Characterisation of Coincidence Data of the Gerda Experiment to Search for Double Beta Decays to Excited States

Dissertation

zur Erlangung des akademischen Grades
Doctor rerum naturalium
(Dr.rer.nat.)

vorgelegt der
Fakultät Mathematik und Naturwissenschaften
der Technischen Universität Dresden

von
Thomas Wester
geboren am 12.12.1986 in Meißen

Gutachter: Prof. Dr. Kai Zuber
Prof. Dr. Allen Caldwell

Datum der Einreichung: September 2018

Autorenreferat

Das Gerda Experiment sucht nach dem neutrinolosen doppelten Beta-Zerfall ($0\nu\beta\beta$-Zerfall) von ^{76}Ge. Damit versucht es zwei noch unbeantwortete Fragen zu klären: „Wie groß ist die Masse der Neutrinos?“ und „Ist das Neutrino ein Dirac oder Majorana Teilchen?“. Außerdem würde eine Beobachtung bedeuten, dass die Leptonenzahl keine Erhaltungsgröße ist. Dies würde helfen, die Asymmetrie zwischen Materie und Antimaterie im Universum zu erklären.

Die effektive Majorana-Neutrino Masse kann aus der Halbwertszeit des $0\nu\beta\beta$-Zerfalls abgeleitet werden. Allerdings entstehen dabei große Unsicherheiten durch Kernmatrixelemente, welche mit Hilfe einer Vielzahl verschiedener Kernmodelle berechnet werden. Zusätzliche Beiträge durch Experimente können helfen diese Modelle anzupassen und dadurch die Genauigkeit der Berechnungen zu verbessern. Diese Beiträge kann man unter anderen dadurch erhalten, indem man theoretische Vorhersagen der Modelle für den neutrinobegleiteten doppelten Beta-Zerfall ($2\nu\beta\beta$-Zerfall) in den Grundzustand, aber auch für Zerfallsmodi in angeregte Zustände des Tocherkerns mit Messungen vergleicht. Die letztgenannten Zerfallsmodi wurden dazu noch nie für ^{76}Ge beobachtet.

Ereignisse durch Übergänge zu angeregten Zuständen sind begleitet durch Gammastrahlung, welche bei der Abregung des Tocherkerns entsteht. Das Gerda Experiment betreibt eine Anordnung von Germanium Halbleiterdetektoren in einem Flüssigargonkryostat. Diese Anordnung ist geeignet, um mit Daten mit koinzidenten Energieeinträgen in mehreren Detektoren nach solchen Übergängen in $2\nu\beta\beta$- und $0\nu\beta\beta$-Zerfällen zu suchen.

Diese Arbeit stellt die Aufbereitung und Charakterisierung dieses Datensatzes vor. Dazu gehört die Auswertung und Korrektur des elektromagnetischen Übersprechens zwischen den Detektorkanälen, die Bestimmung der Energieauflößung der Detektoren und die Beschreibung des Untergrunds.

In einer Auswertung von 22 kg·yr Phase I Daten kombiniert mit den ersten 35 kg·yr Phase II Daten von Gerda wurde kein Signal für $2/0\nu\beta\beta$-Zerfälle von ^{76}Ge in die energetisch niedrigsten drei angeregten Zustände von ^{76}Se gefunden. Neue verbesserte Halbwertszeitgrenzen für die $2\nu\beta\beta$-Zerfallsmodi wurden mit einem Bayesschen Ansatz zu 90% Kredibilität aufgestellt: $T^{2\nu}_{1/2}(0^+_{g.s.} \rightarrow 0^+_1) > 3.1 \cdot 10^{23}\,\mathrm{yr}$, $T^{2\nu}_{1/2}(0^+_{g.s.} \rightarrow 2^+_1) > 3.4 \cdot 10^{23}\,\mathrm{yr}$ und $T^{2\nu}_{1/2}(0^+_{g.s.} \rightarrow 2^+_2) > 2.5 \cdot 10^{23}\,\mathrm{yr}$. Die entsprechenden Sensitivitäten sind $3.6 \cdot 10^{23}\,\mathrm{yr}$, $6.7 \cdot 10^{23}\,\mathrm{yr}$ bzw. $3.7 \cdot 10^{23}\,\mathrm{yr}$. Erste Grenzen für die $0\nu\beta\beta$-Zerfallsmodi in der Größenordnung von $(10^{24} - 10^{25})\,\mathrm{yr}$ wurden außerdem gesetzt. Mit dem Erreichen der angestrebten Datenmenge von 100 kg·yr in Phase II, wird eine Sensitivitätssteigerung von bis zu 50% erwartet.

Abstract

The GERDA experiment is searching for the neutrinoless double beta ($0\nu\beta\beta$) decay of ^{76}Ge. By that, it tries to answer two long standing questions about the neutrino: "How large is the neutrino mass?" and "Is the neutrino either Dirac or Majorana particle?". Additionally, an observation would imply that lepton number is not conserved, which is an important puzzle piece for theories explaining the asymmetry between matter and anti-matter in the universe.

The effective Majorana electron neutrino mass can be extracted from the half-life of the $0\nu\beta\beta$-decay. However, during that conversion large uncertainties are added through nuclear matrix elements, that are calculated by a variety of theoretical models. Experimental input is required to constrain such models and their parameters to improve the reliability of the calculations. Additional input can be obtained by comparing the model predictions for the two neutrino double beta ($2\nu\beta\beta$) decay to the ground state, but also for decay modes to excited states of the daughter nuclid with measurements. The latter decay modes have not yet been observed in the case of ^{76}Ge.

The event signature of transitions to excited states is enhanced by de-excitation γ-rays. The GERDA experiment employs an array of bare germanium semi-conductor detectors in a liquid argon cryostat. This array is suited to search for excited state transition in the $2\nu\beta\beta$ and $0\nu\beta\beta$-decay modes using data with coincident energy depositions in multiple detectors.

This work presents the preparation and characterisation of this data set, which includes the evaluation and correction of crosstalk between detector channels, the determination of the energy resolution of the detectors and the modelling of background.

In an analysis combining 22 kg·yr of Phase I data with the first 35 kg·yr of Phase II data of GERDA, no signal has been observed for $2/0\nu\beta\beta$-decays of ^{76}Ge to the energetically lowest three excited states in ^{76}Se. New limits have been set for the two neutrino decay modes at $T^{2\nu}_{1/2}(0^+_{g.s.} \rightarrow 0^+_1) > 3.1 \cdot 10^{23}$ yr, $T^{2\nu}_{1/2}(0^+_{g.s.} \rightarrow 2^+_1) > 3.4 \cdot 10^{23}$ yr and $T^{2\nu}_{1/2}(0^+_{g.s.} \rightarrow 2^+_2) > 2.5 \cdot 10^{23}$ yr with 90% credibility using a Bayesian approach, improving upon the limits obtained in Phase I. The corresponding sensitivities are $3.6 \cdot 10^{23}$ yr, $6.7 \cdot 10^{23}$ yr and $3.7 \cdot 10^{23}$ yr, respectively. First limits are set for the neutrinoless decay modes in the order of $(10^{24} - 10^{25})$ yr. Reaching the desired Phase II exposure of 100 kg·yr, the sensitivities will increase by up to 50%.

Contents

Appendices

Chapter 1

Introduction

Even 60 years after its discovery, many questions about the neutrino have not yet been answered. Obvious is the question about its mass. So far neutrinos were treated as mass-less in the Standard Model of particle physics, but observations of neutrino flavor oscillations have proven this to be false. However, the absolute mass scale is currently still unknown. Another question addresses the nature of the neutrinos: Are neutrinos Dirac particles with distinct neutrinos and anti-neutrinos or are they of Majorana nature so that neutrinos are identical to their respective partner under charge conjugation?

The neutrinoless double beta ($0\nu\beta\beta$) decay is a major topic in modern neutrino physics. This second order weak decay proposed in the 1930s is only possible, if neutrinos are at least partially Majorana particles. Hence, an observation of $0\nu\beta\beta$-decay answers the question about the neutrino nature and in case the Majorana nature is dominant, information about the absolute neutrino mass scale can be derived from the decay rate. Apart from that, $0\nu\beta\beta$-decay violates lepton number conservation, an important ingredient for the theories of lepto- and baryogenesis which try to explain the asymmetry of matter and anti-matter in the universe.

The GERDA experiment is one of many modern experiments searching for the $0\nu\beta\beta$-decay. It employs an array of bare germanium detectors in a liquid argon cryostat. The detectors are enriched in ^{76}Ge, which is one isotope potentially undergoing $0\nu\beta\beta$-decay. ^{76}Ge is of special interest, since a subgroup of the HDM experiment published a controversial claim of discovery over 10 years ago. GERDA was able to reject this claim with high probability after the first phase of the experiment concluded and set a new lower half-life limit of $T_{1/2} > 2.1 \cdot 10^{25}$ yr (90% C.L.) with a sensitivity of $2.4 \cdot 10^{25}$ yr [1]. In a second phase, after performing several upgrades to the detector setup, the experiment now aims for a background index of 10^{-3} counts/(keV·kg·yr) and a sensitivity beyond 10^{26} yr [2], which translates to an effective Majorana neutrino mass of (0.11-0.23) keV.

The range of masses is due to calculations of nuclear matrix elements. Those calculations, which are based on different nuclear models with different assumptions, add large uncertainties during the conversion from the decay half-life to the neutrino mass. To help to refine those models, additional experimental input is very valuable. This additional input can come on the one hand from the neutrino accompanied double beta ($2\nu\beta\beta$) decay, whose half-life in the case of ^{76}Ge has been measured by GERDA with unprecedent precision [3]. On the other hand, additional input can also come from decay modes to excited states of the daughter nuclide, which is a major subject of this work.

New world best lower half-life limits for three $2\nu\beta\beta$-decay modes to excited states from the first phase of GERDA have already been published in 2015 [4]. This work improves upon these limits by adding the first one and a half years of data from the second phase of GERDA. Additionally, a corresponding search for $0\nu\beta\beta$-decays modes to excited states is presented for the first time in the case of ^{76}Ge. Both analyses are heavily making use of data with coincident particle interaction in two germanium detectors. This data set is free of events from the $0^+_{\text{g.s.}} \rightarrow 0^+_{\text{g.s.}}$ $2\nu\beta\beta$-decay mode, which otherwise poses an irreducable background. Though, before this data set can be utilized for physics analyses, it needs to be prepared and characterised. This includes the correction of distortions of the reconstructed energy values introduced by electromagnetic coupling between the detector channels, referred to as crosstalk. Without correction, this distortion results in a worsening of the energy resolution by up to about 25% and in a shift of peaks by up to 1 keV with respect to their expected position. Furthermore, the characterisation of the data set includes the determination of the energy resolution in dependence of the energy, which is a necessary parameter for most physics analyses.

Another important characteristic is the background of the data set. Because events from $2\nu\beta\beta$-decays to ground state and α contaminations do not cause coincident hits in more than one detector, the background is dominated by γ induced events. The different composition of background can provide supplementary information on background sources and their location to that obtained from anti-coincidence data. γ-lines in the spectrum are identified and a background model is constructed, which can be compared to the anti-coincidence model and which also serves as one of the guidelines to optimize the searches for excited states decay modes.

Hence, this thesis is structured as follows: In Chapter 2 the theory of neutrino physics and double beta decay is presented. Chapter 3 is dedicated to basic knowledge related to low background experiments, including typical background sources, detector technology and methods of statistical data analysis. Selected modern double beta decay experiments are presented at the end of the chapter. The GERDA experiment is introduced in Chapter 4, going through details of the setup, analysis strategies and results of the first and second phase. The subject of Chapter 5 is the coincident data set with a multiplicity of two. In that respect, the evaluation and correction of crosstalk distortions of the reconstructed energy values and the determination of energy resolution curves are presented. The background in the coincident data set is evaluated and modelled in Chapter 6. The two previous chapters are important pre-requisites for the searches for $2\nu\beta\beta$ and $0\nu\beta\beta$-decay modes of ^{76}Ge to excited states, which are described in Chapters 7 and 8, respectively. A summary of this work is given in Chapter 9.

Chapter 2

Neutrino physics

2.1 Introduction

The neutrino is one of the few particles that was first postulated before its discovery. This postulation was based on observations of the electron energy spectrum in β-decays, which is continuous, in contrast to what was expected from a two-body decay. To solve this problem without having to abandon energy conservation, Wolfgang Pauli came up with a new particle in 1930 [5], which is also emitted in β-decays and escapes the detector. Pauli called this particle the neutron, later renamed to neutrino after the discovery of the nucleon today known as the neutron.

A direct detection of the neutrino (ν), or more precisely the electron anti-neutrino (ν_e^c), was only achieved in 1956 by Cowan and Reines [6], using the reaction $\nu_e^c + p \rightarrow e^+ + n$ (inverse β-decay) on protons in water. They built a water tank loaded with $CdCl_2$, which was positioned close to nuclear power reactors in the U.S.A., a strong source for electron anti-neutrinos. Surrounding the tank were liquid scintillators, used to detect the γ-rays from the positron annihilation γ-ray. Additionally, the neutron was captured by ^{113}Cd(n,γ)^{114}Cd, which results in high energetic γ-rays in coincidence to the annihilation.

Despite more than 60 years have passed since its discovery, the neutrino is still posing a lot of questions about its nature, its mass, the number of neutrino families or its role as a dark matter candidate. The reason for this are its extremely low cross-sections when interacting with other particles, which makes it very difficult to observe it with high statistics and low background. Furthermore, its mass is much lower in comparison to all other particles in the Standard Model of particle physics and was long believed to be zero.

Modern experiments in particle and nuclear physics as well as in cosmology are addressing these questions by investigating neutrinos from various sources like the sun, the atmosphere or nuclear power reactors. Different experiments are searching for the so-called neutrinoless double β-decay, which is the gold-plated process to answer the question about the nature of the neutrino and would furthermore give information about the absolute neutrino mass scale. The challenge is often to build very large detectors in an ultra radio-pure environment in order to compensate for the low cross-sections.

This chapter first introduces the integration of the neutrinos in the Standard Model of particle physics in Sec. 2.2. It then presents the phenomenon of neutrino oscillations in Sec. 2.4 and ways to create neutrino masses in theory in Sec. 2.5, which goes beyond the Standard Model. Sec. 2.6 discusses the phenomena of double β-decays.

2.2 Neutrinos in the Standard Model

The **Standard Model (SM)** of particle physics is a quantum field theory based on gauge symmetries, which describes the currently known fundamental particles and their interactions via electromagnetic, weak and strong force. For this chapter it is sufficient to concentrate on the electroweak sector of the SM, that is based on the symmetry group $\mathrm{SU(2)_L \times U(1)_Y}$.

This symmetry group results in four gauge bosons, B and $W_{1,2,3}$, which mix to γ, $W^{\pm}$ and Z^0 and two charges, the electromagnetic charge and the weak isospin.

Following an experiment by Wu et al [7] investigating the angular distribution of electrons from the decay of polarized ^{60}Co atoms, parity is maximally violated in weak interactions. As a result, $W^{\pm}$ only couple to left-handed fermions and right-handed anti-fermions, which have a weak isospin charge of $\pm\frac{1}{2}$. Right-handed fermions and left-handed anti-fermions have a weak isospin charge of zero.

Therefore, together with the left-handed leptons e_L, μ_L and τ_L, the left-handed neutrinos $\nu_{e\mathrm{L}}$, $\nu_{\mu\mathrm{L}}$ and $\nu_{\tau\mathrm{L}}$ form weak isospin doublets:

$$\begin{pmatrix} \nu_e \\ e \end{pmatrix}_\mathrm{L} \qquad \begin{pmatrix} \nu_\mu \\ \mu \end{pmatrix}_\mathrm{L} \qquad \begin{pmatrix} \nu_\tau \\ \tau \end{pmatrix}_\mathrm{L} \tag{2.1}$$

The right-handed counterparts on the other hand only transform as singlets. Because the right-handed neutrinos do not interact via electromagnetic or strong force either, they would be sterile in the SM and have thus been left out.

This has the consequence, that Yukawa mass terms do not exist for neutrinos, coinciding with the fact that neutrinos were thought to be mass-less for a long time, until the observation of neutrino flavor oscillations.

2.3 Dirac or Majorana particles

For most fermions in the SM, a clear distinction between fermion and anti-fermion is made because of their electric charge. They are so-called Dirac particles. From this point of view, neutrinos could potentially be identical to their anti-neutrino, because they are electric neutral, which would make them Majorana particles.

In two experiments by Ray Davis Jr. in the 1950s, he showed that ν_e^c from nuclear power reactors do not trigger the reaction $\nu_e^c + {}^{37}\mathrm{Cl} \to e^- + {}^{37}\mathrm{Ar}$ [8]. Later he furthermore showed, that ν_e from the sun do indeed cause this reaction [9]. Thus, ν_e and ν_e^c can not be identical.

However, as seen from neutrino oscillations (see Sec. 2.4), ν_e are flavor eigenstates of neutrinos, which are a mixture of the mass eigenstates $\nu_{1,2,3}$. Today, the question still stands if $\nu_{1,2,3}$ are invariant under charge conjugation. This question can be addressed by a search for neutrinoless double β-decay (see Sec. 2.6).

In the Lagrangian, Majorana neutrinos are characterised by the presence of lepton number violating Majorana mass terms (compare Sec. 2.5). Violation of lepton number conservation is an important ingredient for leptogenesis and consequently baryogenesis, which give an explanation for the asymmetry between matter and anti-matter in the universe [10].

2.4 Neutrino oscillations

Starting in the late 1960s, the HOMESTAKE experiment by Ray Davis and John N. Bahcall [9] measured the flux of the solar neutrinos using a chlorine based detector. Like in Ray Davis' previous experiments in the 1950s, the reaction $\nu_e^c + {}^{37}\mathrm{Cl} \to e^- + {}^{37}\mathrm{Ar}$ was used to detect and count neutrinos by extracting the Ar atoms. Subsequently, the Cherenkov detector experiments SUPER-KAMIOKANDE [11] and SNO [12] followed years later and came to the same conclusions: the measured solar flux of ν_e is only 1/3 of the flux expected from solar models. This deficit became known as the "solar neutrino problem".

In 1962, Maki, Nakagawa and Sakata proposed the idea of neutrino flavor mixing [13], analogous to the flavor mixing in the quark sector. Pontecorvo and Gribov further discussed in 1968 [14], that through this mixing the neutrino flavor oscillates in vacuum. This oscillation offered an explanation of the disappearance of ν_e from the sun, because many of the ν_e had already changed to other flavors while traveling towards the earth.

The outstanding feature of the SNO experiment, was the ability to not only observe the deficit of ν_e from the sun, but also to detect the ν_μ, which the ν_e have oscillated to. They

could show, that in sum both neutrino flavors were in agreement with the production of ν_e in the sun [12].
With the observation of neutrino flavor oscillations, it was also established that at least two neutrinos have a non-vanishing rest mass.
A review of neutrino oscillations can be found in [15].

2.4.1 Formalism

For massive neutrinos, the mass eigenstates can mix analogous to the quarks as follows:

$$|\nu_\alpha\rangle = \sum_i U_{\alpha i}|\nu_i\rangle \qquad \text{and} \qquad |\nu_i\rangle = \sum_\alpha U^*_{\alpha i}|\nu_\alpha\rangle \tag{2.2}$$

with α the index of the flavor, e, μ or τ and U^* the complex conjugated matrix. For anti-neutrinos, U has to be replaced with U^* and vice versa.
The unitary mixing matrix for the neutrinos is called the PMNS-matrix, named after Pontecorvo, Maki, Nakagawa and Sakata, and can be displayed like this:

$$\begin{aligned} U_{\mathrm{PMNS}} &= \begin{pmatrix} 1 & 0 & 0 \\ 0 & c_{23} & s_{23} \\ 0 & -s_{23} & c_{23} \end{pmatrix} \begin{pmatrix} c_{13} & 0 & s_{13}e^{-i\delta_{\mathrm{CP}}} \\ 0 & 1 & 0 \\ -s_{13}e^{i\delta_{\mathrm{CP}}} & 0 & c_{13} \end{pmatrix} \begin{pmatrix} c_{12} & s_{12} & 0 \\ -s_{12} & c_{12} & 0 \\ 0 & 0 & 1 \end{pmatrix} \\ &= \begin{pmatrix} c_{12}c_{13} & s_{12}c_{13} & s_{13}e^{-i\delta_{\mathrm{CP}}} \\ -s_{12}c_{23} - c_{12}s_{23}s_{13}e^{i\delta_{\mathrm{CP}}} & c_{12}c_{23} - s_{12}s_{23}s_{13}e^{i\delta_{\mathrm{CP}}} & s_{23}c_{13} \\ s_{12}s_{23} - c_{12}c_{23}s_{13}e^{i\delta_{\mathrm{CP}}} & -c_{12}s_{23} - s_{12}c_{23}s_{13}e^{i\delta_{\mathrm{CP}}} & c_{23}c_{13} \end{pmatrix} \end{aligned} \tag{2.3}$$

where $c_{ij} = \cos\theta_{ij}$ and $s_{ij} = \sin\theta_{ij}$ with θ_{ij} the mixing angle between the i-th and j-th mass eigenstate, δ_{CP} the CP-violating phase. In case of Majorana neutrinos, the phases can not be simply redefined. Therefore, to handle the remaining degrees two additional Majorana phases need to be added.
With the mixing matrix, the transition probability for $\nu_\alpha \to \nu_\beta$ after propagation of the distance L in vacuum with an energy E can be obtained with:

$$P_{\nu_\alpha \to \nu_\beta}(t) = \sum_i \left|U_{\alpha i}U^*_{\beta i}\right|^2 + 2\mathrm{Re}\sum_{j>i} U_{\alpha i}U^*_{\alpha j}U^*_{\beta i}U_{\beta j}\exp\left(-i\frac{\Delta m^2_{ij}}{2}\frac{L}{E}\right) \tag{2.4}$$

$$= \delta_{\alpha\beta} - 4\sum_{j>i} U_{\alpha i}U_{\alpha j}U_{\beta i}U_{\beta j}\sin^2\left(\frac{\Delta m^2_{ij}}{4}\frac{L}{E}\right) \tag{2.5}$$

with $\Delta m^2_{i,j} = m^2_i - m^2_j$ the quadratic difference of the neutrino masses, assuming CP invariance in the second line.
This oscillation probability is the basis for every experiment investigating the oscillation parameters. Experiments can be divided into two classes: disappearance and appearance experiments. While in the former class, the experiments measures a deficit of a certain neutrino flavor that is expected from the neutrino source, the latter class of experiments is searching for an increase of a certain flavor or the addition of a new flavor not present in the original neutrino source. Neutrinos of the various flavors are usually detected by observing the corresponding leptons that are created by the charged current interactions $\nu_\alpha/\nu^c_\alpha + \mathrm{N}_1 \to l^-/l^+ + \mathrm{N}_2$.
Different sources of neutrinos offer the possibility to research a different set of the oscillation parameters, depending on their distance to the detector and the flavor and energy of the neutrinos. Neutrinos from nuclear power plants (ν^c_e), the sun (ν_e) and the atmosphere (ν_μ) and the information obtain from these are discussed in the following sections.

2.4.2 Solar neutrinos (θ_{12})

Solar neutrinos are created by the various fusion processes in the sun. The neutrinos are classified according to the process that generated them, which also defines their energy range. The highest flux of solar neutrinos of $5.98 \cdot 10^{10}\,\mathrm{cm}^{-2}\mathrm{s}^{-1}$ [16] are generated by the fusion of two hydrogen nuclei:

$$\mathrm{p} + \mathrm{p} \rightarrow {}^{2}\mathrm{D} + e^{+} + \nu_e. \tag{2.6}$$

Thus, they are called pp-neutrinos. However, with a very low energy of $E_\nu < 0.42\,\mathrm{MeV}$, experiments based on Cherenkov light detection like SNO and SUPER-KAMIOKANDE were not able to measure pp-neutrinos. They had a threshold energy of around 5 MeV due to the relative high natural background, although SNO tried to lower the threshold reaching 3.5 MeV in the attempt [17]. BOREXINO is the first experiment managing a direct measurement pp-neutrinos in its second phase after further reducing the background, allowing a energy threshold of only about 50 keV [18]. Additionally, plans are to attempt to directly measure CNO neutrinos for the first time, which originate from the sun's CNO cycle.

Among the solar neutrinos with the highest average energy are neutrinos generated by the decay of ${}^{8}\mathrm{B}$:

$$\begin{aligned} {}^{7}\mathrm{Be} + \mathrm{p} &\rightarrow {}^{8}\mathrm{B} + \gamma + 0.14\,\mathrm{MeV} \\ {}^{8}\mathrm{B} &\rightarrow {}^{8}\mathrm{Be}^{*} + e^{+} + \nu_e + \approx 15\,\mathrm{MeV} \end{aligned} \tag{2.7}$$

with up to $E_\nu \approx 15\,\mathrm{MeV}$ and a flux of $5.58 \cdot 10^{6}\,\mathrm{cm}^{-2}\mathrm{s}^{-1}$. ${}^{8}\mathrm{B}$ neutrinos played the dominant role for SNO and SUPER-KAMIOKANDE.

Oscillation effects are enhanced in the sun for higher energetic neutrinos due to the high electron density, which increases the effective mass of ν_e through charged current elastic scatter processes (so-called MSW effect [19, 20]). Results of HOMESTAKE [9], GALLEX [21], SNO [12] and SUPER-KAMIOKANDE [11] give two allowed regions in the Δm^2_{21} versus $\tan^2\theta_{12}$ plane [15]. One of the regions was ruled out later by the KAMLAND experiment based on reactor ν_e^c survival data, leaving only the so-called "large mixing angle" (LMA) solution [22].

Combining all results, yields $\Delta m^2_{21} = 7.59^{+0.21}_{-0.21} \cdot 10^{-5}\,\mathrm{eV}^2$ and $\tan^2\theta_{12} = 0.47^{+0.06}_{-0.05}$ [15].

2.4.3 Reactor neutrinos (θ_{13})

Nuclear power reactors are sources for ν_e^c, which are emitted in the various β-decays of neutron rich fission products. Just like in solar neutrino experiments, only disappearance measurements are possible due to the relatively low neutrino energy of a few MeV. This is too low to generate muons or taus.

The first reactor neutrino experiments were conducted in a distance (baseline) of about 1 km and less from the power plants. Results from solar neutrino experiments suggested to go to larger baselines in the order of 100 km. The KAMLAND detector was constructed in the Kamioka mine, surrounded by over 50 power plants in Japan and South Korea, delivering a total flux of $4 \cdot 10^{6}\,\mathrm{cm}^{-2}\mathrm{s}^{-1}$. Evidence for neutrino oscillations was found and best fit values of $\Delta m^2_{21} = 7.58^{+0.21}_{-0.2} \cdot 10^{-5}\,\mathrm{eV}^2$ and $\tan^2\theta_{12} = 0.56^{+0.14}_{-0.09}$ were obtained [22].

Reactor experiments have also access to θ_{13}, important for the search of CP violation. However, as θ_{13} is very small, it requires a good understanding of the systematic uncertainties of the experiment. A popular choice among modern reactor neutrino experiments is to employ two detectors in different distances of the neutrino source. By this approach, many systematic uncertainties cancel out. DAYA BAY [23], RENO [24], DOUBLE CHOOZ [25] (disappearance experiments) and the accelerator experiment T2K [26] (appearance of ν_e in ν_μ beam) are representatives for such experiments. The combined results yield $\sin^2\theta_{13} = 0.10 \pm 0.01$ [15].

Accelerator experiments:

Particle accelerators can provide an intense neutrino beam. The LSND experiment [27] is a short baseline experiment (30 m), where a ν_μ, ν_μ^c and ν_e neutrino beam is generated by a proton beam with an energy of 800 MeV hitting a water target. This first creates positively charged pions, which then decay to ν_μ and μ^+ which produce ν_μ^c and ν_e in their decay. In the $\nu_\mu^c \rightarrow \nu_e^c$ oscillations the experiment measured a Δm^2 in the order of 1 eV. Furthermore, they found evidence for $\theta_{13} > 0$.

MINIBOONE [28] is a new generation experiment at Fermilab Booster, where a 8 GeV proton beam is directed at a Be target. The detector is positioned 500 m away. The experiment found a combined excess of ν_e (in a ν_μ beam) and ν_e^c (in a ν_μ^c beam) of $4.8\,\sigma$, which increases to $6.1\,\sigma$ when also considering the LNSD results. The best fit yields $(\Delta m^2, sin^2 2\theta) = (0.037\,\mathrm{eV}^2, 0.958)$ in a two-neutrino oscillation model [15].

2.4.4 Atmospheric neutrinos (θ_{23})

Neutrinos in the energy range of GeV are generated in the atmosphere by the decay of muons and mesons. Thus ν_e, ν_μ and ν_e^c, ν_μ^c are created. Cherenkov detectors have measured the ratio between "downgoing" and "upgoing" ν_μ and ν_e in order to cancel out systematic uncertainties, by detecting the muons and electrons created by the neutrinos. Downgoing ν_μ approximately travel 10 km before reaching the detector, too short of a distance for oscillations to take effect. Upgoing ν_μ on the other hand travel through the earth a distance of about 6000 km. On this distance, a significant part of the ν_μ changed to ν_τ.

The Super-Kamiokande experiment, measured a ratio of $0.65 \pm 0.05 \pm 0.001$ for sub-GeV μ-like events and $0.52 \pm 0.05 \pm 0.006$ for multi-GeV μ-like events [29]. These results translate to values for the oscillation parameters of $1.9 \cdot 10^{-3}\,\mathrm{eV}^2 < m_{23}^2 < 3.0 \cdot 10^{-3}\,\mathrm{eV}^2$ and $\sin 2\theta_{23} > 0.90$.

2.4.5 Oscillation parameters: A global fit

A global fit of all neutrino oscillation experiments in a three flavor model has been done by NuFIT.

The resulting values obtained from the information available in January 2018 are listed in Tab. 2.1.

2.5 Neutrino mass mechanism

Masses of neutrinos can be generated in the SM by extending its particle content. The simplest way is to add right handed neutrinos, which open the possibility for three new

parameter	normal ordering	inverted ordering
$\sin^2\theta_{12}$	$0.307^{+0.013}_{-0.012}$	$0.307^{+0.013}_{-0.012}$
$\sin^2\theta_{23}$	$0.538^{+0.033}_{-0.069}$	$0.554^{+0.023}_{-0.033}$
$\sin^2\theta_{13}$	$0.02206^{+0.00075}_{-0.00075}$	$0.02227^{+0.00074}_{-0.00074}$
δ_{CP}	234^{+43}_{-31}	278^{+26}_{-29}
$\frac{\Delta m^2_{21}}{10^{-5}\mathrm{eV}^2}$	$7.40^{+0.21}_{-0.20}$	$7.40^{+0.21}_{-0.20}$
$\frac{\Delta m^2_{3\ell}}{10^{-3}\mathrm{eV}^2}$	$+2.494^{+0.033}_{-0.031}$	$-2.465^{+0.032}_{-0.031}$

Table 2.1.: Experimental oscillation parameters obtained from a global fit of all experimental data for normal and inverted neutrino mass hierarchy (see Sec. 2.5.2), done by NuFIT v3.2 [30] (date: January 2018).

Yukawa couplings for the neutrinos, analogous to the other fermions.

$$\mathcal{L}_{\mathrm{Yuk}} = -c_\nu \bar{\nu}_{\mathrm{R}} \begin{pmatrix} \nu_{e\mathrm{L}} \\ e_{\mathrm{L}} \end{pmatrix} + h.c. \tag{2.8}$$

Alternatively, if no more fermions are added to the SM, Yukawa couplings can be introduced for Majorana neutrinos by enlarging the Higgs sector.

To generate neutrino masses that are much smaller than the mass of the other fermions, the Yukawa couplings have to be chosen accordingly. However, as this does not give a natural explanation of the smallness of the neutrino masses, different models that go beyond the SM are preferred.

In the most general way, mass terms for the neutrinos are introduced to the SM by adding all possible terms that are gauge invariant. This leads to a Lagrangian as follows:

$$\mathcal{L} = m_{\mathrm{D}} \left(\bar{\nu}_{\mathrm{L}} N_{\mathrm{R}} + (\bar{N^c})_{\mathrm{L}} (\nu^c)_{\mathrm{R}} \right) + m_{\mathrm{L}} \bar{\nu}_{\mathrm{L}} (\nu^c)_{\mathrm{R}} + m_{\mathrm{R}} (\bar{N^c})_{\mathrm{L}} N_{\mathrm{R}} + h.c. \tag{2.9}$$

or in matrix writing:

$$\mathcal{L} = \begin{pmatrix} \bar{\nu}_{\mathrm{L}} \\ (\bar{N^c})_{\mathrm{L}} \end{pmatrix} \begin{pmatrix} m_{\mathrm{L}} & m_{\mathrm{D}} \\ m_{\mathrm{D}} & m_{\mathrm{R}} \end{pmatrix} \begin{pmatrix} (\nu^c)_{\mathrm{R}} \\ N_{\mathrm{R}} \end{pmatrix} + h.c., \tag{2.10}$$

where the m_{D} denote Dirac mass terms that connect left and right handed neutrino fields, while m_{L} and m_{R} denote left- and right-handed Majorana mass terms, that violate lepton number by two units.

2.5.1 See-saw mechanism

By diagonalizing the mass matrix the mass eigenvalues are obtained as the diagonal elements $m_{1,2}$, which are the masses of two independent Majorana fields. In case of $m_{\mathrm{R}} >> m_{\mathrm{D}}$ and $m_{\mathrm{L}} = 0$, one obtains the popular **see-saw** model, with:

$$m_1 = \frac{m_{\mathrm{D}}^2}{m_{\mathrm{R}}} \qquad m_2 = m_{\mathrm{R}} \left(1 + \frac{m_{\mathrm{D}}^2}{m_{\mathrm{R}}^2} \right). \tag{2.11}$$

From this it is visible, that with a very heavy m_{R}, one heavy Majorana neutrino with $m_2 \approx m_{\mathrm{R}}$ and one light Majorana neutrino with $m_1 \approx 0$ are obtained.

2.5.2 Mass hierarchy

Neutrino oscillation experiments only allow to measure the difference of the squared neutrino masses Δm^2_{ij}. Additionally, the sign of Δm^2_{21} is known from matter effects in solar neutrino oscillations. The sign of Δm^2_{23} however has still not been determined. Consequently, there is currently still freedom in the ordering of neutrino mass values. One distinguishes between the normal mass hierarchy $m_1 < m_2 < m_3$ and the inverted hierarchy $m_3 < m_1 < m_2$.

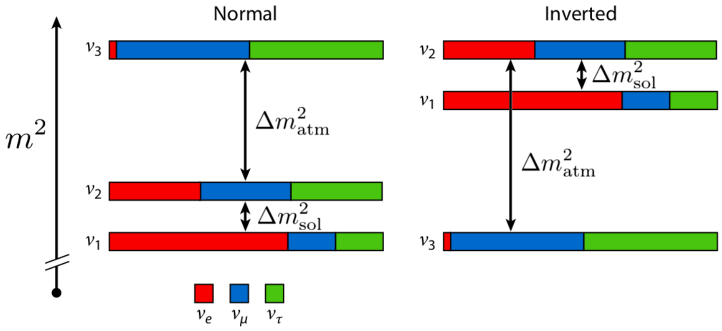

Figure 2.1.: Scheme of the neutrino mass hierarchies: normal (*left*) and inverted (*right*). Adapted from [31]. $\Delta m^2_{\mathrm{sol}}$ refers to Δm^2_{21}, while $\Delta m^2_{\mathrm{atm}}$ refers to Δm^2_{23}.

Limits obtained from double beta decay experiments and cosmological observations are not strong enough to rule out one of the hierarchies. Recent cosmological results as well as results by long baseline experiments only slightly prefer normal hierarchy [32, 33, 34].

2.6 Double beta decay

In β-decay, one of the more common types of radioactivity, a nucleus with Z protons and N neutrons transforms spontaneously into a nucleus with $Z \pm 1$ protons and $N \mp 1$ neutrons, while emitting an electron and a ν_e^c (β^--decay), or a positron and a ν_e (β^+-decay), respectively. While β^+-decay is only possible in case the Q-value[1] of the decay is larger than two electron masses, $2m_e$, alternatively the nucleus can also perform an electron capture (EC) without this energetic penalty. In this case one electron of the atomic shell is absorbed by a proton in the nucleus and only a mono-energetic ν_e is released. The three decay modes can be written on a nucleon level like this:

$$\begin{aligned} \beta^- :&\quad n &&\rightarrow p + e^- + \nu_e^c && (2.12)\\ \beta^+ :&\quad p &&\rightarrow n + e^+ + \nu_e \quad (\text{if } Q > 2m_e) && (2.13)\\ \mathrm{EC} :&\quad p + e^- &&\rightarrow n + \nu_e && (2.14) \end{aligned}$$

2.6.1 $2\nu\beta\beta$-decay

In 1935, Goeppert-Mayer proposed a double β-decay ($\beta\beta$-decay)[35], which describes in general two simultaneous β-decays of the same nucleus. As a result of this process the number of protons and number of neutrons of the nucleus changes by two units, while two

---

[1] The Q-value of a decay is defined as the mass difference between initial and final atom.

electrons/positrons and two ν_e^c/ν_e are emitted. Double EC, as well as a combination of EC and β^+-decay modes are also possible:

$$\beta^-\beta^- : \quad 2n \rightarrow 2p + 2e^- + 2\nu_e^c \tag{2.15}$$

$$\beta^+\beta^+ : \quad 2p \rightarrow 2n + 2e^+ + 2\nu_e \quad (\text{if } Q > 4m_e) \tag{2.16}$$

$$\beta^+/\text{EC} : \quad 2p + e^- \rightarrow 2n + e^+ + 2\nu_e \quad (\text{if } Q > 2m_e) \tag{2.17}$$

$$\text{EC}/\text{EC} : \quad 2p + 2e^- \rightarrow 2n + 2\nu_e \tag{2.18}$$

Because $\beta\beta$-decay is a second order process of weak interaction, half-lives are expected to be extremely long. To date, the $\beta^-\beta^-$-decay mode has been observed for 11 isotopes with half-lives in the range of $10^{18} - 10^{24}$ yr (see Tab. A.1), while the first direct observation goes back to 1987 [36]. A table with half-life measurements of $2\nu\beta\beta$-decays can be found in Appendix A.1.

The lepton number[2] is conserved by all four modes of $\beta\beta$-decay.

Decay rate

The decay rate of $\beta\beta$-decay is defined by two components: 1) the nuclear matrix elements $M^{2\nu}_{\mathrm{GT/F}}$ describing the transition strength between the initial state in the (A,Z) nucleus, the virtual intermediate states in the (A,Z±1) nucleus and the final state in the (A,Z±2) nucleus, and 2) the phase space factor $G^{2\nu}$, which scales with Q^{11}:

$$\left[T^{2\nu}_{1/2}(0^+_{\mathrm{g.s.}} \rightarrow 0^+_{\mathrm{g.s.}})\right]^{-1} = |M^{2\nu}_{\mathrm{GT}} + \tfrac{g_{\mathrm{V}}^2}{g_{\mathrm{A}}^2} M^{2\nu}_{\mathrm{F}}|^2 G^{2\nu}(Q, Z) \tag{2.19}$$

$$G^{2\nu} \propto Q^{11} \tag{2.20}$$

Due to selection rules, Fermi transitions are strongly suppressed for the $0^+ \rightarrow 0^+$ transitions of $\beta\beta$-decay [37] and can be neglected.

2.6.2 $0\nu\beta\beta$-decay

Besides the neutrino accompanied $\beta\beta$-decay (from here on referred to as $2\nu\beta\beta$-decay), Furry discussed the possibility of a neutrinoless decay mode ($0\nu\beta\beta$) in 1939 [38]. In this scenario, the neutrino stays virtual, emitted as a right-handed anti-neutrino by one nucleon and absorbed as a left-handed neutrino by the other nucleon, hence no neutrinos in the final state. This process violates lepton number conservation by two units.

The neutrino needs to fulfill two requirements in order to make this kind of $0\nu\beta\beta$-decay possible:

1) Neutrinos must be Majorana particles, meaning that neutrino and anti-neutrino are identical. This requirement obviously refers to the mass eigenstates. As a result, $0\nu\beta\beta$-decay violates lepton number conservation by two units.

2) The mass of the neutrinos must be larger than zero. This is necessary to allow the helicity[3] to flip from right-handed to left-handed. For mass-less particles the helicity is fixed as they travel with the speed of light.

---

[2] The lepton number is defined as the sum of leptons minus the sum of anti-leptons. In the SM the lepton number is conserved.

[3] The helicity of a particle is the projection of its spin onto the direction of its momentum.

The non-zero mass for neutrinos was already established by the observation of neutrino flavor oscillations, as discussed in Sec. 2.4. The observation of the $0\nu\beta\beta$-decay is the only way to decide whether neutrinos are Majorana particles in a model independent way. The mechanism discussed above is the often regarded as the standard theoretical description of $0\nu\beta\beta$-decay, referred to as **light Majorana neutrino exchange** mechanism. The corresponding Feynman graph can be seen in Fig. 2.2.

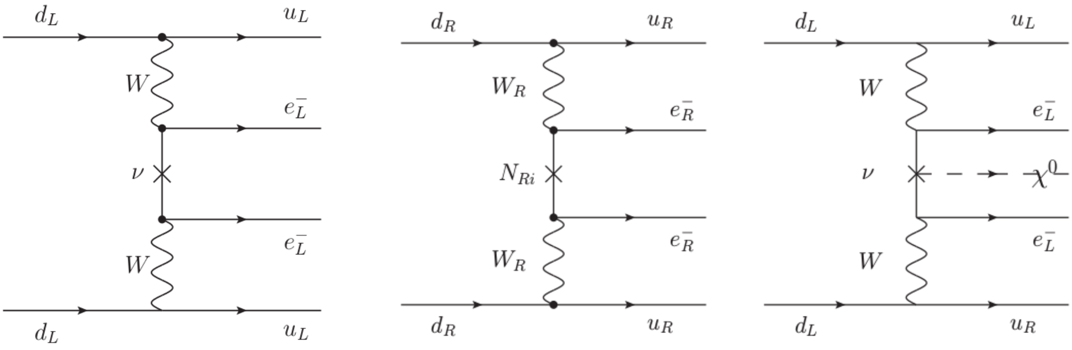

Figure 2.2.: Feynman graphs for various $0\nu\beta\beta$-decay mechanisms: Light Majorana neutrino exchange (*left*), right-handed currents (*middle*) and Majoron emission (*right*).

Decay rate

The propagator of the graph is proportional to the "effective Majorana neutrino mass" of the ν_e^c, which is defined as the coherent sum:

$$\langle m_{\beta\beta}\rangle = |\sum_j U_{ej}^2 m_j|. \tag{2.21}$$

Due to the complex Majorana phase in the mixing matrix, it is possible the contributions by the m_i cancel each other. Thus, even with non-zero m_i, there is no lower limit for $\langle m_{\beta\beta}\rangle$. Unfortunately, without a lower limit, an observation of $0\nu\beta\beta$-decay might be impossible if light Majorana exchange is the dominating mechanism.
Analogous to the $2\nu\beta\beta$-decay, the decay rate is additionally dependent on a nuclear matrix elements and the phase space factor, which is in this case proportional to Q^5:

$$\left[T_{1/2}^{0\nu}(0^+_{\text{g.s.}} \to 0^+_{\text{g.s.}})\right]^{-1} = |M_{\text{GT}}^{0\nu} - \tfrac{g_{\text{V}}^2}{g_{\text{A}}^2} M_{\text{F}}^{0\nu}|^2 G^{0\nu}(Q,Z) \left(\tfrac{\langle m_{\beta\beta}\rangle}{m_e}\right)^2 \tag{2.22}$$

$$G^{0\nu} \propto Q^5. \tag{2.23}$$

From this equation it is visible, that from a measurement of the half-life of $0\nu\beta\beta$-decay, the effective Majorana neutrino mass can be deduced. However, nuclear matrix elements enter in this conversion step, which have to be calculated and add large theoretical uncertainties.

Alternative mechanisms

Eq. 2.22 is only true, if light Majorana neutrino exchange is the only mechanisms contributing to $0\nu\beta\beta$-decay. However, several alternative mechanisms have been proposed [39, 40]:

1) **Right handed currents**: In addition to the V-A structure of the weak interaction, there might be an V+A contribution, which leads to right handed charged currents. This way a helicity match is not necessary, instead the right handed ν_R can interact at the second vertex with W^-_R.

The decay rate in this case is determined by the coupling constants of the right-handed currents, λ (right-handed hadronic and right-handed leptonic currents) and η (right-handed hadronic and left-handed leptonic currents) ($\ll 1$):

$$\left[T_{1/2}\right]^{-1} = C_\lambda \langle\lambda\rangle^2 + C_\eta \langle\eta\rangle^2 + C_{\lambda\eta}\langle\lambda\rangle\langle\eta\rangle, \tag{2.24}$$

with

$$\langle\lambda\rangle = \lambda \sum_j U_{ej} V_{ej} \qquad \langle\eta\rangle = \eta \sum_j U_{ej} V_{ej}. \tag{2.25}$$

Left-handed hadronic with right-handed leptonic currents are neglected. The sums run over the light neutrinos (<10 MeV).

If all m_j are light, then the sums disappear because of orthogonality. Then $\langle\eta\rangle = 0$ and $\langle\lambda\rangle = 0$, which means there is no contribution to $0\nu\beta\beta$-decay from right handed currents. Therefore, there needs to be at least one heavy Majorana neutrino.

For $0^+_\mathrm{g.s.} \to 2^+$ decay modes it was thought, that there is no light Majorana neutrino exchange mechanism, because of angular momentum conservation. But by taking the recoil corrections of the nuclear currents into account, it was found that $0^+_\mathrm{g.s.} \to 2^+$ modes have the same relative senstivity to $\langle\eta\rangle$ and $\langle m_{\beta\beta}\rangle$ like $0^+_\mathrm{g.s.} \to 0^+$ modes, but are relatively more sensitive to $\langle\lambda\rangle$ [41].

2) **Majoron emission**: A violation of lepton number can also be achieved by a spontaneous breaking of the global $(B-L)$ symmetry. A spontaneous symmetry breaking gives birth to a Goldstone boson χ, which in this case is referred to as Majoron. The Majoron can be emitted in $0\nu\beta\beta$-decays, as visible in Fig. 2.2. Within the theory of Majoron emitting decay modes, there are several models with singlet, doublet or triplett Majoron, Majorons with leptonic charge or decays where multiple Majorons are emitted. Each model results in differences in the spectral shape of the electron sum energy E_{ee}. The predicted shape can be given by:

$$\frac{\mathrm{d}N}{\mathrm{d}E_{ee}} \propto \left(Q - E_{ee}\right)^n \cdot f\left(E_{ee}\right), \tag{2.26}$$

where n is the spectral index, which can assume values of 1, 2, 3 and 7 for the different Majoron models and 5 for the $2\nu\beta\beta$-decay.

The half-life of Majoron decay modes is proportional to the coupling strength $\langle g_{\nu\chi}\rangle$ between Majoron and neutrino ($n = 1$). Recent upper limits on the $\langle g_{\nu\chi}\rangle$ have been set by Gerda [3], KamLand-Zen [42] and EXO-200 [43].

3) Multiple decay mechanisms exist, that involve the exchange of supersymmetric particles. For more details, see the references [44, 45] or the reviews in [39, 40].

In principle all mechanisms can be realized simultaneously in nature, but no matter which or how many of the mechanism are realized, observing $0\nu\beta\beta$-decay will imply a Majorana neutrino mass term exists. This is the general statement of the ”black box theorem”, also known as **Schechter-Valle theorem** [46]. However, especially given the normal hierarchy, where neutrino masses can be extremely tiny, the Majorana mass term contribution might be negligible [47].

2.6.3 Phase space factors

The phase space factor (PSF) is a measure for the number of final states in terms of momentum, spins, angular momentum of the final particles. In general for $2/0\nu\beta\beta$-decay, the higher the energy available to the $e^{\hat{a}}$Ąż (and ν_e^c), the higher the PSF. Previously, PSF have been calculated by approximating the electron wave functions. A recent work has improved upon these calculations by using exact numerical calculations of the electron wave functions [48]. The left plot in Fig. 2.3 shows the PSF obtained in this publication for important $0\nu\beta\beta$-decay isotopes isotopes. The PSF of the considered isotopes are spread in a range of two orders of magnitude, where isotopes like ^{150}Nd, ^{96}Zr and ^{116}Cd are favorable due to their high Q-value in $0\nu\beta\beta$-decay.

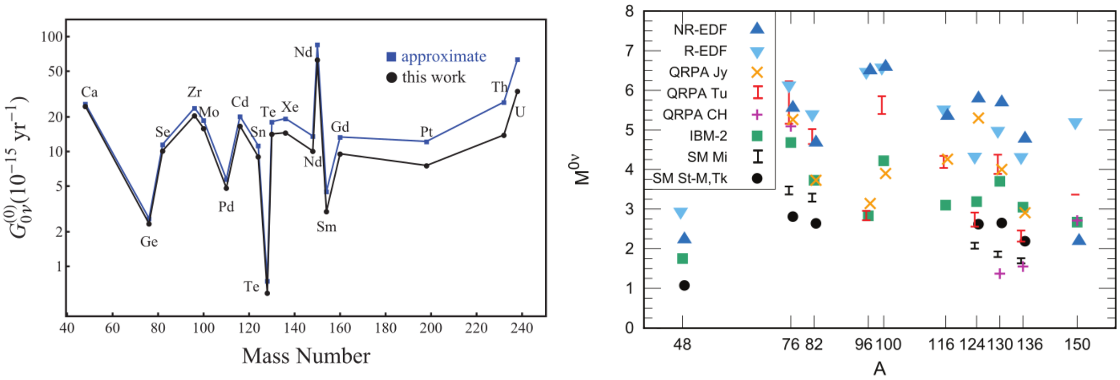

Figure 2.3.: *Left:* Phase space factors calculated for various $0\nu\beta\beta$-decay isotopes [48]. ”approximate” refers to calculations using approximated electron wave functions. ”this work” refers to exact calculations. *Right:* Nuclear matrix elements for several $0\nu\beta\beta$-decay isotopes calculated with various models: the shell model (SM) [49, 50, 51], the interacting boson model (IBM-2) [52], quasiparticle random-phase approximation (QRPA) [53, 54, 55], the relativistic and non-relativistic energy density functional theory (EDF) [56, 57, 58]. $g_A = 1.26$ has been used in all cases. The plot has been taken from [40].

2.6.4 Nuclear matrix elements

The NME describe the strength of transition of a nucleus from an initial state to a final state. In case of $\beta\beta$-decays, the transition can be divided into two steps. First the transition from the initial state i in (A,Z) to an intermediate state m of $(A,Z \pm 1)$ and then the transition from this intermediate state to the final state f in $(A,Z \pm 2)$. All possible states of $(A,Z + 1)$ need to be taken into account, though the higher the energy, the lower the contribution to the total transition rate. For $2\nu\beta\beta$-decay the NME M_{if} can be written as:

$$M_{if} = \sum_m \frac{\langle f|H_{if}|m\rangle\langle m|H_{if}|i\rangle}{E_i - E_m - E_\nu - E_e} \tag{2.27}$$

Selection rules only allow Gamow-Teller transitions to intermediate states with 1^+. Fermi transitions are strongly suppressed. For $0\nu\beta\beta$-decay, there are no selection rules.

NME of $2\nu\beta\beta$-decays and single β-decays can be measured by determining the half-life of the decays. Because the $0\nu\beta\beta$-decay rate also depends on the unknown neutrino mass scale, NME for such processes have to be calculated. The calculations of NME is however not as straightforward like the PSF, because they are extremely sensitive to the description of nuclear deformations. Hence, they adds a huge uncertainty to the prediction of $0\nu\beta\beta$-decay half-lives. Fortunately, a lot of progress in nuclear-structure calculations has been made recently.

Several nuclear structure models are in use to calculate NME. The **Shell Model** is a many-body method which takes all correlations between the nucleons into account. However, due to the high number of these correlations, a sacrifice needs to be made: The calculations have to concentrate on nucleons near the Fermi level, i.e. only a few single particle orbitals in one major oscillation shell, known as the valence space are taken into account. This method describes ground state properties of medium and heavy nuclei very well, like masses, separation energies and charge radii. However, the limitations in the configuration space has a big impact on the predicted $0\nu\beta\beta$-decay matrix elements.

By comparing the NME calculations with the measured values of $2\nu\beta\beta$-decays and single β-decays, it has been found that the calculations almost always overestimate the NME. This is attributed to a quenching of the g_A coupling parameter in the order of 20-30% with respect to the unquenched value of around 1.26. If this is taken into account, there is a good agreement with between experiment and theoretical calculations.

The **quasi-random phase approximation (QRPA)** on the other hand can handle a higher number of single particle orbitals (all orbitals within one or two oscillations shells). The disadvantage in this method is the limited set of correlations, which require stronger modifications of the effective nucleon-nucleon potential, especially in the proton-neutron channel. A renormalized version (RQRPA) attempts to fix the unrealistically high sensitivity with the proton-neutron pairing channel.

The **interacting boson model (IBM)** is a relatively new approach, which tries to combine the strengths of both. It describes nucleon pairs and quadrupol phonons as bosons. As there are no data for $0\nu\beta\beta$-decays, effective parameters have to be mapped based on the shell model approach.

Fig. 2.3 shows the calculated NME for various isotopes of interest and various nuclear models. It can be seen that ^{48}Ca in general shows unfavorable NME, while no conclusive statement can be made about the other isotopes, due to the large spread with different models. The spread ranges up to a factor of 2-3, which directly translated to an uncertainty of $\langle m_{\beta\beta}\rangle$ in case of an observation and to an order of magnitude uncertainty in the predicted half-lives. Consequently, improvements of the calculations are still necessary.

The two transitions in Eq. 2.27 correspond to β^+/EC or β^- transitions. Therefore, experimental input from single β-decays but also from $2\nu\beta\beta$-decay modes for different isotopes can be very valuable to verify and adjust nuclear structure models, because the NME for these processes can be measured independent of neutrino properties for ground state and excited state transitions. Recently, also charge exchange reactions are used to investigate the strength for the transition to the intermediate state [59].

A review of NME calculations and additional literature on each method can be found in [40].

2.6.5 Experimental considerations

Experimentally, the $2\nu\beta\beta$ and $0\nu\beta\beta$-decay are easily distinguished by their $2e^-$ energy spectrum. In the $2\nu\beta\beta$-decay case, the two ν_e^c carry away part of the decay energy. Thus the $2e^-$ spectrum is continuous, similar to a single β-decay spectrum. The energy spectrum of one of the e^- of $2\nu\beta\beta$-decay can be calculated [60] as (using Primakoff-Rosen approximation to simplify Fermi function):

$$\frac{\mathrm{d}N}{\mathrm{d}E_e} \approx (E_e+1)^2\,(Q-E_e)^6\left[(Q-E_e)^2+8\,(Q-E_e)+28\right] \tag{2.28}$$

with E_e in units of m_e. The sum energy E_{ee} is calculated with:

$$\frac{\mathrm{d}N}{\mathrm{d}E_{ee}} \approx E_{ee}\,(Q-E_{ee})^5\left(1+2E_{ee}+\frac{4E_{ee}^2}{3}+\frac{E_{ee}^3}{3}+\frac{E_{ee}^4}{30}\right) \tag{2.29}$$

The maximum of the spectral distribution is at about $0.32\cdot Q$.
After integration over E_{ee} it becomes visible that the total rate scales with Q^{11} as mentioned in Sec. 2.6.
In the $0\nu\beta\beta$-decay, the $2e^-$ carry the full decay energy. Therefore most detectors measure a single peak at the Q-value. An illustration of the $2\nu\beta\beta$ and $0\nu\beta\beta$-decay $2e^-$ signature is shown in Fig. 2.4.

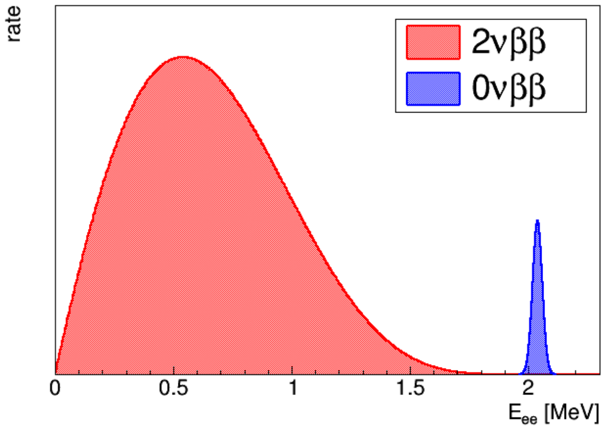

Figure 2.4.: Scheme showing the $2e^-$ sum energy spectrum of $2\nu\beta\beta$ and $0\nu\beta\beta$-decay. The $0\nu\beta\beta$ peak has been smeared with an energy resolution of 1%. The rate of this peak relative to the $2\nu\beta\beta$-decay spectrum has been increased for visibility.

The energy resolution of the experiment is important to distinguish the $0\nu\beta\beta$ peak from the endpoint of the $2\nu\beta\beta$ spectrum. Though the $2\nu\beta\beta$-decay decreased quickly when getting closer to the endpoint, the finite energy resolution of the detector system can cause a significant part of the $2\nu\beta\beta$ spectrum to be smeared towards the $0\nu\beta\beta$ peak.
In case of the Gerda experiment using germanium detectors with an energy resolution in the order of 0.1%, the irreducible $2\nu\beta\beta$ background is negligible at the Q-value. For scintillator based experiments on the other hand energy resolutions in the order of 10%

are common. Such experiments need to either take the $2\nu\beta\beta$-decay spectrum into account during the fit procedure, or sacrifice part of the $0\nu\beta\beta$-decay peak window.

Isotopes of interest

Furthermore, the choice of the isotopes is very crucial. Ideally, Isotopes of interest have a high Q-value, due to the strong scaling of the $2/0\nu\beta\beta$-decay half-lives with it. $\beta^+\beta^+$ and β^+/EC-decay modes are suppressed, because their Q-value is reduced by $4m_e/2m_e$ relative to EC/EC-decay modes. Additionally, a high natural abundance saves effort and costs related to an enrichment process of the material.
Only nuclei whose binding energy is lower than the binding energy of the $(A{,}Z{\pm}2)$ daughter nuclei can undergo $\beta\beta$-decay. Furthermore, single β-decay should be energetically not allowed, or strongly suppressed by isospin configurations. If this is not the case, the continuous e^- spectrum easily covers the $2/0\nu\beta\beta$-decay spectrum by several orders of magnitude. To understand how such a nuclei mass configuration is possible, the Bethe-Weizsäcker equation can be utilized, which offers a semi-empirical description of the mass of a nucleus in dependence of A and Z.

$$B(A,Z) = a_{\mathrm{V}}A - a_{\mathrm{S}}A^{2/3} - a_{\mathrm{C}}\frac{Z(Z-1)}{A^{1/3}} - a_{\mathrm{A}}\frac{(A-2Z)^2}{A} + \delta(A,Z) \tag{2.30}$$

$$\text{with} \quad \delta(A,Z) = \begin{cases} +\delta_0 & \text{even-even nucleus} \\ 0 & \text{even-odd/odd-even nucleus}\ . \\ -\delta_0 & \text{odd-odd nucleus} \end{cases}$$

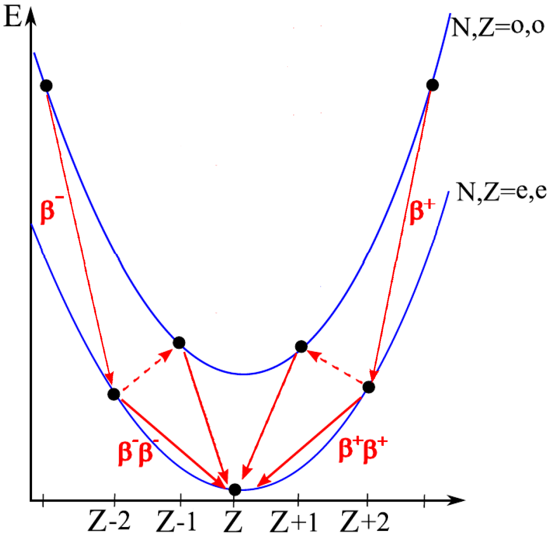

Figure 2.5.: Mass parabola for odd-odd and even-even nuclei with fixed A and in dependence of Z as calculated by the empirical Bethe-Weizäcker equation. Indicated are allowed β-decays and $\beta\beta$-decays (either β^+ or β^-) with continuous lines. Energetically forbidden β-transitions are indicated with dashed lines.

The equation consists of a volume term (a_{V}), a surface term (a_{S}), a Coulomb term (a_{C}), an asymmetry term (a_{A}) and the pair term $\delta(A,Z)$.

The pair term is of special interest here. All β-decays are isobaric transitions, meaning the number of nucleons A is left unchanged. For nuclei with fixed A, Eq. 2.30 creates two parabola for even-even and odd-odd nuclei, which are relatively shifted in energy by $2\delta_0$. This can be seen in Fig. 2.5. During single β-decay, the nucleus makes a transition from one of the parabola to the other. Consequently, $\beta\beta$-decay leads to transitions within the same parabola. Knowing this, configurations can be found, where single β-decay is energetically forbidden, while $\beta\beta$-decay is allowed, which is also indicated in Fig. 2.5. There are 35 $\beta^-\beta^-$ and 6 EC/EC isotopes which are known with a configuration like this [60]. The mother and daughter nucleus of $\beta\beta$-decay in such an case is always even-even and therefore has an isospin 0^+.

For even-odd or odd-even nuclei, single β-decay as well as $\beta\beta$-decay causes transitions only within the same parabola, which lies in between the one from even-even and odd-odd nuclei. Hence, a configuration as described above can not exist.

A strong suppression of single β-decay can also be sufficient, which can be achieved through a high difference in the nuclear spin and angular momentum configuration. In the case of ^{48}Ca, single β-decay has a Q-value of about 278 keV, which only allows a transition from the 0^+ ground state to the three lowest 4^+, 5^+ and 6^+ states of ^{48}Sc. The high isospin difference suppresses the single β-decay so strongly, that it has not yet been observed, while $2\nu\beta\beta$-decay has been observed with a half-life of $T_{1/2} = \left(6.4^{+0.7+1.2}_{-0.6-0.9}\right) \cdot 10^{23}\,\text{yr}$ [61].

2.6.6 Experimental results

The isotope ^{76}Ge is one of the first to be pursued for $0\nu\beta\beta$-decay searches, thanks to the available highly advanced germanium detector technology, which allows an excellent energy resolution with very low background. Starting in the 1980s, the two experiments HdM and IGEX became the leading experiments in the early search for $0\nu\beta\beta$-decays. After publishing lower limits on the $0\nu\beta\beta$-decay half-life of $T_{1/2} > 1.9 \cdot 10^{25}\,\text{yr}$ (90%) (2001 [62]) and $T_{1/2} > 1.57 \cdot 10^{25}\,\text{yr}$ (90%) (2002 [63]), a sub-group of the HdM collaboration first announced an evidence giving a best fit of $T_{1/2} = \left(1.19^{+0.37}_{-0.23}\right) \cdot 10^{25}\,\text{yr}$ [64] (**HdM 2004**) and later an observation with $6.4\,\sigma$ significance [65] after a re-analysis with pulse shape discrimination (**HdM 2006**). However, the claim of observation was met with criticism in the $0\nu\beta\beta$-decay community. Problems with the uncertainty and signal efficiency in the latter publication were pointed out [66], which is why HdM 2006 is not accepted by the GERDA collaboration.

The GERDA experiment (discussed in more detail in Ch. 4) was able to verify the HdM claim of 2004 directly without the influence of NME. The combined data of HdM, IGEX and Phase I of GERDA could reject it with a Bayes factor of $2 \cdot 10^{-4}$ in favor of the background only hypothesis, setting a limit of $T_{1/2} > 3.0 \cdot 10^{25}\,\text{yr}$ (90%) on the half-life. Adding the first 23.2 kg·yr of data of Phase II of GERDA could improve upon the limit, setting a new one at $T_{1/2} > 8.0 \cdot 10^{25}\,\text{yr}$ (90%) [67], which corresponds to $\langle m_{\beta\beta}\rangle < 0.12 - 0.26\,\text{eV}$ using the phase space factors of [48], the NME of [49, 51, 52, 54, 55, 56, 58] and the standard $g_A = 1.27$.

On the other side, KamLAND-Zen set a new limit on the half-life of ^{136}Xe of $T_{1/2} = 10.7 \cdot 10^{25}\,\text{yr}$ (90%), which translates to $\langle m_{\beta\beta}\rangle < 0.06 - 0.17\,\text{eV}$.

Fig. 2.6 shows the allowed bands of $\langle m_{\beta\beta}\rangle$ in dependence of the lightest neutrino mass in case of the normal (NH) and inverted hierarchy (IH). On the right of the figure, the current upper limits of experiments searching for $0\nu\beta\beta$-decay are shown for the candidate isotopes. The current limits are right on the upper end of the IH band. Next generation experiments plan to fully explore the IH region [68, 69, 70].

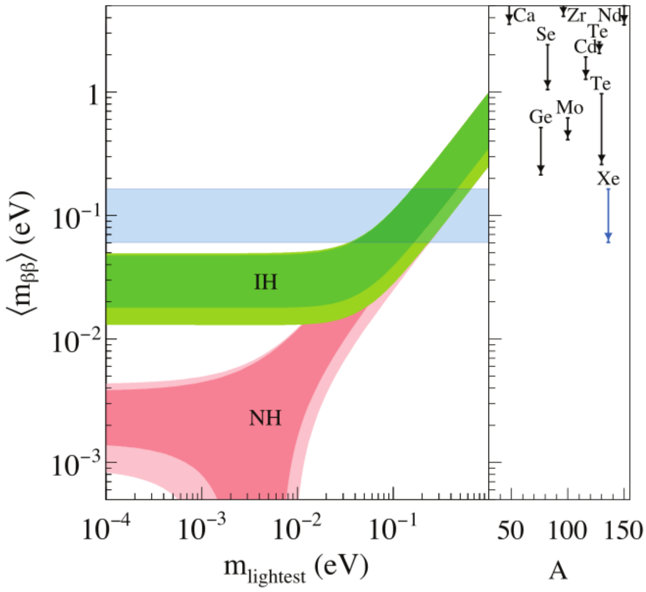

Figure 2.6.: Plotted is the effective electron neutrino mass versus the lightest neutrino mass, m_1 in case of normal hierarchy (NH), m_3 in case of inverted hierarchy (IH). The uncertainty bands of $\langle m_{\beta\beta} \rangle$ are drawn in the case of IH (*green*) and NH (*red*), calculated taking the experimental uncertainties of the oscillation parameters into account and leaving the Majorana phases free. The right side shows the current upper limits on $\langle m_{\beta\beta} \rangle$ from experiments investigating various isotopes. The range of the limits comes from a range of NME. The current best limit was achieved by ^{136}Xe experiments, which is also shown as blue band in the left plot. [40]

The quasi-degenerated region where NH and IH overlap, is almost completely excluded by direct neutrino mass searches and cosmological observation [71, 72]. Cosmological observations furthermore slightly prefer the normal hierarchy [32]. In the framework of the normal hierarchy, the contribution of light Majorana neutrino exchange can be very low, in which case a different mechanism needs to step in, in order to make $0\nu\beta\beta$-decay observable.

2.7 Direct neutrino mass searches

A direct kinematic search for neutrino masses can be done by investigating the endpoint of a single β-decay spectrum using large electron spectrometers. Due to a non-zero electron (anti-)neutrino mass, the spectral shape changes, especially at the end-point, which is additionally shifted by the mass value. Difficulties arise from the very low statistic of electrons with an energy close to the end-point and the very low neutrino mass, which requires a very precise energy measurement.

The MAINZ [73] and TROITSK [74] experiments evaluated tritium decays, which only have a Q-value of 18.6 keV. Additionally, with $Z = 1$, distortions of the electron energy by the Coulomb field are easier to calculate. Upper limits for the mass of $m_{\nu_e^c} < 2.3\,\text{eV}$ and

$m_{\nu_e^c} < 2.05\,\mathrm{eV}$ (95% C.L.) could be set, with

$$m_{\nu_e^c}^2 = \sum_j |U_{ej}^*|^2 m_j^2. \tag{2.31}$$

KATRIN [72] is a new generation experiment also investigating tritium decays, that aims for a sensitivity down to 0.2 eV. The experiment started taking data with a tritium source in 2018 and expect first results in 2019.

Chapter 3

Low background experiments

3.1 Introduction

With the currently present limits on rare processes like $\beta\beta$-decays or dark matter searches, experimentalists often only anticipate a few signal events per year. The biggest effort with new experiments therefore goes to constructing larger detectors with as much source mass or detection medium as possible, while still reducing the background to often only a fraction of an event in the region of interest. In this chapter, first the important parameters of an experiment are discussed in Sec. 3.2. Then the next sections are dedicated to typical background sources, that rare-event experiments have to face (Sec. 3.3) and the description of interaction processes of α, β and γ-radiation with matter (Sec. 3.4). Furthermore, the chapter discusses the basics of some of the most common detector technologies in Sec. 3.5, semi-conductor detectors (especially germanium detectors) and scintillators. The chapter will also deal with the statistical tools necessary to extract information about the required quantity from the data in Sec. 3.6. Finally, some of the currently leading double beta decay experiments are shortly introduced in Sec. 3.7.

3.2 Experimental parameter

The sensitivity of an experiment is a measure of how far it can be expected to probe a particular parameter space. In case of experiments searching for decay processes, the sensitivity to set a limit on the half-life of the decay is often simply estimated by:

$$S = \ln(2) \cdot N_A \cdot \frac{\varepsilon \frac{m}{M} \cdot t \cdot f}{N} = \ln(2) \cdot N_A \frac{\varepsilon \cdot f}{M} \sqrt{\frac{m \cdot t}{\Delta E \cdot B}}, \tag{3.1}$$

where N_A is Avogradro's constant, m is the total source mass, M is the molar mass of the source material, f is the atomic fraction of the source isotope in the source material, t is the live-time of the experiment, N the corresponding limit on the expected number of counts from the signal process, ΔE the signal window width determined by the energy resolution of the experiment and B is the background index. The limit on the expected number of signal counts is here estimated by taking one standard deviation[1] of the background expectation, entering the equation in form of the background index given in units of cts/(keV·kg·yr).

- **Efficiency ε:** The efficiency to detect the signal process. It is defined by the geometry of the source and the detector. In many experiments the detection medium is also the source at the same time, or the source is incorporated into the detection medium to maximize the geometrical efficiency. Furthermore, the efficiency is affected by any additional data selection cuts, which are usually enforced in order to reduce the background. Additional background veto systems can induce a dead time to the experiment, in which it is not sensitive to the signal process.

  The efficiency enters the equation linearly, thus maximizing it is very important.

- **Source mass m and isotopic fraction f:** Modern day liquid scintillator experiments can reach source masses of several tons by dissolving the source material into the liquid. The next generation semi-conductor experiments are aiming for a combined detector mass in the order of several 100 kg [68]. The source mass increases the

---

[1] This assumes a Gaussian distributed uncertainty. Hence this sensitivity approximation is not suited for very low background experiments with count expectations in the Poisson regime

number of source nuclei, that can potentially decay. However, with larger detectors usually the background also increases due to the necessity of additional material (structural) or the increased absorption efficiency of background radiation in the detection medium. Hence the background index is usually given in kg^{-1} and the sensitivity only increases with the square root of m.

The isotopic fraction (sometimes also enrichment fraction) denotes the ratio of a certain isotope in the material. An higher isotopic fraction for the specific source isotopes results in a higher ratio of source nuclei to the total number of nuclei in the source mass, and thus a better source mass to background ratio. Source isotopes with a very high natural abundance are desirable as for example ^{130}Te with 35%. Other isotopes like ^{76}Ge with a low natural abundance require additional steps to enrich the source material. However, this can be very cost intensive.

- **Live-time t:** The live-time is in many cases equivalent to the source mass. A lack of source material can be compensated by a larger measuring time, although additional operation and maintaining costs need to be taken into account.

- **Background index B:** The background index is an extremely important and difficult to estimate parameter of each experiment. Big progress has been made in recent experiments to reduce the background as much as possible, as is visible in case of the GERDA experiment, further discussed in Ch. 4. The background index is usually given in cts/(keV·kg·yr), so that different experiments with different technologies can be compared even if they strongly vary in size and energy resolution. Typical background sources are discussed in Sec. 3.3 in more detail.

- **Energy resolution σ/Peak window ΔE:** The energy resolution is very important for peak searches. With a better energy resolution, the signal peak is confined to a smaller range in energy, and thus can be discriminated against background more easily. Given a flat background around the signal peak, the background below the peak decreases linearly with better energy resolution.

  Especially for the search of the $0\nu\beta\beta$-decay, the continuous $2\nu\beta\beta$-decay spectrum poses an irreducible background which enters into the $0\nu\beta\beta$ signal peak region due to the finite energy resolution of the detectors. With a better energy resolution, the $0\nu\beta\beta$ signal can be distinguished much better from the $2\nu\beta\beta$ spectrum. Typical energy resolutions range from 0.1% like for germanium semi-conductor detectors, for which the background of the $2\nu\beta\beta$-decay is no problem in current and near future experiments, to 10% like for scintillator based experiments, where already a significant part of the $2\nu\beta\beta$ spectrum affects the $0\nu\beta\beta$ region of interest. In this case, the $2\nu\beta\beta$ spectrum needs to be accounted for in the fit or alternatively only the right part of the signal region is analysed.

  A better energy resolution also enables a better identification of background peaks.

In case of a background free experiment (i.e. only a fraction of an event is expected in the region of interest) the sensitivity scales approximately linearly with the mass and the live-time:

$$S \propto \varepsilon \cdot m \cdot t. \tag{3.2}$$

3.3 Background sources

This section discusses the different sources of background in a typical rare-event experiment. In that, it follows the description of background sources in [75], which divides the background in environmental background, impurities in detector and shielding material and cosmic-ray and neutron induced background.

3.3.1 Environmental radiation

The origin of environmental radioactivity can be categorized mostly into primordial, cosmogenic and anthropogenic radiation.

Primordial background:

Primordial isotopes ^{232}Th, ^{235}U and ^{238}U as well as ^{40}K are present in the earth's crust since its birth. They still remain due to their extremely long half-lives in the order of $10^8 - 10^{10}$ yr. The decay of the former three isotopes is followed by a long chain of predominantly α and β-decays until a stable isotope of lead is reached. The majority of γ-radiation low-background experiments need to handle, is emitted by several of the isotopes within the chains. Most importantly, ^{208}Tl with a Q-value of 5 MeV emits the energetically highest natural occurring of all γ-rays with a noteworthy emission probability ($\sim$100%), prominent in most background spectra at 2.614 MeV. Other isotopes of interest in regard of γ-ray emission are ^{212}Bi, ^{214}Bi, ^{228}Ac and ^{214}Pb. A list of γ-rays from the decay chains is given in Appendix B.1. An average concentration of 100 Bq/kg ^{232}Th and 36 Bq/kg ^{238}U in the continental upper crust are given in [76]. However, the concentration can vary substantially depending on the rock type. Granites and pegmatites exhibit the highest concentration.

Secular equilibrium can be assumed for some of the isotopes in deeper rock, which means that the activity of the parent and daughter nuclei is the same.

Radon:

^{222}Rn is a member of the ^{238}U chain. It often escapes from the rock into the air because of the recoil from the α-decay or by diffusion. A ^{222}Rn activity of 1300 Bq/(m^{2}d) [77] is released from the earth land surface and is present in laboratory air in a concentration of $\sim$40 Bq/m^3. ^{220}Rn from the Th chain has a much shorter half-life of about 1 min and has a smaller diffusion length during that life-time. Hence the concentration in air is negligible compared to ^{222}Rn ($\sim$1%). Additionally, the ^{220}Rn family dies out with a half-life of only 11 h with the longest living isotope being ^{212}Pb. On the other hand, the longest living isotope of the ^{222}Rn daughters is ^{210}Pb with a half-life of 22 yr.

The positively charged Rn progenies can get attached to statically charged surfaces such as plastics or glass, Rn is also very soluble in water. Concentrations in big water tanks can reach 100 Bq/l of ^{222}Rn.

Cosmogenic background:

Cosmic rays consisting primarily of protons (almost 90%) and α-particles create particle showers when hitting atoms in the atmosphere. One consequence of this can be the activation of nuclids found in the atmosphere. This leads primarily to the production of

^{7}Be and ^{10}Be. Additionally, produced in the rare gases of the air are ^{37}Ar, ^{39}Ar, ^{42}Ar, ^{85}Kr and ^{81}Kr. This cosmogenic background however becomes only relevant in experiments employing material won from the atmosphere, like experiments based on liquid argon as scintillator detector.

Anthropogenic background:

Anthropogenic background describes artificial, man-made background. Through extensive nuclear weapon testing and accidents in nuclear power plants, fission products have found their way into the atmosphere, predominantly ^{137}Cs and ^{90}Sr. Furthermore, ^{85}Kr is released into the air by nuclear fuel reprocessing plants.

3.3.2 Impurities in detector and shielding material

Spores of Th and U, but also K can be present in detector and shielding materials, due to their presence in ores and other raw material. Furthermore, during the often long and multiple staged production cycles of the detector components, it is difficult to prevent contaminations from being transferred onto them. Nuclides from the chains can be separated in the process, due to the different chemical and physical properties of the elements, resulting in isolated impurities of ^{210}Pb and ^{228}Th among others.

In order to reduce those contaminations, materials can be purified during the production. Copper for example can be refined electrolytically after smelting to impurity levels of $<0.1\,\mu$Bq U/kg Cu [78] and is therefore a very popular shielding material.

Material for semi-conducting detectors needs to be purified extensively to warrant functionality as detector. Upper limits contaminations with long lived daughter nuclides of the U and Th chains of the GERDA germanium detectors are given at a few nBq/kg Ge [79].

A second source for internal radioactivity of detector components is the activation of the material during processing and transport above ground by cosmic-rays. In case of germanium semi-conductor detectors, this can result in the formation of ^{68}Ge and ^{60}Co isotopes in the bulk. To circumvent the production of additional radioisotopes, the time of the material above ground needs to be minimized, ideally shielded from cosmic-rays. Short lived isotopes created this way, can be removed by storing the material underground long before it is employed in the experiment, which is often done with lead and copper shielding material.

3.3.3 Muon induced background

Particles of the atmospheric radiation that reaches to the earth surface consist to more than 60% out of muons created in the higher atmosphere (>10 km) by the decay of pions, which in turn are created by the interaction of cosmic radiation. Muons in the energy range of a few GeV are minimal ionizing particles, which enables them to easily penetrate kilometers of rock.

In detectors they typically deposit a varying amount of energy ranging up to several 10 MeV, depending on the path length and therefore the angle they hit the active volume of the detector. Thus they can directly enter the background in the region of interest in a wide energy range. Additionally, they create showers of pair production, bremsstrahlung and ionization processes, hitting many detectors simultaneous, if available.

Muons also create secondary radiation by interacting with the rock, the shielding material, or any other material in the vicinity of the detector. This includes high energetic bremsstrahlung and neutrons.

3.3.4 Neutron induced background

Neutrons represent about 20% of the atmospheric radiation at sea level. However, in contrast to muons they are strongly attenuated by inelastic scatter processes with a mean length of 200 g·cm^{-2} in standard rock [80]. As a result, atmospheric neutrons become negligible after already 10 m w.e. (water equivalent) of shielding. On the other hand, neutrons produces by muon captures or photonuclear reactions as a result of fast muons in high Z material like lead shielding, as well as neutrons as products of spontaneous fission and (α,n) reactions in the rock become more important for underground laboratories. The dependence of the neutron flux on the laboratory depth is shown for each component in Fig. 3.1.

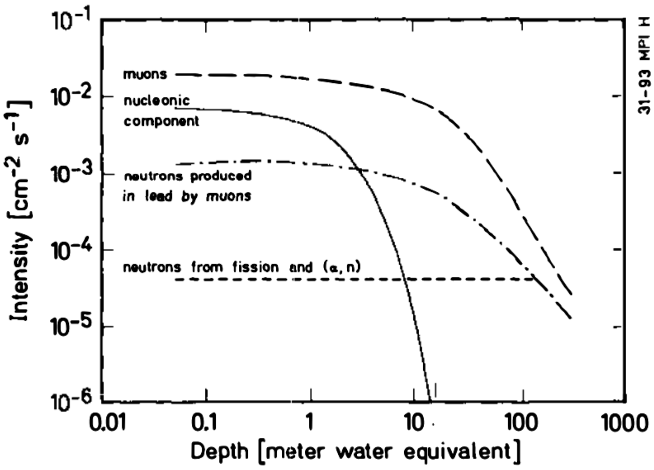

Figure 3.1.: Flux of muons and different neutron components (nucleonic cosmic ray secondaries and tertiary produced) in dependence of the depth in a typical Pb shield. Taken from [75].

In dark matter experiments, neutrons can mimic the nuclear recoil signature of WIMP particles. Inelastic scattering and thermal neutron capture in material close to the detectors can create unstable isotopes and γ-rays.

The contribution by muon induced neutrons is usually strongly suppressed by employing a muon veto. Neutrons from the rock can be effectively shielded by water or borated polyethylene.

3.4 Low energy particle interactions with matter

In order to observe particles they are required to interact with the active volume of the particle detector. The specific processes they interact with the detector material and what kind of signature they imprint depend on the particle type and their energy, but also the detector material itself.

This section shortly discusses the possible interactions of γ, β and α-radiation with matter. For a detailed discussion see [81] and [82]

3.4.1 γ-radiation

The interaction of γ-rays with an energy of several keV to a few MeV with matter is characterized by the processes of photoelectric absorption, coherent and incoherent scattering and pair production.
Because γ-rays are neutral particles, their mean free path[2] and consequently their range is usually much larger than that of β or α particles, reaching up to several tenth of meters in water. They typically interact with shell electrons, thus their cross sections are enhanced for material with high electron density, i.e. a high atomic density and high nuclear charge Z. Fig. 3.2 shows the cross sections of γ-ray interactions in germanium ($Z = 32$) in total and for the four above mentioned processes in dependence of the photon energy E_γ.

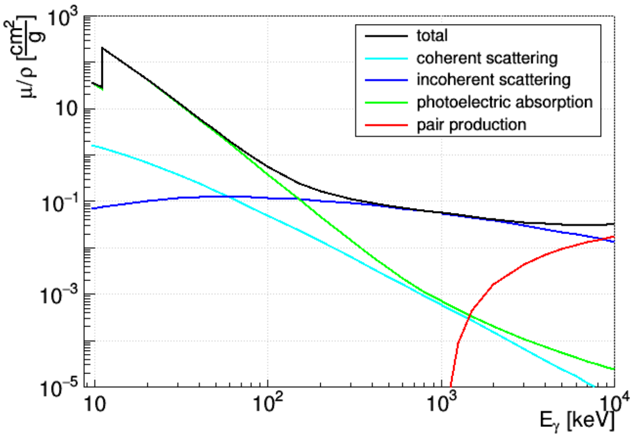

Figure 3.2.: Mass attenuation μ/ρ for γ-rays with an energy between 10 keV and 10 MeV in germanium. Shown is the total attenuation and the attenuation by the four most important processes in this energy range separately. Data taken from [83].

Photoelectric absorption

The photoelectric effect describes the complete absorption of the γ-ray by an electron of the atomic shell. As a consequence, the electron is released from the shell. Its kinetic energy is equal to E_γ reduced by the binding energy of the electron. X-rays or Auger electrons can be emitted in the process, when electrons from energetically higher shells fill the vacancy left by the ejected electron.
The photoelectric absorption is the dominating process for γ-rays with an energy up to a few hundred keV. Its cross-section, given as mass attenuation μ/ρ, rapidly decreases proportional to $E_\gamma^{-7/2}$, and at energies above the electron mass m_e proportional to E_γ^{-1}:

$$\frac{\mu}{\rho} \propto \frac{Z^5}{E_\gamma^{7/2}} \qquad \text{for } E_\gamma < m_e, \tag{3.3}$$

$$\frac{\mu}{\rho} \propto \frac{Z^n}{E_\gamma} \qquad \text{for } E_\gamma \gg m_e, \text{ with } n = 3..3.6. \tag{3.4}$$

The strong Z dependency derives from the dependency on the electron density. Additionally, when E_γ exceeds the binding energy of a certain shell, a sharp rise in the cross-section

---

[2] The mean free path of a particle refers to the average distance between two interactions.

can be observed as there are additional electrons available for the process.
In calorimetric measurements, photoelectric absorption will be visible as sharp peak like signatures in the energy spectrum.

Coherent and incoherent scattering

Incoherent scattering, often also referred to as Compton effect, describes the inelastic scattering of γ-rays at shell electrons. In the process, the direction of the γ-ray is changed and a part of its energy is transferred to the electron. The final energy of the γ-ray E'_γ depends on the scattering angle and can be calculated with:

$$E'_\gamma = \frac{E_\gamma}{1 + \frac{E_\gamma}{m_e}(1 - cos\theta)}, \tag{3.5}$$

where θ is the angle between initial and final momentum of the γ-ray. The maximum energy transfer occurs for a scattering angle of 180°. For very small γ-ray energies ($E_\gamma << m_e$), almost no energy is transferred.
The Compton scatter cross-section was described by Klein and Nishina in 1929 [84] and can be given in differential form for a single electron as follows:

$$\begin{aligned} \frac{d\sigma_e}{d\Omega} &= r_0^2 \left(\frac{1}{1 + \frac{E_\gamma}{m_e}(1 - cos\theta)} \right)^2 \left(\frac{1 + cos^2\theta}{2} \right) \\ &\cdot \left(1 + \frac{\frac{E_\gamma^2}{m_e^2}(1 - cos\theta)^2}{(1 + cos^2\theta)[1 + \frac{E_\gamma}{m_e}(1 - cos\theta)]} \right), \end{aligned} \tag{3.6}$$

where r_0 is the classical electron radius and Ω the solid angle. Note that this cross-section is calculated with the assumption of a quasi-free electron, thus it only gives an approximation.[3]

For most materials, incoherent scattering becomes the dominant process in the range of a few hundred keV to several MeV. The Z dependence of the atomic cross section comes mostly from the number of electrons in the atomic shell. It is therefore roughly proportional to Z. The energy dependence, on the other hand, is more complicated. For photon energies larger than m_e it can be written as empirical relation as proportional to E_γ^{-n}, with n between 0.5 and 1.
The varying scatter angle leads to a continuous distribution of deposited energies in the detector. This energy spectrum has a minimum at 0 corresponding to forward scattering and a maximum, the so-called Compton edge, at $E_{\max} = E_\gamma - E'(180°)$ in case of backscattering. Multiple scattering of the same γ-ray inside the detector can lead to energy depositions above $E_{\max}$. Often the energy spectrum also features another edge at $E_\gamma - E_{\max}$. This edge has its origin in a γ-ray with initial energy E_γ, which was scattered outside the detector volume by 180° and then being fully absorbed inside the detector.

At low energies the incoherent scattering competes with coherent scattering, which refers to an elastic scatter process between a γ-ray and a bound electron. The γ-ray does not lose

---

[3] For a more precise description of the scatter cross-section, $\frac{d\sigma}{d\Omega}$ needs to be folded with a so-called incoherent scattering function, which takes into account effects like the electron bounds and the electron distribution in the shell.

energy in the process, but changes its direction. The momentum difference is absorbed by the nucleus. Because it is only of interest at very low γ-ray energies and no energy is deposited, it is of no importance for this work.

Pair production

With an energy larger than $2\,m_e$, a γ-ray is able to convert into a pair of electron and positron, while within the coulomb field of a nucleus. The energy is almost evenly distributed among the electron and the positron. Both of these particles undergo several more interaction in the matter, until they come to a halt, as will be described in the next section. The positron will annihilate together with another electron from the material, creating two photons in the process. The photons move in the diametrically opposed direction with each an energy of m_e. There is also a small chance of annihilation while the positrons kinetic energy is non-zero, which would then result in higher energetic annihilation photons, whose momentum is slightly shifted in the direction of the positron momentum.
This process is the dominant process for photon matter interactions in the energy range of several MeV and above. Its cross-section increases proportional to $\ln(E)$ and roughly quadratically with the nuclear charge Z. Thus, the important dependencies of the pair production cross section are as follows:

$$\frac{\mu}{\rho} \propto Z^2 \ln E_\gamma, \qquad \text{for } E_\gamma > 1.022\,\text{MeV}. \tag{3.7}$$

Much like in the case of the photoelectric absorption, pair production results in a peak signature at the position of E_γ in the measured energy spectrum, but only if the electron and both annihilation photons deposit all their energy inside the detector. Two additional peak signatures are created at $E_\gamma - 511\,\text{keV}$ (Single escape peak, SEP) and $E_\gamma - 2\cdot 511\,\text{keV}$ (Double escape peak, DEP), when either one or both of the annihilation photons escape the detector. This case is more likely with smaller detectors or low Z material. A schematic of the pair production process as well as the expected signature in an energy spectrum is shown in Fig. 3.3 together with the other processes.

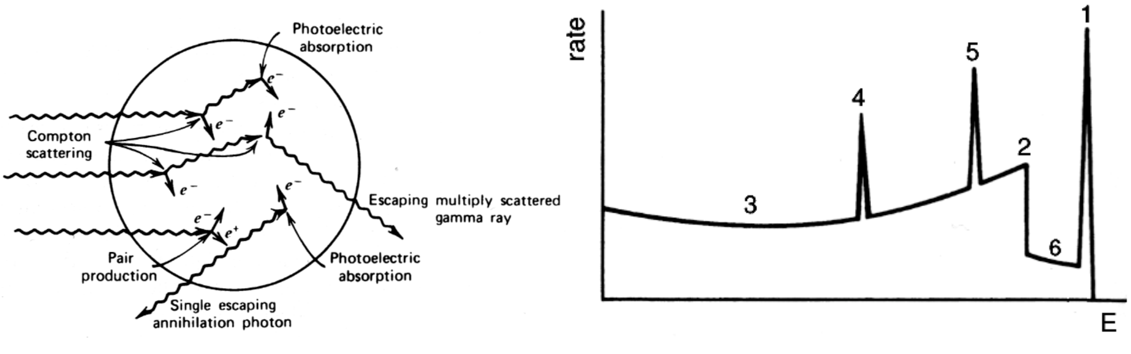

Figure 3.3.: *Left:* Scheme visualizing the three important processes for low energetic γ-rays: Photoelectric absorption, incoherent scattering (Compton) and pair production. In case of pair production, the scenario is shown that leads to a single escape peak. *Right:* Schematic showing the different γ-ray signatures in an energy spectrum: (1) full energy (photo) peak, (2) Compton edge, (3) Compton continuum, (4) double escape peak, (5) single escape peak and (6) multiple Compton scatter continuum. Adapted from [82].

3.4.2 α- and β-radiation

The energy loss of charged particles in matter can be described by the linear stopping power S, i.e. energy loss per path length, which can be written as:

$$S = \frac{dE}{dx} = \left(\frac{dE}{dx}\right)_c + \left(\frac{dE}{dx}\right)_r . \tag{3.8}$$

As can be seen in the equation, the total stopping power is composed of two components. First, the collisional stopping power wich describes the energy loss by ionization and excitation of atoms by collisions with their shell electrons.
A relativistic and quantum theoretical description of the collisional stopping power is given by the Bethe equation:

$$-\left(\frac{dE}{dx}\right)_c = \frac{4\pi e^4 z^2 N}{m_e v^2}\left(\ln\frac{2 m_e v^2}{I} - \ln\left(1-\frac{v^2}{c^2}\right) - \frac{v^2}{c^2}\right), \tag{3.9}$$

where e is the elementary charge, v and z the velocity and charge number of the ionizing particle, N the electron density of the material, c the vacuum speed of light and I the average excitation and ionization potential of the material.
The energy loss is therefore proportional with the electron density of the material, the squared charge of the ionizing particle, i.e. $z = 2$ for α-particles and inverse proportional to its energy in case of a non-relativistic velocity. The latter inverse proportionality causes a much higher specific energy loss at the end of the track of the charged particles, which is known as the Bragg peak.
Due to their much lower mass, which is of the same size like the mass of the shell electrons they are interacting with, the collisional stopping power of β-particles can not be described with the standard Bethe equation. β-particles take a very diffuse path through matter, because their momentum direction changes abruptly with each collision. A modified version of the Bethe equation for β-particles is given with:

$$\begin{aligned} -\left(\frac{dE}{dx}\right)_c = \frac{2\pi e^4 N}{m_e v^2} \Bigg(& \ln\frac{m_e v^2 E}{2I^2\left(1-\left(\frac{v}{c}\right)^2\right)} - (\ln 2)\left(2\sqrt{1-\left(\frac{v}{c}\right)^2} - 1 + \left(\frac{v}{c}\right)^2\right) \\ & + \left(1-\left(\frac{v}{c}\right)^2\right) + \frac{1}{8}\left(1-\sqrt{1-\left(\frac{v}{c}\right)^2}\right)^2 \Bigg) . \end{aligned} \tag{3.10}$$

The second term in Eq. 3.8 is called radiative stopping power, which accounts for the energy loss of charged particles by interaction with the coulomb field of nuclei or electrons from the shell. In the process, the particle is deflected and emits radiation, often referred to as bremsstrahlung. The radiative stopping power can be written as:

$$-\left(\frac{dE}{dx}\right)_r = \frac{NEZ(Z+1)e^4}{137 m_e^2}\left(4\ln\frac{2E}{m_e} - \frac{4}{3}\right). \tag{3.11}$$

As visible from the factor m_e^2 in the denominator, bremsstrahlung occurs more frequently for lighter particles, which is why it is much more important for β-particles than for α-particles and ions, where it can be neglected for low energies.

The ratio between collisional and radiative stopping power for β-particles can be given roughly as:

$$\frac{\left(\frac{dE}{dx}\right)_r}{\left(\frac{dE}{dx}\right)_c} \approx \frac{ZE}{1600 m_e}, \tag{3.12}$$

with E in units of MeV. For β-particles in germanium ($Z = 32$) with an energy of $2 \cdot m_e$, the ratio is 4%.

Bremsstrahlung, though usually low in energy, may escape small detectors and result in a deficit in energy measurements [85].

CSDA range:

Due to their diffuse path through matter, it is difficult to define a range to which β-particles penetrate material. An estimate for the average range can be obtained by the continuous-slowing-down-approximation (CSDA), which assumed that the energy loss is equal to the total stopping power at every point along the path. A β-particle with an energy of $2 \cdot m_e$ has a CSDA range of 1.2 mm in germanium. A database of CSDA values can be found at [86].

3.5 Particle detector technology

To obtain information about particles, an interaction between them and a particle detector is required. From the previous section, it is apparent, that detector mediums with high nuclear charge Z and high density benefit the interaction probability of γ-rays and β-particles.

Besides simply counting the number of interactions with the detector, more advanced devices furthermore allow to extract information like the kinetic energy of the particle, its momentum or its electrical charge from the detector signals. This section will concentrate on calorimetric detector devices though, more precisely semi-conductor detectors and scintillators, because they are of relevance for the GERDA experiment. The major reference for this section is [82], which includes a much more complete discussion of the most common particle detectors.

Semi-conductor detector technology became practically available in the 1960s. As solid state detectors, semi-conductor detectors offer a much higher density compared to earlier gas volume detectors and hence have a higher detection efficiency for the relevant particles while still maintaining reasonable dimensions. Furthermore, especially germanium and silicon based semi-conductor detectors exhibit an excellent energy resolution.

Although scintillating material was already used in the very early 20th century, modern use really gained traction in the 1940s with the invention of the photomultiplier tube, which allowed the electronic read-out of such detectors. Scintillator detectors are usually very low in production cost and much more flexible in shape and form compared to semi-conductors, which often makes them the optimal choice wherever energy resolution is not of high importance.

3.5.1 Semi-conductor detectors

Due to the periodicity of the crystal structure in crystalline material, the states in that electrons are allowed are strongly degenerated so that they form continuous bands.

In a metallic conductor, the valence band is only partly occupied by outer-shell electrons. Therefore, electrons can drift from one state to another free state. Applying an electrical field, the electrons will move in the opposite direction of the field lines.

Given an insulator, the valence band is fully occupied by electrons. Hence, without a free state in the valence band to move to, the electrons remain stationary and no current can flow. The energetically next higher band, the conductor band, is vacant of electrons. Separating the conductor from the valence band is a gap of forbidden energies, where no electrons are allowed, which is referred to as band gap. Insulators typically have band gaps larger than 5 eV, usually too wide for electrons to cross.

In the ground state, semi-conducting material has the same configuration as an insulator and thus behaves identical. However, the band gap is much smaller with typically values lower than 1 eV. As a result, through thermal energy electrons can be lifted to the conducting band where they can drift through the crystal. Additionally, the electrons will leave free states in the valence band which represent a net positive charge, referred to as holes. The electron-hole pair will ultimately recombine after some time of diffusion movement. By applying an electrical field, the electrons in the conductor band are able to move against the field lines. Simultaneously, electrons in the valence band will occupy the holes left in the valence band. Thus, the holes are seemingly moving in the direction of the field lines. Both electrons and holes contribute to the conductivity of semi-conducting material.

Apart from thermal energy, incident ionizing radiation can also creates electron-hole pairs along its path, which then cause a small detectable current. The thermal excitation usually dominates at room temperature though, so that semi-conducting material has to be cooled down to enable the use as radiation detectors. Furthermore, intrinsic semi-conductors require completely pure material so that the number of electrons in the conduction band is identical to the number of holes in the valence band. Achieving such purity is however not possible. Small concentrations of impurity atoms (e.g. 1 part per million) in the crystal lattice will occupy places usually occupied by a normal atom of the lattice. They will either create donor or acceptance levels within the band gap very close to the conductor band or the valence band, in case they have one more or one less valence electron, respectively. As a consequence, electrons provided by the donor levels can easily be lifted into the conductor band by a small amount of thermal energy and will dominate the number of electrons in the conductor band. The higher concentration of electrons will lead to a higher recombination rate between electrons and holes, which in equilibrium will lead to a lower number of holes in the valence band. Hence, the conductivity of such n-type material is almost completely provided by the electrons of the donor impurities. In this case the electrons are called the majority carries, while the holes are the minority carriers. Analogously, acceptance levels provide holes to the valence band, leading to holes as majority and electrons as minority carries.

Though practically impossible to achieve perfectly, the properties of an intrinsic semiconductor can be mimicked by material with an equal amount of n-type and p-type impurities, which will lead to a compensation due to electrons from donor levels being caught in acceptor levels. As alternative, by bringing together n-type and p-type semi-conductor material, a zone bereft of free charge carriers can be created in between the n-type and the p-type sides, called the depletion region. In practice, this is done by starting with a p-type material (analogous for n-type material) and purposely changing the impurity concentration on one side of the material by doping it with a uniform concentration of n-type impurities. The donor electrons from the n-type side will migrate by diffusion into the p-type region and occupy the acceptor sites. In the following, the caught electrons and holes will build up a negative and positive space charge at the p-n junction, respectively, which consequently will create an electrical potential across the junction. At equilibrium, the potential will stop the further migration of electrons and holes across the p-n junction. However, the potential created this way is very small in the order of 1 V, which is insufficient to make charge carriers created in the depletion region by ionizing radiation move quickly enough. Instead they are likely being trapped or recombine. This can be circumvented by applying an external potential in reverse bias direction, which means applying a negative potential to the p-type side so that it supports the potential created by the p-n junction. In this direction, the minority carriers are attracted across the junction and because of their low concentration, only a very small current can flow. Additionally, a high external potential will increase the depletion region, increasing the ”active” volume for the collection of charge carriers generated by ionizing radiation.

The current signal on the contacts is induced by the charge carriers drifting through the active detector volume. The relation between total induced charge Q on an electrode i at time t and the drifting charge is given by the Shockley-Ramo theorem [87, 88]:

$$Q(t) = q \cdot V_{w,i}(x(t)), \tag{3.13}$$

where q is the drifting charge in the detector and $V_{w,i}(x(t))$ is the dimensionless weighting potential of electrode i at the position $x(t)$ of the drifting charge. The weighting potential is a mathematical tool, which is obtained by solving Laplace's equation while fixing the potential of electrode i to 1 and all other electrodes to 0.

Germanium semi-conductors

In the following, semi-conductor detectors based on germanium are further discussed, because they are of relevance for this work. To reduce thermal noise to an acceptable level, germanium semi-conductors have to be cooled down to liquid nitrogen temperatures (∼77 K). At that temperature, germanium has a band gap of about 0.7 eV [82]. The average energy to create an electron-hole pair is 3 eV. The resulting charge carrier statistics allows for an excellent energy resolution of down to 0.1% at 2.6 MeV.

With germanium of normal semi-conductor purity, only depletion regions of 2-3 mm are possible, even with very high potentials applied. The resulting active volume of the detector is too small for spectroscopy of γ-rays of 1 MeV. One approach to enlarge the region of depletion to a sufficient volume is to reduce the impurity concentration by further purification steps to a level of 1 in 10^{12}. Detectors with this high purity, so-called HPGe[4] detectors, became available in the 1980s. This was made possible by zone refinement techniques [89], in that the material is locally heated and a melted zone is dragged from one end of the material to the other. Impurities tend to be more soluble in the heated material, hence they are driven to the end of the sample by following the molten zone. This step can be repeated multiple times to reduce the impurity concentration even further. Given germanium with the purity levels achieved by this method, depletion regions with a thickness of a few cm can be reached.

Additionally, an increase in the active volume is enabled by abandoning a planar detector geometry. Instead coaxial or semi-coaxial detectors geometries are used, which consist of a cylindrical crystal, where in the core a cylindrical shaped piece of material is removed.

---

[4] High Purity Germanium

This has the advantage, that one contact can be implemented at the inner surface of the detector and the full width of the material (minus the removed portion in the core) can be made active. On p-type coaxial germanium detectors, the outer surface n^+ contact is usually created by lithium evaporation and diffusion on the surface, which results in a contact thickness and hence dead layer of about 1 mm. At the inside, a p^+ blocking contact is created by implanting pentavalent boron atoms. The resulting dead layer is typically much smaller than on the n^+ contact, with values in the order of $100\,\mu$m.
New developments are steering towards detectors with very small or point-like anode read-out contacts. The small contact has the advantage of a low capacitance, which lowers the induced noise and subsequently improves the energy resolution. Examples for such detectors are the BEGe detector type produced by Canberra [90] and inverted[5] semi-coaxial detectors, like the Canberra SAGe type. BEGe detectors are heavily used in the GERDA experiment and further discussed in Ch. 4.2.8. Inverted semi-coaxial detectors are one option for future germanium based $0\nu\beta\beta$-decay experiments.

3.5.2 Scintillator detectors

The scintillation process describes the emission of light by a material penetrated by ionizing radiation. This principle belongs to one of the oldest utilized to detect radiation. Detectors based on scintillating material usually consist of two major components: the scintillating material itself and a photo detector which is necessary to convert the scintillation light into an electrical signal.
Scintillators are available in various shapes and forms and all aggregate states. Organic scintillators solved in plastic are easy to fabric and hence a popular choice due to the low costs. Gaseous and liquid scintillators are ideal, when big volume detectors of several meters are required. In liquid state, the density is additionally sufficiently high to offer a decent absorption efficiency for γ radiation. Furthermore it is possible to solve the radioactive sample in the liquid scintillators to maximize the detection efficiency which then reaches almost 100%. The SNO+ experiment for example aims to solve 3.9 t of natural tellurium in a volume of 780 t of organic scintillator LAB[6] to search for the $0\nu\beta\beta$-decay of ^{130}Te [91].
The exact light production mechanism differs for the different mediums. As a result, the light yield and respond time of the detector is highly dependent on the medium. Inorganic scintillators typically exhibit the highest light yield per deposited energy of the radiation, but they are slower in their light output. Organic detectors on the other hand are usually faster on the cost of a lower light yield. The light production will be discussed in the following for the case of liquid argon (LAr) scintillator, which finds application in the GERDA experiment.

Liquid argon as scintillator

The rare gas argon exhibits scintillating abilities in the gaseous and liquid states. Liquid argon has a density of about $1.4\,\mathrm{g{\cdot}cm^{-1}}$ at 87 K and atmospheric pressure.
The scintillation process in argon is based on the excitation or ionization of argon atoms by ionizing radiation. The excited or ionized argon atom than hits another argon atom and

---

[5] In contrast to conventional semi-coaxial detectors, which have the read-out contact inside the borehole, the inverted version has a small contact on the outer surface, opposite of the borehole.

[6] Linear Alkylbenzene

forms a two-argon state, referred to as dimers. The excited dimers decay, accompanied by the emission of UV light with a maximum in the emission spectrum at 128 nm [92]. The ionized dimer neutralizes with a thermal electron, also under the emission of light, and subsequently decays analogous to the former case. In liquid argon, the ionization dominates by a factor of 5 relative to the excitation [93].

Dimers as two-argon states can be formed as singlet (spin 0) or triplets (spin 1). As the decay of the triplet state is connected with a change of spin, it is forbidden and hence has a longer life-time in the order of microseconds, compared to the decay of singlet states with life-times in the order of nanoseconds. As a result, the emitted light is divided into a fast component, known as fluorescence, and a slow component, referred to as phosphorescence. The population of the singlet and triplet states depend on the ionization density of the ionizing particle. The population of singlet states relative to the population of triplet states is larger for smaller ionization densities, like caused by electrons compared to higher ionization densities by alphas or nucleon recoils. The resulting difference in the ratio between fast and slow light component can be used to identify different particles, like electrons and alphas [94]. Additionally, as a consequence of the higher ionization densities of α-particles, a higher amount of dimer will decay radiation-less by transferring the energy to neighboring dimers, known as ”quenching”. The light yield in pure argon is about 40,000 light photons given an electron with 1 MeV, while it is reduced by about 12% for α-particles [93].

The scintillation properties are highly dependent on the concentration of oxygen and other impurities in the LAr [95]. Impurities often boost the radiation-less de-excitation of triplet states reducing the light yield or increase the self absorption in LAr. The self absorption length only becomes important for big volume detectors. For detectors with complex geometries, the scattering length for light photons needs to be considered. Because of the different varying impurity concentrations of different LAr volumes, such parameters optimally need to be measured inside the actual detector as they are very important for the understanding of the response of the detector.

To increase the transparency of the scintillation medium for its own scintillation light, a wavelength shifter is often solved in the liquid, which absorbs the scintillation light and re-emits it with a longer wavelength. Additionally, wavelength shifters are used to adjust the wavelength of the light so that it aligns with the maximum in quantum absorption efficiency of the photo detector.

Photodetector

The most commonly used form of photo detectors are photomultiplier tubes (PMT). PMTs are evacuated tubes that consist in principal of a photocathode and a secondary electron multiplicator. The **photocathode** converts the light photons into electrons through photoabsorption. The light needs to supply an energy high enough for the electron to migrate to the surface of the cathode material and overcome the surface potential barrier. The quantum efficiency of photocathodes i.e. the probability that a photon is converted to a photo-electron, is in practice in the range of 20-30% and depends on the wavelength of the incident light. The primary electrons need to be multiplied in order to produce a measurable signal. The **electron multiplication** is based on secondary electron emission. The primary electrons are accelerated towards a dynode by a potential of typically in the order of 100 V. At the dynode they deposit kinetic energy by hitting the surface, which results in the emission of several secondary electrons. Theoretically $\sim$30 electrons are excited by electrons accelerated to 100 eV, but only a small fraction are released from the surface. With the help of multiple dynode stages, a multiplication factor of 10^6 can be reached. A schematic of a PMT can be seen in Fig. 3.4.

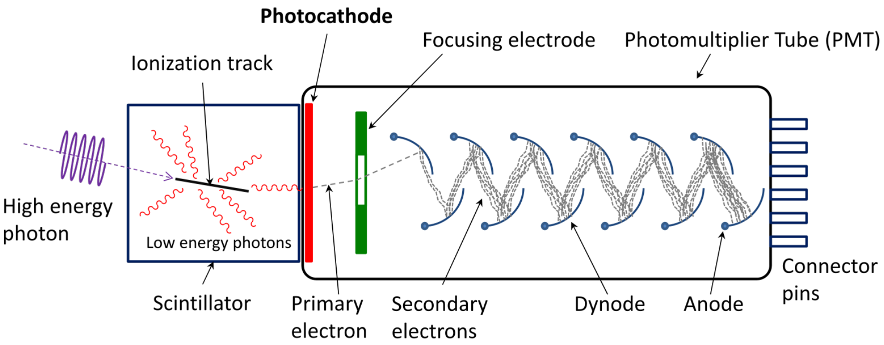

Figure 3.4.: Schematic view of a scintillator attached to a photomultiplier tube. A description can be found in the text. Taken from [96].

Alternatively to PMTs, photo diodes operated with avalanche multiplication are used. Such devices only reach an amplification of 100, but have a higher quantum efficiency, less power consumption and are smaller in volume. In experiments which require to operate the photodetector in a magnetic field, PMTs are not an option and photo diodes are used instead.

The energy resolution of scintillators can not compete with semi-conductor detectors. Typically, a resolution of 6-10% can be achieved at energies of a few MeV. On average about 100 eV per photo-electron are necessary considering the initial photon creation process and quantum efficiency of the photo detector. Compared to the 3 eV which are required to create one electron-hole pair in germanium detectors, the number and hence statistics of information carriers are much lower. Additionally, the statistical multiplication of electrons is further reducing the energy resolution.

3.6 Data analysis & statistics

Experiments usually produce large amounts of data. The goal however, is often to obtain only a single value for a particular parameter found in some theoretical physics model. In nuclear and particle physics, parameters of interest are for example the half-life of a decay process or cross sections for some kind of particle interaction. The desired value, called an estimate, needs to be extracted from the data and should preferably be as close as possible to the unknown true value of the parameter. Its actual value is subject to statistical fluctuations and depends on the specific set of data. Additionally, one usually wants to know the uncertainty of the estimated value, which quantifies how reliable or precise the estimated value is. The task of a typical analyst is therefore to prepare and select the data and find a way to break it down to a single number.

An infinite number of estimators exist, but only a few of them perform as desired. From a ”good” estimator, one expects three basic properties: the estimator should be consistent, unbiased and efficient. In case of a **consistent** estimator, the difference between estimated value and true value of a particular parameter vanishes for an infinitely large data sample. **Unbiased** means, that the expectation value of estimated values is equal to the true value. For a large data sample any consistent estimator is also unbiased. An estimator

is called **efficient**, if the variance (or uncertainty) of estimated values is small, close to minimum variance bound, the lowest possible variance among all estimators. Two of the most commonly estimators are discussed in the following.
Further information with respect to this chapter can be found in [97].

3.6.1 Maximum likelihood estimator

The observed data is drawn from a probability density distribution. Assuming a model, this distribution is known in dependence of a set of parameters $\mathbf{a}$. For any given $\mathbf{a}$, the probability of drawing a set of data points $\mathbf{x}$ can be calculated as the product of the probability of each data point x_i:

$$\mathcal{L}(\mathbf{a}|\mathbf{x}) = \prod P(x_i, \mathbf{a}). \tag{3.14}$$

The product $\mathcal{L}$ is called the likelihood, describing the probability of $\mathbf{x}$ given specific values of $\mathbf{a}$. The values for $\mathbf{a}$, for which the likelihood of the observed data is maximized is a commonly used estimator, called the maximum likelihood. Often, the logarithm $\ln \mathcal{L}$ is used, because it simplifies the likelihood expression in many cases and is in general easier to compute.
The maximum likelihood estimator is usually consistent, but in general biased. However, as already mentioned, for large data samples the bias of consistent estimator disappears. It can be shown, that for large data samples, the likelihood function equals a Gaussian function with a variance which is equal to the variance of the estimator [97]. Thus the uncertainty of the estimator can be easily obtained from the likelihood function, i.e. the 1σ uncertainty is obtained from the value, where $\ln \mathcal{L}$ decreased by 0.5. This method of obtaining the uncertainty is often referred to as likelihood ratio method.
If only a subset $\mathbf{a}'$ of the parameters is of interest, while the remaining $\mathbf{a}''$ are nuisance parameters, a so-called **profile likelihood** can be created,

$$\mathcal{L}_{\mathbf{a}''_{\max}}(\mathbf{a}'|\mathbf{x}) = \max_{\mathbf{a}''} \mathcal{L}(\mathbf{a}', \mathbf{a}''|\mathbf{x}), \tag{3.15}$$

which is a function of only the parameters of interest and often results in better constrains of them.
In an **extended likelihood**, the condition that the normalization of the probability density distribution $P(x, \mathbf{a})$ is 1 is removed. This is helpful, when the expected total number of counts in a spectrum is not known. An additional term can then be added to the likelihood, which takes the Poisson probability of the total number of counts N into account:

$$P(N|\lambda(\mathbf{a})) = \frac{\lambda^N}{N!} e^{-\lambda}, \tag{3.16}$$

where λ is the expected total number of counts in dependence of $\mathbf{a}$.

A fit of an energy spectrum in the range from E_1 to E_2 shall serve as an example. In this case, a function $f(E, \mathbf{a})$ is constructed, where $\int f(E, \mathbf{a}) \mathrm{d}E$ gives the number of expected counts in the energy range $\mathrm{d}E$ in dependence of the parameter set $\mathbf{a}$ with

$$\mu(\mathbf{a}) = \int_{E_1}^{E_2} f(E, \mathbf{a}) \mathrm{d}E.$$

Given the full energy range is divided into k energy bins $\mathrm{d}E_i$, the likelihood is defined as in Eq. 3.14 with x_i being the number of observed counts in bin $\mathrm{d}E_i$, and $P(x_i, \mathbf{a})$ the Poisson probability (as in Eq. 3.16) of observing x_i given an expectation $\lambda_i(\mathbf{a}) = \int f(E, \mathbf{a})\mathrm{d}E_i$:

$$\mathcal{L}(\mathbf{a}|\mathbf{x}) = \prod \frac{(\int f(E_i, \mathbf{a})\mathrm{d}E_i)^{x_i}}{x_i!} e^{-\int f(E_i,\mathbf{a})\mathrm{d}E_i}. \tag{3.17}$$

Using unbinned data, the transition from the binned case can be made by letting the bin width decrease towards zero, so that each bin $\mathrm{d}E_i$ has 1 count and each bin $\mathrm{d}E_j$ no count. The **unbinned likelihood** can then be written as

$$\begin{aligned} \mathcal{L}(\mathbf{a}|\mathbf{E}) &= \prod_i \frac{(f(E_i, \mathbf{a})\mathrm{d}E_i)^1}{1!} e^{-f(E_i,\mathbf{a})\mathrm{d}E_i} \prod_j \frac{(f(E_j, \mathbf{a})\mathrm{d}E_j)^0}{0!} e^{-f(E_j,\mathbf{a})\mathrm{d}E_j} \\ &= e^{-\mu(\mathbf{a})} \prod_i f(E_i, \mathbf{a}). \end{aligned} \tag{3.18}$$

3.6.2 Least squares estimator

The method of least squares minimizes the squared difference between a set of measured values and the predicted values. With a set of data pairs (x_i, y_i), where the x_i are precisely known and the true values of y_i can be expressed as a function $y_i^t = f(x_i, \mathbf{a})$ in dependence of the parameters $\mathbf{a}$, the squared differences known as χ^2 can be written as:

$$\chi^2 = \sum \frac{(y_i - f(x_i, \mathbf{a}))}{\sigma_i^2}, \tag{3.19}$$

where the squared difference for each data point is weighted according to the Gaussian uncertainty σ_i of y_i. The values for $\mathbf{a}$ which minimize χ^2 is one of the most widely used estimators.

As a note, the least square method is based on the maximum likelihood, assuming a Gaussian uncertainty of y_i. In this case the logarithm of the likelihood can be written as $\ln \mathcal{L} = -\sum \frac{(y_i - f(x_i, \mathbf{a}))}{2\sigma_i^2}$. Hence, a maximization of $\ln \mathcal{L}$ is equivalent to a minimization of χ^2.

3.6.3 Frequentist and Bayesian: Two ways of interpretation

When it comes to the interpretation of the results of an experiment, two fundamentally different ways have been established and are frequently used in the particle physics. Most commonly used in the past is the Frequentist interpretation. Frequentists are interested in the frequency with that a certain value is observed, given a particular model. They do **not** make a statement about the probability of the true value. However, this often gives rise to misinterpretations of the results [98].

On the other hand, the Bayesian interpretation does make a statement about the true value and the probability (credibility) that it assumes a certain value. Though, in order to do this, Bayes theorem needs to be applied, which requires the statisticians to include his own subjective view of what prior information to consider, which previous experiments to trust, which not to trust. Due to the high effort in integrating over large parameter spaces, Bayesian statistics has found more and more application with the advent of Markov chain Monte Carlo methods.

Both ways are mathematically sound and correct. To avoid misinterpretations, it should always be stated precisely what has been done and which prior information has been used.

3.6.4 Frequentist statistics

Frequentist probabilities are defined as the relative frequency of identical experiments giving a particular result under the assumption that a certain model and model parameter values are true. Hence, they make a statement about the probability $P(x|a_0)$, i.e. the frequency distribution of x given a_0. A Frequentist confidence interval is a measure of the information content of an experiment. It does not make a statement about the true value of a, instead it rather covers the true value or it does not. In that regard, a confidence interval is not meant to be used on its own. By repeatedly conducting an experiment, multiple confidence intervals are obtained of which a fraction of α intervals covers the true value of a, where α is the confidence level of the interval. The confidence interval obtained by an experiment is not unique. It depends on the precipe after which it is constructed. Care has to be taken in the construction to ensure that the correct coverage of α is achieved independent of the unknown true value of a. If for a certain set of values for a less than a fraction of α of the intervals cover the true value on average, then this is called ”undercoverage”, which is regarded as problematic. If on the other hand a higher fraction of intervals cover the true value, this is referred to as ”overcoverage” or a ”conservative interval”, which often is accepted although strictly the intervals are not correct confidence intervals.

The above discussed uncertainties of the likelihood estimator span one such confidence interval. The likelihood ratio method directly follows from the classic interval construction by Neyman.

Neyman interval construction

Assuming the frequency distributions $P(x|a)$ are known for all values of a. Then for every value of a an interval can be created so that the probability that x lies within the interval is α: $P(x \in [x_0, x_1]|a) = \alpha$ [99]. Some freedom is left in the choice of the interval. Commonly used intervals are symmetric intervals, where the maximum of $P(x|a)$ is in the middle of the interval, the smallest intervals, which minimize the distance between x_1 and x_0, and the central interval, where the integral over $P(x|a)$ within the interval to the left and right of its maximum is equal to $\alpha/2$. Furthermore, there is the choice whether a two-sided or one-sided interval is created.

Subsequently, after measuring a value x_0, a confidence interval for a is obtained by including every value of a, where x_0 is included in the interval $[x_0, x_1]$. By construction the correct coverage is guaranteed for all a.

Intervals created like this can have a few undesired properties. Especially when introducing physical boundaries to the values of a parameter and the best estimated value is close to, or beyond such a boundary. This can lead to confidence intervals that are partly or even completely contained in the nonphysical range, i.e. the interval is empty if restricted to the physical range. Although this is strictly not a problem as one simply obtained one interval from the fraction $1 - \alpha$ of intervals that do not cover the true value, such a result is rather unsatisfying. Furthermore, if the choice to make a one-sided interval (often in the case of a signal compatible with zero) or a two-sided interval (in the case of a signal observation) is done on the base of the data (”flip-floping”), it can lead to undercoverage. Feldman and Cousins tried to address these problems by making adjustments to the interval creation.

Feldman-Cousins ordering principle

Feldman and Cousins made use of the freedom of choice that remains in Neymans classical interval creation to suggest an alternative ordering principle, on which the intervals $[x_0, x_1]$ are created for each value of a [100]. This principle uses the likelihood ratio

$$R(x) = \frac{P(x|a)}{P(x|a_{\text{best}})}, \tag{3.20}$$

where a_{best} is the estimated best value of a, to find the interval $[x_0, x_1]$ for which $R(x_0) = R(x_1)$ and $\int\limits_{x_0}^{x_1} P(x|a)dx = \alpha$.

Empty confidence intervals are avoided using this ordering principle. Additionally, the transition from a one-sided to a two-sided limit is made automatically, preventing the problem of ”flip-floping”.

Still, in an example of a Poisson process with known background, observing less events than expected from the background will lead to very small intervals, that give a misleading view of the information content of the experiment.

Toy Monte Carlo experiments

In practice, it is not possible to repeat an experiment unlimited times. Thus, frequency distributions are usually determined with the help of Monte Carlo (MC) simulations. The simulations are used to generate toy experiments under the assumption of a range of a values. Each toy experiment is then treated exactly like the acxtual experiment to extract the measured value x.

3.6.5 Bayesian statistics

Bayesian statistic is interested in the probability or the degree of belief in a certain model and its parameters given new and old information obtained in experiments. At the basis, Bayes theorem is taken connecting the conditional probabilities $P(x|a_i)$ of the data given the parameter value a_i and $P(a_i|x)$, the posterior probability of the parameter value a_i given the new information x:

$$P(a_i|x) = \frac{P(x|a_i) \cdot P(a_i)}{P(x)} = \frac{P(x|a_i) \cdot P(a_i)}{\sum P(x|a_i)P(a_i)}. \tag{3.21}$$

$P(x)$ is typically just a normalization. $P(a_i)$ describes the prior knowledge of the parameter a, i.e. how much one beliefs the value a_i is true. With Bayes theorem $P(a_i|x)$ can be extracted, which makes a direct statement about the parameter a by assigning a degree of belief to a range of parameter values.

The prior information can be obtained from former experiments if available. Eq. 3.21 basically gives the prescription for an update procedure of the degree of belief of parameter a with every new information obtained by experiments: The posterior information $P(a_i|x)$ of a former experiment can be entered in the analysis of future experiments as the prior information $P(a_i)$ and will be supplemented with the new information gained.

The choice of prior information is often a point for criticism in Bayesian statistic, because it constitutes a subjective choice of information. The prior is a result of ones personal beliefs, which results of former experiments can be trusted and therefore included as prior information or which results not to trust and hence to exclude. Furthermore, in case no former results are available, there is no other choice than to ”make up” the initial prior information. In such a case it is preferably to at least chose prior information that is weak compared to the new information provided by the experiment. Additionally, when stating the results of the experiment, it is necessary to clearly define the prior information that has been used.

Bayesian credibility intervals

Bayesian credibility intervals are simply intervals that contain a certain fraction of the posterior probability density distribution. The interval, similar to Frequentist confidence intervals, is not unique. In general, it is advisable to always provide the full information obtained by the experiment in form of the full posterior probability density distribution. This allows other experiments to include this information as prior.

Bayes factor

Given are two models $H_{1,2}$, and two parameter vectors $\mathbf{a}_{1,2}$. The Bayes factor B is then defined as

$$B = \frac{P(x|H_1)}{P(x|H_2)} = \frac{\int P(\mathbf{p}_1, H_1) \cdot P(x|\mathbf{p}_1, H_1) d\mathbf{a}_1}{\int P(\mathbf{p}_2, H_2) \cdot P(x|\mathbf{p}_2, H_2) d\mathbf{a}_2}. \tag{3.22}$$

The Bayes factor is a form of hypothesis testing. It makes a statement about how much one model is supported by the data compared to another model. It can be used to reject or accept one model in favor of another one. A popular example where this is often used is when searching for a new process. By calculating the Bayes factor between the signal hypothesis and the null hypothesis without signal the decision can be made to either reject or accept the new process.

In order to find the Bayes factor between two different values of one parameter, the two models $H_{1,2}$ can be chosen as the same model with the parameter of interest fixed at the two different values. The integration in Eq. 3.22 is then done over the remaining parameters of the model.

For an interpretation of the Bayes factor ranges in terms of preference or evidence of one model over another model, Kass and Raftery [101] give the following ranges: 1-3: ”Not worth more than a bare mention”, 3-20: ”Positive”, 20-150: ”Strong”, >150: ”Very strong”.

p-value

A p-value is a form of hypothesis testing of a model without making reference to other models. p-values are defined on the basis of a certain discrepancy variable. A discrepancy variable is a test statistic which measures the goodness of a fit, i.e. how well a model describes the data. One of the most commonly used discrepancy values in this regard is the χ^2 variable, introduced in Sec. 3.6.2. Because the model is assumed, the frequency distribution $P(R|H_1)$ for the discrepancy variable R can be calculated or generated using the toy MC approach. The p-value is a one-sided probability on that frequency distribution, determined as $P = \int\limits_{R>R_1} P(R|H_1) dR$, where R_1 is the observed value. In other words, a p-value is the probability that in another iteration of the experiment, the discrepancy variable will imply a worse agreement (in this case a smaller value) between data and the model prediction. On basis of the p-value one can decide if a model is acceptable or not, and in case none of the models at hand describe the data well enough, it motivates the search for new models.

Given the true model and a correction description of the data fluctuations, the p-value will be uniformly distributed between 0 and 1. In case the model parameters have been estimated with the help of the data, when the p-value will be biased to higher values. In general, the bias becomes small with increasing degrees of freedom, i.e. a large number of data points. The distribution of the p-value assuming a wrong model should look significantly different from a flat distribution, usually peaking at values close to 0. If this is not the case, the discrepancy variable might not be sensitive to the source of disagreement between data and model. A small example: a background spectrum is fit with a function that omits a peak in the spectrum. Hence, in the small range of the peak, a consecutive number of data points are above the expectation estimated by the fit. Apart from that, the fit agrees very well with the spectrum. Using the standard χ^2 as discrepancy value can lead to a p-value signifying good agreement, if the omitted peak is rather weak or the overal spectrum range is large compared to the peak range. The problem here is, that the standard χ^2 is not sensitive to the order of the data points, i.e. runs of fluctuations in one direction. A modified χ^2_{run} variable calculated on the range of consecutive data points that results in the largest χ^2 value, would be better suited as discrepancy variable in such a case, as suggested in [102].

The motivation for p-values to evaluate models can be derived from Bayesian statistics [103].

BAT

The Bayesian Analysis Toolkit (BAT) is a flexible analysis framework based on C++ for data analysis using Bayesian statistics. The toolkit utilizes Markov chains to sample the full posterior probability density distribution in high dimensional parameter spaces. At the same time the one-dimensional space of each parameter is sampled to extract the marginalized posterior probability distributions of each single parameter. It allows formulation of arbitrary models and features common ways of parameter estimation and interval construction based on the multi parameter and one-dimensional posterior probability distributions. Emphasis is put on evaluating model validities and comparing the to different models. The goodness-of-fit is determined using well-established methods, like χ^2 and p-values among other model tests.

BAT is developed by the Max Planck Institute for Physics in Munich and is available at no charge [104].

Markov chain Monte Carlo

The most popular Markov chain Monte Carlo (MCMC) algorithm is the Metropolis algorithm, which is implemented in the BAT framework. MCMC are used to effectively sample posterior probability distributions in high dimensional parameter spaces. Before the introduction of MCMC, the application of Bayesian statistics was only limited to a few trivial cases, where the probability distributions can be calculated analytically.

MCMC employ a random walk to sample the parameter space. At first, a starting point a_i is randomly chosen within the allowed parameter space. Based on a proposal function

$g(a_i, b)$ which depends on the start point a_i, a new point b is proposed. The value of the probability distribution $P(a_i|x)$ and $P(b|x)$ is then evaluated at the point a_i and b. A random variable r is generated between 0 and 1. In case of the inequality $\frac{P(b|x)}{P(a_i|x)} \geq r$ then the next point a_{i+1} is set to b, otherwise it is set to a_i. By obtaining a_{i+1} the next iteration step begins. Several of such chains can run in parallel, each with a separate starting point. The proposal function g is first set to a flat function in the allowed parameter space, but later optimized during a pre-run so that the acceptance ratio of new points is in a desired range. The pre-run furthermore ensures that each of the Markov chains converges towards the distribution, which is sampled.

3.7 Modern double beta decay experiments

This section gives a quick overview of current double beta decay experiments, their detector setup and results in terms of $0\nu\beta\beta$-decay. Because this work is done in the framework of the GERDA experiment, it will be discussed in separate chapter in much more detail.

3.7.1 Majorana

The MAJORANA collaboration is currently operating a demonstrator experiment in the Sanford Underground Research Facility in South Dakota [105]. This demonstrator is meant to explore and demonstrate the techniques necessary for future $0\nu\beta\beta$-decay experiments and, like GERDA employs germanium semi-conductor detectors enriched in the double beta decay isotope ^{76}Ge.

The demonstrator houses in total 35 point contact HPGe[7] detectors with a combined mass of over 40 kg in a modular setup consisting of two cryostats. The cryostats are made from ultra-pure electroformed copper. The shielding comprises an inner layer of electroformed copper, an outer layer of oxygen-free high thermal conductivity copper, a layer of high purity lead and a layer of borated polyethylene. Up to the layer of lead, the setup is enclosed in radon exclusion box which is flushed with nitrogen. Scintillator panels are utilized as active muon veto. The first data set were taken in the second half of 2015 and the early months of 2016 with one of the cryostats. After all data selection cuts a background level of 23^{+13}_{-10} cts/(3.1 keV·kg·yr) was achieved with an exposure of 3.03 kg·yr. No events have been observed in the region of interest and the demonstrator could derive a limit of $3.7 \cdot 10^{24}$ yr for the $0\nu\beta\beta$-decay at 90% C.L.

The demonstrator makes use of the powerful pulse shape discrimination (PSD) capabilities provided by the point contact HPGe detectors. The PSD is able to reject more than 90% of multi-site events with a single-site survival efficiency of 90% and to reduce the Compton background in the region of interest by 50%, as measured with a ^{232}Th calibration source. Additionally, the PSD is used to reject events caused by alpha contaminations on the surface of the detectors.

The goal of MAJORANA is to achieve a background level as low as or lower than 1 cts/(4 keV·kg·yr), which is necessary to probe the parameter space of the inverted hierarchy neutrino mass. To reach this goal, improvements to the PSD and localization and removal of γ-ray background sources within the cryostats shall help.

---

[7] High Purity Germanium

3.7.2 KamLAND-Zen

KamLAND-Zen is the direct successor of the KamLAND experiment and utilizes the already existing infrastructure [106]. A scheme of the KamLAND-Zen detector can be seen in Fig. 3.5. The setup consists of a large 13 m diameter spherical outer balloon which is contained in a vessel and filled with 1 kt liquid scintillator. In the center is another spherical balloon with a diameter of 3.08 m made out of 25 μm thick transparent nylon film. The inner balloon is filled with 13 t of Xe-loaded liquid scintillator. The xenon is enriched in ^{136}Xe to 90%. Almost 2000 PMTs are installed at the inner wall of the vessel to read out the scintillation light. The light produced within the outer balloon serves as active background veto. By measuring the arrival time differences of the scintillation light at the different PMTs, the event position can be reconstructed with a resolution of 2 cm.
In its first phase, KamLAND-Zen set a limit of $1.9 \cdot 10^{25}$ yr at 90% C.L. on the half-life of the $0\nu\beta\beta$-decay of ^{136}Xe. The sensitivity was largely limited by an unexpected background peak of ^{110m}Ag close to the region of interest. Hence, the end of phase 1 was followed by an 18 month purification campaign as an attempt to reduce the ^{110m}Ag contamination among other background sources. Phase 2 took data from December 2013 to October 2015.

The final exposure of phase 2 amounted to 504 kg·yr given the complete volume of the inner balloon. The ^{110m}Ag background was found to be reduced to less than 10%. In the second half of phase 2, no ^{110m}Ag was observed, which was assumed to have sunken the bottom of the inner balloon. The background of ^{214}Bi on inner balloon turned out to be one of the dominant sources. Due to the worse energy resolution compared to germanium detectors, the background in the region of interest is not flat, additionally the tail of the $2\nu\beta\beta$-decay needs to be accounted for. Hence, the background modeling is very important for scintillator based experiments. To constrain the different components, the background study uses also events from outside the inner 2 m volume. The data selection cuts include cuts on the reconstruction vertex (which has to be within a 2 m radius to reduce the ^{214}Bi background), muon induced events and delayed coincidences by Bi-Po and reactor anti-neutrino events.

With the phase 2 data, a limit of $9.2 \cdot 10^{25}$ yr at 90% C.L. could be set, while the sensitivity was estimated with $4.5 \cdot 10^{25}$ yr. The combination of phase 1 and phase 2 data results in a limit of $1.07 \cdot 10^{26}$ yr at 90% C.L., which can be converted to a limit of $\langle m_{\beta\beta} \rangle < (61 - 165)$ meV on the effective Majorana neutrino mass, using common NME calculations and a g_A of 1.27.

The next upgrade will introduce a new larger more radio-pure inner balloon loaded with a total mass of 800 kg of Xe.

3.7.3 EXO-200

The EXO-200 detector is a time projection chamber (TPC) 44 cm high with a diameter of 40 cm located in the underground laboratory at the Waste Isolation Pilot Plant in New Mexico [109, 110]. The chamber is filled with liquid xenon enriched in ^{136}Xe to 80%. The detector is able to simultaneously read out the scintillation light by avalanche photodiodes and the ionization charges via a cathode in the center of the chamber. This information is used to reconstruct the energy as well as the position with a resolution of a few millimeters of the event. The position information can be used to discriminate between single-site and multi-site events, i.e. $0\nu\beta\beta$-decay events and γ-ray background. The chamber is shielded

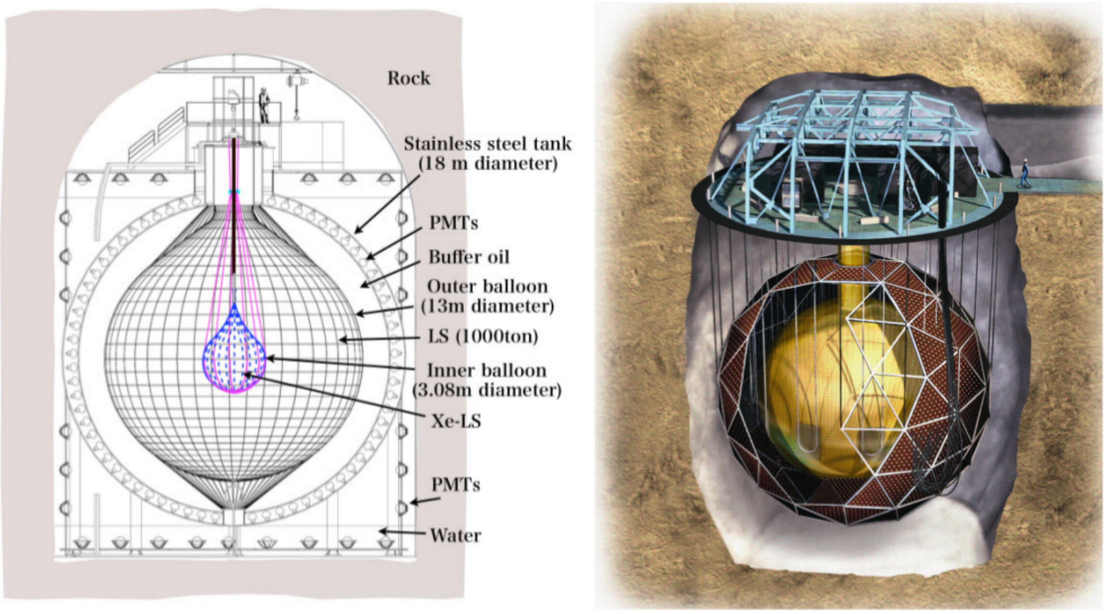

Figure 3.5.: Schemes of the KamLAND-Zen setup [107] (*left*) and the SNO+ setup [108] (*right*).

by 50 cm HFE-7000 cryofluid at 167 K inside a copper croystat, 25 cm of lead and an active muon veto consisting of scintillator panels on 4 sides of the clean room.

The physics data set was taken from September 2011 to September 2013. The fiducial volume cut includes 76.5 kg of ^{136}Xe, which results in an exposure of 100 kg·yr. The background in the region of interest amounts to $(1.7 \pm 0.2) \cdot 10^{-3}$ cts/(keV·kg·yr), where the limiting background sources are the primordial decay chains of ^{232}Th and ^{238}U on material surrounding the liquid xenon volume and ^{137}Xe from the activation of ^{136}Xe by muons.

The experiment could set a limit on the $0\nu\beta\beta$-decay half-life in 2014 at $1.1 \cdot 10^{25}$ yr (90% C.L.), while the sensitivity was given as $1.9 \cdot 10^{25}$ yr [111].

For the future, 5 t liquid xenon TPC experiment with the name nEXO was proposed as the successor of EXO-200 [69]. The bigger xenon volume results in a much better self-shielding effect of the xenon volume. Additionally, improved low noise electronics are expected to improve the energy resolution.

3.7.4 SNO+

The SNO+ experiment is a multi-physics experiment operated in the SNOLAB in Vale's Creighton mine in Sudbury, Canada [91]. The experiments main goal is to search for the $0\nu\beta\beta$-decay of ^{130}Te. Other physics topics that SNO+ is able to contribute include the observation of geoneutrinos, constraints of the neutrino oscillation parameters with reactor anti-neutrinos, the measurement of low energy solar neutrinos, the detection of supernova neutrinos and other exotic physics.

SNO+ is the successor of the SNO experiment and reuses parts of the detector infrastructure. This includes a spherical acrylic vessel with 6 m radius, which will be filled with 780 t of the liquid scintillator LAB[8]. LAB was chosen due to its stability, radio-purity

---

[8] Linear Alkylbenzene

and advantageous optical properties as a scintillator. To reduce the cosmogenic activation time, the liquid scintillator is produced in Quebec relatively close to SNOLAB. Furthermore, LAB was purified to a level of 10^{-17} g/g$_{\mathrm{LAB}}$ for ^{238}U and ^{232}Th contaminations and to remove metals and optical impurities, like gases and residual water.

The scintillation and Cherenkov light is detected by over 9000 PMTs, which cover the inner wall of a stainless steel structure with 8.9 m radius. To adjust the wavelength of the scintillation light to the absorption spectrum of the PMTs, a wavelength shifter is added to the liquid. 7 kt of ultra-pure water are filled in between the acrylic vessel and the steel structure, shielding the scintillator from the rock and the PMTs. The vessel is hold down and in place by a system of ropes, because LAB is lighter than water. Fig. 3.5 shows a drawing of the SNO+ detector on the right.

The physics program of SNO+ is planned in a three phase approach: First the water phase, currently ongoing, second the LAB phase, and third the $0\nu\beta\beta$-decay phase (5 years). In the $0\nu\beta\beta$-decay phase the liquid scintillator will be loaded with 2.3 t of natural tellurium, while still remaining a good stability and optical properties. The large natural abundance of ^{130}Te of 34% does not require to enrich the material. Additionally, the long $2\nu\beta\beta$-decay half-life of ^{130}Te is advantageous, because it will pose a background in the region of interest due to the relatively large energy resolution of 10%. The position of particle interactions inside the vessel can be reconstructed with an average position resolution at center at the Q-value is 15 cm by evaluating the PMT event time profile. This allows to set a fiducial volume cut, only selecting the inner 20% of the acrylic vessel volume. A large suppression of external background from Th and U contaminations on the acrylic vessel surface, the water shielding, the rope system and other components is expected from this.

The biggest background for $0\nu\beta\beta$-decay analysis is expected from internal U and Th contaminations, mostly from Bi-Po decays, and the elastic scattering of ^{8}B neutrinos, as well as the $2\nu\beta\beta$-decay.

Chapter 4

The Gerda experiment

4.1 Introduction

The GERmanium Detector Array (Gerda) experiment was proposed in 2004 [112] as the successor of the Heidelberg-Moscow experiment (HdM). Gerda uses germanium detectors to search for the $0\nu\beta\beta$-decay of ^{76}Ge. As a first step, the experiment aimed to prove or disprove the controversial claim of observation made by a subgroup of HdM [64].
The ultimate goal of Gerda is to push the half-life limit of the decay beyond the order of 10^{26} yr and to pioneer new strategies to reduce the experimental background by 2 to 3 orders of magnitude. In that regard, Gerda followed the novel idea suggested in [75] to operate germanium detectors naked in a cryogenic liquid. This brings two advantages: Firstly the liquid serves as the cooling medium for the detectors, whose operation temperature is typically at about 90 K. Secondly, the detectors are shielded by the ultra-pure liquid from radiation originating from outside the cryostat, but also from contaminations on components of the detector array itself, most dominantly γ-radiation. Initially, liquid nitrogen was chosen for this purpose. However, liquid argon (LAr) was selected instead, because it additionally functions as a scintillator bringing the advantage that background interactions inside the liquid can be vetoed actively with the help of photo detectors. Additionally, due to the higher nuclear charge, LAr is better suited to shield from radiation than liquid nitrogen.
Phase I (PI) of the experiment came to conclusion in May 2013 with the result, that the claim by the HdM subgroup could be rejected with high probability. For this purpose, about 20 kg·yr of data with a background index of 10^{-2} cts/(keV·kg·yr) in the region of interest had been collected during a run time of about 460 days.
After the success of the PI results, the work on the Phase II (PII) upgrade of the detector system started, followed by another extensive commissioning phase. The big goal of PII is to reduce the background index by another order of magnitude to 10^{-3} cts/(keV·kg·yr). PII is projected to collect 100 kg·yr of data within three years and push the half-life sensitivity for the $0\nu\beta\beta$-decay of ^{76}Ge to 10^{26} yr.
The means to reduce the background are threefold:

- Employing lighter and more radio-pure material close to the detectors, e.g. new detector holder design
- Instrumentation of the LAr sctintillator with a light read out upgrade to the cryostat
- Improvements in pulse shape discrimination (PSD) by shifting the focus on new small read-out electrode detectors of the Canberra BEGe[1] design

In addition to the background reduction, the germanium source mass has been increased by a factor of 2, due to the inclusion of 30 newly produced BEGe detectors.
The following sections will give an overview of the detector setup and each major component. In Sec. 4.3 the PSD techniques of Gerda are presented. Sec. 4.4 and 4.5 the data and analysis of PI and PII are discussed. An introduction of the data processing chain is given in Sec. 4.6.

4.2 General detector setup

The construction of the setup was finished in 2009 in the Laboratori Nazionali del Gran Sasso [113]. The detector setup can be seen in Fig. 4.1. The main components of Gerda

---

[1] Broad Energy Germanium

give a good insight in the background reduction strategies of the experiment. Hence a short discussion of each component is given in the next sections. For an extensive description of the detector setup, refer to [2, 114].

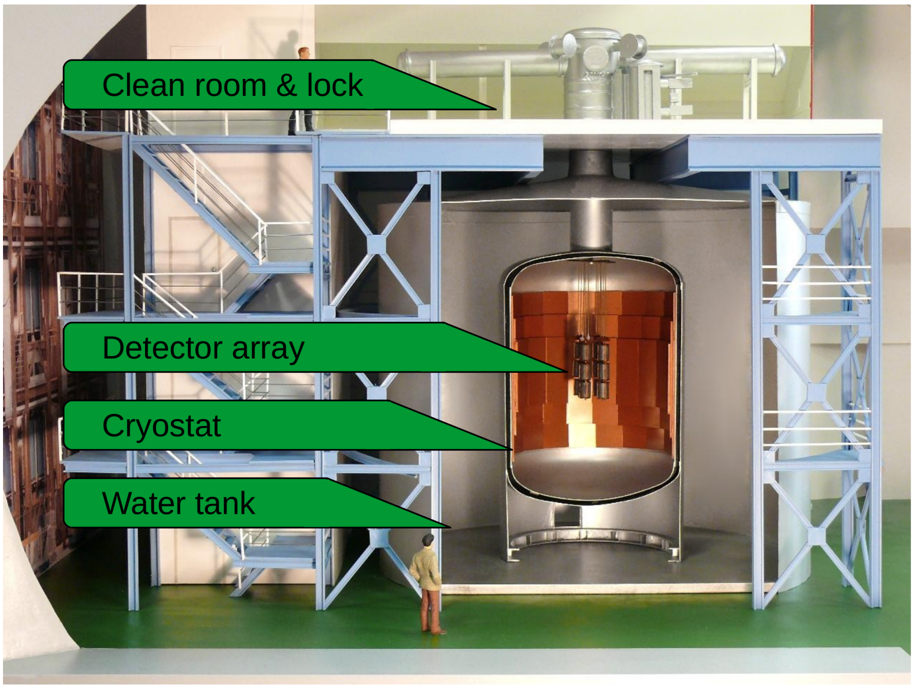

Figure 4.1.: Setup of the GERDA experiment situated in the LNGS. Labeled are the main components. For a description of the setup refer to the text. Picture taken from [115].

4.2.1 LNGS

The Laboratori Nazionali del Gran Sasso (LNGS) [113] of the Istitute Nazionali di Fisica Nucleare (INFN) is one of the worlds largest underground laboratories in the field of nuclear and astroparticle physics, established in 1989. It is situated in the center of Italy, close to the village of Assergi near the Gran Sasso mountain. The surface facilities provide offices, laboratories and workshops on an area of 23 acres. The underground laboratory can be accessed via a 10 km long freeway tunnel that connects the towns of L'Aquila and Teramo.

The laboratory is directed at experiments that require an ultra-low background environment. The 1400 m of rock above the laboratory provides about 3500 m of water equivalent shielding from cosmic radiation. This reduces the muon flux by about 6 orders of magnitude and the neutron flux by 3 orders of magnitude compared to the surface. Several neutrino, dark matter and astroparticle physics experiments are housed in the three 100 m long, 20 m wide and 18 m tall main experimental halls. Among these are for example XENON1T, CUORE, C0BRA, LUNA, BOREXINO and GERDA. GERDA is located in Hall A of the underground laboratory.

4.2.2 Clean room

The class 10,000 clean room is located on top of the experiment. It includes a glove box for the handling of germanium detectors in a nitrogen atmosphere and a lock system to insert the detector array into the cryostat.

4.2.3 Water tank and muon veto

The stainless steel water tank with a diameter of 10 m and a height of 8.90 m is filled with 590 m^3 of radioactively ultra pure water. It shields the inner detector parts from radiation from outside, especially γ-rays and neutrons. Furthermore, the water tank is lined from the inside with reflective VM2000 foil and instrumented with 66 photomultiplier (PMT) that detect and veto the Cherenkov light from muons passing through the water. Additionally five diffuser balls are located in the water tank, that feature an LED to test the PMTs with controlled light pulses. The neck of the tank with the lock system creates a dead zone for the water Cherenkov detector. Therefore an additional 36 plastic scintillator panels are placed in three layers on top of the clean room, allowing to also veto muons coming from straight above.

The trigger condition for the water Cherenkov veto requires that at least 5 of the PMTs detect a signal within 60 ns. Each PMT has an efficiency of about 80% to detect a single photon. The trigger of the scintillator panels requires a triple coincidence by the muon passing through the three layers. The triggers of the combined system requires either one of the triggers of both separate systems. The combined muon veto has a muon detection efficiency of 99.9% and reduces the muon induced background in the region of interest to a level of 10^{-5} cts/(keV·kg·yr) [116].

4.2.4 LAr cryostat

The double walled stainless steel cryostat filled with 64 m^3 LAr is placed inside the water tank. At the inner wall of the cryostat a copper shield is mounted, consisting of 16 t of radioactively pure copper plates with a combined thickness of 6 cm at the center and 3 cm at the top and bottom.

The LAr is at a temperature of about 90 K and keeps the germanium detectors at their operation temperature. It provides an additional layer of passive shielding. LAr has a density of 1.4 $\mathrm{g/cm}^3$ and atomic number of 18. This results in an attenuation length of about 12 cm for 1 MeV γ-rays or 18 cm for 2 MeV γ-rays (based on cross section data for photoelectric effect, incoherent scattering and pair production from [83]).

The central LAr volume with a diameter of 75 cm and 3 m height is enclosed by a 30 μm thick copper foil. This so-called radon shroud prevents the radon emanated from the cyostat wall to reach the germanium detector array in the center by convection.

Unfortunately, an unexpected high concentration of ^{42}Ar was found in the cryogenic LAr itself. ^{42}Ar is radioactive with an half-life of 33 yr, however it only emits a beta particle with an end point energy of 600 keV. A bigger problem is posed by its short lived ($T_{1/2} = 12\,\mathrm{h}$) daughter nuclide ^{42}K. The decay of ^{42}K has a Q-value of 3.5 MeV and can add substantially to the background in the region of interest of the experiment. Therefore, the collaboration made big effort during the commissioning phase of the experiment to estimate and mitigate the ^{42}K borne background, which is discussed further in the next section.

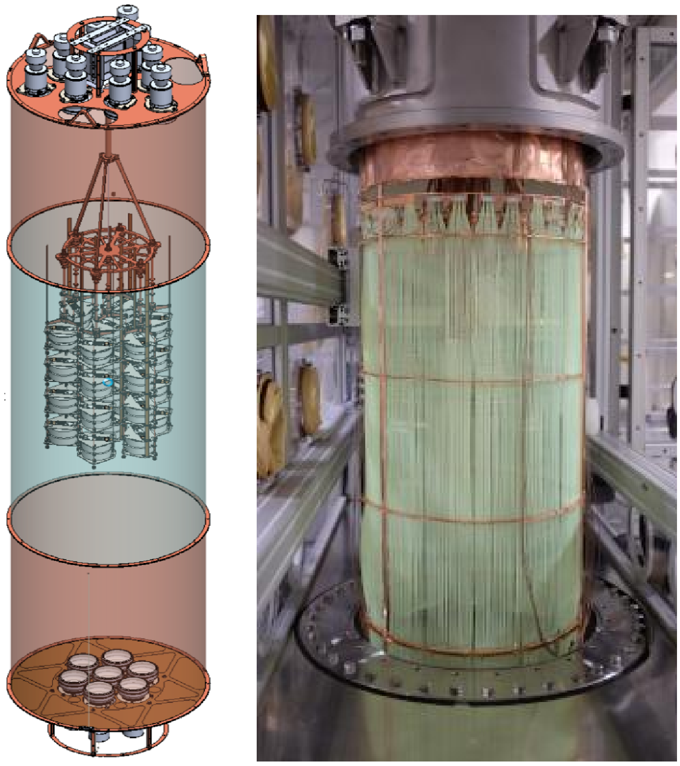

Figure 4.2: *Left:* Schematic of the LAr veto system. The veto consists of nine and seven PMT above and below the detector array, respectively, that are each surrounded by a copper cylinder which is lined with reflective foil and TPB. In the middle, the detector array is enclosed by a shroud of TPB coated fibers, that are read out by SiPMs on both ends. The detector strings are contained in transparent TPB coated nylon minishrouds. *Right:* Photo of the middle section of the LAr veto, showing the top copper cylinder and the fibershroud.

LAr is a scintillator, emitting light with a wavelength of 128 nm. A light read out instrumentation to actively veto particle interactions in the LAr is first introduced as part of the PII upgrade program and discussed below.

4.2.5 LAr veto

The final design of the LAr veto system was the result of a large Monte Carlo campaign. It consists of a twofold redundant light read out system, which is shown in Fig. 4.2. At the top and bottom of the central LAr volume, nine respectively seven PMT are mounted. They are surrounded by two 60 cm high thin copper cylinders that are lined with a reflective Tetratex foil and the wavelength shifter TPB[2]. The two copper cylinders close up a central volume with a height of 1 m on both sides. The central volume includes the detector array and is surrounded by 810 fibers also coated with TPB. The fibers are read out by SiPM[3] arrays. The copper minishrouds that were used in PI had to be replaced with transparent, TPB coated nylon minishrouds, so that the scintillation light from within the array is not blocked off. The performance of the LAr veto system has been studied extensively with MC simulations and in an experimental test setup, called LArGe. For more information see Sec. 4.5.1.

4.2.6 Detector array

The germanium detector array is the heart of the experiment. The detectors are positioned in light holders that are attached to several strings. The modularisation allows to veto

---

[2] Tetraphenyl butadiene, shifts the scintillation light of LAr with a wavelength of 128 nm to a wavelength of 425 nm

[3] Silicon photomultiplier

coincidences between two or more detectors. This makes use of the fact that $0\nu\beta\beta$-decays mostly deposit energy in only one detector. On the other hand, background decays often cause energy depositions in more than one detector, especially due to multiple γ-rays emitted by one decay or due to Compton scattering.
The configuration of the detector array changed over time and varies between PI and PII.

4.2.7 Phase I detector array

The twin lock system of PI allowed to employ one arm with three strings with three detectors each and another arm with only one string, initially equipped with two detectors. The detector holders are mainly constructed from low mass and highly radioactively pure copper (80 g), with small components made from silicon. This is essential to remain an ultra low background from sources close to the detectors. Additionally, the detector needs to be electrically insulated from the holder structure, which is realized with PTFE[4] components. The electrical read-out contact is achieved with a conical copper piece, which is pressed onto the detectors p^+ contact by a silicon spring.
The detectors employed in PI are semi-coaxial p-type detectors, refurbished from previous experiments. These include five enriched detectors from the HdM experiment (ANG1-5) and three enriched detectors from the IGEX experiment (RG1-3). Three natural detectors from the GENIUS Test Facility (GTF32/45/112) are also included to increase the detector anti-coincidence veto capability and cross-check the spectrum from the enriched detectors. The masses and ^{76}Ge fraction are given in Tab. C.1 in the Appendix. The positions of the detectors in the full array are shown in Fig. 4.3.

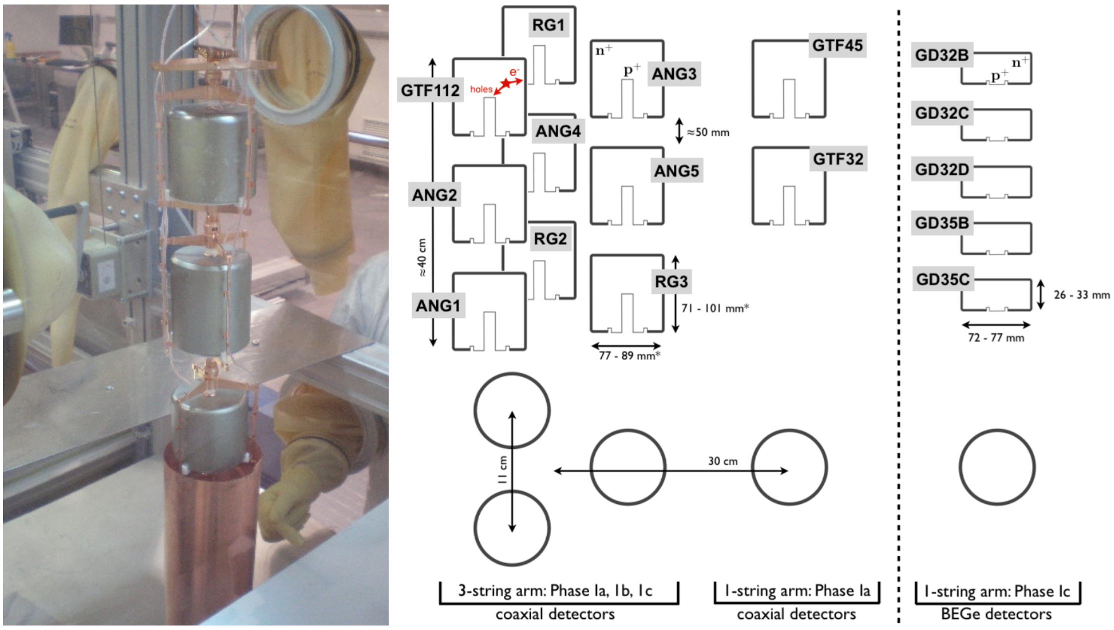

Figure 4.3.: *Left*: String 1 of the PI detector array. The string is being inserted in the copper minishroud, which can be seen at the bottom. *Right*: A scheme of the detector array with labeling of each detector.

After six months of data taking, the detectors on the one-string arm were removed and replaced one month later with five newly produced BEGe detectors for the remainder of

---

[4] Polytetrafluoroethylene

PI, in order to explore their long term stability in the LAr environment for future use in the second phase of the experiment. The production and advantages of the BEGe detectors are discussed in Sec. 4.2.8.

Each detector string is individually surrounded by a 60 μm thick coppershroud, referred to as "minishroud". This prevents the positively charged ^{42}K ions from the ^{42}Ar decays to get caught in the electrical field of the detectors and drift towards them. The minishroud can be seen at the bottom of Fig. 4.3, left side.

4.2.8 Phase II detector array

In PII, the detector array additionally holds 30 new enriched BEGe detectors, corresponding to an increase of germanium mass of 20 kg. The array structure was re-designed to be able to hold the increased weight, now split among seven strings. The full array can be seen in Fig. 4.4.

Also shown are the new detector holders. Most of the copper components have been replaced with mono crystalline silicon, making them even lighter and more radio-pure. Originally it was planned that each module holds two BEGe detectors back to back, bringing them closer together, which improves the anti-coincidence veto and reduces the material per detector even more. However, during commissioning runs, some of the BEGe detectors positioned with their groove pointing up showed problems with leakage current. It is assumed that this is caused by dust that had fallen in the groove during the mounting of the detector pairs. As a countermeasure, all but six back to back detector pairs were separated and instead mounted similar to the semi-coaxial detectors. The very front end (JFET[5], feedback resistor and capacitor) is positioned very close to the detectors on a silicon holder board. The contacts to the electrodes of the detector are now achieved with wire bonds. The flexible signal and high voltage (HV) cables run along the side of the modules to the pre-amplifier, which is located about 50 cm above the top of the array. All the materials for cables, electronics and holder structure have been screened before production to ensure that they satisfy the requirements of radio-purity.

Because of the increased size of the array, the lock had to be replaced by a new lock with a wider diameter of 50 cm. It is accessible from within a glove box, so that detectors as well as the LAr veto can be assembled in dry nitrogen atmosphere and lowered into the cryostat together.

BEGe detectors

The 30 new BEGe detectors have been produced in close collaboration with Canberra [90]. They are the primary detector choice for PII of GERDA. The detectors are significantly smaller than the semi-coaxial detectors, weighting between 400 and 800 g. They are made from p-type germanium. The low capacity and therefore low noise point like p^{+} signal contact results in an excellent energy resolution of typically about 3 keV full width at half maximum at $Q_{\beta\beta}$.

The charge collection especially in the corners is improved by the impurity profile in the detector, which is responsible for the transport of charge carriers in most parts of the detector. The majority of the signal though, is produced close to the p^{+} contact, where the charge carriers are collected due to the applied electrical potential. This leads to a very uniform signal for single-site bulk events, which is advantageous for the discrimination

---

[5] Junction Field Effect Transistor

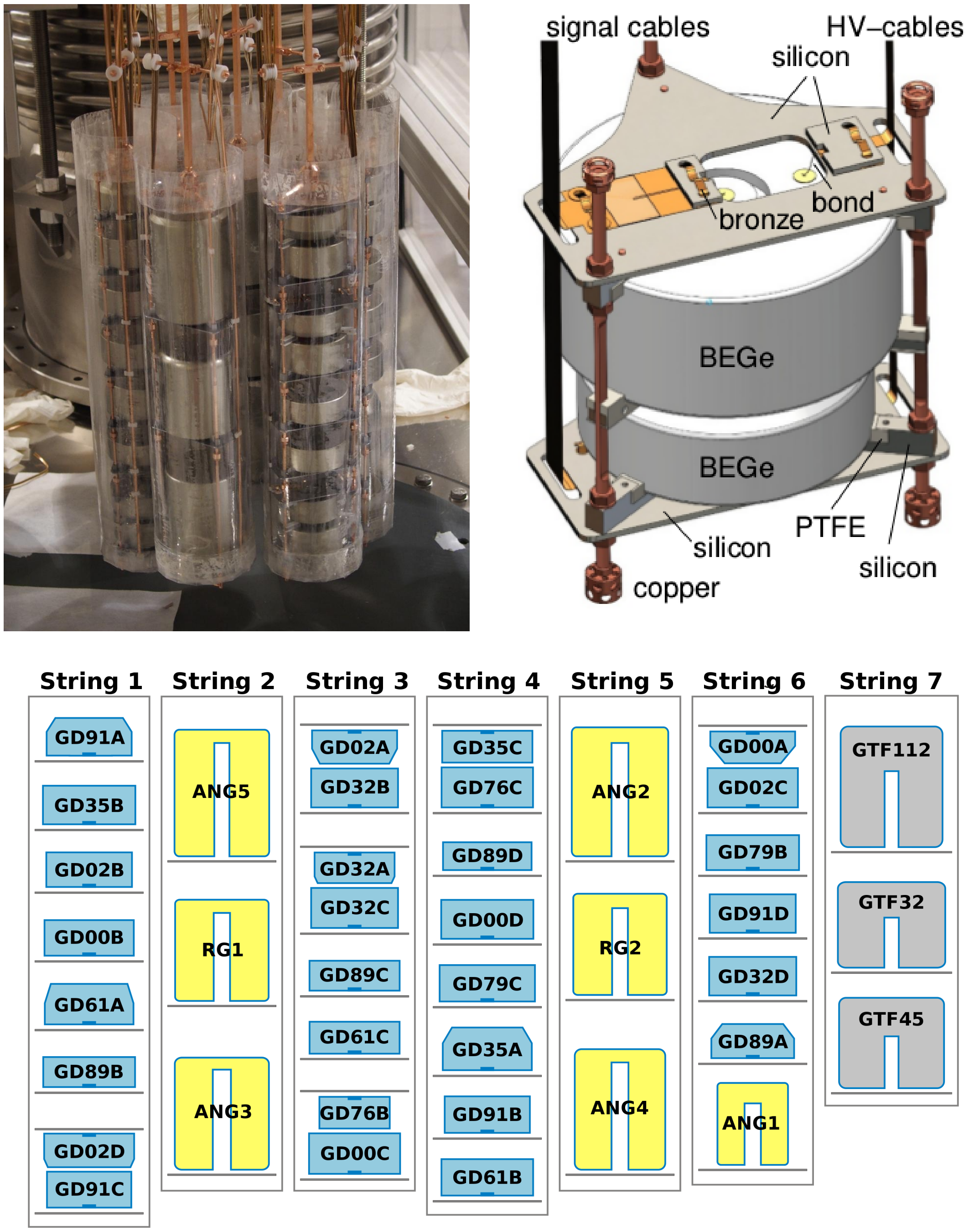

Figure 4.4.: *Top left*: PII detector array. The seven detector strings are enclosed in transparent nylon minishrouds. *Top right*: A scheme of the PII detector holder. *Bottom*: A scheme of the detector array, with labels of the detector names. String 7 is placed in the middle of the array, surrounded by the other 6 strings. BEGe detectors are filled in blue, enriched semi-coaxial detectors in yellow and natural semi-coaxial detectors in grey.

between single-site and multi-site events or bulk and surface events with the help of pulse shapes.

Production

The production and characterisation of the detectors was thoroughly planned to maximize the material yield and minimize the exposure to cosmic radiation [117]. The natural germanium was first enriched in 2005 at the Svetlana Department of the Joint Stock Company ”Production Association Electrochemical Plant” in Zelenogorsk in Russia. The result was 53.4 kg of germanium oxide corresponding to 37.5 kg enriched germanium. From 2006 to 2010, the material was stored underground in the HADES laboratory in Mol, Belgium. In a next step, the material was reduced to metallic germanium and purified via zone refinement to 6N[6] at PPM Pure Metals GmbH in Langelsheim and later further zone-refined to 11N at Canberra Industries Inc. in Oak Ridge. From the purified material, Canberra then grew two batches of crystal ingots. The first two ingots were grown in 2011 out of which seven crystal slices were cut. In the second batch seven more ingots were grown and cut into 23 crystal slices in 2012. The production of the slices was optimized in order to use as much of the raw material as possible. In total, the mass yield of all slices was 20.8 kg.

The slices were converted to BEGe detectors at Canberra Semiconductors N.V. in Olen, Belgium. Out of the 30 slices, 29 detectors could be produced that met the requirements of the collaboration on energy resolution, stable operational voltage and leakage current. The remaining detector (GD02D) was not able to reach full depletion voltage, due to an unsuitable impurity concentration. It was still deployed in GERDA with the option to exclude it from the analysis.

After the production chain, the 30 detectors were transported to the HADES underground laboratory to start a characterisation campaign, to determine important detector parameters like the energy resolution and the active volume. Furthermore, the pulse shape discrimination capabilities were tested.

The transportation of the germanium from one site to the next was done in a big container on truck or ship. To minimize the activation of the material, it was surrounded by a 14.5 t steel cylinder. Additional salt water tanks were used to fill out the empty space between the steel cylinder and the container roof. A reduction factor of 20 and 30 for the production of ^{68}Ge and ^{60}Co atoms inside the germanium could be reached with this shielding.

The complete history of processing steps, transportation and characterisation of the detectors was tracked in a database. The expected number of atoms of ^{68}Ge and ^{60}Co by cosmic radiation could be calculated from this database at any given time. As a result, the expected background index from these nuclides at $Q_{\beta\beta}$ is $1.8 \cdot 10^{-4}$ cts/(keV·kg·yr) before PSD and below 10^{-5} cts/(keV·kg·yr) after PSD. Hence, their contribution to the total background index of PII is negligible.

4.3 Pulse shape discrimination

Pulse shape discrimination (PSD) is a powerful tool to distinguish the signal from $0\nu\beta\beta$-decays from background events, especially from high energetic γ-rays and surface contam-

---

[6] A purity specifications of 6N, or 6-nines, refers to a purity of 99.9999%, or 1 ppm. 11N then corresponds to a purity of 99.999999999%

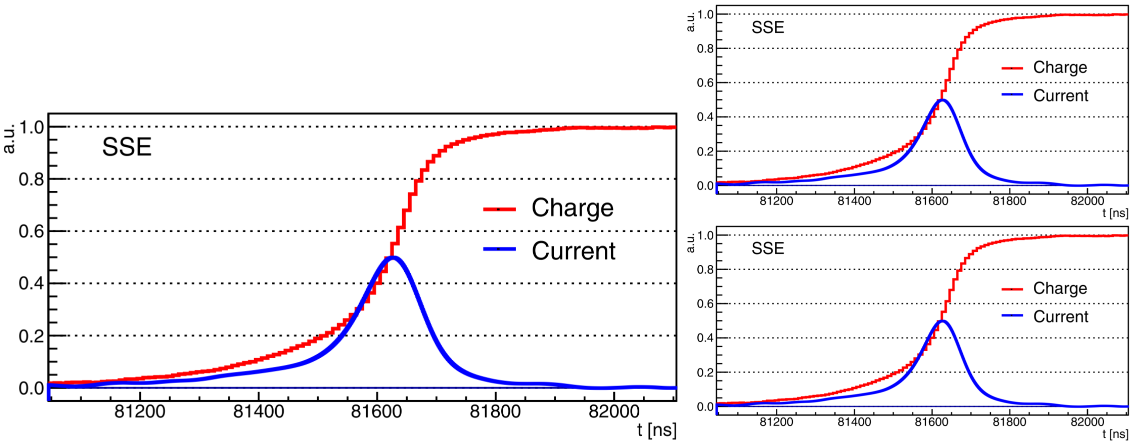

Figure 4.5.: *Left*: Enriched germanium oxide. *Top right*: Germanium ingot. *Bottom right*: Germanium diode.

inations. A detailed documentation of the PSD techniques of GERDA can be found in [118].

$0\nu\beta\beta$-decays are dominantly of single-site character. The range of 1 MeV electrons in germanium is about 1-2 mm [86]. Hence the energy depositions of the electrons from $0\nu\beta\beta$-decay of ^{76}Ge are typically constrained to a small volume of less than 8 mm^3. Only one localized charge cloud is created inside the crystal. Exceptions can be caused by the emission of bremsstrahlung by one or both of the electrons.

High energetic γ-rays on the other hand are very likely to either scatter inside the crystal or to convert into an electron-positron pair. In both cases, energy can be deposited in two (or more) distinct volumes of the crystal, resulting in two separate charge clouds.

While each charge cloud drifts along the electrical field lines, a current signal is induced on the contacts of the detector. A single charge cloud typically induces a peak-like current signal. The current signal from multiple charge clouds is the superposition of the signal from each charge cloud separately.

4.3.1 PSD for BEGe detectors

The BEGe geometry provides a big advantage regarding PSD. The current signal induced on the p$^+$ contact is mostly generated from holes drifting in the region with a high gradient in the weighting potential, i.e. in the region close to the p$^+$ contact. Other than in this region, the weighting potential is very homogeneous, which is why the electrons that drift towards the n$^+$ contact barely contribute to the signal. The holes approach the p$^+$ contact on similar paths largely independent of their origin. Hence, all single-site pulses have approximately the same shape and the current pulse amplitude only depends linearly on the deposited energy. The parameter A/E, where A is the amplitude of the current pulse and E the deposited energy, is therefore a constant for all single-site pulses like they are expected from $0\nu\beta\beta$-decays.

Three different types of events can lead to a divergent A/E parameter, an example pulse shape for each can be seen in Fig. 4.6:

- **Multi-site events**: In the case of a multi-site event, the current pulse is separated into two peaks by the different drift time of both charge clouds. If both contributions

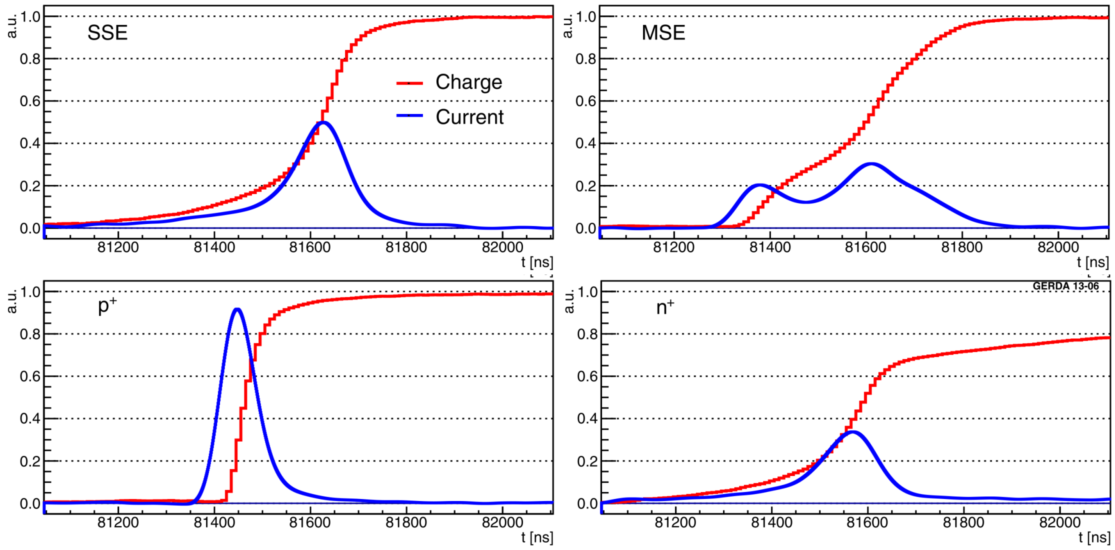

Figure 4.6.: Simulated charge (red) and current (blue) pulses of a BEGe detector for a charge cloud generated in the bulk of the detector (*top left*), at two distinct locations in the bulk of the detector (*top right*), close to the p$^+$ contact (*bottom left*) and close to the n$^+$ contact (*bottom right*) [118].

are not overlapping, then A is simply the amplitude of the current pulse generated by the larger energy deposition. In any case, A/E is lower than for a single-site pulse. Hence, rejecting events with a low A/E parameter will significantly reduce the multi-site background induced by highly energetic γ-rays.

- **n$^+$ surface events**: The electrical field disappears outside of the active volume. Holes created in the dead layer can only reach the active volume by diffusion, a comparatively slow process. Hence, the resulting current pulse is broader albeit with a lower amplitude and consequently a lower A/E parameter than for bulk events. In addition, some of the free charges can recombine before reaching the active volume, which results in a decrease of measured energy. Background events that are affected by this are mostly β-decays of surface contaminations.

- **p$^+$ surface events**: The dead layer at the p$^+$ contact is much thinner in the order of a few hundred μm so that surface β and even α-decays will be able to penetrate the active volume of the detector. The charges will be created in a very high gradient of the weighting potential. In this case, both electrons and holes contribute to the charge pulse, which consequently rises very fast. The amplitude of the current pulse and thus also the A/E parameter is much higher than for bulk events. Thus a high A/E cut is used to reject p$^+$ surface background.

The calibration of the A/E parameter is done with the data from calibration runs with a ^{228}Th source. The goal is to determine the $0\nu\beta\beta$ signal efficiency and the background rejection for a given A/E cut. The ^{208}Tl double escape peak functions as a proxy for the $0\nu\beta\beta$ signal as it mostly constitutes of single-site events. On the other hand, the single escape peak and the full energy peak are dominated by multi-site events and can be used as background sample. In addition, pulse shape simulations are used to study the influence of the high A/E cut on the signal efficiency and estimate systematic uncertainties for the

low cut stemming from the different bremsstrahlung probabilities between double escape events of ^{208}Tl and the $0\nu\beta\beta$ signal process.
Double escape events of ^{208}Tl are not homogeneously distributed in the detector, because the photons have a higher chance to escape when the interaction happened close to the surface. Because of this, the signal efficiency is additionally cross-checked with $2\nu\beta\beta$ events in the physics data and events from the Compton continuum in calibration data. The latter is also used to correct a small energy dependence of A/E. A very good agreement is found between physics and calibration data. The small remaining differences are considered in the systematic uncertainties.
The A/E cut is adjusted so that a signal efficiency of about 92% is reached. Given this cut, the surviving fraction of the single escape peak is about 16%. The pulse shape discrimination based on A/E was successfully tested in PI with the first four BEGe detectors. In a 400 keV region around $Q_{\beta\beta}$, only 7 out of 40 events survive the A/E cut. This reduced the background index to $0.007^{+0.004}_{-0.002}$ cts/(keV·kg·yr) for the BEGe detectors.

4.3.2 PSD for semi-coaxial detectors

In contrast to BEGE detectors, the geometry of semi-coaxial detectors does not allow pulse shape discrimination based on a simple variable like A/E. The gradient of the weighting potential is relatively high in most of the detector volume, so that electrons and holes are contributing to the pulse shape. Because of that, the current pulse looks different depending on the radius where the energy deposition in located.
An artificial neural network (ANN) is used to obtain the information of how signal like a pulse shape looks. 50 timing information are extracted from the charge pulse and used as input for the ANN. To train the network, events from the double escape peak of ^{208}Tl are used as signal like samples, while events from the 1621 keV full energy line of ^{212}Bi are used as background samples. The response of the ANN is a number between 0 and 1, which describes how signal like a pulse shape is. The accepted range of the response is chosen so that a it results in a 90% survival fraction for double escape peak events. This tuning is done for each of the semi-coaxial detectors separately. The signal efficiency obtained from the double escape peak survival fraction agrees again well with the survival of $2\nu\beta\beta$ events and events close to the Compton edge in the calibration data. In PI, 43 out of 96 event in a 230 keV wide window around $Q_{\beta\beta}$ are rejected by ANN. 90% of these events are also rejected by two different methods that are used as a cross-check.

4.4 Phase I analysis

PI of GERDA officially started data taking at the end of 2011. The main goal in PI was to verify the claim of the HDM subgroup. GERDA was the only experiment at this point, that was able to achieve this independently of matrix element calculations.
The upcoming sections will discuss the data taking period, the background modeling and the analysis and results of PI.

4.4.1 Data taking

Following an extensive commissioning phase, data taking for PI started in November 2011 and ended in May 2013, with a total run time of 460 days. The full exposure of ^{76}Ge during that time accounts to 21.6 kg·yr [1].

PI can be divided in three periods according to changes to the detector array: November 2011 until May 2012, with two natural detectors (GTF32, GTF45) on the one-string arm, from May 2012 to July 2012 without the one-string arm and from July 2012 until May 2013 with the re-inserted one-string arm, equipped with five BEGe detectors. From here on, these periods are labeled as PIa, PIb and PIc, respectively.

Furthermore, the data taking period was separated into individual physics runs, with a run time of typically about one month. During each run, the configuration of the array and status of each detector channel was constant. The list of physics runs in PI can be found in Tab. C.2. The runs were interrupted for (bi-)weekly calibrations with ^{228}Th sources, to monitor the stability of the energy resolution and scale of the detectors. Additionally, the leakage current of the detectors was monitored constantly. One of the IGEX detectors (RG3) started drawing strong leakage current and hence showed instabilities from the beginning of PI. Another detector (ANG1) started to show the same problems in February 2012. Subsequently their bias voltage was reduced leaving them not fully depleted until the end of PI. In that state they could not be included in the analysis, but could still be used as anti-coincidence veto. Similarly, one of the five BEGe detectors (GD35C) was also excluded entirely from the analysis due to stability problems. A few other detectors showed instabilities during single runs and were omitted from the analysis of these runs only. The stability of the electronics chain was monitored with a pulser, that feeds the pre-amplifier with a charge signal of well defined height. The status of each detector during each physics run is visible in Fig. C.1.

The charge pulses of the germanium detectors are digitized by FADCs with a sampling rate of 100 MHz. The pulse shape as well as a preliminary energy information determined by the FADC[7] is recorded to disc in a raw file format, together with the corresponding meta data. For more information on the data processing of GERDA, see Sec. 4.6.

In subsequent processing steps, all events within a window of ±20 keV around the two-electron sum energy of the $0\nu\beta\beta$-decay ($Q_{\beta\beta}$) were omitted and not available to the collaboration until the full analysis chain was fixed. This so-called "blinding" of the data is meant to prevent the introduction of human bias while tuning the analysis parameters.

4.4.2 Background analysis

An important quantity for the GERDA experiment is the background index (BI) at $Q_{\beta\beta}$. Together with the signal detection efficiency, the energy resolution and the exposure of the experiment it defines the sensitivity for the half-life of the $0\nu\beta\beta$-decay (see Ch. 3.2). Given a background expectation in the sub count region ("background free" scenario) allows the sensitivity to increase linearly with the exposure instead of the typical square root behavior.

Studying the background in the full energy range from 0 to 7.5 MeV provides valuable information about the present background sources and the origin of the background contamination. From this information, one can infer the expected background at $Q_{\beta\beta}$. Furthermore, the assumption of a flat background in and surrounding the blinded region can be verified and potential γ-lines in the vicinity of $Q_{\beta\beta}$ can be identified.

Additionally, knowing the origin of the background sources is helpful to pinpoint contaminated components of the detector array in order to possibly replaced them with more radio-pure alternatives in later stages of the experiment.

---

[7] Fast Analog to Digital Converter

Hence, a background model was created for PI of Gerda, which is discussed in the following sections. The model is based on the data taken up to March 2012.
The background contaminations in Gerda are simulated using the MaGe software (see Sec. 4.7) in order to obtain their expected contributions to the energy spectrum, which are available as histograms with a binning of 30 keV. Those histograms are fit to the data spectrum using the BAT framework. At first, the energy range from 3.5 MeV to 7.5 MeV is fit using α-contaminations. Secondly, the lower energetic range is fit with γ-emitting contaminations and the $2\nu\beta\beta$-decay of ^{76}Ge, while the results from the α-model are used as prior information input. This second step is done in two variations: By using the minimal amount of background components necessary to reproduce the physics data, a "minimum model" is created. The BI predictions for the $Q_{\beta\beta}$ region by this model is then cross-checked with the predictions from a "maximum model", which takes into account additional background components, most of them in larger distance from the detector array.
For a more in detail discussion of the PI background, see [119, 120, 121]. In Ch. 6 the background is specifically discussed for the coincidence data of Gerda, i.e. events with energy depositions in multiple detector per event.

Expected background sources

Typical background that experiments like Gerda have to face, was already discussed in Ch. 3.3.
The background contributions taken into account for the background model are mostly chosen based on two criteria. Firstly, the materials employed in the experiment, especially the components close to the detectors, have been screened for their radio-purity prior to the installation using HPGe screening facilities and ICP-MS measurements [114]. From this, expected contributions are coming from ^{226}Ra as well as ^{222}Rn and their daughters ^{214}Bi and ^{214}Pb in the detector array, on the p^{+} surface of the detectors and the LAr due to a ^{226}Ra contamination on the detector surface and ^{222}Rn emanation [122] in the cryostat. ^{214}Bi and ^{214}Pb are assumed to be in equilibrium and are the only isotopes in the respective decay chain that emit high energetic γ-rays. ^{228}Th contaminations are expected on the front end electronics, the detector assembly, minishroud, radon shroud and the heat exchanger. From the ^{228}Th only ^{208}Tl and ^{212}Bi contribute significantly to the energy spectrum and are assumed to be in equilibrium as well.
Secondly, structures observed in the energy spectrum like γ-lines also give hints about additional background contributions. One of such is ^{42}K, the ionized decay product of ^{42}Ar with a short half-life of 12.3 h. The positively charged ^{42}K ions can drift within the electric fields close to the detectors and hence the distribution can deviate from the homogeneous distribution of ^{42}Ar inside the LAr. The 1525 keV γ-line of ^{42}K is clearly visible in the energy spectrum. Another isotope observed in the spectrum is ^{40}K.
Additionally, contributions from ^{60}Co are expected due to the cosmogenic activation history of the detectors.
The background contribution from muon induced events are efficiently vetoed by identification of Cherenkov light emitted by muons passing the water tank to more than 99%. This reduces the muon induced background at $Q_{\beta\beta}$ to less than 10^{-3} cts/(keV·kg·yr)
The neutron induced background was estimated to be of the order of 10^{-5} cts/(keV·kg·yr) [123]. The contribution by ^{222}Rn is reduced by the radon shroud and contributions by ^{42}K to the $Q_{\beta\beta}$ region are significantly reduced by the implementation of the minishrouds.

Background locations

Background locations considered are the bulk of the germanium detectors, their n^+ and p^+ surface, as well as a LAr volume close to the p^+ surface and a bigger homogeneous volume of LAr enclosing the full array.
The remaining background locations of several components of the detector array and suspension system are divided into near (up to 2 cm from the detector), medium (2-30 cm) and far (>30 cm) distance components. To the near location belong components of the detector assembly and the minishroud. Medium locations are the radon shroud, the front end electronics and the cable suspension system. The heat exchanger at the top of the cryostat is the only far location considered. From those locations, only γ-rays can contribute to the background spectrum. It turned out, that the resulting expected γ-ray spectra are very similar for locations within a distance class (near, medium, far) and indistinguishable given the available exposure. As a result, only one representative location is chosen per class, which is the detector assembly for near, the radon shroud for medium and the heat exchanger for far sources.
The expected γ-ray spectra from locations of different classes typically differ by the increased peak to Compton ratio for near sources and the absence of summation peaks for far sources. α-radiation becomes only relevant for contaminations on the p^+ contact of the detectors, because of the very thin dead layer. β-radiation can additionally contribute through the n^+ surface, more so for BEGe detectors than for semi-coaxial detectors.

Background spectrum

The background spectrum of the Gold-coax data set for the first 16.7 kg·yr can be seen in Fig. 4.7.

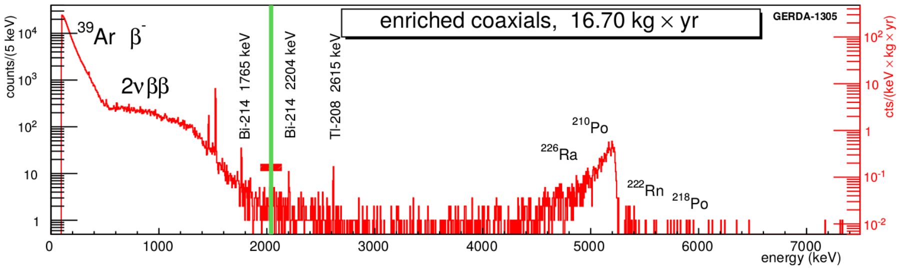

Figure 4.7.: The background spectrum of the Gold-coax data set of PI of GERDA for the first 16.7 kg·yr. Taken from [119].

In the low energy region up to 565 keV the spectrum in all detectors is dominated by the beta spectrum of ^{39}Ar, which is cosmogenically produced in the LAr. There are differences in the spectral shape of the beta spectrum between semi-coaxial and BEGe detectors, due to differences in the detector surface geometry.
In the medium energy region between 600 keV and 1500 keV, contributions to the spectrum in the enriched detectors come mostly from the $2\nu\beta\beta$-decay of ^{76}Ge with γ-lines from ^{42}K, ^{40}K, ^{208}Tl, ^{214}Bi, ^{228}Ac and ^{60}Co overlayed on top. The $2\nu\beta\beta$ spectrum is suppressed in the natural detectors, hence the γ-lines are more dominant.
In the high energy region, several peak like structures especially at 5.3 MeV, but also at 4.7 MeV, 5.4 MeV and 5.9 MeV can be observed. Those can be attributed to the alpha decay of ^{210}Po, ^{226}Ra, ^{222}Rn and ^{218}Po, respectively.

Alpha model

Above the Q-value of ^{42}K of 3.5 MeV the major contribution to the background comes from α-decays on the detector p$^+$ surface. α-decays on the n$^+$ surface can not contribute, due to the larger dead layer thickness.

First, from the time distribution of the α event rate, it became apparent, that the strongest contribution comes from ^{210}Po α-decays with a half-life of 138.4 d in addition to a time constant contribution by isotopes with longer half-lives like ^{210}Pb (22.3 yr) from the ^{226}Ra chain, which is clearly broken at ^{210}Pb.

Thus, in addition to ^{210}Po, the energy spectrum is fitted with contribution of all the α-decays in the ^{226}Ra chain up to ^{210}Pb. The expected spectra from these contributions have their maximum shifted with respect to the original α energy, because of a part of the energy being deposited in the dead layer.

Additionally, the fit includes simulations of the decays in a 1 mm thick volume of LAr in contact with the p$^+$ surface, which result in a broad energy spectrum without peak, which extends to lower energies reaching inside the $Q_{\beta\beta}$ region. The best fit is illustrated in Fig. 4.8. From the alpha model a BI of $(2.4\pm0.1)\cdot10^{-3}$ cts/(keV·kg·yr) is expected at $Q_{\beta\beta}$.

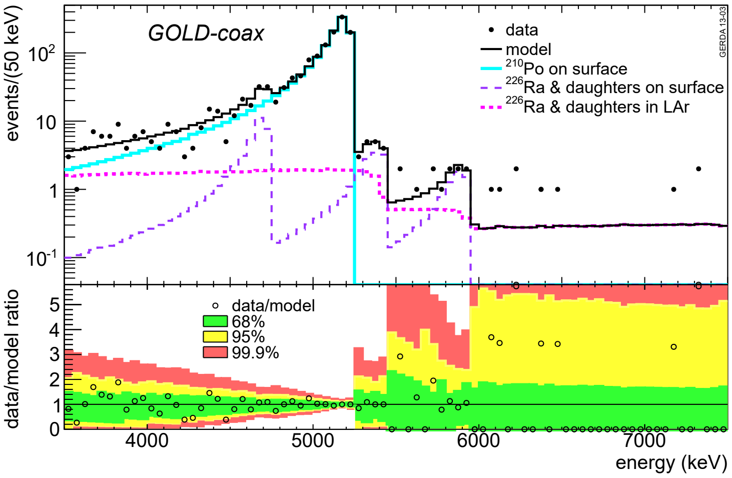

Figure 4.8.: Alpha model fit of the Gold-coax data set with components of ^{210}Po on the detector surfaces and members of the ^{226}Ra chain on and in the LAr close to the detector surfaces. In the bottom plot the ratio between the observed counts in the data and the best fit prediction for each bin is shown, together with the smallest 68%, 95% and 99.9% intervals. Taken from [119].

Full background model

The energy spectrum in the range of 570 keV to 7.5 MeV was used for a complete background fit. Two fits were performed using a different set of background contributions. The minimum model concentrates on the minimum amount of well motivated background sources necessary to describe the observed energy spectrum. Those include the $2\nu\beta\beta$-decay of ^{76}Ge, ^{40}K, ^{60}Co, ^{228}Th, ^{228}Ac and ^{214}Bi on the detector assembly, ^{42}K homogeneously distributed in the LAr and the best fit alpha model. This includes ^{214}Bi on the p$^+$ surface,

which is constrained by a Gaussian prior according to the ^{226}Ra activity obtained from the alpha model.
The fit with the minimum model can be seen in Fig. 4.9.

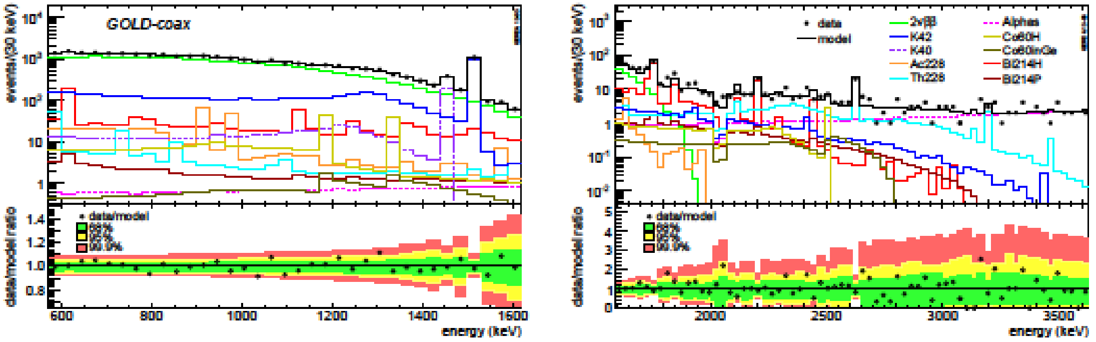

Figure 4.9.: Minimum model best fit of the GOLD-coax data set. Shown are the contributions by each background component in two energy ranges of [570,1620] keV (*left*) and [1620,3620] keV (*right*). The first range is dominated by the $2\nu\beta\beta$-decay component, the second range is dominated by ^{214}Bi and ^{228}Th as well as surface α-decays at higher energies. The bottom plots, show the ratio between the observed counts in the data and the best fit prediction for each bin, together with the smallest 68%, 95% and 99.9% intervals. Taken from [119].

In the maximum model also sources from medium and far distances are included. This includes ^{42}K on the n$^+$ surface, ^{228}Th on the radon shroud and the heat exchanger, ^{228}Ac and ^{214}Bi on the radon shroud and ^{214}Bi in the LAr close to the p$^+$ contact.

All contamination that are expected from the screening measurements have also been observed in the background spectrum. However, they do not account for the total background. The fit returns larger contamination levels than expected from the screening, suggesting that there are additional sources present.
The minimum model describes the spectrum sufficiently well with a p-value greater than 0.1. The results from the maximum model for the same isotope on different location reveal strong correlations. With the available exposure, no discrimination between the near, medium and far locations is possible for ^{214}Bi, ^{228}Th and ^{228}Ac.
The background model was cross-checked on several ways, including the determination of the $2\nu\beta\beta$ decay half-life, γ-line intensities (especially the 352 keV line of ^{214}Pb, which is not included in the fit range), using different binnings to test the stability of the fit, making an estimation on the time coincidence of ^{214}Bi and ^{214}Po alpha decays, identifying events on the p$^+$ surface using PSD and comparing to a background model fit based on coincident events (see Ch. 6).
According to the background model, the main background around $Q_{\beta\beta}$ comes from alpha decay in the ^{226}Ra chain, as well as ^{42}K, ^{60}Co, ^{214}Bi and ^{228}Th with individual contributions in the range of $1\text{-}5\cdot10^{-3}$ cts/(keV·kg·yr). The background around $Q_{\beta\beta}$ is expected flat without any peaks within the blinded region. The minimum and maximum model predict a BI of $18.5^{+0.8}_{-0.9}$ and $21.9^{+1.9}_{-1.2} \cdot 10^{-3}$ cts/(keV·kg·yr), respectively. The energy range from 1930-2190 keV, with a total width of 200 keV (excluding two small region with expected γ-lines from ^{208}Tl and ^{214}Bi and the 40 keV blinded region) was used to determine the experimental BI. A value of $17.5^{+2.6}_{-2.4} \cdot 10^{-3}$ cts/(keV·kg·yr) was found for the enriched semi-coaxial detectors, well in agreement with the prediction of both models.

BEGe background model

Due to the lower mass of the BEGe detectors the detection efficiency for full energy peaks is reduced. Additional, the exposure is much lower compared to the enriched semi-coaxial data sets. As a result, less γ-lines can be identified in the spectrum and hence constraining background sources is more difficult.

Only a minimum model fit is done for the BEGe data set. This model uses the same components as before, in addition to ^{68}Ge ($T_{1/2}$= 271 days) in the bulk of the detectors, as it is expected due to cosmogenic activation. This component could be neglected for the semi-coaxial detectors, because they have been stored underground for many years. From the recorded activation history of the BEGe detectors, an upper limit to the contributions by ^{68}Ge as well as the cosmogenic ^{60}Co is imposed at 0.32 cts/day) and 0.05 cts/day), respectively.

Furthermore, ^{42}K is included on the n^{+} surface. This component is expected to have a higher contribution to the spectrum due to the thinner dead layer.

The best fit model describes the observed spectrum very well, a p-value of 0.5 was obtained. It predicts a total of $((38.1^{+5.2}_{-5.9})\cdot 10^{-3}$ cts/(keV·kg·yr) in the region of interest. The biggest contribution of $(21.8^{+2.9}_{-14.0})\cdot 10^{-3}$ cts/(keV·kg·yr) is indeed expected from ^{42}K on the detector surface, followed by ^{214}Bi and ^{228}Th on the detector assembly. From the observed counts in the 200 keV region around $Q_{\beta\beta}$, a BI of $(36.1^{+13.2}_{-9.7})\cdot 10^{-3}$ cts/(keV·kg·yr) could be obtained by interpolation, which is in agreement with the prediction.

Subsequently, after fixing the calibration parameters and the background model, a part of the blinded window was opened, only keeping a central 10 keV (8 keV) region blinded for the enriched semi-coaxial (BEGe) detectors. The events observed in the unblinded region were consistent with the prediction from the background models.

Lastly, it should be noted, that all the BI values in the above sections are given without the application of PSD cuts. No deviation from the flat background is expected after PSD cuts are applied.

4.4.3 Data sets and analysis parameters

Data cuts

The data have to pass several basic cuts that ensure the integrity and physicality of each event. These quality cuts are a set of multi parameter requirements to the pulse shapes, e.g. a stable baseline, a physical charge pulse rise time or the rejection of discharge pulses [124]. They remove less than 1% of events above 500 keV, excluding pulser events [125].

In a next step, several background cuts are imposed on the data. The anti-coincidence cut rejects events with energy depositions in more than one germanium detector, like they are produced by multiple scattered γ-rays for example. This removes about 3% of the events above 500 keV and 15% around $Q_{\beta\beta}$. A different anti-coincidence cut rejects events that happen within 1 ms from each other in order to remove background from decay chains like the subsequent decays of ^{212}Bi and ^{212}Po, which affects less than 1% of events. Furthermore, all events that happened within 8 ms of a trigger from the muon veto system are also discarded, which are less than 1% overall and 7% in the $Q_{\beta\beta}$ region [1]. The dead time introduced by these cuts is negligible.

Finally, a cut based on PSD is applied as discussed in Sec. 4.3.

Data sets

For the purpose of the $0\nu\beta\beta$-analysis, the data are divided in three distinct data sets. The ”golden” data set includes most of the data from the enriched semi-coaxial detectors (Gold-coax). The only exception is the period of PIb, in which a significantly higher background was observed after operations on the detector array. These data are labeled as ”silver” data set (Silver-coax). The BEGe data constitute the third data set.
The natural detectors constitute their own data set, which is not utilized for the $0\nu\beta\beta$-decay search.

Analysis parameters

Given Eq. 3.1, the important parameters for the analysis are the energy resolution of the detectors, the signal efficiency and the exposure of the experiment.
The energy scale of each detector is calibrated using the (bi-)weekly calibration runs. In the process, the **energy resolution** is extracted at the position of several lines of ^{208}Tl in the spectrum resulting in a calibration curve for each calibration and detector. The values for the resolution at $Q_{\beta\beta}$ is obtained from these curves and combined to a single value for the data set, taking into account the live-time, that each calibration is valid, and the exposure of each detector [126].
The **signal efficiency** ϵ of each detector is a combination of several factors:

$$\epsilon = f_{76} f_{\mathrm{av}} \epsilon_{\mathrm{FEP}} \epsilon_{\mathrm{PSD}} \tag{4.1}$$

with:

- f_{76}, the isotope fraction of ^{76}Ge of the enriched material.

- f_{av}, the active volume fraction of the detectors, which is equal to the detector volume reduced by the volume of the dead layer[8]. The dimensions of the semi-coaxial detectors have been measured by Canberra after reprocessing. To obtain the dead layer, the full energy efficiency was measured for a ^{60}Co source in GDL[9]. The dead layer in MC simulations was then adjusted to fit the measured spectrum. Similar measurements with the BEGe detectors have been done in the HADES underground laboratory [127].

- ϵ_{FEP}, the fraction of $0\nu\beta\beta$-decays in the active volume that are reconstructed at $Q_{\beta\beta}$, which was determined with MC simulations. A loss of energy can happen when bremsstrahlung, created by the β -particles, escapes the detector. Additionally, decays at the edge of the active volume can lead to a partial energy deposition in outside the active volume. The fraction of decays affected by this is in the order of 10%.

- ϵ_{PSD}, the fraction of signal events that survive the PSD cuts , see Sec. 4.3.

---

[8] Within the dead layer thickness, there exists a transition layer from which charges can enter the active volume via diffusion and contribute to the spectrum, though with a deteriorated reconstructed energy value. Hence, the dead layer is actually not completely ”dead”. A better fitting term coined in [127] is ”Full Charge Collection Depth” (FCCD)

[9] GERDA Detector Laboratory, a test facility for detector characterisations at the LNGS.

Data set	$\mathcal{E}$ [kg·yr]	ϵ	FWHM [keV]	BI [cts/(keV·kg·yr)]
Gold-coax	17.9	$0.62^{+0.04}_{-0.07}$	4.8±0.2	$(11\pm2)\cdot10^{-3}$
Silver-coax	1.3	$0.62^{+0.04}_{-0.07}$	4.8±0.2	$(30\pm10)\cdot10^{-3}$
BEGe	2.4	0.66±0.02	3.2±0.2	$(5^{+4}_{-3})\cdot10^{-3}$

Table 4.1.: Data sets of PI, their germanium exposure $\mathcal{E}$, the exposure weighted efficiency ϵ, the energy resolution FWHM (Full Width at Half Maximum) and the background index BI after PSD cuts.

The signal efficiency for each detector was furthermore combined to a single value for the data set, calculating the detector exposure weighted sum.

The final **background index** was estimated by counting the background events in a 260 keV window around the region of interest. Known γ-lines by ^{214}Bi and ^{208}Tl and a 10 keV (8 keV) window around $Q_{\beta\beta}$ have been excluded from this region in the enriched semi-coaxial (BEGe) data set. The GERDA background model predicts a flat background in this region. It also gives an estimation for the background index before PSD of $18.5^{+0.8}_{-0.9}$ cts/(keV·kg·yr) ("minimum model", compare Sec. 4.4.2) for the Gold-coax data set.

The calculation of the **exposure** of each data set requires the mass of the active volume and the live-time of each detector. The live-time is measured by counting the recorded pulser signals of the detector channels.

The necessary analysis parameters for each data set are collected in Tab. 4.1.

Values for the number of observed $0\nu\beta\beta$-decay events $N^{0\nu}$ can be translated to the half-life of the decay via the following relation:

$$T^{0\nu}_{1/2} = \frac{(\ln 2) N_{\mathrm{A}}}{m_{\mathrm{enr}} N^{0\nu}} \mathcal{E}\epsilon, \tag{4.2}$$

where m_{enr} is the molar mass of the enriched material, $\mathcal{E}$ the exposure and ϵ the combined signal efficiency.

4.4.4 Results

The data in the window around $Q_{\beta\beta}$ was fully unblinded in July 2013 after all analysis parameters were fixed. The combined final spectrum of the enriched detectors of PI in the region of interest is shown in Fig. 4.10. The figure shows the spectrum and before and after applying PSD. Quality cuts, muon veto and the anti-coincidence cut are applied in both cases. Seven events are counted in a ±5 keV region around $Q_{\beta\beta}$ before PSD, while 5.1±0.5 counts are expected given the background index. After PSD, 3 events remain in the Gold-coax and Silver-coax data set, while none remain in the BEGe data set. The observed counts are in agreement with the background expectation.

To obtain the signal strength, a spectral fit of the three data sets is performed. For this purpose a profile likelihood is constructed. The fit function consists of a constant background term and a Gaussian signal term. Therefore the fit has 4 free parameters: $T^{-1}_{1/2}$ which is common to all data sets and the background indices of each of the three data sets. The systematic uncertainties coming from the analysis parameters are included by a MC method, taking correlations into account.

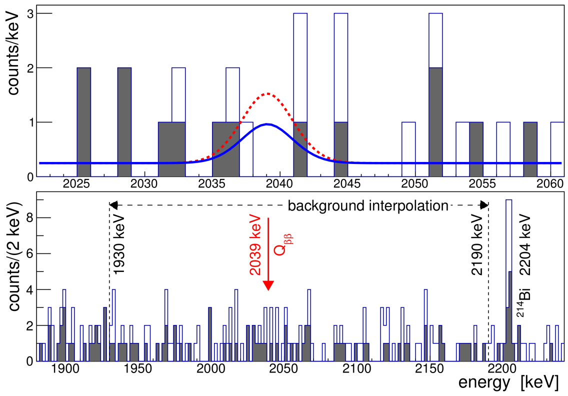

Figure 4.10.: Anti-coincidence energy spectrum of the combined data of all enriched detectors of PI before (empty histogram) and after (grey filled histogram) PSD cut. The bottom plot shows the region, which is used for the background interpolation. The top shows a zoom on the $Q_{\beta\beta}$ region. Also shown are the expectations assuming $T_{1/2}^{0\nu} = 1.19 \cdot 10^{25}$ yr (central value of the 2004 claim [64]) as red dashed line and $T_{1/2}^{0\nu} = 2.1 \cdot 10^{25}$ yr (90% C.L. lower limit of Gerda PI) as blue solid line. Taken from [1].

The fit returns a best fit value of 0 counts, i.e. no indication of a signal has been found. Consequently a Frequentist coverage limit of $T_{1/2}^{0\nu} > 2.1 \cdot 10^{25}$ yr has been extracted at 90% confidence level, while the median sensitivity is $2.4 \cdot 10^{25}$ yr [1]. A Bayesian analysis has been performed as well using the same likelihood and a flat prior probability density distribution for $T_{1/2}^{-1}$. A 90% credibility limit of $T_{1/2}^{0\nu} > 1.9 \cdot 10^{25}$ yr was obtained with a median sensitivity of $2.1 \cdot 10^{25}$ yr.

The Bayes factor between the model with the signal peak scaled according to the 2004 claim of the HdM subgroup and the model without any signal has been calculated. A value of 0.024 has been obtained, meaning that the claimed half-life is disfavored by the Gerda data compared to the background only scenario.

By performing a combined profile likelihood fit of the Gerda spectra and the energy spectra from the HdM (Fig. 4 in [62]) and IGEX (Tab. II in [63]) experiments, a 90% C.L. half-life limit of $T_{1/2}^{0\nu} > 3.0 \cdot 10^{25}$ yr was obtained. This limit translates to a lower limit on the effective electron neutrino mass of $\langle m_{\beta\beta} \rangle < 0.2 - 0.4$ eV, using the phase space factors of [48] and the NME calculation from [49, 54, 55, 128, 129, 130, 131]. With the three experiments combined, the Bayes factor from above yields a value of $2 \cdot 10^{-4}$, strongly disfavoring the claim.

4.5 Phase II analysis

At the time of writing, PII is still ongoing. Hence, several steps of the analysis chain are still work in progress and preliminary results reported here (also see the disclaimer in Appendix I).

4.5.1 Data taking

Data taking for the official PII data set started in December 2015. This work considers data taken until April 2017. A duty cycle of 93% was reached for this period. In general, all

40 detector channels are working during PII. However, two detectors are excluded from all physics analyses: GD91B showed strong leakage current and is operated at a lower voltage and GD02D is not fully depleted [127]. Additionally, some detectors showed instabilities only during a subset of runs. Like in PI, the data from those detectors during the affected runs were omitted from the analysis. About 80% of the recorded data was stable enough to be used for analysis. A list of physics runs in PII can be found in Tab. C.3, while the detector status for each run can be viewed in Fig. C.2.

The data available for the analysis are blinded in a 50 keV window around $Q_{\beta\beta}$ again and it was decided to do a first unblinding after the sensitivity of PI was doubled. This goal was reached in June 2016 with a collected exposure of 5.0 kg·yr with the semi-coaxial detectors and 5.8 kg·yr with the BEGe detectors [132]. This period is refered to as PIIa.

A second unblinding of the BEGe data set was done after an exposure of 18.2 kg·yr in April 2017. By that point 16.2 kg·yr had been taken with the semi-coaxial detectors. However, it was decided to not unblind the additional data in this set, in order to gain additional time to adjust parameters for more efficient PSD cuts. This second period will be called PIIb from here on.

A third unblinding, including a full unblinding of the Coax data set is planned for May 2018.

Fig. 4.11 shows the energy spectra of the BEGe and enriched semi-coaxial detectors after basic cuts as already discussed in Sec. 4.4.3 as well as after PSD and LAr veto cuts. A zoom in on the spectra of the BEGe and enriched semi-coaxial data sets in the region of interest is shown in Fig. 4.12. After all cuts, only 4 events remain in each data set in the energy range from 1930 keV to 2190 keV. No event is found in a ±5σ window around $Q_{\beta\beta}$. Consequently, the background index for the BEGe data set is $1.0^{+0.6}_{-0.4} \cdot 10^{-3}$ cts/(keV·kg·yr), which fulfills the goal of GERDA PII.

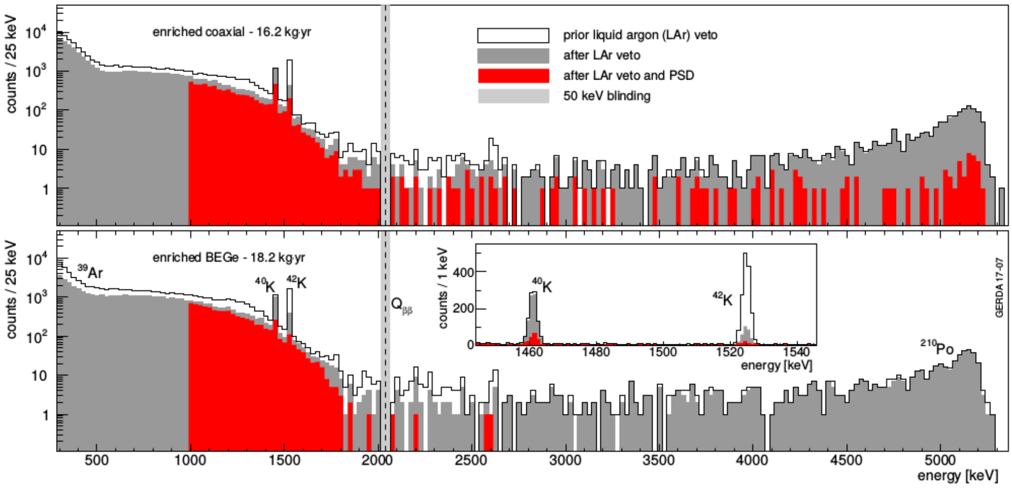

Figure 4.11.: The energy spectrum of the enriched semi-coaxial detectors (*top*) and the BEGe detectors (*bottom*) of PII data up to April 2017 (PIIa and PIIb) [67]. In the bottom, some of the stronger background features are labeled. The inlay shows a zoom in on the ^{40}K and ^{42}K full energy lines.

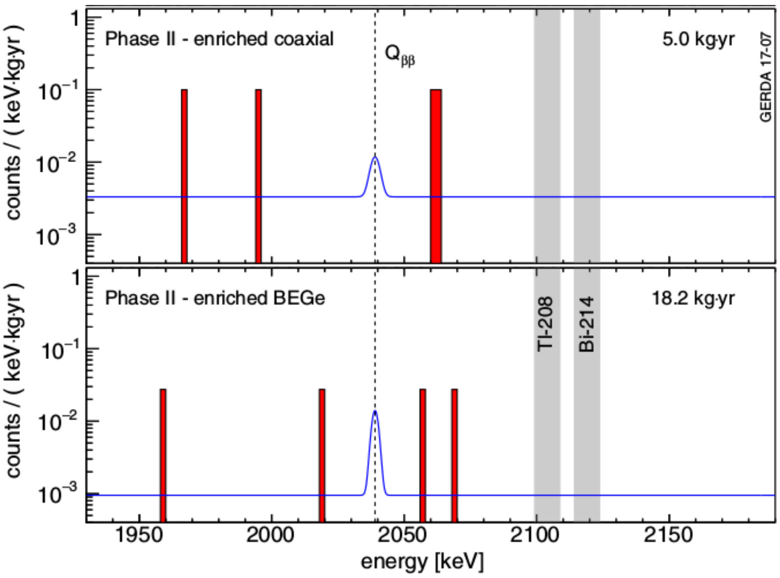

Figure 4.12.: The energy spectrum of the enriched semi-coaxial detectors (*top*) and the BEGe detectors (*bottom*) of PII data up to April 2017 (PIIa and PIIb) in the region of interest [67]. Shown are the events after all cuts, including PSD and LAr veto. Also shown is the expected distribution of counts corresponding to the 90% C.L. half-life limit of $T_{1/2} > 8.0 \cdot 10^{25}$ yr (blue line). The shaded regions are excluded from the fit, because two background lines are expected there.

LAr veto performance

Background that deposits energy in the LAr in coincidence to the energy deposited in a germanium detector can be rejected with the LAr veto system. This concerns especially decays of ^{42}K where β-particle is released in the LAr, but also high energetic γ-rays like from ^{214}Bi and ^{208}Tl.

The probability that a background event is vetoed is described by the background rejection efficiency. This efficiency depends heavily on the type and position of background source, the geometry of the detector array and the scintillation properties of LAr. The LAr veto was heavily studied with the help of MC simulations, utilizing MaGe [133].

As an input, MaGe requires the optical properties of LAr like for example its light yield, which can vary strongly with the purity of the LAr. Hence, results from other experiments can only be used as starting point and have been adjusted in MaGe by a comparison with measurements in the LArGe test facility [134] and during the GERDA commissioning phase in June 2014.

After these optimizations, final suppression factors in the $Q_{\beta\beta}$ region for important background sources were estimated using a tentative PII detector array with all channels active. This resulted in a factor of about 130 for ^{208}Tl and a factor of 3 for ^{214}Bi on the detectors holders and a factor of 2-3 for ^{42}K homogeneously distributed in LAr among others [127]. The optimization of the MC simulations using the actual physics data of PII is still ongoing at the time of writing. Hence, simulations are not ready yet to precisely reproduce the energy spectrum after LAr veto.

The LAr veto system runs stable since March 2016, which is monitored continuously during physics data taking by evaluating the noise levels and gain of each PMT and SiPM channel. The additional dead time induced to the setup by random coincidences between

the LAr veto and the germanium detectors reduces the signal acceptance by a factor of (97.7±0.1)%. This was estimated using events from the ^{40}K full energy peak, which come from electron captures without any energy deposited in the LAr. The full energy peak of ^{42}K on the other hand is strongly suppressed by a factor of 5, which can be seen in the inlay of Fig. 4.11.
The performance was further studied with ^{228}Th and ^{226}Ra calibration runs, which yielded suppression factors for events in the $Q_{\beta\beta}$ region of about 100 and 6, respectively. These are lower than the suppression factors measured in LArGe, which can be attributed to several factors related to geometry differences, but especially the lower purity of the LAr in GERDA.

4.5.2 Background analysis

One big improvement to the setup while progressing from PI to PII was the replacement of material that will be located close to the detectors, by more radio-pure components. The new detector holder is manufactured mostly from mono-crystalline silicon with only small parts of copper. As another measure to reduce the material close to the detectors, the front end electronics were pushed to a larger distance from the detectors. Furthermore, the activation history of each detector was well documented and the time above ground was kept as short as possible during its full production cycle.
With these arrangements, contaminations close to the detectors from ^{228}Th and ^{214}Bi are expected to be greatly reduced in comparison to PI.

Material screening results

Samples of the materials close to the detector array have been screened for their radiopurity through methods of gamma spectromety, ICPMS (Inductively Coupled Plasma Mass Spectrometer), NAA (Neutron Activation Analysis) and Radon emanation measurements [2]. The results can be converted to limits on the activity of the employed detector components and can enter the background analysis as prior information or simply serve as a cross-check of the results obtained from the background modeling. Tab. 4.2 lists the obtained values for ^{228}Th, ^{226}Ra, ^{60}Co and ^{40}K. This data has been gathered and converted by von Sturm, Schütz and Pertoldi [135, 136]. The screened materials include the silicon of the detector holders (Holders), the high voltage and signal cables (Cables), the front end electronics (Front End), the coating and glue of the minishrouds (Minishroud) and several components of the LAr veto system: the Fibers, the SiPM, the PMTs (LArPMT) and the copper and tetratex of the coppershrouds (Coppershroud). The limits given for the holder component by gamma spectroscopy (^{228}Ac, ^{60}Co, ^{238}U) are rather weak. The silicon is expected to be much cleaner, as shown by the limits for ^{226}Ra and ^{228}Th, which are obtained by NAA.

Initial observations from γ-lines

An initial investigation of the γ-lines in the M1 energy spectrum using the data until October 30th, 2016 was presented in [138]. The results show an increase of the counts in the ^{42}K line by a factor of 2 and in the ^{40}K line by a factor of 4. The increase of ^{42}K can likely be attributed to the non-metallic minishrouds utilized in PII, that do not block the electric field lines of the germanium detectors. The additional ^{40}K is not fully understood as of the time of writing. It needs to be noted though, that this does not increase the BI

component	activity
^{228}Ac	
Holders	(<0.25) mBq
Cables	(<0.443) mBq
Front end	(0.770±0.385) mBq
Minishroud	(18±5) μBq
Fibers	(49±5) μBq
SiPM	(<7.3) μBq
Coppershroud	(31.2±3.1) μBq
^{226}Ra: ^{214}Bi(1), ^{214}Pb(1)	
Holders	($<6.4\cdot10^{-5}$) μBq
Cables	(662±208) μBq
Front end	(2.530±0.330) mBq
SiPM	(351±97) μBq
LArPMT	(<45) mBq
Coppershroud	(125±13) μBq
^{228}Th: ^{212}Bi(1), ^{208}Tl(0.3594)	
Holders	($<6.4\cdot10^{-4}$) μBq
Cables	(<414) μBq
Front end	(0.770±0.440) mBq
Minishroud	(18±5) μBq
Fibers	(49±5) μBq
SiPM	(<223) μBq
LArPMT	(<39) mBq
Coppershroud	(31.3±3.1) μBq

component	activity
^{60}Co	
Holders	(<0.102) mBq
Cables	(<0.343) mBq
Front end	(<0.297) mBq
^{40}K	
Holders	(2.75±0.58) mBq
Cables	(5.82±1.97) mBq
Front end	(14.3±4.4) mBq
Minishroud	(1.7±0.5) mBq
Fibers	(391±78) μBq
SiPM	(2.4±1.8) mBq
LArPMT	(<330) mBq
Coppershroud	(18±2) mBq
^{238}U: ^{234m}Pa(1)	
Holders	(<6.2) mBq
Cables	(<53.8) mBq
Front end	(<20.9) mBq
Minishroud	(43±13) mBq
Fibers	(36±4) μBq

Table 4.2.: Constraints on the activity for several components of the detector array as obtained from screening measurements. Results collected by von Sturm, Schütz and Pertoldi. For the decay chains of ^{228}Th and ^{226}Ra, the chain members of interest are given in combination with their branching ratio in brackets. Values are from January 2018. Final values will be in [136, 137].

in the $Q_{\beta\beta}$ region, because this requires the β-particle to be detected besides the γ-ray. Furthermore, a top-bottom detector asymmetry was observed in the count rate of the ^{42}K line, which points to a higher concentration of ^{42}K above the array.
Contributions by ^{214}Bi have found to be up to around a factor 2 lower than in PI, although the statistics are rather low and the values agree within one or two standard deviations. Similar rates have been found for lines fo ^{208}Tl when comparing PII to PI.

Preliminary background model

As of the time of writing, the background model process of PII is still work in progress. Hence, this chapter only shortly discusses the analysis steps and preliminary results as of January 2018. A documentation of the background model in PII will eventually be available in [136, 137].
The data is again divided into a Coax data set including the enriched semi-coaxial detectors and a BEGe data set. All detectors are used according to their run status.
The same approach as in PI has been chosen at first. Components to consider in the background are selected according to screening measurements and observations in the physics data. An α-model is created, whose results are used as prior input for the "minimum" and "maximum" model fit of the energy range from 500 keV to 3500keV. Additionally, prior information for the latter fits are applied according to the expectations from the screening measurements. Furthermore, prior information for the ^{42}K component in the LAr above the array has been obtained from sub fits of the energy spectra of the top, middle and bottom detectors.
Results from the first 10.8 kg·yr of PII data have been published in [132]. Further results are presented in [2], discussing the upgrade of GERDA from PI to PII. sing the first 34.4 kg·yr PII data to model the background, it has been found that with one exception, the data spectrum is well represented by assuming the contaminations observed in the screening measurements. This points at a well understood background, because the major background components have been covered and expected by the comprehensive material screening. The one exception is ^{40}K, for which an additional component is required. In this stage of the background model process, this component was attributed to the fibershroud of the LAr veto, which results in contamination levels that are a factor of about 200 higher than expected. Furthermore, in [138] it has been found that especially the natural detector GTF112 shows an increased intensity of the ^{40}K full energy line. This hints at a hot spot of this isotope directly above this detector. A possible source can be the glue utilized to close the nylon minishrouds. The exact amount of glue employed in the setup has not been recorded.
The higher concentration of ^{42}K in the top detectors has been taken into account by an additional component of this isotope in a cylindrical volume above the array, which .
The preliminary minimum model predicts a BI in the region from 1930−2190 keV of $(14 \pm 1) \cdot 10^{-3}$ cts/(keV·kg·yr) for the BEGe data set and $(19 \pm 1) \cdot 10^{-3}$ cts/(keV·kg·yr) for the enriched semi-coaxial data set before PSD and LAr veto cuts, to which degraded α-decays, ^{42}K and ^{214}Bi/^{208}Tl contribute each by about a third.
Complementary, a background model using the M2 data of PII has been constructed, which is discussed in Ch. 6. This model by itself can be compared to the findings of the preliminary M1 model, in order to check for inconsistencies or additional information that can be obtained from M2 data.
However, the final goal is to create a global model by performing a combined fit, using

the M1 and two-dimensional M2 data. In this global model, the γ-lines by ^{42}K and ^{40}K will be treated separately on a detector to detector bases to retain as much of the position sensitive information as possible, similar to the procedure described in Ch. 6.6.2 and 6.6.3. The work on the combination of M1 and M2 data is currently still ongoing.

4.5.3 Data sets and analysis parameters

Data cuts

Around 78% of all triggered events are accepted by the quality cuts, excluding test pulses and injected baseline pulses [139]. Of the events around $Q_{\beta\beta}$, 99.9% are accepted and all pulse shapes of events above 1.6 MeV have been visually inspected to verify that no nonphysical events have passed. In addition to several basic background cuts that are already applied in PI (anti-coincidence cut [9% above 500 keV], a time correlation cut, muon veto cut about [0.35%]) in PII the LAr veto cut is applied, which rejects about 40% of all physical events, which are within 5 μs of a LAr veto trigger. The new dead time introduced by the LAr was measured to be (2.3±0.1)% by studying the events in the ^{40}K background peak [132] and (2.45±0.02)% by counting the number of injected baseline pulses, that are flagged by the LAr veto [139].

Data sets

The signal efficiency is again calculated by the multiplication of several factors: the isotope fraction of ^{76}Ge (87%), the active volume fraction (87-90%) of the germanium detector, the fraction of $0\nu\beta\beta$ events reconstructed at $Q_{\beta\beta}$ (92%), the PSD signal efficiency (79-92%) and the live-time fraction (97.7%). The PSD cuts have been re-adjusted for each detector.

The analysis uses the PII BEGe and coax data set as well as the Gold-coax, Silver-coax and BEGe data set of PI. The PI data haves been reprocessed using a new energy reconstruction filter developed for PII (see Sec. 4.6). However, the data selection has been left unchanged. In addition, another semi-coaxial data set is included in the analysis, which was taken after the official end of PI with only the three string arm. This data set is labeled as ”Phase I extra”. All data sets and their parameters are listed in Tab. 4.3. Note, that the PI efficiencies have been reduced in comparison to Tab. 4.1, as they were corrected for the difference in survival fractions of DEP and $0\nu\beta\beta$-decay events, which was evaluated with MC data [140].

4.5.4 Results

A Frequentist approach was chosen to fit all six data sets simultaneously. The fit is based on a two sided test statistic, that uses an unbinned extended profile likelihood function. The fit function for each data set includes a flat background term and a Gaussian term for the signal. The strength of the Gaussian signal is proportional to the exposure and the signal efficiency of the data set, as well as to the inverse half-life which is a shared parameter between all data sets. The width of the Gaussian is restricted by the energy resolution of the respective data set. The systematic uncertainties of the efficiencies, the energy resolutions and a systematic energy shift are considered in the fit.

The best fit is returned for zero signal and a 90% C.L. limit of $8.0 \cdot 10^{25}$ yr is obtained, with a median sensitivity of $5.8 \cdot 10^{25}$ yr [67]. Furthermore, a Bayesian approach, which is

Data set	$\mathcal{E}$ [kg·yr]	ϵ	FWHM [keV]	BI [cts/(keV·kg·yr)]
PI Gold-coax	17.9	0.57±0.03	4.3±0.1	$(11\pm2)\cdot10^{-3}$
PI Silver-coax	1.3	0.57±0.03	4.3±0.1	$(30\pm10)\cdot10^{-3}$
PI BEGe	2.4	0.66±0.02	2.7±0.2	$(5^{+4}_{-3})\cdot10^{-3}$
PI Extra	1.9	0.58±0.04	4.2±0.2	$(5^{+4}_{-3})\cdot10^{-3}$
PII Coax	5.0	0.53±0.05	4.0±0.2	$(3.5^{+2.1}_{-1.5})\cdot10^{-3}$
PII BEGe	18.2	0.60±0.02	2.93±0.06	$(1.0^{+0.6}_{-0.4})\cdot10^{-3}$

Table 4.3.: Data sets for the search for the $0\nu\beta\beta$-decay ($0^+_{\text{g.s.}} \rightarrow 0^+_{\text{g.s.}}$) as of April 2017, their germanium exposure $\mathcal{E}$, the exposure weighted efficiency ϵ, the energy resolution FWHM (Full Width at Half Maximum) and the background index BI after PSD cuts.

based on the same likelihood function and uses a flat prior for the inverse half-life between 0 and $10^{-24}\,\text{yr}^{-1}$ returns a 90% credibility limit of $5.1\cdot10^{25}$ yr. The median sensitivity for the Bayesian analysis is $4.5\cdot10^{25}$ yr. Assuming light Majorana neutrino exchange and the matrix elements from [49, 51, 52, 54, 55, 56, 58] the Frequentist half-life limit translates to $\langle m_{\beta\beta}\rangle < 0.12 - 0.26$ eV.

With the background index reached in the BEGe data set, only a fraction of one event is expected in the region of interest even up to the design exposure of 100 kg·yr. Thus, the experiment will remain "background free" and the sensitivity will increase approximately linearly with the exposure. The ultra low background sets the GERDA experiment apart from other experiments in the field. Its current sensitivity is on a comparable level to that of the KAMLAND-ZEN experiment, which is $5.6\cdot10^{25}$ yr [106]. However, due to the lower background and much better energy resolution, GERDA reaches that sensitivity with only a tenth of the exposure of KAMLAND-ZEN.

4.6 Gerda germanium detector signal processing

4.6.1 Data tier structure

The data processing chain of GERDA is divided into four steps, starting with the digitization of the germanium detector signals, which are then used to reconstruct information about the events in the next steps. The steps and the corresponding data are referred to as "tiers", ranging from tier0 to tier4.

FADC to tier0

The signals of the germanium detectors are digitized via several FADC modules. The FADCs shapes the signal with a trapezoidal filter after digitization and a trigger signal is given when the shaped signal exceeds a programmable trigger threshold (normally set to 30 keV in PI and around 150 keV for PII). With the trigger the signals are recorded to disc in a binary raw data format, known as tier0, and are later available for analysis in the tier1 ROOT format [141].

In addition to the rising edge of the signal, about 80 μs of samples are recorded before and after the trigger position. This serves the purpose to obtain information about the pre and post trigger baseline of the signal, which is used to judge the quality of a signal (e.g. by the baseline RMS). During physics data taking, the signal of all channels is recorded

as soon as one signal triggers (*physics mode*). Due to the much higher rate of data in calibrations, only the triggered channel is recorded (*calibration mode*).
In PI, 16384 samples with a sampling frequency of 100 MHz are recorded per triggered signal. Due to the increase in channels and consequently an increase in data volume in PII, the sampling frequency was reduced to 25 MHz with 4096 samples recorded per triggered signal by adding up every 4 samples. Additionally a full frequency (100 MHz) version of the signal within 5 μs around the rising edge was recorded for the purpose of pulse shape analysis.

tier0 to tier1 (MGDO)

The raw data of the germanium array as well as the raw data of other detector systems (muon veto, LAr veto) are converted to a common structure, consisting of custom MGDO data objects which are stored in a ROOT file format. MGDO (MAJORANA-GERDA Data Objects) is a framework, developed within the GERDA and MAJORANA collaborations, which provides a number of general purpose analysis tools to process experimental and simulated signals. The collection of MGDO objects stored in the ROOT file format is called tier1.
Furthermore, the blinding of the data is performed during the conversion step from tier0 to tier1. Events within a certain range around $Q_{\beta\beta}$ are not converted and instead saved in a backup copy of the Raw data format.

tier1 to tier2 (Gelatio)

The tier1 format is processed using the GELATIO (GErda LAyouT for Input/Output) framework [142], developed by the GERDA collaboration. GELATIO contains multiple analysis modules that use the tier1 data objects as input. Some of the more common tasks include the copying of FADC information to the new output (GEMDFADC), correction of the baseline offset, the correction of the exponential tail in case of pile-up, a signal polarity check (GEMDBaseline), the calculation of the trigger position and threshold (GEMDTrigger/GEMDFTTrigger), the calculation of the energy according to the corresponding filters (GEMDEnergyGauss, GEMDGenericShaping) and the calculation of the amplitude of the current signal (GEMDCurrentPSA). This data is again stored in ROOT files and is referred to as tier2.

tier2 to tier3/4 (gerda-ada)

Further processing of the data from tier2 to tier3 is done via separate scripts provided within the GELATIO framework (PI) or the gerda-ADA (GERDA Advanced Data Analysis) framework (PII). In tier3 calibrated energy and A/E values are included as well as quality flags for events and signal traces, which makes this tier ready to be used for individual physics analysis by the members of the collaboration.
As of PII, tier3 files exists for each of the detector systems. The combination of all the information of each detectors systems constitutes tier4.

In summary the basic tier structure of the data:

- **tier0**: binary raw data format

- **tier1**: digitized signal traces, timestamp, trigger counter, FADC energy, FADC flags (contains all the information of the raw format)
- **tier2**: GELATIO module specific output, e.g. reconstructed energies, baseline, risetime, A/E (in general information extracted from the recorded waveforms)
- **tier3/4**: calibrated energies and A/E values (information from tier2 combined with meta data as obtained from calibration runs for example)

4.6.2 Reconstruction of energy

In the following the reconstruction of the energy from the signals and the current signal amplitude are explained in more detail.
The energy is in principle proportional to the amplitude of the charge signal, or equivalently to the integral of the current signal. The existence of noise makes it necessary to modify or shape the signal in order to increase the precision. GERDA uses three different energy reconstruction methods. An online method using a trapezoidal filter, and two offline methods using a pseudo Gaussian and a ZAC filter. In principal, the offline analysis allows to reprocess the data using any given shaping filter.

Pseudo Gaussian filter

The filter is called pseudo Gaussian because the shaped signal looks like a Gaussian. The raw and shaped signal is shown in Fig. 4.13. The shaping itself is comprised by the following steps:

a) a delayed differentiation (typically 5 μs)

b) a number n moving average operations with window length δ (PI: $n = 25$, $\delta = 5\,\mu$s, PII: $n = 13$, $\delta = 10\,\mu$s)

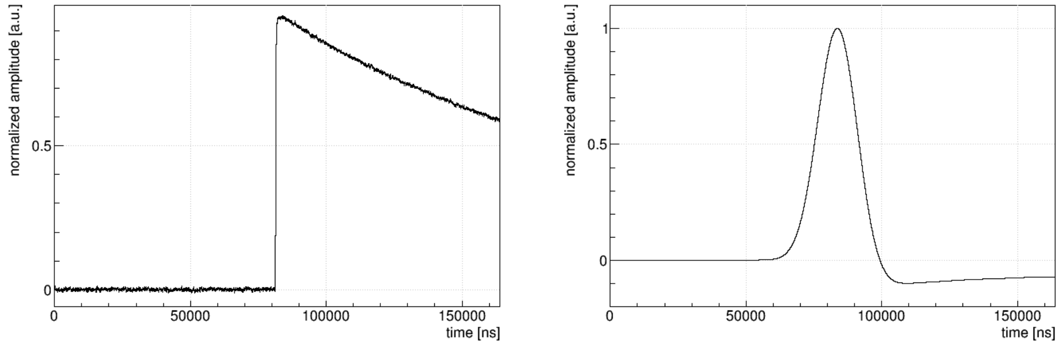

Figure 4.13.: Example of a raw (left) and shaped signal (*right*) using the pseudo Gaussian filter.

This shaping procedure is close to ideal in case only high frequency noise is present. However, in GERDA there is a significant low frequency noise component, e.g. from microphonics due to mechanical vibrations of the 30-60 cm long cables connecting the detectors to the pre-amplifiers.
The pseudo Gaussian filter was the go-to filter in PI.

ZAC filter

For δ-like signals it as been shown that a Cusp filter is optimal [143]. With PII, a modified finite Cusp filter, so-called ZAC (Zero Area Cusp) filter, was developed, which can be seen in Fig. 4.14. The modifications implemented consist of a flat top necessary because of the finite charge collection time in the order of 1 μs and the subtraction of two parabolas from the sides of the filter to adjust the total area to 0, so that low frequency noise mostly cancels out. The filter is convoluted with the inverse pre-amplifier response function to take into account the exponential decay of the signals. Furthermore, the filter parameters, i.e. length, length of the flat top and the shaping time are optimized for each detector channel using calibration data. This is preferable, because each detector has a different noise spectrum due to the different capacitances and leakage currents.
The integration window is defined by the width of the flat top and is shorter in comparison to the pseudo Gaussian filter. This can be detrimental for slow pulses originating from the n^+ surface of the detectors, because it can lead to an underestimation of the energy, though such events are usually cut by PSD.

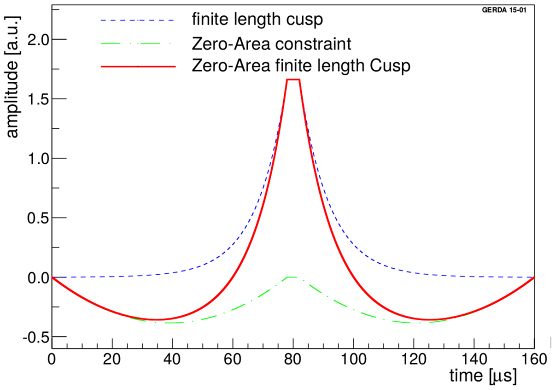

Figure 4.14.: ZAC filter. Taken from [126, 144].

4.6.3 Reconstruction of the current signal amplitude

The amplitude A of the current signal is one of the two parameters necessary for the pulse shape discrimination applied in the GERDA experiment. A is hereby extracted by differentiation of the charge pulse, followed by a pulse smoothing operation and the determination of the maximum of the processed pulse. Noise is the limiting factor for a precise determination of A and consequently the A/E parameter, especially in the low energy regions, where the A/E resolution exceeds 10%.

4.7 MaGe

MaGe (MAjorana-GErda) [133] is a Geant4 [145] based simulation framework for particle propagation and interactions, which has been developed by the GERDA and MAJORANA collaborations. The complete detector setup of GERDA and MAJORANA has been implemented in MaGe, as well as many test setups related to detector characterisations, like the test stands in the HADES laboratory or LArGe [134]. The software uses a dedicated physics list for low energy processes.

The geometry, the primary particle source and the output format can be configured using text based macro files. The detector geometries and their position in the GERDA array are also included via text based files, which list the detector names and their dimensions like height, radius, groove radius or dead layer depth.
MaGe is capable of tracking scintillation photons, although at the cost of a very high processing time.

Chapter 5

Coincidence data set of the Gerda experiment

5.1 Introduction

The main purpose of the GERDA experiment is to search for the neutrinoless double beta decay of ^{76}Ge. In that regard, the germanium detector array offers an additional powerful background veto, referred to as anti-coincidence (AC) veto: Events in which more than one germanium detector measures an energy deposition, are rejected for the analysis.

However, valuable information can be obtained from this multi-detector data. Valuable information especially about background from γ-rays as they are very likely to deposit their energy in more than one detector by Compton scattering or pair production, but also information about alternative $\beta\beta$-decay modes, namely decay modes of ^{76}Ge into excited states of ^{76}Se.

Before this data can be utilized for analysis, it needs to be prepared. The crosstalk between multiple detector channels is a problem only for such events, which needs to be taken care of. The correction of the crosstalk can not be done perfectly. Consequently energy deteriorations can remain even after the correction is applied. As a result, the energy resolution needs to be characterised also for the coincidence data.

This chapter is structured as follows: First the data sets are defined in Sec. 5.2. Parameters like the detector energy threshold and the multiplicity of an event which are strongly connected to coincidence data are discussed in Sec. 5.2.1 and Sec. 5.3. In the following, the chapter will concentrate on data with a multiplicity of two. Sec. 5.5 presents the evaluation and correction of the crosstalk. In Sec. 5.6, the energy resolution is determined for the coincidence data and compared to the energy resolution of the anti-coincidence data. This section also compares the efficiency of the different crosstalk corrections.

The remaining sections are dedicated to the analysis of coincidence data. Sec. 5.7 takes a quick look at the data, discussing the energy spectrum and the distributions of the events among the detector array.

5.2 Data sets

The analysis presented here, is based on data from PI and PII of GERDA. The PI data was taken between the 2nd of December 2011 and the 21st of May 2013, which is further divided into PIa (December 2011 to May 2012) and PIc (July 2012 to May 2013). The intermediate period of PIb is not taken into account due to the higher background observed. The PII data was taken between the 20th of December 2015 and the 15th of April 2017. This is further divided into PIIa (December 2015 to June 2016) and PIIb (June 2016 to April 2017). As of the time of writing, data taking of PII is still ongoing. However, the additional data is not taken into account for any of the analyses presented here.

As mentioned in Ch. 4, data taking runs are divided into shorter run periods of a typical duration of one month, which allows to exclude periods, where the detector setup behaved unstable. GD91B and GD02D are excluded from all analyses (see Ch. 4.5.1. Additionally, GTF32 is excluded as well from any physics analysis based on the coincidence data set due to reoccuring instabilities, which are also visible in the crosstalk behavior as seen in Sec. 5.5.7.

The PI data predominantly consists of data from semi-coaxial detectors, but also data with very low statistics from BEGe detectors from the fourth detector string in the second half of PI (PIc). PII on the other hand features almost equal masses of enriched semi-coaxial detectors and BEGe detectors.

Events with a multiplicity of 2 always consist of two energy depositions in two detectors.

Thus, instead of single detectors, one needs to look at detector pairs. Strictly dividing the full data set into semi-coaxial detector pairs and BEGe detector pairs discards the part of the data with mixed detector pairs. In PI, this is done as a consequence of excluding events between the three string arm and fourth string from the analysis, because the relative positioning between these strings is not precisely known. However, due to the relatively large distance between the three string arm and the fourth string, less than 4% of events are affected by this.

In PII, mixed detector pairs represent 40% of the valid coincidence data, because the outer strings are alternating between semi-coaxial and BEGe detectors.

As a result, in both phases, semi-coaxial and BEGe detector data are combined to one data set.

5.2.1 Exposure of ^{76}Ge

The main analysis of the GERDA experiment presented in [1, 132] gives exposure values, which account for all active detectors during each data taking run period (”active exposure” of ^{76}Ge).

However, the exposure for an analysis of ^{76}Ge decays using the coincidence data needs to take into account, that detectors excluded from an analysis are still contributing as a source of ^{76}Ge decays. This ”passive exposure” of ^{76}Ge is calculated using the total mass of ^{76}Ge in an array configuration (e.g. PIa/PIc/PII) and multiplying it with the live-time of that particular configuration.

The total detector masses in PI are given in [114]. The isotopical fraction of ^{76}Ge are also given, but were later re-evaluated and summarized in [146]. The isotopical fractions of the HdM detectors were measured with the Heidelberg MP-Tandem accelerator mass spectrometer using small samples of Ge residues after crystal production [147] The isotopical fraction of the IGEX detectors have been measured by the Botchvar Institute, Moscow [146].

The isotopical fraction of the BEGe detectors have been measured by neutron activation in Geel [148], by the ECP[1] and by ICPMS [149]. The weighted average of the three measurements is used.

The total masses and isotopic fractions of the relevant detector subsets are given in Tab. 5.1. Tab. C.1 in the appendix gives details on the masses, isotopic fractions and active volumes of each detector employed in GERDA.

Furthermore, the live-time of the experiment is important, which is measured by counting the number of pulser events in the physics data. The live-time of PIa is 174.1 d, PIc is 285.6 d, PIIa is 131.1 d and PIIb is 274.0 d. The uncertainty on the live-time is negligible.

The PI and PII data sets correspond to a passive exposure of (22.13 ± 0.31) kg·yr and (35.04 ± 0.40) kg·yr, respectively.

The uncertainty is coming from the fractions of each isotopes and the resulting uncertainty of the averaged molar mass. The correlation between the isotopic fractions has been taken into account by a toy MC approach.

---

[1] Currently known as Joint Stock Company ”Production Association Electrochemical Plant” (JSC ”PA Electrochemical Plant”, uranium enrichment enterprise of the State Atomic Energy Corporation ”Rosatom”.

detector	data set	m [g]	m_{76} [g]	f_{76}	$\bar{A}$ [g/mol]	$\mathcal{E}'$ [kg·yr]
ANG1	PI/PII	958	823(28)	0.859(29)	75.616(63)	
ANG2	PI/PII	2833	2453(71)	0.866(25)	75.633(55)	
ANG3	PI/PII	2391	2111(62)	0.883(26)	75.678(55)	
ANG4	PI/PII	2375	2050(31)	0.863(13)	75.624(49)	
ANG5	PI/PII	2746	2351(36)	0.856(13)	75.610(48)	
RG1+2+3	PI	6368	5445(96)	0.855(15)	75.601(31)	
RG1+2	PII	4281	3660(64)	0.855(15)	75.601(31)	
BEGe combined	PIc	3630	3184(47)	0.877(13)	75.668(28)	
BEGe combined	PII	20013	17551(260)	0.877(13)	75.668(28)	
GTF112	PI/PII	2965	231(3)	0.078(1)	72.638	
GTF32+45	PIa/PII	4643	362(5)	0.078(1)	72.638(8)	
	PIa	25261	15819±247			7.54±0.14
	PIc	24258	18640±251			14.58±0.20
	PI	24638	17571±248			22.13±0.31
	PIIa	43205	31602±352			11.34±0.13
	PIIb	43205	31602±352			23.70±0.27
	PII	43205	31602±352			35.04±0.40

Table 5.1.: Total detector masses m, ^{76}Ge masses m_{76}, the isotopical fraction of ^{76}Ge f_{76}, the averaged molar mass $\bar{A}$ of the detector material and the passive ^{76}Ge exposure $\mathcal{E}'$.

5.3 Detector energy thresholds

Due to the presence of noise on the detector signals, an energy threshold is applied during data taking. This means, for a primary detector signal to be written to disk, the amplitude of the (shaped) detector signal needs to exceed this threshold. During usual data taking this in addition triggers all other detector channels (secondary channels) to be recorded. No energy threshold is enforced upon the secondary channels. However, the electronic noise presents a threshold that prevents low physical amplitudes from being detected by the offline trigger algorithm.

To apply the energy threshold during data taking, the signal height determined by the FADC with a trapezoidal filter is used. The resulting value is not calibrated, thus the actual energy threshold can be different for each detector, according to its energy calibration.

The energy reconstruction used for data analysis on the other hand is done offline with a different reconstruction algorithm (see Ch. 4.6). As a result, the offline reconstructed energy values can differ slightly from the values determined by the FADC. Consequently, this energy is not strictly subject to the same constant energy threshold. Instead, the threshold varies from event to event. As an example, the energy of two events is reconstructed by the FADC as 100 keV, while the offline energy reconstruction can result in an energy of 95 keV for one event, and 105 keV for the other event. Thus, also energy values below the energy threshold can be found in the data sets.

In PI, an energy threshold of about 100 keV was set. For PII, the threshold was increased and ranges from 150-200 keV, for the separate detector channels. The inherent noise threshold on the secondary channel is at around 50 keV for semi-coaxial detectors and

30-40 keV for BEGe detectors in PI and at around 20-40 keV in PII.
The energy threshold determines the multiplicity of an event. Hence the threshold has an important impact on the anti-coincidence veto efficiency and efficiencies of multi-detector signals, which require MC data to calculate. Because it is difficult to reproduce the "non-constant" nature of primary threshold (energy reconstruction/calibration) and secondary threshold (noise) in MC data, an offline threshold is applied in this work, which is the same for each detector channel and event. This threshold is chosen at 100 keV for PI and 200 keV for PII. The same threshold is chosen for both, the primary and secondary channel. This in addition avoids problems, that arise from the efficiency of quality cuts, that is not known very well in the low energy region below 100 keV [4]. In this region, a part of physical events might be removed by quality cuts, due to the low signal to noise ratio.

5.4 Multiplicities

The default multiplicity of an event is given by the FADC trigger on the primary channel and the number of secondary channels with triggers as reconstructed by the offline trigger algorithm. The multiplicity used for the analysis of coincidence data can differ from the default value, because an additional energy threshold is forced in the offline analysis. Because this threshold is higher than the default thresholds, consequently the multiplicity value of a specific event is potentially decreased. Additionally, detectors that are excluded from the analysis for a particular run due to instabilities, as explained in Ch. 4.4, are not counted towards the multiplicity and instead are completely disregarded in the presented coincidence data analyses. This is done, because the reconstructed energy of instable detectors can not be trusted, which would have an impact on multi-detector events and would therefore introduce a large uncertainty on efficiencies of multi-detector signal searches as done in later chapters. [2]
Data with a given multiplicity are referred to as Mx data in the following, where x is the multiplicity value (e.g. M2 data refers to all events with a multiplicity of 2).
Tab. 5.2 lists the number of events with a certain multiplicity value in the PI and PII data sets. Given are the values for an offline threshold of 100 keV for PI and 200 keV for PII, as used for this work. The PI values for a threshold of 200 keV are additionally given for comparison. The increase of the threshold from 100 keV to 200 keV reduces the number of M2 events roughly by half.
Going from PI to PII, the number of M1 events with a threshold of 200 keV increased by 68%, which roughly corresponds to the 60% higher germanium exposure in PII. The number of M2 events increased by a factor of 4 in addition to the exposure ratio, which is a result of the more compact and granular detector array in PII, primarily employing lower mass BEGe detectors in contrast to the high mass semi-coaxial detectors with higher γ-ray absorption efficiency.

5.5 Crosstalk evaluation and correction

In electronics, a signal transmitted on one channel can cause a noise signal on other channels by electromagnetic interference. As most of the material in the GERDA setup is

---

[2] For the $0\nu\beta\beta$-decay analysis which is solely based on anti-coincidence data, unstable detectors are still used as anti-coincidence veto.

Multiplicity	1	2	3	4	5	6+
PI (100 keV)	726934	2711	81	2	1	0
PI (200 keV)	221601	1241	20	0	0	0
PII (200 keV)	371738	7720	339	15	1	0

Table 5.2.: Number of events in the PI and PII data sets with a specified multiplicity given a low energy threshold of 100 keV/200 keV on all detector channels.

not shielded against electromagnetic interferences, detector channels can ”talk” to other detector channels on this way, which is referred to as crosstalk. Crosstalk can happen through capacitive or inductive coupling between any two unshielded components in the electronic cycle, including the detectors (surface), the cables or the front end electronics. Theoretically, it can be modeled with the help of the telegraph equations [150], which is however out of the scope of this thesis. A thorough discussion and analysis of crosstalk can be found in [151].

The size of the crosstalk effect depends on the geometry and the relative positioning of the various crosstalking components and can therefore be different for each channel pair. In general, two components very close to each other typically show a stronger crosstalk relation. The shape of the crosstalk signal furthermore depends on whether the coupling is capacitive or inductive. In case of capacitive coupling via electric field, the current induced by crosstalk is defined by the capacitance between the two components (e.g. two parallel running cables) and is proportional to the original current. Inductive coupling on the other hand referres to crosstalk, which is induced on one component by the changing magnetic field of another component and is thus proportional to the current gradient of the original signal.

In the following, then referring to the crosstalk from channel i to channel j, the notation $(i \to j)$ is used. Furthermore, channel i in this case is referred to as the ”trigger channel”, while channel j is referred to as the ”crosstalk channel”.

Given energy conservation, a partial transfer of a signal from one channel to another channel results in the reduction of the amplitude of the original signal. This is in principle not a problem for the majority of the GERDA data, as the loss of amplitude is compensated for by the energy calibration assuming the crosstalk amplitudes are proportional to the amplitude of the trigger signal. Knowledge of the actual size of the crosstalk effect is not necessary in this case. However, for coincidence events, multiple trigger signals of different channels are affecting each other. This results in a distortion of the signal amplitudes by a varying amount depending on which channel contributes to the signals. Following this, the energy information extracted from the signal amplitudes will also get distorted. The polarity of the crosstalk signal dictates whether the amplitude of each signal is reduced or increased.

The extent of the crosstalk effect shall be illustrated by a simple example. ^{208}Tl is a typical isotope found in the background of GERDA data and is also used as the primary calibration isotope. It emits a highly energetic 2.6 MeV γ-ray in combination with several other γ-rays. In case this γ-ray is fully absorbed in one detector while one of the other γ-rays deposits energy in a second detector and assuming a typical crosstalk effect of 0.1% (i.e. the size of the amplitude in the crosstalk channel is altered by an amount equivalent to 0.1% of the amplitude of the trigger channel), then this results in a 2.6 keV energy distortion in the second detector. This distortion is comparable to the energy resolution

and one order of magnitude larger compared to the usual energy shift of less than 0.2 keV [126] observed after calibration. Hence, it is important to correct for this effect.
To restore the original amplitudes and energy information, it is required to characterise and quantify the crosstalk effect between each channel. This information is then filled into a matrix $\mathbb{M}$, where $\mathbb{M}_{ij}$ describes the size of the crosstalk effect for the case $(i \rightarrow j)$.
In the scope of this section, first examples of crosstalk signals are given as studied by a visual inspection. In a next step, two methods are presented to quantify the crosstalk. The first one was used in PI and is based on the signal amplitudes. It makes several assumption with respect to the shape of the crosstalk signal. However, those assumptions are not true for all the crosstalk in GERDA, therefore the precision of this method is not always sufficient. Furthermore, this method is susceptible to noise, which prohibits the determination of smaller crosstalk effects. Consequently, an improved method was developed in PII to more accurately quantify the crosstalk effect based on averaged waveforms. With both methods, matrices are constructed for the PI and PII data, which are then used to correct the signal amplitudes of coincidence events. Both methods are compared by evaluating the energy resolution and position of various peaks in the crosstalk corrected calibration data in Sec. 5.6.

5.5.1 Data sets for crosstalk evaluation

PI is clearly separated into three periods by the removal of natural detectors and insertion of BEGe detectors on the one-string arm. Such a big change in the setup is expected to change the crosstalk behavior. In PII, the detector array stayed constant so far. Though, an exchange of the cables leading to the electronics cabinet between Run 71 and 72 in September 2016 can potentially affect the crosstalk matrix. Thus especially the periods PIa, PIc, PIIa and PIIb are of interest for the crosstalk determination.
The crosstalk matrix can in principal be determined with any data recorded in *physics mode*. Single physics runs usually suffer from very low statistics in each channel pair and are therefore not suited very well for this analysis. However, a combination of all the physics runs in the above mentioned periods is one of the options, and in fact the only available option for PIa. In addition, during all periods excluding PIa, at least one calibration has been taken in *physics mode*, which provide more than enough statistics to determine the crosstalk matrix very accurately. The calibrations are listed in the following:

- **C1302:** Taken during Run 43 on the 22nd of February, 2013. This calibration was specifically done to study the crosstalk. Only one ^{228}Th source was employed at a time to reduce the number of random coincidences. The sampling frequency of the germanium signals was reduced to 25 MHz. Live-time: 24 min.

- **C1602:** Taken during Run 57 on the 21st of February, 2016, specifically to study the crosstalk. The calibration uses three ^{228}Th sources. Live-time: 45 min.

- **C1605:** Taken during Run 63 on the 17th of May, 2016. This calibration was again done to study the crosstalk, because the previous calibration had relatively low statistics. All three ^{228}Th sources were employed. Live-time: 5 h.

- **C1702:** Taken over five days at the end of Run 76 from the 5th to 9th of February, 2017. This calibration was done using a ^{226}Ra source to study the LAr veto suppression, but also to study the crosstalk after the cable change. The energy threshold was set to about 1 MeV. Live-time: >60 h.

- **C1504:** Taken during PII integration tests on April 30th, 2015.

5.5.2 Crosstalk examples

To gain a first insight into what kind of crosstalk induced signals to expect, waveforms of the PI data set were visually inspected using the graphical user interface provided in the Gelatio framework. To quantify by how much crosstalk changes the extracted energy values of physical signals, several questions regarding the shapes and forms of crosstalk signals need to be answered: Of what size are the expected crosstalk induced signals? What is the polarity of those signals? What is the time structure of the crosstalk signals and are are they similar to the physical trigger signals? Are there different crosstalk signal shapes depending on the channel combination? Is the crosstalk shape independent from the amplitude of the trigger signal? Is there a time dependence (on a run to run basis) of the crosstalk?

In the following some examples for crosstalk signals are given. Fig. 5.1 shows a typically example of a trigger signal in channel 3 and crosstalk signals in channels 2 and 6, as raw signals and shaped signals using the pseudo Gaussian filter. Firstly, it is visible that the polarity of the crosstalk amplitude is reversed in comparison to the trigger signal amplitude. This is also the case for the other channels judging by the visual inspection. The amplitude of the crosstalk signal from channel 3 to channel 6 is about 3% of the amplitude of the trigger signal. The crosstalk can therefore be expected to reach up to a few percent. For some channels, no crosstalk is visible, which may also be hidden below the noise. As can be seen in Fig. 5.1, the crosstalk signal in channel 6 looks very close to the trigger. In consequence, the position of the amplitude maximum of both signals roughly aligns with each other. On the other hand, the crosstalk signal in channel 3 is rather delayed compared to the trigger signal, thus the maximum of the amplitude of the shaped crosstalk signal comes much later.

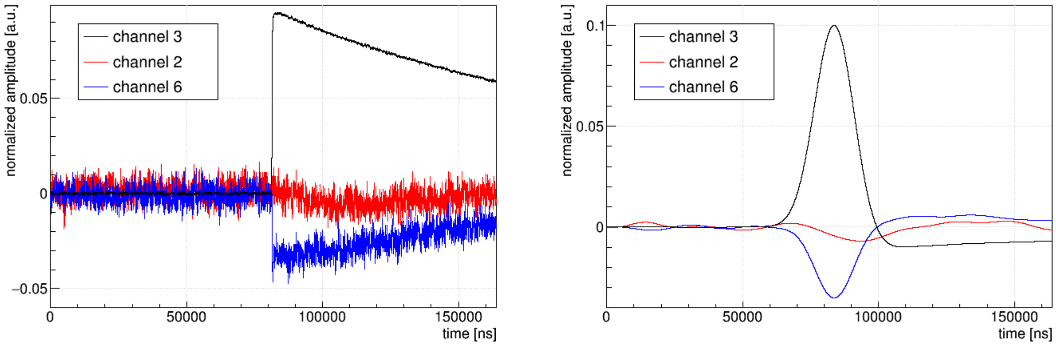

Figure 5.1.: Examples of crosstalk signals (channel 2 and 6), raw (*left*) and shaped with the pseudo Gaussian filter (*right*). The amplitudes of the signals are normalized by a common factor of $\frac{1}{A_{\mathrm{trig}}}$, where A_{trig} is the amplitude of the trigger signal. The trigger signal (channel 3) is additional scaled by a factor of 0.1.

By combining multiple signals of the same channels, one can obtain a clearer view of the crosstalk. Fig. 5.2 shows four examples of different crosstalk signals. The data was collected during a special calibration run in PIc (C1302), for further information see Sec. 5.5.1. To correct for the variation of the trigger position of the trigger signal in a range of 2 μs, the signals are time shifted so that the maximum of the shaped trigger signals align. The crosstalk signals are shifted accordingly by the same amount.

The first plot (2 → 4) shows crosstalk, with a very sharp time profile, i.e. a very quick rise and a fast decline with negative polarity. The width of the sharp spike is in the order of one microsecond and could therefore be caused by inductive coupling by the rising edge of the trigger signal. In rare cases in PI and the majority of PII (often much stronger) this spike feature has positive polarity, like for (13 → 11). Furthermore, the crosstalk signal sometimes shows two spikes with opposing polarity, like (13 → 12), from coupling between two different components. Both examples can be seen in Appendix D.1. This spike like feature only appears for same string channel pairs and is not limited to neighboring detectors, which hints at crosstalk between cables or channels on the front end board. It does not affect the reconstructed energy values, because it cancels out in the shaping process.

The second plot (2 → 5) shows a very slowly rising signal, with the maximum of the amplitude located several $10\,\mu$s behind the trigger signal. Delayed crosstalk signals can be expected due to the long signal cables. The delay is not limited to same string channel pairs, can reach up to about $50\,\mu$s as for (6 → 4) and is also present in PII, e.g. (3 → 36) or (18 → 27). Examples can again be found in Appendix D.1.

The third plot (3 → 6) shows one of the examples from Fig. 5.1. The signal is rather similar to a trigger signal (capacitive coupling), except for a spike at the rising edge similar to the first example, which was previously not visible. Additionally, another delayed maximum can be found about $10\,\mu$s after the rising edge, before it decays with the usually decay time. In PII, (38 → 23) and (39 → 23) among others also show a crosstalk signal very similar to the trigger signal. GD79C (channel 23) and GTF32/GTF45 (channel 38/39) are neither neighboring detectors nor within the same string, but they use neighboring channels on the front end electronics board because the original channel for GD79C is broken. Thus, this crosstalk signal is likely transmitted via the front end electronics.

The fourth plot shows the baseline of channel 11, while a trigger signal is detected in channel 3. No measurable crosstalk signal is visible. The same is true for all channel combinations between the three-string arm and the one-string arm of the detector array in PI.

5.5.3 Amplitude based crosstalk determination

The crosstalk matrix element $\mathbb{M}_{ij}$ in PI was determined by the mean of the distribution of ratios between the maximum negative amplitude A_{xt} of the shaped crosstalk waveform in channel j and the maximum positive amplitude A_{trig} of the shaped trigger waveform in channel i:

$$R^{ij} = \frac{A^j_{\text{xt}}}{A^i_{\text{trig}}} \tag{5.1}$$

The shaping was done using the pseudo-Gaussian filter and the amplitudes were calculated by the corresponding GELATIO energy reconstruction module (GEMDEnergyGauss).

Small physical signals from coincidences can superimpose the crosstalk signal and consequently distort the determination of the crosstalk amplitude. Therefore, events with a low probability to create coincidences should be selected. Potential candidates are events from the ^{42}K full energy peak at 1525 keV or alpha events in the range of 3-5 MeV.

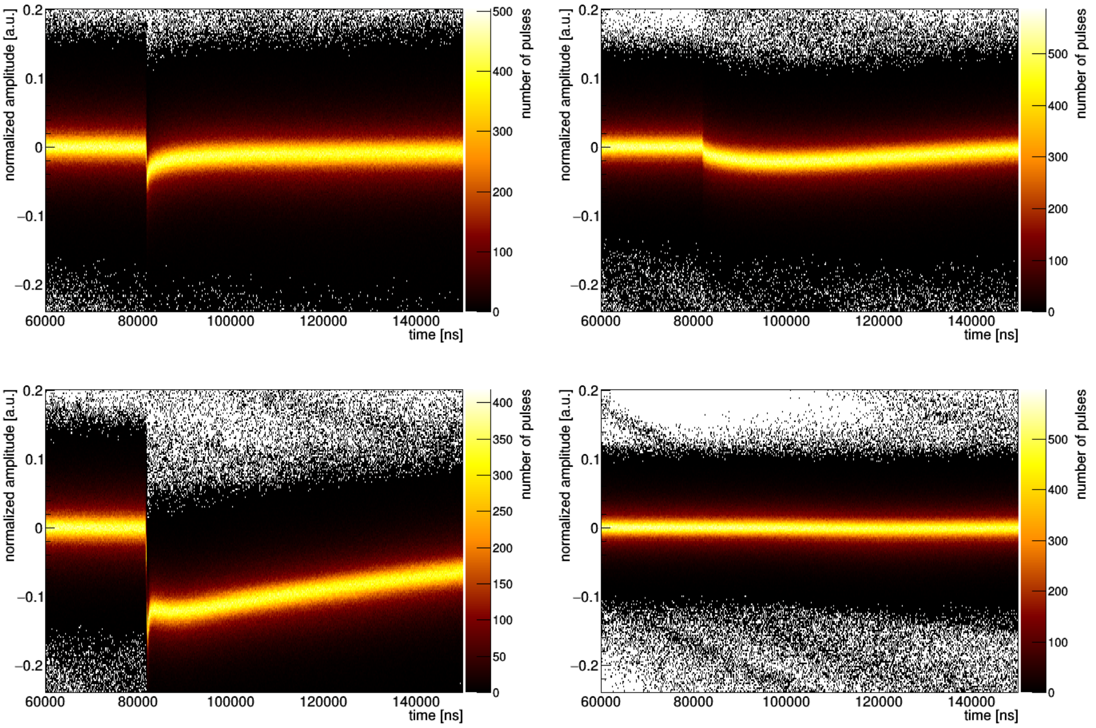

Figure 5.2.: Three examples of crosstalk signatures for $(2 \rightarrow 4)$, $(2 \rightarrow 5)$ and $(3 \rightarrow 6)$ and a typical baseline without measureable crosstalk in case of $(3 \rightarrow 11)$ (*bottom right*). Using the data from calibration C1302.

The accuracy of this method is limited by the noise of the shaped waveforms. The threshold lies at about 5 keV in PI for the semi-coaxial detectors. Thus, using events from the ^{42}K full energy peak, the crosstalk can be determined down to a threshold of about 0.3%. With alpha events the threshold lies at about 0.1%. However, the number of alpha events in the PI data is usually limited to less than 10 per run. Nevertheless, the alpha events are chosen as the preferred event class for the crosstalk determination, because they allow a higher precision and a lower crosstalk threshold due to the increased crosstalk signal to noise ratio.

To compensate for the low statistics of alpha events per run, the data of Run 26 to Run 39 are combined. For each channel pair $(i \rightarrow j)$ a distribution of amplitude ratios R are obtained from the alpha events, which can be seen exemplary for the channel pairs $(4 \rightarrow 3)$ and $(4 \rightarrow 10)$ in Fig. 5.3. The corresponding matrix element is obtained from the mean of the distribution.

The time correlation between the position of the maximum amplitudes from trigger and crosstalk waveforms can be used to decide whether the negative amplitude of the crosstalk waveform is actually caused by crosstalk or just by noise. The amplitude of the pseudo-Gaussian shaped trigger signals lies usually at around 144 μs into the waveform. Hence, the crosstalk amplitude is expected at about the same time. An example is shown in the right plot of Fig. 5.3 for the aforementioned channel pairs. For channel pair $(4 \rightarrow 3)$ the amplitudes of the crosstalk are clearly correlated to the maximum of the trigger signal.

On the other hand, no correlation is visible for channel pair (4 → 10)[3]. Therefore, one can deduce that the crosstalk amplitude is lower than the noise threshold for the latter pair. In such a case, the matrix element is set to 0.

A crosstalk amplitude that is much delayed with respect to the trigger amplitude can indicate a slow rising crosstalk signal, whose trace is very distinct to that of the trigger signal.

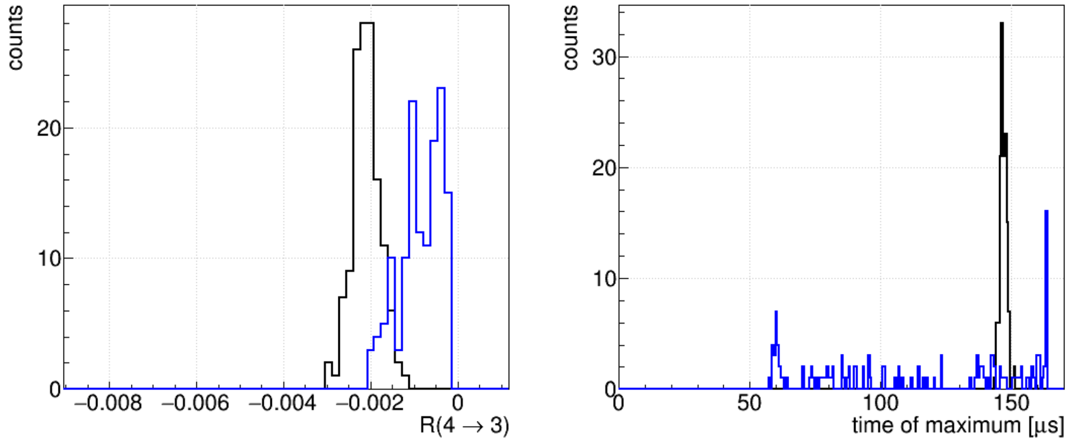

Figure 5.3.: *Left:* Ratios R between the maximum negative amplitude of the crosstalk signal and the maximum positive amplitude of the trigger signal, both after Gaussian shaping. In black for channel pair (4 → 3), in blue for channel pair (4 → 10). *Right:* Position of the maximum negative amplitude in the crosstalk waveform.

It should also be noted, that this method assumes that the polarity of the crosstalk amplitude is reversed to that of the trigger amplitude. From a visual inspection of various crosstalk signals no same polarity crosstalk was apparent. Furthermore, it is assumed that the maximum amplitudes of crosstalk and trigger signals align with each other. In cases where this is not valid, the crosstalk will be overestimated.

This method is in the following referred to as *amp* method.

5.5.4 Averaged waveform based crosstalk determination

Because the *amp* method is extracting information on a waveform by waveform basis, the noise threshold poses a limit to the accuracy of this method. In order to determine the crosstalk matrix elements below the 0.1% level, the information of all crosstalk waveforms of a channel pair need to be combined. For this purpose, the waveforms are first shaped by the energy reconstruction module (pseudo-Gaussian or ZAC), before an average waveform is calculated for each channel pair. The following steps are taken to obtain the matrix element for $(i \rightarrow j)$.

---

[3] The sharp features at the beginning and at the end of the spectrum are artifacts from the shaping algorithm due to the finite waveform length. The shaping algorithm shifts the amplitude by about 60 μs.

Step 1: Waveform selection

The baseline corrected and shaped waveforms used for this task have to fulfill a set of pre-selection criteria:

0) Nonphysical waveforms are excluded, including pulser induced waveforms, discharge events and events that saturate the ADC range (overflow events).
1) The (uncalibrated) energy value of the trigger waveform lies in the selected energy range (typically chosen so that the calibrated energy is roughly >500 keV). Thus, very noisy low energy waveforms are excluded.
2) The maximum of the shaped trigger waveform lies in the selected time window (typically between 60-100 μm, before time offset correction).
3) The trigger waveform only has one trigger as determined by the DAQ. This filters events with pile-up or strong nonphysical signatures.
4) No other waveform within that event has an energy value above a certain threshold (typically corresponding to approximately 30 keV). The goal is to study the crosstalk from one single channel to all other channels.
5) During the early baseline (e.g. first 1000 samples) the normalized crosstalk waveform does not exceed a selected threshold (e.g. 0.015) in positive or negative direction. This criteria is optional and is meant to further filter noisy waveforms.

This selection results in a set of trigger waveforms $\mathbf{W'}^{i}_{n_i}$ in channel i, with $0 < n_i < N_i$, where N_i is the number of selected waveforms.[4] Furthermore, N_{ij} crosstalk waveforms $\mathbf{W'}^{ij}_{n_{ij}}$ in channel j are obtained, with $0 < n_{ij} < N_{ij}$ and $N_{ij} \leq N_i$.

Step 2: Waveform normalization and trigger offset correction

The trigger waveforms in channel i are normalized so that their amplitude value is 1. The waveforms in channel j are scaled accordingly:

$$W^{i}_{n_i}[s] = \frac{W'^{i}_{n_i}[s]}{A'^{i}_{n_i}} \qquad W^{ij}_{n_{ij}}[s] = \frac{W'^{ij}_{n_{ij}}[s]}{A'^{i}_{n_i}},$$

where $A'^{i}_{n_i}$ is the amplitude of the n_i-th trigger waveform pre normalization and s is denoting the samples of a waveform.

Furthermore, to correct trigger position offsets, the waveforms $\mathbf{W}^{i}_{n_i}$ and $\mathbf{W}^{ij}_{n_{ij}}$ for a given event are shifted by a common time so that the maximum of all shaped trigger waveforms align with each other[5].

Step 3: Waveform averaging

To remove remaining outliers like coincidences that fall below the threshold in 4), the averaging process is done in two phases: The converging phase and the averaging phase.

---

[4] The bold notation indicates that a waveform is a vector of ADC sample values.

[5] The ADC trigger is set to about 80 μs. The position of the amplitude maximum relative to the trigger position is dependent on the height of the signal and in general on the signal characteristics. Higher amplitudes will reach the trigger threshold early and reach the maximum later than lower amplitudes.

Converging phase:

The first waveform is accepted. The average $\overline{\mathbf{W}}^{ij}$ is meant to converge towards the global mode of the waveform distribution. Thus, the k-th waveform is only accepted for the average if the residual Δ_k between it and the average waveform $\overline{\mathbf{W}}^{ij}_{k-1}$ obtained from the first $k-1$ waveforms is below a typical value of 0.01. The residual and the new average $\overline{\mathbf{W}}^{ij}_{k}$ are calculated as follows:

$$\Delta_k = \sum_s |\overline{W}^{ij}_{k-1}[s] - W^{ij}_k[s]| \tag{5.2}$$

$$\overline{W}^{ij}_k[s] = \frac{\left(w_{k-1}\overline{W}^{ij}_{k-1}[s]+W^{ij}_k[s]\right)}{w_k}, \tag{5.3}$$

with $w_k = w_{k-1} + 1$ the weight of the k-th average.
The cutoff value for the residual has to be chosen high enough so that the average does not get ”stuck” on a cluster of outlying waveforms but low enough to reject the strongest outliers. The converging phase ends when a typical number of 100 waveforms are accepted for the average. At the end of this phase, the weight of the average is reset to 1.

Averaging phase:

During the averaging phase, the residual threshold is decreased to a typical value of 0.0025. With this only waveforms similar to the average, that in principle are only set apart by noise, are accepted for the final average. Fig. 5.4 shows on the left the residuals of the pre-selected crosstalk waveforms of each channel for the calibration run C1605 (see Sec. 5.5.1). On the right, it shows an example of an averaged crosstalk waveform on top of the distribution of pre-selected waveforms. Also visible are still true coincidences that fall below the threshold applied to the amplitudes (compare item 4 in the above listing).

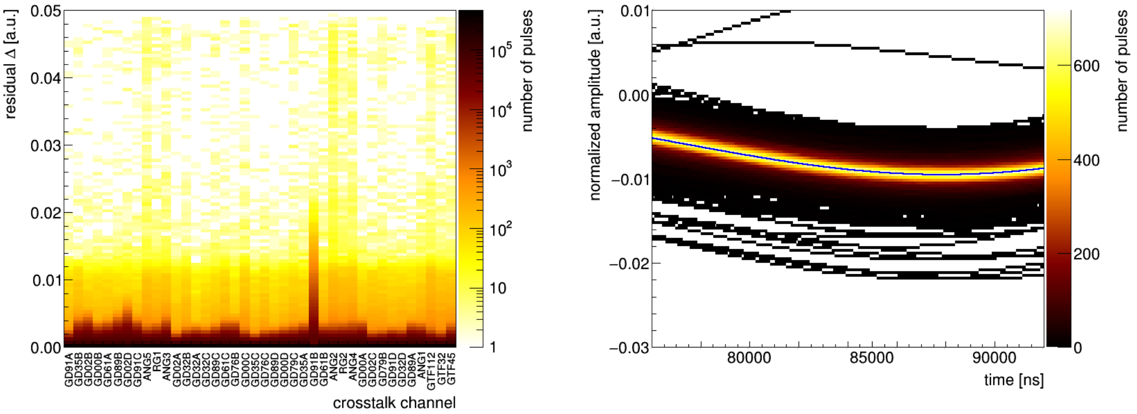

Figure 5.4.: *Left:* Waveform residuals relative to the average waveform during the averaging process. *Right:* Averaged Gaussian shaped crosstalk waveform (blue line) for channel 36, induced by channel 3, zoomed in the region where physical amplitudes are expected in channel 36. The color code shows the distribution of pre-selected waveforms.

The previous steps are processed for all channel combinations. This way, the average trigger waveform $\overline{\mathbf{W}}^{j}_{n_j}$ in channel j is obtained, which is necessary for the following step.

Step 4: Calculation of the matrix element

After the averaging process, the averaged trigger waveform of channel j and the averaged crosstalk waveform for the channel pair $(i \to j)$ are added up:

$$\overline{W}^{j}[s] + \overline{W}^{ij}[s] = \overline{W}^{j+ij}[s]. \tag{5.4}$$

The maximum amplitude $\bar{A}^{j+ij}$ of $\overline{\mathbf{W}}^{j+ij}$ is determined. Because the original amplitude $\bar{A}^{j}$ is normalized to 1, subtracting 1 from $\bar{A}^{j+ij}$ returns the amount by which the original amplitude in channel j is reduced by the crosstalk, relative to the physical trigger amplitude in channel i. This value determines the matrix element $\mathbb{M}_{ij}$:

$$\mathbb{M}_{ij} = \bar{A}^{j+ij} - 1. \tag{5.5}$$

The noise limit of the method is given by the statistics, i.e. the number N_{avg} of waveforms available for the averaging phase. The uncertainty on the average thus decreases with $\frac{1}{\sqrt{N_{\text{avg}}}}$. This method takes additionally into account that the maximum crosstalk amplitude and the maximum trigger amplitude may not align perfectly. Hence, in such cases the crosstalk effect is not overestimated as it is the case for the amplitude method. This method is in the following referred to as *avg* method.

5.5.5 Correction

The correction is applied in the step from tier 2 to tier 3. The reconstructed amplitude A_i of channel i is corrected, using the reconstructed amplitudes of all the other triggered channels j:

$$A'_i = A_i - \sum_{j \neq i} A_j \mathbb{M}_{ij}, \tag{5.6}$$

The correction coming from the largest amplitude is applied to the other amplitudes first. Going on in descending order, the remaining corrections use the already corrected amplitudes. Only one iteration is done, hence second order corrections are mostly neglected.
No correction is applied to channels without trigger. As a result, the crosstalk correction does not change the default multiplicity of an event.

5.5.6 Crosstalk matrix results: Phase I

The crosstalk during PI was determined using the *amp* method explained in Section 5.5.3. During most of PI only physics data was available for the study of crosstalk matrix. A special calibration (C1302) was taken close to the end of PI to verify the matrix.

Amp method

As already mentioned, the event selection in the physics data was concentrating on alpha events at energies between 4-6 MeV. Events are rejected in case the maximum amplitude of the trigger signal is not located in the range of 142-144 μs and in case another channel registers an energy above 100 keV.
The matrix obtained for PIc is shown in Fig. 5.5. Channels 0 and 7 were inactive during most of the PI data taking and are not included in any physics analysis utilizing the

coincidence data. Thus the corresponding matrix elements are set to 0. The average crosstalk between the active channels is $1.6{\cdot}10^{-3}$. As previously expected, the crosstalk can predominantly be found within strings, where the two largest elements are $(3 \to 5)$ and $(5 \to 6)$ with $3.4{\cdot}10^{-2}$ and $3.2{\cdot}10^{-2}$ from string 2. Channel 5 and 6 belong to detectors at the top and at the bottom of the string, respectively. Thus, not only neighboring detectors can show a strong crosstalk relation, hinting at a coupling via cables or front end electronics.

Between pairs of channels from different strings within the three string arm the crosstalk reaches values up to $1.3{\cdot}10^{-2}$. No crosstalk above the noise threshold was observed between the three string arm and the one string arm. The crosstalk between semi-coaxial detectors is on average $1.17{\cdot}10^{-2}$, while the crosstalk between BEGe detectors is on average a factor 10 lower with $1.9{\cdot}10^{-3}$. This can possibly be attributed to the much smaller signal contact surface of the BEGe detectors or the different configuration of the BEGe string, although the electronics are almost identical [117].

This matrix was used for physics analysis in [4].

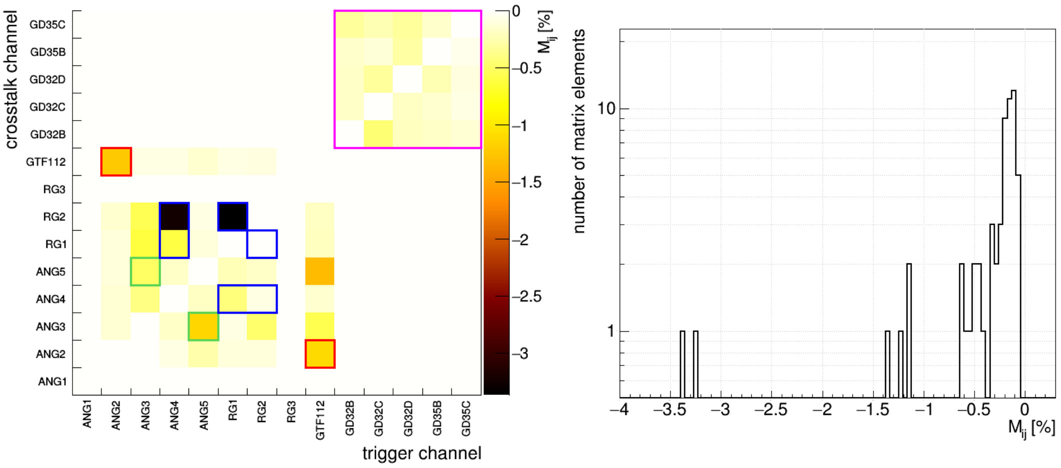

Figure 5.5.: *Left:* Crosstalk matrix determined with alpha events with an energy of 4-6 MeV in Runs 26 to 39. The elements of detector pairs within a string are framed in red (string 1), blue (string 2), green (string 3) and magenta (string 4). The detector names are in the order of their channel number, starting with channel 0 (ANG1) *Right:* Histogram of matrix elements.

Avg **method and stability**

The switch of detectors between PIa and PIc has very likely an effect on the crosstalk matrix, which could not be studied using the *amp* method, due to the low statistics and no *physics mode* calibration was taken during PIa. Hence, the *avg* method is utilized to first investigate potential shifts of crosstalk values during PI, and second to create multiple matrices to account for such a shift if necessary, which would then be used to reprocess the PI data. For this purpose, a crosstalk matrix is extracted from the physics data of each run. To compensate for the low statistics, the event selection was adjusted accordingly: The lower energy threshold was set to 400 (about 200 keV) and the converging phase of the averaging process was already stopped after 15 accepted events. As a result, for each channel pair a few 100 events were accepted for the average, and therefore the uncertainty of the matrix elements is still relatively large. Additionally, the matrix is obtained by combining the Runs 25-30, Runs 25-32, Runs 31-32, Runs 36-46 and from the calibration C1302, using a lower energy threshold of 600 (about 300 keV) and 50 waveforms required for the converging phase. Especially in the calibration data about 10^3-10^4 waveforms are used for the average of each channel pair.

In Fig. 5.6 the matrix element $\mathbb{M}_{18}$ is shown for each run. Indeed, a jump of about $2.5{\cdot}10^{-3}$ is observed between Run 32 and Run 36, which can be attributed to the operations on the detector array. This is the largest jump observed from all matrix elements, while for the majority of matrix elements the jump is smaller than $1{\cdot}10^{-3}$. No deviation from a constant matrix element during PIa and during PIc is visible. The values obtained from the combined physics runs and from the calibration agree with each other within statistical fluctuations. Consequently, two matrices are obtained, using the combination of Runs 25-32 for PIa and the calibration C1302 for PIc.

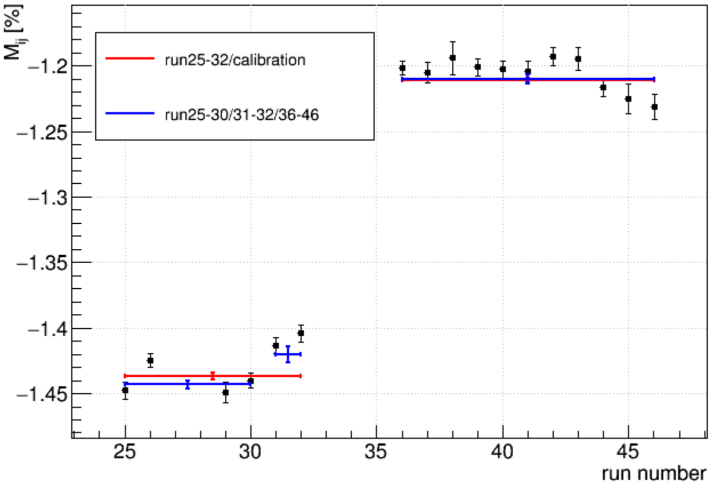

Figure 5.6.: The matrix element $\mathbb{M}_{18}$ determined based on physics runs from Run 25 to 46. Additionally, the element was determined with the combined data of Run 25-32 (red), Run 25-30 (blue), Run 31-32 (blue), Run 36-46 (blue) and the dedicated crosstalk calibration C1302 (red).

For the crosstalk induced on channel 2 and 4, a jump in the crosstalk value already occurred between Run 30 and 31. Run 31 was very unstable and noisy with a drift in the pulser position of 5-7 keV for several channels. The reason for this remains unexplained, but a coincident change of the crosstalk seems reasonable. Thus for those channels, the matrix for PIa was separated into two, for which the elements were obtained from the combination of Runs 25-30 and of Runs 31-32.

In addition to taking the jumps into account, this method was able to determine the matrix elements with a statistical precision in the order of $1{\cdot}10^{-4}$ (single runs) and $1{\cdot}10^{-5}$ (calibration and combined runs), while the *amp* method is limited to $1{\cdot}10^{-3}$. The crosstalk between the three string arm is different to 0 for several elements, with values up to $5{\cdot}10^{-4}$, with the average value below $1{\cdot}10^{-4}$. Furthermore, 3 channel pairs with regular (positive) polarity crosstalk could be identified: $(1 \rightarrow 4)$ with $4{\cdot}10^{-4}$, $(3 \rightarrow 4)$ post Run 36 with $7{\cdot}10^{-4}$ and $(6 \rightarrow 5)$ with $4.5{\cdot}10^{-3}$. The latter can be seen in Appendix D.1.

The matrices obtained with the *avg* method are shown in Appendix D.2 in color code and as table in Appendix D.3. The resulting improvement in the energy resolution and peak positions in the calibration data are discussed in Sec. 5.6.

5.5.7 Crosstalk matrix results: Phase II

Amp method

The *amp* method has been applied at the beginning of PII based on the C1602 calibration. This work was conducted by D'Andrea [138] and uses events over 2 MeV from the ^{228}Th source. As the resulting matrix was only temporarily used and did not impact any final physics results, it should only be mentioned here for reference later on, when studying the energy resolution for the coincidence data in Sec. 5.6.

Avg method

In the following, the crosstalk matrix in PII is determined with the *avg* method using the calibrations C1605 (PIIa) and C1702 (PIIb). Only a subset of the data of the latter calibration was used to decrease processing time, while still keeping sufficient statistics. Events with a physical energy higher than about 500 keV (1500 in uncalibrated energy values) have been used. The number of waveforms accepted for the average varies with each channel pair depending on the source positioning. In both calibrations at least 10^3 and up to 10^5 waveforms have been accepted per pair.
The matrix obtained from C1605 is displayed in Fig. 5.7. The matrix elements that correspond to channel pairs within one string are framed with a red border.
The average of the absolute value of all crosstalk elements is $6{\cdot}10^{-4}$. Only 13 elements have positive polarity, all of them with a value below $4{\cdot}10^{-4}$. The crosstalk is in general the largest for neighboring channels within one string. The average for BEGe detectors is hereby $2.1{\cdot}10^{-3}$, while the average of semi-coaxial detectors is $3.8{\cdot}10^{-3}$. However, the largest two elements are $\mathbb{M}_{3823}$ and $\mathbb{M}_{3923}$ with about $1.6{\cdot}10^{-2}$, which is a result of their neighboring channels on the front end electronics board, as mentioned in Sec. 5.5.2. Also noteworthy is, that the crosstalk between BEGe pairs at the bottom half of the strings with an average of $3.3{\cdot}10^{-3}$ is larger than at the top half with an average of $1.6{\cdot}10^{-3}$. A possible explanation is that the cables of the bottom detectors are longer and run along the side of all detectors above. The uncertainty of the matrix elements is smaller than 10^{-4}, for most elements even an order of magnitude below that.
Fig. 5.8 shows the distribution of matrix element differences between the PIIa and PIIb matrix. Channel 7 has been switched off completely after Run 69 during the first period, because of a broken JFET. The average value only decreases slightly to $5.8{\cdot}10^{-4}$ since the previous calibration. About 60% of the matrix elements have decreased in the PIIb matrix, while the largest change is an increase of $8{\cdot}10^{-4}$ in the channel pair $(38 \rightarrow 23)$.[6] All the other changes are below $4{\cdot}10^{-4}$, thus effects of the cable change or possible shifts over time are rather minor.

Difference between using pseudo-Gaussian and ZAC shaped waveforms

The matrices discussed above have been obtained using waveforms shaped with the pseudo-Gaussian filter, in the following denoted as $\mathbb{M}^{\mathrm{Gauss}}$. Because many crosstalk signals look

---

[6] Channel 38 (GTF32) is excluded from the physics analyses in this work, due to his reoccurring instabilities.

different than typical physical signals and show various shapes as displayed in 5.5.2, different shaping filters are expected to result in different crosstalk amplitudes. Therefore, due to the ZAC filter being the new standard energy reconstruction filter starting with PII, which has in general a shorter integration window, the crosstalk matrix has additionally been studied with ZAC shaped waveforms, denoted as $\mathbb{M}^{\text{ZAC}}$. The ZAC filter parameters are usually optimized for every calibration. As there are only two calibrations taken in *physics mode* for the crosstalk determination, only the two parameter sets optimized based on these calibrations are utilized. The effect of different filter parameters on the matrix can therefore not be studied in detail. However, it is expected to be small compared to the difference to $\mathbb{M}^{\text{Gauss}}$.

Fig. 5.8 also shows the difference of the matrices of the C1602 calibration between the pseudo-Gaussian and ZAC shaping filter on the right. On average, the crosstalk values differ in the order of 10^{-4}. The biggest differences are found for the channel pairs ($38 \to 23$) and ($39 \to 23$) with an increase of about $1.1{\cdot}10^{-3}$ with respect to $\mathbb{M}^{\text{Gauss}}$. Over 80% of the matrix elements are smaller by $1{\cdot}10^{-4}$ on average. The average of the elements of $\mathbb{M}^{\text{ZAC}}$ is $5.5{\cdot}10^{-4}$.

Additionally shown in the left plot in Fig. 5.8 are the differences between $\mathbb{M}^{\text{ZAC}}$ for the C1602 and the C1702 calibrations. Again, the largest changes are found in the channel pairs ($38 \to 23$) and ($39 \to 23$) with an increase of $7.7{\cdot}10^{-4}$. About half of the elements increased, the other half decreased, indicating that there is no big systematic change. The average of the crosstalk values only changes marginally to $5.4{\cdot}10^{-4}$.

The matrices of PII as obtained with the *avg* method and ZAC shaping are given as a table in Appendix D.3.

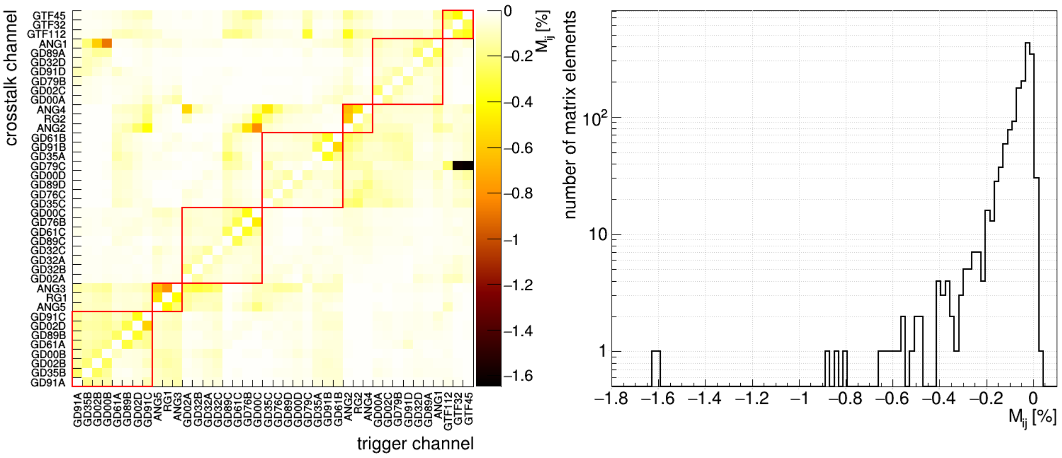

Figure 5.7.: *Left:* Crosstalk matrix extracted from the C1605 calibration. *Right:* Histogram of matrix entries.

In Ch. 5.6 the energy resolution curves and peak shifts are determined for the coincidence data. This chapter will also include an evaluation of the efficiency of the crosstalk correction using the various methods discussed above.

Stability

As in PI, a crosstalk matrix is extracted from each physics run to study the run to run stability. The same averaging parameters are used as in PI.

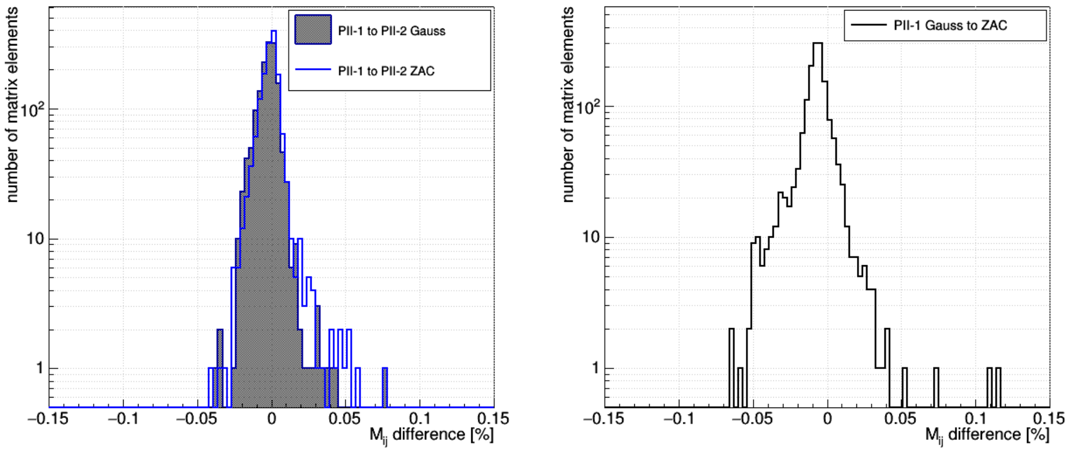

Figure 5.8.: Difference between elements of matrices *Left:* from PIIa to PIIb, *Right:* determined with pseudo-Gaussian shaped and ZAC shaped waveforms.

Because there are many more detector pairs, it is not feasable to visually inspect the stability of each. Instead, runs and detector pairs, where the matrix element from the physics data differs to the matrix element obtained from the corresponding calibration (C1605 until Run 71, C1702 from Run 72 onwards) by more than three sigma are counted. Fig. 5.9 shows on the left the total counts for each run. The most pairs with three sigma deviations are counted in the early runs of PII (up to 90) and in Run 70 and 71 (~140). Additionally shown are histograms limited to pairs with a deviation larger than $0.5{\cdot}10^{-3}$ and $1.0{\cdot}10^{-3}$. On the right side of Fig. 5.9 are shown for each combination of trigger and crosstalk channel the number of runs with a three sigma deviation larger than $0.5{\cdot}10^{-3}$. Especially GTF32 (channel 38) stands out with the most counts. The deviation can be mostly found in the early PI runs. This detector channel also caught attention by its reoccurring stability problems in calibration runs (pulser drifts). It was therefore decided to exclude it completely from further physics analyses using the M2 data.

Furthermore, the upper half of the first string and the second string show the majority of counts, which can mostly be found in Runs 70 and 71. Possible reasons are a short power cut between Run 69 and 70 and a major earthquake in this region on the 24th of August, although the latter should only affect Run 71.

The average of the deviations larger than three sigma is $4.9{\cdot}10^{-4}$, $4.1{\cdot}10^{-4}$ without GTF32 and $5.5{\cdot}10^{-4}$ for only Run 70 and 71. The crosstalk is mostly overestimated by the calibrations.

No actions have been taken so far to take care of these crosstalk stability problems. Two possible ways to proceed are:

a) to use selected matrix elements obtained from the physics runs for periods with larger deviations, or determine the matrix elements from a combination of physics runs, e.g. Run 70 and 71, to increase the statistics.

b) to exclude specific combinations of trigger and crosstalk channels for runs with larger deviations.

The decision will be made before the final data processing and selection of PII (see also the disclaimer in Appendix I).

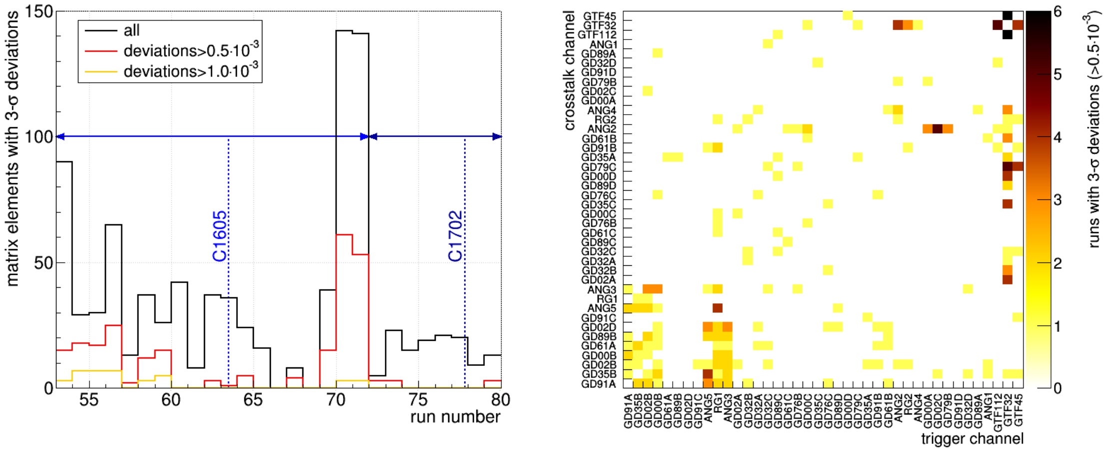

Figure 5.9.: *Left:* The number of crosstalk matrix elements determined from the physics run itself, that deviate from the element as determined from the respective calibration by more than three sigma. The red and orange histograms additional put a lower limit on the absolute deviation. The blue dashed lines indicate when the calibrations have been taken, while the arrows span over the runs for which the corresponding calibration is used for the crosstalk determination. *Right:* The number of runs for each combination of trigger and crosstalk channel, for which the matrix elements determined from the physics run and the matrix elements determined from the calibration deviate by three sigma.

5.5.8 Systematic uncertainties and cross-checks

Energy dependence

By selecting events from a wide range of energies, one has to assume that the crosstalk effect is energy independent, i.e. the amplitude of the crosstalk signal is proportional to the amplitude of the trigger signal.

A quick check is performed using the calibration C1702. Two crosstalk matrices are extracted. For the first, only events with a trigger amplitude between 1500 and 4000 (corresponds to an energy of about 500-1300 keV, though an online threshold of 1 MeV is set during the calibration run) are used, while the second matrix is based on events with an amplitude larger than 4000. The average energies of the selected events are roughly 1.1 MeV and 1.6 MeV, respectively.

The mean difference between all matrix elements of both matrices is $3{\cdot}10^{-6}$, while the standard deviation of the distribution of differences is $2{\cdot}10^{-5}$. It can be concluded, that the amplitude of the crosstalk signal is directly proportional to the trigger amplitude, i.e. no energy dependence has been observed within the required precision.

Difference between calibration and physics runs

The calibrations runs usually take a few hours up to a few days in case of C1702. Therefore, parameters extracted from these runs only represent the status of the experiment during that day. On the other hand, the live-time of physics runs can be in the order of months. During this long time, drifts might happen in experimental parameters like the energy calibration, but also in the crosstalk.

A cross-check was done of the matrix obtained from C1702, by extracting a matrix from the three combined physics Runs 77-79 and evaluating the differences between both matrices (see Fig. D.4). The standard deviation of the differences has been found to be $6{\cdot}10^{-5}$, which corresponds to an energy of 0.06 keV, if the crosstalk is induced by a 1 MeV signal. Thus, on base of this exemplary comparison one can deduce that the calibration runs represent the physics runs with respect to the crosstalk behavior within the necessary precision.

Additional noise induced by crosstalk

Noise in the crosstalk effect will add to the already existing electronic noise on the waveforms. To estimate this additional noise contribution, the width of the waveform distributions can be compared at several positions. Three positions in the waveform have been used: before the trigger at $40\,\mu$s, at the maximum of the trigger signal at $84\,\mu$s and at the maximum of the crosstalk signal at $89\,\mu$s. Since events with varying energies are considered, the profiles consists of a sum of Gaussian distributions with varying widths, e.g. high energy events will lead to a small width and vice versa. Neither of the three profiles shows any significant deviation from the others. The added noise from the crosstalk is therefore negligible.

Time alignment of maximum amplitudes

The averaged crosstalk signal in channel j is aligned to the position of the maximum amplitude of the trigger signal in channel i, that induced the crosstalk. To determine the crosstalk effect, the averaged crosstalk signal is applied to the averaged trigger signal in channel j though. A mismatch of the position of the maxima of the signal in the first and the second channel i and j of a M2 event will lead to an inaccuracy in the crosstalk correction. This uncertainty can be evaluated with M2 events in calibration data. Doing this, it turns out that the maxima are usually very well in sync, i.e. for the majority of events within one sample, with a few events in a range of $\pm 0.8\,\mu$s.

Using this range, a quite conservative estimation of the crosstalk uncertainty can be given by shifting the averaged crosstalk signals by $0.8\,\mu$s during the calculation of the crosstalk matrix. By comparing the altered matrix obtained this way to the original matrix, an average difference of all matrix elements of $2{\cdot}10^{-5}$ has been observed, which corresponds to an energy shift of only 0.02 keV if the crosstalk is induced by a 1 MeV signal.

Different weighting of averaged crosstalk signal

When extracting the matrix elements, the averaged crosstalk signal, induced by a trigger signal with amplitude 1, is added to the averaged trigger signal with amplitude 1 in the second channel (1 to 1 weighting). In the data, e.g. a 2.6 MeV signal crosstalks to a channel with a 583 keV signal (5 to 1 weighting). The different weighting can shift the position of the amplitude of the combined signal and result in a slightly different size of the crosstalk effect.

This uncertainty is estimated by applying different weightings of up to 20 to 1 (and vice versa) to the averaged signals and subsequently re-extracting the matrix elements. The comparison of the modified matrices and the original matrix yield an average difference of $2{\cdot}10^{6}$, which corresponds to 0.002 keV, if the crosstalk is induced by a 1 MeV signal. The maximum difference for a single matrix element corresponds to 0.1 keV. Since these shifts are all smaller than the energy resolution and the peak shifts in the data, this uncertainty is negligible.

5.6 M2 energy resolution and peak positions

In this chapter, the energy resolution is determined for the semi-coaxial and BEGe data in the M2 coincidence data. This process is done similarly to the work presented in [126], where the energy resolution was determined for the M1 data. The M2 energy resolution is compared to the one obtained from the M1 data and reasons for a degradation of the energy resolution in the M2 data are discussed. Additionally, the stability of the energy resolution and peak position is investigated and energy resolution curves are obtained for both data sets.

Weekly calibration measurements have been taken with ^{228}Th sources. The recorded spectra feature various γ-ray peaks that can be used to determine the energy resolution at different positions in the spectrum. In addition, the calibration data has been processed multiple times using different crosstalk matrices to evaluate the efficiency of the crosstalk correction. The following matrices are considered, which are discussed in Sec. 5.5:

1) $\mathbb{M}^{\text{unit}}$: a unit matrix (i.e. no crosstalk correction)
2) $\mathbb{M}^{\text{amp}}$: a matrix determined with the *amp* method
3) $\mathbb{M}^{\text{avg}}$: a matrix determined with the *avg* method using waveforms shaped with the semi-Gaussian filter
4) $\mathbb{M}^{\text{ZAC}}$: a matrix determined with the *avg* method using waveforms shaped with the ZAC filter (PII only).

For the M1 data, 9 peaks of the ^{228}Th spectrum have been used for this task. The statistics in the M2 data are about one order of magnitude lower compared to the M1 data. As a result only 4 of the peaks are usable. The peaks are located at 583 keV, 860 keV, 1593 keV and 2615 keV. The calibration spectra are divided into spectra of semi-coaxial detectors and spectra of BEGe detectors. Each event features an energy deposition in two detectors, thus two entries per event are added to the spectra. An example spectrum for the BEGe detectors is displayed in Fig. 5.10 for the calibration from the 17th of May, 2016 using the ZAC energy reconstruction[7].

The fitting of the peaks is done using a Gaussian function, with a low energy tail, a low energy step and otherwise a linear background [152]. The peak width is hereby extracted directly from the fit function at the half maximum of the peak height. The uncertainty of the peak width is taken as the uncertainty of the standard deviation of the Gaussian part, scaled to the width extracted in the previous step. The low energy tail is especially important in case of an imperfect crosstalk correction (or none at all), as the energy tends to be underestimated by the reconstruction. For peaks with a low number of counts (less than 1000) it was refrained from using a function as complex and instead only a Gaussian function with a linear background was used, to achieve a more stable fit.

---

[7] The annihilation peak at 511 keV and the single escape peak at 2104 keV are excluded, due to a increased width related to the kinematics of the annihilation process.

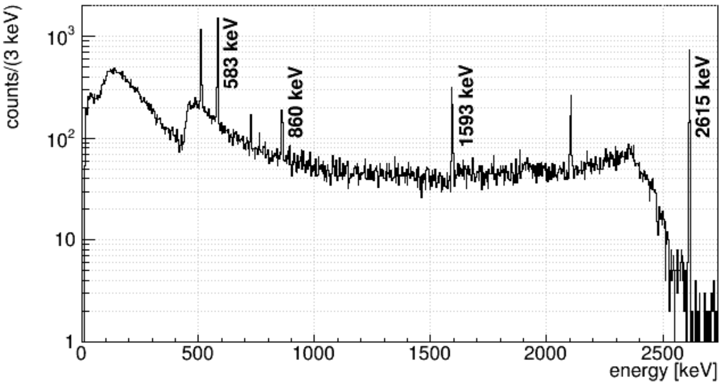

Figure 5.10.: Example of a ^{228}Th calibration spectrum of the BEGe detectors. Labeled are the γ-lines used to extract energy resolution and peak position.

5.6.1 FWHM and peak shifts

The standard deviation σ of the peaks is extracted together with the peak mean for each calibration spectra. Fig. 5.11 shows the distribution of the Full Width at Half Maximum (FWHM $= 2.35 \cdot \sigma$) and the deviation of the peak mean to the literature value (peak shift) respectively for the four peaks in the calibration spectra of the BEGe data set. The corresponding plot for the semi-coaxial data set can be found in Appendix D.5. The average FWHM (solid lines) is improved by up to 13% with crosstalk matrix $\mathbb{M}^{\mathrm{amp}}$ for the two lower energetic peaks. The higher energetic peaks are not affected as much by the crosstalk, due to the energy in coincidence to the two higher energetic peaks being on average about three times lower than for the lower energetic peaks as investigated with ^{208}Tl simulation data. Crosstalk matrix $\mathbb{M}^{\mathrm{avg}}$ and $\mathbb{M}^{\mathrm{ZAC}}$ improve the resolution by up to 20%.

Without crosstalk correction, on average the peaks are shifted by typically 0.5 keV below the literature value and up to 0.9 keV for the 583 keV peak in the semi-coaxial data set. The crosstalk matrix $\mathbb{M}^{\mathrm{amp}}$ overcompensates for the shift. The peaks are located by up to 1 keV above the literature value. This is a problem of the noise threshold of this crosstalk determination method, which results in an overestimation of most of the smaller matrix elements and thus a too large correction factor. With crosstalk matrix $\mathbb{M}^{\mathrm{ZAC}}$, the average peak shifts are within 0.3 keV. Crosstalk matrix $\mathbb{M}^{\mathrm{avg}}$ results in only slightly larger shifts. The spread of the peak shifts around the average value is in most cases also well within 0.2 keV.

A shift of about 0.2 keV has also been observed in the M1 calibration data. Hence, it can be assumed that the shift seen in the M2 data largely stems from the shift already inherent to the energy calibration, which is based on the M1 data. The origin of this shift is currently under investigation.

5.6.2 Stability

The energy resolution and peak shift extracted from each calibration is shown in Fig. 5.12 for PI (using $\mathbb{M}^{\mathrm{avg}}$) and in Fig. 5.13 for PII (using $\mathbb{M}^{\mathrm{ZAC}}$), in both cases for the peak at 2615 keV. The corresponding plots for the other peaks can be found in the Appendix D.5. The FWHM does not show a strong time dependence in PI. Deviations of single calibra-

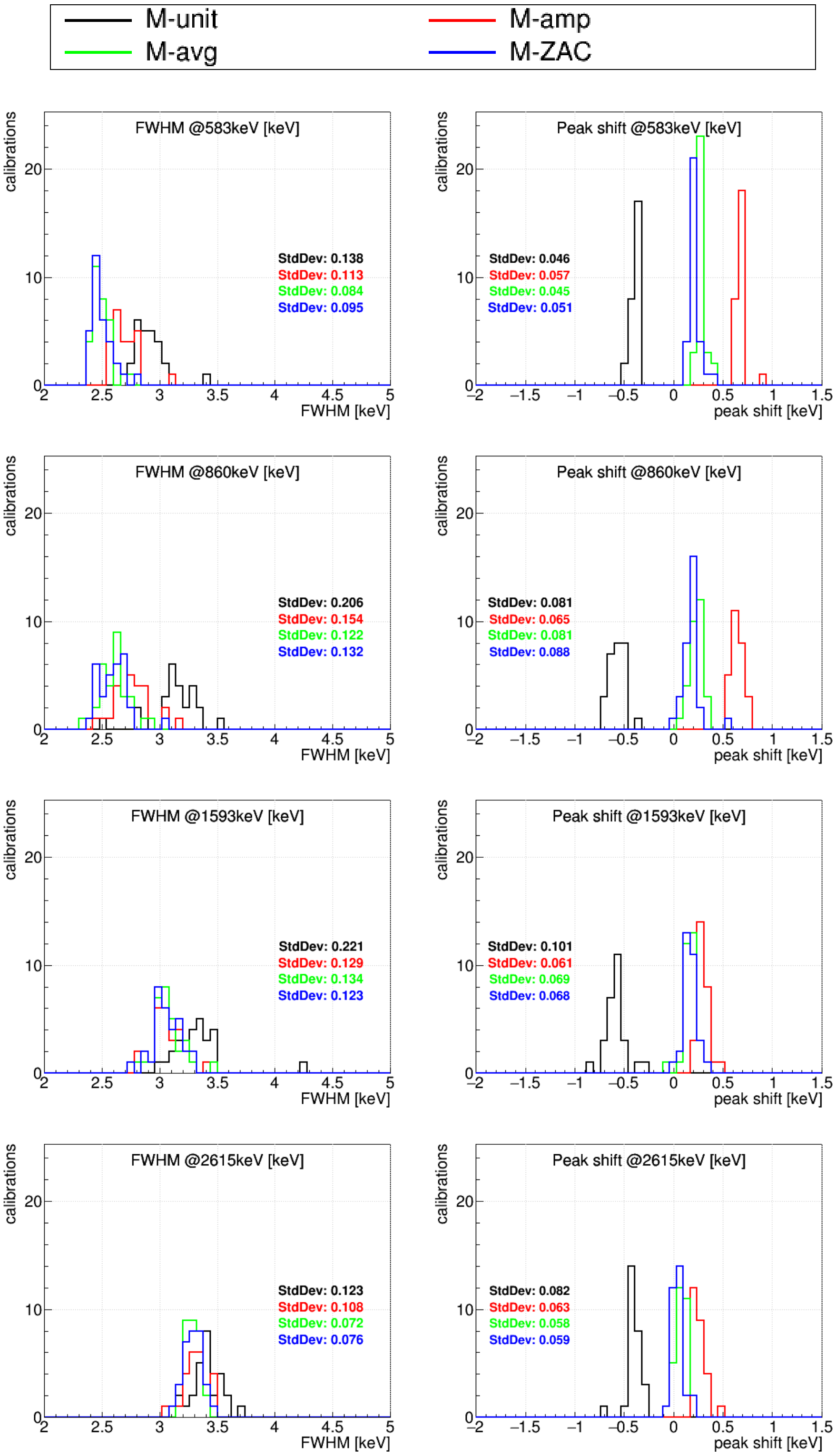

Figure 5.11.: Illustrated is the distribution of the FWHM (*left*) and the peak shift (*right*) obtained from 4 peaks of ^{208}Tl in the BEGe data of the PIIa calibration runs. The plots compare the distributions obtained without crosstalk correction ($\mathbb{M}^{\text{unit}}$) and with the three different crosstalk correction methods ($\mathbb{M}^{\text{amp}}$, $\mathbb{M}^{\text{avg}}$, $\mathbb{M}^{\text{ZAC}}$). Also given is the standard deviation of each distribution.

tions from the mean are largely within statistical expectations. Furthermore, jumps of the detector performance in a few calibrations are expected considering data taking period lasted over a year and are all within an acceptable range. Periods with larger jumps are already excluded from the data sets by the M1 analysis.

Data points with very large uncertainty point to either a calibration with very low statistics or a problem with the fit. Due to their high uncertainty, these points do not contribute to the mean value in a significant way. Problematic fits that led to values with an unnatural low uncertainty have been removed, which concerns not more than three data points in each data set.

PII shows some stronger deviations from the mean for the 583 keV line (see Fig. D.12). In February of 2016, several calibrations showed an increase in the FWHM in the semi-coaxial data set, though none larger than 0.5 keV. Additionally, the performance of the semi-coaxial detectors improved after the end of PIIa. Furthermore, the BEGe detectors show an improvement in the peak shift during PIIb.

As the origin of the peak shifts has not been understood yet, it is difficult to make assumptions about the cause of instabilities of them. A connection to time variations in the crosstalk seems plausible though, which would also explain why they are mostly observed for the 583 keV line.

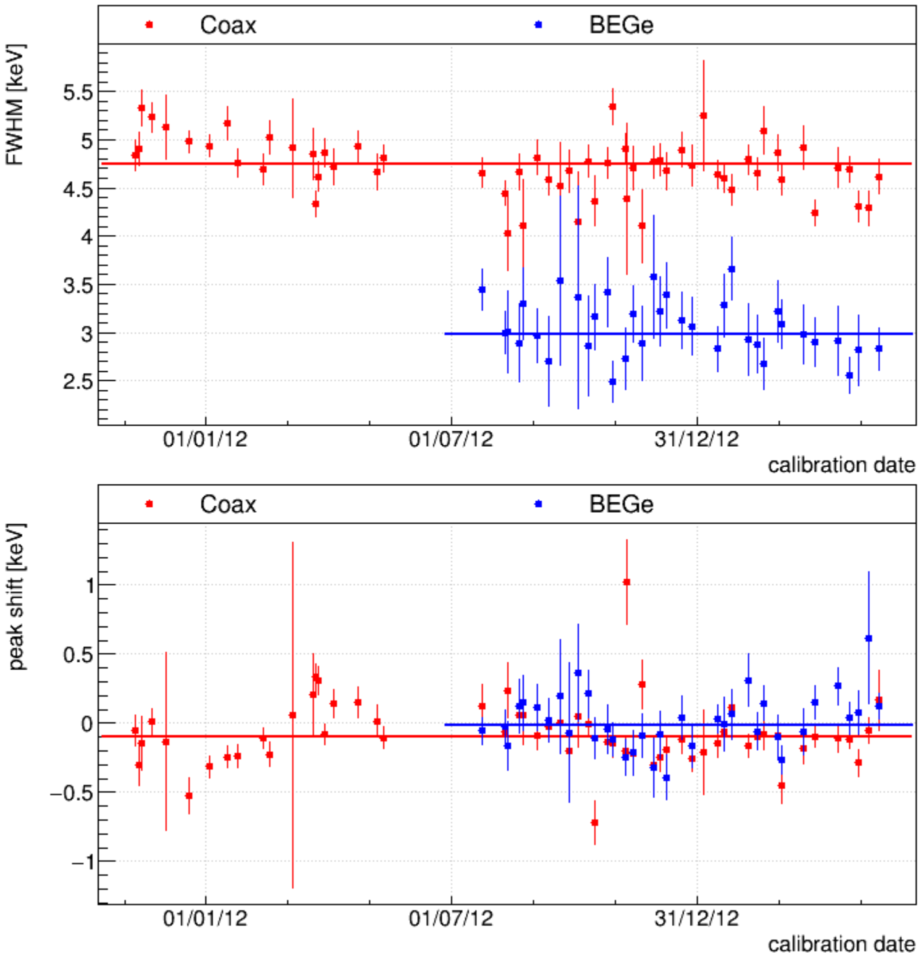

Figure 5.12.: FWHM (*top*) and peak shift (*bottom*) of the 2615 keV γ-line of ^{208}Tl extracted from the PI calibration runs for the semi-coaxial and BEGe data.

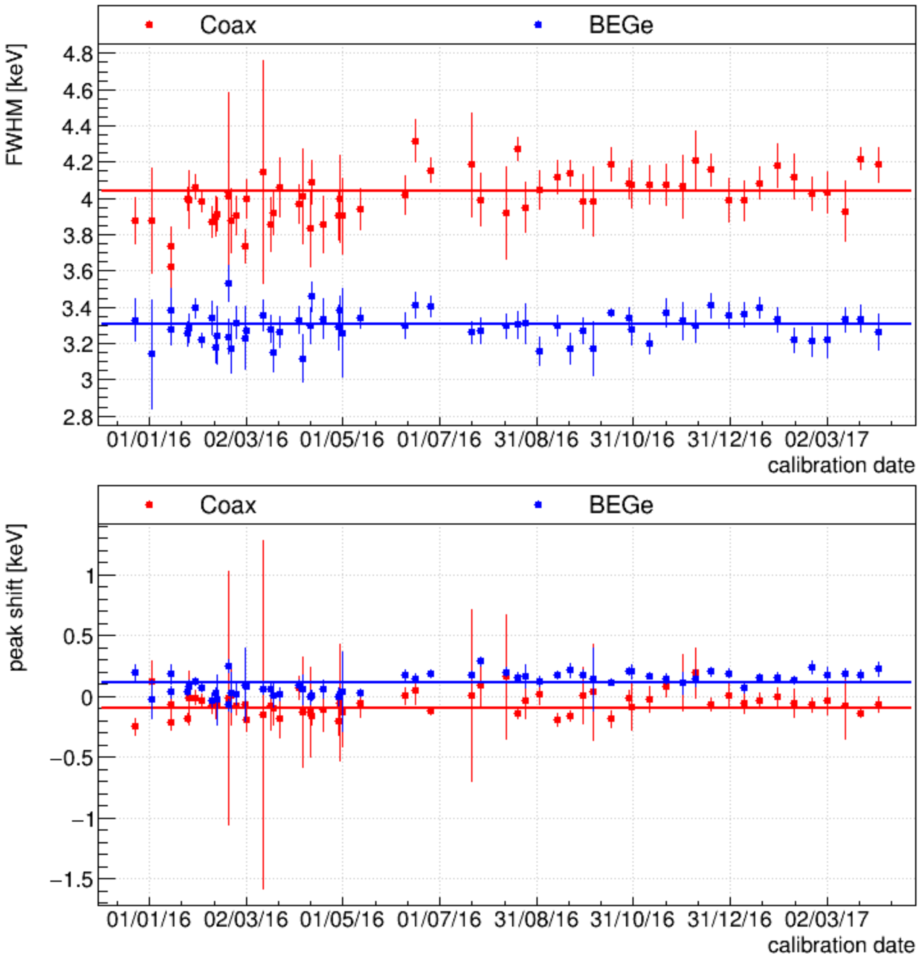

Figure 5.13.: FWHM (*top*) and peak shift (*bottom*) of the 2615 keV γ-line of ^{208}Tl extracted from the PII calibration runs for the semi-coaxial and BEGe data.

5.6.3 Validity time weighted energy resolution

To estimate the energy resolution in the physics data from the calibration data, each calibration needs to be weighted with the live-time of the corresponding physics data that the calibration is applied to, i.e. the time of validity.

In a first step, the energy resolution values FWHM, as extracted from each calibration and each peak, are fit with the following curve, which takes into account the peak width caused by the limited number of charge carriers and the one caused by the electronic noise:

$$\mathrm{FWHM}(E) = \sqrt{p_0^2 + p_1 \cdot E} \tag{5.7}$$

A different energy resolution curve was also suggested [153]:

$$\mathrm{FWHM}(E) = \tilde{p}_0 + \tilde{p}_1\sqrt{E} \tag{5.8}$$

The first equation is used to obtain the mean FWHM values at any given energy, while the second equation is used to study the systematic uncertainty coming from the choice of fit function.

The FWHM_i of each calibration at a given energy are then combined weighted with the time of validity:

$$\mathrm{FWHM} = \frac{\sum\limits_i \frac{\mathrm{FWHM}_i \cdot t_i}{\Delta\mathrm{FWHM}_i^2 \cdot T}}{\sum\limits_i \frac{t_i}{\Delta\mathrm{FWHM}_i^2 \cdot T}}, \tag{5.9}$$

$$\frac{1}{\Delta\mathrm{FWHM}^2} = \sum_i \frac{t_i}{\Delta\mathrm{FWHM}_i^2 \cdot T}. \tag{5.10}$$

The second equation is giving the uncertainty on the combined value, with t_i the corresponding physics live-time of calibration i and $T = \sum\limits_i t_i$.

The weighted values for FWHM and the peak shift are given in Tab. 5.3 comparing the values before and after crosstalk correction for PIIa.

5.6.4 Comparison to combined calibration spectrum

In the previous section, the FWHM of the peaks has been combined without taking into account, that each calibration can have a different shift in the order of 0.1 keV. These shifts can lead to an additional broadening of the combined peak, although this effect is expected to be small as the shifts are in general small compared to the energy resolution. To check if this is indeed true, in this section the peaks are fit in the combined calibration spectra, i.e. the sum of all calibration spectra. Tab. 5.3 additionally gives the FWHM and peak shifts obtained from the combined calibration spectrum.

The energy resolution in the combined calibration spectrum and the validity time weighted values from 5.6.3 usually agree within the uncertainty. This shows that the individual shifts of each calibration does not contribute significantly to a degradation of the FWHM, as expected. The FWHM obtained from the combined spectrum is actually slightly better in all cases, which likely comes from the different weighting of the calibrations (live-time weighting versus validity time weighting).

The peaks in the combined calibration spectrum are shifted by less than 0.2 keV for the PI data and by less than 0.3 keV for the PII data using the best crosstalk correction.

Fig. 5.14 shows a comparison of the 583 keV peak in the combined calibration spectra using the different crosstalk correction matrices. The improvement of energy resolution of the *avg* method is clearly visible. The residuals in Fig. 5.14 reveal deviations from a Gaussian shape of the peaks. The thinner top and tails to both sides are expected from the fact, that the combined calibration spectra contain data from various calibrations and detectors, each with a different energy resolutions. Hence, the peaks are actual a sum of multiple Gaussians with varying widths. The tail towards the higher energy side seems slightly stronger, which is possibly caused by remaining imperfections in the crosstalk correction, for example from small variations of the crosstalk over time. It should also be noted, that the calibration data discussed here is exaggerating the crosstalk effect in comparison to the typical physics data, due to the high average energy of over 800 keV that comes in coincidence to the 583 keV peak energy.

5.6.5 Energy resolution curves

The aim of this section is to esimate the energy resolution at any energy by determining the energy resolution curves, i.e. the dependence of the energy resolution on the energy.

Phase I		583 keV	860 keV	1593 keV	2615 keV
Coax	FWHM	5.119±0.111	5.217±0.027		5.800±0.167
$\mathbb{M}^{\text{unit}}$	Shift	-0.687±0.021	1.061±0.051		-1.124±0.021
BEGe	FWHM	2.587±0.066	2.525±0.084		3.247±0.059
$\mathbb{M}^{\text{unit}}$	Shift	-0.382±0.014	-0.484±0.039		-0.365±0.028
Coax	FWHM	4.053±0.019	4.163±0.052		4.802+-0.029
$\mathbb{M}^{\text{avg}}$	Shift	-0.018±0.013	-0.138±0.028		-0.101+-0.013
BEGe	FWHM	2.188±0.063	2.327±0.083		3.063±0.051
$\mathbb{M}^{\text{avg}}$	Shift	0.022±0.011	-0.203±0.027		-0.014±0.024

Phase IIa		583 keV	860 keV	1593 keV	2615 keV
Coax	FWHM	3.523±0.013	3.755±0.036	4.084±0.063	4.164±0.025
$\mathbb{M}^{\text{unit}}$	Shift	-0.716±0.008	-0.651±0.017	-0.122±0.030	-0.490±0.018
BEGe	FWHM	2.886±0.011	3.094±0.031	3.298±0.020	3.420±0.017
$\mathbb{M}^{\text{unit}}$	Shift	-0.391±0.007	-0.565±0.013	-0.582±0.010	-0.401±0.010
Coax	FWHM	3.071±0.009	3.096±0.026	3.798±0.055	3.933±0.021
$\mathbb{M}^{\text{ZAC}}$	Shift	-0.015±0.004	0.166±0.012	0.272±0.026	-0.107±0.015
BEGe	FWHM	2.479±0.007	2.572±0.021	3.053±0.017	3.285±0.012
$\mathbb{M}^{\text{ZAC}}$	Shift	0.220±0.003	0.164±0.010	0.160±0.008	0.063±0.007

Phase I combined calib		583 keV	860 keV	1593 keV	2615 keV
Coax	FWHM	4.021±0.026	4.158±0.178	4.357±0.094	4.762±0.030
$\mathbb{M}^{\text{avg}}$	Shift	0.002±0.019	-0.039±0.206	-0.023±0.079	-0.027±0.029
BEGe	FWHM	2.147±0.020	2.200±0.063	2.879±0.078	2.963±0.142
$\mathbb{M}^{\text{avg}}$	Shift	0.035±0.010	-0.178±0.032	-0.130±0.040	0.039±0.247
Phase IIa combined calib		**583 keV**	**860 keV**	**1593 keV**	**2615 keV**
Coax	FWHM	3.005±0.008	3.005±0.042	3.746±0.088	3.921±0.022
$\mathbb{M}^{\text{ZAC}}$	Shift	-0.021±0.004	0.200±0.033	0.277±0.046	-0.069±0.021
BEGe	FWHM	2.376±0.007	2.449±0.030	2.921±0.036	3.254±0.016
$\mathbb{M}^{\text{ZAC}}$	Shift	0.218±0.003	0.189±0.020	0.172±0.028	0.054±0.009

Table 5.3.: Averaged FWHM and peak shifts of 4 γ-lines of ^{208}Tl for the calibration data of PI and PIIa. Given are the values for data without crosstalk correction and data using the $\mathbb{M}^{\text{avg}}$ ($\mathbb{M}^{\text{ZAC}}$) crosstalk correction. Also given are the FWHM and peak shifts of the same γ-lines extracted from the combined spectra of all calibrations (*bottom*).

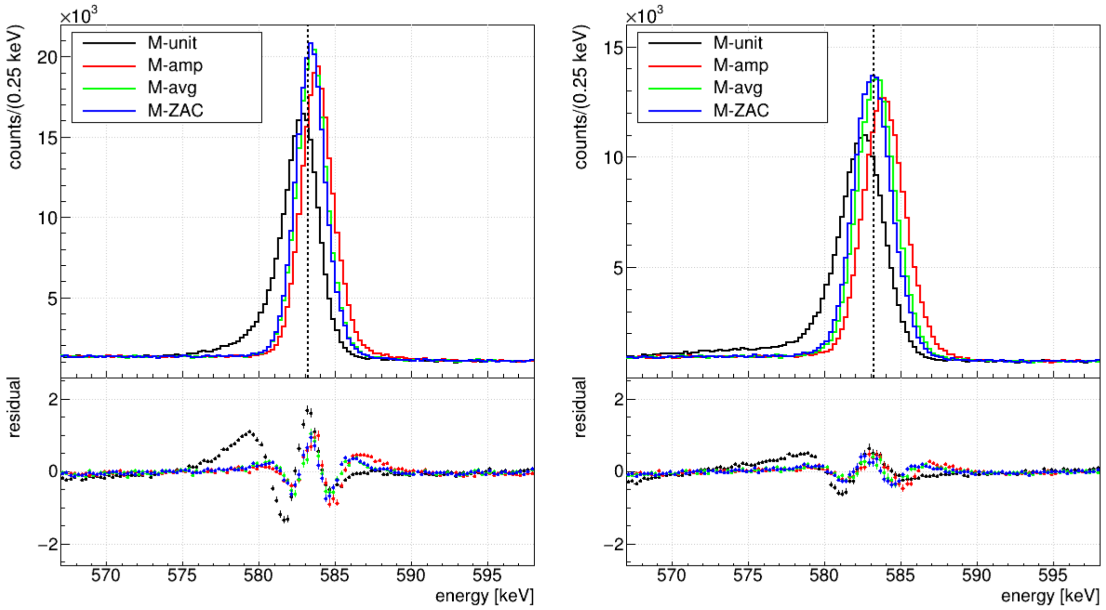

Figure 5.14.: Comparison of the peak at 583 keV in the PII combined calibration data of the BEGe detectors (*left*) and semi-coaxial detectors (*right*) using the ZAC energy reconstruction and different crosstalk corrections as labeled in the legend. In the bottom, the residual of the peaks compared to a fit, using a Gaussian and a linear background component, is shown.

In Tab. 5.4 and 5.5 the combined FWHM are given at the four energies of the ^{208}Tl peaks for the current PII data set, obtained as discussed in the previous section. Additionally, the combined FWHM at the ^{40}K and ^{42}K peaks are given.
The total uncertainty is a combination of uncertainties gained from the propagation in Eq. 5.10, the difference to the FWHM value obtained with the second energy resolution equation and the difference to the value obtained from the final energy resolution curve, in case they differ by more than one standard deviation.
These values are again fit with the above function to obtain the final energy resolution curves. The parameters of the curves of PI and PII are given in Tab. 5.6.
Additionally, the parameters of the energy resolution curves for the combined BEGe and semi-coaxial data sets are also given.

5.6.6 Comparison to energy resolution in physics data

If the possibility exists, the energy resolution just obtained from the calibration data should be compared to values extracted from the physics data. In the M1 data, this is done with the help of the ^{40}K and ^{42}K peaks. The M2 data spectrum does not have sufficient statistics in any peak for this purpose, though. However, both lines are visible in the spectrum of the sum energy of an event. In this case, the width of the peaks is a result from folding the width of the energy depositions in two detectors. Using Eq. 5.7 the energy resolution in the sum spectrum can be obtained with:

$$\sigma_{\text{sum}}(E = E_1 + E_2) = \sqrt{p_0^2 + p_1 \cdot E_1 + p_0^2 + p_1 \cdot E_2} = \sqrt{2} \cdot \sigma(E/2). \tag{5.11}$$

The values extracted from the physics data of PII are listed in Tab. 5.7. Comparing those

Energy [keV]	PI Coax		PI BEGe	
	amp	*avg*	*amp*	*avg*
583	4.832±0.098	4.053±0.019	2.278±0.021	2.188±0.063
860	4.877±0.030	4.163±0.052	2.405±0.042	2.327±0.083
1593	4.996±0.087	4.441±0.072	2.712±0.047	2.659±0.076
2615	5.157±0.176	4.802±0.029	3.090±0.080	3.063±0.051
1525	4.985±0.080	4.416±0.073	2.685±0.049	2.631±0.078
2039	5.067±0.131	4.602±0.058	2.884±0.049	2.843±0.057

Table 5.4.: Averaged FWHM given in keV at 6 energies of interest (4 γ-lines of ^{208}Tl, one γ-line of ^{42}K, $Q_{\beta\beta}$ of ^{76}Ge) for the PI Coax and BEGe data sets. Given are the values using the data corrected with *amp* and *avg* crosstalk correction methods.

Energy [keV]	PII Coax *ZAC*	PII BEGe *ZAC*
583	2.978±0.020	2.475±0.002
860	3.160±0.019	2.609±0.027
1593	3.597±0.030	2.934±0.036
2615	4.129±0.029	3.335±0.011
1525	3.559±0.032	2.905±0.038
2039	3.839±0.011	3.116±0.020

Table 5.5.: Averaged FWHM given in keV at 6 energies of interest (4 γ-lines of ^{208}Tl, one γ-line of ^{42}K, $Q_{\beta\beta}$ of ^{76}Ge) for the PII semi-coaxial and BEGe data sets.

	p_0 [keV]	p_1 [keV]	$\tilde{p}_0$ [keV]	$\tilde{p}_1$ [keV]
PI Coax$_{amp}$	4.734	$1.600{\cdot}10^{-3}$	4.203	$2.204{\cdot}10^{-2}$
PI BEGe$_{amp}$	1.984	$2.149{\cdot}10^{-3}$	1.583	$2.944{\cdot}10^{-2}$
PI Coax$_{avg}$	3.811	$3.264{\cdot}10^{-3}$	3.390	$2.814{\cdot}10^{-2}$
PI BEGe$_{avg}$	1.862	$2.264{\cdot}10^{-3}$	1.509	$3.069{\cdot}10^{-2}$
PII Coax$_{ZAC}$	2.554	$4.029{\cdot}10^{-3}$	1.940	$4.227{\cdot}10^{-2}$
PII BEGe$_{ZAC}$	2.166	$2.460{\cdot}10^{-3}$	1.711	$3.156{\cdot}10^{-2}$

Table 5.6.: Parameters p_0 and p_1 of the FWHM function (5.7), and $\tilde{p}_0$ and $\tilde{p}_1$ of the alternative FWHM function (5.8) for the semi-coaxial and BEGe data set of PI and PII.

	Coax		BEGe	
	calibration	physics	calibration	physics
^{40}K	4.35	3.98±0.47	3.60	3.34±0.24
^{42}K	4.38	4.12±0.26	3.62	3.20±0.12

Table 5.7.: Comparison of the energy resolution (FWHM in keV) of the sum energy of a M2 event in the calibration and the physics data. The uncertainties of the values obtained from the calibration are much smaller than from the physics FWHM.

to the values obtained from the calibration using Eq. 5.11, shows that the energy resolution seems to be better in the physics data.

It is important to note, that the contribution of each detector to the spectra is different between calibration and physics runs. In the calibration data, the ^{228}Th sources are positioned so that each detector collects sufficient statistics and contributes similarly to the spectrum of the full array. In case of the physics data, a higher concentration of ^{42}K has been observed in the top detectors (see Ch. 4.5.2). The top detectors typically exhibit a better resolution than the bottom detectors because of the shorter signal cables, introducing less noise. Therefore, the energy resolution of the ^{42}K peak is expected to be better than interpolated from the calibration data. In case of ^{40}K, a contamination on the cables and the front end electronics can also create a higher concentration in the top detectors, although the deviation between physics and calibration is anyhow in agreement with the statistical expectation.

In general, because of the different irradiation profile of the detector array by different sources, a single energy resolution curve is not sufficient to precisely predict the energy resolution in the physics data from the calibrations. Using MC data, it can be shown, that the difference in the expected energy resolution between sources from above the array (e.g. the front end electronics) and sources below the array (bottom coppershroud) can reach up to 20%, while even for sources closer to the array (e.g. SiPMs and cables) a difference of 5% can be reached.

5.6.7 Comparison to M1 energy resolution

The M2 energy resolution curves are compared to the M1 curves in [132] in Fig. 5.15. For the M1 curves, the combined spectra of all detectors has been used, thus the weighting of each detector is comparable to the M2 curves.

In Sec. 5.6.1 it was found that the crosstalk correction significantly improves the FWHM (by up to 20%) as well as the shifts and quality of peaks. However, comparing the M2 resolution curves to the ones obtained from the M1 data, it becomes clear that there is still a constant degradation of about 0.2 keV (corresponding to 10-6%) for the BEGe detectors and up to about 0.3 keV (corresponding to 9%) at 2.6 MeV for the semi-coaxial data set. A potential reason are the inclusion of the GTF detectors in the M2 data set and jumps in the crosstalk behavior for certain runs in the long period of data taking, which still need to be taken care of.

5.6.8 Uncertainties

As mentioned before, the uncertainties given for the FWHM values are obtained from the statistical uncertainties of the peak fits, from the difference to the value obtained with the

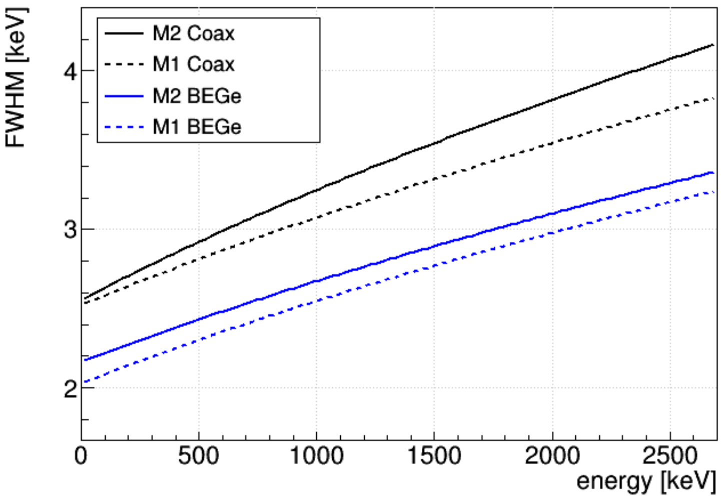

Figure 5.15.: Comparison of the energy resolution curves obtained from the M1 and M2 calibration data of the semi-coaxial and BEGe data sets in PII.

alternative energy resolution equation and the difference to the value obtained from the final energy resolution curve.

However, another systematic uncertainty has also been mentioned before, which is the dependence of the weight of each detector pair on the expected distribution of events among them for a particular source. In principle, one would need to determine the resolution for each of the pairs separately, in order to combine them with the correct weight afterwards. As this is not possible due to the lack of statistics, instead the difference in resolution for several sources within the setup has to be estimated. For this purpose, the M1 resolution curves for each detector are utilized and combined, with a weight according to the event distribution of the source. From a ^{40}K source on holders, cables, fibers and minishroud, a maximum difference of 3.6% was observed. The difference from a location on the n^+ surface of BEGe detectors to semi-coaxial detectors amounts to 9.5%. From these results, the uncertainty for the M2 resolution is extrapolated with a very conservative 10%[8].

5.7 M2 coincidence spectrum

There are multiple ways of representing the energy spectrum of M2 events. Fig. 5.16 shows the two-dimensional spectra of events with a multiplicity of 2 in the PI and PII data. Plotted is one of the energies of such events versus the other energy. The order in which the two energies are plotted is determined by the detector ID number, i.e. the energy deposited in the detector with the lower detector ID is attributed to the x-coordinate.

Fig. 5.16 additionally also shows two one-dimensional representations of both spectra in the bottom row plots: 1) the ”single energy spectrum” showing the sum of the projections of the two-dimensional spectrum to each axis, 2) the ”sum energy spectrum” showing sum of both energies of an event, i.e. the projection of the two-dimensional spectrum on the diagonal line.

---

[8] The actual difference for the M2 resolution is likely even lower than for the M1 resolution, because the requirement of two detector events adds a smearing effect to the location of the source

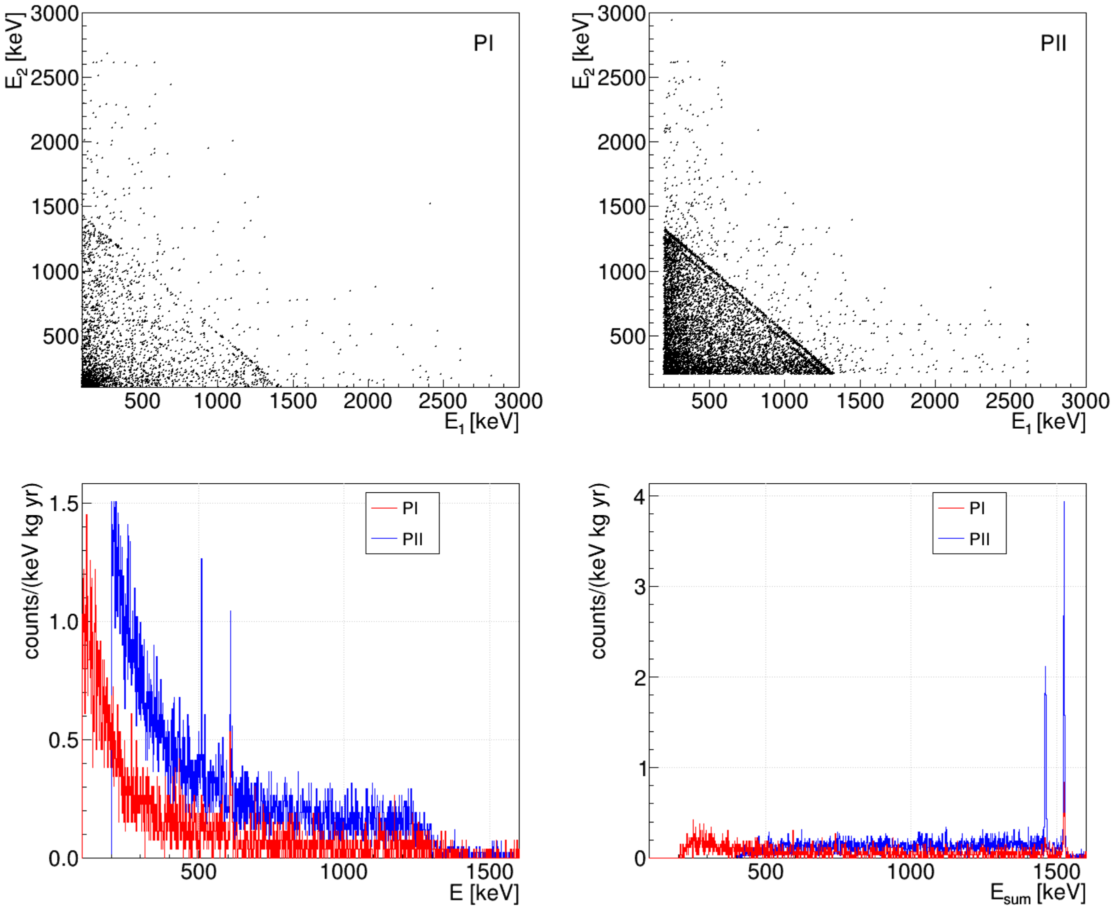

Figure 5.16.: *Top:* Two-dimensional energy spectra, *Bottom left:* single energy spectra and *Bottom right:* sum energy spectra of M2 events in the PI and PII physics data.

The most prominent structure in the energy spectrum are the γ-lines from ^{42}K and ^{40}K, visible in the sum energy spectrum at 1460 keV and 1525 keV and as diagonal lines in the two-dimensional spectrum. The single energy spectrum additionally shows a γ-line by ^{214}Bi at 609 keV and the 511 keV γ-line predominantly in the PII data. Hints are found for the 434 keV line from ^{108m}Ag (PI only) and the 583 keV line from ^{208}Tl. The Compton edge of the ^{42}K line is visible at around 1300 keV. PII in addition shows the Compton edge of the ^{40}K line at a slightly lower energy. Below the two potassium lines, the spectrum is in general dominated by the Compton continuum of both lines. The contribution by ^{39}Ar only turns significant below 200 keV in the single energy spectrum and below 400 keV in the sum energy spectrum. Therefore, with the applied thresholds, it is only visible in the PI spectrum.

In Fig. 5.17, the distribution of M2 events among the detector pairs are shown. In PI the majority of events are concentrated in the six lateral pairs of the three string arms (ANG2/ANG4/ANG5 in the middle of the strings and RG1/ANG3/GTF112 at the top of the strings[9]) with over 50% of all M2 events (200-300 counts each pair).

In PII, the middle string (GTF) is contributing to the majority of events (34%) as well as

---

[9] Because two detectors at the bottom of the string are de-activated (ANG1 and RG3), three lateral pairs are excluded.

pairs of neighboring detectors within a string (33%, diagonal). Especially the three back to back BEGe pairs at the top of the strings contain the highest amount of events of any pairs (∼200 events, 2-3% each), due to their proximity and the higher ^{42}K concentration at the top of the array. Also visible is a higher concentration of events with an energy deposition in the enriched semi-coaxial detectors (29%, ANG/RG) and a slightly higher concentration in pairs of neighboring strings (off-diagonals).
The next chapter will be dedicated to a more in detail analysis of the background spectrum in the M2 data.

5.8 Summary

The anti-coincidence cut requiring that only one detector registers an energy deposition, is a powerful cut helping the search for the $0\nu\beta\beta$-decay into ground state by effectively reducing the γ-ray background. But because of different background expectation, especially the absence of the $2\nu\beta\beta$-decay spectrum of ^{76}Ge, coincidence data with a multiplicity of two can be helpful for analysis of the Gerda background and alternative physics goals.
For this purpose, this data set needs to be characterised. The chapter concentrated on the full Phase I data and Phase II data taken between December 2015 and April 2017. By evaluating the energy resolution and peak shifts with the help of ^{228}Th calibration data, it has been found that the FWHM is deteriorated compared to the anti-coincidence data by up to almost 30%, while peaks are shifted by up to 1 keV relative to their expected position. These problems can be attributed to the presence of electronic crosstalk between the detector channels.
This chapter presented two methods to correct for the energy information of each combination of two channels for the crosstalk effect. While the first one is based on distributions of amplitude ratios between single crosstalk and trigger signals, it is limited by the noise threshold. A much higher precision is obtained with the second method, which first averages waveforms and then determines the crosstalk effect based on those.
The efficiency of the crosstalk correction has again been investigated with the calibration data. An improvement of the energy resolution of up to 20% was reached, though in certain cases still 10% worse than in the anti-coincidence data.
Study of crosstalk on a run by run basis in Phase II revealed runs with several matrix elements that deviate from the currently utilized crosstalk matrix (obtained from special calibrations) by more than three sigma. A separate treatment or exclusion of these cases from data set, could lead to an additional improvement. This decision will be made with the final Phase II data processing.
The energy resolution curves were extracted for the semi-coaxial and BEGe data sets, which are used for further going analyses of the coincidence data in subsequent chapters. A first look at the coincidence data has been given.

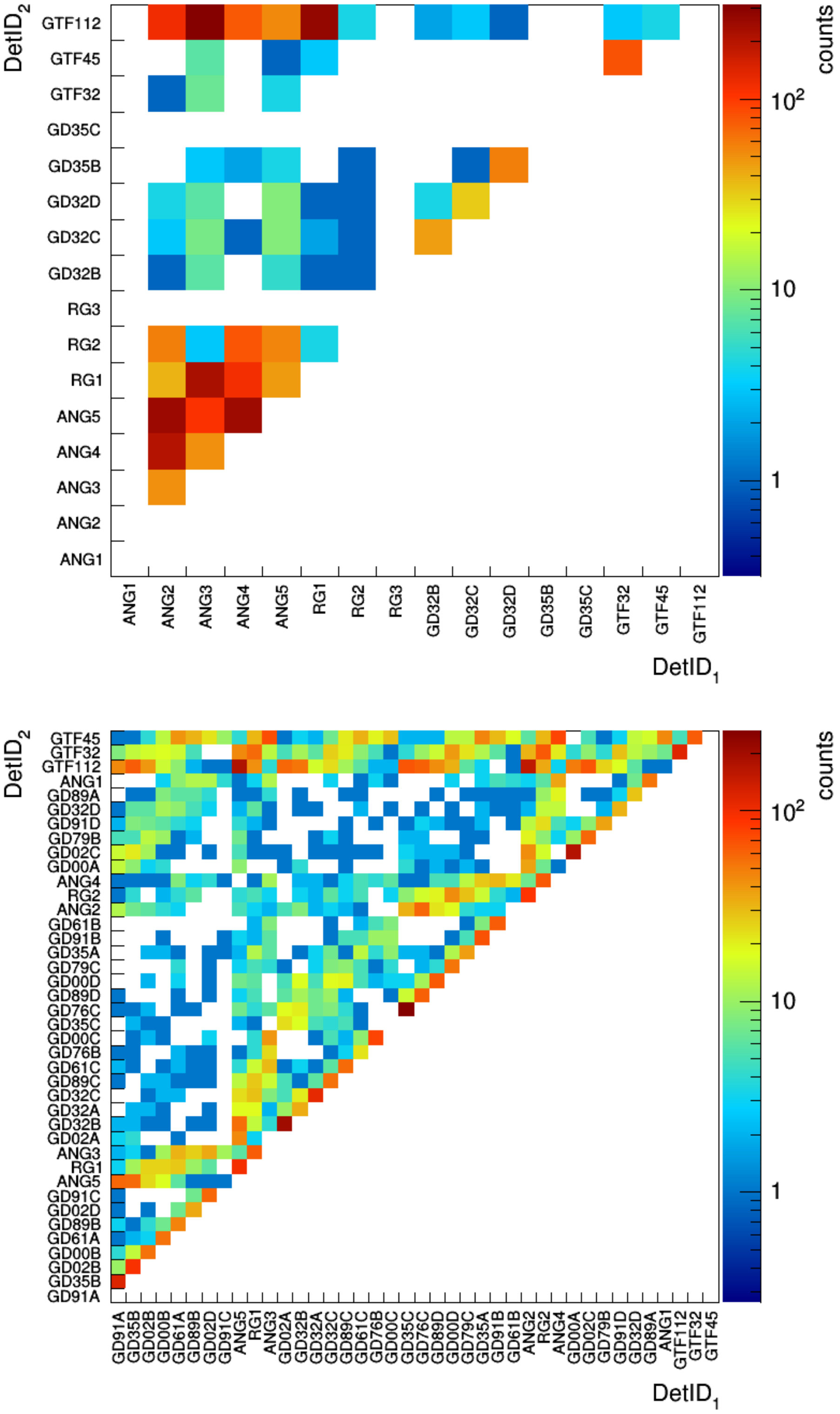

Figure 5.17.: Distribution of M2 events among the detector pairs in the PI (*top*) and PII (*bottom*) physics data.

Chapter 6

Coincidence data set background analysis

6.1 Introduction

This section is dedicated to the evaluation of the background spectrum and the construction of a background model using the M2 data for PI and PII of Gerda.

The motivation for the PI background model with M2 data was primarily to cross-check the model created for the M1 data [120, 121]. For this purpose, the model uses the same background components to fit the energy spectrum, so that the results can be directly compared to the results obtained from the M1 data. This step is presented in Sec. 6.5. Subsequently, this model was adjusted and proved to be a helpful tool in designing the analysis of ^{76}Ge decays to excited states, as presented in Ch. 7.

From the beginning, the PII background model presented in Sec. 6.6 was designed to serve the analysis of ^{76}Ge decays to excited states. Additionally, it is again utilized as a cross-check of the M1 model, but also as a means to check if additional information about some background sources like ^{42}K can be obtained, which can help to refine the M1 model. Despite that the M2 data offers much lower statistics compared to the M1 data, it should in principle be sensitive to the location especially of sources that emit a multitude of γ-rays and are very likely to create multi-detector hits. Besides that, purely β-decaying isotopes such as ^{39}Ar as well as the $2\nu\beta\beta$-decay to the ground state play no important role and can only potentially contribute by bremsstahlung to the M2 spectrum. Contaminations on the detector surfaces that lead to α-decays do not contribute.

The experience from the M2 background model is very valuable to achieve the ultimate goal of a combined fit of the M1 and M2 background spectra. This step is still work in progress at the time of writing and will eventually be presented in [136] and in a dedicated journal publication.

A summary of the background model process is given in Sec. 6.7.

The first application of the M2 background model is presented in Sec. 6.8, in which the efficiency of the anti-coincidence veto in dependence on the energy threshold is investigated. This efficiency is of importance for the evaluation of the background index for the $0\nu\beta\beta$-decay analysis. Other analyses based on coincidence data that make use of the background model are presented in Ch. 7 and 8.

6.2 γ-line intensities

A first evaluation of the γ-line intensities in the PI and PII data can already give valuable information about relevant background sources and gives an idea about which sources need to be considered in the background model. Additionally, it reveals changes in PII with respect to PI.

This study is done for γ-lines of the most relevant background sources. γ-lines in a single detector with another detector in coincidence, but also γ-lines in the sum of two detectors are considered.

To obtain the γ-line counts, first the number of counts n within an energy window including ±3 standard deviations of the peak are determined. Second, the continuum below the peak is estimated with two energy bands positioned to the left and right of the peak. The number of counts in those bands are denoted as m.

The quantities n and m enter a likelihood, which is written as follows:

$$\mathcal{L}(n, m|s, b) = \left(e^{-b}\frac{b^m}{m!}\right) \cdot \left(e^{-(s+b/\tau)}\frac{(s + b/\tau)^n}{n!}\right), \tag{6.1}$$

where s are the expected γ-line counts, b are the expected counts in the two energy bands to the left and right of the peak and τ the ratio between the energy range in which m and n are counted. Using BAT [104] the marginalized posterior probability density distribution for s is extracted. The prior probability density distribution is chosen as flat for s and b. Tab. 6.1 presents the marginalized mode for s as well as the smallest 68% interval of the marginalized distribution. In case this interval is compatible with 0, the 90% quantile is given as an upper limit.

A big difference between PI and PII is the increase in ^{40}K and ^{42}K γ-line counts by factors of 12 and 4, respectively. An increase of a factor of 4 and 2, respectively, has been observed in the M1 data [2]. The additional ^{42}K contribution is due to the application of non-metallic nylon minishrouds in PII, that do not enclose the electrical field lines of the germanium detectors. This leads to an increased drift of the positively charged ^{42}K ions towards the detector array. The additional factor of 2-3 comes from the higher detector array efficiency in regard of coincident data. A potential source for the increase of ^{40}K is the glue which has been applied to assemble the minishrouds.

Sources by ^{214}Bi and ^{208}Tl have been reduced through the careful material selection. In the M1 data, this is visible in an reduction of the γ-line counts by up to a factor of about 2 [138]. Given this reduction and considering the higher array efficiency for M2 events, the observation of similar line counts between PI and PII in the M2 data are in agreement.

In PI, lines at 434 keV and 723 keV of ^{108m}Ag ($T_{1/2} = 438\,\text{yr}$ [154]) have been observed in the M2 spectrum. Another line with comparable emission probability at 614 keV is inseparable from the 609 keV line of ^{214}Bi. ^{108m}Ag was previously not included in the background model process of M1 data. Screening measurements of PI cables show a positive result for ^{108m}Ag. None was observed in the PII material screening, which is reflected in the obtained line counts. No evidence for ^{108m}Ag has been found in the PII M1 data either.

Furthermore, no evidence has been found for ^{228}Ac in PII, neither in the M1 nor in the M2 data. For ^{207}Bi, a significantly positive result was only obtained for the line at 1064 keV in the $^{\text{enr}}$Coax data set in the M1 data in PII. None has been observed in the M2 data.

6.3 Background simulations

To study the background in more detail for the full energy range and in order to compare it to expectations from screening measurements, MC simulations of the background sources are necessary.

The MC simulations have been performed within MaGe. The tracking of the scintillation photons in the LAr is extremely time intensive and has thus been disabled for all simulations. As a result, the background study presented here is done without application of the LAr veto.

The energy of the events in the simulation data is smeared using the energy resolution curves determined in Ch. 5.6.5. From this simulation data, MC histograms are created for the single and sum energy of the M2 data, as well as DetID (detector ID) histograms with the total counts in each detector (pair). Hereby, an energy threshold of 200 keV is enforced on all channels. A default binning of 30 keV is used in PI for the energy histograms, the same as for the M1 background model. For the PII histograms, a 4 keV binning is used. Additionally, a binning of 10 keV is used to evaluate the systematic effect of the bin size on the results.

One histogram is created for each of the components and for each detector configuration

single energy				
E [keV]	Phase I		Phase II	
^{228}Ac				
911	0.77	(0.51,1.07)	0.09	<0.37
^{108m}Ag				
434	0.79	(0.52,1.07)	0.22	<0.65
723	0.39	(0.24,0.60)	0.36	(0.17,0.59)
^{110m}Ag				
658	0.07	<0.33	0.00	<0.29
885	0.03	<0.26	0.02	<0.32
Annihilation				
511	0.62	(0.33,0.87)	1.89	(1.56,2.28)
^{207}Bi				
570	0.00	<0.28	0.06	<0.44
1064	0.00	<0.19	0.00	<0.20
^{214}Bi				
609	1.49	(1.23,1.81)	1.88	(1.56,2.15)
1120	0.26	(0.13,0.45)	0.38	(0.20,0.58)
^{60}Co				
1173	0.23	(0.11,0.40)	0.00	<0.26
1332	0.00	<0.18	0.34	(0.22,0.47)
^{40}K				
1461	0.00	<0.12	0.00	<0.09
^{42}K				
1525	0.13	(0.07,0.23)	0.35	(0.25,0.46)
^{208}Tl				
583	0.56	(0.34,0.80)	0.62	(0.36,0.85)
2615	0.25	(0.16,0.37)	0.36	(0.27,0.46)

sum energy				
E [keV]	Phase I		Phase II	
^{110m}Ag				
658	0.02	<0.29	0.00	<0.29
885	0.22	(0.04,0.41)	0.23	(0.04,0.43)
Annihilation				
511	0.00	<0.31	0.87	(0.55,1.18)
1022	0.15	<0.45	0.62	(0.36,0.90)
^{207}Bi				
570	0.00	<0.24	0.11	<0.46
1064	0.31	(0.14,0.52)	0.00	<0.36
^{214}Bi				
609	0.03	<0.37	0.33	(0.08,0.53)
1120	0.55	(0.34,0.77)	0.35	(0.13,0.57)
1377	0.06	<0.39	0.06	<0.46
1730	0.00	<0.17	0.12	(0.04,0.20)
1764	0.19	(0.08,0.31)	0.36	(0.27,0.50)
1847	0.00	<0.16	0.04	<0.17
2204	0.14	(0.05,0.25)	0.10	(0.04,0.17)
^{60}Co				
1173	0.00	<0.24	0.29	(0.06,0.47)
1332	0.13	<0.46	0.00	<0.25
^{40}K				
1461	0.59	(0.35,0.85)	6.77	(6.30,7.30)
^{42}K				
1525	3.32	(2.99,3.80)	14.39	(13.76,15.01)
^{208}Tl				
2615	0.13	(0.06,0.24)	0.20	(0.12,0.28)

Table 6.1.: The γ-line strength observed at the corresponding line energy of several background isotopes, given in counts/(kg·yr). The left table shows the number of counts for γ-lines in one detector with a coincidence in another detector. The right table shows the number of counts for γ-lines in the sum energy of two detectors. Given are the marginalized mode and the 68% smallest interval in case this interval does not include 0. Otherwise the 90% upper limit is given.

as found in the physics runs. The histograms of the different configurations are combined with a weight corresponding to the live-time of the physics runs.

Parts of the minishroud (tub, top and bottom) and parts of the cables (cable at holder and cables from holder to electronics plate) have been simulated and processed separately. The MC histograms obtained for each part have then been combined, weighted according to the mass of each individual part.

As the detectors can have a conical shape, the vertex positions for events on the surface of the detectors have been generated separately for each detector using the general surface sampler (GSS) implemented in MaGe. The vertex positions are saved to a file and the n^+ surface position is extracted in a post processing step. The MC simulations itself are done for all detectors combined, by sampling vertex positions from the files according to the surface area ratio of each detector.

For ^{42}K and ^{39}Ar Decay0 [155] was used to generate the initial particle momenta. The other sources are generated using the G4gun.

For decay chains of ^{228}Th and ^{226}Ra, only the relevant members have been simulated separately, which are ^{208}Tl, ^{212}Bi and ^{214}Bi. The remaining chain members mostly do not emit γ radiation or only emit low energetic γ-rays so that they play no role in the M2 data (e.g. ^{214}Pb). The histograms of ^{208}Tl and ^{212}Bi are combined according to the branching in a ratio of 0.3594 to 1. The chain is assumed to be in secular equilibrium for those two isotopes.

As discussed in Ch. 4.4.2, the sources can be divided into groups according to their distance to the detector array. In general, far sources lead to a suppression of low energetic γ-lines and lines corresponding to the summation of multiple γ-rays. Additionally, the γ-lines from far sources have a higher presence in the sum energy spectrum than in the single energy spectrum of the M2 data, relative to near sources. This is due to the smaller solid angle in which γ-rays can be emitted in order to move in the direction of the detector array. Hence, the probability of one γ-ray making it to the array and being scattered from one detector to another is higher, than two γ-rays being emitted in the direction of the detector array and being absorbed in two different detectors.

6.4 Fit procedure

A template fit is performed, in which the MC histograms are fit to the data histogram. The weights $\boldsymbol{\lambda}$ of the MC histograms are free parameters. The MC histograms are prescaled to an activity of 1 Bq, thus λ_c corresponds to the activity of the component c in Bq. From the weighted sum of all MC histograms, the expected background b_i for each bin i can be deduced. Given this background expectation, the Poisson probability to observe the number of counts n_i in a bin i as observed in the data is calculated as

$$P(n_i|b_i(\boldsymbol{\lambda})) = e^{-b_i(\boldsymbol{\lambda})}\frac{b_i(\boldsymbol{\lambda})^{n_i}}{n_i!}. \tag{6.2}$$

The likelihood for the full energy spectrum is defined as the product of the Poisson probability of each bin:

$$\mathcal{L}(\mathbf{n}|\mathbf{b}(\boldsymbol{\lambda})) = \sum_i P(n_i|b_i(\boldsymbol{\lambda})) = \sum_i e^{-\sum\limits_c b_{c,i}(\boldsymbol{\lambda})}\frac{\left(\sum\limits_c b_{c,i}(\boldsymbol{\lambda})\right)^{n_i}}{n_i!}, \tag{6.3}$$

where c is the index running over all considered background components.

The background model fit uses the Bayesian Analysis Toolkit (BAT) to extract the posterior probability density distribution (posterior in the following) for the $\boldsymbol{\lambda}$ parameter space utilizing the likelihood and the prior probability density distribution (prior) for each λ_c. The prior is chosen as flat distribution if not otherwise noted.

The best fit is defined as the global mode (maximum) of the posterior. Marginalized posteriors are created for each particular λ_c by integrating the multi-dimensional posterior over the remaining λ'_c ($c' \neq c$), to obtain information about each of the components separately.

6.5 Background modeling: Phase I

The initial motivation to create a background model based on the M2 data of Gerda PI was to cross-check the model obtained from the semi-coaxial detectors in the M1 data. Following that, the model was expanded to include the BEGe detectors to allow it to be used as a guideline for physics analysis based on M2 data.

6.5.1 Cross-check of the M1 background model

The statistics in the PI M1 data set does not allow to precisely pinpoint each contamination in the detector setup. Thus, the selection of components to include into the background model is mostly steered by prior results from the material screening measurements.

The M2 data set offers complementary information on the background, that, if the model components are correct, should agree with the results from the M1 data set. A contradiction between the results from both data sets can either mean, that there are additional background sources not regarded in the model, or assumptions made about the location of background sources are not correct. In such a case, the model can be revised if necessary by identifying and adding the missing background components, which subsequently can lead to a difference for the predicted background at $Q_{\beta\beta}$.

A meaningful cross-check can only be done when using the identical background components for the M1 and M2 model fit. The cross-check uses the background components included in the minimum model. Those components are mostly comprised of contaminations on the detector assembly, as motivated by screening measurements [119] showing contaminations especially on the PTFE parts of the detector holders. In the following, given in brackets is the name of the component and the number of generated decays in the MC simulations for PIa and PIc each. The contaminations on the holders include ^{214}Bi (Bi214Holder, $5{\cdot}10^{8}$), ^{228}Th (Th228Holder, $5{\cdot}10^{8}$ for ^{212}Bi and ^{208}Tl each), ^{60}Co (Co60Holder, $1{\cdot}10^{8}$), ^{40}K (K40Holder, $1{\cdot}10^{8}$) and ^{228}Ac (Ac228Holder, $5{\cdot}10^{8}$). Additionally included are ^{214}Bi on the detector's p^{+} surface (Bi214Pplus, $1{\cdot}10^{7}$ per detector) and ^{42}K homogeneously distributed in a 9.5 t volume of LAr with a height of 2 m and a radius of 1 m surrounding the array (K42LAr, $1{\cdot}10^{10}$).

The PI background modeling for the M1 data is based on a subset of the full data set, ending with the beginning of March, 2013, corresponding to runs 25 to 43 (excluding the silver data set). For the purpose of the cross-check, the identical period is used for the M2 data. Only the 6 semi-coaxial detectors (ANG2-5, RG1-2), that are never excluded from the physics analysis for any run between 25 and 43 (compare Tab. C.1 in the appendix) are considered in this section. The BEGe detector string is neglected entirely and consequently the BEGe background model is not cross-checked with the M2 data. The reason is that the BEGe detectors were only employed in the second half of PI and are spatially separated (by

		M1	M2	
component	unit	minimum model	single energy	sum energy
Ac228Holder	[μBq/det]	17.8 (10.0,26.8)	<47	44 (30,63)
Bi214Holder	[μBq/det]	35 (31,39)	50.4 (42.1,58.8)	40 (28,52)
Bi214Pplus	[μBq]	2.9 (2.3,3.9)	2.9 (1.5,4.6)	2.8 (1.6,4.6)
Co60Holder	[μBq/det]	4.9 (3.1,7.3)	4.3 (2.0,7.0)	<5.3
K40Holder	[μBq/det]	152 (136,174)	<520	238 (150,350)
K42LAr	[μBq/kg]	106 (103,111)	124 (98,166)	168 (146,190)
Th228Holder	[μBq/det]	15.1 (12.7,18.3)	20.5 (17.4,25.0)	24.0 (19.5,28.5)

Table 6.2.: Comparison of the activities for the background components of the M1 minimum model [119] to the values obtained from a fit of the sum and single energy spectrum of the M2 data in PI. A Gaussian prior was set for Bi214Pplus, obtained from the alpha model. Given are the marginalized modes and the 68% interval. In case this interval is compatible with 0, the 90% upper limit is given instead. The contaminations on holder components are given in μBq/det, because the number of detectors and thus the number of holders was not a constant during PI.

>15 cm) from the other detectors. Hence the BEGe data set exhibits very low statistics (10% compared to the six semi-coaxial detectors). As a result, the whole data taking period can be simplified to one array configuration, comprising the three string arm with six working detectors, two detectors not working and one natural detector. A 30 keV binning was used for the M1 background modeling as well as for the cross-check with M2 data.

The activities resulting from the best fit of the single and the sum energy spectrum are collected in Tab. 6.2 in comparison to the values of the M1 minimum model.

In general, the fits from the single energy and the sum energy agree with each other within one standard deviation. They also agree very well with the results obtained from the M1 data, usually within two standard deviations. This indicates that a revision of the background model is not necessary. The only bigger discrepancy comes from the K42LAr component, where the value obtained from the sum energy spectrum differs by about 2.7 standard deviations from the results from the M1 model. This difference might be a hint, that the assumption of a homogeneous distribution of the positively charged ^{42}K ions is not true. A more conclusive statement about the actual distribution can not be made though, due to the lack of sufficient statistics.

6.5.2 Adjustments for the final model

In order to utilize the M2 background model for the physics analyses based on coincidence data, some adjustments were made to the model. At first, the data set used for the modeling process has been extended to the full PI period, which comprises runs 25-46 (excluding the silver data period). The other adjustments are given in the following sections.

Addition of ^{39}Ar

^{39}Ar decays by β -decay. Bremsstrahlung emitted by the β -particles is necessary in order to create an M2 event. The activity of ^{39}Ar in LAr has been measured to be about 1 Bq/kg [156].

A component of ^{39}Ar homogeneously distributed in the LAr was added to the model. The decays in the simulation (Ar39LAr, $1{\cdot}10^{10}$) are confined to a 110 kg volume with a height of 60 cm and radius of 21 cm surrounding the three string arm.

This component is fixed in the model to the measured activity. With that, it is one of the biggest contributors to the spectrum in the low energy region below 200 keV in the single energy spectrum and especially below 400 keV in the sum energy spectrum.

Furthermore, it should be noted that the contribution is strongly affected by the dead layer thicknesses of the detectors, which have a large uncertainty themselves. Additionally, the implementation of the dead layers in the simulation framework assumes that they are homogeneous, which is not necessarily the case in reality [117]. This adds a large systematic uncertainty on the spectrum contribution of ^{39}Ar. Another, factor is the spectral shape of the distribution of the initial energy of the β-particle, which just recently has been calculated for the first time to the next-to-leading order [157]. A comparison of this calculation with experimental data is still pending. Decay0 was utilized to generate the initial momenta of the β-particles, which uses the model from [158].

Addition of ^{108m}Ag

^{108m}Ag on the cables (Ag108mCables, $1{\cdot}10^{8}$) was added to the M2 model, because the γ-lines at 434 keV and 723 keV have been observed in the single energy spectrum (see Tab. 6.1). The asymmetric ^{214}Bi line at 609 keV further hints at the presence of the 614 keV line of ^{108m}Ag. Additional, screening measurements report a positive result for ^{108m}Ag on the cables [159]. The ^{108m}Ag spectrum is characterised mostly by the mentioned three γ-lines. The continuum can be neglected in comparison, hence the inclusion of ^{108m}Ag has only a minor effect on the results for the remaining components.

To include the 434 keV line in the fit, the fit range was extended to 420-3000 keV.

Inclusion of BEGe detectors

As the BEGe M2 data is very limited in its statistics, a separate fit is not worthwhile. Instead, the values obtained from the M1 BEGe model [121] are directly translated to the M2 model. Neither of the background components from the BEGe string influences the model of the semi-coaxial detectors significantly. The only component that is shared between both detector types is K42LAr. Hence, K42LAr is fixed to the value obtained from the M1 BEGe model and to compensate a potential discrepancy of ^{42}K in the semi-coaxial detector data set, an additional component of ^{42}K is added on the n^+ surface of the semi-coaxial and BEGe detectors (K42Nplus, $1{\cdot}10^{8}$ per detector).

6.5.3 Final M2 background model

With the above adjustments, the sum and single energy spectrum are fit again in the range of 420-3000 keV. To achieve a combined model, the results for the ^{228}Ac, ^{40}K and ^{42}K components are taken from the sum energy model and are fixed to these values in the single energy spectrum fit. The values for the remaining components are then taken from the fit of the single energy spectrum. The best fit activities obtained from the global mode are given in Tab. 6.3. Additionally, the best fit is illustrated in Fig. 6.1 and 6.2 for the single and sum energy spectrum, respectively, with the 30 keV binning as it was used in the fit. Corresponding plots with a finer 4 keV binning are shown in the Appendix E.1.

The dominant background component for a large energy range is ^{42}K up to the full energy peak at 1525 keV in the sum energy spectrum and the Compton edge at about 1350 keV in the single energy spectrum. About 42% of all events in the fit range below these structures are expected from ^{42}K. Besides this, another notable contribution in this region comes from ^{214}Bi (about 22%). Together with ^{208}Tl (40-50%), ^{214}Bi (33-43%) takes the top spot in the higher energy region.

At the low energy end of the spectra below the fit range (below 350 keV in the sum energy spectrum and below 150 keV in the single energy spectrum), the biggest contribution comes from the ^{39}Ar β-decay. The concentration of 1 Bq/kg clearly underestimates the amount of ^{39}Ar in GERDA. Alternatively, ^{39}Ar events are highly sensitive to the dead layer of the detectors and thus the homogeneous dead layer model implemented in the MC simulations does not offer a sufficiently accurate description of such low energetic events. Nonetheless, the background model in this region is not used for any physics analysis so that this discrepancy is not a major problem. Also, from the plots in Appendix E.1, it is apparent that the statistic in the MC simulations of ^{39}Ar is not sufficient to support a 4 keV binning.

The final background model describes the single energy spectrum very well. p-values of 0.53 and 0.19 have been calculated (using the description given in the appendix of [103]) for the 30 keV and 4 keV binning, respectively. The number of data points within each colored band are in very good agreement with the expectations (71% within green, 95% within yellow, 100% within red for 30 keV binning and 74% within green, 96% within yellow, 99.5% within red for 4 keV[1]).

For the sum energy spectrum, p-values of 0.10 and 0.07 have been obtained for the 30 keV and 4 keV binning, respectively. Although these values are much smaller, they still signal a decent agreement between the model and the data. For data points with a strong excess of counts, like at 740 keV (better seen with 4 keV binning), it has been checked if there are fitting isotopes emitting γ-rays with the corresponding energy. However, no candidates have been found.

The number of data points within each colored band are close to the expectations (62% within green, 91% within yellow, 100% within red for 30 keV binning and 70% within green, 94% within yellow, 99.7% within red for 4 keV).

The distribution of total counts per detector, shown in Fig. 6.3, is mostly defined by the size and the live-time of the detectors and their position in the array. Only two data points are within the green 68% probability band expected from the model. However, the model has not been tuned to fit the individual contributions by each detector. Contaminations are assumed to be homogeneous over the corresponding setup components. Considering this, an agreement on this level is already very convincing.

An excess of events is observed in all the BEGe detectors in comparison to the model expectations, which is likely due to the extrapolation of the M1 model values to the M2 case.

---

[1] Bins including peaks related to the annihilation process at 511 keV, 1022 keV and 2104 keV are not counted in the case of the 4 keV binning, due to their increased width, which is not taken into account in the smearing of the MC data.

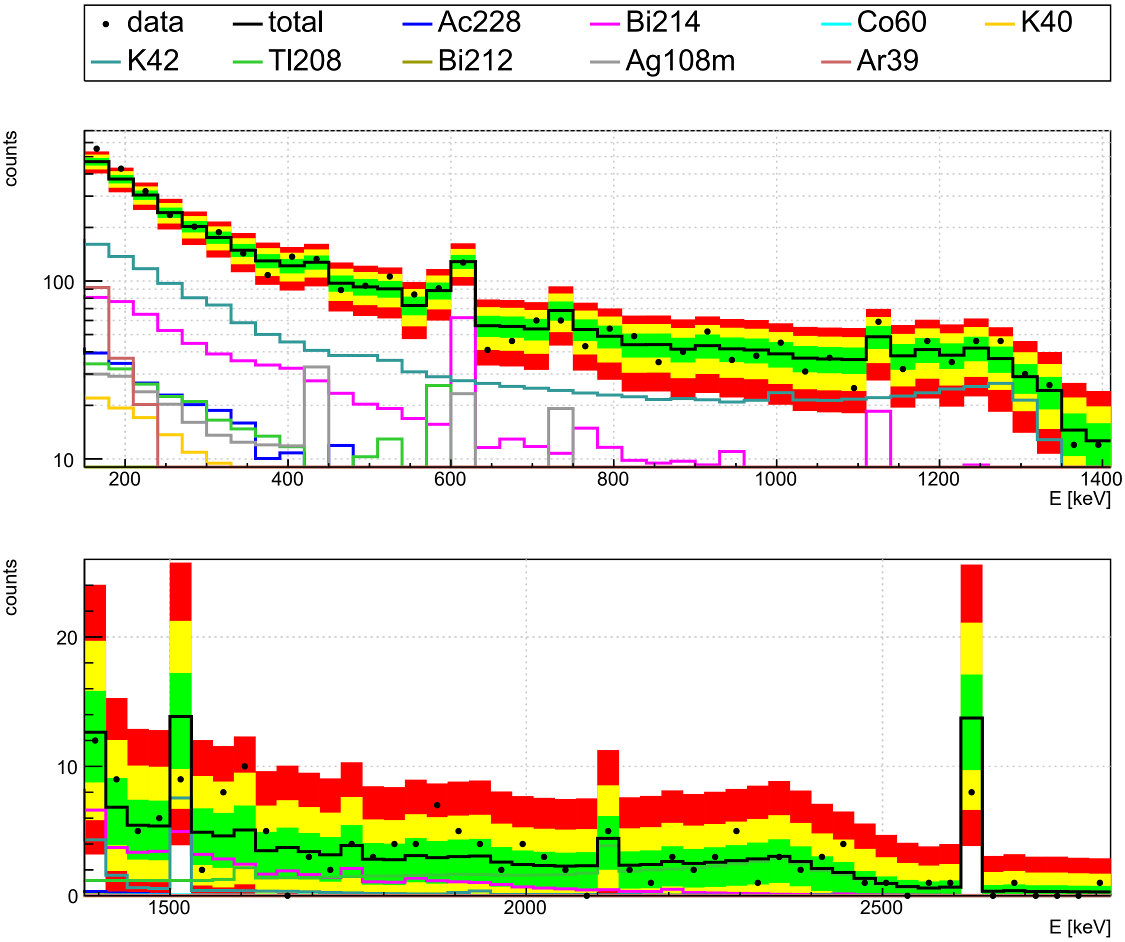

Figure 6.1.: The M2 data of PI in form of the single energy spectrum in comparison to the final background model. The green, yellow and red band indicate for each bin the 68%, 95% and 99.7% smallest probability intervals of the Poisson distribution, with the expectation value given by the background model expectation. Additionally shown are the expected spectra of the individual background isotopes. Note, that the upper plot is in logarithmic scale. A 30 keV binning is used for the spectra. An alternative version with 4 keV binning can be found in the Appendix E.1 (Fig. E.1).

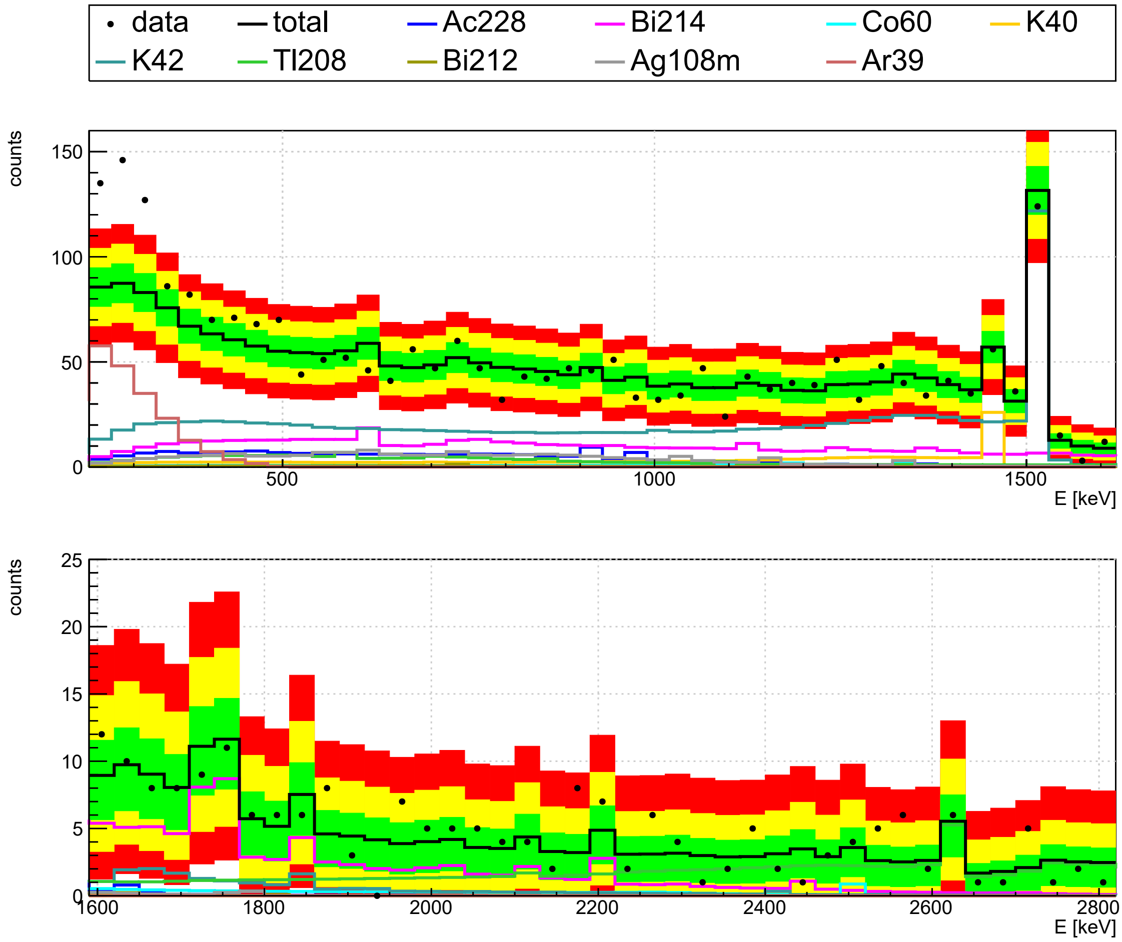

Figure 6.2.: The M2 data of PI in form of the sum energy spectrum in comparison to the final background model. The green, yellow and red band indicate for each bin the 68%, 95% and 99.7% smallest probability intervals of the Poisson distribution, with the expectation value given by the background model expectation. Additionally shown are the expected spectra of the individual background isotopes. A 30 keV binning is used for the spectra. An alternative version with 4 keV binning can be found in the Appendix E.1 (Fig. E.2).

component	unit	activity	
		semi-coaxial	BEGe
Ac228Holder	[μBq/det]	27.1	-
Ag108mVertBars	[μBq/det]	4.3	-
Bi214Holder	[μBq/det]	34.9	14
Bi214Pplus	[μBq]	3	1
Co60Holder	[μBq/det]	2.2	-
K40Holder	[μBq/det]	258	82
K42LAr	[μBq/kg]	85	
K42Nplus	[μBq/det]	136	80
Th228Holder	[μBq/det]	23.7	1.6

Table 6.3.: Final model component activities. BEGe values taken from [121].

6.6 Background modeling: Phase II

The background model for the PII M2 data presented in this chapter is based on runs 54 to 79, which correponds to the period from December 2015 to April 2017. Prior results from material screening measurements are available and are given in Ch. 4.5.2. Because PI and the first data of PII showed hints that ^{42}K is not homogeneously distributed in the LAr, the events in the ^{42}K full energy peak in the sum energy spectrum will be treated separately from the rest of the spectrum. The same procedure will be performed with events in the full energy peak of ^{40}K in an attempt to gain information about the cause of the strong increase of ^{40}K in PII.

This section is thus structured like follows: First, the background components that are expected and simulated and their expected spectra are discussed in Sec. 6.6.1. Sec. 6.6.2 and Sec. 6.6.3 present the separate treatment of the ^{42}K and ^{40}K full energy peak entries. Consequently, both energy spectra are fit in Sec. 6.6.4 and the results are combined to a final model in Sec. 6.6.5, followed by small notes about cross-checks of the M1 model and a discussion of remaining problems in the final sections.

6.6.1 Background components

The background components are selected mostly based on the screening results. Preliminary MC simulations with only about a hundredth of the final generated decays are used to estimate the impact of each component of a certain isotope to the expected spectrum, given the values reported in Tab. 4.2. This impact has been quantified by the total integral of the events in the simulated M2 spectrum. Components that are expected to contribute significantly to the spectrum of each isotope are ^{228}Ac, ^{214}Bi, ^{208}Tl and ^{212}Bi and ^{60}Co on cables and ^{40}K on holders, cables and minishroud. Additionally, medium/far distance components are added in some cases to cover potential contaminations not considered on base of the screening measurements. One example being the copper support structure of the fibershroud, which has not been screened before installation.

As reported in [138], a hint of the presence of ^{207}Bi was found in the enriched semi-coaxial data set. Because the 570 keV γ-line of ^{207}Bi is in close proximity to the region of interest of the analysis of $2\nu\beta\beta$-decays to excited states presented in Ch. 7, a component of ^{207}Bi on the minishrouds is added as well.

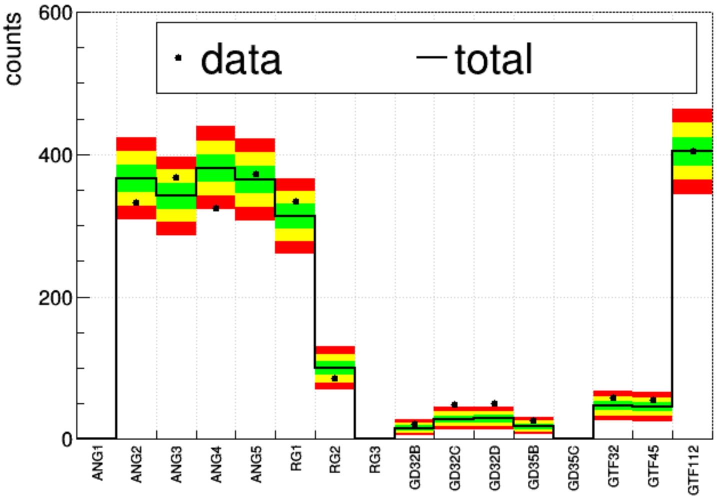

Figure 6.3.: Comparison of the distribution of total counts per detector in the M2 data to the expected distribution from the final coincidence background model in PI of GERDA. Only events above a sum energy of 400 keV are chosen, which excludes contributions from ^{39}Ar.

In addition several components of ^{42}K are considered, which are discussed in more detail in a dedicated Sec. 6.6.2. The components of ^{40}K are discussed in Sec. 6.6.3. The remaining background isotopes are discussed in the following paragraphs. The simulated single energy, sum energy and detector distributions for each considered component can be found in the Appendix E.3. The number of generated decays in the MC simulations is given in brackets.

^{214}Bi:

From the screening measurements, positive results for ^{214}Bi are available for the contaminations on the cables, front end, SiPM and coppershroud (tetratex). However given these results, Bi214Cables ($1{\cdot}10^9$) has by far the highest expected contribution to the spectrum. Additionally, Bi214Fibers ($1{\cdot}10^8$) and Bi214CopperShroud ($1{\cdot}10^{10}$) are included as a medium and far distance components.

The most intense γ-lines in the single energy MC spectrum of ^{214}Bi are found at 609 keV (emission probability 45%) and 1120 keV (15%). Further lines are visible at 1238 keV (5.8%), 1661 keV (1.0%), 1764 keV (15%) 1847 keV (2.0%) among several lesser lines. In the sum energy spectrum, other than the 609 keV line, the lines at 1730 keV (2.9%) and 1764 keV (15%) are of the most interest, as they are located above the ^{42}K γ-line.

For the Bi214CopperShroud component, the γ-lines are barely visible, only the Compton continuum and the annihilation peak remains. Due to the larger distance to the detector array, only one of the emitted γ-rays will reach the detector array in most cases. Hence, in order to create a coincidence, the γ-ray needs to be Compton scattered and will not be detected as a line in the single energy spectrum, but instead in the sum energy spectrum. The single energy spectrum of the Bi214Fibers component as a medium distance source is in between the spectrum of the other two components.

The distribution of total counts per detector is shifted towards the upper detectors of a string for the Bi214Cables component, because the cables are running from top to the respective detector. The distribution is shifted to the lower detectors of a string for the Bi214CopperShroud component, because the lower coppershroud cylinder is much closer to the detector array (about 8 cm from the bottom detectors) than the upper cylinder (about 40 cm from the top detectors). For the Bi214Fibers component, less events are expected in the middle string.

^{228}Th (^{208}Tl & ^{212}Bi):

For ^{228}Th positive values were obtained for contaminations on the front end (less than two standard deviations), minishrouds, fibers and coppershroud. The limit obtained for contaminations on the cables is not very strict in comparison and allows the cables to be the dominant background source of ^{228}Th. Therefore, three components are considered for the model: Th228Cables ($1 \cdot 10^8$), Th228Fibers ($1 \cdot 10^8$) and Th228CopperShroud ($1 \cdot 10^{10}$) as near, medium and far distance sources. Only the isotopes ^{208}Tl and ^{212}Bi are included. A multitude of γ-lines appear in the single energy MC spectrum of mostly ^{208}Tl. Those include a line at 511 keV (23% and annihilation), 583 keV (85%), 861 keV (13%), 2615 keV (100%) and the SEP and DEP at 2104 keV and 1593 keV. The γ-line to Compton ratio is much lower for larger distance sources as is visible for the Th228Fibers and especially the Th228CopperShroud component The γ-lines at 583 keV and 861 keV are barely visible for the latter. The 2615 keV line and its SEP and DEP are not weakened as much in comparison, due to the very high energy. The annihilation component of the 511 keV line also survives mostly with larger distance.
In the sum energy MC spectrum, additionally lines at 727 keV (6.7%) from ^{212}Bi and the summation line of the 511 keV and 583 keV (Th228Cables only) are featured.

^{228}Ac:

^{228}Ac is a member of the ^{232}Th chain. The screening measurements for ^{228}Ac show similar results than for ^{228}Th. Judging by the observed γ-lines, its contribution to the energy spectrum is expected to be much lower though, therefore only a near (Ac228Cables, $1 \cdot 10^8$) and far (Ac228CopperShroud, $1 \cdot 10^{10}$) distance component are considered for the fit.
The single energy MC spectrum of ^{228}Ac is characterised mostly by the 911 keV (26%) and 969 keV (16%) γ-lines and their Compton continuum. Additional lines can be seen at 209 keV (3.9%), 270 keV (3.5%), 328 keV (3.0%), 338 keV (11%), 409 keV (1.9%), 463 keV (4.4%) and 795 keV (4.3%). For the Ac228CopperShroud component, the γ-lines are not visible, only the Compton continuum remains.
In the sum energy spectrum, two additional lines are visible at 1588 keV (3%) and 1630 keV (1.5%) which are only emitted in coincidence with very low energetic γ-rays. Furthermore, summation lines are found between 1 and 1.5 MeV. For the Ac228CopperShroud component, those summation effects disappear. Besides that the low energy γ-lines are reduced in comparison to the Ac228Cables component.

^{60}Co:

The activation time of the materials employed close to the detector array has been carefully documented and minimized. No positive result was obtained for contaminations with the cosmogenic ^{60}Co from screening measurements. However, for the holders and cables, only weak upper limits of <0.11 mBq and <0.34 mBq have been obtained, which translate to

comparable contributions to the spectrum. Additionally, there is a positive result for at least the 1332 keV γ-line in the data (see Tab. 6.1). As the holder plates are expected to be much cleaner than the corresponding limit suggests, the Co60Cables ($1{\cdot}10^7$) component is included. Additionally, Co60Fibers ($1{\cdot}10^7$) is included as a medium distance source.
The two lines at 1173 keV and 1332 keV, both γ-rays emitted with almost 100% probability, are the distinct feature of ^{60}Co, visible in both the single and sum energy spectrum. In the single spectrum, both lines are more dominant for close distance sources like Co60Cables than for medium or far distance sources like Co60Fibers. The sum energy spectrum additionally shows the summation line at 2506 keV and the corresponding Compton spectrum, which is weaker with larger distance from the array.

^{207}Bi:

As already discussed shortly before, Bi207Minishroud ($1{\cdot}10^8$) is included as only component of ^{207}Bi.
The MC spectra of ^{207}Bi is dominated by the two lines at 570 keV (98%) and 1064 keV (75%). In the sum energy spectrum, also the summation of both γ-lines is visible at 1634 keV.

$^{234\text{m}}$Pa:

^{234m}Pa is not expected to contribute due to the low emission probability of the γ-rays.

6.6.2 Fit of ^{42}K peak entries

The LAr borne ^{42}K is represented by several components, whose motivation is described in the following:

> **K42LAr** - ^{42}K homogeneously distributed in the LAr: ^{42}K is the daughter of ^{42}Ar. As ^{42}Ar is homogeneously distributed in the LAr, ^{42}K initially will be as well. This homogeneously distribution is used as basis of the overall distribution. In the MC simulations, ^{42}K decays have been confined to a cylindrical volume of 2.6 m height and 1 m radius, centered around the center of the detector array, which corresponds to 11.3 t of LAr. This volume includes more than 99% of the ^{42}K that contributed to the M2 spectra. $1{\cdot}10^{11}$ decays have been generated in the simulation. There are reasons for inhomogeneities in the distribution, which led to additional components, as described in the following.
>
> **K42NplusCoax/BEGe** - ^{42}K on the n^+ surface of the semi-coaxial and BEGe detectors: ^{42}K is created as a positively charged ion, which will drift in the electrical field lines of the detectors. The distribution of ^{42}K close to the detectors is likely not homogeneous for that reason. For simplicity, a component on the n^+ surface of the detectors is taken into account, which also allows the β-particle from the ^{42}K decay to enter the active volume by overcoming the dead layer. $1{\cdot}10^8$ and $1{\cdot}10^7$ decays have been generated for the component on the semi-coaxial and BEGe detector surface, respectively.
>
> **K42Minishroud** - ^{42}K on the minishroud surface: Because non-metallic minishrouds are used in PII, the electric field lines of the detectors are not constrained to the small volume inside the minishrouds. Hence, ions from outside the volume

will drift towards the detectors and get stuck on the surface of the minishrouds. It is possible that the minishrouds of the outer strings will have an higher concentration of ^{42}K stuck to their surface, because they shield the inner minishroud from the ions outside of the array. $1{\cdot}10^8$ decays have been generated.

K42LArAbove - ^{42}K homogeneously distributed in a small volume above the array: As observed in the data, the detectors at the top of each string exhibit a higher number of counts originating from ^{42}K. One reason could be the unshielded cables above the array that attract the positive ions. A cylindrical ^{42}K volume of 0.25 m height and 1 m radius was simulated, at about 5 cm above the top detectors. This volume corresponds to 270 kg of LAr. $1{\cdot}10^9$ decays have been generated.

K42LArRing80 - ^{42}K homogeneously distributed in a cylindrical shell with an inner and outer radius of 80 cm and 100 cm, respectively. This volume corresponds to about 3.3 t of LAr. A mismatch between the Compton continuum and the full energy line of ^{42}K was observed in the sum energy spectrum if only a homogeneous distribution is assumed. The ratio between full energy line and Compton continuum is smaller for a source with a larger distance to the detector array, thus the outer shell of the homogeneous volume is additionally employed as a separate volume. $3.6{\cdot}10^{10}$ decays have been generated.

A comparison between the expected single and sum energy spectra for the different components can be found in the Appendix E.3.
The Compton continuum of the 1525 keV (18%) γ-ray defines the single energy MC spectrum of ^{42}K. The Compton edge is located at about 1300 keV. Additionally visible are the SEP at 1014 keV and the DEP at 503 keV as well as the 511 keV annihilation line. The further the distance between source and detector array, the more flattened becomes the Compton edge. Also the γ-line intensity is reduced with larger distance. No lines are visible for the K42LArRing80 component, because the γ-ray loses energy in most cases before reaching the detector array.
The β-particle (with an end point energy of 1566 keV) can be detected by one detector for the K42NplusCoax/BEGe and to lesser degree also the K42LAr component. Additionally, bremsstrahlung from the β-particle can be detected for close distance sources, including K42NplusCoax/BEGe, K42LAr and K42Minishroud. The detection of either the *beta*-particle or its bremsstahlung allows the γ-ray to be fully detected in a second detector. Thus the full energy line is visible for those components at 1525 keV in the single energy MC spectrum.
In the sum energy MC spectrum, the full energy line at 1525 keV is the most important feature. The high distance K42LArRing80 component shows a significantly lower full energy to Compton ratio by about a factor of 1.5. The Compton continuum has a small maximum at about 1330 keV. For the K42NplusCoax/BEGe components, the continuum fall of at lower energies, because the detected β-particle causes a shift to higher energies. The K42Minishroud component is very similar to the K42LAr component in all three spectra. In preliminary fits, it turned out that it is not possible to disentangle both components using the data. A global mode for the K42Minishroud component of 0 was found. Therefore the K42Minishroud component will be left out for the remaining background model process.

As all detectors are combined to one data set, information about the location of the background contamination is lost in the energy spectrum. Hence, the idea is to use the

component		global	marg.	68% interval	90% quant.
K42LAr	[μBq/kg]	119	96	(62,114)	<109
K42LArAbove	[mBq/kg]	1.93	1.93	(1.74,2.07)	<2.11
K42NplusBEGe	[mBq]	0	0.5	(0,1.4)	<2.2
K42NplusCoax	[mBq]	0	0.7	(0,1.4)	<2.3
p-value: 0.38		data points in interval:		68.0%:	26 (70%)
		(out of 37)		95.0%:	35 (95%)
				99.7%:	37 (100%)

Table 6.4.: Results from the fit of the detector distribution for events with a sum energy of (1524.7±7.5) keV. Given is the obtained global mode, marginalized mode, the 68% smallest interval containing the marginalized mode and the 90% quantile of the marginalized posterior densitity distribution.

events and their distribution among the detectors in the ^{42}K full energy line in the sum spectrum in an attempt to better define some of the ^{42}K components, especially the K42LArAbove and K42NplusBEGe/Coax components. The continuum underneath the full energy line which is not caused by ^{42}K can be estimated from the spectrum at the right side of the line. 583 counts are observed in total in the peak window of ±7.5 keV, while from the range of 1532.2 keV to 1720.0 keV, 9±1 counts are expected underneath the peak from background sources other than ^{42}K. Thus, the continuum can be neglected in the following.

The expected detector distribution can also be found in the Appendix E.3. The detector distribution for the K42LAr component is affected by the size of the detector, in that larger detectors have a higher γ-ray absorption probability, but also a lower probability that a scattered γ-ray can escape and deposit energy in a second detector. Furthermore, the position of the detector in the array is relevant. Back to back detector pairs like GD35C and GD76C are expected to contribute more to the full energy line. On the other hand, detectors on either end of a string contribute in general less, because they only have one neighbor in vertical direction.

For the K42LArAbove component the intensity of the expected full energy line decreases from the top of the string to the bottom. The K42NplusBEGe and K42NplusCoax components have a higher concentration of events in their respective detector type. The detector distributions of the K42LArRing80 and K42LArMinishroud components are very similar to the K42LAr component. Thus, a separation can not be achieved via the distribution of peak counts per detector and only the K42LAr component is used, representing also the other components.

The right plot in Fig. 6.4 shows the fit of the detector distribution. The fit results in a p-value of 0.38, which means that the observed distribution can be reconstructed with the considered components very well. The results for the n$^+$ components are compatible with zero. This indicates that no larger concentration of events has been observed in neither of the detector types, that is not already explained by the other components. Additionally, both n$^+$ components are correlated, so that a higher weight of the BEGe component requires also a higher weight of the Coax component in order to remain the balance between both detector types. Furthermore, as a consequence the K42LAr component is strongly (anti-)correlated with the two detector surface components. On the other hand, the K42LArAbove component is well defined by the fit. The two-dimensional posterior of the K42NplusBEGe/Coax components, as well as the posterior of the K42LArAbove component will be used as prior distribution for the fit of the energy spectrum. An illustration of both distributions can be found in the Appendix E.4.

The energy range below the ^{42}K full energy peak and above the ^{40}K peak is dominated by the Compton continuum of ^{42}K, with lesser contributions by other sources emitting high energetic γ-rays, especially ^{214}Bi and ^{208}Tl. The range from 1468.32 keV to 1517.20 keV is chosen to cross-check the findings from the full energy peak.

The posteriors obtained for the ^{42}K components from the full energy peak fit are used as prior input. For the Th228Cables, Th228Fibers and Bi214Cables, the prior is constrained at the upper end by preliminary results obtained from the M1 model. This means the prior is chosen flat until 0.51 mBq, 0.35 mBq and 0.08 mBq, respectively, and then falls to 0 quickly.

The p-value obtained for this fit is 0.33, which means the results obtained from the full energy line also described the Compton continuum sufficiently well. However, a three sigma deviation was found between the new global mode and the previous results, related to an increase of the K42NplusBEGe/Coax components. This is due to the lower full energy to Compton ratio in the data than compared to the MC of K42LAr and K42NplusBEGe/Coax components. Repeating the fit with the K42LArRing80 component in addition, a p-value of 0.47 has been obtained and the results are in very good agreement with the results obtained from the full energy line. Calculating the Bayes factor between the model with and without the K42LArRing80 component, returns a value of larger than 200, indicating that the fit strongly prefers an additional component in larger distance to the detector array. This is another hint for an inhomogeneity of the ^{42}K inside the LAr.

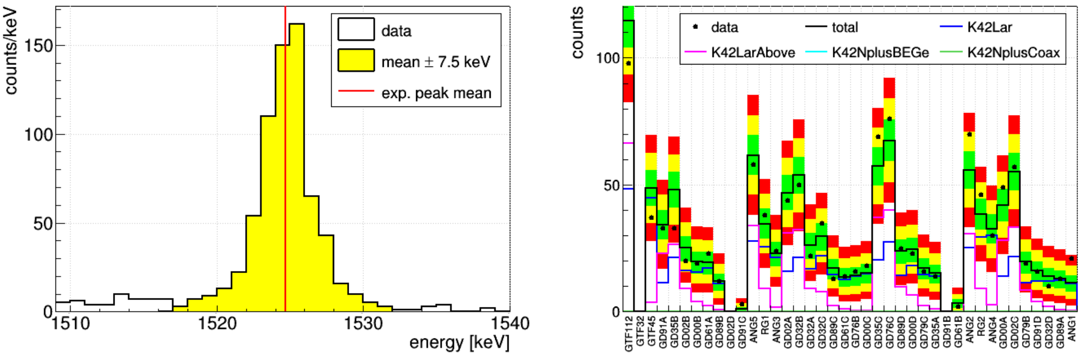

Figure 6.4.: Comparison of the total counts in each detector for events within the ^{42}K peak region of (1524.7±7.5) (keV) (region illustrated on the *left*) as observed in the data and as expected from the best fit using the given background components. The colored bands correspond to the smallest 68%, 90% and 99.7% probability intervals expected from a Poisson distribution with expectation value equal to the best fit value.

6.6.3 Fit of ^{40}K peak entries

For ^{40}K, four components are considered. The idea is the same as for ^{42}K. The full energy peak at 1461 keV in the sum energy spectrum is cut, and the distribution of total events per detector is used to get some first information about the components:

K40Minishroud - ^{40}K on the minishrouds surrounding the detector strings: Observed in the screening measurements of the glue, used to close the lateral surface and add the top and bottom part. The events are mostly evenly distributed among the detectors according to their mass and position in the array. $1{\cdot}10^8$ decays have been generated.

K40Holder - ^{40}K on the detector assembly: Observed in the screening measurements. The events are similarly distributed among the detectors like for the component of K40Minishroud, with a slightly higher weight on the upper detectors of the strings. $1{\cdot}10^8$ decays have been generated.

K40Cables - ^{40}K on the signal and HV cables running along side of the detetor strings: Observed in the screening measurements. A higher concentration of events is expected in detectors at the top of the strings, because all cables for the lower detectors run along the side of them, while the bottom detectors are only close to their own cables. $1{\cdot}10^8$ decays have been generated.

K40Fibers - ^{40}K on the fibershroud (part of the LAr instrumentation): Although ^{40}K was observed on the fibers in the screening measurements, its contribution is small compared to the previous components. Still, this component is added as a medium distance source of ^{40}K. As the fibers are surrounding the detector array, less events are expected in GTF detectors in the middle string. $1{\cdot}10^9$ decays have been generated.

^{40}K only emits one γ-ray with an energy of 1461 keV (11%). The single energy spectrum therefore reveals the Compton continuum of this line with the edge at about 1240 keV in addition to the single escape (SEP), double escape (DEP) line at 950 keV and 439 keV, respectively, as well as the line at 511 keV from electron positron annihilation as a result of pair production. For the close distance components, K40Holder, K40Minishroud and K40Cables, the single energy spectrum looks very similar. In case of the K40Fibers component, the Compton edge is flattened and the lines slightly reduced in comparison to the Compton continuum, because less of the γ-rays reach the detector array with their full energy.
In the sum energy spectrum, the full energy line at 1461 keV is the dominant feature. This line is less intense for the K40Fibers component, compared to the other three. Furthermore, there are comparably more low energetic Compton scattered events.

Unlike for the ^{42}K full energy peak, the background below the ^{40}K peak can not be neglected. Using the range between 1468.32 keV to 1517.20 keV, an estimate of $56{\pm}4$ events can be given for the ±7.5 keV region around the peak center, which contains 333 events itself. To constrain this background, the results obtained in the previous section for the continuum in the above given range will be entered here as prior information.
Given the results obtained from the screening measurements for the four components mentioned above (see Tab. 4.2), in total only $179{\pm}32$ events are expected in the ^{40}K peak, which is more than three standard deviations below the observed number of events. Positive screening results are also available for the PMTs, the coppershroud and the SiPM of the LAr veto. An estimation based on MC simulations shows that this translates into an expected contribution of those components, which is less than 5% of the already included components and are therefore no candidates to explain the observed excess of events. This is evidence, that there is an additional source of ^{40}K not recorded in the screening

component		global	marg.	68% interval	90% quant.
K40Holder	[mBq]	0	0	(0,2.3)	<4.0
K40Minishroud	[mBq]	0	0	(0,3.9)	<6.7
K40Cables	[mBq]	6.4	5.6	(2.6,8.2)	<9.2
K40Fibers	[Bq]	0.11	0.04	(0.01,0.08)	<0.10
p-value: 0.33		data points in interval:		68.0%:	24 (65%)
		(out of 37)		95.0%:	35 (95%)
				99.7%:	37 (100%)

Table 6.5.: Results from the fit of the detector distribution for events with a sum energy of (1460.8±7.5) keV. Given is the obtained global mode, marginalized mode, the 68% smallest interval containing the marginalized mode and the 90% quantile of the marginalized posterior density distribution.

measurements. As a consequence, the fit is first performed with flat priors, in order to check if the excess of events can be absorbed by any of the considered components.

Indeed, the detector spectrum is described well by only the four components, yielding a p-value of 0.33. The right plot in Fig. 6.5 illustrates the fit. The three components K40Holder, K40Minishroud and K40Fibers have only small differences in the expected detector distribution and therefore can not be distinguished by the fit. As a result, the mode obtained for the respective λ is compatible with 0 on the 68% level for the K40Holder and K40Minishroud components and on the 95% level for the K40Fibers component. The K40Cables component is well defined by the fit and differs from 0 by about two standard deviations. A marginalized mode and 68% interval of $(5.6^{+2.6}_{-3.0})$ mBq can be obtained which is in accordance with the result obtained from the screening measurements of (5.8±2.0) mBq. Its posterior will be used in subsequent fits and can be seen in Appendix E.4.

As a result of the excess of observed events, the best fit prefers the activity for the K40Fibers component to be higher by a factor of 200 ($\lambda = (0.11 \pm 0.02)$ Bq) than expected from the screening measurements.

In a second step, the screening results for the four ^{40}K components are added as priors in the fit. Additional, to compensate the excess two components K40Near (copy of K40Holders) and K40Far (copy of K40Fibers) with a flat prior are added. In regard of the detector distributions, these two components can alternatively be understood as components ”inside” and ”outside” the detector array, because their main difference is the reduced expectation in the natural detectors in the middle string for the K40Far component. Thus, information to discriminate both components comes mostly from the natural detectors.

A model test can be performed by calculating the Bayes factor between the models with K40Near (near model) or K40Far (far model) and the model with neither of the two components (base model). A Bayes factor of about 40 has been obtained between the near model and the base model, while a factor of about 5 has been obtained between the far model and the base model. As expected, an additional component is preferred in addition to the ones expected from screening measurements, especially a component close or inside the detector array. A good candidate for this component is the glue that is applied to close the minishrouds and which has been found to be the main source of the ^{40}K contamination on the minishrouds. A vertical glue stripe is used to close the tub, while a ring of glue connects the top and the bottom piece to the tub. The glue

is applied manually by hand, thus its distribution among each minishroud is expected to be inhomogeneous. For that reason, it is possible that the calculations of the prior information does not take the full mass of glue into account.
When only including the K40Near component, a marginalized mode of $(3.5^{+1.0}_{-1.3})$ mBq for λ_{K40Near} and a p-value of 0.15 is obtained. Only including the K40Far component returns a marginalized mode of (59^{+16}_{-19}) mBq for λ_{K40Far} and a p-value of 0.25.

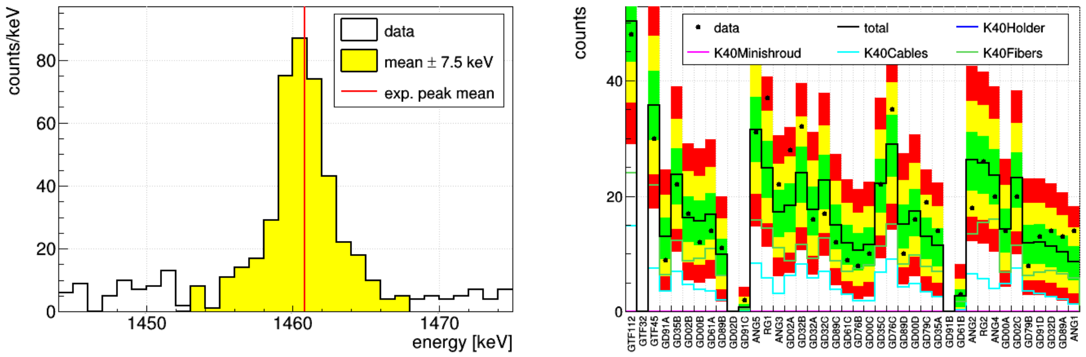

Figure 6.5.: Comparison of the total counts in each detector for events within the ^{40}K peak region of (1460.82±7.50) keV (region illustrated on the *left*) as observed in the data and as expected from the best fit using the given background components. The colored bands correspond to the smallest 68%, 90% and 99.7% probability intervals expected from a Poisson distribution with expectation value equal to the best fit value.

6.6.4 Energy spectrum fit

Because single and sum energy spectra are just two ways of representing the same data, there are correlations between both spectra. Hence, it is not advised to perform a combined fit, if those correlations are not taken into account. However, a fit of both energy spectra is performed and compared to each other. As each of the energy spectra puts emphasis on different features of each component, some components might be better defined by one fit than by the other.
The fit of the sum energy and single energy spectra is performed separately in the range of 450 to 3000 keV and 250 to 3000 keV, respectively. The lower end was chosen to be 50 keV above the low energy threshold in the energy spectra of 2·200 keV (sum) and 200 keV (single). The annihilation peaks at 511 keV and 1022 keV are excluded from the fit, because the larger peak width is not taken into account in the MC data.
The fits are done in multiple steps: First, all components are used for the fit, as they are listed in Sec. 6.6.1, 6.6.2 and 6.6.3. All priors are chosen as flat, with the exception of the following: the prior for the K42LArAbove component is chosen as an asymmetric Gaussian corresponding to $(1.93^{+0.14}_{-0.19})$ mBq/kg (compare Sec. 6.6.2), a two-dimensional prior is set for the K42NplusBEGe/Coax components according to the right figure in Fig. E.12 and an asymmetric Gaussian prior is chosen for the K40Cables component, which corresponds to $(5.6^{+2.6}_{-3.0})$ mBq (compare Sec. 6.6.3). The resulting fits are then compared to the results from the screening measurements as well as to each other.
In a second step, to attempt a more minimalistic approach, components that lead to degeneracies or strong correlations are removed from the model or prior information is added from the screening measurements if available.

The fits initially use a 4 keV binning. The fits are repeated with a 10 keV binning to evaluate the systematic influence from the bin size.

Preliminary fits

The results of the fits of the sum and single energy spectra are listed in Appendix E.2. The fits yield p-values of 0.83 and 0.51, respectively and therefore agree very well with the data. In the sum energy spectrum no data point lies outside of the 99.7% Poisson interval, while two events are expected to fall outside of that interval by pure statistical fluctuations. In the single energy spectrum, four events are outside the 99.7% Poisson interval.

With the information in the sum energy spectrum, it is not possible to distinguish the two components of ^{228}Ac. The components are determined by the γ-lines at 911 keV and 969 keV, whose ratio is similar for the Ac228Cables and Ac228Coppershroud components. The sum energy spectrum is not sensitive to the different peak to Compton ratio of both components.
From the single energy spectrum, no valuable information for ^{228}Ac can be obtained. The posterior is compatible with 0 within the 68% interval and the upper limits on both components are well above the limits that can be obtained from the sum energy spectrum.

The posteriors obtained for Bi207Minishroud are compatible with 0 within the 68% and the 90% interval for the single and sum energy spectrum, respectively. Thus, no significance of ^{207}Bi has been found in the data. The sum energy spectrum is slightly more sensitive to ^{207}Bi, because the low energy lines are located in a region with a lower background level, in addition to the existence of a summation line above the ^{42}K full energy line.

Due to the presence of the 609 keV and 1120 keV γ-lines in both energy spectra, the Bi214Cables component is well defined. The presence of the lines is stronger in the single energy spectrum. The results obtained from both spectra are compatible with each other. Furthermore, they are compatible with the limits obtained from screening measurements. Both global and marginalized modes of the Bi214Fibers component are found at 0 for both energy spectra. The posteriors for the Bi214Coppershroud component are compatible with 0 within the 68% interval. This component is moderately anti-correlated with the Bi214Fibers component in the single energy spectrum (correlation coefficient: -0.43) and with the Bi214Cables component in the sum energy spectrum (-0.69).

In the case of ^{60}Co, only the two γ-lines are of importance. However, both lines are relatively close to each other in energy, so that the line ratio is largely independent of the source distance. Therefore, the data is not suited to discriminate between both components. However, a difference between both components is expected when comparing the results of single and sum energy spectrum. For far distance sources, the lines are expected to be stronger in the sum energy spectrum relative to the single energy spectrum. Hence, two additional fits are performed with each including only one of both components. With only the Co60Cables component, marginalized modes of $(109^{+38}_{-42})\,\mu$Bq and $(33^{+17}_{-15})\,\mu$Bq have been obtained for the sum and single energy spectra fits, while with the Co60Fibers component $(765^{+330}_{-325})\,\mu$Bq and $(855^{+513}_{-336})\,\mu$Bq has been obtained. The Co60Fibers component results in a better match between both energy spectra and is therefore used in the model. It should be noted though, that the Co60Cables component still results in a reasonable match, with the results only differing by less than two sigma.

The K40Holder and K40Minishroud components are largely degenerate (correlation coefficient -0.81 and -0.61 for single and sum spectra), but preferred to K40Fibers, which is compatible with 0 within the 68% interval. The gain in information about the K40Cables component is negligible compared to the prior information added from Ch. 6.6.3. In summary, all four components are compatible with the results from the screening measurements, however the statistics are too low to make any additional conclusive statements.

Compatible results have been obtained for the K42LAr component from the single and sum energy spectrum fit. An anti-correlation has been observed between this component and the K42LArRing80 component in the sum energy spectrum (-0.59) and to a lesser extent in the single energy spectrum (-0.23) and a strong correlation between K42LAr and the K42NplusCoax/BEGe components of about -0.8 (sum) and -0.7 (single). An additional far distance component of ^{42}K (K42LArRing80) is not needed by the single energy spectrum, depsite the two sigma overestimation of the full energy peak by the best fit. Possibly the much stronger Compton continuum in the low energy range of K42LArRing80 is incompatible with the data. Also in the sum energy spectrum, the posterior is compatible with 0 within the 68% interval.
No additional information about the K42LArAbove component is included in either of the energy spectra, as has been expected.
Both energy spectra prefer the presence of K42NplusCoax/BEGe components, indicated by the exclusion of 0 from the 95% interval of the corresponding posteriors. The features very likely responsible for that are the more pronounced Compton edge in the single energy spectrum and the lower Compton continuum in the low energy region in the sum energy spectrum.

The results for the Th228Cables component is consistent with the limit obtained from the screening measurements ($<$0.41 mBq) for both energy spectra fits with $(0.36^{+0.07}_{-0.06})$ mBq and $(0.31^{+0.07}_{-0.06})$ mBq (sum and single). The two additional medium and far distance components, Th228Fibers and Th228Coppershroud, are degenerate and the posterior is fully compatible with 0. Without any of those two components, the Th228Cables component is pushed higher and slightly conflicts with the limit from the screening measurements.

A cross-check with a binning of 10 keV verifies that the fit is stable in regard of the bin size. For the sum model, the significance of the Ac228Holder and Co60Holder components are slightly reduced to below two sigma, because the γ-lines are washed out due to the larger bin size. The p-value decreases to 0.59, but still signifies a very good agreement between data and model. For two bins, an observation outside the 99.7% interval expected from the best fit model has been made, 0.8 are expected from statistical fluctuations. The first is at an energy of 1022 keV which is discussed in Sec. 6.6.7. The second is right below the ^{42}K full energy line, which is likely related to a tailing effect, which is not taken into account in the MC energy smearing.

Final fit

The following adjustments are made:

- Ac228Coppershroud, Bi214Fibers, Co60Cables and Th228Fibers are removed from

		sum fit			single fit		
component		global	marg.	68%/90%	global	marg.	68%/90%
Ac228Cables	[μBq]	320	308	(169,475)	214	34	<543
Bi207Minishroud	[μBq]	61	59	(20,93)	8	8	<39
Bi214Cables	[μBq]	614	591	(456,759)	611	617	(533,706)
Bi214Coppershroud	[mBq]	69	76	(30,122)	209	179	(128,226)
Co60Fibers	[mBq]	0.8	0.8	(0.4,1.1)	1.0	0.9	(0.5,1.4)
K40Holder	[mBq]	2.7	2.7	(2.1,3.3)	2.7	2.8	(2.2,3.3)
K40Cables	[mBq]	5.6	5.4	(3.5,7.3)	5.8	5.8	(3.8,7.7)
K40Minishroud	[mBq]	1.7	1.7	(1.2,2.2)	1.7	1.6	(1.2,2.2)
K40Fibers	[μBq]	391	397	(313,468)	391	393	(313,468)
K40Near	[mBq]	5.3	3.5	(1.2,5.2)	10.5	9.7	(6.9,12.3)
K40Far	[mBq]	0	1	<61	0	1	<49.0
K42LAr	[μBq/kg]	18	30	(10,69)	82	49	(14,71)
K42LArRing80	[mBq/kg]	4.8	2.7	(0.6,3.9)	0.0	0.1	<2.9
K42LArAbove	[mBq/kg]	1.9	1.9	(1.7,2.1)	1.9	1.9	(1.7,2.1)
K42NplusBEGe	[mBq]	2.5	2.2	(1.3,2.8)	0.5	1.2	(0.5,1.7)
K42NplusCoax	[mBq]	2.6	2.2	(1.4,2.9)	0.5	1.1	(0.5,1.8)
Th228Cables	[μBq]	468	471	(425,529)	394	400	(352,440)
p-value:		data points in interval:			data points in interval:		
0.81 (sum)		(out of	68.0%:	463 (73%)	(out of	68.0%:	528 (77%)
0.50 (single)		632)	95.0%:	611 (97%)	685)	95.0%:	659 (96%)
			99.7%:	632 (100%)		99.7%:	681 (99.4%)

Table 6.6.: Results from the final fit of the sum and single energy spectrum with a reduced number of components . Given are the global mode, the marginalized mode and the 68% smallest interval. If this interval is compatible with 0, the 90% upper limit is given instead as obtained from the 90% quantile of the marginalized posteriors. Additionally given at the bottom are the p-value of the fit and the number of data points (bins) within the 68%, 95% and 99.7% probability bands given the global mode as expectation value.

the fit.

- A Gaussian prior is set for Bi214Cables to (662±208) μBq.
- Gaussian priors are set for the K40Holder, K40Minishroud, K40Cables and K40Fibers components to (2.8±0.6) mBq, (1.7±0.5) mBq, (5.8±2.0) mBq and (391±78) μBq, respectively according to the screening measurements (compare Tab. 4.2). These screening results are all compatible with the results from the first fit within one sigma. Additionally, copies of the K40Holder and K40Fibers components are added with a flat prior as K40Near and K40Far, to take into account that there might be a missing component.

The results are given in Tab. 6.6 and are illustrated und Fig. 6.6.
The best fit is illustrated in Fig. 6.7 and Fig. 6.8 for the sum and single energy spectrum, respectively. Plots for the best fit with 10 keV binning can be found in the Appendix E.2. The p-values of the fits changed insignificantly to 0.81 and 0.50. The degeneracies have been largely resolved. A comparison between the results from the single and sum energy spectrum fit reveals a consistent picture. Thus given those results, no major component seems to be missing in the background model or misplaced in the setup.
Notable changes are summarized in the following:

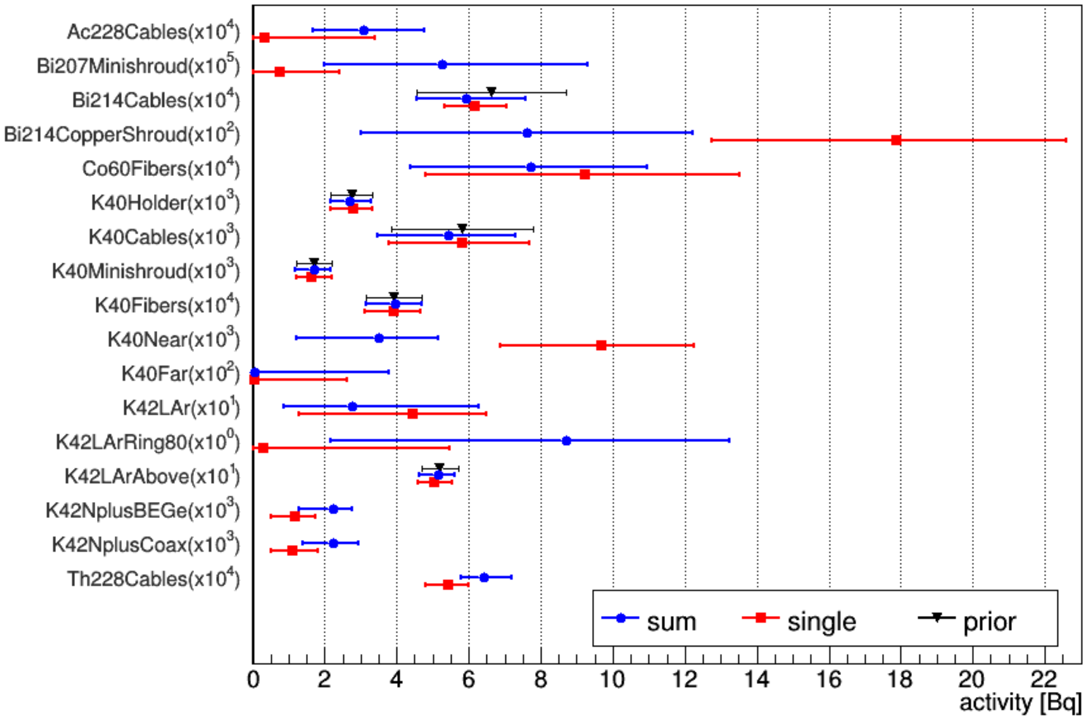

Figure 6.6.: Marginalized modes and 68% smallest intervals for the activities of the background model components as obtained from the final fit of the sum (*blue*) and single (*red*) energy spectrum. The prior information is shown as well, where available (*black*). The values of each component are scaled by a factor given behind the components name.

For Ac228Cables as the only lasting component of ^{228}Ac, global and marginalized modes of the sum energy spectrum fit of $(321{\pm}158)\,\mu$Bq and $(318^{+157}_{-150})\,\mu$Bq were obtained, respectively, which is consistent with the limit obtained from the screening measurements of $<443\,\mu$Bq. The results from the single energy spectrum fit agrees with the above results within one standard deviation: $(244{\pm}251)\,\mu$Bq and $(79^{+262}_{-79})\,\mu$Bq.

Prior information was added to the Bi214Cables component, which was observed with three sigma in both preliminary fits. The new information from the sum and single energy spectrum fit results in a decrease of the mean value of less than one standard deviation to $(617{\pm}163)\,\mu$Bq and $(608^{+152}_{-150})\,\mu$Bq (global and marginalized modes from sum) and $(611{\pm}86)\,\mu$Bq and $(617^{+89}_{-84})\,\mu$Bq (global and marginalized modes from single) in comparison to the prior information from the screening measurements of $(662{\pm}208)\,\mu$Bq. Additionally, the uncertainties are reduced by up to a factor of 2, especially from the single energy spectrum.

The results obtained for the additionally included far component Bi214Coppershroud hints, that either the screening results underestimate the contribution on the cables or that there is another source of ^{214}Bi contributing to the spectra. Especially the posterior extracted from the single energy spectrum, which excludes 0 from the 99.7% interval. A slight discrepancy between the results obtained from both fits of about two standard deviations might point to an additional contamination in a different location, though. Furthermore, the obtained values are well above the result obtained for the coppershroud from the screening measurements. However, a more precise localisation of the contami-

nation is not possible given the current statistics in the coincidence data set as has been shown in the results of the preliminary fits.
A correlation between both components has been observed with a correlation coefficient of -0.79 and -0.46 from the sum and single energy spectrum fit.

The sole component of ^{60}Co (Co60Fibers) has already been discussed before. Both fits return results compatible within one standard deviation for the global and marginalized mode, different from 0 by about three standard deviations.

An additional near distance component of ^{40}K is largely preferred in favor of a far distance source by both energy spectra fits. Both fits return global and marginalized modes of 0 for K40Far, while K40Near excludes 0 by even the 99.7% interval in the single energy spectrum fit. The resulting posteriors have a slight discrepancy of about two sigma, which is understandable since the exact position of the additional ^{40}K contamination is not known and very likely affects the balance between both spectra.
Both K40Near and K40Far are correlated with a correlation coefficient of -0.67 and -0.43 in the sum and single energy spectrum fit.
With the addition of the K40Near and K40Far components and to absorb the excess of ^{40}K events in comparison to the expectation from the screening measurement results, it is not surprising that there is barely any update of the prior information added to the fit.

Th228Cables as the only component of ^{228}Th is sufficient to describe the data. Both results from the single (global and marginalized mode: $(468\pm51)\,\mu$Bq and $(468^{+51}_{-52})\,\mu$Bq) and sum energy spectra (global and marginalized mode: $(393\pm43)\,\mu$Bq and $(400^{+47}_{-40})\,\mu$Bq) agree just within one standard deviation. The results are close to the limit obtained from the screening measurements of $<414\,\mu$Bq. The addition of additional components remove weight from the Th228Cables component. However, the coincidence data is not able to constrain such a component.

6.6.5 Combined model

In the previous sections, two background models have been created from the coincidence data using the single and sum energy spectra. Both models are compatible with each other in all components. The results of both models are combined here to obtain one model that can help to steer analyses based on coincidence data, like presented in Ch. 7 and 8. For this purpose, the global modes for each component are averaged, weighted with the inverse of one standard deviation. The resulting values are listed in Tab. 6.7.
Strictly, the correlation between single and sum energy spectrum needs to be taken into account, which however, are difficult to estimate. Since the values obtained here are just meant as a middle way between the two models and are only used as full model with all components combined, the correlations are neglected and no uncertainties are given. The uncertainties on the combined components are small compared to the statistical fluctuations in the data. Using the total counts below the Compton edge or the full energy peak of ^{42}K in the single and sum energy spectrum, respectively, the uncertainty in this region can be estimated with about 1%. In the higher energy region, an estimate of about 5% can be given this way.
For information about each single component, it is recommended to refer to the results in the previous sections.

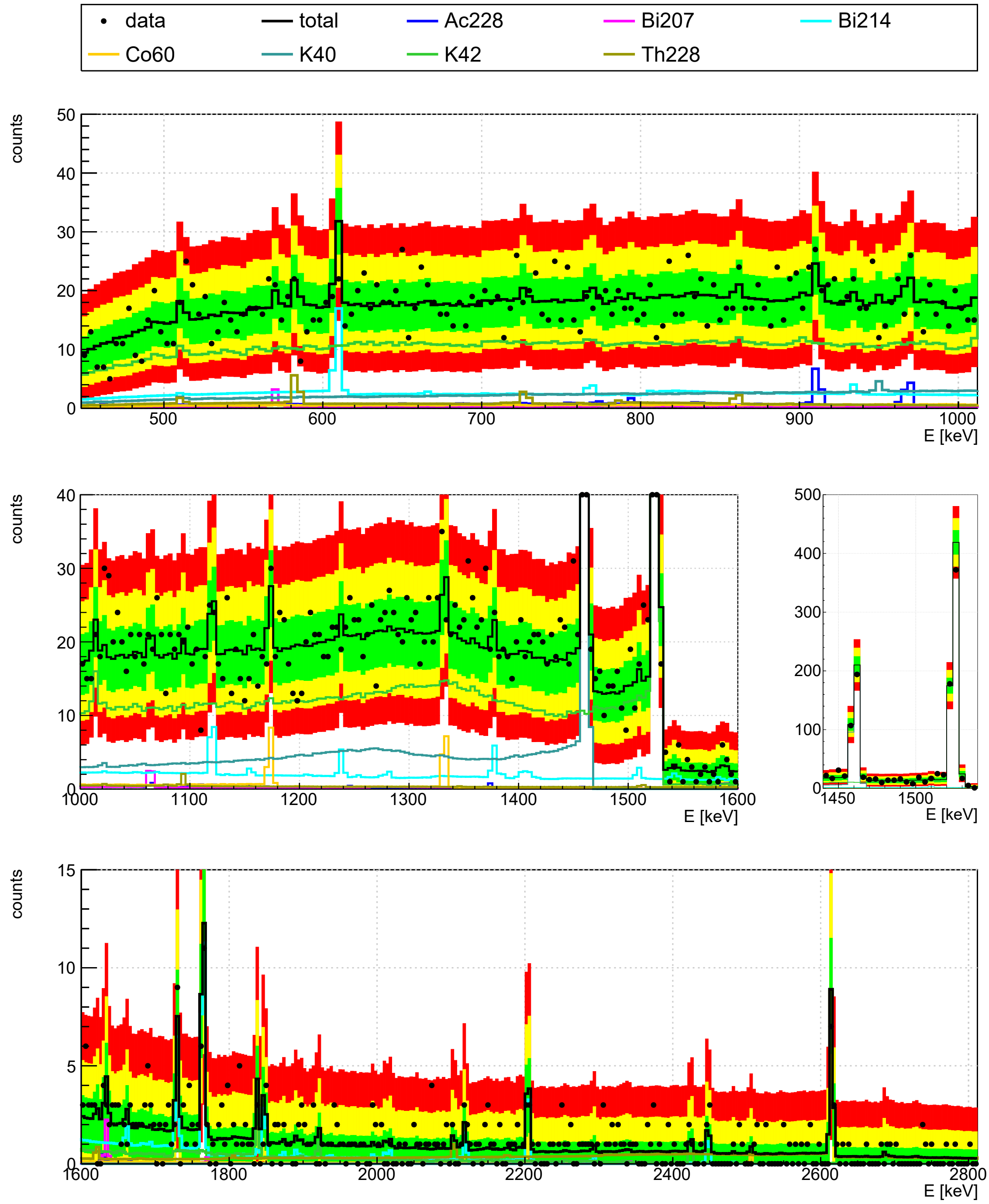

Figure 6.7.: Best fit of the sum energy spectrum of the PII M2 data with a 4 keV binning. Also shown are the expected contribution by each background isotop. The green, yellow and red band indicate for each bin the 68%, 95% and 99.7% smallest probability intervals of the Poisson distribution, with the expectation value given by the best fit. An alternative version with 10 keV binning can be found in the Appendix E.2 (Fig. E.3).

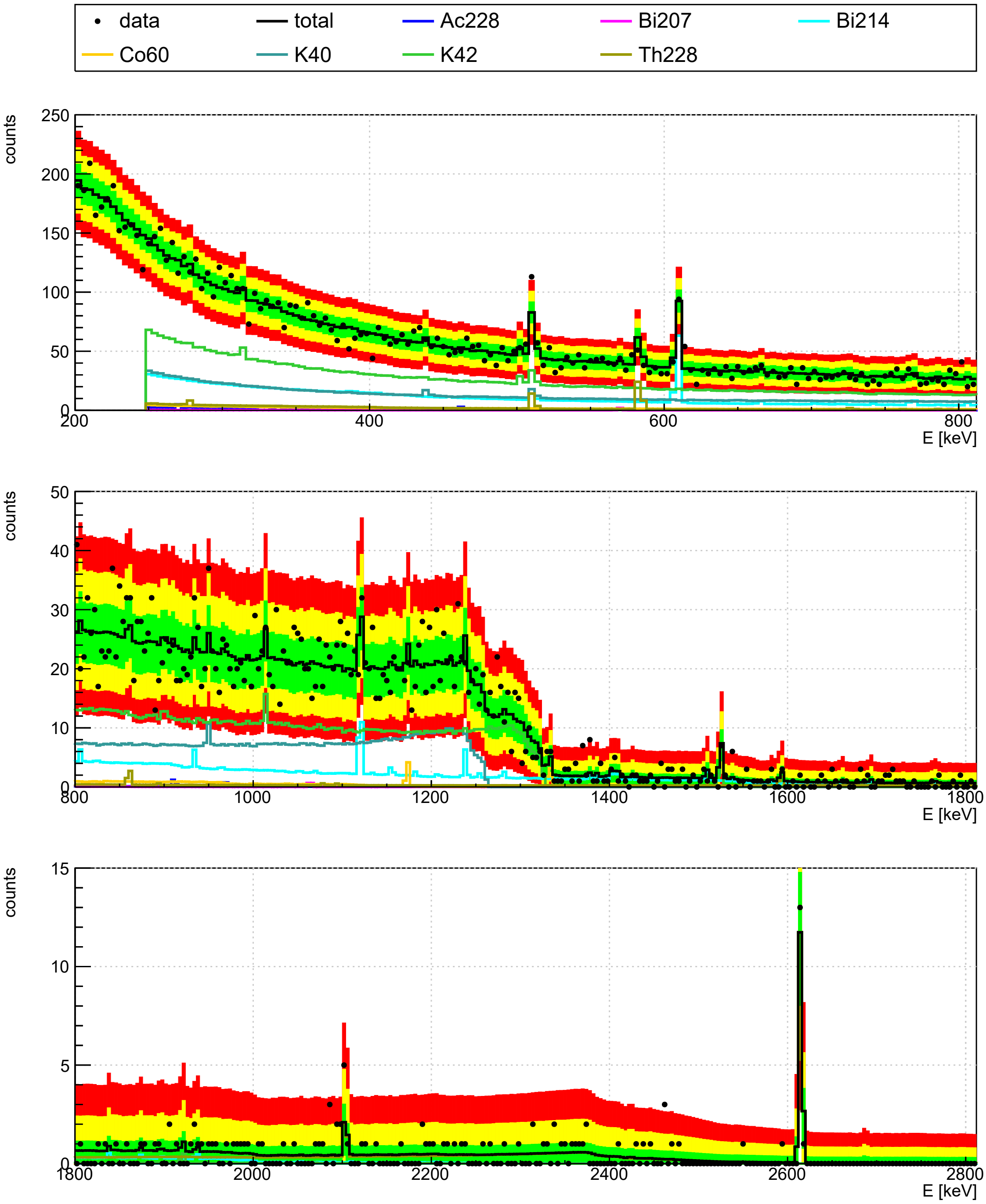

Figure 6.8.: Best fit of the single energy spectrum of the PII M2 data with a 4 keV binning. Also shown are the expected contribution by each background isotop. The green, yellow and red band indicate for each bin the 68%, 95% and 99.7% smallest probability intervals of the Poisson distribution, with the expectation value given by the best fit. An alternative version with 10 keV binning can be found in the Appendix E.2 (Fig. E.4).

component	unit	activity	component	unit	activity
Ac228Cables	[μBq]	299	K42LAr	[μBq/kg]	58.7
Bi207Minishroud	[μBq]	40	K42LArAbove	[mBq/kg]	1.9
Bi214Cables	[μBq]	612	K42LArRing80	[mBq/kg]	3.0
Bi214Coppershroud	[mBq]	146	K42NplusBEGe	[mBq]	1.7
Co60Fibers	[μBq]	910	K42NplusCoax	[mBq]	1.8
K40Holder	[mBq]	2.75	Th228Cables	[μBq]	435
K40Cables	[mBq]	5.71			
K40Minishroud	[mBq]	1.70			
K40Fibers	[μBq]	391			
K40Near	[mBq]	7.3			

Table 6.7.: Activities of the components of the final coincidence background model, combining the results obtained from the single and sum energy spectra fits.

6.6.6 Overall detector distribution

A cross-check of the model is made by comparing the distribution of the total counts among the detectors in the M2 data set to the predicted distribution from the model. This is illustrated in Fig. 6.9.

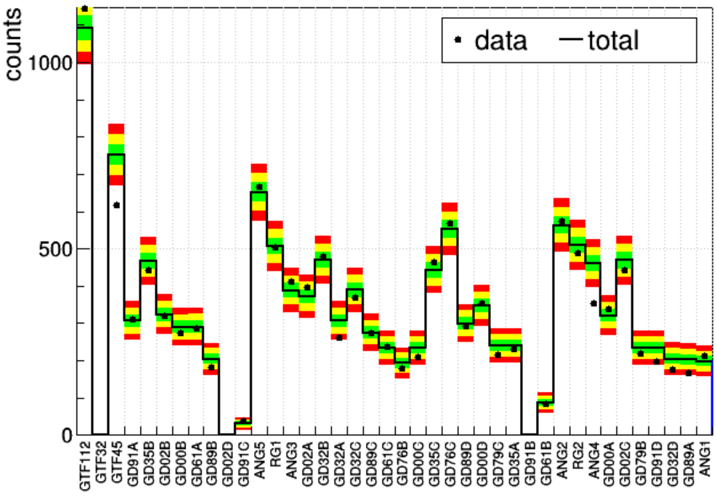

Figure 6.9.: Comparison of the distribution of total counts per detector in the M2 data to the expected distribution from the combined coincidence background model.

The energy spectra are not very sensitive to differences of background contaminations between different components of one type, e.g. different detector holders, minishrouds or cables. Because of this, even if the energy spectra agree very well to the predicted spectra from the background model, this might not necessarily be true for the distribution of events among the detectors.

As can be seen in Fig. 6.9, for 51% of detectors the data point is within the green band (66.8% probability interval) from the model prediction, 84% are within the yellow band (95%) and 95% are within the red band (99.7%). This makes six detectors that are outside the yellow band, two of them (GTF45, ANG4) clearly outside the red band. Judging solely by statistics, the model does not reproduce the data very well in this respect.

However, the model performs surprisingly well, if one takes into account that a strong assumption has been made for the simulations of the background contaminations. All components of a certain type are assumed to be homogeneously contaminated. This means for example for a particular source, the activity per gram of nylon from the minishrouds in the MC simulations is the same for all minishrouds and all parts they consist of. This is of course not true in reality. In some cases large deviations from that assumption are expected. A good example is the glue on the minishrouds, which can vary significantly between the different glue locations. This can not be accurately reproduced in the MC simulations.

Instead it requires more granularity in the model components, which on the other hand over-complicates the model as it opens too many different possibilities that would lead to degeneracies given the limited statistics in the GERDA data.

Differences in the GTF detectors could be explained by the sparse data quality control applied to the natural detectors, because they are not needed for the main $0\nu\beta\beta$-decay analysis. However, they play a very important role for the M2 data, because they are placed in the middle of the detector array. Furthermore, as of the time of writing, a more thorough investigation of the data quality of the natural detectors is going on. For these reasons, it was decided to keep GTF112 and GTF45 for the analysis. It should be noted though, that the revision of the natural detector data set can potentially lead to differences in the final background model.

6.6.7 Additional hints for inhomogeneities

The previous section already revealed, that there are very likely inhomogeneities in the contamination of components of a certain type, which are not taken into account in the model.

Apart from that, peaks connected to the annihilation process have been excluded from the fit, due to their increased width, which is not reproduced in the simulated spectra. Still, they are included in the visualization of the fits in Fig. 6.8 and 6.7. As can be seen, both the peak at 511 keV in the single energy spectrum and the peak at 1022 keV (corresponding to $2 \cdot 511$ keV) in the sum energy spectrum are well above the prediction from the model, outside the 99.7% interval. The origin of this is currently not known. Considering that the two annihilation photons are emitted in diametrical direction and an inhomogeneity of contaminations is expected, a different distribution of contaminations that allow pair production could have a big impact on the annihilation peaks.

Also in case of the two dominant γ-lines of ^{40}K and ^{42}K, the data points are below the model expectation by two to three standard deviations. This hints to a mismatch between the counts in the peak and the Compton continuum, as already discussed in Sec. 6.6.2. Despite the inclusion of K42LArRing80, which has a much higher Compton to peak ratio than the other components, this problem is not solved in the final model. One reason could be the shape of the Compton continuum of the K42LArRing80 component, that does not match the data due to the strong slope.

6.6.8 Background composition

The spectra can be divided into two regions with differing background compositions, due to the contributions from ^{40}K and ^{42}K. Below the Compton edge of ^{42}K at about 1350 keV in the single energy spectrum and below the respective full energy lines in the sum energy spectrum, the dominant contributions come from the aforementioned ^{42}K with about 50-60% of the total events and ^{40}K with around 20%. Additionally of interest in this region is also ^{214}Bi with about 15%. The high energetic end of the spectra is dominated by ^{214}Bi and ^{228}Th with each about 40% of the total expected contributions. Due to the low Q-value, ^{40}K does not add at all to the region above its full energy line. ^{42}K can enter the higher energetic region in the case the β-particle or its bremsstrahlung is detected as well. Still, almost 20% of the total events above 1530 keV in the sum energy spectrum are caused by ^{42}K.

6.6.9 Cross-check of the M1 model

As of the time of writing, the M1 background model process is still ongoing. Thus no results from the M1 data are discussed here quantitatively and only a few short remarks are given about the consistency between the models obtained from M1 and M2 data.

Comparison of the results obtained in this work with preliminary fits of the M1 data show in general a good agreement. This is also mostly a consequence that most components are determined by the prior information, as has been seen in previous sections. Only the results for K42LArAbove and the missing ^{40}K component led to mismatches. A possible explanation are wrong assumption of the locations of those contaminations. For ^{42}K, only an arbitrary cylindrical volume has been chosen, which can be altered and shifted towards or away from the array. The missing ^{40}K component currently positioned on the fibers, can be placed on different material of which the glue rings at the end of the minishrouds are a hot candidate.

In any case, the final goal is to combine M1 and M2 data in one single fit. This combined fit and the separate treatment of the pottassium lines in the M1 data analogous to the procedure presented in Sec. 6.6.3 and 6.6.2 is expected to shed more light on the location of those components.

6.7 Summary of background modeling

A background model for the coincidence M2 data of GERDA PI and PII has been developed. The fits were done using a Bayesian approach with the help of the BAT software.

The PI background models from single and sum energy spectrum were used to cross-check the results of the background model obtained from the M1 data [119, 120]. No big discrepancies between the models were found, except for the ^{42}K component, which hints at an inhomogeneous distribution of the positively charged ^{42}K ions in the LAr or in the setup in general, which may drift in the electromagnetic field lines by the detectors. The M2 models were combined to a final model, which was used to guide the search for $2\nu\beta\beta$-decay to excited states, as presented in [4, 127] and continued with PII data in Ch. 7.

Similarily, background models for the single and sum energy spectrum were created for the PII data set. This time the ^{40}K and ^{42}K lines are treated separately first by fitting the total counts in those peaks in each detector. By this approach more information about the location of the ^{40}K and ^{42}K was preserved. This was necessary especially for ^{42}K, because PII clearly shows an inhomogeneity of the ^{42}K distribution in the LAr, which was already hinted at in PI. Supposedly, the much higher concentration above the detector array is caused by unshielded high voltage cables, which attract the ^{42}K ions.

The fit of the energy spectrum was done in two steps. First, components that are expected to contribute significantly judging by prior screening measurements are included. The M2 data is often not sufficient to discriminate between several components of one isotope. Therefore, in a second step, the components were reduced to remove degeneracies and components with no significant contribution. Additionally, the results from the screening measurements are added as prior information to the Bayesian fit. For the final model, the models from the two energy spectra were again combined. This model was again used to help with the analysis of $2\nu\beta\beta$-decays to excited states in Ch. 7.

In both phases, the data is represented very well by the models. The screening measurements are already sufficient to describe the PII data, with the exception of ^{40}K, which requires an additional source. However, the model does not describe the total counts per detector as well, which is understandable given all the contaminations are assumed to be homogeneously distributed among the respective parts. Inhomogeneities (except for ^{42}K) are not taken into account during the analysis. Furthermore, the annihilation peaks are underestimated by the model. No conclusive statement can be made so far about what causes this discrepancy.

The PII model furthermore agrees with the observation from the M1 model [136]. As already mentioned, the excess of ^{40}K observed in the M1 data compared to the expectation from the screening measurements can also be verified by the M2 data. An additional component near or inside the detector array is preferred by both, the distribution of events from the full energy peak of ^{40}K among the detectors, but also by a comparison of the fit of single and sum energy spectrum. One potential source of this contamination could be the glue used to close the minishrouds, which is applied by hand and thus potentially not fully taken into account in the expectations from the screening measurements.

For the final GERDA background model, currently in work, both M1 and M2 data will be fit in combination. The approach to treat the two pottasium peaks separately will be adapted. Additionally, instead of independently fitting the single and sum energy spectrum, the so-called "global fit" will utilize the two-dimensional information of both detector's energy depositions.

6.8 Anti-coincidence veto efficiency

The anti-coincidence (AC) veto effectively removes background events originating from high energetic γ-rays from the M1 data set and consequently reduces the backgound for the analysis searching for a signal of the $0\nu\beta\beta$ $0^+_{\text{g.s.}} \rightarrow 0^+_{\text{g.s.}}$ decay. Signal events in this case are expected to produce point like energy depositions constrained to 1-2 mm inside the germanium detector, hence they survive the AC veto cut to almost 100%.

As discussed in Ch. 5.3, each secondary channel has an inherent threshold (AC threshold), due to electronic noise hiding the small signal amplitude from the offline trigger algorithm. This threshold lies in the range of 20-40 keV in PII. It reduces the efficiency of the AC veto.

Furthermore, in order to model the AC veto in the MC simulations, it is necessary to apply an energy threshold in the post processing of the MC data. This can be done by either applying each channel's individual threshold or by applying a common threshold of 40 keV larger than the individual thresholds to all channels in the MC data and also the physics data. The former option would require to precisely determine the threshold for each channel, which can be difficult especially for detectors that are only accepted as AC veto for the analysis, due to shifts or jumps in the energy scale. Hence, their threshold

can be time dependent. The second option further reduces the AC veto efficiency.
The reduction of the AC veto efficiency can be studied in dependence of the AC threshold setting using the M2 background model. The effect of events with multiplicity higher than 2 is smaller than 5% with respect to that of M2 events and will be neglected.
Fig. 6.10 shows the background model in the E_1 versus E_2 plane, where $E_1 > E_2$, for all events and for events with E_1 inside a window of ±200 keV around $Q_{\beta\beta}$. ^{39}Ar homogeneously distributed in the LAr was added to the background model with an activity of 1 Bq/kg [156].

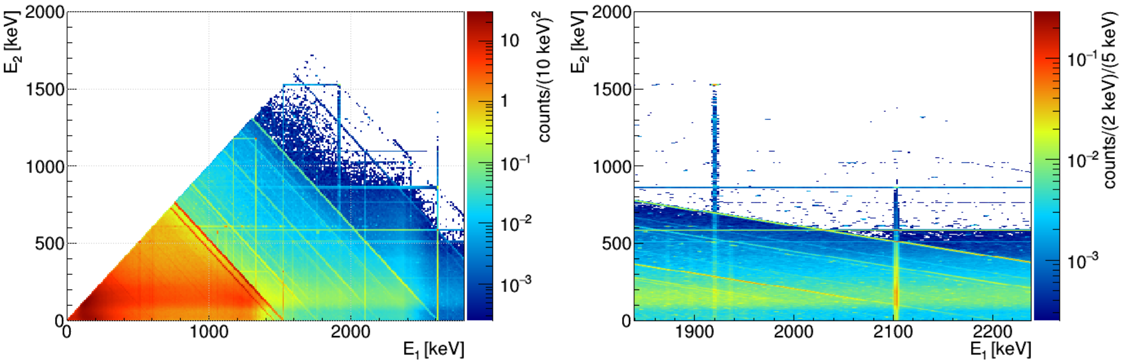

Figure 6.10.: M2 background spectrum with $E_1 > E_2$. The right plot shows a zoom in to $Q_{\beta\beta}$±200 keV on the E_1-axis.

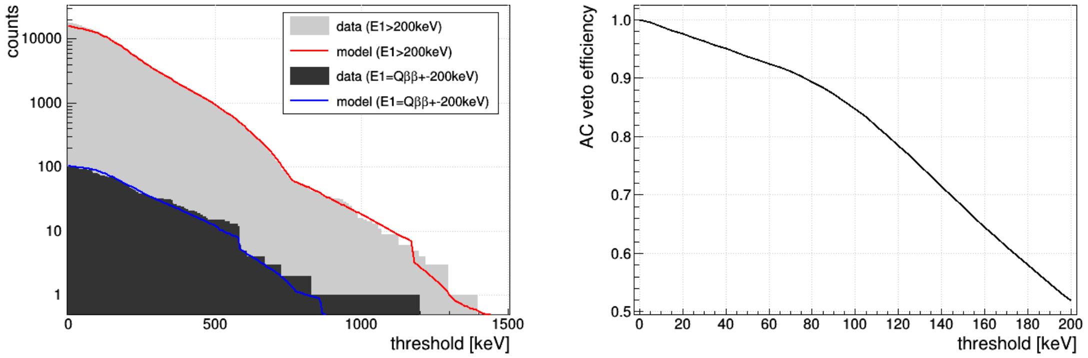

Figure 6.11.: *Left*: The plot illustrates the number of M2 events in the PII data in dependence of the AC threshold. The histogram is drawn for two cases: in light grey are shown all events with the larger energy greater than 200 keV, which avoids problems from threshold differences of the primary channels. In darker grey are shown all events with the larger energy inside a window of $Q_{\beta\beta}$±200 keV. Both histograms are compared to the expectation from the M2 background model (red and blue line). *Right*: The AC veto efficiency in dependence of the AC threshold for events that fall into the ±200 keV region around $Q_{\beta\beta}$.

In the following, a scan of the AC threshold is performed by incrementing the threshold on E_2 in steps of 10 keV from 0 to 1500 keV. For each step, the number of remaining M2 events are counted by integrating from the set threshold upwards. The integrated number of events is shown in Fig. 6.11 in a comparison between model prediction and actual events in the PII data for two cases: the larger energy E_1 above 200 keV and E_1

within $Q_{\beta\beta}\pm 200$ keV.

It should be noted that neighboring bins in the histogram are strongly correlated, because lower bins share all the events with higher bins. Taking this into account, model and data agree within one standard deviation, except for the differences in the low threshold region of the light grey histogram. These differences are very likely due to the uncertainty of the detector dead layers, which have a big impact on the attenuation of low energetic γ-rays and the electrons from ^{39}Ar decay of which there are about 600 and 1200 events expected above 200 keV with an AC threshold of 40 keV and 0 keV, respectively.

In total 107 are removed by the AC veto from the $Q_{\beta\beta}$ region. Those are almost a third of all events after muon veto cut. At a threshold setting of 15 keV, the first events will leak the AC veto cut, while 3 events and 6 events will slip through the cut with a threshold of 20 keV and 40 keV, respectively. Events with a secondary energy below 15 keV are already not caught by the AC veto cut, because they are not recognized by the offline trigger.

The right plot in Fig. 6.11 depicts the AC veto efficiency for the $Q_{\beta\beta}$ region for a AC threshold between 0 and 200 keV. The efficiency has been obtained by normalizing the blue curve from the left plot, so that the AC veto efficiency is 1 for no AC threshold, which corresponds to vetoing all coincidence events that would fall in the $Q_{\beta\beta}$ region. Efficiencies of 0.976 ± 0.006 and 0.951 ± 0.013 are obtained for a threshold of 20 keV and 40 keV, respectively. With the inherent trigger thresholds, the efficiency is expected to be somewhere between the two values given. By setting a fixed threshold of 40 keV, about 5 events in the considered PII data are expected to leak the AC veto cut in the $Q_{\beta\beta}$ region. According to the M2 background model, the highest contribution to the $Q_{\beta\beta}$ region that is cut by the AC veto comes from contaminations of ^{208}Tl (65%) and ^{214}Bi (23%).

The uncertainty was estimated from the dead layer uncertainties of the detectors. For this purpose, two classes of γ-ray induced events have to be considered. In the first, a higher energetic γ-ray enters the detector and is forward scattered, depositing an energy of 40 keV. This class of events is largely unaffected by the attenuation of the dead layer. The second class are events, where a 40 keV γ-rays enters the detector from outside and is absorbed in the active volume. A change of 0.2 mm of the dead layer will affect the attenuation of such a low energetic γ-ray by roughly 50%. A very conservative assumption is made, that the second class of events make up half of the total number of events with a secondary energy of 40 keV.

Uncertainties from the background model have been evaluated by determining the AC veto efficiency with the model obtained from the sum energy best fit and the single energy best fit from Sec. 6.6.4 and comparing the results. The difference was found to be negligible compared to the contribution from the dead layer uncertainty. This is largely due to the efficiency being calculated as a ratio between the expected events for a particular threshold to the expected events without threshold. Uncertainties of a background component (e.g. ^{208}Tl) in the model will have almost the same effect on both values, hence the efficiency will not change.

Chapter 7

$2\nu\beta\beta$-decay to excited states

7.1 Introduction

The $2\nu\beta\beta$-decay to excited states has so far only been observed for two isotopes, ^{100}Mo [160] and ^{150}Nd [161, 162]. Several limits have been set for the $2\nu\beta\beta$-decay of ^{76}Ge to excited states of ^{76}Se. The latest before the GERDA experiment at $T_{1/2}$>6.2·10^{21} yr (90% C.L.) for the $0^+_{g.s.} \rightarrow 0^+_1$ transition has been achieved in the framework of the IGEX experiment [163].

As is the case for the $0\nu\beta\beta$ ground state decay, a vast variety of nuclear models exist, predicting a large range of half-lives for the $2\nu\beta\beta$-decay of ^{76}Ge to excited states. While the $0\nu\beta\beta$ and the $2\nu\beta\beta$ nuclear matrix elements are numerical different, calculations rely on similar model assumptions. Hence, the value of an observation of excited state transitions lies not only in the constraint of the model parameters describing the $2\nu\beta\beta$-decay process, but also in a refinement of the $0\nu\beta\beta$-decay predictions.

A collection of half-life predicitions for three decay modes is given in Tab.7.1, taken from [4, 127]. Many of the predictions are older than 20 years, giving a typical half-life range in the order of 10^{21}-10^{23} yr for the $0^+_{g.s.} \rightarrow 0^+_1$ transition.

New results have been published recently by the GERDA collaboration using PI data [4] with an exposure of approximately 22 kg·yr. Additional information can be found in [127]. No signal has been found in the analysis of GERDA PI data and new Frequentist and Bayesian half-life limits for the three decay modes $0^+_{g.s.} \rightarrow 0^+_1$, $0^+_{g.s.} \rightarrow 2^+_1$ and $0^+_{g.s.} \rightarrow 2^+_2$ have been extracted. The Bayesian 90% credibility limits have been set at $T_{1/2}(0^+_{g.s.} \rightarrow 0^+_1) > 2.7 \cdot 10^{23}$ yr, $T_{1/2}(0^+_{g.s.} \rightarrow 2^+_1) > 1.3 \cdot 10^{23}$ yr and $T_{1/2}(0^+_{g.s.} \rightarrow 2^+_2) > 1.8 \cdot 10^{23}$ yr, respectively. Based on this data, Bayes factors have been calculated between the theoretical half-lives and the null hypothesis, ruling out most of the older predictions. However, the GERDA results gave a push for three new calculations reaching in the order of 10^{24} yr, one order of magnitude above the previous values [164, 165, 166].

With PII of GERDA and an exposure of 100 kg·yr, a sensitivity of $1 \cdot 10^{24}$ yr is envisioned [127], that can fully test the calculations of [164].

So far, up until mid 2017, GERDA has taken 35 kg·yr of data in PII. In this chapter the analysis of the $2\nu\beta\beta$-decay to excited states is presented, combining the GERDA data of PI and PII. First, Sec. 7.2 will take a look at the decay schematics of the signal process, followed by an discussion of the signal signatures as expected from MC data in Sec. 7.3. In Sec. 7.4, the important parameters of the data sets that are used for this analysis are summarized.

An overview of the analysis procedure, followed by a more in detail discussion of every step is given in Sec. 7.5. The results are presented in Sec. 7.6

7.2 Decay schematics

The Q-value of the $\beta\beta$-decay of ^{76}Ge is Q =(2039.061±0.007) keV [174]. This allows the decay in general to occupy the energetically lowest ten nuclear states in the ^{76}Se level scheme [175]. However, the more energy is spend for the excitation of the daughter nucleus, the less energy is left for the emitted electrons and neutrinos, effectively reducing the phase space and consequently the rate of the decay. Thus it was decided to concentrate on the first three excited states. The decay scheme is shown in Figure 7.1. Apart from the phase space, the nuclear spin configuration of mother and daughter nuclei are important to the decay rate. The decay from the 0^+ ground state of ^{76}Ge to the second excited state with a 0^+ configuration is favored over the decay to the first and third excited state (both

$2\nu\beta\beta$-decay	$T_{1/2}$ [yr]	model	year	ref.
$0^+_{g.s.} \rightarrow 2^+_1$	$1.2 \cdot 10^{30}$	ShM	1984	[37]
	$5.8 \cdot 10^{23}$	HFB	1994	[167]
	$5.0 \cdot 10^{26}$	QRPA	1994	[168]
	$2.4 \cdot 10^{24}$	QRPA	1996	[169]
	$7.8 \cdot 10^{25}$	MCM-QRPA	1996	[170]
	$1.0 \cdot 10^{26}$	RQRPA	1997	[171]
	$(2.4 - 4.3) \cdot 10^{26}$	RQRPA	1998	[172]
	$(2.0) \cdot 10^{27}$	RQRPA	2014	[173]
$0^+_{g.s.} \rightarrow 0^+_1$	$1.32 \cdot 10^{21}$	HFB	1994	[167]
	$4.0 \cdot 10^{22}$	QRPA	1994	[168]
	$4.5 \cdot 10^{22}$	QRPA	1996	[169]
	$7.5 \cdot 10^{21}$	MCM-QRPA	1996	[170]
	$(1.0 - 3.1) \cdot 10^{23}$	RQRPA	1997	[171]
	$(1.2 - 5.8) \cdot 10^{23}$	RQRPA	2014	[164]
	$6.4 \cdot 10^{24}$	IBM-2	2014	[165]
	$(2.3 - 2.6) \cdot 10^{24}$	ShM	2014	[166]
$0^+_{g.s.} \rightarrow 2^+_2$	$1.0 \cdot 10^{29}$	QRPA	1994	[168]
	$1.3 \cdot 10^{29}$	MCM-QRPA	1996	[170]
	$(0.7 - 2.2) \cdot 10^{28}$	RQRPA	1997	[171]

Table 7.1.: Summary of half-lives for the $0^+_{g.s.} \rightarrow 0^+_1$, $0^+_{g.s.} \rightarrow 2^+_1$ and $0^+_{g.s.} \rightarrow 2^+_2$ $2\nu\beta\beta$-decay modes predicted by various nuclear models (ShM: Shell Model, HFB: Hartree-Fock-Bogoliubov, QRPA: Quasi-random phase approximation, MCM-QRPA: multiple commutator method QRPA, RQRPA: renormalized QRPA, IBM: Interacting boson model). The table is taken from [127], the reference for each prediction is given in the table.

with a 2^+ configuration) out of that reason. Predicted half-lives for each decay mode are typically in the orders of 10^{26}-10^{27} yr for the $0^+_{g.s.} \rightarrow 2^+_1$ transition, 10^{23}-10^{24} yr for the $0^+_{g.s.} \rightarrow 0^+_1$ transition and 10^{28}-10^{29} yr for the $0^+_{g.s.} \rightarrow 2^+_2$ transition.

In the neutrino accompanied decay modes the available energy from the difference between initial and final state is divided among the two electrons and two neutrinos. The detector is only able to measure the continuous spectrum of the electron sum energy with an end point equal to the respective Q-value. For the neutrinoless decay modes, the two electrons will share the full energy available and the energy spectrum will feature a single line at the position corresponding to the Q-value.

The decay signature is additionally enhanced by one or more γ-rays that are emitted by the de-excitation of the daughter nucleus. In the de-excitation of the 2^+_1 state, one γ-ray with an energy of 559.1 keV is emitted. The de-excitation of the 0^+_1 state happens via the intermediate 2^+_1 state. Thus an additional γ-ray with an energy of 563.2 keV is emitted in coincidence to the 559.1 keV γ-ray. The de-excitation of the 2^+_2 state can follow two branches. The first branch (B1) with a branching ratio of 64% makes again an intermediate transition to the 2^+_1 state and therefore emits a 657.0 keV γ-rays in addition to the 559.1 keV γ-ray. In the second branch (B2) with a branching ratio of 36%, the transition follows directly to the ground state, which results in one emitted γ-ray with an energy of 1216.1 keV.

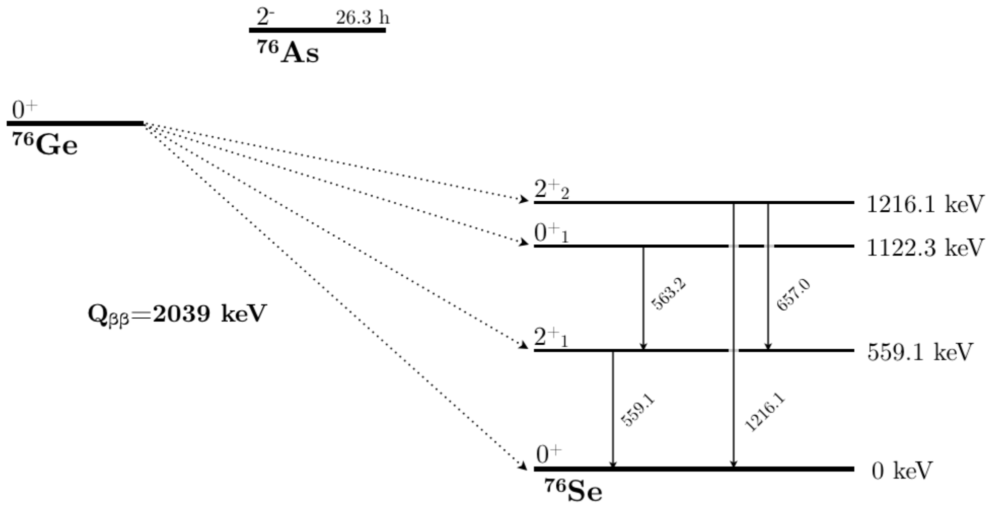

Figure 7.1.: Decay scheme of the double beta decay of ^{76}Ge to ^{76}Se. Shown are the ground state and the lowest three excited states in ^{76}Se [4, 127].

decay mode		$Q_{\beta\beta}$[keV]	$E_{\beta\beta}^{\max}$ [keV]	E_γ [keV]	p_γ
$0^+_{g.s.} \rightarrow 2^+_1$		1480.0	600	559.1	100%
$0^+_{g.s.} \rightarrow 0^+_1$		916.8	250	559.1, 563.2	100%
$0^+_{g.s.} \rightarrow 2^+_2$	B1	823.0	330	559.1, 657.0	64%
	B2			1216.1	36%

Table 7.2.: Electrons and γ-rays emitted by the $0\nu\beta\beta$ and $2\nu\beta\beta$-decays of ^{76}Ge and the subsequent de-excitation of the ^{76}Se daughter nucleus. Given are the end point energy (2ν) and the sum energy (0ν) $Q_{\beta\beta}$ of the two electrons, respectively, as well as their most likely sum energy $E_{\beta\beta}^{\max}$ (2ν). Also given are the energies of the γ-rays and their emission probability p_γ.

The γ-rays from the 0^+_1 state and B1 of the 2^+_2 state are emitted with an angular correlation, which is given by $W(\theta) \propto 1 - 3\cos^2\theta + 4\cos^4\theta$ and $W(\theta) \propto 1 - \frac{15}{13}\cos^2\theta + \frac{16}{13}\cos^4\theta$, respectively [176].

γ-rays may escape the detector where the decay happened and may deposit their energy fully or partially inside one or more other detectors. This potential to create multi-detector coincidences differentiates decays to excited states from the $0^+_{\text{g.s.}} \rightarrow 0^+_{\text{g.s.}}$ decay mode. For the $2\nu\beta\beta$-decay modes to excited states, the coincidence data set is very important to the search, because the continuous energy spectrum of the electrons from the $0^+_{\text{g.s.}} \rightarrow 0^+_{\text{g.s.}}$ decay poses a large and irreducible background to the likewise continuous spectrum expected from the excited state decay modes. For the search for $0\nu\beta\beta$-decay modes, the coincidence data set can be used as additional data set to improve the sensitivity.

Tab. 7.2 lists the energies of the electrons and γ-rays emitted by each decay mode.

7.3 Signal Monte Carlo

For each decay mode and each array configuration (PIa/PIc, PII), 10^9 decays have been simulated within each detector in the array. The primary momenta of the electrons and

γ-rays have been generated using the decay0 software [155]. The position of the decays has been confined to the full germanium volume of the detector, which includes the active volume as well as the dead layer. For the $0^+_{g.s.} \rightarrow 0^+_1$ and $0^+_{g.s.} \rightarrow 2^+_2$ decay modes, the angular correlation between the γ-rays has been taken into account.

As only coincident data is of interest for this analysis, events with an energy deposition in only one detector are removed from the files to allow a faster and more effective processing. The energies of the events are smeared with the help of the energy resolution curves as collected in Sec. 7.4. The default low energy threshold of 100 keV and 200 keV is applied for the PI and PII data, respectively, i.e. an event with exactly two energy depositions above this threshold is classified as M2 event.

Fig. 7.2 shows the two-dimensional spectra of M2 events for all three decay modes. The order in which the two energies are plotted is determined by the detector ID number, i.e. the energy deposited in the detector with the lower detector ID is attributed to the x coordinate.

Visible in the spectra are several horizontal and vertical lines. It is apparent that the highest concentration of signal events can be found in those lines forming a ”cross-like” pattern. The lines correspond to the energy of the γ-rays in one detector. In the other detector, the energy corresponds in most cases to the energy of the two electrons and possibly a part of the energy of the second γ-ray.

For the $0^+_{g.s.} \rightarrow 0^+_1$ decay mode, the ”cross” shape consists of a double line, because the energies of the two γ-rays are inseparable with 559.1 keV and 563.2 keV. The signal cut requires one of the energies of an event to match either of those given a certain energy window defined by the energy resolution.

The $0^+_{g.s.} \rightarrow 2^+_1$ decay mode spectrum initially looks very similar, the difference being that there is only a single line at a γ-ray energy of 559.1 keV. Hence, the signal cut requires one energy to match 559.1 keV.

The $0^+_{g.s.} \rightarrow 2^+_2$ decay mode has two separate de-excitation branches. The first manifests itself as two ”cross-like” shapes corresponding to γ-ray energies of 559.1 keV and 657.0 keV. The second branch is visible as a vertical and horizontal line at 1216.1 keV. The projection of those lines are purely the two-electron spectrum with the end point at 823 keV. Due to the limited MC statistics and the low population of the high energy tail of the two-electron spectrum, the lines appear to reach only up to about 700 keV.

Fig. 7.3 also shows the two one-dimensional representations of this spectrum, the single energy spectrum and the sum energy spectrum.

The signal MC data is used to identify the signal regions and construct the signal cuts, as well as to calculate the signal cut efficiencies.

Importance of detector size and position

The search for the $0^+_{\mathrm{g.s.}} \rightarrow 0^+_{\mathrm{g.s.}}$ mode prefers larger detectors, because this minimizes the amount of electronics and other material close to the detector that is potentially contaminated. Additionally, the probability that bremsstrahlung from the signal decay escapes the detector is minimized. On the other hand, the search for excited states decay modes which concentrates on coincident events instead, prefers a higher granularity of the detector array. Smaller detectors largely increase the fraction of M2 events caused by signal decays, due to less self absorption of the de-excitation γ-rays. Fig. 7.4 shows the fraction of $0^+_{g.s.} \rightarrow 0^+_1$ signal decays that are detected as M1, M2 or M3 events for each detector (higher multiplicities are negligible) with a low energy threshold of 200 keV.

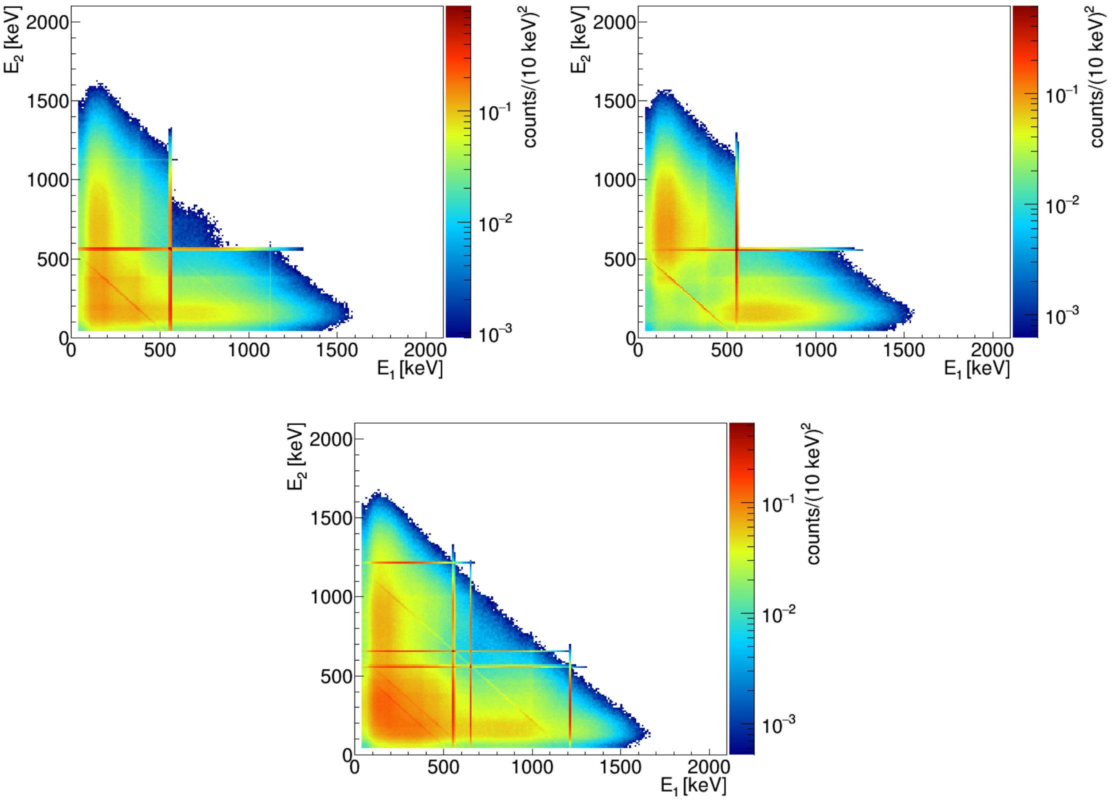

Figure 7.2.: Signal MC spectrum. Shown is the energy of one detector against the energy of the second detector of M2 events for the three decay modes $0^+_{g.s.} \rightarrow 0^+_1$ (*top left*), $0^+_{g.s.} \rightarrow 2^+_1$ (*top right*) and $0^+_{g.s.} \rightarrow 2^+_2$ (*bottom*). The signal has been scaled to correspond to a half-life of 10^{23} yr.

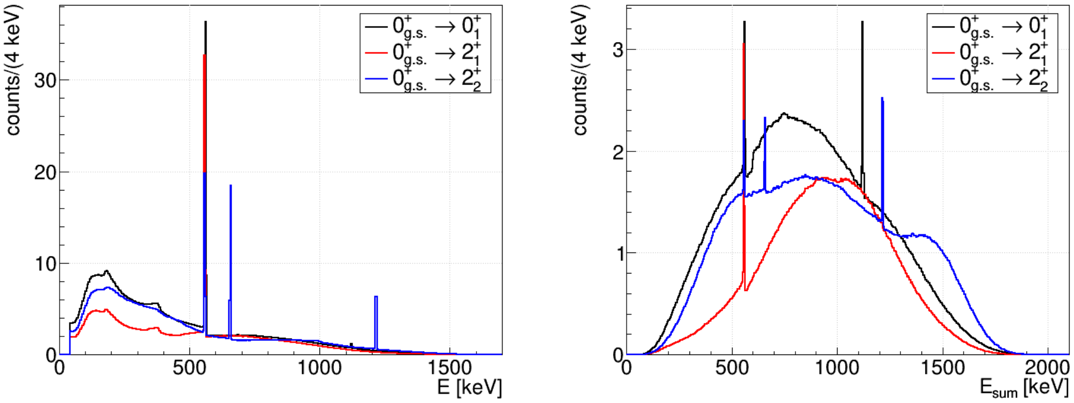

Figure 7.3.: Signal MC data. Shown are two one-dimensional representations of the M2 data for all three decay modes: *Left:* the single energy spectrum. *Right:* the sum energy spectrum. The signal has been scaled to correspond to a half-life of 10^{23} yr.

The fraction of M2 events created by signal decays in BEGe detectors is about twice as high than for the larger semi-coaxial detectors (ANG). Furthermore, the position of the detector in the array is important. Detectors that are surrounded by other detectors show a higher fraction of M2 events. These are detectors in the middle of a string and especially the GTF detectors in the middle of the array. GTF112 is comparable to ANG2 and ANG5 by its size, while GTF32 and GTF45 are comparable to ANG3 and ANG4. By comparing similar size detectors, the effect of self absorption is canceled and it becomes visible, that detectors on the middle string generate 1.7 to more than twice as many M2 events per signal decay.
Unfortunately, the advantage of the middle string position is not utilized, because the GTF detectors are not enriched and thus generate only very few signal decays. However, plans are to replace the existing GTF detectors with enriched inverted coaxial detectors, to explore their potential for the future LEGEND experiment [68].

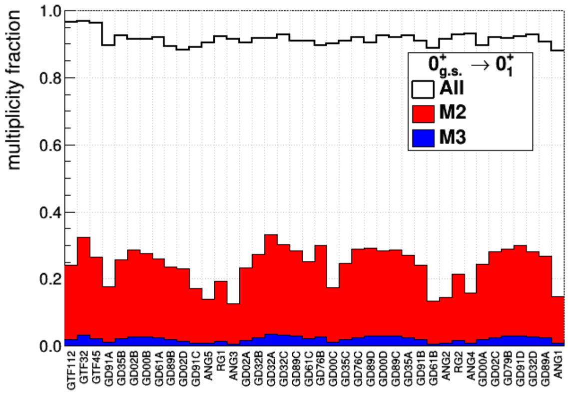

Figure 7.4.: The fraction of $0^+_{g.s.} \rightarrow 0^+_1$ signal decays for each detector in PII, that generate an event of a specific multiplicity. The histograms are stacked.

7.4 Data sets

The analysis is purely based on the coincidence data of Gerda PI and PII up until the mid 2017. Only M2 events are used. Higher multiplicities are barely sensitive to the signal process due to a very low efficiency.
The data sets used are described in Ch. 5.2 and summarized in the following, providing the necessary analysis parameters:

- **Phase I (Coax & BEGe):**
    - Start: November 9th, 2011 / End: July 2nd, 2013
    - Runs 25-47 (excluding: 33-35)
    - Exposure: 22.11±0.31 kgyr
    - Livetime: 459.7 d
    - Total detector mass: 24.3/25.3 kg (PIa/PIc)
    - Energy reconstructed with the pseudo-Gaussian shaping filter
    - FWHM= $\sqrt{p_0^2 + p_1 E}$
      Coax: $p_0 = 3.81$, $p_1 = 0.0033$, BEGe: $p_0 = 1.86$, $p_1 = 0.0023$

- **Phase II (Coax & BEGe):**
  - Start: December 20th, 2015 / End: April 15th, 2017
  - Runs 53-79 (excluding: 66, 68)
  - Exposure: 35.04±0.40 kgyr
  - Livetime: 405.1 d
  - Total detector mass: 43.2 kg
  - Energy reconstructed with the ZAC shaping filter
  - FWHM= $\sqrt{p_0^2 + p_1 E}$
    Coax: $p_0 = 2.55$, $p_1 = 0.0040$, BEGe: $p_0 = 2.17$, $p_1 = 0.0025$

The M2 data potentially has a worse energy resolution than the M1 data, due to imperfections in the crosstalk correction. Therefore, energy resolution curves are additionally extracted for the M2 data. This procedure is described in Ch. 5.6.1. The curves are used to smear the output of signal and background MC simulations. Given these curves, the energy resolution at several energies of interest are listed in Tab. 7.3.

energy [keV]	FWHM [keV]			
	PI Coax	PI BEGe	PII Coax	PII BEGe
560	4.04±0.02	2.18±0.06	2.96±0.02	2.46±0.01
657	4.08±0.03	2.23±0.07	3.03±0.01	2.51±0.01
823	4.15±0.05	2.31±0.08	3.14±0.02	2.59±0.03
917	4.19±0.06	2.35±0.09	3.20±0.02	2.64±0.03
1122	4.26±0.07	2.45±0.09	3.32±0.03	2.73±0.04
1216	4.30±0.07	2.49±0.09	3.38±0.03	2.77±0.04
1382	4.36±0.07	2.57±0.08	3.48±0.03	2.84±0.04
1480	4.40±0.07	2.61±0.08	3.53±0.03	2.89±0.04
sum energy				
1382	5.79±0.05	3.17±0.10	4.31±0.02	3.58±0.02
1460	5.82±0.06	3.20±0.11	4.35±0.03	3.60±0.03
1480	5.82±0.06	3.21±0.11	4.36±0.03	3.61±0.03
1525	5.83±0.06	3.22±0.11	4.38±0.03	3.62±0.03
2039	5.98±0.09	3.40±0.12	4.61±0.05	3.79±0.05

Table 7.3.: Energy resolution given as Full Width as Half Maximum (FWHM) at several energies of interest for the M2 data sets of PI and PII.

The shift of the peak positions compared to its literature value is smaller than 0.2 keV for the M1 data, as given in [126]. In case of the M2 data, the average shift of the 4 peaks are not greater than 0.3 keV when looking at the averaged value for all calibrations and also the combined spectrum of all calibrations. Therefore, the uncertainty of the energy scale is taken as 0.2 keV and 0.3 keV for the M1 and M2 data, respectively.

7.5 Analysis

7.5.1 Overview

The analysis is based on a cut and count method and was also presented in [4], on the basis of the PI data. A short overview is given here first. Afterwards the analysis steps are discussed in more detail by applying the analysis to the new PII data.

With an energy threshold of 200 keV on both channels, over 7000 M2 events are expected from the background in the region below 2039 keV. This can be compared to 200 to 300 signal M2 events for the different decay modes, assuming a half-life of 10^{23} yr. The signal to background ratio can be improved significantly by selecting only certain regions in the two-dimensional energy spectrum that facilitate the expected signal counts. Such signal cuts are chosen based on the decay signature of each decay mode and the signal MC data. At the beginning, the width and length of the signal cuts are set to default values. Those values are optimized in a next step to maximize the sensitivity, but also to provide an objective way to select cut parameters in order to minimize the introduction of subjective bias. The sensitivity is calculated with the help of a figure of merit, involving the signal cut efficiency and the expected background after the cut. Thus, MC data of the signal and background processes are heavily utilized in this step. The optimization also involves the introduction of additional background cuts to eliminate very prominent background lines (e.g. from ^{42}K). The option to improve the sensitivity by excluding certain detector pairs from the analysis is also investigated. The final sensitivity given the optimized signal cuts is determined with the help of toy MC experiments.

The optimized signal cuts are applied to the experimental data to obtain a number of counts for the signal region. Additionally, the same cuts are applied to the signal MC data to derive the signal cut efficiency.

The aim is to decouple the experimental half-life results from the background MC data. Therefore, the background after applying the signal cuts needs to be estimated based on the experimental data alone. For that purpose sideband cuts are constructed, so that the expected background in the signal cut region can be inferred as accurate as possible from the background in the sideband cut regions.

Given the signal region counts and the counts in the sideband regions, a Bayesian analysis was chosen to extract the marginalized posterior probability density for the half-life of the signal process. From this distribution a 90% credibility interval is obtained.

7.5.2 Signal cuts

The following chain of cuts is applied to the data:

Basic cuts

Before any analysis specific cuts are applied, basic cuts like quality cuts and the muon veto cut are enforced (see Ch. 4.4.3 and 4.5.3).

The effect of the quality cuts on physical signals is expected to be smaller than 0.1% [125, 132] for energies above 100 keV. The muon veto cut vetoes about 0.4% of the physical events in PI and PII. The LAr veto cuts roughly 40% of all physical events [139]. However, it can not be used for all decay modes in this analysis, as part of the energy can also be deposited in the argon by the γ-rays emitted in the signal process. It is used though for all signal regions, where the full decay energy is detected in the germanium detectors. The LAr veto introduces a dead time of (2.3±0.1)% [132]. No PSD cuts are applied.

Coincidence cut

Second, a coincidence cut is applied, which requires the energy of two detectors to be above 100 keV and 200 keV for PI and PII data respectively. A threshold of 100 keV is the minimum threshold to ensure that the quality cuts are working properly without removing a significant amount of physical events due to a low signal to noise ratio. The threshold of some detectors in PII is set much higher, so that 200 keV is chosen as common value (see also Ch. 5.3). Changing the threshold will have an effect on the multiplicity: A higher threshold can degrade higher multiplicity events to lower multiplicities and vice versa. In the PI analysis, this threshold was optimized to increase the sensitivity of the signal search. In the PII analysis, instead the low energy end of the signal cuts is optimized (see Sec. 7.5.4). The energy threshold is kept constant to preserve the default multiplicities.

Signal cut

The main signal region cut is applied in a next step, which is specific to each decay mode. This cut imposes requirements on the energy depositions of both detectors to select the "cross-like" regions with a high signal concentration according to the MC spectrum shown in Fig. 7.2. Hence, the signal cut requires one of the detectors to register an energy equivalent to the energy of one of the γ-rays. The energies have to match within a certain signal cut window which is defined by the energy resolution. The default value for the window width is chosen as twice the energy resolution ($2\sigma_E$). The low energy end is set by default to the energy threshold. At higher energies, the signal cut is limited by a diagonal line, which corresponds to a sum energy equivalent to the Q-value of the decay. The window width as well as the low and high energy end of the cut region are subject to an optimization as presented in Sec. 7.5.4.
For the different decay modes, the signal cut looks as follows:

- $0^+_{g.s.} \to 0^+_1$: The base signal cut requires the energy deposition in one detector to either be within (559.1±3.6) keV or within (563.2±3.6) keV. For a width larger than ±2.05 keV the windows of both γ-rays are connected. The energy deposition in the second detector can occupy any value in the range between the low and high energy end of the cut region.

- $0^+_{g.s.} \to 2^+_1$: The energy deposition of either detector has to be within a window of (559.1±3.6) keV.

- $0^+_{g.s.} \to 2^+_2$: The two branches of this decay mode are handled with two separate cut regions.

  For the first de-excitation branch (B1) the energy deposition of either detector has to be within a window of (559.1±3.6) keV or within a window of (657.0±3.0) keV. The two γ-rays lead to two regions that are not connected. The window width of the second region is restricted to ±3.0 keV due to a ^{214}Bi background line at 665.4 keV. As it will be seen in Sec. 7.5.4, the optimized width is smaller than 3.0 keV, thus the restriction imposed by the background line will have no impact on the final result. The second energy deposition is constrained to below 1193.0 keV in order to prevent it to fall together with the region of the second branch.

  The signal cut for the second branch (B2) requires one of the energy depositions in the detectors to be within (1216.1±4.0) keV.

Each decay mode is evaluated separately from each other, because the ratio between the decay rates for each mode are not known. That means, when analysing one decay mode, the others are assumed to be non-existent. As long as no signal is observed, this assumption is insignificant. In case of an observation, more thought needs to be put into

discriminating between the decay modes. This can be done with the help of the secondary γ-ray of some of the decay modes or the LAr veto, because only some of the decay modes deposit energy in the LAr for events selected by the signal cut. Judging by the half-life predictions, the $0^+_{g.s.} \rightarrow 0^+_1$ mode should be the dominant decay mode, contributing the majority of signal counts.
Because all decay modes share a signal cut in the region around the 559.1 keV signal line, the results will be correlated.

Background cut

Fig. 7.5 shows the sum energy spectra of the background model after the signal cut has been applied. While the signal spectra is rather homogeneous over the energy range, the background peaks at positions of prominent background lines. Background lines that cross the signal region cut are in general no problem, if they are properly accounted for in the estimated background expectation. Lines with a high intensity can dominate the background expectation though. Hence, additional background cuts to remove those lines can lead to an increase in the sensitivity, as they cut a significant amount of background while leaving the cut efficiency almost untouched. The two most prominent lines in the spectrum are the ^{42}K line at 1525 keV and the ^{40}K line at 1460 keV in the sum energy spectrum. Both lines are excluded by a ±5 keV window around the line energy. By removing both background lines, the sensitivity improves by about 5%, 15%, 10% and 45% for the $0^+_{g.s.} \rightarrow 0^+_1$, $0^+_{g.s.} \rightarrow 2^+_1$ and B1 and B2 of the $0^+_{g.s.} \rightarrow 2^+_2$ decay modes, respectively. The second branch of $0^+_{g.s.} \rightarrow 2^+_2$ experiences the biggest improvement, because the background is dominated by the two high energetic γ-lines of ^{40}K and ^{42}K in the region of 1200 keV.

7.5.3 Signal cut efficiency

Efficiency calculation

The efficiencies of the signal cuts are calculated based on the signal MC data. For this purpose, 10^6 signal decays have been simulated in each detector. This MC data is then converted to the same structure as the physics data so that both data can be processed by

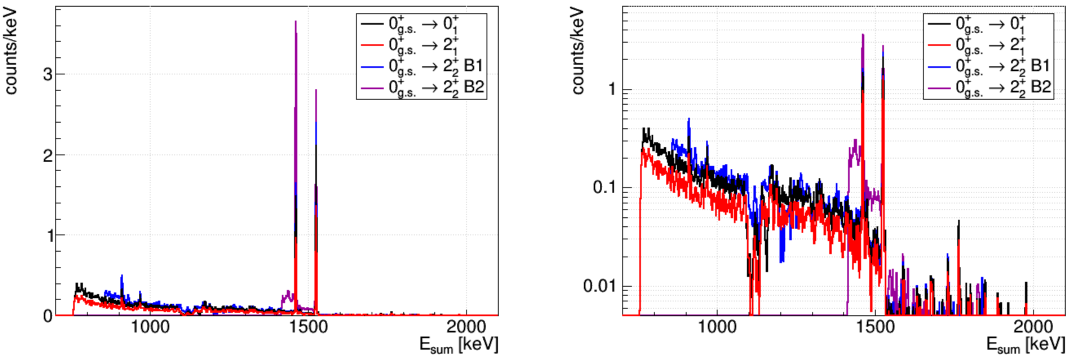

Figure 7.5.: The sum energy spectrum of the background model after the signal cut for each decay mode has been applied (*left*: linear scale, *right:* logarithmic scale). Clearly visible are the γ-lines of ^{42}K at 1525 keV and ^{40}K at 1460 keV.

the same analysis framework. This framework applies the whole cut chain and extracts a number of counts surviving all cuts. The multiplicity in the signal MC data is calculated for each run separately according to the status of each detector during that run.
In a first step, the efficiency $\varepsilon_{d,r}$ is calculated for signal decays in detector d and run r by taking the number of surviving counts and dividing them by the number of total generated events in detector d. The continuous spectrum of the signal below the respective γ-line will be counted towards the background and is thus subtracted from the surviving counts when calculating the efficiency. This is done with the help of sideband regions, as explained later in Sec. 7.5.5.
The efficiency obtained is then summed to a run efficiency of the whole detector array

$$\varepsilon_r = \frac{\sum\limits_d \varepsilon_{d,r} \cdot m_{76,d}}{\sum\limits_d m_{76,d}}, \tag{7.1}$$

weighted with the source mass (mass of ^{76}Ge m_{76}) of the detectors.
In the final step, the run efficiencies are summed to the global efficiency of the experiment, weighted with the sum of the source mass and the live-time of each run:

$$\varepsilon = \frac{\sum\limits_r \varepsilon_r \cdot \sum\limits_{d_r} m_{76,d_r} \cdot t_r}{\sum\limits_r \sum\limits_{d_r} m_{76,d_r} \cdot t_r}. \tag{7.2}$$

Default signal cut efficiencies

Given the default signal cut region as explained in Sec. 7.5.2, the global signal cut efficiency was calculated. It amounts to 2.70% for the $0^+_{g.s.} \rightarrow 0^+_1$ decay mode, 1.62% for the $0^+_{g.s.} \rightarrow 2^+_1$ decay mode and 1.77% and 0.43% for the two branches of the $0^+_{g.s.} \rightarrow 2^+_2$ decay mode for the PII data.

Uncertainties

The uncertainties to the efficiency come from three big contributions. The change in efficiency due to each source of uncertainty was evaluated by changing the corresponding parameter by ±1 standard deviation in the signal MC data and re-calculating the efficiency.

- **The active volume/dead layer thickness uncertainty of each detector.** The active volume directly affects the efficiency by affecting the detection probability of the γ-rays and two electrons. A thicker dead layer reduces the probability that γ-rays are detected. Furthermore, the chance that a signal decay happens in the dead layer increases and likewise the chance that the two electrons are lost and their energy deposition is not registered.

  For the dead layer thickness of the BEGe detectors in PII, uncorrelated and correlated uncertainty terms are available (see Tab. C.1). To account for the correlated term, all dead layers in the signal MC data were changed by ±1 standard deviation. To account for the uncorrelated term, only the dead layer by one representative detector (GD61A) was changed. The effect of the dead layer thickness uncertainty of the other BEGe detectors was assumed to be similar, so that the combined effect due to the uncorrelated uncertainty term could be taken as $\sqrt{n_{\mathrm{BEGe}}} \cdot \sigma^{\mathrm{uncorr}}_{\varepsilon,\mathrm{BEGe}}$, where

n_{BEGe} is the number of BEGe detectors in the array and $\sigma^{\text{uncorr}}_{\varepsilon,\text{BEGe}}$ is the resulting uncertainty of the signal efficiency by changing the dead layer of GD61A. The typically asymmetric uncertainties of the efficiency are approximated by a symmetric uncertainty by taking the maximum of the positive and negative part. The correlation exists for all BEGe detectors employed in GERDA. Thus, the resulting uncertainty on the efficiency is also correlated between PI and PII. The uncertainty stemming from the uncorrelated term is assumed to be uncorrelated between PI and PII, because the BEGe detectors in PI are only a small subset of the PII BEGe detectors.

For the semi-coaxial detectors only one uncertainty for the dead layer thickness is available. To stay conservative, the uncertainty is assumed to be 100% correlated. Hence a set of MC data is produced where the dead layer thicknesses of all semi-coaxial detectors have been changed by ±1 standard deviation. The uncertainty of the semi-coaxial detectors is correlated between PI and PII, because the same detectors have been used, with the exception that RG3 has been excluded.

Typical values for the uncertainty introduced by the dead layer thickness are in the range of 1-5%.

- **The uncertainty of the energy resolution and energy scale.** The signal cut window width is defined based on the energy resolution. Only a certain fraction of the signal peaks are included in the cut window. A change in the energy resolution affects the fraction of the signal peaks that is included in the cut window and hence affects the cut efficiency. For example, for a broader signal peak a lower fraction of signal events will be counted in the cut region.

  Similar to a change in the energy resolution, shifts of the peak position due to an uncertainty in the energy scale will also move a fraction of the signal peak out of one side of the cut window and therefore change the cut efficiency as well.

  The smearing of the signal MC data is done during the post processing of the MC data to save computing time. Because of this, in contrast to the evaluation of the dead layer uncertainty, no new MC data needs to be created. Both parameters, the energy resolution and the energy shift, are varied in a post processing step and the efficiency is re-calculated to obtain the efficiency uncertainty caused by the respective parameter.

  The energy resolution for semi-coaxial and BEGe detectors is changed independently from each other. This results in one efficiency uncertainty term for each detector set. To account for the shift in the peak position, instead the signal cut region is shifted by a value of 0.3 keV (compare Ch. 5.6.1). A single final uncertainty value is obtained by combining the individual values from BEGe and semi-coaxial energy resolution and peak shift quadratically.

- **The uncertainty on the signal MC data.** A 4% uncertainty is taken due to the physical processes implemented in the Geant4 based MC framework MaGe [177]. The statistical uncertainty of the MC data is in general negligible.

7.5.4 Signal cut optimization

The signal cut window width and low and high energy end are optimized based on a figure of merit which represents the half-life sensitivity. This optimization is meant to maximize the sensitivity of the analysis as well as to provide an objective way of the choice of the signal cut shape. For this purpose, the optimization is entirely based on MC data of the signal process and the background model.

Figure of merit

A figure of merit for the sensitivity to set a lower limit on the half-life is calculated based on a Feldman-Cousins approach. For this, Feldman-Cousins limits are obtained for a range of counts n_s in the signal region and the background expectation b from the MC data. The range for n_s is adjusted according to a Poisson distribution with the expectation value identical to the background expectation. The figure of merit is determined by dividing the efficiency by the upper count limits, weighted with the Poisson probability of the corresponding n_s.

$$F = \frac{\varepsilon}{\sum\limits_{n_s}(P(n_s,b)FC(n_s,b))} \tag{7.3}$$

where $P(n_s, b)$ the Poisson distribution with expectation value b and $FC(n_s, b)$ the upper count limit obtained with Feldman-Cousins.
This approach was cross-checked using a toy MC approach with BAT for several of the optimization runs. Qualitatively the results obtained with both approaches are in agreement. Consequently the much faster Feldman-Cousins approach is utilized to perform the full optimization runs.

Optimization of the low energy end

Because the background drops of very quickly with higher energies in the low energy region and the single energy signal spectrum is mostly that of the two electrons with a maximum at roughly 1/3 of the endpoint energy, the optimal value of the low energy end is expected close to that maximum. The low energy end E_{low} is varied from the minimum value of 200 keV in PII up to 500 keV in steps of 10 keV. For each value, the figure of merit is determined as stated above purely based on MC data. Fig. 7.6 shows the optimization curves of E_{low} for the three decay modes on the left side. The optimal values obtained are 250 keV, 400 keV, 250 keV and 250 keV for the $0^+_{g.s.} \rightarrow 0^+_1$, $0^+_{g.s.} \rightarrow 2^+_1$ and the first and second branch of the $0^+_{g.s.} \rightarrow 2^+_2$ transition, respectively.

Optimization of the high energy end

On the other hand, the signal spectrum drops off quickly close to its endpoint, while there are higher energetic background components. This is the reasoning to shorten the cut region at the higher energy end. The high energy end E_{high} is varied from 2050 keV down to 1500 keV in 50 keV steps and is applied to the sum energy. The right plot in Fig. 7.6 shows the curve of the figure of merit for each decay mode. The optimal values are found for 1850 keV, 1750 keV and 1850 keV for the $0^+_{g.s.} \rightarrow 0^+_1$, $0^+_{g.s.} \rightarrow 2^+_1$ and the $0^+_{g.s.} \rightarrow 2^+_2$ B2 transition, respectively. The optimization curve for the $0^+_{g.s.} \rightarrow 2^+_2$ B1 transition reveals no maximum, because the cut region is already restricted at high energies by the cut region of the second branch.

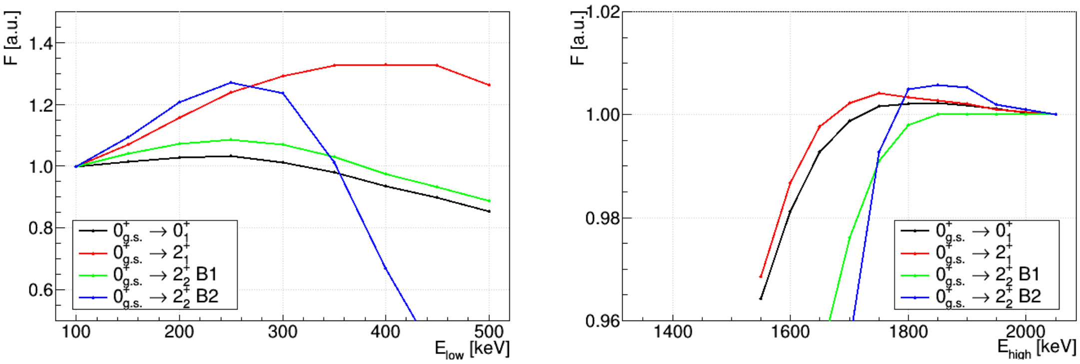

Figure 7.6.: Optimization curves for the low energy end E_{low} (left) and the high energy end E_{high} (right) of the signal cut region for all decay modes. The figure of merit F on the y-axis is discussed in Sec. 7.5.4

Optimization of the window width

For the signal cut width an optimal value is expected depending on the underlying constant background level. The window width w is varied from 1.0 keV to 4.0 keV in steps of 0.2 keV. Fig. 7.7 shows the optimization curves obtained for the three decay modes. The optimal values are smaller than in PI, which can be attributed to the improved energy resolution and the higher ratio of BEGe detectors in the array. Optimal values of 2.0 keV, 1.8 keV, 1.6 keV and 2.2 keV are found for the $0^+_{g.s.} \to 0^+_1$, $0^+_{g.s.} \to 2^+_1$ and the first and second branch of the $0^+_{g.s.} \to 2^+_2$ transition, respectively.

For the $0^+_{g.s.} \to 0^+_1$ decay mode, the figure of merit increases strongly while reducing the window width down to 2.0 keV. This can be explained due to the two γ-lines, that are only separated by 4.1 keV. Hence for a window width higher than 2.05 keV the windows of both γ-lines are connected. For values lower than 2.05 keV there are two separate windows and a fraction in the middle of the double line is excluded from the cut region. The optimal window width is set to the more precise 2.05 keV.

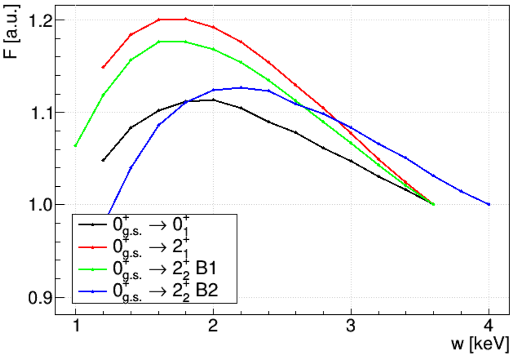

Figure 7.7.: Optimization curve for the signal cut region window width w for all decay modes. The figure of merit FS on the y-axis is discussed in Section 7.5.4

Detector pair selection

When looking at the M2 data, with two energy depositions in two separate detectors, it makes sense to divide the array into pairs of detectors. In PI the array consisted of 22 and 27 operational pairs during PIa and PIc, respectively. Given the 40 detectors in PII, the number of pairs has been increased immensely to 780 pairs.

The signal cuts enable to distinguish between the γ-ray absorbing detector and the detector with the signal decay, observing the energy deposition of the two electrons. Taking this into account, the number of pairs are effectively doubled.

The contribution of each pair to the total signal efficiency and background is different. A pair of neighboring detectors adds a larger amount to the efficiency compared to a pair of detectors on opposing ends of a string, because of the smaller distance and less γ-ray absorbing material in between. Additionally, larger detectors are more likely to fully absorb γ-rays of other detectors. Hence, their contribution is typically larger compared to smaller detectors. Obviously, pairs with a natural detector as the signal decay detector typically add very little to the efficiency.

The background is not affected in the same way as the signal, due to the different energy of γ-rays and the origin of the radiation outside of the detectors. Some pairs can add much more to the background than they contribute to the signal efficiency. Excluding such pairs from the analysis can increase the total sensitivity.

In order to objectively choose the pairs that are included in the analysis, the pairs are ranked using the ratio s between their contribution to the signal efficiency ε and their contribution to the background $\sqrt{B}$ as estimated from the background model. Pairs with a ratio above a certain cut value will be accepted, pairs with a ratio below the cut value will be removed. To maximize the sensitivity, the cut value is iterated over the full range of ratios. For each iteration, the total sensitivity of the accepted pairs is estimated using the figure of merit F. The cut value resulting in the largest value for F is selected for the analysis.

Fig. 7.8 shows a map of all detector pairs during PII and their normalized ratio s for the $0^+_{g.s.} \rightarrow 0^+_1$ decay mode, with the γ-ray detector on the x-axis and the signal decay detector on the y-axis. The framed detector pairs are selected for the analysis. The selected pairs can be divided into several groups. Close to the diagonal of the map, are pairs of neighboring detectors within a string, which add the most to the total sensitivity. The highest contributions come from neighboring semi-coaxial detectors and back to back positioned BEGe detectors like GD76C/GD35C and GD00C/GD76B. Additional groups are found in the off-diagonals close to the center, consisting of pairs of BEGe detectors from the neighboring strings 3 (GD02A to GD00C) and 4 (GD35C to GD61B), and close to the edges of the map, consisting of pairs of BEGe detectors from neighboring strings 1 (GD91A to GD91C) and 6 (GD00A to ANG1). Strings 2 and 5 with the semi-coaxial detectors result in bands of selected detectors, especially in vertical direction, due to their large mass and high γ-ray detection probability. The natural GTF detectors are also largely accepted as γ-ray detector and in a few cases even as signal decay detector, thanks to their position in the middle string.

For the $0^+_{g.s.} \rightarrow 0^+_1$ decay mode, 425 out of 1332 considered pairs are accepted by an optimized cut value of $s = 6.5 \cdot 10^{-4}$. The pair selection results in an increase of 3% of the figure of merit. The $0^+_{g.s.} \rightarrow 2^+_1$ decay mode results in 561 pairs with a optimized cut value of $s = 0.40 \cdot 10^{-4}$ and an increase of 7% in the figure of merit. For the first branch of the $0^+_{g.s.} \rightarrow 2^+_2$ decay mode, 545 pairs survived the cut with an optimized cut value of

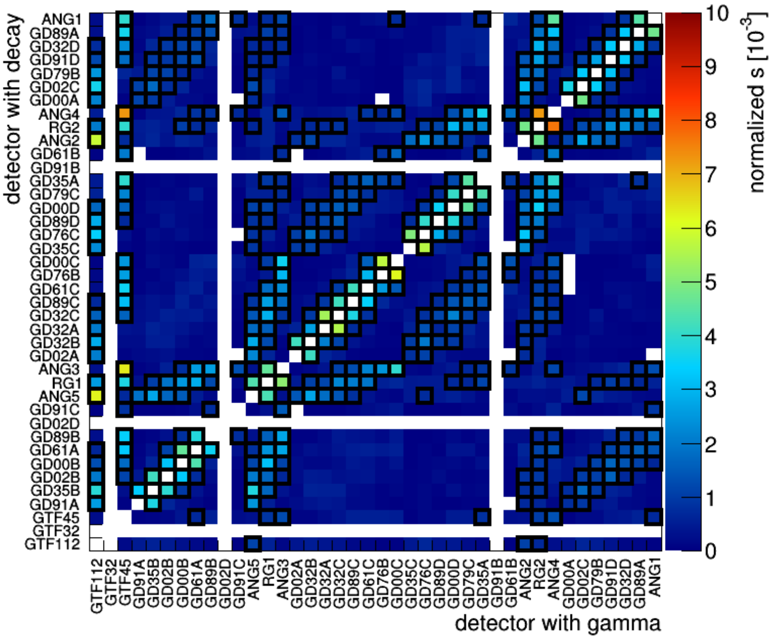

Figure 7.8.: A map of detector pairs in PII, with the detector with the γ-ray energy deposition on the x-axis and the two electron energy deposition (signal decay) on the y-axis. The color code indicates the contribution of each pair to the total sensitivity to the $0^+_{g.s.} \rightarrow 0^+_1$ decay mode, as determined by the ratio between signal efficiency contribution and background contribution. Pairs with a high individual contribution are accepted for the analysis and are framed in black. A discusson of the different regions of accepted pairs can be found in the text.

$s = 5.0 \cdot 10^{-4}$ and a figure of merit increase of 2% Due to the higher γ-ray energy, more pairs are accepted for B2, namely 652 with an optimized cut value of $s = 4.5 \cdot 10^{-4}$ and a figure of merit increase of 3%. The increase of the figure of merit is largest for the decay modes with only one de-excitation γ-ray. The corresponding maps for the other decay modes can be found in Appendix F.2.

Those results are similar to the ones obtained for PI in [127]. Pairs in top-down direction contributed the most to the total sensitivity, followed by pairs in lateral direction on neighboring strings. Around 37 out of 56 considered pairs are included for each of the decay modes.

Summary of optimization

Tab. 7.4 lists the selected cut regions with the optimized parameters for all decay modes. Additionally, the efficiency and background expectations are listed. Also listed is the increase in sensitivity achieved by the optimization. An increase between 6% and 27% has been achieved depending on the decay mode.

7.5.5 Background estimation

The expected background in the signal cut region can be obtained from the background model. However, the background model was constructed by using one-dimensional pro-

decay mode		E_{low}	E_{high}	w	ε [%]		b		$1-\frac{F_{\text{opt}}}{F_{\text{def}}}$
$0^+_{g.s.} \rightarrow 0^+_1$		250	1850	2.05	2.157	(81%)	47.0	(55%)	6%
$0^+_{g.s.} \rightarrow 2^+_1$		400	1750	1.80	1.122	(70%)	11.4	(25%)	27%
$0^+_{g.s.} \rightarrow 2^+_2$	B1	250	2050	1.60	1.263	(72%)	32.7	(41%)	8%
	B2	250	1850	2.20	0.286	(71%)	2.8	(20%)	26%

Table 7.4.: The values for the optimized signal cut paramters in PII: the low and high end of the cut window E_{low} and E_{high}, as well as the window width w given in units of keV. Also given are the efficiency ε and background expectation b after the optimization and their fraction compared to the default cuts. The last column lists the gain in sensitivity with respect to the default parameter values.

jections of the data. The signal cuts, on the other hand, are a small selection of events in the two-dimensional energy space. Because of this, the background model might not predict the experimental background sufficient enough.

Alternatively, an estimation of the expected background counts is obtained from the event counts in so-called sidebands (SBs). Sidebands are regions that are shifted by a few keV with respect to the signal region, but are otherwise equivalent to it.

It is important to ensure, that the background is flat or at least linear in good approximation around the signal regions. Otherwise, the sidebands will not give a good estimation for the expected background in the signal region. Furthermore, background lines need to be excluded from any sideband. In order to stay as much independent from the background model as possible, it is attempted to exclude even very small background lines. Background lines are allowed to cross a sideband if they are also included in other sidebands and the signal region to the same extent.

The selection of the position of the sidebands is supported by the MC data of the relevant background processes. The background model of Ch. 6.6 is again utilized for this purpose. Events that are located in multiple cut regions (ROI or SBs) are removed to prevent complications that arise from counting one event twice. Therefore, every event that enters the final analysis can be assigned exclusively to exactly one region.

The selection of the sideband regions is discussed in the following for each decay mode. The uncertainty on the MC count expectations for each cut region (SBs and ROI) is in the order of 0.1 counts and lower and thus much smaller than the fluctuations in the data.

- $0^+_{g.s.} \rightarrow 0^+_1$: Background lines around the region of interest include the 511 keV line, the 583 keV line from ^{208}Tl, the 609 keV line of ^{214}Bi and potentially a line of ^{207}Bi at 569.7 keV. Four sidebands are positioned, of which each consists of two connected regions due to the double signal line. One sideband has a combined width of 8.2 keV. On the higher energetic side, two sidebands can be positioned in the flat area between the ^{208}Tl and ^{214}Bi line (between 585 keV and 605 keV). The position on the lower energetic side is weaker restricted by background lines. Hence, two sidebands are placed symmetrically to the first two sidebands with respect to the signal region.

  Given these sidebands, the background model predicts a count expectation $\bar{N}^{\text{SB}}_{\text{MC}}$ averaged over all sidebands of 47.3 , while it predicts an expectation value $\bar{N}^{\text{SB}}_{\text{MC}}$ of 47.4 counts in the ROI. Both values agree very well with each other. However, a background line of ^{228}Ac is located inside the signal region at 562.5 keV. The expected number of counts from this line is evaluated in Sec. 7.6.5 based on the background model and the γ-line ratio to other observed lines of ^{228}Ac.

- $0^+_{g.s.} \to 2^+_1$: The region of interest is the same as for the $0^+_{g.s.} \to 0^+_1$ decay mode. Due to the smaller window width of 1.8 keV compared to the $0^+_{g.s.} \to 0^+_1$ decay mode and only a single signal line, eight sidebands are placed in total. Furthermore, the smaller window width allows to place one sideband between the ^{207}Bi and the ^{208}Tl lines and three sidebands between the ^{208}Tl and the ^{214}Bi lines. The sidebands on the lower energetic side are again positioned symmetrically to the other four sidebands with respect to the signal region.

  From the background model follows an expected 12.6 counts for the averaged sidebands. For the ROI, 12.5 counts are expected. Both values agree again very well.

- $0^+_{g.s.} \to 2^+_2$: The first decay branch is divided into two region of interest. The first region is the same as for the other decay modes. Because the window width is also similar to the $0^+_{g.s.} \to 2^+_1$ decay mode, the sideband positions are adopted. In the second region, no background lines are expected. Four sidebands are placed in the region between 670 keV and 690 keV and four more sidebands are placed symmetrically on the other side of the signal region.

  The expected counts from the background model for the averaged sidebands and the ROI agree sufficiently within on count with 34.6 and 34.1 counts, respectively.

  In the region of interest of the second decay branch, only one background line of ^{214}Bi is expected at 1238 keV. Three sidebands are fit between the signal region and this line. A fourth sideband is set on the right side of the ^{60}Co line. The sidebands on the lower energetic side are again positioned symmetrically with respect to the first four sidebands and the signal region.

  From the averaged sidebands 3.3 counts are expected, while in the ROI 3.4 counts are expected.

  Due to the SBs of the second branch, the boundary of the cut region of the first branch at high energies is shifted from 1193.0 keV down to 1184.0 keV in order to prevent counting events twice for both branches.

The positions of the final sidebands and the expected background counts in each sideband derived from the background model are listed in Tab. 7.5. Additionally, the signal region and the sidebands are visualized in Fig. 7.9 together with the background model.

Background composition

The expected background in the ROI of the $0^+_{g.s.} \to 0^+_1$ mode is composed mainly of ^{42}K with 27 counts (56%), ^{40}K with 8.4 counts (18%) and ^{214}Bi and ^{214}Pb with 7.7 counts (16%). For the $0^+_{g.s.} \to 2^+_1$ and the $0^+_{g.s.} \to 2^+_2$ B1 mode the composition is similar with the major contribution coming from ^{42}K with 7.3 counts (57%) and 20 counts (57%), respectively. The ^{40}K background does not enter the ROI of the $0^+_{g.s.} \to 2^+_2$ B2 mode. The biggest contributors are in this case again ^{42}K with 2.1 counts (67%) and ^{214}Bi and ^{214}Pb with 0.9 counts (26%).

$0^+_{g.s.} \rightarrow 0^+_1$		
SB	E_center [keV]	N^SB_MC
0	519.1 ∨ 523.2	52.4
1	528.1 ∨ 532.2	50.7
2	590.1 ∨ 594.2	43.3
3	599.1 ∨ 603.2	43.0
window: ±2.05 (eff. width: 4.10x2)		
$\bar{N}^\text{SB}_\text{MC}$:		47.3
N^ROI_MC:		47.4

$0^+_{g.s.} \rightarrow 2^+_1$		
SB	E_center [keV]	N^SB_MC
0	520.1	14.4
1	524.1	14.1
2	528.1	13.8
3	541.1	13.1
4	577.1	11.9
5	590.1	11.4
6	594.1	11.1
7	598.1	11.1
window: ±1.80 (eff. width: 3.60)		
$\bar{N}^\text{SB}_\text{MC}$:		12.6
N^ROI_MC:		12.5

$0^+_{g.s.} \rightarrow 2^+_2$ B1		
SB	E_center [keV]	N^SB_MC
0	520.1 ∨ 629.0	37.8
1	524.1 ∨ 633.0	37.0
2	528.1 ∨ 637.0	36.6
3	541.1 ∨ 641.0	35.5
4	577.1 ∨ 673.0	33.5
5	590.1 ∨ 677.0	32.2
6	594.1 ∨ 681.0	32.0
7	598.1 ∨ 685.0	32.4
window: ±1.60 (eff. width: 3.20x2)		
$\bar{N}^\text{SB}_\text{MC}$:		34.6
N^ROI_MC:		34.1

$0^+_{g.s.} \rightarrow 2^+_2$ B2		
SB	E_center [keV]	N^SB_MC
0	1187.1	4.3
1	1201.1	3.5
2	1206.1	3.4
3	1211.1	3.3
4	1221.1	3.3
5	1226.1	3.1
6	1231.1	3.0
7	1245.1	2.4
window: ±2.20 (eff. width: 4.40)		
$\bar{N}^\text{SB}_\text{MC}$:		3.3
N^ROI_MC:		3.4

Table 7.5.: The positions of the sidebands (SBs) for all decay modes by their center energy and the window width. Also given is the expected background N^SB_MC in each SB estimated from the background model, the average of those background expectations $\bar{N}^\text{SB}_\text{MC}$ and for comparison the background expectation in the ROI N^ROI_MC.

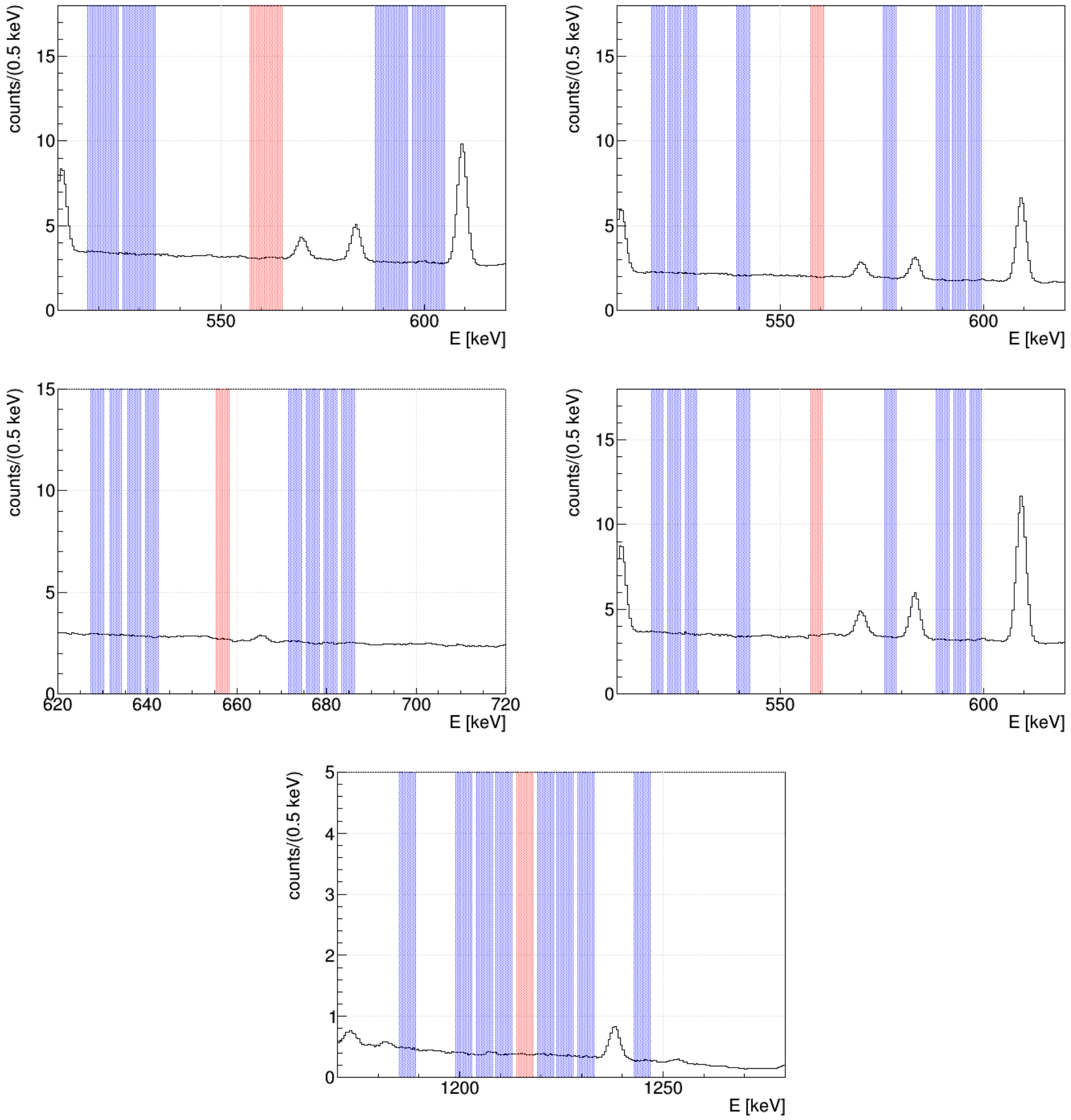

Figure 7.9.: Visualisation of the signal regions (red shade) and the sidebands (blue shade) together with the background model for all decay modes: *Top left*: $0^+_{g.s.} \rightarrow 0^+_1$, *Top right*: $0^+_{g.s.} \rightarrow 2^+_1$, *Middle left*: $0^+_{g.s.} \rightarrow 2^+_2$ B1 first region, *Middle right*: $0^+_{g.s.} \rightarrow 2^+_2$ B1 second region, *Bottom*: $0^+_{g.s.} \rightarrow 2^+_2$ B2.

7.5.6 Update of Phase I analysis

Because the complete GERDA data is utilized for the analysis, the opportunity is taken to update the PI data with the improved crosstalk correction. This can have have impact on the event counts in each region and on the energy resolution and can consequently change the signal region window width and efficiencies slightly.

Some additional changes are implemented, as listed in the following:

1) The optimization obtained for PI is cross-checked using the figure of merit from Sec. 7.5.4.

2) The lower energy threshold, which determines the multiplicity of an event is fixed at 100 keV and independent from the lower energy end of the signal cut region. As a consequence, no events with multiplicity of 3 or higher are shifted to the M2 spectrum by optimizing the signal cut region.

The optimization of signal region parameters is repeated to check if the previously obtained values are still valid with the changes applied. It was found that the newly found optimized parameter values remain consistent with the previous analysis. If at all, the optimal parameter values only change slightly in comparison to those found in [127]. At best, an improvement of the sensitivity of 3% is obtained for the $0^+_{g.s.} \rightarrow 2^+_1$ decay mode for the newly optimized cut regions in comparison to the old regions. The improvement for the other decay modes is below 1%, which is considered negligible. Hence for simplicity, the optimized signal cut regions are kept as they are in [127].

The updated efficiencies and counts in the signal cut regions and in the sidebands are listed in Tab. 7.6. Events that either are removed from or added to the selection due to the changes in comparison to the previous analysis are listed in Appendix F.1.

7.5.7 Efficiency and background: Phase I and Phase II

Compared to PI, the efficiencies in PII have increased by a factor of 2-3, due to the more compact detector array and the higher detector mass in general. The exposure increased by a factor of about 1.6. Thus, the overall expected signal counts for any given half-life has increased by a factor of 3.5-5, depending on the decay mode.

However, the absolute background also increased. The BI is not ideal to compare for coincidence events, because not only the detector mass and the live-time are important. Additionally, the different detector array configuration has a large impact on the background detection. The background increased by a factor of 4-7, which is more than the signal increase. The reason for this is the significant increase of the ^{42}K and ^{40}K background components. Another reason is the sub-optimal placement of the natural detectors in the middle of the array as discussed in Section 7.5.3, which hurts the signal efficiency. At the same time, the natural detectors do add additional background, as does the LAr in the middle of the array, which has a high chance of triggering coincident events in the germanium detectors.

The simplified sensitivity for PII given Eq. 3.1 is by a factor of about 1.5 for the $0^+_{g.s.} \rightarrow 0^+_1$ and $0^+_{g.s.} \rightarrow 2^+_2$ decay modes and 2.1 for the $0^+_{g.s.} \rightarrow 2^+_1$ decay mode larger than that of PI.

decay mode		ε [%]	N^{ROI}	N^{SB}	$\bar{N}^{\mathrm{SB}}$	$N^{\mathrm{ROI}}_{\mathrm{MC}}$		$\bar{N}^{\mathrm{SB}}_{\mathrm{MC}}$	
Phase I									
$0^+_{g.s.} \rightarrow 0^+_1$		0.899	5	8,7,9,8	8.0	7.6	(4.5,10.0)	7.3	(5.9,8.6)
$0^+_{g.s.} \rightarrow 2^+_1$		0.406	3	2,4,0,5	2.75	2.4	(0.6,3.5)	2.3	(1.5,3.0)
$0^+_{g.s.} \rightarrow 2^+_2$	B1	0.591	8	5,6,3,11	6.25	8.3	(5.1,10.8)	8.3	(6.9,9.6)
	B2	0.096	0	0,1,0,1	0.5	0.4	(0,0.9)	0.5	(0.1,0.7)
Phase II									
$0^+_{g.s.} \rightarrow 0^+_1$		2.167	50	48,41,41,35	41.3	47.4	(40.2,53.9)	47.3	(43.8,50.6)
$0^+_{g.s.} \rightarrow 2^+_1$		1.136	17	14,12,3,12 15,11,5,9	10.1	12.5	(8.7,15.7)	12.6	(11.3,13.8)
$0^+_{g.s.} \rightarrow 2^+_2$	B1	1.255	38	45,29,24,40 33,31,23,30	31.9	34.1	(28.0,39.6)	34.6	(32.5,36.6)
	B2	0.288	4	8,2,9,2 4,2,6,2	4.4	3.4	(1.3,4.8)	3.3	(2.6,3.9)

Table 7.6.: The number of counts surviving the optimized signal cuts N^{ROI} and the sideband cuts N^{SB} and their average $\bar{N}^{\mathrm{SB}}$ for the PI and PII data sets. Additionally, given are the expected values for each region obtained from the background model together with the 68% Poisson interval and the signal cut efficiencies ε.

7.6 Count results

In Tab. 7.6 the resulting counts after the signal cut and the sideband cuts are listed for each decay mode for PI and PII. Additionally given are the signal cut efficiencies and the background expectation obtained from the background model.

7.6.1 Sideband counts

A p-value for the observed number of counts in the SBs has been calculated. For this purpose, the MC expectations for each SB given in Section 7.5.5 are approximated by a linear background function in dependency of the energy. This linear background is than scaled to the observed average of all SB counts $\bar{N}^{\mathrm{SB}}$ and used to obtain the expectation value for a Poisson distribution for each SB position. Toy MC experiments are generated given these Poisson distributions and the likelihood is calculated for each one of them. The p-value is obtained by taking the ratio of toy experiments with a likelihood lower than that of the data. This results in a p-value of 0.93, 0.08, 0.26 and 0.21 for the $0^+_{g.s.} \rightarrow 0^+_1$, $0^+_{g.s.} \rightarrow 2^+_1$ and $0^+_{g.s.} \rightarrow 2^+_2$ branch 1 and 2 decay modes, respectively. The lowest p-value was obtained for the $0^+_{g.s.} \rightarrow 2^+_1$ decay mode. The value of 0.08 still signifies an acceptable agreement with the linear model.
The background model describes the observed counts in the SBs in general well enough. $\bar{N}^{\mathrm{SB}}_{\mathrm{MC}}$ and $\bar{N}^{\mathrm{SB}}$ of the first three modes agree within the 95% Poisson interval. $\bar{N}^{\mathrm{SB}}$ for the second branch of $0^+_{g.s.} \rightarrow 2^+_2$ is just outside the 95% interval. The p-values calculated with the unscaled linear background function directly obtained from the $N^{\mathrm{SB}}_{\mathrm{MC}}$ are 0.48, 0.04, 0.19 and 0.04 and thus only slightly worse than the ones obtained with the scaled function. The only exception is the second branch of the $0^+_{g.s.} \rightarrow 2^+_2$ decay mode, where the difference in expected counts between $\bar{N}^{\mathrm{SB}}_{\mathrm{MC}}$ and $\bar{N}^{\mathrm{SB}}$ has a bigger impact due to the small count values. Anyway, $\bar{N}^{\mathrm{SB}}_{\mathrm{MC}}$ will not enter in the process of extracting half-life informations from the observed counts.

7.6.2 Region of interest counts

The number of counts N^{ROI} in the ROI in PII are in most cases (except $0^+_{g.s.} \rightarrow 2^+_2$ B2) above the background expectation from the SBs. It should be noted though, that the N^{ROI} for $0^+_{g.s.} \rightarrow 0^+_1$, $0^+_{g.s.} \rightarrow 2^+_1$ and the first branch of $0^+_{g.s.} \rightarrow 2^+_2$ are correlated, because they use the same ROI with the 559 keV γ-line. Hence all three are affected by an excess of events in this region. The probability to observe a background fluctuation of at least the size as observed assuming the no signal case, while also taking the fluctuations in the SBs into account, is 10%, 3%, 16% and 64%, for the $0^+_{g.s.} \rightarrow 0^+_1$, $0^+_{g.s.} \rightarrow 2^+_1$ and $0^+_{g.s.} \rightarrow 2^+_2$ B1 and B2, respectively.

7.6.3 Detector and time distribution of surviving events

The probability of observing a count in one detector depends on the size of the detector in two ways and on its position in the array. Larger detectors are more likely to absorb a γ-ray. On the other hand, it is less likely that γ-rays from a decay inside the detector can escape it, thus there is a higher probability for a M1 event than in smaller detectors. Fig. 7.10 left shows the total counts surviving the signal cut per detector for the $0^+_{g.s.} \rightarrow 0^+_1$ decay mode. Normalizing to the detector mass, the BEGe detectors register about 5-6 counts/kg. The semi-coaxial detectors only register about half of that, due to the higher self absorption of γ-rays generated inside the detector itself.

The upper detectors of the strings detect a higher number of counts, which is in accordance with the observation of a higher ^{42}K concentration above the array. Otherwise, the number of counts are evenly distributed among a specific type of detectors without any significant outlier.

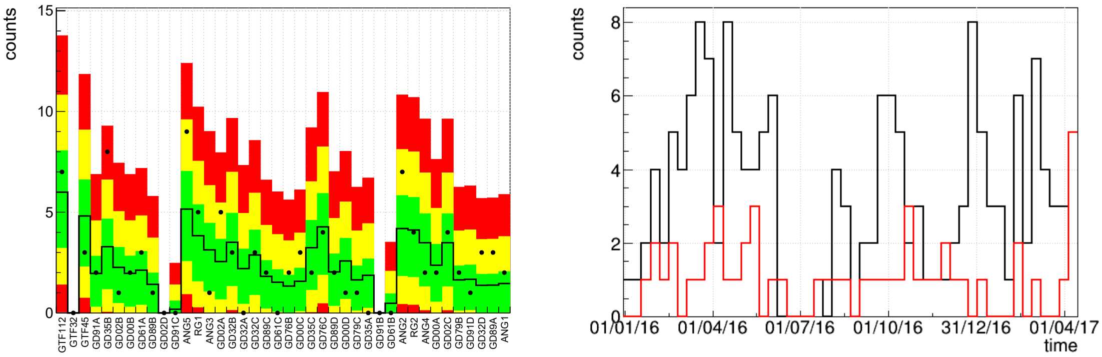

Figure 7.10.: *Left:* The number of counts surviving the signal cut per detector for the $0^+_{g.s.} \rightarrow 0^+_1$ decay mode in PII in comparison to the expectation from the background model. *Right:* The timestamp distribution of the events surviving the signal cut (red) and the sideband cuts (black) for the $0^+_{g.s.} \rightarrow 0^+_1$ decay mode.

Fig. 7.10 right shows the distribution of timestamps of the surviving events.

The corresponding plots for the other decay modes as well as a list of all the events surviving the signal cut (ROI) with their timestamp, energies and LAr veto can be found in the Appendices F.4, F.5 and F.6.

Only one data point has been observed outside of the 99.7% interval, which is the counts in ANG2 for the ROI of the second branch of the $0^+_{g.s.} \rightarrow 2^+_2$ decay mode. This is within the expectation from statistical fluctuations.

7.6.4 LAr veto

In the search for the $0\nu\beta\beta$-decay to the ground state the LAr veto is a powerful tool to reduce the background, because the signal process is expected to store all of the released energy in only one detector in most cases. For the search for decays to excited states, the LAr veto can not be applied as simply, because even the signal process can deposit energy in the LAr via the de-excitation γ-rays.

As of the time of this work, the MC simulations of GERDA are not able to sufficiently reproduce the LAr veto efficiency, due to parameters like the light yield or the attenuation length of the light in LAr that are not known very well, although attempts are taken to measure them [178]. Thus, the probability that a signal decay triggers the LAr veto can not be determined precisely.

As a rough estimate, MC simulations can be used to determine how many of the signal decays deposit energy in the LAr, neglecting the light propagation process. In the case of the $0^+_{g.s.} \rightarrow 0^+_1$ mode, about 63% of decays that survive the signal cut deposit any energy in the LAr, while 48% of them deposit an energy larger than 200 keV. For the $0^+_{g.s.} \rightarrow 2^+_2$ B1 mode, about 67% deposit any energy and 55% deposit an energy larger than 200 keV. Taking the light propagation into account will obviously reduce those numbers.

The signal cuts for the $0^+_{g.s.} \rightarrow 2^+_2$ B2 and $0^+_{g.s.} \rightarrow 2^+_1$ modes ask for an energy deposit in one detector equivalent to the energy of the only γ-ray emitted in the decay mode. Though, this energy can be mimicked by the electrons which would leave the γ-ray free to deposit some energy in the LAr, such events will not contribute to the peak structure and instead contribute to the continuous background. Therefore, the $0^+_{g.s.} \rightarrow 2^+_2$ B2 and $0^+_{g.s.} \rightarrow 2^+_1$ decay mode are the exception, for which the LAr veto can be applied with only an insignificant loss in the signal cut efficiency due to bremsstrahlung emitted by the electrons.

The LAr veto can still be applied to all decay modes in order to study the background in the SBs and ROI. Tab. 7.7 shows the number of counts that are vetoed and not vetoed for the optimized cuts. The sum of vetoed and not vetoed counts is identical to the counts given in Tab. 7.6. About 80-90% of the events are vetoed by the LAr veto which is expected given the dominant background components are isotopes that emit multiple γ-rays like ^{214}Bi and γ-rays from ^{42}K and ^{40}K that only deposit a part of their energy in the two detectors, considering their full energy peak is cut from the signal region.

In the ROI of the $0^+_{g.s.} \rightarrow 0^+_1$, 8.7 counts above the SB background estimation of 41.3 counts have been observed. Applying the LAr veto, 3.7 counts are observed above the background estimation for the vetoed events, and 5.0 are observed above the background estimation for the non vetoed events.

7.6.5 ^{228}Ac γ-line

^{228}Ac produces a γ-line at 562.5 keV and hence coincides with the 563.2 keV signal line of the $0^+_{g.s.} \rightarrow 0^+_1$ decay mode. This line is in fact contained to 100% within the ROI. The other decay modes are barely affected. Only less than 10% of the ^{228}Ac are contained in the 559.1 keV ROI of the $0^+_{g.s.} \rightarrow 2^+_1$ and $0^+_{g.s.} \rightarrow 2^+_2$ B1 decay mode.

The strength b_{Ac} of that line can be estimated using the background model. Using the same ROI and SBs to subtract the flat background as for the analysis of the $0^+_{g.s.} \rightarrow 0^+_1$ decay mode, this results in 0.74 counts for $b^{\mathrm{MC}}_{\mathrm{Ac}}$ for the global mode and the smallest 68% credibility interval of [0.40,1.15] counts.

decay mode		N^{ROI}	N^{SB}	$\bar{N}^{\mathrm{SB}}$
vetoed				
$0^+_{g.s.} \to 0^+_1$		40	42,34,39,30	36.3
$0^+_{g.s.} \to 2^+_1$		13	12,10,3,9,14,11,5,6	8.8
$0^+_{g.s.} \to 2^+_2$	B1	30	38,26,19,33,30,29,20,26	27.6
	B2	3	4,1,9,1,2,1,4,2	3.0
not vetoed				
$0^+_{g.s.} \to 0^+_1$		10	6,7,2,5	5.0
$0^+_{g.s.} \to 2^+_1$		4	2,2,0,3,1,0,0,3	1.4
$0^+_{g.s.} \to 2^+_2$	B1	8	7,3,5,7,3,2,3,4	4.3
	B2	1	4,1,0,1,2,1,2,0	1.4

Table 7.7.: Number of counts surviving the ROI and SB cuts separated by their LAr veto flag.

Additionally, b_{Ac} can be deduced from the strength $b^{\mathrm{obs}}_{\mathrm{Ac}}$ of the other γ-lines in the physics data. For this purpose , the ratios between the line strengths need to be determined with MC data which is dependent on the location of the contamination. The lines close in energy to the 562.5 keV line behave similar with changing distance between the source and array. ^{228}Ac is included on the cables in the background model. In Tab. 7.8 the peak integrals, ratios and observed ($b^{\mathrm{obs}}_{\mathrm{Ac}}$) and deduced ($b^{\mathrm{R}}_{\mathrm{Ac}}$) expectation for the 562.5 keV line are given. $b^{\mathrm{obs}}_{\mathrm{Ac}}$ has been determined by defining a ROI and SBs around the line energy. The cut regions feature the same low and high energy end as for the $0^+_{g.s.} \to 0^+_1$ decay mode. Lines with too many other lines in close vicinity are excluded. The results of all the lines agree very well with each other and also with the peak integrals from the background model. From the lower energetic lines, only an upper limit could be extracted due to the higher background.

Both methods are not independent of each other, because the background model is constructed using the physics data. While the background model combines the information of the full spectrum, the results for $b^{\mathrm{R}}_{\mathrm{Ac}}$ obtained from each separate line can be utilized to cross-check if the assumption of the location of the contamination holds. As no discrepancies have been found for the results from the different lines, this assumption seems to hold within the uncertainties.

Combining all $b^{\mathrm{R}}_{\mathrm{Ac}}$ an upper limit of $b_{\mathrm{Ac}} < 1.55$ is obtained. By only combining the two lines closest to the 562.5 keV line, results in a marginalized mode of 1.28 [0.20,2.33]. The latter is used as prior information in the statistical analysis of the $0^+_{g.s.} \to 0^+_1$ decay mode to estimate the impact of this line on the extracted half-life.

7.7 Statistical analysis

The analysis uses a Bayesian approach to extract information about the decay half-life. A likelihood function is constructed taking into account the number of observed counts in the ROI and SBs, as well as the systematical uncertainties on the efficiency and exposure. Using Bayes theorem, the likelihood density is converted to a posterior probability density using prior information for each of the free parameters. The inverse half-life $T^{-1}_{1/2}$ of the decay mode is the free parameter that connects the data sets and decay branches.

BAT is used to sample the multi-dimensional posterior probability density distribution (in

E_{line} [keV]	I_{peak}	R	$b_{\text{Ac}}^{\text{obs}}$	b_{Ac}^{R}
321	1.37	1.85	<12	<6.49
328	4.00	5.51	<15	<2.72
338	3.95	5.36	<12	<2.34
409	1.91	2.59	<13	<5.02
463	4.20	5.70	<18	<3.09
795	2.06	2.79	7.3 [2.0,12.8]	2.61 [0.72,4.59]
911	2.49	3.38	9.5 [3.8,15.5]	2.81 [1.12,4.59]

Table 7.8.: The peak integral I_{peak} from the MC data and expected counts $b_{\text{Ac}}^{\text{obs}}$ as obtained from the physics data, determined for several of the peaks of ^{228}Ac. Also given is the ratio R between the peak integrals and the peak integral of the 562.5 keV peak and the expected counts b_{Ac}^{R} estimated for this peak given R and I_{peak} of the other peaks. Upper limits are given with 90% and two sided intervals are given with 68% credibility.

the following only called posterior), which is marginalized in regard of the inverse half-life to obtain an interval with 90% credibility.

7.7.1 Likelihood function

The likelihood function consists of two terms. The first term accounts for the ROI, which includes contributions by the signal and background. The second term accounts for the corresponding SBs, including only background and no signal contribution. The likelihood function combining multiple data sets and decay branches can then be written as:

$$\mathcal{L}\left(\mathbf{n},\mathbf{m}|\mathbf{s},\mathbf{b}\right)=\prod_{d,r}\left[\tfrac{(s_{d,r}+b_{d,r}/\tau)^{n_{d,r}}}{n_{d,r}!}\cdot e^{-(s_{d,r}+b_{d,r}/\tau_{d,r})}\right]\cdot\left[\frac{b_{d,r}^{m_{d,r}}}{m_{d,r}!}\cdot e^{-b_{d,r}}\right], \tag{7.4}$$

with $n=N^{\text{ROI}}$ and $m=\sum\limits_{i}N_i^{\text{SB}}$, $s_{d,r}$ the expected signal counts in data set d and decay branch r, $b_{d,r}$ the expected background counts in the combined SBs of data set d and branch r and $\tau_{d,r}$ the ratio between the $b_{d,r}$ and the expected background counts in the ROI, i.e. the number of SBs provided the background is flat and each SB has the same size as the ROI.

The signal count expectation s is connected to the half-life of the decay as follows:

$$\begin{aligned} s_{d,r} &= T_{1/2}^{-1}\cdot\varepsilon_{d,r}\cdot\frac{\ln 2\cdot N_A\cdot m_{\text{enr},d}\cdot f_{76,d}\cdot t_d}{M_{\text{enr}}} && (7.5)\\ &= T_{1/2}^{-1}\cdot\varepsilon_{d,r}\cdot\ln 2\cdot N_A\cdot\mathcal{E}_{76,d}, && (7.6)\end{aligned}$$

where $T_{1/2}$ is the half-life of the signal decay, N_A Avogadro's constant, m_{enr_d} the total mass of enriched germanium, M_{enr_d} the molar mass of enriched germanium, f_{76_d} the isotopic fraction of ^{76}Ge in the enriched germanium and $\mathcal{E}_{76,d}$ the ^{76}Ge exposure of data set d.

Additionally, an alternative likelihood function is constructed for the PII data set in the case of the $0^+_{g.s.}\rightarrow 0^+_1$ decay mode, adding the contribution of the ^{228}Ac γ-line to the signal region. The expected counts from this line are denoted with b_{Ac} and are added to all occurrences of s in Eq 7.4.

7.7.2 Prior probability density distribution

The prior probability density distribution (in the following only called prior) for the inverse half-life $T_{1/2}^{-1}$ is defined as a flat distribution in the range of $[0,2]\cdot 10^{-23}\,\mathrm{yr}^{-1}$.
The prior for $b_{d,r}$ is also defined as a flat distribution. The range is defined between -5$\sqrt{m_{d,r}}$ (but minimum 0) and +5$\sqrt{m_{d,r}}$ (but minimum 10).
The prior of b_{Ac} is defined as a Gaussian distribution with mean 1.28 and standard deviation 1.05 (compare Section 7.6.5) in the range [0,10].

7.7.3 Systematical uncertainties

Section 7.5.3 describes how the uncertainties on the efficiency are obtained. To include the uncertainties of the efficiency in the fit, it is written as follows:

$$\begin{aligned}\varepsilon_{d,r} = \tilde{\varepsilon} \; &+ \; \sigma_{d,r}^{\mathrm{MC}} + \sigma_{d,r}^{\mathrm{FWHM,BEGe}} + \sigma_{d,r}^{\mathrm{FWHM,Coax}} + \sigma_{d,r}^{\mathrm{Shift}} \\ &+ \; \sigma_{d,r}^{\mathrm{corr,BEGe}} + \sigma_{d,r}^{\mathrm{uncorr,BEGe}} + \sigma_{d,r}^{\mathrm{corr,Coax}}, \end{aligned} \tag{7.7}$$

with the σ as the uncertainties coming from the MC processes, the FWHM, the energy scale shift and correlated and uncorrelated active volume values. Each σ is hereby a product of the one standard deviation uncertainty $\tilde{\sigma}$ and a free parameter a, which is defined in a range from -5 to 5. The prior for a is a Gaussian distribution with mean 0 and standard deviation 1. The correlation of the dead layer uncertainties between data sets (PI and PII and different de-excitation branches) is taken into account by using a shared a parameter for these data sets. For simplification, uncertainty contribution without correlation between data sets are combined into one. Furthermore, the uncertainty of the BEGe dead layer in PI is neglected, because they only contribute a small fraction to the global efficiency.
The uncertainty on the exposure was calculated in Ch. 5.2.1. The exposure is written as

$$\mathcal{E}_d = \left(\tilde{\mathcal{E}}_d^{\mathrm{Coax}} + \sigma_d^{\mathcal{E},\mathrm{Coax}}\right) + \left(\tilde{\mathcal{E}}_d^{\mathrm{BEGe}} + \sigma_d^{\mathcal{E},\mathrm{BEGe}}\right), \tag{7.8}$$

where the uncertainties σ are again expressed with a floating parameter a. The correlation between PI and PII data sets is taken into account for the semi-coaxial detectors via the a parameter. Due to the low contribution of the BEGe detectors in PI, their uncertainty to the exposure is neglected.
Table 7.9 lists the different uncertainties and their relative values. The biggest contribution comes from the dead layer uncertainties. Especially in PI, they result in efficiency uncertainties of about 10%.

7.7.4 Sensitivity

The final sensitivity of the experiment to set a 90% credibility limit on the half-life has been calculated with a toy MC approach. The toy experiments are generated assuming no signal and only background. For each toy experiment, the number of counts in the ROI are sampled from a Poisson distribution with an expectation value of $N_{\mathrm{MC}}^{\mathrm{ROI}}$.The number of counts in the combined SBs are sampled as well from a Poisson distribution, with an expectation value of $\tau \cdot N_{\mathrm{MC}}^{\mathrm{ROI}}$.The calculations for the LAr veto mode use $\bar{N}^{\mathrm{SB}}$ instead, because no MC estimation is available. The efficiency is sampled according to all of its uncertainties.

Uncertainty [%]	$0^+_{g.s.} \rightarrow 0^+_1$	$0^+_{g.s.} \rightarrow 2^+_1$	$0^+_{g.s.} \rightarrow 2^+_2$ B1	$0^+_{g.s.} \rightarrow 2^+_2$ B2
		Phase I		
FWHM	2.3	4.4	4.1	4.3
Shift	0.5	0.7	0.5	0.6
Combined Energy	2.4	4.4	4.2	4.3
DLCoax	9.8	14.7	11.7	14.0
DLBEGe	-	-	-	-
MC processes	4	4	4	4
Exposure	1.4	1.4	1.4	1.4
		Phase II		
FWHM	1.0	2.9	3.5	2.6
Shift	0.6	1.3	1.2	0.8
Combined Energy	1.2	3.2	3.7	2.7
DLCoax	2.8	4.4	2.5	4.5
DLBEGe	1.2	3.6	1.1	4.7
MC processes	4	4	4	4
Exposure	1.1	1.1	1.1	1.1

Table 7.9.: Summary of the systematical uncertainties of the expected signal counts derived from the energy resolution (FWHM), the energy scale shift (Shift), the dead layer/active volume uncertainties (DLCoax, DLBEGe), the MC physics processes and the Exposure for each data set and decay mode.

decay mode			S_{PI} $[10^{23}\,\mathrm{yr}]$	S_{PII} $[10^{23}\,\mathrm{yr}]$	$S_{\mathrm{PI+PII}}$ $[10^{23}\,\mathrm{yr}]$
$0^+_{g.s.} \rightarrow 0^+_1$			1.65	3.07	3.62
$0^+_{g.s.} \rightarrow 2^+_1$			1.09	2.97	3.38
	(+LAr)		-	-	6.65
$0^+_{g.s.} \rightarrow 2^+_2$		B1	1.14	2.15	2.51
		B2	0.38	1.24	1.46
		B1+B2	1.32	2.61	3.06
	(+LAr)	B1+B2	-	-	3.46

Table 7.10.: The sensitivities to set a 90% credibility half-life limit of the PI, PII and combined data of Gerda, determined with a toy MC approach as explained in the text.

10^4 toy experiments are generated for each decay mode and the marginalized one-dimensional posterior of $T^{-1}_{1/2}$ as well as an upper 90% credibility limit $T^{-1}_{1/2,\mathrm{upper}}$ is extracted for each experiment. The sensitivity is then defined as the median of the $T^{-1}_{1/2,\mathrm{upper}}$ distribution. This results in $3.62 \cdot 10^{23}$ yr, $3.38 \cdot 10^{23}$ yr and $3.06 \cdot 10^{23}$ yr for the $0^+_{g.s.} \rightarrow 0^+_1$, $0^+_{g.s.} \rightarrow 2^+_1$ and $0^+_{g.s.} \rightarrow 2^+_2$ decay modes for the combined PI and PII of Gerda. The application of the LAr significantly improves the sensitivity for the $0^+_{g.s.} \rightarrow 2^+_1$ decay mode to $6.65 \cdot 10^{23}$ yr. The sensitivity for the $0^+_{g.s.} \rightarrow 2^+_2$ decay mode only slightly improves to $3.46 \cdot 10^{23}$ yr, because the LAr veto is only applied for the second branch. The sensitivities of the combined data sets as well as the PI and PII sets separately are given in Tab. 7.10. The sensitivities of PI are identical to the ones given in [127].

Without the systematical uncertainties the sensitivities improve by 1-2%, which was evaluated by repeating this procedure while fixing the efficiency and exposure.

7.7.5 Limit extraction

The best fit value is defined as the value at which the maximum of this distribution is located. A non-zero best fit value was obtained for the inverse half-life $T^{-1}_{1/2}$ for all decay modes. After marginalization, the one-dimensional posterior $p(T^{-1}_{1/2}|\mathbf{n},\mathbf{m})$ for $T^{-1}_{1/2}$ is obtained, which is shown in Fig. 7.11. In all cases, 0 is within or just outside the smallest 68% interval. Hence, no signal has been observed. As a result, the 90% upper credibility limit is obtained from $p(T^{-1}_{1/2}|\mathbf{n},\mathbf{m})$. The best fit value and 90% credibility limit for $T_{1/2}$, the equivalent in the signal count expectation $s_{d,r}$ and the $b_{d,r}$ are given in Tab. 7.11.

Just like the sensitivities, the limits improve by 1-2% when the systematic uncertainties are neglected.

The Bayes factor between several of the theoretical predicted half-lives (given in Tab. 7.1) and the null hypothesis was calculated using BAT. For the models in [167, 168, 169, 170] the Bayes factor is below 10^{-5} and thus they are excluded by the combined data set of Gerda PI and PII. For the model of [171] a range of Bayes factors was obtained, ranging from $3 \cdot 10^{-5}$ to 0.64. The model of [164] yields a range from $7 \cdot 10^{-4}$ to 1.3. Model [165] and [166] result in a Bayes factor slightly above 1, which signifies a light preference over the null hypothesis.

decay mode		ε [%]	$s_{d,r}^{\text{best}}$	$s_{d,r}^{\text{marg}}$ (68%)	$s_{d,r}^{\text{limit}}$	$\frac{b_{d,r}^{\text{marg}}}{\tau}$ (68%)	$T_{1/2}^{\text{limit}}$
Phase I							
$0^+_{g.s.} \to 0^+_1$		0.899	0.8	1.0 (0.0,2.3)	3.6	7.1 (6.0,8.5)	
$0^+_{g.s.} \to 2^+_1$		0.406	1.3	1.3 (0.5,2.2)	2.7	2.7 (1.9,3.4)	
$0^+_{g.s.} \to 2^+_2$	B1	0.591	1.0	1.0 (0.0,2.1)	3.2	6.2 (5.2,7.5)	
	B2	0.096	0.2	0.2 (0.0,0.3)	0.5	0.4 (0.2,0.8)	
Phase II							
$0^+_{g.s.} \to 0^+_1$		2.167	3.1	3.8 (0.0,8.8)	13.7	41.4 (38.7,44.8)	3.05
$0^+_{g.s.} \to 0^+_1$	$(+b_{\text{Ac}})$	2.167	1.8	1.5 (0.0,7.9)	12.7	41.6 (38.5,44.6)	3.29
$0^+_{g.s.} \to 2^+_1$		1.136	5.9	5.8 (2.4,9.8)	12.0	10.2 (9.1,11.3)	1.82
$0^+_{g.s.} \to 2^+_2$	B1	1.255	3.3	3.5 (0.0,7.1)	10.8	32.1 (30.1,34.0)	2.23
	B2	0.288	0.8	0.8 (0.0,1.6)	2.5	4.2 (3.6,5.0)	
Phase II + LAr							
$0^+_{g.s.} \to 2^+_1$		1.136	2.7	2.5 (0.9,5.0)	6.5	1.6 (1.2,2.1)	3.37
$0^+_{g.s.} \to 2^+_2$	B1	1.255	2.1	1.9 (0.0,6.0)	9.5	32.3 (30.4,34.4)	2.54
	B2	0.288	0.5	0.4 (0.0,1.4)	2.2	1.2 (0.9,1.7)	

Table 7.11.: Given are the best fit values and 90% credibility limits for the half-life $T_{1/2}$ for the combined fit of PI and PII data. Also given are the global and marginalized mode of the signal count expectation $s_{d,r}$, as well as the marginalized mode for the background expectation in the combined SBs $b_{d,r}$. The indices d and r denote the data set and decay branch, respectively. Half-life values are given in units of 10^{23} yr.

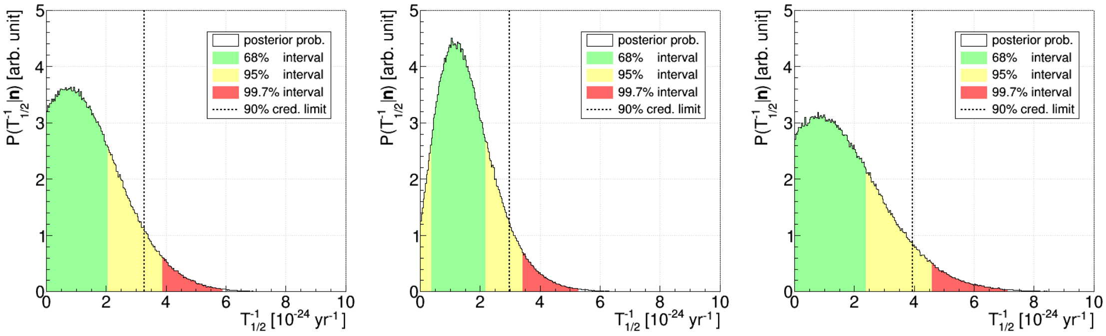

Figure 7.11.: Shown is the marginalized posterior probability density distribution for $T_{1/2}^{-1}$ obtained for the $0^+_{g.s.} \rightarrow 0^+_1$ (left), $0^+_{g.s.} \rightarrow 2^+_1$ (middle) and $0^+_{g.s.} \rightarrow 2^+_2$ (right) decay modes. The smallest 68%, 95% and 99% intervals are filled in color. Additionally, the 90% credibility upper limit is shown as dashed line.

7.7.6 Discussion

The combination of the PI data with the first 35 kg·yr of PII data boosts the sensitivity by a factor 1.5 to 2, depending on the decay mode. The inclusion of the LAr veto increases the sensitivity of the $0^+_{g.s.} \rightarrow 2^+_1$ mode by another factor of 2. Only one of the branches of the $0^+_{g.s.} \rightarrow 2^+_2$ mode profits from the LAr veto. Thus the sensitivity is increased only by about 13%.

Due to an excess of events in the region around the expected 559.1 keV signal line, a non-zero best fit value was obtained for the signal strength and hence the experimental limits are below the sensitivity for all modes. Despite that, the limits improve upon the previous results, even without utilization of the LAr veto. The new limit for the $0^+_{g.s.} \rightarrow 0^+_1$ mode of $T_{1/2}>3.1 \cdot 10^{23}$ yr corresponds to a 14% improvement on the PI limit of $T_{1/2}>2.7 \cdot 10^{23}$ yr. Taking into account the ^{228}Ac line, the limit increases by 7%. In light of the observed excess of events, not taking into account this background line thus leads to a more conservative limit. In case of an observation, its constribution needs to be thoroughly studied, because it directly affects the measurement of the $0^+_{g.s.} \rightarrow 0^+_1$ half-life.

The new limit for the $0^+_{g.s.} \rightarrow 2^+_1$ mode with LAr veto of $T_{1/2}>3.4 \cdot 10^{23}$ yr increases the PI limit of $T_{1/2}>1.7 \cdot 10^{23}$ yr by a factor of 2. The new limit for the $0^+_{g.s.} \rightarrow 2^+_2$ mode with LAr veto of $T_{1/2}>2.5 \cdot 10^{23}$ yr is an increase of 39% compared to the PI limit of $T_{1/2}>1.8 \cdot 10^{23}$ yr. No additional predictions can be ruled out by the new results in favor of the no signal case. In general, the Bayes factors are higher than the values obtained in PI, due to the non-zero best fit value for the signal count expectation with the combined PI and PII data set.

7.8 Summary and outlook

New 90% credibility limits have been obtained for the $2\nu\beta\beta$-decay of ^{76}Ge to the first three excited states of ^{76}Se combining 22 kg·yr of Phase I data and the first 35 kg·yr of Phase II data of the GERDA experiment. The analysis is based on the data with a germanium detector multiplicity of 2 and employs a cut and count procedure, searching for the coincidence of the signal of the two electrons in one detector and the signal of one of the de-excitation γ-rays in another detector. The limits are set to:

- $0^+_{g.s.} \rightarrow 0^+_1$: $T^{2\nu}_{1/2} > 3.1 \cdot 10^{23}$ yr with a sensitivity of $S^{2\nu} = 3.6 \cdot 10^{23}$ yr
- $0^+_{g.s.} \rightarrow 2^+_1$: $T^{2\nu}_{1/2} > 3.4 \cdot 10^{23}$ yr with a sensitivity of $S^{2\nu} = 6.7 \cdot 10^{23}$ yr
- $0^+_{g.s.} \rightarrow 2^+_2$: $T^{2\nu}_{1/2} > 2.5 \cdot 10^{23}$ yr with a sensitivity of $S^{2\nu} = 3.5 \cdot 10^{23}$ yr

A non-significant excess of events is found for all three decay modes, hence the limits are below the sensitivity. As only a subset of the final Phase II data is used, these results are preliminary and will be updated with the final data set, once it is available (see the disclaimer in Appendix I).

Reaching the design goal exposure of GERDA of 100 kg·yr, the sensitivities will be expected to increase by about 50%, reaching $5.1 \cdot 10^{23}$ yr, $1.1 \cdot 10^{24}$ yr and $5.0 \cdot 10^{23}$ yr for the three decay modes.

The improvement in sensitivity compared to Phase I is hampered due to a significant increase of the ^{42}K and ^{40}K background in Phase II, which are the dominant backgrounds for this analysis. The LAr veto can help to reduce this background. The $0^+_{g.s.} \rightarrow 2^+_1$ mode employs the LAr veto fully, while the $0^+_{g.s.} \rightarrow 2^+_2$ mode employs it for one of its two de-excitation branches. With a better understanding of the light propagation processes in the LAr and improved simulations, the background for the $0^+_{g.s.} \rightarrow 0^+_1$ mode could be cut immensely by up to 90%. However, this requires to sacrifice 50% of the signal efficiency. A sensitivity of $6.5 \cdot 10^{23}$ yr can be expected, still short of the envisioned sensitivity of $1{\cdot}10^{24}$ yr.

Additionally, the LAr veto can be used to distinguish between the $0^+_{g.s.} \rightarrow 0^+_1$ and $0^+_{g.s.} \rightarrow 2^+_1$ modes, which is otherwise not possible, due to the same energy γ-rays.

Furthermore, it is planned to replace the natural detectors in the middle of the detector array by new enriched inverted coaxial detectors after 100 kg·yr have been reached. Because the middle position in the detector array offers the highest potential for the emitted γ-rays to be absorbed by the surrounding detector, the signal detection efficiency is expected to be significantly increased.

Chapter 8

$0\nu\beta\beta$-decay to excited states

8.1 Introduction

Following the search for the $2\nu\beta\beta$-decay of ^{76}Ge to excited states of ^{76}Se presented in the previous chapter, this chapter discusses the corresponding search for the $0\nu\beta\beta$-decay modes.

The basics of the decay schematics of the $0\nu\beta\beta$-decay modes into excited states are the same like in the case of the $2\nu\beta\beta$-decay modes, as already discussed in Ch. 7.2. The important difference is, that without the emission of neutrinos, the full decay energy will be shared solely among the two electrons. Therefore, the energy deposited in the detector by the electrons is usually discrete, unless the decay happens inside or close to the dead layer.

The analysis of the $0\nu\beta\beta$-decay modes to the excited states employs again the M2 data sets as discussed extensively in Ch. 5 and summarized in Ch. 7.4. Additionally, the discrete two-electron energy in the $0\nu\beta\beta$-decay modes and hence the discrete line signature of the signal (see Sec. 8.3.3) makes it viable to consider the M1 data set, as well.

For this reason, this analysis is divided into two parts. First, Sec. 8.3 will present the analysis of the M1 data set, followed by the M2 data set in Sec. 8.4. Finally, the results of both parts are combined and discussed in Sec. 8.5.

8.2 Motivation

Matrix elements for the $0^+_{g.s.} \rightarrow 2^+_1$ decay mode of ^{76}Ge have been investigated in [41, 179]. By considering the recoil corrections of the nuclear currents, it has been found that this decay mode has the same relative sensitivity to $\langle m_{\beta\beta} \rangle$ and $\langle \eta \rangle$ than the $0^+_{\mathrm{g.s.}} \rightarrow 0^+_{\mathrm{g.s.}}$ mode, but is more sensitive to $\langle \lambda \rangle$. Half-lives are expected about three orders of magnitude above the $0^+_{\mathrm{g.s.}} \rightarrow 0^+_{\mathrm{g.s.}}$ mode, which is due to the lower phase space and the higher partial waves that are required for the emitted electrons. A lower limit of $T_{1/2}(0^+_{\mathrm{g.s.}} \rightarrow 2^+_1) > 8.2 \cdot 10^{23}$ yr (90% C.L.) by the HdM experiment is given in [180].

The $0^+_{g.s.} \rightarrow 0^+_1$ decay mode is investigated in [181], which is preferred due to the $s_{1/2}$ wave of the electrons. The phase space factor is one order of magnitude lower than for ground state decays. A half-life larger by a factor of about 50-100 compared to the ground state transition is predicted for the light Majorana neutrino exchange ($\mathcal{O}(10^{28})$ for $\langle m_{\beta\beta} \rangle = 0.1$ keV) and a factor of about 50-1000 for right-handed current mechanisms.

A signal discovery of excited states decay modes for the $0\nu\beta\beta$-decay is therefore not expected, because the predicted half-lives exceed the current sensitivity of Gerda by several orders of magnitude. Only limits will be set, which before Gerda only exist for the $0^+_{g.s.} \rightarrow 2^+_1$ mode, as mentioned above.

Additionally, this chapter provides a blueprint of an analysis to search for those decay modes, which can be applied to future experiments like LEGEND, in which the sensitivity for the $0^+_{\mathrm{g.s.}} \rightarrow 0^+_{\mathrm{g.s.}}$ mode is planned to approach the order of 10^{28} yr [68].

It is still an open question if experiments can have a comparable sensitivity to the lepton number violating parameters of different $0\nu\beta\beta$-decay mechanism by investigating excited state transitions like when investigating ground state transition [181].

8.3 M1 data analysis

The goal of this section is to perform spectral fits of the data in multiple regions, where peaks are expected from the signal decay. For this purpose, the separate data sets first needs to be discussed (see Sec. 8.3.1). Second, the regions of interest (ROI) need to be determined with the help of MC simulations of the signal process and the expected background. The shape of the background in these ROI will also largely define the fit functions. Additionally, the signal MC data is utilized to determine the signal efficiencies for each ROI. This process is presented in Sec. 8.3.3 and Sec. 8.3.4. In Sec. 8.3.5 onwards, the technicalities of the fit procedure, the fit results and the determination of sensitivities are presented.

8.3.1 Data selection/Data sets

Quality cuts, muon veto and LAr veto are enforced as discussed in the previous Ch. 7.5.2. Additionally, the anti-coincidence cut is applied for this part of the analysis, which removes about 3% of the events above 500 keV in PI and about 9% in PII.

The M1 data is separated into BEGe data ($^{\mathrm{enr}}$BEGe) and data from the enriched semi-coaxial detectors ($^{\mathrm{enr}}$Coax). Both detector types differ significantly in energy resolution as well as in their background structures, due to the different size, dead layer thickness and detector assembly. The data of the natural semi-coaxial detectors ($^{\mathrm{nat}}$Coax) is not utilized due to the low isotopic fraction of ^{76}Ge.

This results in 4 data sets: PI-$^{\mathrm{enr}}$Coax, PI-$^{\mathrm{enr}}$BEGe, PII-$^{\mathrm{enr}}$Coax and PII-$^{\mathrm{enr}}$BEGe. The PI data corresponds to an exposure of 22.1 kg·yr with a live-time of 459.7 d, while the PII data sums up to an exposure of 35.1 kg·yr with a live-time of 405.1 d. The exposure is calculated taking the total mass of ^{76}Ge during the specific phase into account.

Note, that in the case of the PII-$^{\mathrm{enr}}$Coax data set, the region around 2039.1 keV is only unblinded up to June 2016 as of the writing of this work. Hence, the analysis of this region uses the PIIa-$^{\mathrm{enr}}$Coax data set, with an exposure of 11.3 kg·yr and a live-time of 131.1 d.

The energy spectrum up to 3 MeV is shown in Fig. 8.1 for the four data sets. Below 570 keV the spectra are dominated by the beta spectrum of ^{39}Ar. Above 570 keV and up to 2 MeV the majority of events can be attributed to the $2\nu\beta\beta$-decay of ^{76}Ge with γ-lines on top. The two most intense γ-lines by ^{40}K and ^{42}K are clearly visible. Above 2 MeV, the spectrum consists of entries caused by high energy γ-rays and degraded alphas on the p^{+} surface of the detectors.

8.3.2 Energy resolution

The energy reconstruction for all the M1 data is done with the ZAC (Zero Area Cusp) shaping filter. It has been determined in [126] for the PI data, based on the weekly calibration data. This process was explained and repeated in Ch. 5.6 for the M2 data. Due to the higher statistics in the M1 data, energy resolution values were obtained for each detector. Those values are then weighted and averaged to one single value for the corresponding data set.

The energy resolution curves for the PII data are presented in [132]. A correction term of (0.50±0.07) keV and (0.01±0.06) keV is added to the values of the PII-$^{\mathrm{enr}}$Coax and PII-$^{\mathrm{enr}}$BEGe data, respectively, due to a discrepancy between the energy resolution obtained from the calibrations and the one obtained from the ^{42}K peak at 1525 keV in the physics data. In PI, the correction term is already included in the detector specific energy resolutions for detector ANG2 and GD32D.

The analysis of M1 data is based on spectral fits of small energy regions in which signal peaks are expected. Thus the energy resolution is required only at the position of each of

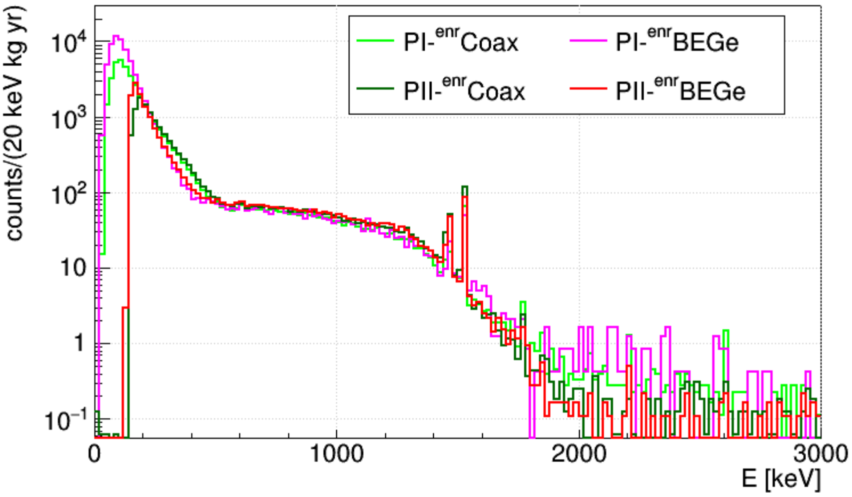

Figure 8.1.: The experimental spectra for the ^{enr}Coax and ^{enr}BEGe data sets of PI and PII in the energy range up to 3 MeV.

Energy	^{enr}Coax		^{enr}BEGe	
[keV]	PI	PII	PI	PII
823	3.82±0.05	3.35±0.07	2.17±0.10	2.38±0.06
917	3.86±0.05	3.40±0.07	2.22±0.10	2.43±0.06
1382	4.03±0.05	3.62±0.07	2.44±0.10	2.65±0.06
1480	4.07±0.05	3.67±0.07	2.48±0.10	2.70±0.06
2039	4.26±0.06	3.91±0.07	2.72±0.10	2.93±0.06

Table 8.1.: The energy resolution (given as FWHM in keV) in the four anti-coincidence (M1) data sets of PI and PII at several energies of interest for the $0\nu\beta\beta$ decay to excited states analysis.

the expected peaks.

The weighting of the separate detectors is done using the global signal efficiency, which also takes into account the exposure of each detector. Due to the multi-detector event signature, the classification of an event as M1 or M2 event is influenced by the surrounding detectors and thus simply weighting each detector with its exposure would result in a small, though negligible error ($< \mathcal{O}(0.01)$). The signal detection efficiency of each detector is calculated in Sec. 8.3.4. Tab. 8.1 lists the FWHM at the energies of interest.

The statistical uncertainties of the energy resolution come from the peak fits of the calibration data, which are propagated through the averaging process. In case of detectors/data sets that require the correction term, the uncertainty is a combination of the propagated uncertainty from calibrations and the peak fit uncertainty from the physics data. The statistics in the physics data is much lower compared to the calibration, hence the latter uncertainty contribution is dominating, which is obvious for the PII values.

The uncertainty on the energy scale and peak positions is estimated with 0.2 keV by evaluating the shift of the ^{208}Tl line positions in the calibrations data with respect to their literature values [126].

8.3.3 Signal decay signature

For each decay mode, each detector in the array and each array configuration (PIa/PIc, PII), 10^6 decays have been simulated. Decay0 [155] was used to generate the initial momentum of the decay particles. The simulated energy spectra can be seen in Fig. 8.2. The energy resolution of the detectors is assumed to be perfect in those spectra, i.e. the raw simulation spectra have not been smeared with the experimental energy resolution of the detectors.

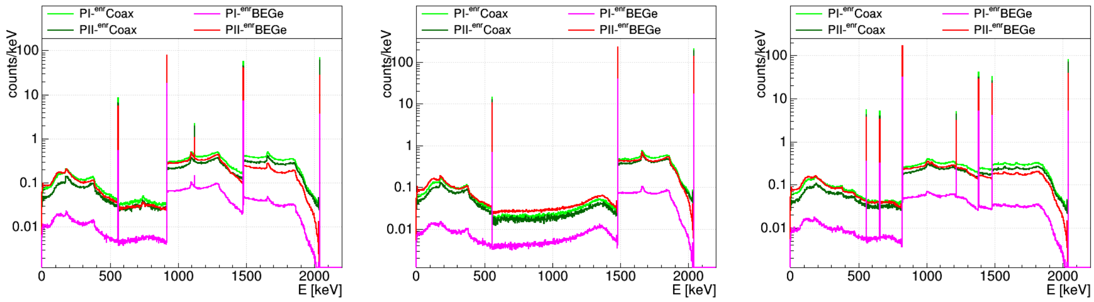

Figure 8.2.: The simulated expected M1 signal spectrum of the $0^+_{g.s.} \rightarrow 0^+_1$ (left), $0^+_{g.s.} \rightarrow 2^+_1$ (middle) and $0^+_{g.s.} \rightarrow 2^+_2$ (right) mode of the $0\nu\beta\beta$-decay. No energy resolution smearing has been applied. The signal has been scaled to a half-life of 10^{23} yr.

The $\mathbf{0^+_{g.s.} \rightarrow 0^+_1}$ decay spectrum shows three major lines, that correspond to the energy of 1) the two electrons at 916.8 keV, 2) the two electrons and either of the γ-rays at 1475.9 keV and 1480.0 keV (note that the two γ-rays differ in their energy by 4 keV, which results in two very close lines at this position), and 3) the two electrons and both γ-rays at 2039.1 keV, respectively. Another double line is visible at the energy of the γ-rays at 559.1 keV and 563.2 keV, which originates from decays in the dead layer of the detectors or in detectors that are omitted from the analysis, so that the energy deposition of the electrons is not registered. The intensity of this line is by a factor of about 10 smaller than the previous lines. An even less intense line can be seen at the sum energy of both γ-rays at 1122.3 keV.

Because of the differences in the intensity, the contribution of the latter two lines to the analysis is negligible and only the numbered lines are considered in the analysis. The regions of interest are therefore chosen as [880,950] keV for line 1 (ROI1), [1420,1510] keV for line 2 (ROI2) and [1930,2095] keV for line 3 (ROI3).

In those regions the background can be sufficiently described by a linear function. ROI1 contains a background peak by ^{228}Ac at 911.2 keV. Another line by ^{214}Bi with an emission probability of 3% is also contained in ROI1. This line is estimated to contribute less than 10 counts by comparing its line ratio to the observed 609.3 keV line. ROI2 contains the background peak by ^{40}K at 1460.8 keV.

In the $\mathbf{0^+_{g.s.} \rightarrow 2^+_1}$ decay spectrum three lines are visible. The two major lines at 1480.0 keV and at 2039.1 keV correspond to the energy of the two electrons and the energy of the two electrons and the 559.1 keV γ-ray, respectively. A less intense line from the γ-ray is visible as well, but omitted from the analysis. The analysis of the $0^+_{g.s.} \rightarrow 2^+_1$ decay mode shares its two regions of interest with the $0^+_{g.s.} \rightarrow 0^+_1$ decay mode at [1420,1510] keV (ROI1) and [1930,2095] keV (ROI2).

The $\mathbf{0^+_{g.s.} \rightarrow 2^+_2}$ decay spectrum shows four major lines at the energy of the two electrons at 823.0 keV, at the energy of the two electrons and either of the two γ-rays of the first de-excitation branch at 1382.1 keV and 1480.0 keV and at the full energy of the decay at 2039.1 keV. Furthermore, two lines can be seen at the energy of either of the γ-rays and one line at the energy of the sum of both γ-rays, which also includes contributions from the γ-ray of the second de-excitation branch. Those lines are not taken into account for the analysis.

The first two regions of interest are set to [790,850] keV (ROI1) and [1340,1410] keV (ROI2). ROI2 contains a background line at 1377.7 keV by ^{214}Bi, which is taken into account. Additional lines of ^{214}Bi with emission probabilities of 1-2% in both regions are a factor of 4-5 less intense. An ^{228}Ac line at 794.9 keV is expected to be a factor 8 less intense than the line at 934.1 keV. The final two regions of interest are again shared with the other two decay modes at [1420,1510] keV (ROI3) and [1930,2095] keV (ROI4).

A zoom in on the five relevant regions can be seen in Fig. 8.3.

8.3.4 Signal peak efficiencies

The signal efficiencies for each peak have been obtained from the MC data. The simulation spectra of decays in each detector are combined by weighting them with the ^{76}Ge mass of the corresponding detector. Furthermore, the spectra of each detector are weighted with the live-time of the detector in each run and summed up to a final spectrum for each data set. The combination of each run factors in the complete period of PI for the $^{\text{enr}}$BEGe data set, which means the period of PIa is added using empty spectra[1].

The integrated efficiency, i.e. the probability that a signal decay anywhere in the detector array creates a M1 event in one of the data sets, is about 60% for the PI-$^{\text{enr}}$Coax, 8% for the PI-$^{\text{enr}}$BEGe and about 30% for the PII-$^{\text{enr}}$Coax and PII-$^{\text{enr}}$BEGe data sets with small variations depending on the decay mode.

The signal efficiency ε for each line results from the ratio of the entries in the line to the number of weighted generated decays. The continuum below the peaks is subtracted from the peak entries, though in general it can be neglected. The LAr veto is enforced for PII data only in regions containing the full energy deposition of the signal decay, i.e. the line at 2039.1 keV. As this introduces an experimental dead time of 2.3% due to random coincidences in the veto system [132], a factor of 0.977 is multiplied to the efficiency in those cases.

The efficiency for each line, decay mode and data set is given in Table 8.2. The combined signal efficiency of the PII-$^{\text{enr}}$Coax data set for the $0^+_{g.s.} \rightarrow 0^+_1$ decay mode is about 10%, divided into four signal lines with 2-3% efficiency each. The combined efficiency of the PII-$^{\text{enr}}$BEGe data set is similar, though the weighting of each line is different. Due to the smaller size of the BEGe detectors, it is more likely that both γ-rays escape the detector and hence less likely that the total decay energy is contained in the active volume. The same trend is observed for the other decay modes.

The efficiency of the semi-coaxial detectors is roughly twice as high in PI as compared to PII. This is due to the fact, that they make up the majority of the total detector mass in PI and only half of the total mass in PII. The efficiency of the $^{\text{enr}}$BEGe data set is a

---

[1] This is an arbitrary choice. If factoring in the complete phase, the total exposure can be used to scale the signal. Otherwise, the exposure needs to be limited to the PIc period.

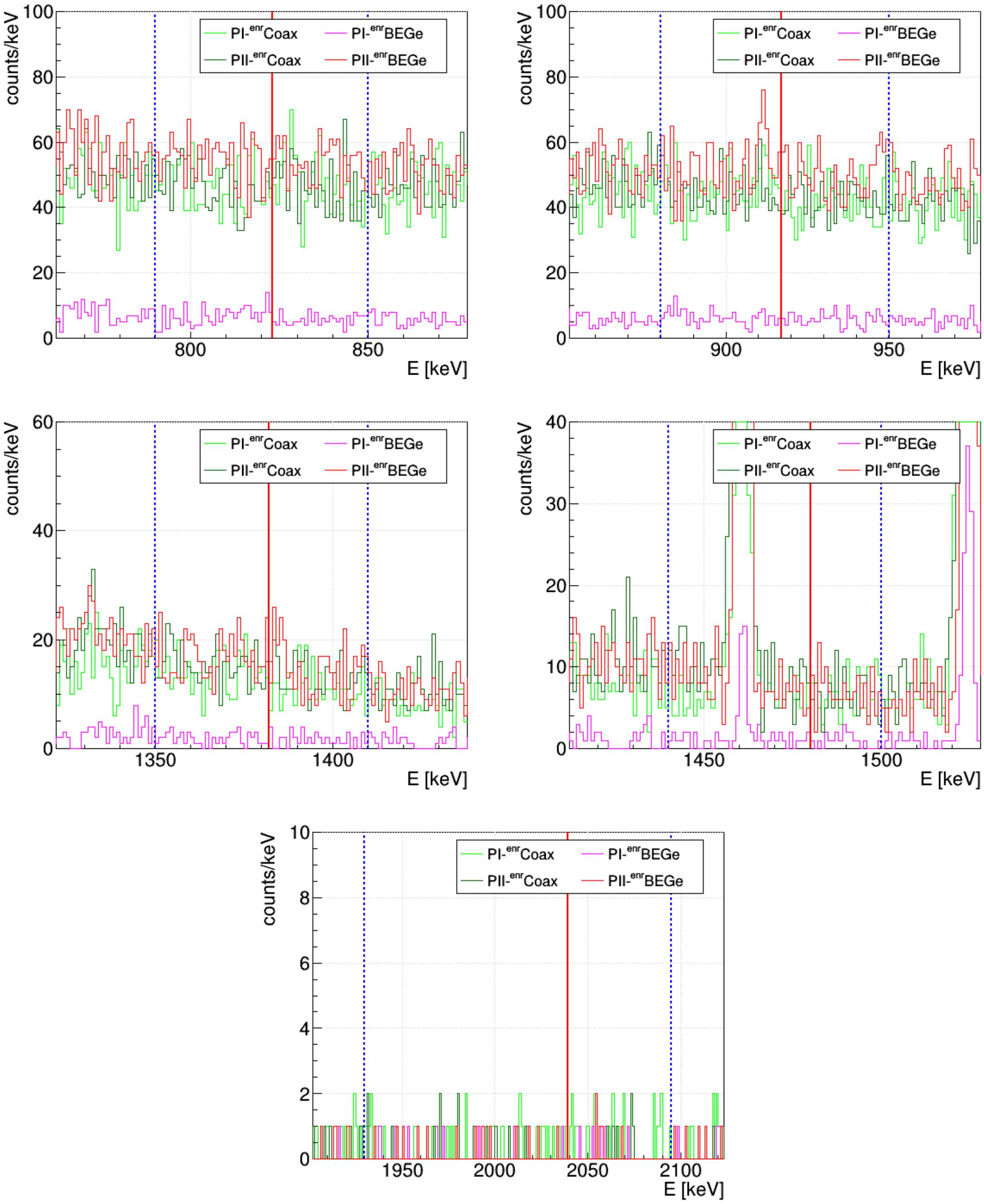

Figure 8.3.: The experimental spectra for the $^{\mathrm{enr}}$Coax and $^{\mathrm{enr}}$BEGe data sets of PI and PII around the expected signal lines at 823.0 keV, 916.8 keV, 1382.1 keV, 1480.0 keV and 2039.1 keV, which are indicated by the vertical red line. The dashed blue lines confine the regions of interest (fit range).

Energy	$^{\text{enr}}$Coax		$^{\text{enr}}$BEGe	
[keV]	PI	PII	PI	PII
$0^+_{g.s.} \to 0^+_1$				
916.8	0.057(1)	0.025(0)	0.0151(2)(1)	0.0405(0)(1)
1480.0	0.048(2)	0.023(1)	0.0069(2)(1)	0.0204(1)(1)
2039.1	0.057(6)	0.030(3)	0.0030(2)(1)	0.0139(2)(1)
$0^+_{g.s.} \to 2^+_1$				
1480.0	0.167(5)	0.084(2)	0.0324(8)(4)	0.1176(3)(1)
2039.1	0.173(13)	0.091(7)	0.0145(7)(4)	0.0695(8)(4)
$0^+_{g.s.} \to 2^+_2$				
823.0	0.121(3)	0.059(2)	0.0254(5)(3)	0.0839(3)(1)
1382.1	0.033(2)	0.016(1)	0.0041(1)(1)	0.0139(1)(0)
1480.0	0.027(1)	0.013(1)	0.0033(1)(1)	0.0112(1)(0)
2039.1	0.068(7)	0.036(3)	0.0043(3)(2)	0.0198(2)(1)

Table 8.2.: The table lists the efficiencies for the considered signal lines in the four data sets. Note, that in the case of the PII $^{\text{enr}}$Coax data, only the first period (PIIa) is used to determine the efficiency of the 2039 keV line. Further note, that in case of the $0^+_{g.s.} \to 0^+_1$ decay mode, the value for the 1480.0 keV line is used also for the very close 1475.9 keV line. The uncertainties from the dead layer thickness of the detectors is given in brackets, first the correlated and second the uncorrelated value. Only a correlated value is used for the $^{\text{enr}}$Coax data set. In case the uncertainty is 0, it is below the precision given and below the uncertainty of 4% from the MC physics processes.

factor of 3-4 lower in PI, due to the lower mass ratio and their presence only in the second period, PIc.

Uncertainties

The statistical uncertainty of the signal efficiency from the line entries in the MC data is negligible. The two largest contributions to the systematical uncertainty are a 4% uncertainty assigned to the physics processes in the MC simulations [177] and the dead layer thickness/active volume uncertainty of the detectors. Both contributions were also discussed in case of the $2\nu\beta\beta$-decay to excited states in Ch. 7.5.3.

MC simulations have been generated with the dead layer thickness altered according to the correlated and uncorrelated uncertainty values of the detectors. With the modified MC data, the efficiency of each detector was again determined. The corresponding uncertainty of the efficiency is calculated as the difference between the values of the modified MC data and the original values. To obtain the uncertainty for a full data set, the correlated uncertainties are summed linearly, while the uncorrelated uncertainties are combined quadratically. The uncertainty available for the $^{\text{enr}}$Coax detectors is assumed to be fully correlated.

With a decrease of the active volume, two effects work in opposite directions for the lines at 823.0 keV, 916.8 keV, 1382.1 keV and 1480.0 keV: On the one hand, events are removed from the line, if one of the particles is depositing its energy partially in the increasing inactive volume. On the other hand, for the same reasons, events can newly enter the line if they degrade from a higher energetic line (or continuum), e.g. an event originally in the 1480 keV line will drop down to the 916.8 keV line if the γ-ray deposited its energy in the now additional inactive volume. For the line at 2039.1 keV, only the first effect comes into play, thus the uncertainties are typically larger in comparison. They reach up to about 10% for the $^{\mathrm{enr}}$Coax data set and up to 7% (correlated) and 4% (uncorrelated) for the $^{\mathrm{enr}}$BEGe data set. The uncertainties for the $^{\mathrm{enr}}$Coax data sets are obviously larger than for the $^{\mathrm{enr}}$BEGe data sets as they are assumed to be fully correlated.

8.3.5 Fit procedure

A combined spectral fit of all data sets and signal regions is performed. The fit is based on an unbinned likelihood function which is defined as follows:

$$\mathcal{L}(\mathbf{p}|\mathbf{n}) \quad \propto \quad \prod_d \mu_d^{N_d} e^{-\mu_d} \prod_i^{N_d} \frac{1}{\mu_d} P_d(E_{d,i}|\mathbf{p}) \tag{8.1}$$

with the extended pdf $P_d(E|\mathbf{p})$ and its integral $\mu_d = \int dE P_d(E|\mathbf{p})$. N_d is the number of events within any of the selected signal regions in the data set d, $\mathbf{p}$ the set of parameters describing the fit function and $\mathbf{n}$ the collective data.
The extended pdf of data set d and region r consists of a Gaussian signal peak, a linear background component and, if necessary, a Gaussian background peak:

$$\begin{aligned} P_d, r(E|\mathbf{p}) \quad &= \quad \frac{1}{\sqrt{2\pi}\sigma_{d,r}} \left(s_{d,r} e^{\left(-\frac{(E-E_{S,r}+\delta_{d,r})^2}{2\sigma_{d,r}^2}\right)} + b_{d,r} e^{\left(-\frac{(E-E_{B,r}+\delta_{d,r})^2}{2\sigma_{d,r}^2}\right)} \right) \\ &\quad + b_{0,d,r} + b_{1,d,r}\left(E - E_{S,r} + \delta_{d,r}\right). \end{aligned} \tag{8.2}$$

The Gaussian signal is described by the signal count expectation $s_{d,r}$, the standard deviation and energy resolution $\sigma_{d,r}$ and the mean $E_{S,r}$. A free parameter $\delta_{d,r}$ takes the systematic shift of peak position relative to the literature value into account. The background peak with the expected peak counts $b_{d,r}$ and mean $E_{B,r}$ shares the width $\sigma_{d,r}$ and shift $\delta_{d,r}$ with the signal peak. The two parameters $b_{0,d,r}$ and $b_{1,d,r}$ describe the linear background component. The reference point of the linear background is chosen as the signal position $E_{S,r}$, so that $b_{0,d,r}$ corresponds to the expected background below the signal peak.
The expected number of signal counts $s_{d,r}$ is connected to the half-life of the decay:

$$s_{d,r} = \frac{1}{T_{1/2}} \cdot \varepsilon_{d,r} \cdot \frac{\ln 2 \cdot N_A \cdot \mathcal{E}_{76}}{m_{76}} \qquad , \tag{8.3}$$

with $T_{1/2}$ the half-life of the signal decay, $\varepsilon_{d,r}$ the signal efficiency for signal line r in data set d, N_A Avogradro's constant, $\mathcal{E}_{76}$ the exposure of ^{76}Ge and m_{76} the molar mass of ^{76}Ge.

Systematic uncertainties

To include the systematic uncertainties of the efficiency and the exposure, they are substituted by the following expressions:

$$\varepsilon_{d,r} \quad = \quad \tilde{\varepsilon}_{d,r} + a^{\mathrm{corr}}\sigma_{d,r}^{\mathrm{corr}} + a_r^{\mathrm{uncorr}}\sigma_{d,r}^{\mathrm{uncorr}} + a_{d,r}^{\mathrm{MC}}\sigma_{d,r}^{\mathrm{MC}} \tag{8.4}$$

$$\mathcal{E}_{76} \quad = \quad \tilde{\mathcal{E}}_{76} + a^{\mathrm{Coax}}\sigma_d^{\mathrm{Coax}} + a^{\mathrm{BEGe}}\sigma_d^{\mathrm{BEGe}}, \tag{8.5}$$

where $\tilde{\varepsilon}_{d,r}$ and $\tilde{\mathcal{E}}_{76}$ are the mean of the efficiency and exposure, respectively. $\sigma_{d,r}^{\mathrm{corr}}$ and $\sigma_{d,r}^{\mathrm{uncorr}}$ are the uncertainties due to the correlated and uncorrelated dead layer uncertainties, $\sigma_{d,r}^{\mathrm{MC}}$ is the uncertainty due to the MC physics processes and $\sigma_{d}^{\mathrm{Coax}}$ and $\sigma_{d}^{\mathrm{BEGe}}$ the exposure uncertainties. The parameters a are floating in the range between -5σ and +5σ. The inverse half-life $T_{1/2}^{-1}$ is the shared parameter between all data sets and regions. Additionally, the fit includes 3 (2) floating parameters for each region with (without) background peak, not counting the systematic uncertainties. $b_{1,d,r}$ is fixed to 0 for the signal regions containing the 2039.1 keV line. The systematic uncertainties add 6 parameters handling the exposure and dead layer uncertainties, and 12 parameters per signal region for the efficiency uncertainty coming from the MC physics processes, the energy resolution and the energy shift.

A priori probability

The prior probability density distribution (in short: prior) for $T_{1/2}^{-1}$ is chosen as flat between 0 and $1.0 \cdot 10^{-24}\,\mathrm{yr}^{-1}$ for the $0^+_{g.s.} \rightarrow 0^+_1$ and $0^+_{g.s.} \rightarrow 2^+_2$ modes, and $0.3 \cdot 10^{-24}\,\mathrm{yr}^{-1}$ for the $0^+_{g.s.} \rightarrow 2^+_1$ mode. The prior for $b_{0,d,r}$ is chosen flat with a range specifically chosen for each signal region and data set. The prior for $b_{1,d,r}$ is also chosen as flat. The range is limited to negative values. The prior for the a parameters is a Gaussian distribution with the mean at 0 and a width of 1. A Gaussian distribution is also used for the $\delta_{d,r}$ with the meant at 0 and a width of 0.2 keV.

8.3.6 Fit Results

The best fit was obtained by maximizing the posterior probability density distribution (in the following just posterior). The maximum of the posterior could be found for $T_{1/2}^{-1}$ equals zero, hence no signal has been observed for all three decay modes. Consequently, a 90% credibility limit was extracted from the 90% quantile of the marginalized posterior of $T_{1/2}^{-1}$ $P(T_{1/2}^{-1}|\mathbf{d})$. The best fit and the 90% limit is shown in Fig. 8.4 for the sum of all data sets and in Appendix G.1 for all data sets separately (Fig. G.1 and following).
These limits translate to a half-life limit of $T_{1/2} > 3.31 \cdot 10^{24}\,\mathrm{yr}$ for the $0^+_{g.s.} \rightarrow 0^+_1$, $T_{1/2} > 1.14 \cdot 10^{25}\,\mathrm{yr}$ for $0^+_{g.s.} \rightarrow 2^+_1$ and $T_{1/2} > 3.11 \cdot 10^{24}\,\mathrm{yr}$ for $0^+_{g.s.} \rightarrow 2^+_2$ decay mode. When neglecting the systematic uncertainties, the limits would improve by about 1%. The limits correspond to a limit on the expected signal counts of the combined data sets of 20, 10 and 27, with a combined background expectation below the signal peak of 167, 23 and 211 counts/keV for the three decay modes, respectively. The results are listed in Tab. 8.3 for each of the data sets and ROIs separately.
The background peak of ^{214}Bi at 1377.7 keV is compatible with zero at the 68% level for all data sets. Removing this peak from the fit function changes the limit for the $0^+_{g.s.} \rightarrow 2^+_2$ decay mode by less than 1%.
The p-value was calculated for the combined fit and amounts to 0.86, 0.65 and 0.54 for the three decay modes, using the algorithm from [103] signifying a general agreement between the data and the fit model.

Excluding the ROI around the Q-value

The signal peak expected at the full Q-value of the decay at 2039.1 keV does coincide with the signal peak expected from the $0^+_{\mathrm{g.s.}} \rightarrow 0^+_{\mathrm{g.s.}}$ mode. As long as neither of the $0\nu\beta\beta$-

Data set		ε		b_0	s
$0^+_{g.s.} \rightarrow 0^+_1$: $T_{1/2} > 3.3 \cdot 10^{24}$ yr (90% cred.)					
PI-$^{\mathrm{enr}}$Coax	ROI1	0.057		$43.3^{+0.7}_{-0.8}$	0 / <2.1
	ROI2	0.048	(x2)	$6.8^{+0.3}_{-0.4}$	0 / <3.5
	ROI3	0.057		$0.39^{+0.04}_{-0.06}$	0 / <2.1
PI-$^{\mathrm{enr}}$BEGe	ROI1	0.0151		$6.1^{+0.02}_{-0.04}$	0 / <0.6
	ROI2	0.0069	(x2)	$1.0^{+0.1}_{-0.1}$	0 / <0.5
	ROI3	0.0030		$0.11^{+0.02}_{-0.03}$	0 / <0.1
PII-$^{\mathrm{enr}}$Coax	ROI1	0.025		$43.5^{+0.8}_{-0.8}$	0 / <1.5
	ROI2	0.023	(x2)	$7.8^{+0.3}_{-0.4}$	0 / <2.7
	ROI3	0.030		$0.07^{+0.03}_{-0.02}$	0 / <1.7
PII-$^{\mathrm{enr}}$BEGe	ROI1	0.042		$50.3^{+0.9}_{-0.9}$	0 / <2.4
	ROI2	0.021	(x2)	$7.2^{+0.3}_{-0.3}$	0 / <2.4
	ROI3	0.014		$0.10^{+0.03}_{-0.02}$	0 / <0.8
$0^+_{g.s.} \rightarrow 2^+_1$: $T_{1/2} > 1.1 \cdot 10^{25}$ yr (90% cred.)					
PI-$^{\mathrm{enr}}$Coax	ROI1	0.167		$6.8^{+0.3}_{-0.4}$	0 / <1.8
	ROI2	0.173		$0.37^{+0.6}_{-0.4}$	0 / <1.8
PI-$^{\mathrm{enr}}$BEGe	ROI1	0.0324		$1.0^{+0.1}_{-0.1}$	0 / <0.3
	ROI2	0.0145		$0.11^{+0.02}_{-0.03}$	0 / <0.2
PII-$^{\mathrm{enr}}$Coax	ROI1	0.084		$7.8^{+0.3}_{-0.4}$	0 / <1.4
	ROI2	0.091		$0.07^{+0.03}_{-0.02}$	0 / <1.5
PII-$^{\mathrm{enr}}$BEGe	ROI1	0.122		$7.2^{+0.3}_{-0.3}$	0 / <2.0
	ROI2	0.071		$0.11^{+0.03}_{-0.02}$	0 / <1.2
$0^+_{g.s.} \rightarrow 2^+_2$: $T_{1/2} > 3.1 \cdot 10^{24}$ yr (90% cred.)					
PI-$^{\mathrm{enr}}$Coax	ROI1	0.121		$46.6^{+0.9}_{-0.8}$	0.22 / <4.7
	ROI2	0.033		$12.6^{+0.4}_{-0.5}$	0.06 / <1.3
	ROI3	0.027		$6.7^{+0.4}_{-0.2}$	0.05 / <1.0
	ROI4	0.068		$0.38^{+0.05}_{-0.04}$	0.12 / <2.6
PI-$^{\mathrm{enr}}$BEGe	ROI1	0.0254		$6.3^{+0.3}_{-0.3}$	0.05 / <1.0
	ROI2	0.0041		$1.8^{+0.2}_{-0.2}$	0.01 / <0.2
	ROI3	0.0033		$1.0^{+0.1}_{-0.1}$	0.01 / <0.1
	ROI4	0.043		$0.10^{+0.03}_{-0.02}$	0.01 / <0.2
PII-$^{\mathrm{enr}}$Coax	ROI1	0.059		$46.2^{+1.0}_{-0.7}$	0.17 / <3.6
	ROI2	0.016		$14.4^{+0.5}_{-0.4}$	0.05 / <1.0
	ROI3	0.013		$7.8^{+0.03}_{-0.04}$	0.04 / <0.8
	ROI4	0.036		$0.07^{+0.03}_{-0.02}$	0.10 / <2.2
PII-$^{\mathrm{enr}}$BEGe	ROI1	0.087		$54.3^{+0.9}_{-1.1}$	0.25 / <5.3
	ROI2	0.014		$15.6^{+0.6}_{-0.4}$	0.04 / <0.9
	ROI3	0.012		$7.3^{+0.02}_{-0.04}$	0.03 / <0.7
	ROI4	0.020		$0.12^{+0.02}_{-0.03}$	0.06 / <1.2

Table 8.3.: Fit results for the three decay modes. Given are the efficiency for each ROI and data set, the marginalized mode of the background below the peak ($b_{0,d,r}$), as well as the best fit of the signal count expectation ($s_{d,r}$) and its 90% upper limit obtained from the 90% quantile of the marginalized posterior. The uncertainties of $b_{0,d,r}$ are obtained from the smallest 68% interval of the corresponding marginalized posterior.

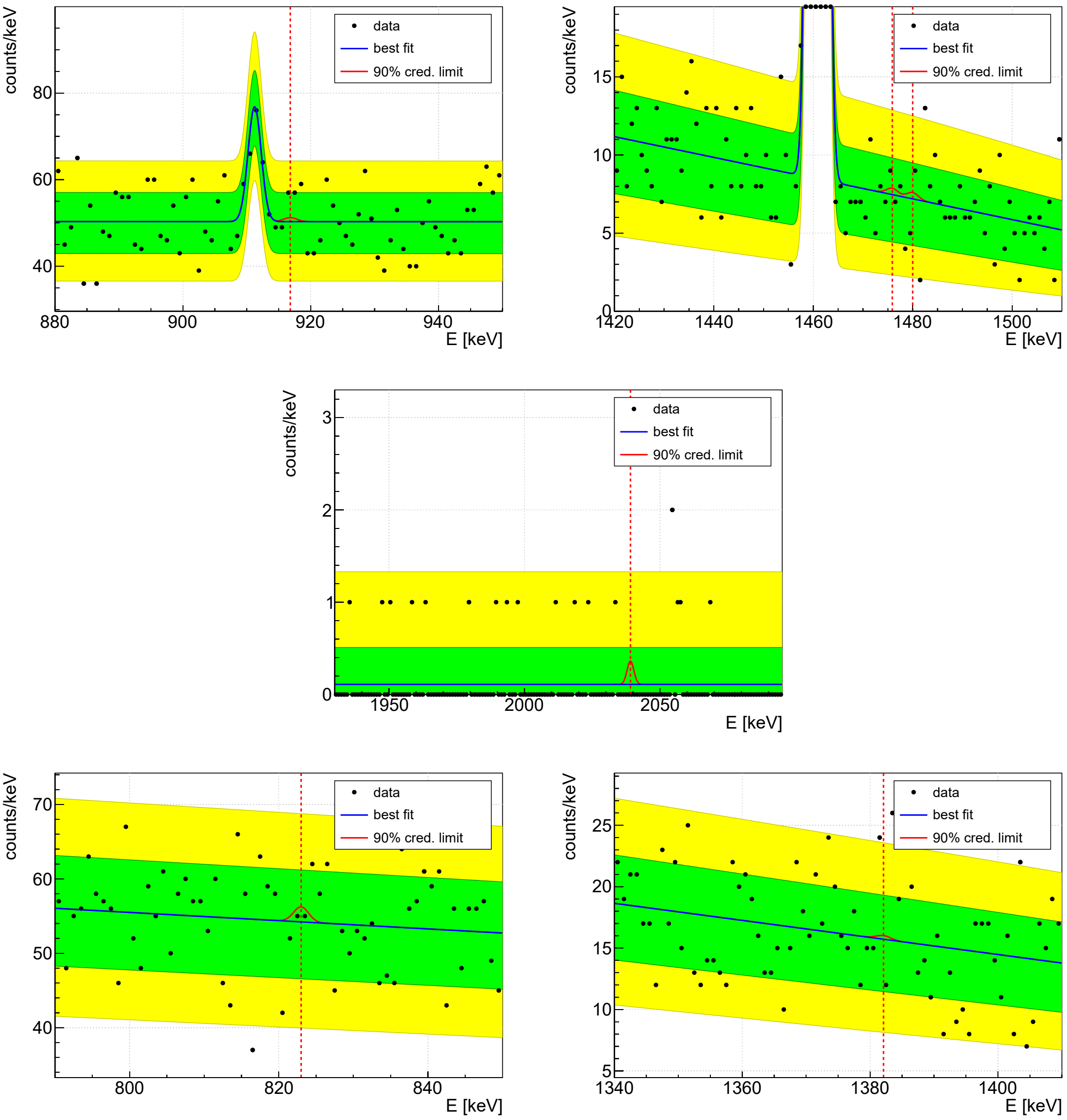

Figure 8.4.: Combined unbinned spectral fit of the M1 data in the ROIs of the $0\nu\beta\beta$-decay analysis. The data points are the sum of all data sets. A binning of 1 keV has been chosen for visualisation. The red dashed line shows the signal position. The limit is scaled to the limit obtained for the $0^+_{g.s.} \rightarrow 0^+_1$ decay in the top three plots and to the limit obtained for the $0^+_{g.s.} \rightarrow 2^+_2$ decay mode in the bottom plots. The green and yellow band represent the 68% and 95% probability band, obtained from a Poisson distribution with an expectation equal to the best fit value.

decay modes are observed, the ROI including the Q-value has value for all decay modes as an almost background free region. On the other hand, in case of an observation of the $0^+_{\text{g.s.}} \rightarrow 0^+_{\text{g.s.}}$ mode, this ROI will lose its value for settings a limit on the excited states decay modes. In such a case, the analysis needs to rely on the remaining ROIs only. Even in a scenario where modes to excited states are observed in addition to the $0^+_{\text{g.s.}} \rightarrow 0^+_{\text{g.s.}}$ mode, the expected signal counts from the former modes will very likely be very small compared to those of the $0^+_{\text{g.s.}} \rightarrow 0^+_{\text{g.s.}}$ mode, due to the several orders of magnitude longer half-life. In such a case, the remaining ROI can be utilized to constrain the contribution of the excited states decay modes to the peak at the Q-value.

Repeating the fit procedure while excluding the ROI at the Q-value results in a best fit of the inverse half-life of 0 for the $0^+_{g.s.} \rightarrow 0^+_1$ and $0^+_{g.s.} \rightarrow 2^+_1$ decay modes, and a best fit of $3.28 \cdot 10^{-25}\,\text{yr}^{-1}$ for the $0^+_{g.s.} \rightarrow 2^+_2$ decay mode. The marginalized posterior for the latter decay mode is still compatible with 0 on the 68% level.

Again, 90% credibility limits are set at values corresponding to half-lives of $T_{1/2} > 1.52 \cdot 10^{24}\,\text{yr}$, $T_{1/2} > 4.11 \cdot 10^{24}\,\text{yr}$ and $T_{1/2} > 0.92 \cdot 10^{24}\,\text{yr}$ for the three decay modes, respectively. The limits are reduced by around 60% for the $0^+_{g.s.} \rightarrow 0^+_1$ and $0^+_{g.s.} \rightarrow 2^+_1$ decay modes and about 70% for the $0^+_{g.s.} \rightarrow 2^+_2$ decay mode compared to the previous result with the Q-value ROI included.

Sensitivity

The sensitivity to set a 90% credibility limit for the different ROIs and PI and PII, as well as for the combined data set has been determined using a toy MC approach. For this purpose, 1000 toy experiments have been generated according to the expected background obtained from a background fit excluding the signal region. No signal contribution was added to the toy experiments. The sensitivity is defined as the median of the distribution of the limits obtained with each toy experiment. The distributions can be seen in Fig. G.5 of the Appendix G.2.

The sensitivities of the combined data sets are $3.00 \cdot 10^{24}\,\text{yr}$, $1.01 \cdot 10^{25}\,\text{yr}$ and $3.29 \cdot 10^{24}\,\text{yr}$ for the three decay modes, respectively. The sensitivity for the $0^+_{g.s.} \rightarrow 2^+_1$ mode is a factor 3 higher than for the other two modes, due to a very high signal efficiency, which is due to the emission of only one γ-ray.

Although, the exposure has increased by a factor of 1.6 in PII, the sensitivity for all decay modes remains roughly the same compared to PI. This is a result of the higher abundance of smaller BEGe detectors and the increased compactness of the detector array that leads to less M1 events in favor of M2 events and hence reduces the mass weighted average of the signal efficiencies of BEGe and semi-coaxial data set. Furthermore, the semi-coaxial data set is only partially unblinded in the Q-value region in PII.

The sensitivities of the different ROIs gives insight on the value of each of them for this analysis. GERDA is designed with the goal of an extremely low background at the Q-value of the $0\nu\beta\beta$-decay. Thus, it is no surprise, that the ROI around the Q-value offers the highest sensitivity. It represents about 90% of the sensitivity of the combined data sets. However, in case of an observation of the $0^+_{\text{g.s.}} \rightarrow 0^+_{\text{g.s.}}$ decay mode, this region will lose its value, as already discussed in the previous section.

Tab. 8.5 lists the obtained sensitivities.

S [10^{24} yr]	$0^+_{g.s.} \rightarrow 0^+_1$	$0^+_{g.s.} \rightarrow 2^+_1$	$0^+_{g.s.} \rightarrow 2^+_2$
Combined	3.00	10.1	3.29
Without ROI$_Q$	1.23	3.24	1.19
PI	2.03	5.81	2.26
PII	1.79	6.68	2.19
ROI1	0.50	3.34	1.01
ROI2	1.16	9.15	0.39
ROI3	2.50	-	0.42
ROI4	-	-	3.16

Table 8.4.: Sensitivity to set a 90% credibility limit on the half-life of the signal decay modes for the combined data set, the combined data set without the Q-value region, only the PI or PII data set, or only using one of the given ROIs. ROI$_Q$ denotes the final ROI for each decay mode, whose range includes the Q-value.

8.4 M2 data analysis

The M2 analysis of the $0\nu\beta\beta$-decay to excited states follows the structure presented in Ch. 7 for the neutrino accompanied decay modes. The same data sets with the same basic analysis cuts are used.

This chapter starts with discussing the signal decay signatures. Potential signal regions are defined using the signal MC data. The feasibility of all regions for the analysis is examined based on their individual sensitivity. The size of regions with a large enough sensitivity, as well as detector pairs considered for this regions are optimized in the following. Regions with low sensitivity are discarded, on the other hand. The background in the signal regions will be estimated using sideband regions, which are placed with the help of the background model.

The statistical analysis combines the surviving count results of each regions into one likelihood, and converts it to a multi-dimensional posterior probability distribution using Bayes theorem. A 90% credibility limit on the half-life of the particular decay mode is extracted from the marginalized posterior.

8.4.1 Signal decay signature

Fig. 8.5 shows the two-dimensional spectra of M2 events for all three decay modes. Plotted is one of the energies of such events versus the other energy. As a result of the discrete energy of the two electrons in the $0\nu\beta\beta$-decay modes, there are a variety of horizontal/vertical and diagonal lines visible in those spectra, that correspond to the different possibilities of detecting the involved electrons and γ-rays with two detectors, either partially or fully.

Fig. 8.6 shows both one-dimensional representations of this spectrum, the single energy spectrum and the sum energy spectrum.

Signal cut regions

The signal MC data is now used to assign a signal cut region (ROI) to the various lines. In the following an overview is given, discussing these signatures. Lines not pre-selected for discussion clearly show a lower intensity in the spectrum and are thus omitted.

$0^+_{g.s.} \rightarrow 0^+_1$:

Seven ROI have been pre-selected, labeled with Cut0-6 and highlighted in the right hand side plots in Fig. 8.5.

Cut0: The signal decay happens either in a detector excluded from the analysis or in the dead layer of a detector, so that the energy of the two electrons is not detected. Both of the two γ-rays are detected fully in two separate detectors.

Cut1: The two electrons are detected in one detector. Additionally, one of the γ-rays may get detected in the same detector, either partially or fully. The other γ-ray is detected fully in a second detector.

Cut2: The two electrons are detected in one detector and one of the γ-rays is detected partially in another detector.

Cut3: The two electrons and one of the γ-rays are detected fully in one detector. The second γ-ray is detected partially in a second detector.

Cut4: The two electrons and part of the energy of one γ-ray is detected in one detector. The same γ-ray deposits its remaining energy in a second detector.

Cut5: The two electrons and one γ-ray deposit the full energy in one detector. The second γ-ray is also partially detected in the same detector. The remaining energy of that γ-ray is detected in a second detector.

Cut6: The two electrons are detected in one detector. Both of the γ-rays deposit energy in a second detector, so that it registers an energy greater than the full energy of one γ-ray alone.

$0^+_{g.s.} \rightarrow 2^+_1$:

Due to emitting just a single γ-ray in this decay mode, only two ROI can be pre-selected, labeled with Cut0-1 in the right hand side plots in Fig. 8.5. The regions correspond to Cut3 and Cut5 of the $0^+_{g.s.} \rightarrow 0^+_1$ decay mode. The difference is that the energy that the second γ-ray would carry, is now included in the energy of the two electrons.

Cut0: The two electrons are detected fully in one detector. The γ-ray is detected partially in a second detector.

Cut1: The two electrons deposit the full energy in one detector. The γ-ray is also partially detected in the same detector. The remaining energy of that γ-ray is detected in a second detector.

$0^+_{g.s.} \rightarrow 2^+_2$:

Seven ROI have been pre-selected, labeled with Cut0-6 in the right hand side plots in Fig. 8.5. The diagonal regions corresponding to Cut4 of the $0^+_{g.s.} \rightarrow 0^+_1$ decay mode are not selected. This is a result from the evaluation of the sensitivity of each region in the next section, which led to Cut4 of the $0^+_{g.s.} \rightarrow 0^+_1$ decay mode being rejected for further analysis and is expected to yield an even lower sensitivity for the diagonal regions of the $0^+_{g.s.} \rightarrow 2^+_2$ decay mode.

Cut0: The two electrons are detected in one detector. The two γ-rays of the first de-excitation branch (B1) deposit all or part of their energy in a second detector.

Cut1: The two electrons and the 559.1 keV γ-ray deposit their energy in one detector. The second γ-ray is detected partially in a second detector.

Cut2: Analogous to Cut1, switching the γ-ray energies.

Cut3: The two electrons are detected fully in one detector in addition to at least a part of the energy of the 657.0 keV γ-ray. The 559.1 keV γ-ray is detected fully in a second detector.

Cut4: Analogous to Cut3, switching the γ-ray energies.

Cut5: The two electrons and either γ-ray deposit their full energy in one detector. The remaining γ-ray shares its energy among the same detector and a second one.

Cut6: In addition to the energy of the two electrons in one detector, the 1122.1 keV γ-ray of the second de-excitation branch (B2) distributes its energy between the same detector and another one. Alternatively, the two γ-rays of B1 share their energy between both detectors.

Region sensitivity

The signal efficiency ε of the various ROI are determined as presented in Ch. 7.5.3. The expected background b is obtained from the background model. Given those two quantities, the sensitivity S_r of each ROI is estimated separately using a toy MC approach. The toy experiments are generated in the background only scenario. The number of counts in the ROI and in the sidebands is sampled according to a Poisson distribution with expectation value b. A 90% credibility upper limit on the expected signal counts is extracted for each toy experiment, by performing the statistical analysis of Ch. 7.7 on each one of them. The inverse of the median of the limit distribution is defined as S_r. Tab. 8.5 lists the efficiency, background expectation and sensitivity for the ROI.

The ROI with the largest S_r for a particular decay mode is labeled with a red checkmark. ROI with a S_r of at least 20% of that of the largest value are accepted for the further analysis, ROI with a S_r below are excluded. With a rough estimation of the combined sensitivity by calculating the quadratic sum of all the separate sensitivities, the loss by excluding those regions is less than 1%. On the other hand, the effort and complexity of the analysis can be kept to a minimum.

For the $0^+_{g.s.} \rightarrow 0^+_1$ decay mode, Cut3 is the most valuable ROI, in PI with a sensitivity more than twice as high as the others. Cut0 is excluded due to the high background of about 18 and 52 expected counts in that low energy region in PI and PII, respectively. Similarly, Cut4 lies in a region of relatively high background of 9 and 16 expected counts and is excluded as well. The lowest value of S_r was obtained for Cut6 due to the very low signal efficiency.

The two ROI of the $0^+_{g.s.} \rightarrow 2^+_1$ decay mode are both accepted. The S_r of Cut0 is five times as high as for Cut1.

For the $0^+_{g.s.} \rightarrow 2^+_2$ decay mode, Cut3,4,6 are excluded in PI due to a very low efficiency. Cut0 has the highest S_r in PI, despite the relatively high background of 9 expected counts thanks to the high efficiency of 2.5%. In PII, the increase in ^{42}K and ^{40}K background strongly affects this region, pushing the expected counts up to 34. As a result, its S_r decreases relative to the other regions[2].

8.4.2 Signal cut optimization

The size of each ROI will be optimized analogously to Ch. 7.5.4 to maximize the sensitivity. Additionally, the detector pairs taken into account are selected for each region separately. Background lines of ^{42}K, ^{40}K and ^{214}Bi (PII only) with a sum energy of 1524.70 keV, 1460.83 keV and 1764.43 keV, respectively, are excluded from the ROI with a ±5 keV window.

---

[2] Some value can likely be obtained by separating Cut0 of the $0^+_{g.s.} \rightarrow 2^+_2$ decay mode into a region above and below the ^{42}K sum energy line.

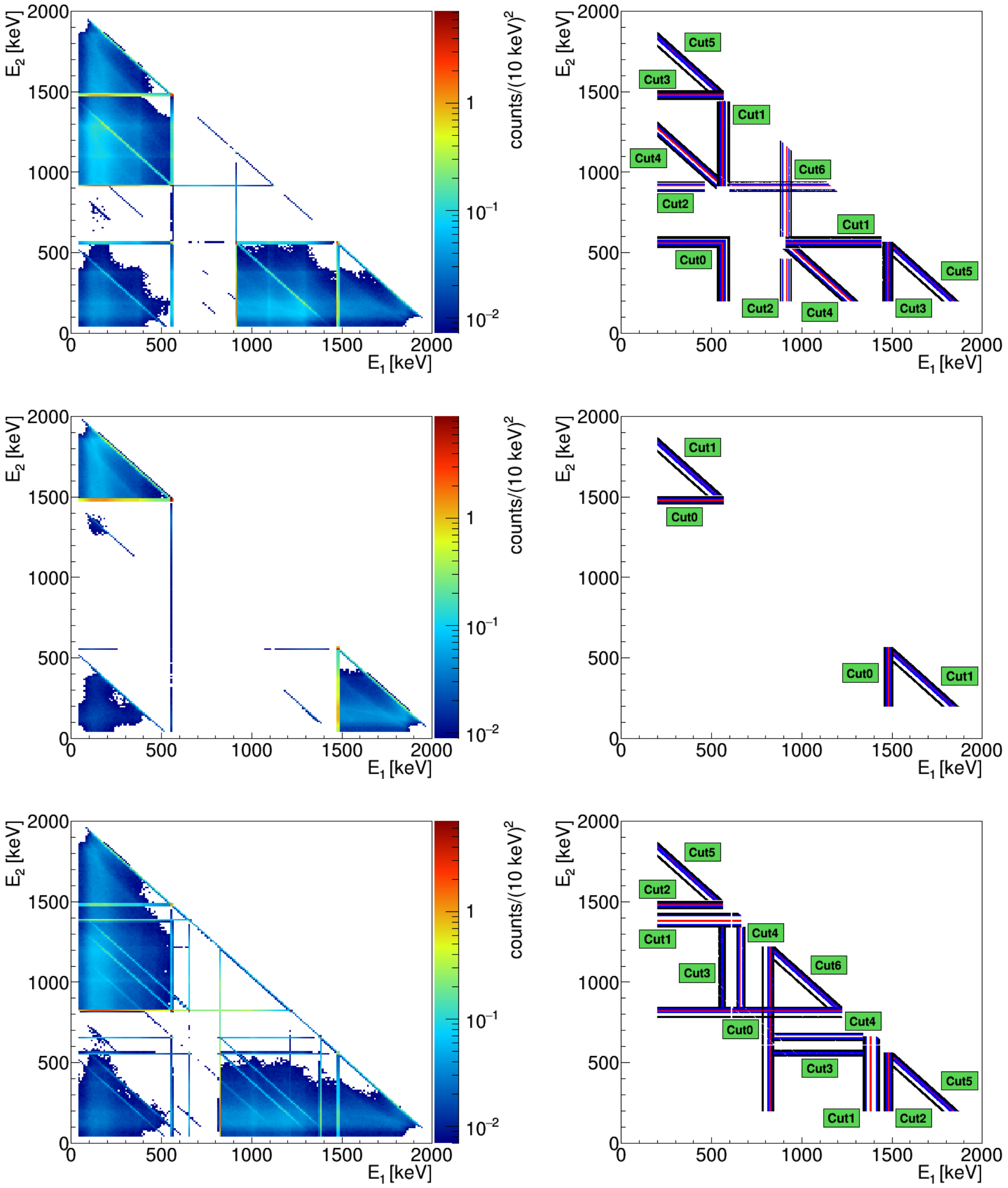

Figure 8.5.: Signal MC spectrum of the $0\nu\beta\beta$-decay to the three lowest excited states of ^{74}Se. Shown is the energy of one detector against the energy of the second detector of multiplicity 2 events for the three decay modes $0^+_{g.s.} \rightarrow 0^+_1$ (top), $0^+_{g.s.} \rightarrow 2^+_1$ (middle) and $0^+_{g.s.} \rightarrow 2^+_2$ (bottom). The plots on the right highlight the pre-selected cut regions in red. Shown in black and blue are temporary sidebands.

	Phase I				Phase II			
Region	ε [%]	b	S_r [a.u.]		ε [%]	b	S_r [a.u.]	
$0^+_{g.s.} \rightarrow 0^+_1$								
Cut0	0.26	17.9	0.7		0.39	52.3	0.8	
Cut1	0.74	1.3	4.4	✓	2.06	3.4	7.4	✓
Cut2	0.94	3.3	4.8	✓	2.17	11.8	3.9	✓
Cut3	1.52	1.5	10.0	✓	2.28	2.6	10.0	✓
Cut4	0.25	9.0	0.9		0.58	16.0	1.2	
Cut5	0.31	0.8	2.3	✓	0.56	1.3	2.9	✓
Cut6	0.04	0.2	0.4		0.15	0.2	1.2	
$0^+_{g.s.} \rightarrow 2^+_1$								
Cut0	2.76	1.2	10.0	✓	5.54	2.0	10.0	✓
Cut1	0.50	0.8	2.0	✓	1.24	1.3	2.5	✓
$0^+_{g.s.} \rightarrow 2^+_2$								
Cut0	2.54	9.0	10.0	✓	5.55	34.0	8.3	✓
Cut1	0.53	2.3	4.6	✓	0.81	3.0	10.0	✓
Cut2	0.44	1.2	4.6	✓	0.64	2.0	9.2	✓
Cut3	0.11	1.1	1.2		0.28	3.7	2.9	✓
Cut4	0.11	0.4	1.4		0.28	1.0	5.0	✓
Cut5	0.26	0.8	2.9	✓	0.54	1.3	8.9	✓
Cut6	0.05	0.1	0.7		0.11	0.27	2.6	✓

Table 8.5.: Signal cut efficiency ε, background expectation b as obtained from the background model and the normalized sensitivity S_r of each considered signal region of the three decay modes of the $0\nu\beta\beta$-decay to excited states.

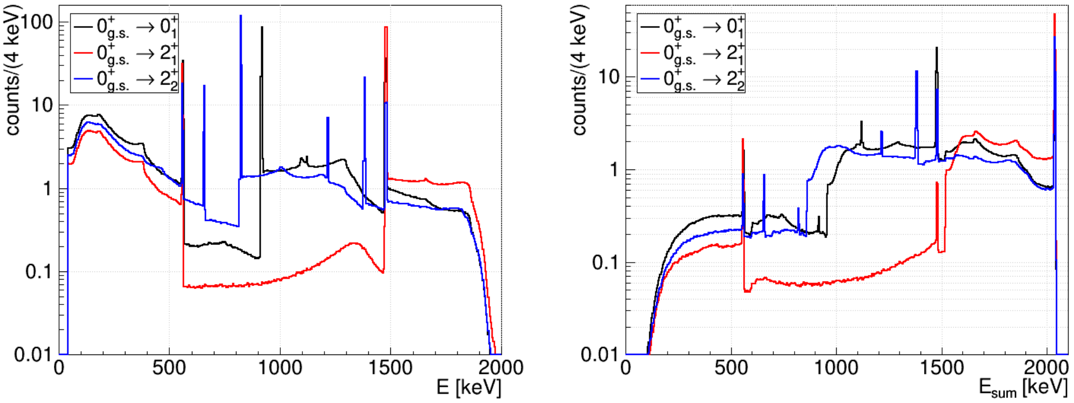

Figure 8.6.: Signal MC data. Shown are two one-dimensional representations of the M2 data for all three decay modes: *Left:* the single energy spectrum. *Right:* the sum energy spectrum.

Region size

The ROI are optimized individually with respect to their window width and their length in order to maximize the sensitivity. To quickly evaluate the change in sensitivity of the regions for a range of region size parameters, the figure of merit F as explained in Ch. 7.5.4 is utilized.

The spectrum along the ROI is typically that of a γ-ray. The default end points of the cut region at both sides are chosen, so that the full energy peaks of the γ-rays (dots in the two-dimensional spectra) are included with 3 standard deviations.

Shortening the length of the cuts does not result in a gain in sensitivity, because it would exclude either the Compton continuum and backscatter maximum on one side of the region or the full energy peak on the other side. This is in contrast to the $2\nu\beta\beta$-decay modes, where the spectrum is that of the two electrons with a maximum at approximately 1/3 of the end point energy. The only exception is the diagonal region at $E_{\text{sum}} = 2039.1$ keV (Cut5/Cut1/Cut5 for the three decay modes, respectively), where a maximum of F was found for a low energy limit of 140 keV. To populate the region below 140 keV, one of the γ-rays would need to deposit most of its energy in the decay detector and then still make it to another detector without getting absorbed on its way, which is highly unlikely.

The cut regions could be fragmented further, by separating the full energy peak of the γ-rays for a potential sensitivity increase. However, it was decided against this, to keep the cut regions more basic. Additionally, some cut regions are already in the background free regime, thus a further segmentation would not result in an improvement of the sensitivity. The latter effect is also the reason why it is preferred to keep some of the regions as large as possible, since they exhibit a very low background especially in PI. In this case, the sensitivity is reduced by the decreasing signal efficiency of smaller cut regions. This can additionally be seen in the window width optimization curves in Fig. 8.7. Initially the window width has been chosen as two standard deviations of the semi-coaxial detector energy resolution in PI. A maximum of F in PI is only present for curves corresponding to regions with a relatively high background, like Cut2 of $0^+_{g.s.} \to 0^+_1$ and Cut0 of $0^+_{g.s.} \to 2^+_2$ with $b > 3$ and to a smaller degree Cut1,3 of $0^+_{g.s.} \to 0^+_1$, Cut0 of $0^+_{g.s.} \to 2^+_1$ and Cut1,2,3 of $0^+_{g.s.} \to 2^+_2$ with $b > 1$. The highest gain of 5% was achieved for Cut0 of $0^+_{g.s.} \to 2^+_2$,

which is also the region with the highest background expectation.
Region Cut2 of $0^+_{g.s.} \rightarrow 0^+_1$ is constrained by a background line of ^{228}Ac at 911.2 keV on the left side. Thus, the cut window is defined asymmetric around the signal line, with an effective width of 4.6 keV.
The optimized window widths in PII are lower compared to the PI values, due to the improved energy resolution, the higher share of BEGe detectors, but also because most cuts are no longer background free with $b > 1$.

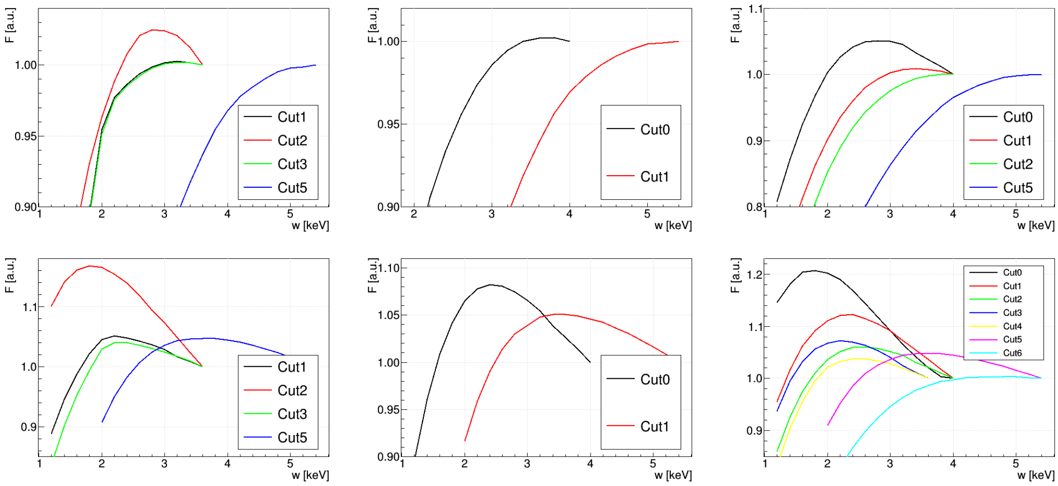

Figure 8.7.: Optimization curve for the signal region window width w for all decay modes, $0^+_{g.s.} \rightarrow 0^+_1$ (*left*), $0^+_{g.s.} \rightarrow 2^+_1$ (*middle*), $0^+_{g.s.} \rightarrow 2^+_2$ (*right*), for PI (*top*) and PII (*bottom*). The figure of merit F on the y-axis is discussed in Sec. 7.5.4. It is normalized so that it results in a value of 1 for the largest width.

Detector pair selection

The detector pairs that are accepted by the signal cut have been selected by an optimization process as explained in Ch. 7.5.4. The optimization procedure uses the optimized ROI as input.
The plots showing the contribution of each detector pair, which also indicate the accepted pairs can be found in Appendix G.3. Assigned to the x-axis is the detector, which is tagged by a discrete energy deposition, i.e. the detector corresponding to the shorter side of the cut regions in the two-dimensional energy spectrum (compare Fig. 8.5). For diagonal cut regions, the detector with the lower energy deposition is tagged. The only exception is Cut6 of the $0^+_{g.s.} \rightarrow 2^+_2$ decay mode, for which both energy depositions are interchangeable. In this case the detector with the lower ID receives the tag, which as a result halves the number of total pairs.
The natural detectors are largely excluded as detectors tagged as the decay detector, which is identified by having registered the electron energy. Besides that, the number of pairs accepted mainly depends on the energy and number of γ-rays, that are available to propagate to the second detector. In case of the $0^+_{g.s.} \rightarrow 0^+_1$ decay mode, for Cut2 both γ-rays are free to move to the second detector, thus most of the pairs contribute (77%). For Cut1 and Cut3 only one of the γ-rays is available, hence only 50%-60% are accepted, which includes most pairs of neighboring strings. The only free γ-ray for Cut5 deposits a

part of its energy in the decay detector. As a result its range with the reduced energy is limited and mostly only pairs of detectors that are direct neighbors in either vertical or lateral direction contribute (32%).

Optimization summary

Tab. G.1 lists the parameters of the optimized cut regions. Given are the center energy of the cut region E_{center}, the window width w and the energies E_{low} and E_{high} that limit the cut region at both ends. The latter two energies are already corrected, so that the cut region and the sidebands described in Sec. 8.4.3 do not overlap. The improvements of F range from only a few percent up to 17%.

8.4.3 Sideband positions

Sidebands to estimate the expected background contribution to the ROI have been positioned with the general approach already discussed in Ch. 7.5.5. A visualization of the sidebands can be found in the Appendix G.5.

The sidebands avoid background lines expected from ^{208}Tl at 583 keV, ^{228}Ac at 911 keV, ^{214}Bi at 665 keV, 934 keV, 1402 keV, 1408 keV and 1509 keV and ^{207}Bi at 570 keV.

Furthermore, they are positioned symmetrically with respect to the ROI. An exception has been made for Cut3 of $0^+_{g.s.} \to 0^+_1$, Cut0 of $0^+_{g.s.} \to 2^+_1$ and Cut2 of $0^+_{g.s.} \to 2^+_2$, due to the location of several background structures that prevent a symmetrical placement close to the ROI. In those cases, it was verified that the expected background is reasonably flat to allow an asymmetrical placement. In this regard, Tab. G.2 to G.8 in Appendix G.5 give the expectation for the number of counts in each sideband ($N^{\text{SB}}_{\text{MC}}$), as obtained from the background model.

The expected counts from the mean of the sideband values ($\bar{N}^{\text{SB}}_{\text{MC}}$) and the expected counts in the ROI ($N^{\text{ROI}}_{\text{MC}}$) agree very well. The differences between both values are well below one count and are compatible with the statistical fluctuations given and the uncertainty of typically 0.1 counts or less. For most cut regions, the differences are below one to two standard deviations. The biggest deviation is found for Cut0 of the $0^+_{g.s.} \to 2^+_2$ decay mode in PII, with about three standard deviations.

For Cut1 of $0^+_{g.s.} \to 2^+_2$, background lines are partially contained within the ROI. Those are two lines of ^{214}Bi at 1378 keV and 1385 keV , which cannot be excluded from this region without losing a significant part of the signal peak. The contribution of both lines to the ROI can be estimated with the background model, which results in $(0.27^{+0.04}_{-0.05})$ counts and $(0.20^{+0.03}_{-0.02})$ counts for PI and PII, respectively. To stay conservative, the models with the largest contribution of ^{214}Bi have been consulted for this purpose. In PI, this is the model obtained from the single energy spectrum fit (compare Tab. 6.2). For PII, values are taken from a model extracted from a sum energy spectrum fit, for which the ^{214}Bi component on the coppershroud was removed.

Hence, given the current data, the expected contribution of the background lines to the ROI is also well below one count.

Background composition

As most of the cut regions are located above the sum energy of the ^{42}K and ^{40}K lines, the dominant background expected from the background model is presented by ^{214}Bi, with a share of typically between 40-70% of the total background. In cut regions with a very

high energy in a single detector (e.g. Cut5 of the $0^+_{g.s.} \rightarrow 0^+_1$ decay mode) the contribution by ^{208}Tl is expected to reach up to 40%.
Still, in those regions up to 20% of the background is expected from ^{42}K, where either the β-particle or bremsstrahlung deposit energy in the detectors. For regions below the ^{42}K full energy line ($0^+_{g.s.} \rightarrow 0^+_1$: Cut1/2, $0^+_{g.s.} \rightarrow 2^+_2$: Cut0/3/4), it adds much more strongly to the total background with 10-50% in PI and 40-60% in PII. Those regions are coincidentally the regions with the highest expected background.
The background in Cut2 of the $0^+_{g.s.} \rightarrow 0^+_1$ decay mode and Cut0,3 of the $0^+_{g.s.} \rightarrow 2^+_2$ decay mode additionally contains a share of 10-20% by ^{40}K in PII, because they reach to the lowest sum energies.

8.4.4 Count results

The number of surviving events contained in each signal (N_{ROI}) and sideband cut region (N_{SB}) are listed in Tab. 8.6. Also given are the expectations from the background model and the corresponding smallest 68% Poisson interval. For only three ROI ($0^+_{g.s.} \rightarrow 0^+_1$: PII Cut1, $0^+_{g.s.} \rightarrow 2^+_2$: PI Cut0 and PII Cut3), N_{ROI} is outside the expected 68% interval, but still within the 99.7% interval. The average of the counts in the sidebands, $\bar{N}_{\mathrm{SB}}$, is always within the expected 95% interval. This indicates that the observed counts in the cut regions are described very well by the background models.
No events are found in the regions containing the full energy of the decay. A total of 4 and 6 events are found in the corresponding sidebands in PI and PII. In PII all these are rejected by the LAr veto.
The distribution of the events in the ROI and in the sidebands among the detectors can be found in Appendix G.7. Note, that in this one-dimensional representation of this distribution, there is a correlation between the entries in each pair of bins, especially between pairs of neighbouring detectors.
There are three occasions with events outside the expected smallest 99.7% percent Poisson interval. It should again be pointed out, that the background model from which the expected values are obtained, has not been tuned to reproduce the event distribution among the detectors (compare Ch. 6.6.6). Additionally, in dependence of which background dominates in the respective ROI, the event distribution is sensitive to the location of different background contaminations.
The first data point outside the 99.7% interval can be found in PI for Cut0 of the $0^+_{g.s.} \rightarrow 2^+_2$ decay mode, where 6 events are observed for both RG1 and GTF112, while only about 1.75 and 1.2 are expected, respectively. Both detectors share 4 of those events, which reminds at the already mentioned correlation especially between bins of neighboring detectors. Taking a look at the timestamps, dectector IDs and energies of all ROI events of Cut0 (see Tab. G.9), it is visible that 4 events are observed in Run26, within a 22 d timespan, and 3 events are observed during Run39a, within a 13 d timespan. However, no clustering of energies is obvious. Also the 4 events with energy depositions in both detectors are not concentrated on a short time period.
The second occasion can be found in the PII data, in Cut3 of the $0^+_{g.s.} \rightarrow 2^+_2$ decay mode. ANG5 registered 4 events, while only 0.3 were expected. Taking a look again on the event list (Tab. G.10), no clustering of events in either timestamp, sum energy or detector pair is visible.
The third case, are the observed counts in GD00B in the combined sidebands of Cut2 of the $0^+_{g.s.} \rightarrow 0^+_1$ decay mode in PII. From the background model, about 5 counts are

expected, while 13 events are observed.
It also needs to be noted, that the probability to observe at least one event outside the 99.7% interval in 80 bins (ROI and sidebands) is about 20%.

8.4.5 Systematic uncertainties and sensitivities

The approach from Ch. 7.5.3 is used to estimate the systematic uncertainties on the signal efficiency, that originate from the implementation of physics processes in the MC simulation, the active volume/dead layer of the detectors and the energy resolution and scale. The uncertainties are summarized in Tab. G.13 in Appendix G.8. The uncertainties from the energy scale are in general larger with a more narrow window size, because a larger portion of the signal peak is situated at the edge of the window. This is lower in PII, because the weight is shifted towards BEGe detectors with a better energy resolution, while the window size also takes into account the larger resolution of the semi-coaxial detectors. The uncertainties from the dead layer are larger for ROI that require the full detection of a γ-ray and even more for the ROI where the full decay energy is detected.
The sensitivity for extracting a 90% credibility lower limit on the half-life of each decay mode has been determined as explained in Ch. 7.7.4. The efficiencies and expected background as obtained from the background model given in Tab. G.1 have been used for this purpose. 10^5 toy MC experiments have been generated for the background only scenario, on the basis of the predicted $N_{\mathrm{ROI}}^{\mathrm{MC}}$ from the background model. The distribution of limits extracted from the toy MC experiments are shown in Fig. G.6. Values of $S = 2.17 \cdot 10^{24}$ yr, $3.79{\cdot}10^{24}$ yr and $1.51{\cdot}10^{24}$ yr have been obtained for the $0^+_{g.s.} \rightarrow 0^+_1$, $0^+_{g.s.} \rightarrow 2^+_1$ and $0^+_{g.s.} \rightarrow 2^+_2$ decay mode, respectively.

8.4.6 Limit extraction

The marginalized posterior $P(T_{1/2}^{-1}|\mathbf{m},\mathbf{n})$ of the inverse half-life is extracted using BAT. The likelihood as defined in Ch. 7.7 is used as basis, where r can be used to indicate the different cut regions. All cut regions of a decay mode and PI and PII data sets are fit in combination.
The priors of $T_{1/2}^{-1}$ has been chosen as flat in the range of $[0,1]{\cdot}10^{-24}\,\mathrm{yr}^{-1}$ ($0^+_{g.s.} \rightarrow 0^+_1$), $[0,3]{\cdot}10^{-24}\,\mathrm{yr}^{-1}$ ($0^+_{g.s.} \rightarrow 2^+_1$) and $[0,1]{\cdot}10^{-24}\,\mathrm{yr}^{-1}$ ($0^+_{g.s.} \rightarrow 2^+_2$).
Fig. G.30 in the Appendix G.9 shows the obtained $P(T_{1/2}^{-1}|\mathbf{m},\mathbf{n})$ for the three decay modes. All of them are compatible with 0, thus no signal has been found and a 90% credibility limit defined by the 90% quantile of the distribution. Those limits translate to half-life limits of $T_{1/2}(0^+_{g.s.} \rightarrow 0^+_1) > 1.88 \cdot 10^{24}$ yr, $T_{1/2}(0^+_{g.s.} \rightarrow 2^+_1) > 4.85 \cdot 10^{24}$ yr and $T_{1/2}(0^+_{g.s.} \rightarrow 2^+_2) > 1.48{\cdot}10^{24}$ yr. The limits are close to the sensitivity and fully compatible with the distribution of limits obtained from toy MC experiments, shown in Fig. G.6.
Without the systematic uncertainties, the limits would improve only slightly by about 1%. The application of the LAr veto on selected cut regions does not alter the limits significantly.

8.5 Combination M1 and M2 results

The analyses of the M1 data (Sec. 8.3) and the M2 data (Sec. 8.4) are combined by propagating the marginalized posteriors for $T_{1/2}^{-1}$ obtained in the former analysis to the latter analysis as prior input.

Region		ε	N_{ROI}	N_{SB}	$\bar{N}_{\mathrm{SB}}$	$N_{\mathrm{ROI}}^{\mathrm{MC}}$		$\bar{N}_{\mathrm{SB}}^{\mathrm{MC}}$	
				$0^+_{g.s.} \rightarrow 0^+_1$					
PI	Cut1	0.712	1	0,1,0,0	0.25	0.95	(0,1.47)	0.92	(0.37,1.30)
	Cut2	1.129	3	4,4,7,4,4,3,2,4	4.00	3.61	(1.42,5.09)	3.69	(2.97,4.32)
	Cut3	1.489	1	0,3,1,1,0,2	1.17	1.20	(0,1.74)	1.19	(0.69,1.57)
	Cut5	0.320	0	0,0,3,0,1,0,0,0	0.50	0.57	(0,1.06)	0.58	(0.27,0.80)
PII	Cut1	1.871	5	5,0,1,1	1.75	2.47	(0.64,3.56)	2.43	(1.57,3.12)
	Cut2	2.251	11	9,6,18,13 8,16,15,18	12.9	13.1	(9.2,16.3)	13.2	(11.3,14.9)
	Cut3	2.033	1	1,2,1,5,1,1	1.83	1.86	(0.26,2.67)	1.86	(1.25,2.35)
	Cut5	0.517	0	1,0,1,0,0,2,0,1	0.63	0.82	(0,1.33)	0.86	(0.49,1.14)
	Cut5*	0.517	0	0,0,0,0,0,0,0,0	0.00	-	-	-	-
				$0^+_{g.s.} \rightarrow 2^+_1$					
PI	Cut0	2.665	0	2,2,0,1,1,0,0,1	0.88	0.90	(0,1.41)	0.75	(0.41,1.01)
	Cut1	0.520	0	0,0,3,0,1,0,0,0	0.50	0.59	(0,1.08)	0.59	(0.28,0.81)
PII	Cut0	4.782	1	1,0,2,3,0,1,0,0	0.88	1.01	(0,1.53)	0.98	(0.59,1.28)
	Cut1	1.127	0	1,0,1,0,0,2,0,1	0.63	0.80	(0,1.31)	0.83	(0.47,1.10)
	Cut1*	1.127	0	0,0,0,0,0,0,0,0	0.00	-	-	-	-
				$0^+_{g.s.} \rightarrow 2^+_2$					
PI	Cut0	2.290	11	8,4,6,7	6.25	5.31	(2.70,7.22)	5.43	(4.19,6.50)
	Cut1	0.491	1	5,0,3,2	2.50	1.51	(0.06,2.13)	1.34	(0.68,1.82)
	Cut2	0.432	0	2,2,0,1,1,0,0,1	0.88	0.90	(0,1.41)	0.75	(0.41,1.01)
	Cut5	0.283	0	0,0,3,0,1,0,0,0	0.50	0.58	(0,1.07)	0.58	(0.27,0.80)
PII	Cut0	4.622	17	18,19,14,13	16.0	16.6	(12.2,20.3)	16.9	(14.8,18.9)
	Cut1	0.714	2	0,2,3,2,3,1,2,0	1.63	1.58	(0.10,2.24)	1.48	(1.01,1.86)
	Cut2	0.571	1	2,0,2,3,0,1,0,1	1.13	1.15	(0,1.68)	1.16	(0.74,1.49)
	Cut3	0.248	6	3,5,3,1,3,2,0,0	2.13	2.45	(0.62,3.53)	2.48	(1.89,2.99)
	Cut4	0.261	1	1,0,0,1,1,1,0,0	0.50	0.99	(0,1.51)	1.01	(0.62,1.32)
	Cut5	0.496	0	1,0,1,0,0,2,0,1	0.63	0.82	(0,1.33)	0.85	(0.49,1.13)
	Cut6	0.107	0	0,0,0,1,0,0,0,0	0.13	0.19	(0,0.61)	0.21	(0.02,0.30)
	Cut5*	0.496	0	0,1,0,0,0,0,0,0	0.125	-	-	-	-
	Cut6*	0.107	0	0,0,0,0,0,0,0,0	0.00	-	-	-	-

Table 8.6.: The number of counts in the optimized signal regions N_{ROI} and in the sideband regions N_{SB} and their average $\bar{N}_{\mathrm{SB}}$. Additionally, given are the expected values for each region obtained from the background model together with the 68% smallest Poisson interval and the signal efficiency ε. The asterisk notes cut regions for which the LAr veto is applied.

The combined and final 90% credibility limits of this analysis are $T_{1/2}(0^+_{g.s.} \rightarrow 0^+_1) > 3.89 \cdot 10^{24}$ yr, $T_{1/2}(0^+_{g.s.} \rightarrow 2^+_1) > 1.44 \cdot 10^{25}$ yr and $T_{1/2}(0^+_{g.s.} \rightarrow 2^+_2) > 3.58 \cdot 10^{24}$ yr. The marginalized posterior distributions are visible in Fig. 8.8. By combining the data sets, total signal efficiencies of 27.8%, 41.9% and 36.0% are reached in PI and 26.6%, 42.7% and 32.7% in PII. The weight of the total M2 efficiency relative to the total M1 efficiency has increased in PII by a factor of about 2-3.

The sensitivities of the combined M1 and M2 data is estimated by summing the separate sensitivities quadratically. This results in values for S of $3.70{\cdot}10^{24}$ yr, $1.08{\cdot}10^{25}$ yr and $3.62{\cdot}10^{24}$ yr, including the region around the Q-value in the M1 analysis.

Refraining from utilizing the Q-value regions for the M1 analysis, combined limits of $T_{1/2}(0^+_{g.s.} \rightarrow 0^+_1) > 2.57 \cdot 10^{24}$ yr, $T_{1/2}(0^+_{g.s.} \rightarrow 2^+_1) > 7.39 \cdot 10^{24}$ yr and $T_{1/2}(0^+_{g.s.} \rightarrow 2^+_2) > 1.64 \cdot 10^{24}$ yr are obtained, which can be compared to the sensitivities of $2.49{\cdot}10^{24}$ yr, $4.99{\cdot}10^{24}$ yr and $1.92{\cdot}10^{24}$ yr.

From the combined results it is visible that the limits are dominantly driven by the Q-value region of the M1 analysis. The inclusion of the M2 data improves the sensitivities by factors of 1.3 for the $0^+_{g.s.} \rightarrow 0^+_1$ decay mode and 1.1 for the remaining decay modes. However, the M2 data becomes more important, if the Q-value region is not utilized, which becomes necessary as discussed in Sec. 8.3.6. In fact, in this case, the sensitivities obtained with the M1 data set are lower than the ones obtained from the M2 data set and are improved by factors of 2.1, 1.6 and 1.7 for the three decay modes when combining both data sets.

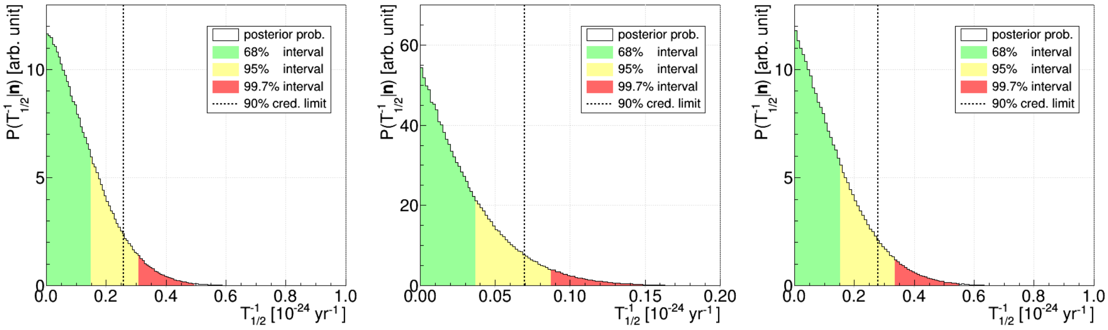

Figure 8.8.: Shown is the marginalized posterior probability density distribution for $T^{-1}_{1/2}$ obtained for the $0^+_{g.s.} \rightarrow 0^+_1$ (*left*), $0^+_{g.s.} \rightarrow 2^+_1$ (*middle*) and $0^+_{g.s.} \rightarrow 2^+_2$ (*right*) decay modes by combining the M1 and M2 data. The smallest 68%, 95% and 99.7% intervals are filled in color. Additionally, the 90% credibility upper limit is shown as dashed line.

8.6 Summary and outlook

A search for the $0\nu\beta\beta$-decay of ^{76}Ge into the first three excited states of ^{76}Se has been presented using the 21 kg·yr of Phase I data and the first 35 kg·yr of Phase II data of the Gerda experiment.

The search uses the anti-coincidence germanium detector data, as well as data with two-detector hits. For the analysis of the anti-coincidence data, a spectral fit of the energy spectrum has been performed in multiple regions, where peaks of the signal are expected. The two-detector data was analysed with a cut and count approach. Signal cut regions in the two-dimensional energy spectrum have been defined, in which a high contribution by

the signal is expected. The number of events observed in these regions are compared to the number of events in background control regions (sidebands) by carrying out a combined fit of all regions.
The combination of both data sets yields total signal efficiencies of 27.8%, 41.9% and 36.0% in Phase I and 26.6%, 42.7% and 32.7% in Phase II, while the relative contribution of the two-detector data in increases by a factor of 2-3 in Phase II.
No signal has been observed in neither of the two data sets. As a result, 90% credibility lower limits on the half-life of each decay mode are extracted using the combined information of both data sets.
The limits are set to:

- $0^+_{g.s.} \rightarrow 0^+_1$: $T^{0\nu}_{1/2} > 3.9 \cdot 10^{24}\,\mathrm{yr}$ with a sensitivity of $S^{0\nu} = 3.7 \cdot 10^{24}\,\mathrm{yr}$
- $0^+_{g.s.} \rightarrow 2^+_1$: $T^{0\nu}_{1/2} > 1.4 \cdot 10^{25}\,\mathrm{yr}$ with a sensitivity of $S^{0\nu} = 1.1 \cdot 10^{25}\,\mathrm{yr}$
- $0^+_{g.s.} \rightarrow 2^+_2$: $T^{0\nu}_{1/2} > 3.6 \cdot 10^{24}\,\mathrm{yr}$ with a sensitivity of $S^{0\nu} = 3.6 \cdot 10^{24}\,\mathrm{yr}$

The limit for the $0^+_{g.s.} \rightarrow 2^+_1$ decay mode improves the previous limit given in [180] by more than one order of magnitude. Note, that while the limit in this work was obtained by a Bayesian approach, the limit in [180] uses a Frequentist analysis.
The inclusion of the two-detector data increases the sensitivity by 8-26%. The two-detector data becomes much more important, in case the Q-value region in the anti-coincidence data is not taken into account, in which the signal is superimposed by the $0^+_{\mathrm{g.s.}} \rightarrow 0^+_{\mathrm{g.s.}}$ mode of the $0\nu\beta\beta$-decay.
As only a subset of the final Phase II data is used, these results are preliminary (see the disclaimer in Appendix I). The analysis will be updated with the remaining data still being taken in Phase II of GERDA. With a combined exposure of 100 kg·yr, the sensitivities are projected to reach $5.9 \cdot 10^{24}\,\mathrm{yr}$, $1.8 \cdot 10^{25}\,\mathrm{yr}$ and $6.4 \cdot 10^{24}\,\mathrm{yr}$ for the three decay modes, respectively.

Chapter 9

Summary

The work presented in this thesis has been carried out in the framework of the GERDA experiment. It takes into account 22 kg·yr of data from Phase I and the first 35 kg·yr of data from one and a half years of Phase II, from December 2011 until May 2013 and December 2015 until April 2017, respectively. The presented analyses concentrate for the most part on the data set of coincident events with hits in two germanium detector. This data set is supplementary to the "standard" data set used for the search for the $0\nu\beta\beta$-decay of ^{76}Ge to the ground state of ^{76}Se, which applies an anti-coincidence cut and thus only utilizes single detector events.

It should be noted, that the results are preliminary for Phase II of GERDA, because the final data selection and processing might be different, as well as the obvious increase of exposure with the complete data.

The energy resolution of the coincidence data set has been evaluated, using data from (bi-)weekly calibration runs. It was found that it is worse by up to 25% compared to the anti-coincidence data set and shifts of γ-ray induced peaks of up to 1 keV with respect to their expected position have been observed. This degradation is caused primarily by electromagnetic interference between multiple detector channels, referred to as crosstalk. An evaluation and correction of the crosstalk has been presented. The correction is based on averaging crosstalk waveforms for each channel pair, which are obtained from dedicated calibration runs. Although the degradation of energy resolution and peak shifts is compensated for the most part, a small worsening still remains (5%) with peak shifts up to 0.3 keV. One potential reason for this are run dependent drifts of the crosstalk signals or problems with calibrations, which are currently under investigation. A couple of runs with jumps in crosstalk values have been found. Subsequently, either affected channel pairs need to be excluded for certain runs from future analyses, or separate crosstalk correction matrices need to be extracted from physics runs instead.

Furthermore, the coincidence data set has been characterised in terms of its background. After evaluating γ-lines in the energy spectrum, a full background model has been created, which describes the energy spectrum with good agreement. This process was done in two steps: First, a fit of the energy spectrum was performed, while including background components expected from screening measurements of materials employed in the detector setup. Additionally, for most isotopes, components with larger distance between background source and detector array have been added to take potential sources into account, that have not been considered in the material screening. However, for most background components, the statistics in the data are not sufficient to distinguish between different locations of the contaminations. Hence, in a second step, the number of components are reduced and prior information from the screening measurements is added. This more minimalistic model, describes the data just as well. Furthermore, no bigger discrepancy between models obtained from coincidence and anti-coincidence data sets have been found.

In comparison to Phase I, background from components of the detector array has decreased in Phase II, thanks to the improved material selection process. However, a 4 times higher contribution by ^{40}K was observed, after correcting for the increased array efficiency. A near source for this contamination is slightly preferred by the data. The glue, which is used to combine the parts of the minishrouds that enclose the detector strings, is one potential candidate. Additionally, the amount of ^{42}K has also increased by a factor of 2, which is thought to be due to the non-metallic nylon minishrouds, in contrast to the copper minishrouds employed in Phase I. Hints that were found in Phase I for an inhomogeneous

distribution of ^{42}K in the LAr were further confirmed in Phase II, in which a much stronger concentration above the array was observed in both anti-coincidence and coincidence data sets. The unshielded cables above the detector array are a possible source for attraction of the ^{42}K ions.
The events in the full energy peak of ^{40}K and ^{42}K have been investigated separate from the rest of the energy spectrum by taking into account the distribution of them among the detectors. This way, information about the location of the background sources is retained. Given the background model, the composition of the background is dominated by ^{42}K with about 50-60% of the total events and ^{40}K with around 20% in the low energetic region below $\sim$1.5 MeV. In the higher energetic region, components by ^{214}Bi and ^{228}Th with each about 40% of the total expected background are the biggest contributions.

The final two analysis chapters presented the search for the $2/0\nu\beta\beta$-decay of ^{76}Ge to the energetically lowest three excited states in ^{76}Se. Both analyses utilize the coincidence data set. A cut and count method is applied, which selects regions in the two-dimensional energy spectrum with a high intensity of the expected signal process. These regions are furthermore optimized in order to increase the sensitivity and remove human bias in the choice of the region size. The contribution of background to the selected regions is estimated with the help of equivalent sidebands, which are positioned next to the signal region. The background model plays a major role in these steps, because it is used as a guideline to position the regions and predict the background contributions in them.
From signal and sideband regions, number of counts are obtained, which enter a Bayesian analysis in order to extract the posterior probability density distribution for the half-life of the particular decay mode. All of these distributions are compatible with 0 within the smallest 95% interval, hence no signal has been observed.
Consequently, for the three $2\nu\beta\beta$-decay modes, new best Bayesian 90% credibility limits have been set, which improve upon the limits set with Phase I of GERDA:

- $0^+_{g.s.} \rightarrow 0^+_1$: $T^{2\nu}_{1/2} > 3.1 \cdot 10^{23}\,$yr with a sensitivity of $S^{2\nu} = 3.6 \cdot 10^{23}\,$yr
- $0^+_{g.s.} \rightarrow 2^+_1$: $T^{2\nu}_{1/2} > 3.4 \cdot 10^{23}\,$yr with a sensitivity of $S^{2\nu} = 6.7 \cdot 10^{23}\,$yr
- $0^+_{g.s.} \rightarrow 2^+_2$: $T^{2\nu}_{1/2} > 2.5 \cdot 10^{23}\,$yr with a sensitivity of $S^{2\nu} = 3.5 \cdot 10^{23}\,$yr .

The theory predictions have large uncertainties due to nuclear matrix element calculations. With the help of these results, several of the calculations can be ruled out, which helps to further refine nuclear models and increases the reliability of half-life predictions, also for the $0\nu\beta\beta$-decay to the ground state.
By reaching 100 kg·yr exposure, the sensitivities are projected to increase by up to 50%. The latter two decay modes already make use of the LAr veto. Applying the LAr veto to the $0^+_{g.s.} \rightarrow 0^+_1$ mode, the sensitivity is expected to increase by another 27%. However, this requires Monte Carlo simulations that model the LAr veto sufficiently well in order to determine the signal efficiency after the veto cut.

In the search for the $0\nu\beta\beta$-decay to excited states, first limits have been set for the three modes:

- $0^+_{g.s.} \rightarrow 0^+_1$: $T^{0\nu}_{1/2} > 3.9 \cdot 10^{24}\,$yr with a sensitivity of $S^{0\nu} = 3.7 \cdot 10^{24}\,$yr
- $0^+_{g.s.} \rightarrow 2^+_1$: $T^{0\nu}_{1/2} > 1.4 \cdot 10^{25}\,$yr with a sensitivity of $S^{0\nu} = 1.1 \cdot 10^{25}\,$yr

- $0^+_{g.s.} \rightarrow 2^+_2$: $T^{0\nu}_{1/2} > 3.6 \cdot 10^{24}\,\text{yr}$ with a sensitivity of $S^{0\nu} = 3.6 \cdot 10^{24}\,\text{yr}$

This search additionally made use of the anti-coincidence data set, due to the discrete line signature of the signal process.

The sensitivities are projected to increase by 35-55% with an exposure of 100 kg·yr. However, the predicted half-lives are still out of reach. Future experiments like LEGEND may be able to approach them, if the ground state decay is observed.

Appendix A

Double beta decay

A.1 2/0$\nu\beta\beta$-decay half-lives

isotope	$T_{1/2}$ [10^{21} yr] ($2\nu\beta\beta$)	ref.	$T_{1/2}$ [10^{23} yr] ($0\nu\beta\beta$)	ref.
^{48}Ca	$0.064^{+0.007+0.012}_{-0.006-0.009}$	[61]	> 0.58	[182]
			> 0.2	[61]
^{76}Ge	1.926 ± 0.094	[3]	$> 8 \cdot 10^2$	[67]
			$> 1.9 \cdot 10^2$	[183]
^{82}Se	$0.096 \pm 0.003 \pm 0.010$	[184]	> 3.6	[185]
^{78}Kr*	$9.2^{+5.5}_{-2.6} \pm 1.3$	[186]	> 0.055	[186]
^{96}Zr	$0.0235 \pm 0.0014 \pm 0.0016$	[187]	> 0.092	[187]
^{100}Mo	$0.00690 \pm 0.00015 \pm 0.00037$	[188]	> 11	[189]
^{116}Cd	$0.0274 \pm 0.0004 \pm 0.0018$	[190]	> 1	[190]
			> 1.7	[191]
^{128}Te	7200 ± 400	[192]	> 1.1	[193]
	1800 ± 700	[194]		
^{130}Te	$0.82 \pm 0.02 \pm 0.06$	[195]	$> 1.5 \cdot 10^2$	[195]
^{130}Ba*	$(0.5-2.7)$	[196, 197]		
^{134}Xe	> 0.87	[198]	> 1.1	[198]
^{136}Xe	$2.165 \pm 0.016 \pm 0.059$	[199]	$> 1.8 \cdot 10^2$	[200]
	$2.38 \pm 0.02 \pm 0.14$	[201]	$> 10.7 \cdot 10^2$	[106]
^{150}Nd	$0.00934 \pm 0.00022^{+0.00062}_{-0.00060}$	[202]	> 0.20	[202]
^{238}U	2.0 ± 0.6	[203]		

Table A.1.: Half-life measurements (68% C.L.) and 90% C.L. limits of 2/0$\nu\beta\beta$-decay isotopes. Isotopes marked with an asterisk decay by EC/EC.

Appendix B

Low background Experiments

B.1 Decay chains and γ-rays

E [keV]	isotope	I [%]	chain
13.52(2)	^{228}Ra	1.60	^{232}Th
46.539(1)	^{210}Pb	44.25(4)	^{238}U
53.2284(18)	^{214}Pb	1.075(7)	^{238}U
99.509(6)	^{228}Ac	1.26(7)	^{232}Th
129.065(1)	^{228}Ac	2.42(9)	^{232}Th
186.211(13)	^{226}Ra	3.64(4)	^{238}U
209.253(6)	^{228}Ac	3.89(7)	^{232}Th
238.632(2)	^{212}Pb	43.6(5)	^{232}Th
240.986(6)	^{224}Ra	4.10(5)	^{232}Th
241.9950(23)	^{214}Pb	7.251(16)	^{238}U
270.245(2)	^{228}Ac	3.46(6)	^{232}Th
277.371(5)	^{208}Tl	6.6(3)	^{232}Th
295.2228(18)	^{214}Pb	18.42(4)	^{238}U
300.087(10)	^{212}Pb	3.30(4)	^{232}Th
328.000(6)	^{228}Ac	2.95(12)	^{232}Th
338.320(3)	^{228}Ac	11.27(19)	^{232}Th
351.9321(18)	^{214}Pb	35.60(7)	^{238}U
409.462(6)	^{228}Ac	1.92(4)	^{232}Th
463.004(6)	^{228}Ac	4.40(7)	^{232}Th
510.77(10)	^{208}Tl	22.60(20)	^{232}Th
562.500(4)	^{228}Ac	0.87(3)	^{232}Th
583.187(2)	^{208}Tl	85.0(3)	^{232}Th
609.320(5)	^{214}Bi	45.49(16)	^{238}U
665.447(9)	^{214}Bi	1.531(6)	^{238}U
674.75	^{228}Ac	2.1(7)	^{232}Th
727.330(9)	^{212}Bi	6.67(9)	^{232}Th
755.315(4)	^{228}Ac	1.00(3)	^{232}Th
763.13(8)	^{208}Tl	1.79(3)	^{232}Th
768.360(5)	^{214}Bi	4.894(11)	^{238}U
772.291(5)	^{228}Ac	1.49(3)	^{232}Th
785.37(8)	^{212}Bi	1.102(13)	^{232}Th
785.96(8)	^{214}Pb	1.06(3)	^{238}U
794.947(5)	^{228}Ac	4.25(7)	^{232}Th
806.180(9)	^{214}Bi	1.264(5)	^{238}U
835.710(6)	^{228}Ac	1.61(6)	^{232}Th
860.557(4)	^{208}Tl	12.50(10)	^{232}Th
911.204(4)	^{228}Ac	25.8(4)	^{232}Th
934.056(6)	^{214}Bi	3.107(10)	^{238}U
964.766(10)	^{228}Ac	4.99(9)	^{232}Th
968.971(17)	^{228}Ac	15.8(3)	^{232}Th
1120.294(6)	^{214}Bi	14.92(3)	^{238}U
1155.210(8)	^{214}Bi	1.633(6)	^{238}U
1238.122(7)	^{214}Bi	5.834(15)	^{238}U
1280.976(10)	^{214}Bi	1.434(6)	^{238}U
1377.669(8)	^{214}Bi	3.988(11)	^{238}U
1401.515(12)	^{214}Bi	1.330(5)	^{238}U
1407.988(11)	^{214}Bi	2.394(7)	^{238}U
1509.210(10)	^{214}Bi	2.130(10)	^{238}U
1588.20(3)	^{228}Ac	3.22(8)	^{232}Th
1620.50(10)	^{212}Bi	1.47(3)	^{232}Th
1630.627(10)	^{228}Ac	1.51(4)	^{232}Th
1661.274(16)	^{214}Bi	1.047(6)	^{238}U
1729.595(11)	^{214}Bi	2.878(8)	^{238}U
1764.491(10)	^{214}Bi	15.30(3)	^{238}U
1847.429(13)	^{214}Bi	2.025(9)	^{238}U
2118.514(19)	^{214}Bi	1.160(6)	^{238}U
2204.059(22)	^{214}Bi	4.924(18)	^{238}U
2447.70(3)	^{214}Bi	1.548(7)	^{238}U
2614.511(10)	^{208}Tl	99.754(4)	^{232}Th

E [keV]	isotope	I [%]	origin
79.131(3)	^{108m}Ag	6.6(5)	cosmo.
433.937(4)	^{108m}Ag	90.5	cosmo.
614.276(4)	^{108m}Ag	89.8(19)	cosmo.
722.907(10)	^{108m}Ag	90.8(19)	cosmo.
446.812(3)	^{110m}Ag	3.70(5)	cosmo.
620.3553(17)	^{110m}Ag	2.73(8)	cosmo.
632.98(5)	^{108}Ag	1.76(10)	cosmo.
657.7600(11)	^{110m}Ag	95.61	cosmo.
677.6217(12)	^{110m}Ag	10.70(5)	cosmo.
687.0091(18)	^{110m}Ag	6.53(3)	cosmo.
706.6760(15)	^{110m}Ag	16.69(7)	cosmo.
744.2755(18)	^{110m}Ag	4.77(3)	cosmo.
763.9424(17)	^{110m}Ag	22.60(7)	cosmo.
818.0244(18)	^{110m}Ag	7.43(4)	cosmo.
884.6781(13)	^{110m}Ag	75.0(11)	cosmo.
937.485(3)	^{110m}Ag	35.0(3)	cosmo.
1077.34(5)	^{68}Ga	3.22	cosmo.
1173.228(3)	^{60}Co	99.85(3)	cosmo.
1332.492(4)	^{60}Co	99.9826(6)	cosmo.
1384.2931(20)	^{110m}Ag	25.1(5)	cosmo.
1460.820(5)	^{40}K	10.66(17)	nat.
1475.7792(23)	^{110m}Ag	4.08(5)	cosmo.
1505.0280(20)	^{110m}Ag	13.33(15)	cosmo.
1524.6(3)	^{42}K	18.08	^{42}Ar
1562.2940(18)	^{110m}Ag	1.22(3)	cosmo.

Table B.1.: γ-rays expected from the natural decay chains (*left* and *top right*) and from other sources (*bottom right*) ordered by their energy. Only γ-rays with an emission probability I larger than 1% are taken into account. The emission of the γ-ray follows the decay of the isotope given in the second column. Data taken from [154].

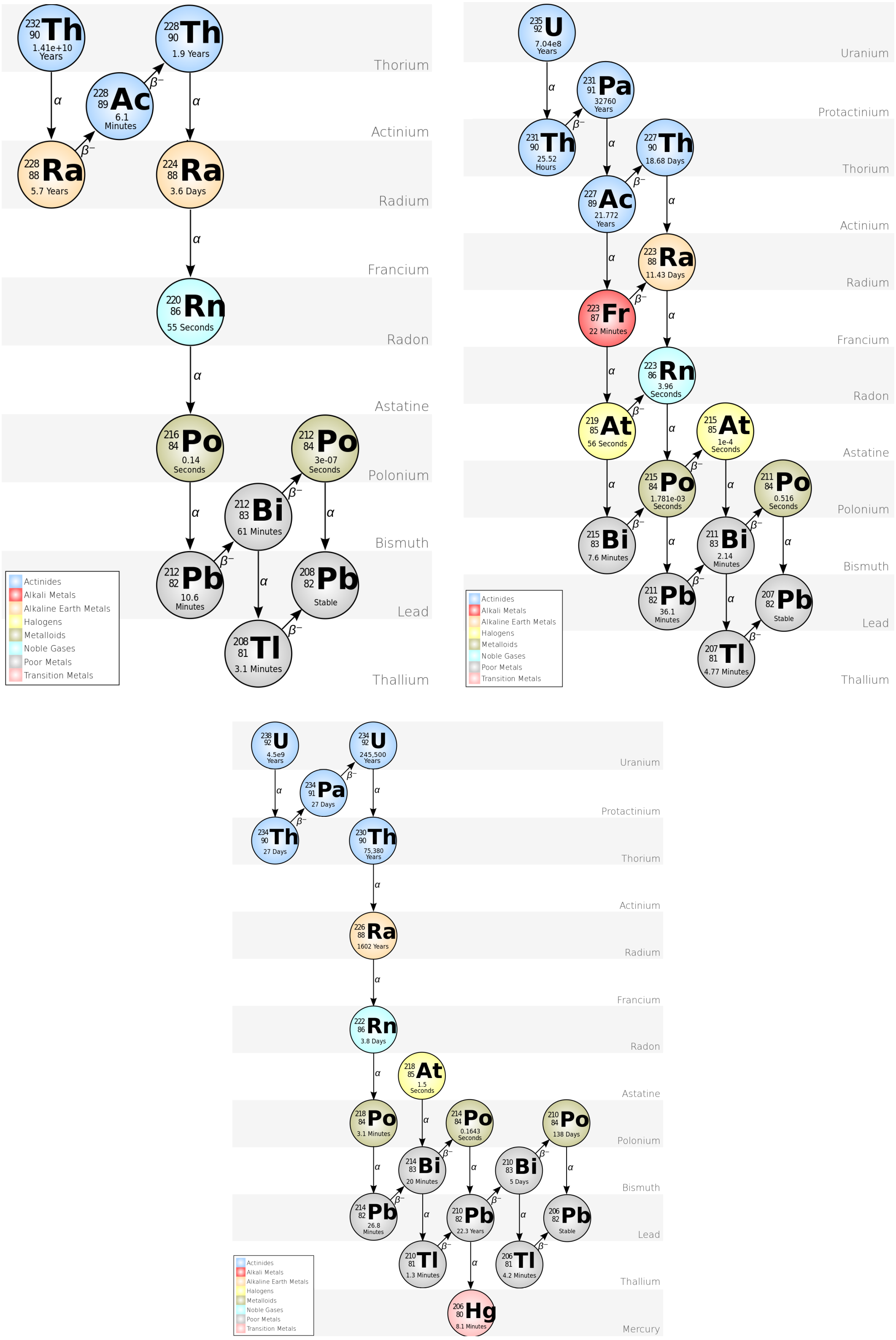

Figure B.1.: Primordial decay chains of ^{232}Th (*top left*), ^{235}U (*top right*) and ^{238}U (*bottom*). Schemes taken from [204].

Appendix C

The Gerda experiment

C.1 Detector list

name	type	m [g]	f_{76}	f_{av}	FCCD (DL) [mm]
ANG1	semi-coaxial	958	0.859(29)	0.830(52)	1.8(5)
ANG2	semi-coaxial	2833	0.866(25)	0.871(51)	2.3(7)
ANG3	semi-coaxial	2391	0.883(26)	0.866(57)	1.9(7)
ANG4	semi-coaxial	2372	0.863(13)	0.901(57)	1.4(7)
ANG5	semi-coaxial	2746	0.856(13)	0.831(48)	2.6(6)
RG1	semi-coaxial	2110	0.855(15)	0.904(59)	1.5(7)
RG2	semi-coaxial	2166	0.855(15)	0.831(53)	2.3(7)
RG3	semi-coaxial	2087	0.855(15)	0.895(54)	1.4(7)
GFT32	semi-coaxial	2321	0.078(1)		0.8^{*}
GFT45	semi-coaxial	2312	0.078(1)		0.8^{*}
GFT112	semi-coaxial	2965	0.078(1)		0.8^{*}
GD32A	BEGe	458	0.877(13)	$0.882^{+0.021+0.008}_{-0.021-0.004}$	$0.91^{+0.17+0.03}_{-0.17-0.06}$
GD32B	BEGe	716	0.877(13)	$0.883^{+0.014+0.006}_{-0.014-0.006}$	$1.05^{+0.13+0.03}_{-0.13-0.06}$
GD32C	BEGe	743	0.877(13)	$0.895^{+0.014+0.006}_{-0.014-0.003}$	$0.96^{+0.13+0.03}_{-0.13-0.06}$
GD32D	BEGe	720	0.877(13)	$0.913^{+0.014+0.007}_{-0.014-0.003}$	$0.77^{+0.13+0.03}_{-0.13-0.06}$
GD35A	BEGe	768	0.877(13)	$0.902^{+0.017+0.004}_{-0.017-0.003}$	$0.95^{+0.17+0.03}_{-0.17-0.04}$
GD35B	BEGe	810	0.877(13)	$0.914^{+0.014+0.006}_{-0.014-0.003}$	$0.78^{+0.13+0.03}_{-0.13-0.06}$
GD35C	BEGe	634	0.877(13)	$0.902^{+0.014+0.007}_{-0.014-0.004}$	$0.79^{+0.12+0.03}_{-0.12-0.06}$
GD61A	BEGe	731	0.877(13)	$0.892^{+0.016+0.005}_{-0.015-0.004}$	$1.01^{+0.15+0.04}_{-0.15-0.05}$
GD61B	BEGe	751	0.877(13)	$0.887^{+0.016+0.007}_{-0.016-0.003}$	$1.00^{+0.15+0.03}_{-0.15-0.06}$
GD61C	BEGe	634	0.877(13)	$0.887^{+0.015+0.008}_{-0.015-0.004}$	$0.92^{+0.13+0.03}_{-0.13-0.07}$
GD76B	BEGe	384	0.877(13)	$0.848^{+0.018+0.009}_{-0.018-0.004}$	$1.14^{+0.14+0.03}_{-0.14-0.07}$
GD76C	BEGe	824	0.877(13)	$0.878^{+0.015+0.006}_{-0.015-0.003}$	$1.14^{+0.15+0.03}_{-0.15-0.06}$
GD79B	BEGe	736	0.877(13)	$0.881^{+0.018+0.007}_{-0.018-0.003}$	$1.04^{+0.16+0.03}_{-0.16-0.06}$
GD79C	BEGe	812	0.877(13)	$0.878^{+0.014+0.006}_{-0.014-0.003}$	$1.10^{+0.13+0.03}_{-0.13-0.06}$
GD89A	BEGe	524	0.877(13)	$0.882^{+0.019+0.006}_{-0.018-0.003}$	$0.99^{+0.16+0.03}_{-0.16-0.05}$
GD89B	BEGe	620	0.877(13)	$0.859^{+0.019+0.007}_{-0.019-0.004}$	$1.13^{+0.16+0.03}_{-0.16-0.06}$
GD89C	BEGe	595	0.877(13)	$0.874^{+0.020+0.009}_{-0.019-0.004}$	$0.99^{+0.16+0.03}_{-0.16-0.07}$
GD89D	BEGe	526	0.877(13)	$0.863^{+0.018+0.009}_{-0.018-0.004}$	$1.02^{+0.14+0.03}_{-0.14-0.07}$
GD91A	BEGe	627	0.877(13)	$0.889^{+0.016+0.005}_{-0.017-0.003}$	$0.99^{+0.16+0.03}_{-0.15-0.05}$
GD91B	BEGe	650	0.877(13)	$0.889^{+0.016+0.007}_{-0.016-0.003}$	$0.96^{+0.14+0.03}_{-0.14-0.06}$
GD91C	BEGe	627	0.877(13)	$0.887^{+0.017+0.007}_{-0.017-0.003}$	$0.96^{+0.15+0.03}_{-0.15-0.06}$
GD91D	BEGe	693	0.877(13)	$0.888^{+0.017+0.007}_{-0.017-0.003}$	$0.99^{+0.16+0.03}_{-0.16-0.06}$
GD00A	BEGe	496	0.877(13)	$0.886^{+0.017+0.006}_{-0.018-0.004}$	$0.91^{+0.15+0.03}_{-0.14-0.05}$
GD00B	BEGe	697	0.877(13)	$0.880^{+0.017+0.007}_{-0.017-0.003}$	$1.04^{+0.15+0.03}_{-0.15-0.06}$
GD00C	BEGe	815	0.877(13)	$0.892^{+0.017+0.006}_{-0.016-0.003}$	$1.01^{+0.16+0.03}_{-0.16-0.06}$
GD00D	BEGe	813	0.877(13)	$0.889^{+0.016+0.006}_{-0.016-0.003}$	$1.02^{+0.15+0.03}_{-0.15-0.06}$
GD02A	BEGe	545	0.877(13)	$0.896^{+0.014+0.006}_{-0.014-0.003}$	$0.86^{+0.12+0.03}_{-0.12-0.05}$
GD02B	BEGe	625	0.877(13)	$0.885^{+0.016+0.007}_{-0.016-0.003}$	$0.97^{+0.14+0.03}_{-0.14-0.06}$
GD02C	BEGe	788	0.877(13)	$0.888^{+0.016+0.006}_{-0.016-0.003}$	$1.03^{+0.15+0.03}_{-0.15-0.06}$
GD02D	BEGe	662	0.877(13)	$0.834^{+0.016+0.000}_{-0.016-0.003}$	$1.45^{+0.15+0.03}_{-0.15-0.00}$

Table C.1.: List of GERDA detectors. Given are their total mass m, their fraction of ^{76}Ge f_{76}, the active volume fraction f_{av} and the dead layer (DL), or more precisely the full charge collection depth (FCCD). ANG detectors are refurbished from the HDM experiment, RG detectors from the IGEX experiment. GTF denote natural detectors from the Genius Test Facility. BEGe detectors labeled with GD are manufactured especially for the GERDA experiment. The Information for the ANG and RG detectors is taken from an internal note [146]. The information for the BEGe detectors is taken from [205]. The values marked with an asterisk are taken from the implementation in the MaGe simulation framework.

C.2 Run list

	run	start	end	live-time [d]	remark
Phase Ia	Run25	Nov 09, 2011	Dec 02, 2011	20.51	not blinded
	Run26	Dec 02, 2011	Jan 11, 2012	39.28	not blinded
	Run27	Jan 11, 2012	Jan 16, 2012	5.18	
	Run28	Jan 16, 2012	Jan 26, 2012	9.57	
	Run29	Jan 26, 2012	Feb 16, 2012	20.41	
	Run30	Feb 17, 2012	Mar 21, 2012	30.94	
	Run31	Mar 24, 2012	Apr 23, 2012	21.60	very unstable, revision in March 2013
	Run32	Apr 23, 2012	May 22, 2012	26.60	
PIb	Run33*	May 31, 2012	Jun 15, 2012	11.22	one-string arm removed, very unstable and not usable for physics analysis
	Run34*	Jun 15, 2012	Jul 02, 2012	14.82	
Phase Ic	Run35*	Jul 08, 2012	Jul 27, 2012	17.77	one-string arm reinserted, carrying five new BEGe detectors
	Run36	Jul 27, 2012	Sep 03, 2012	37.74	
	Run37	Sep 03, 2012	Sep 27, 2012	23.46	
	Run38	Sep 27, 2012	Oct 11, 2012	13.88	
	Run39a	Oct 11, 2012	Oct 29, 2012	15.28	
	Run39b	Oct 29, 2012	Nov 08, 2012	9.47	
	Run40	Nov 08, 2012	Dec 13, 2012	34.53	
	Run41	Dec 13, 2012	Jan 05, 2013	21.50	
	Run42	Jan 05, 2013	Feb 07, 2013	32.04	
	Run43	Feb 07, 2013	Mar 03, 2013	22.78	RG2 probably experienced a discharged and is not usable after this run
	Run44a	Mar 03, 2013	Mar 04, 2013	1.42	all detectors on the three-string arm excluded from analysis, due to large jumps in the pulser position, related to RG2
	Run44	Mar 04, 2013	Mar 28, 2013	22.84	Major blackout at the LNGS on Mar 28
	Run45	Mar 29, 2013	May 02, 2013	33.13	
	Run46a	May 02, 2013	May 14, 2013	12.13	
	Run46b	May 15, 2013	May 21, 2013	5.61	unexplained large shift of pulser position in GD32D
PI-extra	Run47	May 31, 2013	Jul 02, 2013	31.44	not blinded. one-string arm removed
	Run48a	Jul 03, 2013	Jul 30, 2013	10.22	not blinded, water tank emptied during this run
	Run48-coinc	Aug 14, 2013	Aug 21, 2013	6.89	not blinded, only multiplicity>1 events acquired
	Run48b	Aug 21, 2013	Sep 05, 2013	14.66	not blinded, water tank partially filled

Table C.2.: List of PI physics runs. Runs marked with an asterisk are excluded from the golden data set due to a

	run	start	end	live-time [d]	remark
Phase IIa	Run53	Dec 20, 2015	Jan 25, 2016	18.70	not blinded
	Run54	Jan 25, 2016	Jan 29, 2016	3.48	
	Run55	Jan 29, 2016	Feb 03, 2016	4.95	
	Run56	Feb 03, 2016	Feb 19, 2016	14.54	
	Run57	Feb 19, 2016	Feb 24, 2016	4.57	
	Run58	Feb 24, 2016	Mar 09, 2016	11.94	
	Run59	Mar 12, 2016	Mar 17, 2016	4.67	
	Run60	Mar 17, 2016	Apr 06, 2016	18.50	
	Run61	Apr 06, 2016	Apr 12, 2016	2.97	
	Run62	Apr 12, 2016	Apr 29, 2016	15.91	
	Run63	Apr 29, 2016	May 23, 2016	22.36	
	Run64	May 23, 2016	Jun 01, 2016	8.52	
Phase IIb	Run65	Jun 01, 2016	Jun 12, 2016	12.91	
	Run66	Jun 16, 2016	Jun 22, 2016	-	muon veto not active
	Run67	Jun 22, 2016	Jul 01, 2016	8.41	
	Run68	Jul 01, 2016	Jul 21, 2016	-	no test pulses
	Run69	Jul 21, 2016	Jul 27, 2016	5.55	JFET of GD91C not working any longer; short power cut after the run
	Run70	Jul 27, 2016	Aug 23, 2016	25.51	earthquake in the night of August 24, all PMTs tripped
	Run71	Aug 24, 2016	Sep 23, 2016	28.14	
	Run72	Sep 23, 2016	Sep 29, 2016	5.19	change of 75 Ohm cables between flange and electronics cabinet
	Run73	Sep 29, 2016	Oct 30, 2016	30.00	
	Run74	Oct 30, 2016	Dec 01, 2016	30.99	
	Run75	Dec 01, 2016	Jan 09, 2017	38.53	
	Run76	Jan 09, 2017	Feb 09, 2017	26.01	
	Run77	Feb 09, 2017	Mar 13, 2017	31.36	
	Run78	Mar 13, 2017	Apr 04, 2017	21.87	
	Run79	Apr 05, 2017	Apr 15, 2017	9.55	false cryostat alarm caused the water tank to get drained on April 15

Table C.3.: List of PII physics runs.

C.3 Detector status

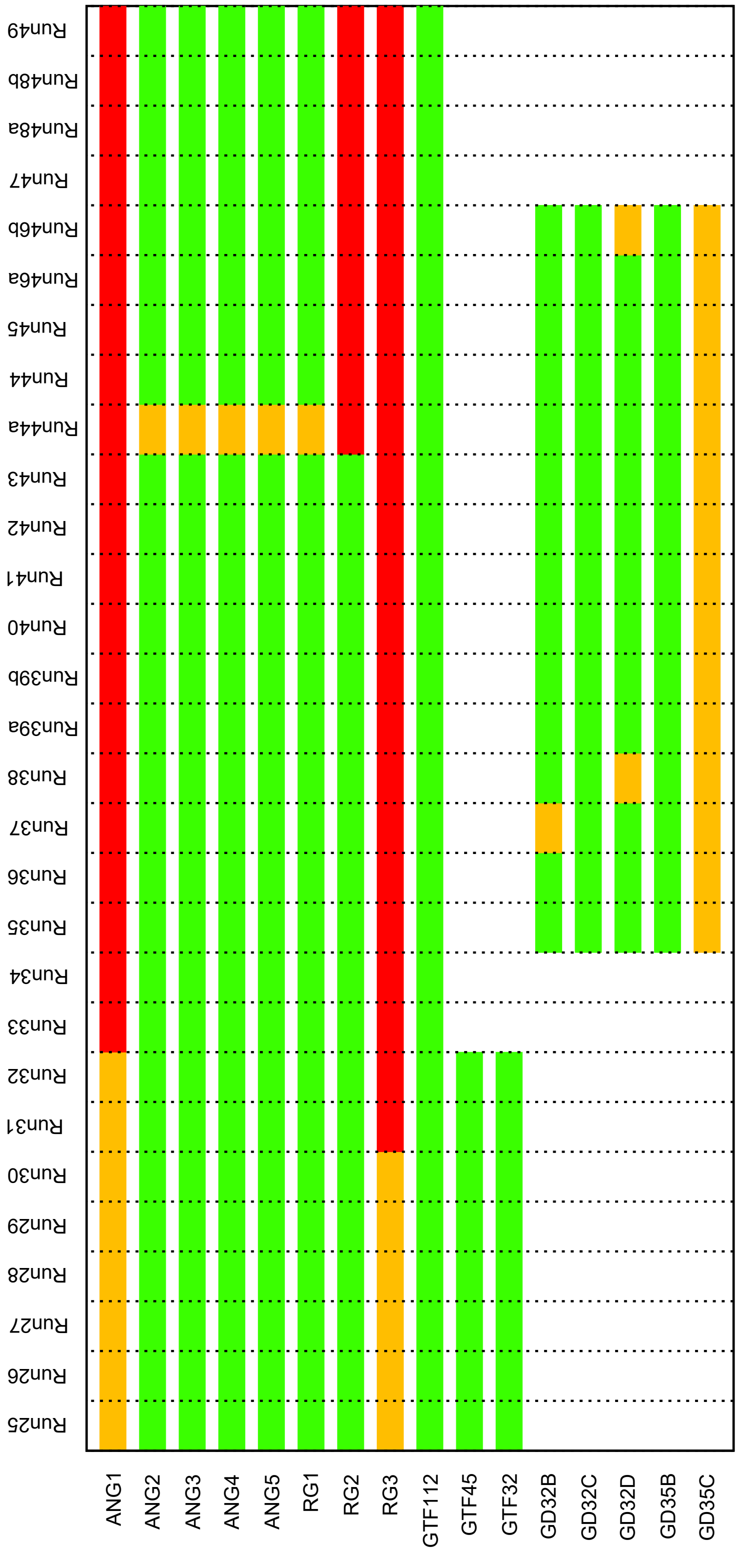

	ANG1	ANG2	ANG3	ANG4	ANG5	RG1	RG2	RG3	GTF112	GTF45	GTF32	GD32B	GD32C	GD32D	GD35B	GD35C
Run25	🟧	🟩	🟩	🟩	🟩	🟩	🟩	🟧	🟩	🟩	🟩					
Run26	🟧	🟩	🟩	🟩	🟩	🟩	🟩	🟧	🟩	🟩	🟩					
Run27	🟧	🟩	🟩	🟩	🟩	🟩	🟩	🟧	🟩	🟩	🟩					
Run28	🟧	🟩	🟩	🟩	🟩	🟩	🟩	🟧	🟩	🟩	🟩					
Run29	🟧	🟩	🟩	🟩	🟩	🟩	🟩	🟧	🟩	🟩	🟩					
Run30	🟧	🟩	🟩	🟩	🟩	🟩	🟩	🟧	🟩	🟩	🟩					
Run31	🟧	🟩	🟩	🟩	🟩	🟩	🟩	🟥	🟩	🟩	🟩					
Run32	🟧	🟩	🟩	🟩	🟩	🟩	🟩	🟥	🟩	🟩	🟩					
Run33	🟥	🟩	🟩	🟩	🟩	🟩	🟩	🟥	🟩							
Run34	🟥	🟩	🟩	🟩	🟩	🟩	🟩	🟥	🟩							
Run35	🟥	🟩	🟩	🟩	🟩	🟩	🟩	🟥	🟩			🟩	🟩	🟩	🟩	🟧
Run36	🟥	🟩	🟩	🟩	🟩	🟩	🟩	🟥	🟩			🟩	🟩	🟩	🟩	🟧
Run37	🟥	🟩	🟩	🟩	🟩	🟩	🟩	🟥	🟩			🟧	🟩	🟩	🟩	🟧
Run38	🟥	🟩	🟩	🟩	🟩	🟩	🟩	🟥	🟩			🟩	🟩	🟧	🟩	🟧
Run39a	🟥	🟩	🟩	🟩	🟩	🟩	🟩	🟥	🟩			🟩	🟩	🟩	🟩	🟧
Run39b	🟥	🟩	🟩	🟩	🟩	🟩	🟩	🟥	🟩			🟩	🟩	🟩	🟩	🟧
Run40	🟥	🟩	🟩	🟩	🟩	🟩	🟩	🟥	🟩			🟩	🟩	🟩	🟩	🟧
Run41	🟥	🟩	🟩	🟩	🟩	🟩	🟩	🟥	🟩			🟩	🟩	🟩	🟩	🟧
Run42	🟥	🟩	🟩	🟩	🟩	🟩	🟩	🟥	🟩			🟩	🟩	🟩	🟩	🟧
Run43	🟥	🟩	🟩	🟩	🟩	🟩	🟩	🟥	🟩			🟩	🟩	🟩	🟩	🟧
Run44a	🟥	🟧	🟧	🟧	🟧	🟧	🟥	🟥	🟩			🟩	🟩	🟩	🟩	🟧
Run44	🟥	🟩	🟩	🟩	🟩	🟩	🟥	🟥	🟩			🟩	🟩	🟩	🟩	🟧
Run45	🟥	🟩	🟩	🟩	🟩	🟩	🟥	🟥	🟩			🟩	🟩	🟩	🟩	🟧
Run46a	🟥	🟩	🟩	🟩	🟩	🟩	🟥	🟥	🟩			🟩	🟩	🟩	🟩	🟧
Run46b	🟥	🟩	🟩	🟩	🟩	🟩	🟥	🟥	🟩			🟩	🟩	🟧	🟩	🟧
Run47	🟥	🟩	🟩	🟩	🟩	🟩	🟥	🟥	🟩							
Run48a	🟥	🟩	🟩	🟩	🟩	🟩	🟥	🟥	🟩							
Run48b	🟥	🟩	🟩	🟩	🟩	🟩	🟥	🟥	🟩							
Run49	🟥	🟩	🟩	🟩	🟩	🟩	🟥	🟥	🟩							

Figure C.1.: Status of the detector in each run of PI (green: running, orange: running but only used as anti-coincidence veto, red: switched off).

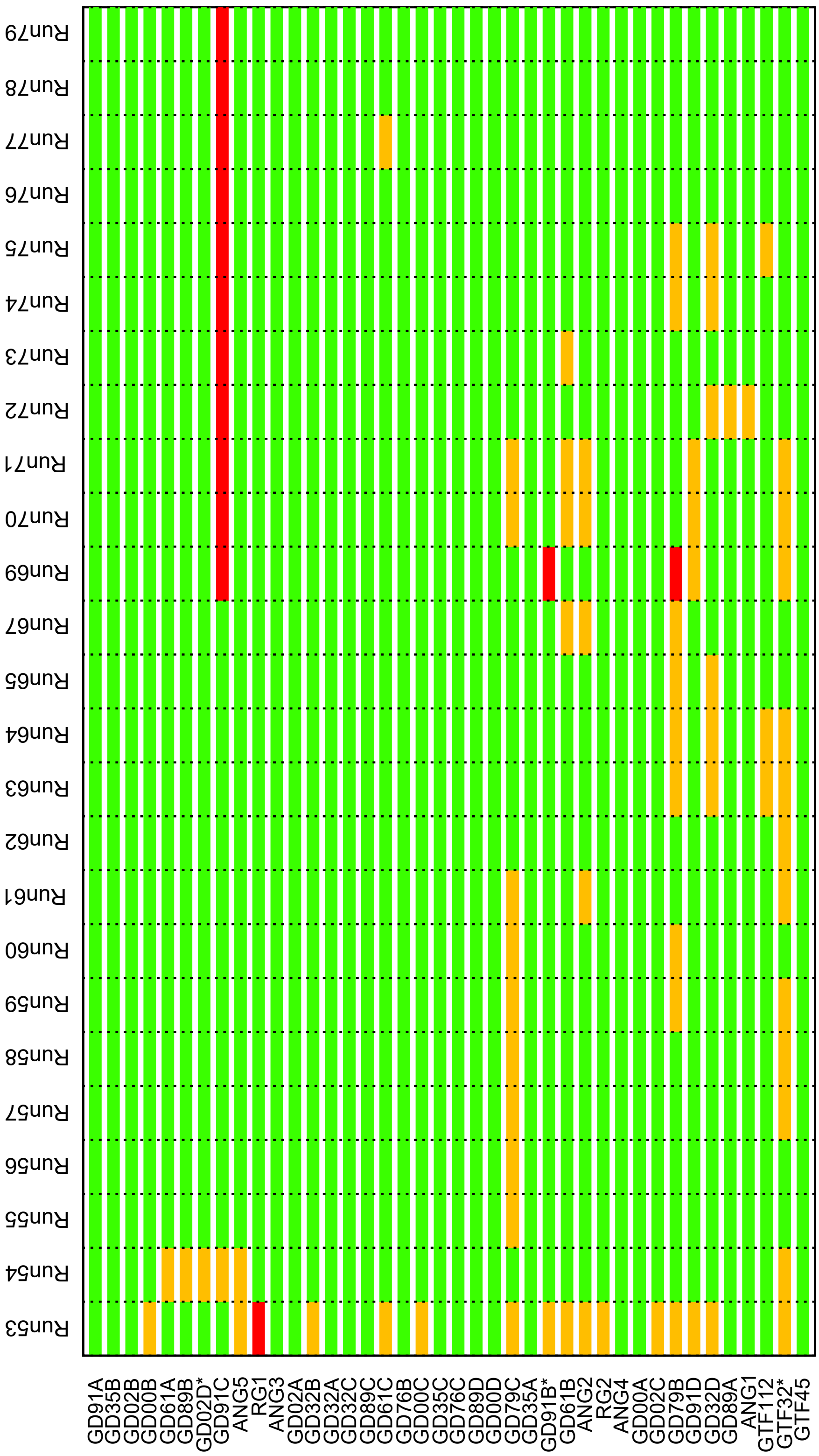

	Run53	Run54	Run55	Run56	Run57	Run58	Run59	Run60	Run61	Run62	Run63	Run64	Run65	Run67	Run69	Run70	Run71	Run72	Run73	Run74	Run75	Run76	Run77	Run78	Run79
GD91A	🟩	🟩	🟩	🟩	🟩	🟩	🟩	🟩	🟩	🟩	🟩	🟩	🟩	🟩	🟩	🟩	🟩	🟩	🟩	🟩	🟩	🟩	🟩	🟩	🟩
GD35B	🟩	🟩	🟩	🟩	🟩	🟩	🟩	🟩	🟩	🟩	🟩	🟩	🟩	🟩	🟩	🟩	🟩	🟩	🟩	🟩	🟩	🟩	🟩	🟩	🟩
GD02B	🟩	🟩	🟩	🟩	🟩	🟩	🟩	🟩	🟩	🟩	🟩	🟩	🟩	🟩	🟩	🟩	🟩	🟩	🟩	🟩	🟩	🟩	🟩	🟩	🟩
GD00B	🟧	🟩	🟩	🟩	🟩	🟩	🟩	🟩	🟩	🟩	🟩	🟩	🟩	🟩	🟩	🟩	🟩	🟩	🟩	🟩	🟩	🟩	🟩	🟩	🟩
GD61A	🟩	🟧	🟩	🟩	🟩	🟩	🟩	🟩	🟩	🟩	🟩	🟩	🟩	🟩	🟩	🟩	🟩	🟩	🟩	🟩	🟩	🟩	🟩	🟩	🟩
GD89B	🟩	🟧	🟩	🟩	🟩	🟩	🟩	🟩	🟩	🟩	🟩	🟩	🟩	🟩	🟩	🟩	🟩	🟩	🟩	🟩	🟩	🟩	🟩	🟩	🟩
GD02D*	🟩	🟧	🟩	🟩	🟩	🟩	🟩	🟩	🟩	🟩	🟩	🟩	🟩	🟩	🟩	🟩	🟩	🟩	🟩	🟩	🟩	🟩	🟩	🟩	🟩
GD91C	🟩	🟧	🟩	🟩	🟩	🟩	🟩	🟩	🟩	🟩	🟩	🟩	🟩	🟩	🟥	🟥	🟥	🟥	🟥	🟥	🟥	🟥	🟥	🟥	🟥
ANG5	🟧	🟧	🟩	🟩	🟩	🟩	🟩	🟩	🟩	🟩	🟩	🟩	🟩	🟩	🟩	🟩	🟩	🟩	🟩	🟩	🟩	🟩	🟩	🟩	🟩
RG1	🟥	🟩	🟩	🟩	🟩	🟩	🟩	🟩	🟩	🟩	🟩	🟩	🟩	🟩	🟩	🟩	🟩	🟩	🟩	🟩	🟩	🟩	🟩	🟩	🟩
ANG3	🟩	🟩	🟩	🟩	🟩	🟩	🟩	🟩	🟩	🟩	🟩	🟩	🟩	🟩	🟩	🟩	🟩	🟩	🟩	🟩	🟩	🟩	🟩	🟩	🟩
GD02A	🟩	🟩	🟩	🟩	🟩	🟩	🟩	🟩	🟩	🟩	🟩	🟩	🟩	🟩	🟩	🟩	🟩	🟩	🟩	🟩	🟩	🟩	🟩	🟩	🟩
GD32B	🟧	🟩	🟩	🟩	🟩	🟩	🟩	🟩	🟩	🟩	🟩	🟩	🟩	🟩	🟩	🟩	🟩	🟩	🟩	🟩	🟩	🟩	🟩	🟩	🟩
GD32A	🟩	🟩	🟩	🟩	🟩	🟩	🟩	🟩	🟩	🟩	🟩	🟩	🟩	🟩	🟩	🟩	🟩	🟩	🟩	🟩	🟩	🟩	🟩	🟩	🟩
GD32C	🟩	🟩	🟩	🟩	🟩	🟩	🟩	🟩	🟩	🟩	🟩	🟩	🟩	🟩	🟩	🟩	🟩	🟩	🟩	🟩	🟩	🟩	🟩	🟩	🟩
GD89C	🟩	🟩	🟩	🟩	🟩	🟩	🟩	🟩	🟩	🟩	🟩	🟩	🟩	🟩	🟩	🟩	🟩	🟩	🟩	🟩	🟩	🟩	🟩	🟩	🟩
GD61C	🟧	🟩	🟩	🟩	🟩	🟩	🟩	🟩	🟩	🟩	🟩	🟩	🟩	🟩	🟩	🟩	🟩	🟩	🟩	🟩	🟩	🟩	🟧	🟩	🟩
GD76B	🟩	🟩	🟩	🟩	🟩	🟩	🟩	🟩	🟩	🟩	🟩	🟩	🟩	🟩	🟩	🟩	🟩	🟩	🟩	🟩	🟩	🟩	🟩	🟩	🟩
GD00C	🟧	🟩	🟩	🟩	🟩	🟩	🟩	🟩	🟩	🟩	🟩	🟩	🟩	🟩	🟩	🟩	🟩	🟩	🟩	🟩	🟩	🟩	🟩	🟩	🟩
GD35C	🟩	🟩	🟩	🟩	🟩	🟩	🟩	🟩	🟩	🟩	🟩	🟩	🟩	🟩	🟩	🟩	🟩	🟩	🟩	🟩	🟩	🟩	🟩	🟩	🟩
GD76C	🟩	🟩	🟩	🟩	🟩	🟩	🟩	🟩	🟩	🟩	🟩	🟩	🟩	🟩	🟩	🟩	🟩	🟩	🟩	🟩	🟩	🟩	🟩	🟩	🟩
GD89D	🟩	🟩	🟩	🟩	🟩	🟩	🟩	🟩	🟩	🟩	🟩	🟩	🟩	🟩	🟩	🟩	🟩	🟩	🟩	🟩	🟩	🟩	🟩	🟩	🟩
GD00D	🟩	🟩	🟩	🟩	🟩	🟩	🟩	🟩	🟩	🟩	🟩	🟩	🟩	🟩	🟩	🟩	🟩	🟩	🟩	🟩	🟩	🟩	🟩	🟩	🟩
GD79C	🟧	🟩	🟧	🟧	🟧	🟧	🟧	🟧	🟧	🟩	🟩	🟩	🟩	🟩	🟩	🟧	🟧	🟩	🟩	🟩	🟩	🟩	🟩	🟩	🟩
GD35A	🟩	🟩	🟩	🟩	🟩	🟩	🟩	🟩	🟩	🟩	🟩	🟩	🟩	🟩	🟩	🟩	🟩	🟩	🟩	🟩	🟩	🟩	🟩	🟩	🟩
GD91B*	🟧	🟩	🟩	🟩	🟩	🟩	🟩	🟩	🟩	🟩	🟩	🟩	🟩	🟩	🟥	🟩	🟩	🟩	🟩	🟩	🟩	🟩	🟩	🟩	🟩
GD61B	🟧	🟩	🟩	🟩	🟩	🟩	🟩	🟩	🟩	🟩	🟩	🟩	🟩	🟧	🟩	🟧	🟧	🟩	🟧	🟩	🟩	🟩	🟩	🟩	🟩
ANG2	🟧	🟩	🟩	🟩	🟩	🟩	🟩	🟩	🟧	🟩	🟩	🟩	🟩	🟧	🟩	🟧	🟧	🟩	🟩	🟩	🟩	🟩	🟩	🟩	🟩
RG2	🟧	🟩	🟩	🟩	🟩	🟩	🟩	🟩	🟩	🟩	🟩	🟩	🟩	🟩	🟩	🟩	🟩	🟩	🟩	🟩	🟩	🟩	🟩	🟩	🟩
ANG4	🟩	🟩	🟩	🟩	🟩	🟩	🟩	🟩	🟩	🟩	🟩	🟩	🟩	🟩	🟩	🟩	🟩	🟩	🟩	🟩	🟩	🟩	🟩	🟩	🟩
GD00A	🟩	🟩	🟩	🟩	🟩	🟩	🟩	🟩	🟩	🟩	🟩	🟩	🟩	🟩	🟩	🟩	🟩	🟩	🟩	🟩	🟩	🟩	🟩	🟩	🟩
GD02C	🟧	🟩	🟩	🟩	🟩	🟩	🟩	🟩	🟩	🟩	🟩	🟩	🟩	🟩	🟩	🟩	🟩	🟩	🟩	🟩	🟩	🟩	🟩	🟩	🟩
GD79B	🟧	🟩	🟩	🟩	🟩	🟩	🟧	🟧	🟩	🟩	🟧	🟧	🟧	🟧	🟥	🟩	🟩	🟩	🟩	🟧	🟧	🟩	🟩	🟩	🟩
GD91D	🟧	🟩	🟩	🟩	🟩	🟩	🟩	🟩	🟩	🟩	🟩	🟩	🟩	🟩	🟧	🟧	🟧	🟩	🟩	🟩	🟩	🟩	🟩	🟩	🟩
GD32D	🟧	🟩	🟩	🟩	🟩	🟩	🟩	🟩	🟩	🟩	🟧	🟧	🟧	🟩	🟩	🟩	🟩	🟧	🟩	🟧	🟧	🟩	🟩	🟩	🟩
GD89A	🟩	🟩	🟩	🟩	🟩	🟩	🟩	🟩	🟩	🟩	🟩	🟩	🟩	🟩	🟩	🟩	🟩	🟧	🟩	🟩	🟩	🟩	🟩	🟩	🟩
ANG1	🟩	🟩	🟩	🟩	🟩	🟩	🟩	🟩	🟩	🟩	🟩	🟩	🟩	🟩	🟩	🟩	🟩	🟧	🟩	🟩	🟩	🟩	🟩	🟩	🟩
GTF112	🟩	🟩	🟩	🟩	🟩	🟩	🟩	🟩	🟩	🟩	🟧	🟧	🟩	🟩	🟩	🟩	🟩	🟩	🟩	🟩	🟧	🟩	🟩	🟩	🟩
GTF32*	🟧	🟧	🟩	🟩	🟧	🟧	🟧	🟩	🟧	🟧	🟧	🟧	🟩	🟩	🟧	🟧	🟧	🟩	🟩	🟩	🟩	🟩	🟩	🟩	🟩
GTF45	🟩	🟩	🟩	🟩	🟩	🟩	🟩	🟩	🟩	🟩	🟩	🟩	🟩	🟩	🟩	🟩	🟩	🟩	🟩	🟩	🟩	🟩	🟩	🟩	🟩

Figure C.2.: Status of the detector in each run of PII (green: running, orange: running but only used as anti-coincidence veto, red: switched off).

Appendix D

Coincidence data set of the Gerda experiment

D.1 Additional crosstalk examples

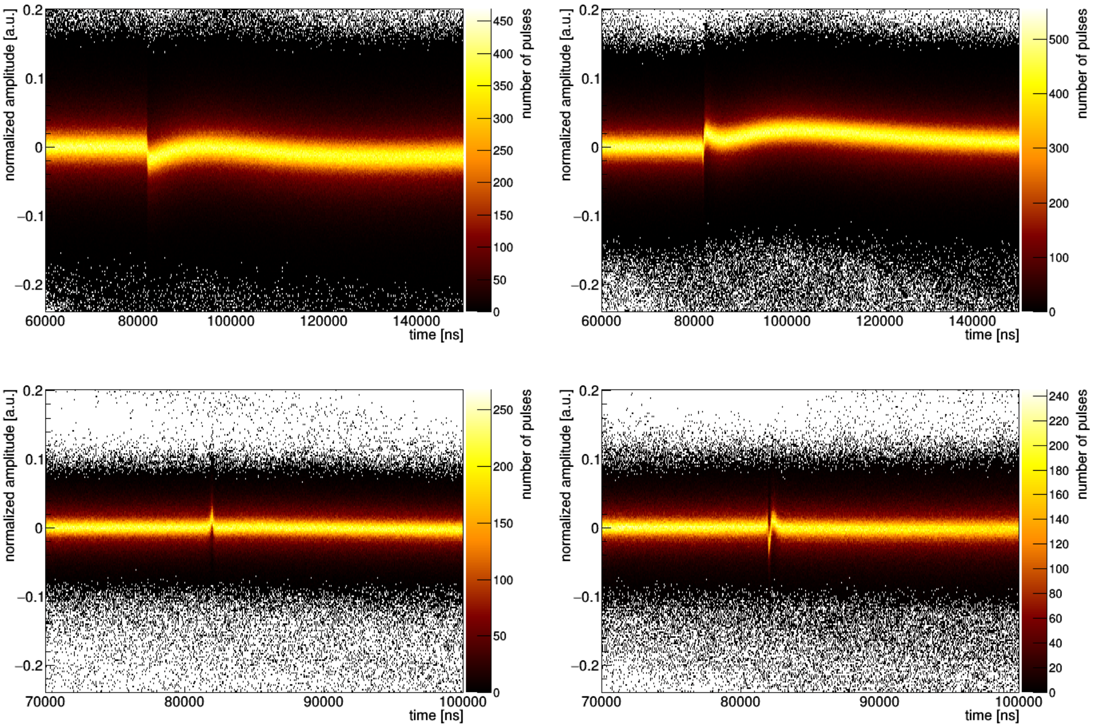

Figure D.1.: Example of crosstalk signatures for (6 → 4), (6 → 5), (13 → 11) and (13 → 12). Using the data from calibration C1302.

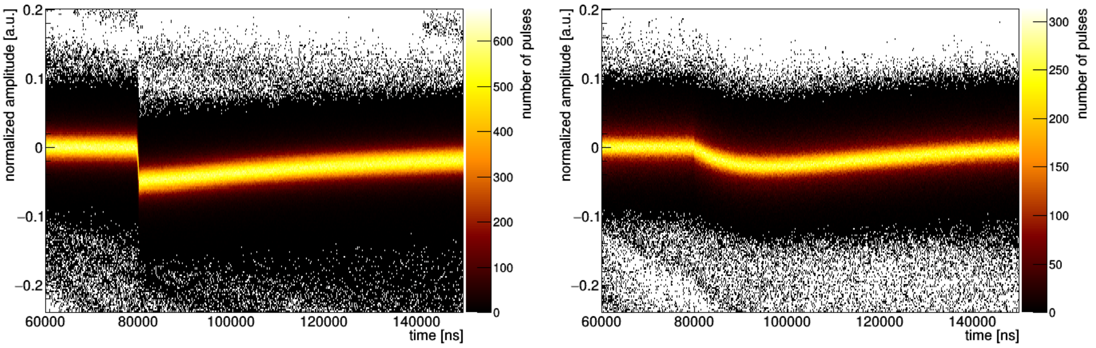

Figure D.2.: Example of crosstalk signatures for (38 → 23) (similar to (39 → 23)) and (3 → 36) (similar to (18 → 27)). Using the data from calibration C1605.

D.2 Phase I matrices with *avg* method

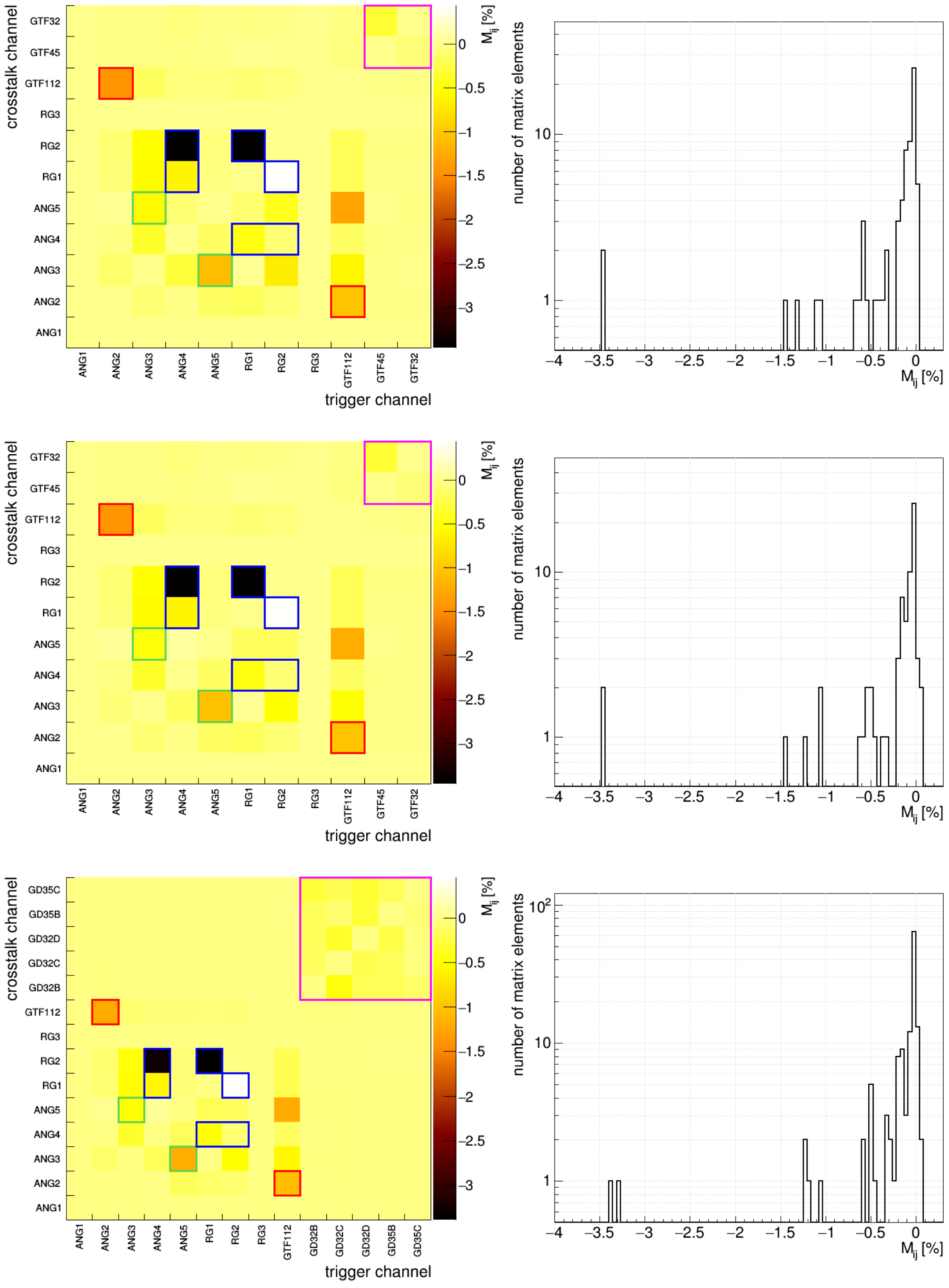

Figure D.3.: Crosstalk matrix determined with *avg* method for PIa from Run 25 to 30 (*top*) and from Run 31 to 32 (*middle*) as well as for PIc for Runs 36 to 46 obtained from calibration C1302 (*bottom*). The elements of detector pairs within a string are framed in red (string 1), blue (string 2), green (string 3) and magenta (string 4). The detector names are in the order of their channel number, starting with channel 0 (ANG1).

D.3 Crosstalk matrices elements values

	0	1	2	3	4	5	6	7	8	9	10
0	0.000	0.000	0.000	0.000	0.000	0.000	0.000	0.000	0.000	0.000	0.000
1	0.000	0.000	-0.117	-0.027	0.028	-0.078	-0.094	0.000	-1.437	-0.012	-0.012
2	0.000	-0.093	0.000	-0.359	-0.580	-0.561	-0.531	0.000	-0.161	-0.021	-0.018
3	0.000	-0.015	-0.303	0.000	-0.090	-0.632	-3.466	0.000	-0.066	-0.024	-0.056
4	0.000	-0.154	-1.097	-0.149	0.000	-0.047	-0.059	0.000	-0.065	-0.012	-0.012
5	0.000	-0.182	0.036	-0.473	-0.100	0.000	-3.450	0.000	-0.093	0.012	-0.022
6	0.000	-0.094	-0.684	-0.098	-0.421	0.438	0.000	0.000	-0.064	0.006	-0.017
7	0.000	0.000	0.000	0.000	0.000	0.000	0.000	0.000	0.000	0.000	0.000
8	0.000	-1.046	-0.589	-0.152	-1.314	-0.204	-0.203	0.000	0.000	-0.051	-0.034
9	0.000	-0.019	-0.010	-0.024	-0.003	-0.017	-0.025	0.000	-0.012	0.000	-0.342
10	0.000	-0.014	0.003	-0.021	-0.022	-0.012	-0.024	0.000	-0.022	-0.081	0.000

Table D.1.: Matrix obtained with the *avg* method which is used for PIa Runs 25 to 30. Each row correspond to a certain trigger channel, while columns correspond to the crosstalk channels. The values are given in %. Note that channels 0 (ANG1) and 7 (RG3) are excluded from all physics analyses.

	0	1	2	3	4	5	6	7	8	9	10
0	0.000	0.000	0.000	0.000	0.000	0.000	0.000	0.000	0.000	0.000	0.000
1	0.000	0.000	-0.074	-0.027	0.054	-0.078	-0.094	0.000	-1.437	-0.012	-0.012
2	0.000	-0.093	0.000	-0.359	-0.497	-0.561	-0.531	0.000	-0.161	-0.021	-0.018
3	0.000	-0.015	-0.170	0.000	0.056	-0.632	-3.466	0.000	-0.066	-0.024	-0.056
4	0.000	-0.154	-1.051	-0.149	0.000	-0.047	-0.059	0.000	-0.065	-0.012	-0.012
5	0.000	-0.182	0.031	-0.473	-0.169	0.000	-3.450	0.000	-0.093	0.012	-0.022
6	0.000	-0.094	-0.531	-0.098	-0.169	0.438	0.000	0.000	-0.064	0.006	-0.017
7	0.000	0.000	0.000	0.000	0.000	0.000	0.000	0.000	0.000	0.000	0.000
8	0.000	-1.046	-0.516	-0.152	-1.242	-0.204	-0.203	0.000	0.000	-0.051	-0.034
9	0.000	-0.019	-0.006	-0.024	-0.005	-0.017	-0.025	0.000	-0.012	0.000	-0.342
10	0.000	-0.014	-0.017	-0.021	-0.008	-0.012	-0.024	0.000	-0.022	-0.081	0.000

Table D.2.: Matrix obtained with the *avg* method which is used for PIa Runs 31 to 32. Each row correspond to a certain trigger channel, while columns correspond to the crosstalk channels. The values are given in %. Note that channels 0 (ANG1) and 7 (RG3) are excluded from all physics analyses.

	0	1	2	3	4	5	6	7	8	9	10	11	12	13
0	0.000	0.000	0.000	0.000	0.000	0.000	0.000	0.000	0.000	0.000	0.000	0.000	0.000	0.000
1	0.000	0.000	-0.099	-0.012	0.043	-0.060	-0.081	0.000	-1.211	-0.019	-0.019	-0.007	-0.007	-0.009
2	0.000	-0.003	0.000	-0.341	-0.487	-0.502	-0.477	0.000	-0.082	-0.009	-0.012	-0.003	-0.001	-0.002
3	0.000	0.006	-0.175	0.000	0.067	-0.579	-3.299	0.000	-0.051	-0.011	-0.012	-0.009	-0.004	-0.006
4	0.000	-0.152	-1.192	-0.153	0.000	-0.050	-0.055	0.000	-0.049	-0.013	-0.018	-0.010	-0.004	-0.005
5	0.000	-0.114	-0.000	-0.489	-0.174	0.000	-3.392	0.000	-0.043	-0.003	-0.007	-0.001	-0.007	-0.001
6	0.000	-0.080	-0.516	-0.070	-0.146	0.454	0.000	0.000	-0.057	-0.008	-0.003	-0.005	-0.005	-0.007
7	0.000	0.000	0.000	0.000	0.000	0.000	0.000	0.000	0.000	0.000	0.000	0.000	0.000	0.000
8	0.000	-1.053	-0.567	-0.136	-1.207	-0.184	-0.184	0.000	0.000	-0.013	-0.013	-0.000	0.001	-0.000
9	0.000	-0.012	-0.015	-0.013	-0.016	-0.014	-0.002	0.000	-0.022	0.000	-0.149	-0.155	-0.164	-0.284
10	0.000	-0.020	-0.017	-0.016	-0.021	-0.018	-0.011	0.000	-0.019	-0.461	0.000	-0.343	-0.082	-0.192
11	0.000	-0.002	-0.006	-0.010	-0.011	-0.006	-0.006	0.000	-0.007	-0.174	-0.198	0.000	-0.285	-0.311
12	0.000	0.001	-0.001	-0.005	-0.010	-0.010	0.002	0.000	-0.004	-0.172	-0.150	-0.238	0.000	-0.178
13	0.000	-0.002	-0.006	-0.008	0.000	-0.010	0.006	0.000	-0.013	-0.110	-0.020	-0.031	-0.067	0.000

Table D.3.: Matrix obtained with the *avg* method from calibration C1302 which is used for PIc Runs 36 to 46. Each row correspond to a certain trigger channel, while columns correspond to the crosstalk channels. The values are given in %. Note that channels 0 (ANG1) and 7 (RG3) are excluded from all physics analyses.

	0	1	2	3	4	5	6	7	8	9	10	11	12	13	14	15	16	17	18	19
0	0.000	-0.237	-0.165	-0.118	-0.156	-0.146	-0.172	-0.154	-0.087	-0.081	-0.124	-0.007	-0.006	-0.028	-0.003	-0.004	-0.025	-0.010	-0.012	0.007
1	-0.201	0.000	-0.241	-0.170	-0.126	-0.116	-0.151	-0.121	-0.065	-0.072	-0.109	-0.023	-0.018	-0.011	-0.013	-0.013	-0.021	-0.023	-0.015	0.007
2	-0.144	-0.256	0.000	-0.245	-0.154	-0.141	-0.152	-0.140	-0.092	-0.100	-0.131	-0.012	-0.011	-0.017	-0.007	-0.005	-0.011	-0.012	-0.012	0.004
3	-0.140	-0.175	-0.294	0.000	-0.195	-0.152	-0.178	-0.158	-0.084	-0.110	-0.156	-0.026	-0.023	-0.016	-0.016	-0.005	-0.016	-0.035	-0.023	0.006
4	-0.030	-0.020	-0.043	-0.098	0.000	-0.257	-0.133	-0.087	-0.027	-0.033	-0.048	-0.015	-0.011	-0.017	-0.014	-0.047	-0.026	-0.016	-0.018	-0.087
5	-0.034	-0.014	-0.045	-0.041	-0.321	0.000	-0.296	-0.131	-0.039	-0.047	-0.060	-0.010	-0.008	-0.017	-0.010	-0.035	-0.043	-0.028	-0.016	-0.064
6	-0.046	-0.041	-0.045	-0.045	-0.139	-0.351	0.000	-0.395	-0.027	-0.033	-0.066	-0.023	-0.021	-0.006	-0.022	-0.016	-0.038	-0.048	-0.015	-0.035
7	-0.116	-0.051	-0.099	-0.065	-0.180	-0.175	-0.566	0.000	-0.073	-0.054	-0.081	-0.009	-0.003	-0.014	-0.008	-0.006	-0.013	-0.033	-0.037	-0.039
8	-0.083	-0.075	-0.114	-0.123	-0.081	-0.077	-0.071	-0.066	0.000	-0.512	-0.634	-0.026	-0.045	-0.057	-0.097	-0.017	-0.044	-0.042	-0.083	-0.001
9	-0.109	-0.113	-0.156	-0.131	-0.094	-0.100	-0.101	-0.085	-0.402	0.000	-0.799	-0.023	-0.022	-0.030	-0.044	-0.035	-0.038	-0.064	-0.090	-0.005
10	-0.128	-0.126	-0.124	-0.113	-0.091	-0.089	-0.113	-0.096	-0.227	-0.372	0.000	-0.033	-0.028	-0.023	-0.025	-0.018	-0.024	-0.036	-0.054	0.006
11	-0.002	-0.015	-0.008	-0.021	-0.007	-0.010	-0.019	-0.005	-0.095	-0.128	-0.237	0.000	-0.200	-0.088	-0.079	-0.062	-0.077	-0.095	-0.072	-0.025
12	-0.024	-0.037	-0.033	-0.060	-0.021	-0.019	-0.040	-0.017	-0.054	-0.088	-0.280	-0.151	0.000	-0.133	-0.093	-0.045	-0.055	-0.071	-0.057	0.000
13	-0.054	-0.043	-0.058	-0.074	-0.032	-0.038	-0.030	-0.045	-0.062	-0.078	-0.253	-0.059	-0.104	0.000	-0.151	-0.046	-0.059	-0.053	-0.051	-0.005
14	-0.048	-0.063	-0.074	-0.094	-0.044	-0.051	-0.070	-0.052	-0.091	-0.067	-0.181	-0.052	-0.068	-0.107	0.000	-0.064	-0.062	-0.057	-0.062	-0.000
15	0.022	0.011	0.017	0.016	-0.024	-0.018	0.004	0.005	0.019	0.011	0.040	-0.037	-0.034	-0.052	-0.100	0.000	-0.264	-0.117	-0.112	-0.127
16	0.002	-0.003	0.011	0.009	0.003	-0.016	-0.018	-0.001	-0.016	0.002	0.018	-0.040	-0.038	-0.047	-0.053	-0.283	0.000	-0.215	-0.160	-0.077
17	0.010	0.003	0.015	-0.010	0.013	-0.008	-0.031	-0.015	-0.060	-0.035	-0.010	-0.063	-0.054	-0.042	-0.054	-0.099	-0.379	0.000	-0.379	-0.044
18	0.011	0.012	0.014	0.004	0.013	0.003	0.004	-0.024	-0.157	-0.072	-0.051	-0.091	-0.051	-0.068	-0.068	-0.085	-0.159	-0.455	0.000	-0.024
19	0.000	0.005	0.004	0.003	-0.016	-0.017	-0.008	-0.033	-0.054	-0.057	-0.066	-0.041	-0.018	-0.025	-0.012	-0.028	-0.024	-0.032	-0.031	0.000
20	-0.005	-0.015	-0.005	-0.018	-0.011	-0.016	-0.022	-0.014	-0.021	-0.037	-0.111	-0.054	-0.040	-0.009	-0.017	-0.013	-0.016	-0.020	-0.013	-0.112
21	-0.012	-0.008	-0.012	-0.026	-0.019	-0.024	-0.016	-0.018	-0.005	-0.016	-0.102	-0.009	-0.037	-0.016	-0.006	0.005	0.010	0.003	0.001	-0.055
22	-0.023	-0.017	-0.025	-0.046	-0.033	-0.026	-0.035	-0.023	-0.024	-0.018	-0.083	0.005	-0.009	-0.032	-0.017	0.004	0.011	0.000	0.006	-0.029
23	-0.013	-0.014	-0.008	-0.025	-0.007	-0.006	-0.008	-0.004	-0.008	-0.012	0.003	-0.063	-0.039	-0.009	-0.009	-0.016	-0.009	-0.032	-0.009	-0.028
24	-0.040	-0.055	-0.053	-0.055	-0.042	-0.042	-0.051	-0.051	-0.041	-0.028	-0.056	-0.025	-0.020	-0.022	-0.046	-0.014	-0.025	-0.018	-0.007	-0.045
25	-0.053	-0.062	-0.061	-0.056	-0.052	-0.044	-0.071	-0.054	-0.012	-0.042	-0.054	-0.043	-0.033	-0.020	-0.027	-0.006	-0.002	-0.016	-0.009	-0.031
26	-0.057	-0.060	-0.057	-0.050	-0.055	-0.053	-0.070	-0.058	-0.006	-0.034	-0.067	-0.087	-0.036	-0.033	-0.017	-0.017	-0.009	-0.036	-0.021	-0.084
27	0.000	0.001	0.004	0.000	-0.007	0.002	0.002	0.003	0.021	0.022	0.027	-0.003	-0.011	-0.013	-0.019	-0.038	-0.040	-0.039	-0.054	-0.231
28	0.003	0.004	0.002	0.006	0.008	0.008	0.009	0.009	0.028	0.025	0.032	-0.005	-0.012	-0.017	-0.029	-0.038	-0.053	-0.046	-0.045	-0.263
29	0.003	0.004	0.005	0.001	0.008	0.004	0.004	0.005	0.021	0.019	0.018	0.002	-0.001	-0.015	-0.023	-0.033	-0.041	-0.027	-0.028	-0.126
30	-0.011	-0.019	-0.013	-0.001	-0.011	-0.012	-0.023	-0.028	-0.005	0.003	-0.006	-0.003	-0.003	-0.011	-0.009	-0.016	-0.019	-0.013	-0.015	-0.122
31	-0.006	-0.012	-0.005	-0.004	-0.013	-0.013	-0.026	-0.024	0.011	0.012	0.008	-0.005	-0.004	-0.005	-0.008	-0.011	-0.014	-0.014	-0.016	-0.141
32	0.004	0.003	0.002	0.004	-0.024	-0.014	-0.004	-0.012	0.005	0.005	-0.003	-0.002	-0.002	-0.005	-0.008	-0.015	-0.012	-0.011	-0.016	-0.115
33	0.003	-0.001	-0.004	-0.003	-0.081	-0.030	-0.016	-0.018	0.007	0.003	-0.002	0.001	0.001	-0.001	-0.004	-0.030	-0.015	-0.007	-0.011	-0.083
34	-0.013	-0.028	-0.014	-0.019	-0.011	-0.021	-0.023	-0.028	-0.015	-0.011	-0.021	-0.048	-0.021	-0.009	-0.006	-0.009	-0.009	-0.009	-0.011	-0.028
35	-0.007	-0.016	-0.013	-0.002	-0.007	-0.011	-0.014	-0.016	-0.002	-0.002	-0.006	-0.030	-0.014	-0.009	-0.002	-0.005	-0.005	-0.006	-0.004	-0.020
36	-0.011	-0.018	-0.008	-0.002	-0.011	-0.018	-0.037	-0.054	-0.002	0.000	-0.005	-0.016	-0.016	-0.014	-0.011	-0.009	-0.007	-0.010	-0.010	-0.052
37	-0.027	-0.016	-0.014	-0.018	-0.012	-0.011	-0.018	-0.023	-0.082	-0.022	-0.030	-0.084	-0.036	-0.015	-0.004	-0.009	-0.020	-0.020	-0.027	-0.029
38	-0.009	0.002	0.001	0.003	0.006	0.008	0.003	0.001	0.007	0.002	0.018	-0.086	-0.054	-0.044	-0.010	-0.015	-0.026	-0.008	-0.021	-0.069
39	0.001	0.005	0.004	0.007	-0.000	-0.003	-0.001	-0.000	0.009	0.007	0.005	-0.036	-0.033	-0.031	-0.014	-0.026	-0.018	-0.023	-0.016	-0.090

Table D.4.: First half of the matrix obtained with the *avg* method from calibration C1605 which is used for PIIa Runs 53 to 64. Each row correspond to a certain trigger channel, while columns correspond to the crosstalk channels. The values are given in %.

	20	21	22	23	24	25	26	27	28	29	30	31	32	33	34	35	36	37	38	39
0	0.007	0.012	0.010	0.006	-0.002	0.008	0.006	0.027	0.022	0.044	-0.012	-0.008	-0.047	-0.106	-0.054	-0.027	-0.045	-0.021	-0.011	-0.011
1	-0.000	0.017	0.013	0.013	0.006	0.018	0.011	0.029	0.026	0.053	-0.017	-0.015	-0.022	-0.105	-0.114	-0.098	-0.212	-0.009	-0.007	-0.009
2	0.002	0.008	0.007	0.003	0.007	0.005	0.006	0.016	0.017	0.039	-0.016	-0.014	-0.009	-0.045	-0.081	-0.168	-0.613	-0.019	-0.008	-0.019
3	0.000	0.002	-0.010	-0.008	0.007	0.006	0.003	0.019	0.022	0.039	-0.002	-0.004	-0.002	-0.023	-0.053	-0.161	-0.940	-0.024	-0.014	-0.015
4	-0.074	-0.075	-0.080	-0.078	-0.148	-0.099	-0.107	-0.054	-0.033	-0.052	0.001	-0.014	-0.023	-0.083	0.001	0.003	0.003	-0.072	-0.014	-0.020
5	-0.054	-0.063	-0.061	-0.092	-0.094	-0.049	-0.069	-0.090	-0.036	-0.058	-0.019	-0.020	-0.024	-0.035	-0.001	-0.001	-0.004	-0.094	-0.041	-0.047
6	-0.041	-0.032	-0.037	-0.048	-0.048	-0.029	-0.034	-0.200	-0.060	-0.056	-0.048	-0.036	-0.022	-0.019	-0.009	-0.009	-0.021	-0.074	-0.053	-0.073
7	-0.023	-0.020	-0.018	-0.022	-0.017	-0.005	-0.009	-0.357	-0.177	-0.129	-0.095	-0.053	-0.040	-0.021	-0.023	-0.022	-0.047	-0.059	-0.043	-0.082
8	0.007	0.007	-0.003	-0.031	-0.033	0.013	0.001	-0.020	-0.013	-0.043	-0.013	-0.004	-0.001	-0.006	-0.002	-0.006	-0.026	-0.051	-0.004	-0.007
9	0.004	0.005	-0.000	-0.023	-0.010	-0.017	-0.017	-0.001	0.002	-0.003	-0.063	-0.022	-0.007	-0.010	-0.002	-0.010	-0.029	-0.007	-0.004	-0.006
10	-0.000	0.001	0.011	-0.012	0.011	0.010	-0.036	0.018	0.020	0.032	-0.110	-0.062	-0.015	-0.008	-0.001	-0.014	-0.031	-0.009	0.003	0.000
11	-0.044	-0.006	0.011	0.013	0.003	0.004	-0.005	0.050	-0.069	-0.539	0.001	0.001	0.003	0.004	0.003	-0.004	-0.006	0.004	0.003	-0.006
12	-0.032	-0.029	-0.004	-0.004	0.004	0.003	0.005	0.047	0.022	-0.064	-0.007	-0.005	-0.003	0.001	0.001	-0.001	-0.012	0.001	-0.000	0.004
13	-0.006	-0.017	-0.030	-0.004	-0.008	0.013	-0.006	0.037	0.014	-0.002	-0.010	-0.002	-0.005	-0.002	0.001	-0.002	-0.017	-0.003	-0.004	-0.000
14	-0.008	0.000	-0.016	-0.004	-0.035	0.003	-0.001	0.036	0.026	0.023	-0.012	-0.008	-0.005	-0.003	0.001	-0.000	-0.013	-0.002	-0.000	0.002
15	-0.101	-0.111	-0.114	-0.143	-0.278	-0.221	-0.171	-0.027	0.002	0.023	0.009	0.002	-0.003	-0.020	0.004	0.002	-0.001	-0.147	-0.036	-0.038
16	-0.060	-0.058	-0.063	-0.125	-0.154	-0.105	-0.093	-0.130	-0.011	0.033	0.005	0.003	0.003	-0.001	0.003	0.001	-0.000	-0.176	-0.091	-0.088
17	-0.037	-0.028	-0.040	-0.059	-0.048	-0.028	-0.036	-0.486	-0.089	0.031	-0.001	0.000	0.003	-0.001	-0.001	-0.006	-0.007	-0.143	-0.111	-0.169
18	-0.007	-0.000	-0.010	0.023	-0.001	0.010	-0.010	-0.799	-0.382	-0.153	-0.000	-0.001	0.004	-0.000	-0.001	-0.006	-0.010	-0.054	-0.066	-0.137
19	-0.128	-0.083	-0.059	-0.134	-0.077	-0.049	-0.048	-0.034	-0.158	-0.452	-0.001	-0.003	0.001	-0.003	0.001	-0.001	-0.009	-0.025	-0.016	-0.035
20	0.000	-0.104	-0.090	-0.028	-0.087	-0.050	-0.047	-0.017	-0.053	-0.190	-0.005	-0.007	0.001	-0.005	0.003	-0.001	-0.004	-0.016	-0.008	-0.019
21	-0.135	0.000	-0.146	-0.006	-0.058	-0.036	-0.052	-0.007	-0.023	-0.050	-0.005	-0.004	0.002	-0.004	0.001	0.004	-0.013	-0.017	-0.002	-0.012
22	-0.045	-0.129	0.000	0.022	-0.070	-0.045	-0.078	-0.018	-0.015	-0.041	-0.007	-0.005	-0.002	-0.006	0.003	-0.005	-0.016	-0.015	-0.006	-0.018
23	-0.029	-0.034	-0.109	0.000	-0.050	-0.029	-0.072	-0.018	-0.034	-0.041	0.002	-0.004	0.002	-0.010	-0.013	-0.038	-0.011	-0.341	-0.125	-0.105
24	-0.056	-0.036	-0.063	-0.012	0.000	-0.228	-0.179	-0.016	-0.010	-0.036	-0.016	-0.015	-0.005	-0.007	-0.001	-0.004	-0.030	-0.017	-0.009	-0.030
25	-0.035	-0.054	-0.063	0.004	-0.381	0.000	-0.368	0.003	-0.011	0.011	-0.036	-0.022	-0.009	-0.009	-0.003	-0.007	-0.039	-0.019	-0.006	-0.016
26	-0.047	-0.118	-0.090	-0.067	-0.198	-0.573	0.000	-0.002	-0.002	-0.001	-0.060	-0.052	-0.024	-0.013	-0.005	-0.012	-0.051	-0.063	-0.022	-0.046
27	-0.139	-0.115	-0.088	-0.171	-0.174	-0.216	-0.287	0.000	-0.604	-0.652	-0.027	-0.081	-0.061	-0.054	-0.027	-0.090	-0.114	-0.353	-0.100	-0.176
28	-0.219	-0.143	-0.081	-0.154	-0.109	-0.151	-0.215	-0.207	0.000	-0.495	-0.014	-0.042	-0.010	-0.016	-0.026	-0.058	-0.058	-0.131	-0.062	-0.096
29	-0.164	-0.218	-0.149	-0.165	-0.090	-0.110	-0.135	-0.102	-0.133	0.000	-0.027	-0.022	-0.003	-0.002	-0.013	-0.025	-0.036	-0.120	-0.042	-0.071
30	-0.126	-0.118	-0.089	-0.059	-0.092	-0.088	-0.115	-0.068	-0.060	-0.090	0.000	-0.234	-0.083	-0.055	-0.066	-0.084	-0.120	-0.072	-0.015	-0.022
31	-0.113	-0.090	-0.080	-0.059	-0.102	-0.087	-0.142	-0.066	-0.064	-0.054	-0.147	0.000	-0.118	-0.083	-0.042	-0.058	-0.074	-0.053	-0.005	-0.006
32	-0.085	-0.084	-0.073	-0.072	-0.122	-0.109	-0.155	-0.068	-0.039	-0.048	-0.053	-0.122	0.000	-0.109	-0.036	-0.051	-0.058	-0.064	-0.011	-0.017
33	-0.069	-0.074	-0.067	-0.092	-0.141	-0.088	-0.119	-0.050	-0.035	-0.045	-0.045	-0.063	-0.174	0.000	-0.059	-0.074	-0.067	-0.071	-0.015	-0.018
34	-0.024	-0.026	-0.036	-0.049	-0.033	-0.044	-0.044	-0.029	-0.037	-0.045	-0.030	-0.039	-0.033	-0.066	0.000	-0.228	-0.146	-0.092	-0.019	-0.020
35	-0.019	-0.021	-0.030	-0.045	-0.027	-0.024	-0.027	-0.031	-0.031	-0.044	-0.029	-0.030	-0.033	-0.048	-0.205	0.000	-0.189	-0.055	-0.020	-0.013
36	-0.046	-0.070	-0.100	-0.052	-0.061	-0.062	-0.064	-0.155	-0.107	-0.124	-0.121	-0.069	-0.080	-0.064	-0.110	-0.283	0.000	-0.171	-0.072	-0.125
37	-0.022	-0.019	-0.016	-0.275	-0.014	-0.003	-0.041	-0.104	-0.029	-0.035	-0.012	-0.011	-0.006	-0.009	-0.051	-0.036	-0.048	0.000	-0.170	-0.281
38	-0.052	-0.056	-0.090	-1.714	-0.038	-0.014	-0.055	-0.034	-0.046	-0.044	0.009	0.005	0.004	-0.001	-0.012	-0.027	-0.024	-0.269	0.000	-0.354
39	-0.064	-0.105	-0.151	-1.741	-0.062	-0.062	-0.075	-0.055	-0.046	-0.089	0.003	0.000	-0.004	-0.003	-0.009	-0.012	-0.051	-0.383	-0.293	0.000

Table D.5.: Second half of the matrix obtained with the *avg* method from calibration C1605 which is used for PIIa Runs 53 to 64. Each row correspond to a certain trigger channel, while columns correspond to the crosstalk channels. The values are given in %.

	0	1	2	3	4	5	6	7	8	9	10	11	12	13	14	15	16	17	18	19
0	0.000	-0.250	-0.172	-0.122	-0.175	-0.166	-0.230	0.000	-0.085	-0.085	-0.123	-0.008	-0.010	-0.022	-0.005	-0.007	-0.007	-0.007	-0.009	0.006
1	-0.196	0.000	-0.202	-0.166	-0.127	-0.139	-0.191	0.000	-0.067	-0.071	-0.107	-0.018	-0.020	-0.005	-0.010	-0.010	-0.008	-0.015	-0.011	0.004
2	-0.153	-0.260	0.000	-0.250	-0.164	-0.161	-0.203	0.000	-0.096	-0.105	-0.134	-0.012	-0.013	-0.013	-0.008	-0.005	-0.005	-0.008	-0.015	0.003
3	-0.135	-0.176	-0.295	0.000	-0.190	-0.159	-0.224	0.000	-0.081	-0.102	-0.158	-0.022	-0.014	-0.008	-0.010	-0.010	-0.014	-0.010	-0.015	0.003
4	-0.054	-0.037	-0.049	-0.095	0.000	-0.236	-0.127	0.000	-0.020	-0.027	-0.053	-0.017	-0.014	-0.028	-0.016	-0.049	-0.029	-0.011	-0.022	-0.086
5	-0.047	-0.042	-0.055	-0.051	-0.309	0.000	-0.305	0.000	-0.040	-0.045	-0.066	-0.013	-0.010	-0.013	-0.011	-0.036	-0.050	-0.014	-0.016	-0.059
6	-0.049	-0.044	-0.047	-0.049	-0.139	-0.351	0.000	0.000	-0.023	-0.030	-0.060	-0.021	-0.008	-0.005	-0.013	-0.014	-0.041	-0.041	-0.018	-0.034
7	0.000	0.000	0.000	0.000	0.000	0.000	0.000	0.000	0.000	0.000	0.000	0.000	0.000	0.000	0.000	0.000	0.000	0.000	0.000	0.000
8	-0.086	-0.099	-0.127	-0.131	-0.086	-0.095	-0.114	0.000	0.000	-0.530	-0.658	-0.023	-0.043	-0.054	-0.098	-0.022	-0.036	-0.038	-0.085	0.006
9	-0.111	-0.131	-0.161	-0.141	-0.098	-0.114	-0.152	0.000	-0.396	0.000	-0.766	-0.024	-0.025	-0.031	-0.048	-0.033	-0.038	-0.051	-0.091	0.004
10	-0.119	-0.133	-0.136	-0.113	-0.101	-0.115	-0.165	0.000	-0.232	-0.359	0.000	-0.030	-0.029	-0.022	-0.020	-0.018	-0.024	-0.029	-0.052	0.004
11	-0.002	-0.013	-0.007	-0.023	-0.007	-0.009	-0.020	0.000	-0.098	-0.130	-0.221	0.000	-0.175	-0.072	-0.067	-0.057	-0.061	-0.072	-0.069	-0.015
12	-0.020	-0.039	-0.033	-0.057	-0.027	-0.027	-0.036	0.000	-0.055	-0.087	-0.269	-0.139	0.000	-0.119	-0.074	-0.037	-0.049	-0.046	-0.048	-0.000
13	-0.051	-0.045	-0.059	-0.080	-0.050	-0.049	-0.058	0.000	-0.059	-0.075	-0.242	-0.051	-0.103	0.000	-0.151	-0.044	-0.042	-0.034	-0.049	0.002
14	-0.047	-0.065	-0.077	-0.098	-0.047	-0.057	-0.095	0.000	-0.090	-0.065	-0.170	-0.046	-0.053	-0.106	0.000	-0.055	-0.056	-0.042	-0.046	0.001
15	0.013	0.008	0.013	0.015	-0.020	-0.016	0.010	0.000	0.019	0.013	0.039	-0.036	-0.036	-0.052	-0.096	0.000	-0.261	-0.118	-0.115	-0.125
16	0.011	0.006	0.014	0.009	0.006	-0.017	-0.014	0.000	-0.005	0.001	0.017	-0.029	-0.030	-0.029	-0.050	-0.279	0.000	-0.261	-0.149	-0.066
17	0.014	0.007	0.013	0.007	0.015	0.001	-0.023	0.000	-0.051	-0.026	-0.016	-0.044	-0.029	-0.029	-0.036	-0.094	-0.353	0.000	-0.359	-0.032
18	0.013	0.013	0.012	0.008	0.012	0.010	0.012	0.000	-0.155	-0.074	-0.053	-0.091	-0.045	-0.065	-0.055	-0.082	-0.141	-0.458	0.000	-0.018
19	-0.004	-0.002	-0.001	-0.003	-0.014	-0.015	-0.011	0.000	-0.051	-0.059	-0.067	-0.031	-0.017	-0.014	-0.013	-0.025	-0.014	-0.023	-0.031	0.000
20	-0.008	-0.015	-0.011	-0.022	-0.016	-0.016	-0.028	0.000	-0.024	-0.040	-0.108	-0.046	-0.035	-0.010	-0.007	-0.009	-0.010	-0.008	-0.014	-0.104
21	-0.014	-0.014	-0.020	-0.029	-0.017	-0.020	-0.034	0.000	-0.009	-0.019	-0.092	-0.005	-0.034	-0.021	-0.003	0.003	0.003	0.005	-0.001	-0.048
22	-0.020	-0.026	-0.030	-0.047	-0.027	-0.029	-0.050	0.000	-0.017	-0.016	-0.080	0.003	-0.009	-0.033	-0.020	0.004	0.005	0.002	0.001	-0.025
23	-0.006	-0.010	-0.004	-0.009	-0.001	-0.008	-0.011	0.000	-0.002	-0.001	-0.002	-0.058	-0.034	-0.010	-0.005	-0.007	-0.010	-0.008	-0.004	-0.018
24	-0.036	-0.054	-0.055	-0.065	-0.040	-0.047	-0.082	0.000	-0.040	-0.031	-0.057	-0.022	-0.021	-0.018	-0.049	-0.007	-0.014	-0.017	-0.010	-0.026
25	-0.047	-0.065	-0.069	-0.059	-0.050	-0.059	-0.095	0.000	-0.018	-0.050	-0.053	-0.042	-0.022	-0.021	-0.020	-0.008	-0.006	-0.016	-0.013	-0.026
26	-0.055	-0.069	-0.064	-0.057	-0.057	-0.064	-0.111	0.000	-0.009	-0.027	-0.063	-0.091	-0.040	-0.032	-0.022	-0.022	-0.013	-0.042	-0.027	-0.076
27	0.001	-0.001	0.005	0.003	-0.005	0.002	-0.000	0.000	0.023	0.023	0.023	-0.005	-0.008	-0.013	-0.021	-0.041	-0.043	-0.036	-0.046	-0.233
28	0.004	0.007	0.006	0.006	0.007	0.008	0.010	0.000	0.025	0.024	0.029	0.002	-0.001	-0.012	-0.020	-0.031	-0.042	-0.030	-0.038	-0.263
29	0.006	0.002	0.009	0.006	0.008	0.008	0.007	0.000	0.022	0.022	0.026	0.001	-0.008	-0.014	-0.024	-0.032	-0.032	-0.022	-0.021	-0.127
30	-0.015	-0.005	-0.006	-0.004	-0.012	-0.012	-0.024	0.000	-0.003	0.001	-0.007	-0.005	-0.003	-0.011	-0.010	-0.015	-0.018	-0.013	-0.018	-0.122
31	-0.007	-0.010	-0.003	-0.003	-0.017	-0.010	-0.023	0.000	0.013	0.009	0.007	-0.007	-0.006	-0.007	-0.012	-0.015	-0.018	-0.011	-0.017	-0.143
32	0.000	-0.001	-0.001	-0.003	-0.022	-0.013	-0.013	0.000	0.004	0.002	-0.003	-0.003	-0.001	-0.007	-0.010	-0.016	-0.013	-0.012	-0.020	-0.116
33	0.001	0.001	-0.005	-0.007	-0.087	-0.034	-0.019	0.000	0.005	0.003	-0.003	0.000	0.001	-0.003	-0.006	-0.031	-0.016	-0.006	-0.013	-0.081
34	-0.013	-0.016	-0.013	-0.021	-0.019	-0.023	-0.032	0.000	-0.015	-0.014	-0.022	-0.040	-0.021	-0.009	-0.006	-0.007	-0.010	-0.009	-0.010	-0.028
35	-0.006	-0.006	-0.005	-0.006	-0.010	-0.015	-0.018	0.000	-0.003	-0.003	-0.006	-0.024	-0.015	-0.006	-0.001	-0.007	-0.004	-0.004	-0.006	-0.022
36	-0.011	-0.007	-0.007	-0.006	-0.013	-0.021	-0.042	0.000	-0.001	-0.000	-0.006	-0.015	-0.014	-0.017	-0.010	-0.010	-0.009	-0.010	-0.011	-0.053
37	-0.022	-0.020	-0.012	-0.012	-0.015	-0.015	-0.024	0.000	-0.080	-0.021	-0.028	-0.076	-0.036	-0.017	-0.006	-0.010	-0.012	-0.013	-0.019	-0.029
38	-0.001	0.000	-0.001	0.002	0.003	-0.002	0.002	0.000	0.005	-0.003	0.014	-0.085	-0.058	-0.040	-0.012	-0.016	-0.010	-0.017	-0.016	-0.061
39	-0.000	0.003	0.004	0.004	-0.001	-0.002	-0.002	0.000	0.008	0.006	0.002	-0.033	-0.034	-0.036	-0.017	-0.019	-0.020	-0.025	-0.019	-0.091

Table D.6.: First half of the matrix obtained with the *avg* method from calibration C1702 which is used for PIIb Runs 65 to 79. Each row correspond to a certain trigger channel, while columns correspond to the crosstalk channels. The values are given in %.

	20	21	22	23	24	25	26	27	28	29	30	31	32	33	34	35	36	37	38	39
0	0.006	0.008	0.010	0.008	0.004	0.008	0.002	0.028	0.023	0.052	-0.013	-0.013	-0.055	-0.102	-0.061	-0.032	-0.049	-0.015	-0.007	-0.012
1	-0.003	0.010	0.007	0.004	0.001	0.007	0.006	0.025	0.027	0.046	-0.000	-0.009	-0.018	-0.087	-0.113	-0.088	-0.207	-0.009	-0.005	-0.007
2	0.001	0.005	0.000	0.007	-0.002	0.000	-0.001	0.018	0.016	0.044	-0.008	-0.007	-0.008	-0.035	-0.088	-0.164	-0.617	-0.018	-0.008	-0.016
3	-0.005	0.007	0.001	0.008	-0.006	0.011	-0.004	0.023	0.018	0.040	-0.011	-0.008	-0.006	-0.023	-0.060	-0.163	-0.959	-0.017	-0.008	-0.015
4	-0.078	-0.074	-0.080	-0.076	-0.145	-0.108	-0.102	-0.054	-0.033	-0.050	0.001	-0.016	-0.029	-0.085	0.000	-0.001	0.000	-0.069	-0.008	-0.012
5	-0.054	-0.055	-0.056	-0.088	-0.088	-0.054	-0.067	-0.100	-0.038	-0.054	-0.018	-0.018	-0.024	-0.034	0.001	0.000	-0.005	-0.082	-0.028	-0.037
6	-0.039	-0.031	-0.030	-0.057	-0.042	-0.023	-0.033	-0.226	-0.063	-0.055	-0.047	-0.037	-0.025	-0.018	-0.012	-0.010	-0.023	-0.065	-0.041	-0.067
7	0.000	0.000	0.000	0.000	0.000	0.000	0.000	0.000	0.000	0.000	0.000	0.000	0.000	0.000	0.000	0.000	0.000	0.000	0.000	0.000
8	0.005	0.007	0.003	-0.022	-0.026	0.004	0.004	-0.012	-0.014	-0.038	-0.012	-0.004	-0.003	-0.007	0.001	-0.004	-0.023	-0.039	0.001	0.002
9	0.006	0.011	0.011	-0.015	-0.014	-0.028	-0.012	-0.001	0.001	0.005	-0.066	-0.021	-0.008	-0.012	-0.001	-0.008	-0.031	-0.003	-0.002	-0.001
10	0.000	0.010	0.013	-0.011	0.009	-0.003	-0.034	0.021	0.021	0.046	-0.112	-0.063	-0.021	-0.012	-0.003	-0.013	-0.033	0.002	0.005	0.001
11	-0.036	-0.002	0.010	0.007	0.006	0.006	-0.006	0.053	-0.066	-0.543	0.002	-0.000	0.003	0.002	0.001	-0.002	-0.004	0.011	0.005	-0.000
12	-0.029	-0.029	-0.006	-0.003	0.002	0.008	-0.003	0.053	0.027	-0.080	-0.006	-0.007	0.000	0.001	-0.001	-0.002	-0.012	0.006	0.004	0.007
13	-0.004	-0.019	-0.028	-0.002	-0.000	0.006	-0.000	0.040	0.026	0.000	-0.011	-0.005	-0.004	-0.001	-0.003	-0.005	-0.013	0.002	0.001	0.005
14	-0.003	0.002	-0.016	-0.003	-0.033	0.001	-0.005	0.037	0.030	0.022	-0.016	-0.011	-0.004	-0.002	-0.002	-0.002	-0.011	0.003	0.001	0.005
15	-0.107	-0.110	-0.115	-0.151	-0.272	-0.211	-0.177	-0.032	0.011	0.032	0.003	0.002	-0.005	-0.022	0.001	-0.001	-0.001	-0.150	-0.022	-0.021
16	-0.065	-0.061	-0.066	-0.142	-0.139	-0.098	-0.096	-0.145	0.003	0.045	0.003	0.002	0.005	-0.003	0.003	0.002	0.003	-0.163	-0.067	-0.080
17	-0.029	-0.021	-0.031	-0.045	-0.049	-0.032	-0.038	-0.506	-0.084	0.034	0.004	-0.001	0.003	-0.000	0.002	-0.003	-0.008	-0.119	-0.092	-0.153
18	-0.007	-0.003	-0.007	0.017	-0.002	0.003	-0.011	-0.827	-0.382	-0.148	0.002	0.000	0.003	0.001	-0.003	-0.008	-0.009	-0.036	-0.050	-0.130
19	-0.125	-0.077	-0.056	-0.141	-0.055	-0.043	-0.039	-0.036	-0.157	-0.452	0.001	-0.002	0.001	-0.003	-0.002	-0.006	-0.010	-0.024	-0.011	-0.036
20	0.000	-0.105	-0.090	-0.032	-0.071	-0.044	-0.048	-0.016	-0.039	-0.201	-0.004	-0.008	0.000	-0.002	-0.002	-0.005	-0.008	-0.025	-0.010	-0.023
21	-0.123	0.000	-0.139	0.002	-0.053	-0.039	-0.041	-0.008	-0.015	-0.052	-0.005	-0.003	-0.002	-0.003	-0.001	-0.001	-0.014	-0.016	-0.008	-0.011
22	-0.047	-0.129	0.000	0.038	-0.070	-0.045	-0.057	-0.013	-0.019	-0.036	-0.005	-0.003	-0.003	-0.004	-0.002	-0.003	-0.020	-0.012	-0.008	-0.017
23	-0.019	-0.024	-0.100	0.000	-0.045	-0.030	-0.070	-0.021	-0.029	-0.040	0.006	0.000	0.006	0.002	-0.023	-0.035	-0.008	-0.327	-0.119	-0.095
24	-0.043	-0.029	-0.066	-0.005	0.000	-0.261	-0.177	-0.011	-0.004	-0.037	-0.013	-0.015	-0.006	-0.007	-0.006	-0.009	-0.029	-0.013	-0.008	-0.033
25	-0.024	-0.047	-0.053	0.002	-0.376	0.000	-0.355	0.005	-0.003	0.011	-0.039	-0.020	-0.012	-0.011	-0.005	-0.011	-0.042	-0.022	-0.010	-0.020
26	-0.046	-0.105	-0.069	-0.067	-0.191	-0.567	0.000	0.003	-0.000	0.007	-0.063	-0.049	-0.024	-0.016	-0.010	-0.015	-0.056	-0.061	-0.024	-0.048
27	-0.144	-0.115	-0.087	-0.173	-0.168	-0.216	-0.286	0.000	-0.609	-0.648	-0.026	-0.081	-0.063	-0.054	-0.034	-0.092	-0.119	-0.348	-0.096	-0.177
28	-0.199	-0.135	-0.083	-0.151	-0.113	-0.143	-0.220	-0.208	0.000	-0.488	-0.015	-0.038	-0.015	-0.018	-0.031	-0.059	-0.062	-0.133	-0.058	-0.099
29	-0.170	-0.217	-0.149	-0.159	-0.097	-0.105	-0.129	-0.101	-0.113	0.000	-0.029	-0.020	-0.004	-0.002	-0.015	-0.026	-0.039	-0.112	-0.040	-0.071
30	-0.125	-0.116	-0.089	-0.066	-0.088	-0.090	-0.118	-0.071	-0.065	-0.093	0.000	-0.219	-0.074	-0.048	-0.074	-0.074	-0.117	-0.072	-0.014	-0.022
31	-0.113	-0.089	-0.077	-0.067	-0.100	-0.094	-0.142	-0.071	-0.064	-0.058	-0.141	0.000	-0.105	-0.080	-0.042	-0.056	-0.074	-0.054	-0.003	-0.006
32	-0.085	-0.083	-0.074	-0.075	-0.121	-0.119	-0.155	-0.071	-0.044	-0.049	-0.050	-0.108	0.000	-0.100	-0.035	-0.047	-0.052	-0.061	-0.008	-0.013
33	-0.069	-0.070	-0.065	-0.092	-0.140	-0.102	-0.117	-0.050	-0.032	-0.046	-0.044	-0.060	-0.166	0.000	-0.067	-0.064	-0.065	-0.074	-0.011	-0.015
34	-0.026	-0.027	-0.038	-0.043	-0.033	-0.036	-0.041	-0.030	-0.033	-0.041	-0.029	-0.027	-0.027	-0.068	0.000	-0.214	-0.134	-0.084	-0.009	-0.010
35	-0.020	-0.022	-0.035	-0.043	-0.028	-0.025	-0.032	-0.035	-0.032	-0.045	-0.022	-0.024	-0.027	-0.031	-0.233	0.000	-0.176	-0.055	-0.015	-0.014
36	-0.049	-0.070	-0.104	-0.049	-0.061	-0.058	-0.067	-0.158	-0.109	-0.126	-0.113	-0.065	-0.071	-0.056	-0.118	-0.285	0.000	-0.167	-0.066	-0.120
37	-0.029	-0.018	-0.018	-0.273	-0.007	-0.005	-0.038	-0.094	-0.027	-0.026	-0.013	-0.012	-0.007	-0.012	-0.060	-0.042	-0.049	0.000	-0.159	-0.281
38	-0.051	-0.066	-0.101	-1.790	-0.024	-0.026	-0.055	-0.030	-0.037	-0.041	0.009	0.006	0.002	-0.002	-0.009	-0.031	-0.031	-0.238	0.000	-0.370
39	-0.066	-0.107	-0.157	-1.757	-0.063	-0.067	-0.078	-0.056	-0.045	-0.087	0.001	0.001	-0.003	-0.005	-0.004	-0.016	-0.052	-0.379	-0.290	0.000

Table D.7.: Second half of the matrix obtained with the *avg* method from calibration C1702 which is used for PIIb Runs 65 to 79. Each row correspond to a certain trigger channel, while columns correspond to the crosstalk channels. The values are given in %.

D.4 Crosstalk matrix comparison

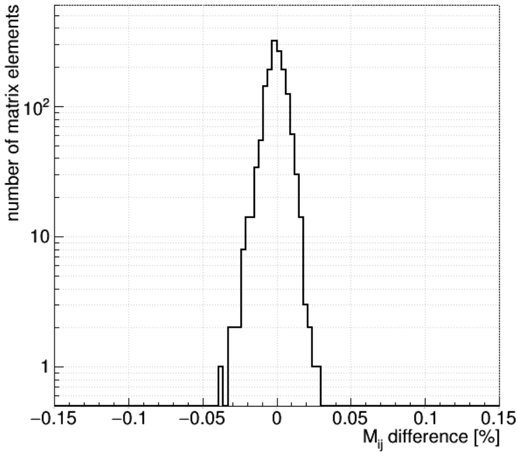

Figure D.4.: Difference between elements of matrices C1702 to the one obtained from the combined physics run 77 to 80.

D.5 Stability plots

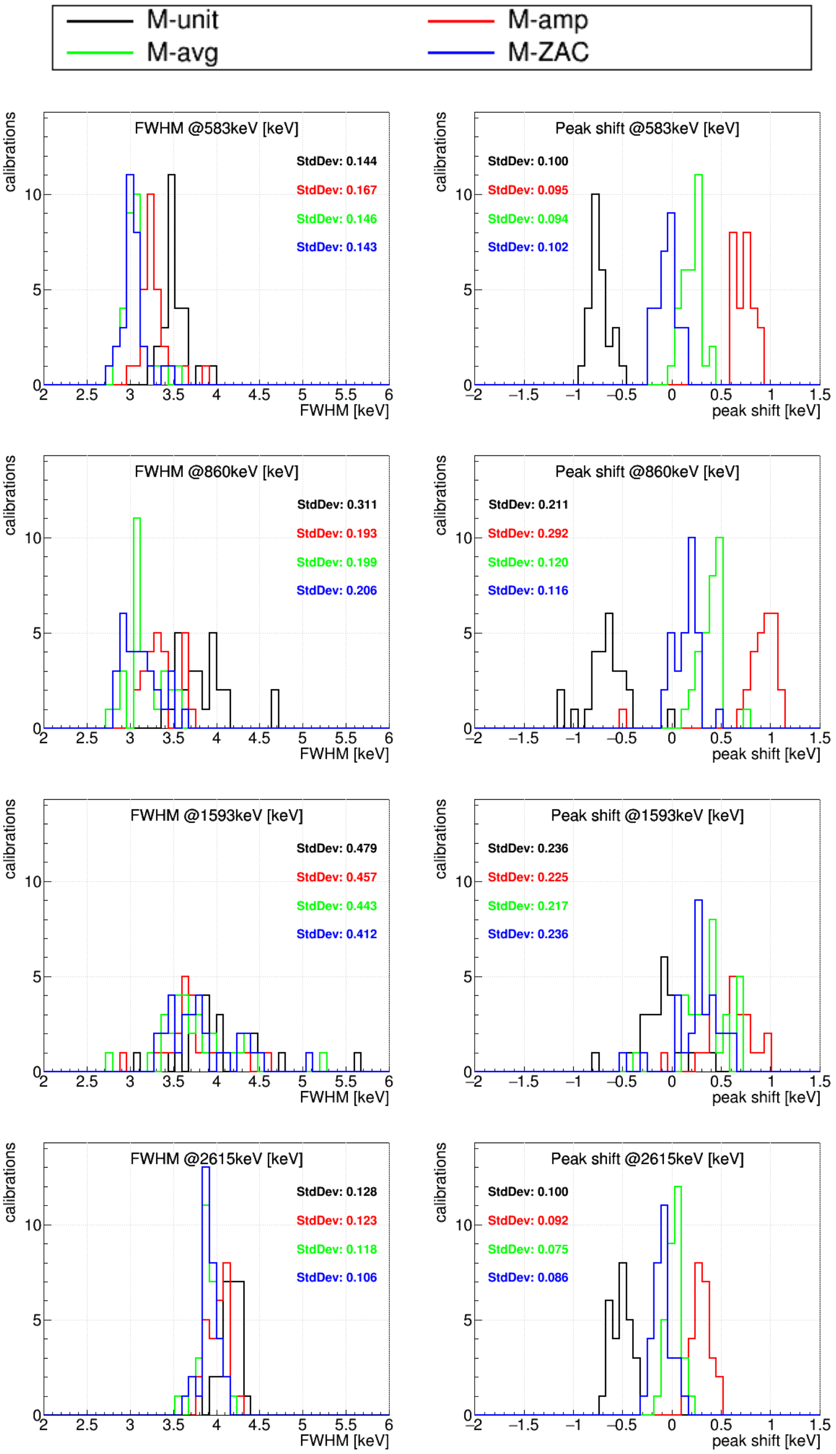

Figure D.5.: Illustrated is the distribution of the FWHM (*left*) and the peak shift (*right*) obtained from 4 peaks of ^{208}Tl in the semi-coaxial data of the PIIa calibration runs. The plots compare the distributions obtained without crosstalk correction ($\mathbb{M}^{\text{unit}}$) and with the three different crosstalk correction methods ($\mathbb{M}^{\text{amp}}$, $\mathbb{M}^{\text{avg}}$, $\mathbb{M}^{\text{ZAC}}$). Also given is the standard deviation of each distribution.

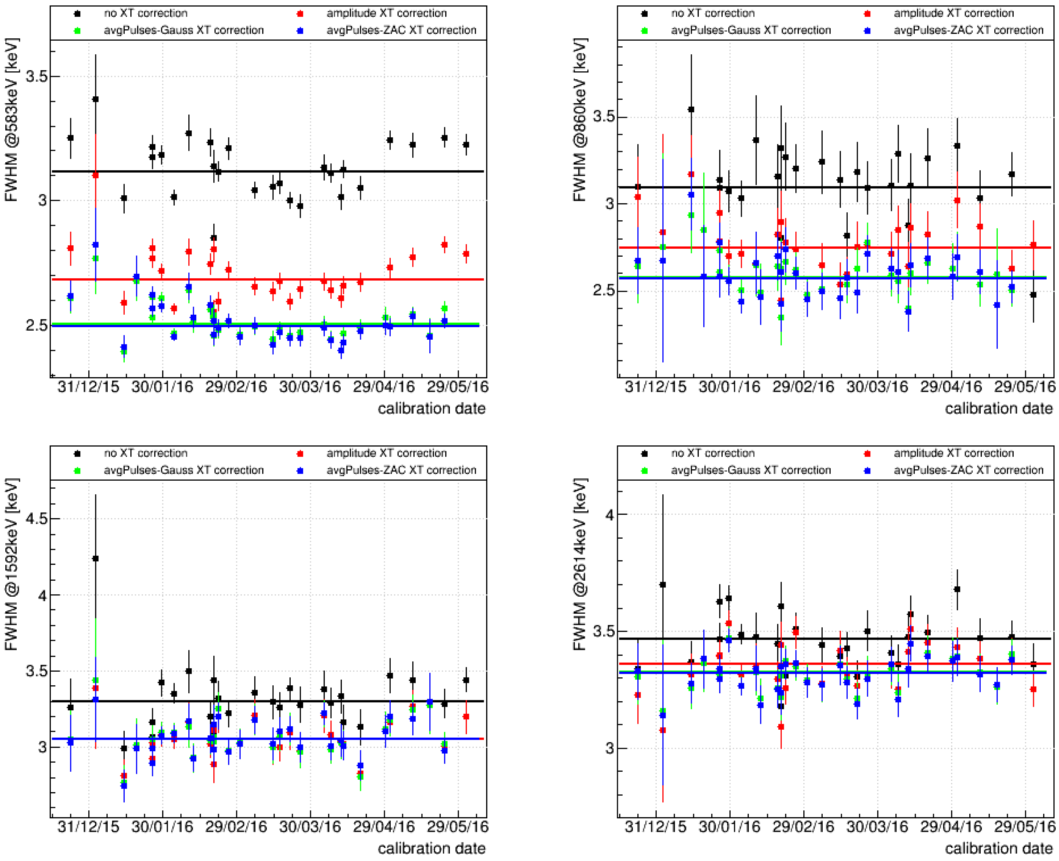

Figure D.6.: The FWHM of the BEGe data set in PIIa as obtained from various calibration runs processed with four different crosstalk matrices (see Ch. 5.6). The colored lines show the corresponding mean values.

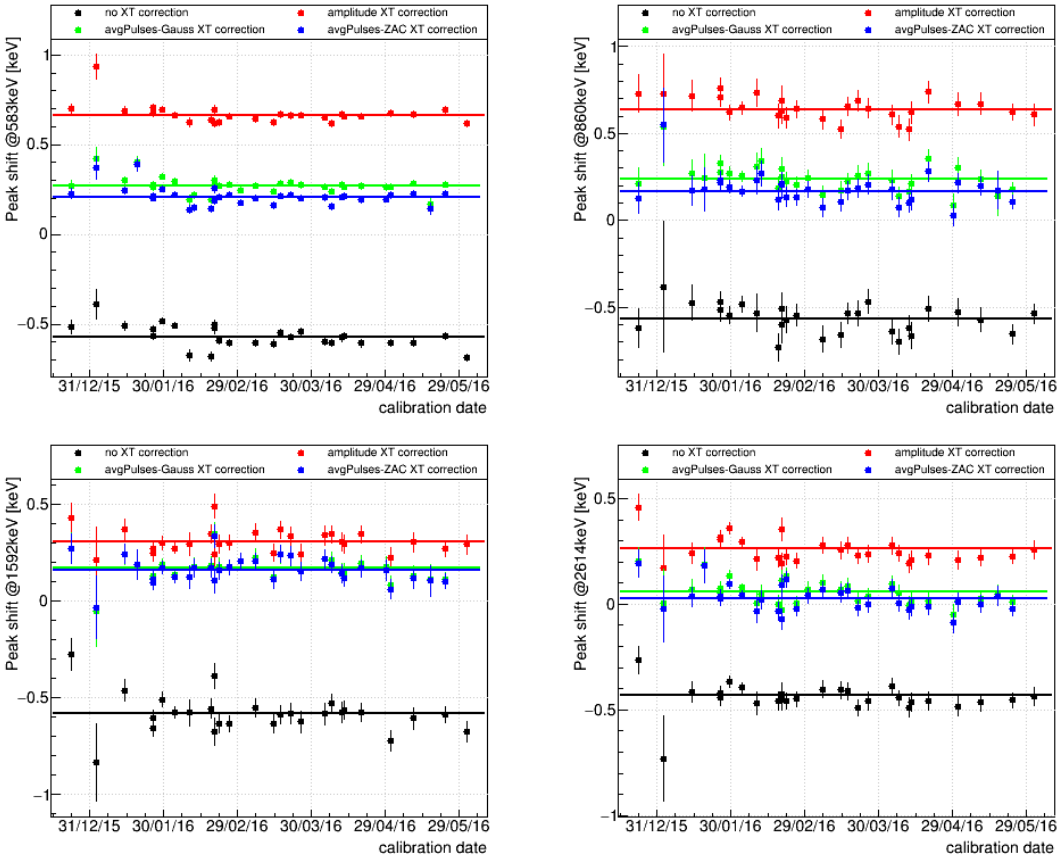

Figure D.7.: The peak shifts of the BEGe data set in PIIa as obtained from various calibration runs processed with four different crosstalk matrices (see Ch. 5.6). The colored lines show the corresponding mean values.

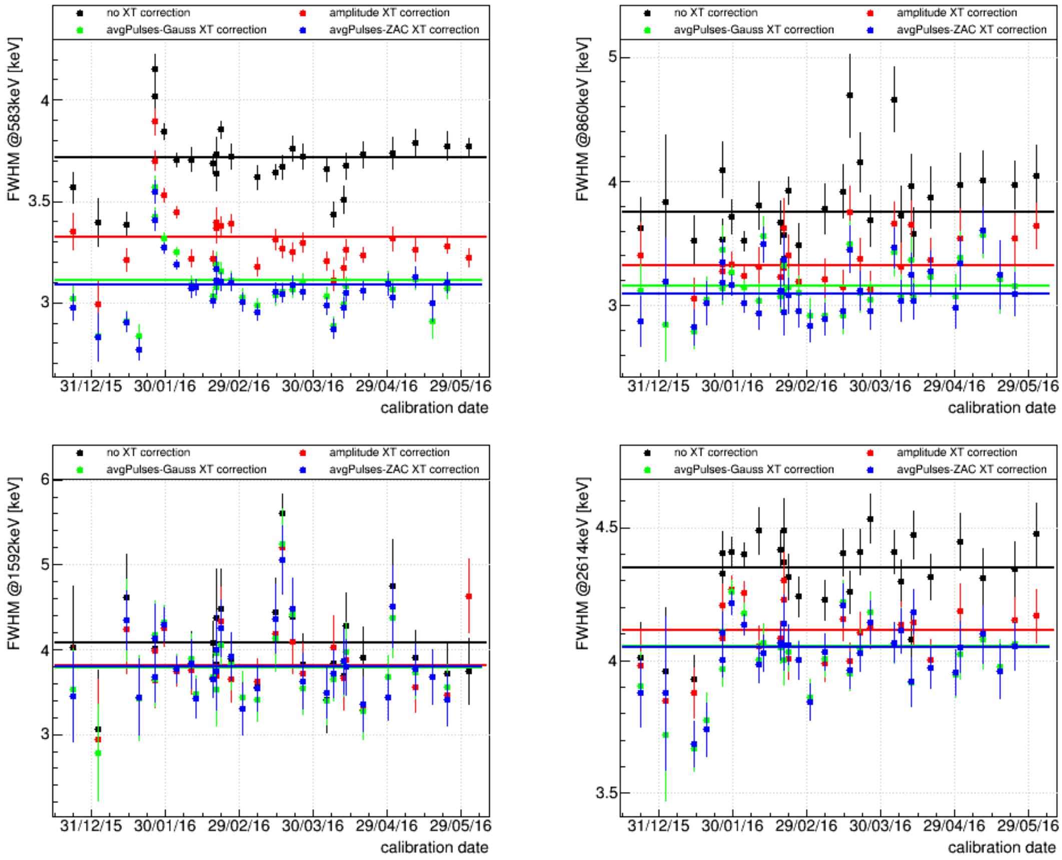

Figure D.8.: The FWHM of the semi-coaxial data set in PIIa as obtained from various calibration runs processed with four different crosstalk matrices (see Ch. 5.6). The colored lines show the corresponding mean values.

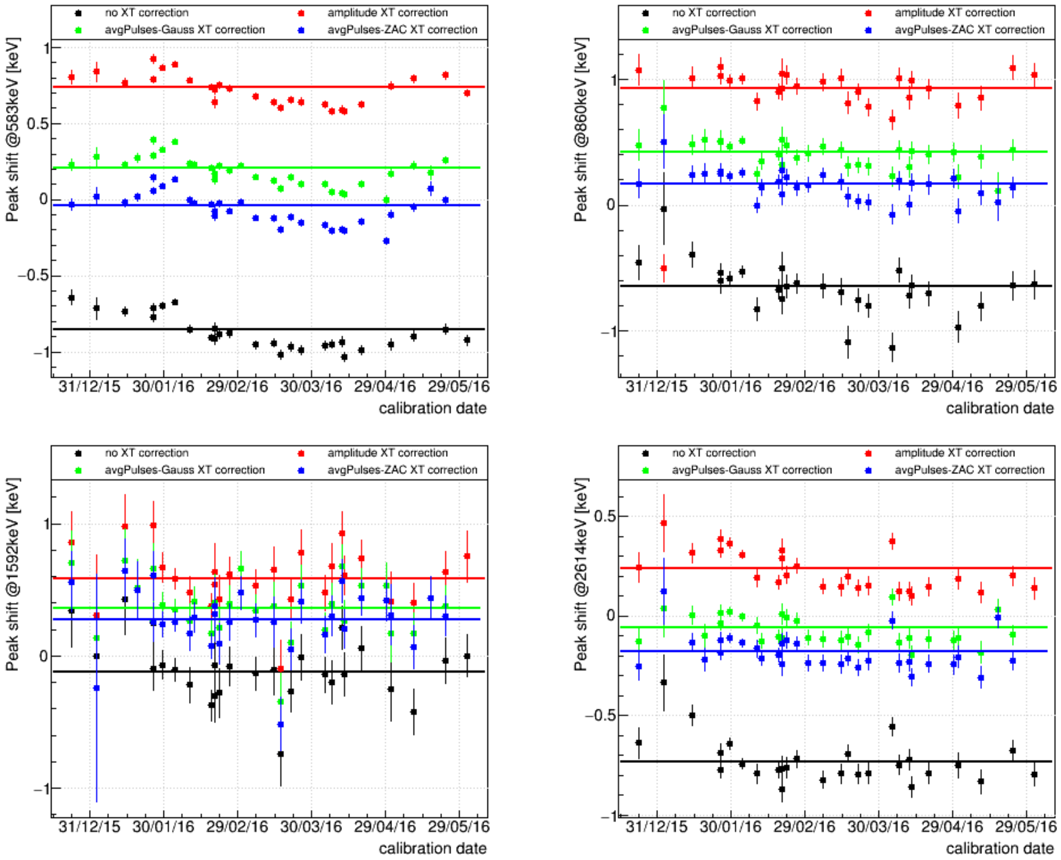

Figure D.9.: The peak shifts of the semi-coaxial data set in PIIa as obtained from various calibration runs processed with four different crosstalk matrices (see Ch. 5.6). The colored lines show the corresponding mean values.

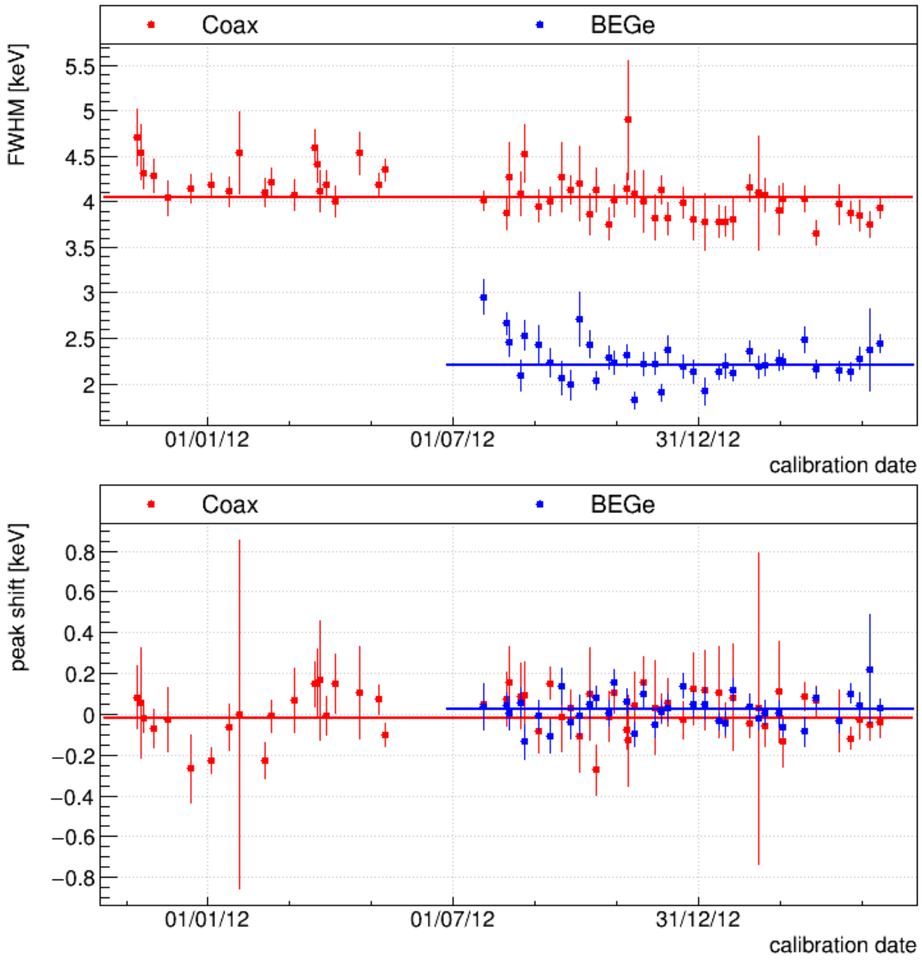

Figure D.10.: FWHM (*top*) and peak shift (*bottom*) of the 583 keV γ-line of ^{208}Tl extracted from the PI calibration runs for the Coax and BEGe data.

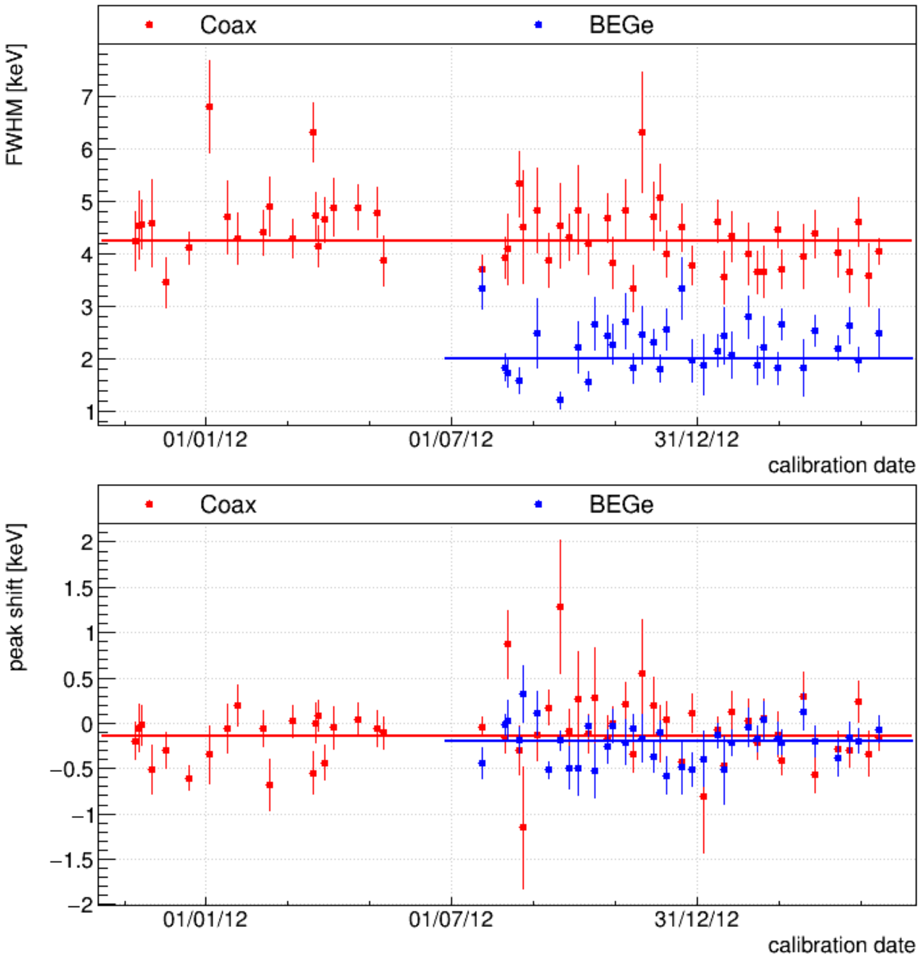

Figure D.11.: FWHM (*top*) and peak shift (*bottom*) of the 860 keV γ-line of ^{208}Tl extracted from the PI calibration runs for the Coax and BEGe data.

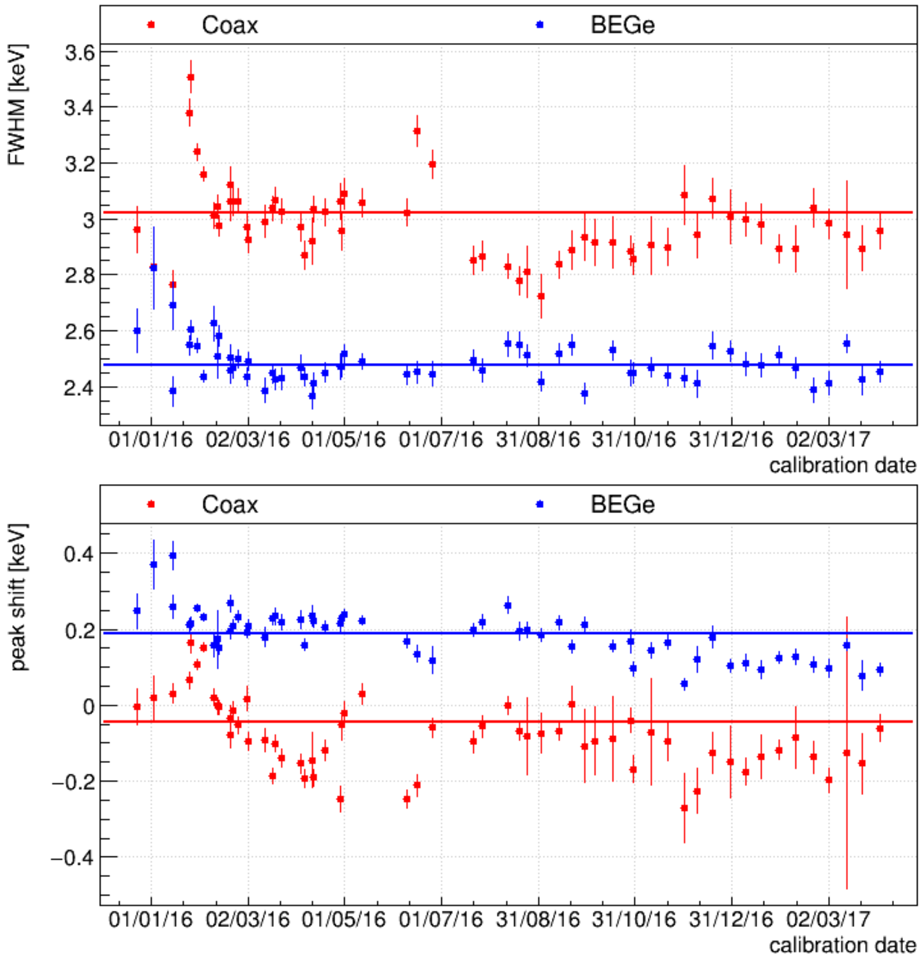

Figure D.12.: FWHM (*top*) and peak shift (*bottom*) of the 583 keV γ-line of ^{208}Tl extracted from the PII calibration runs for the Coax and BEGe data.

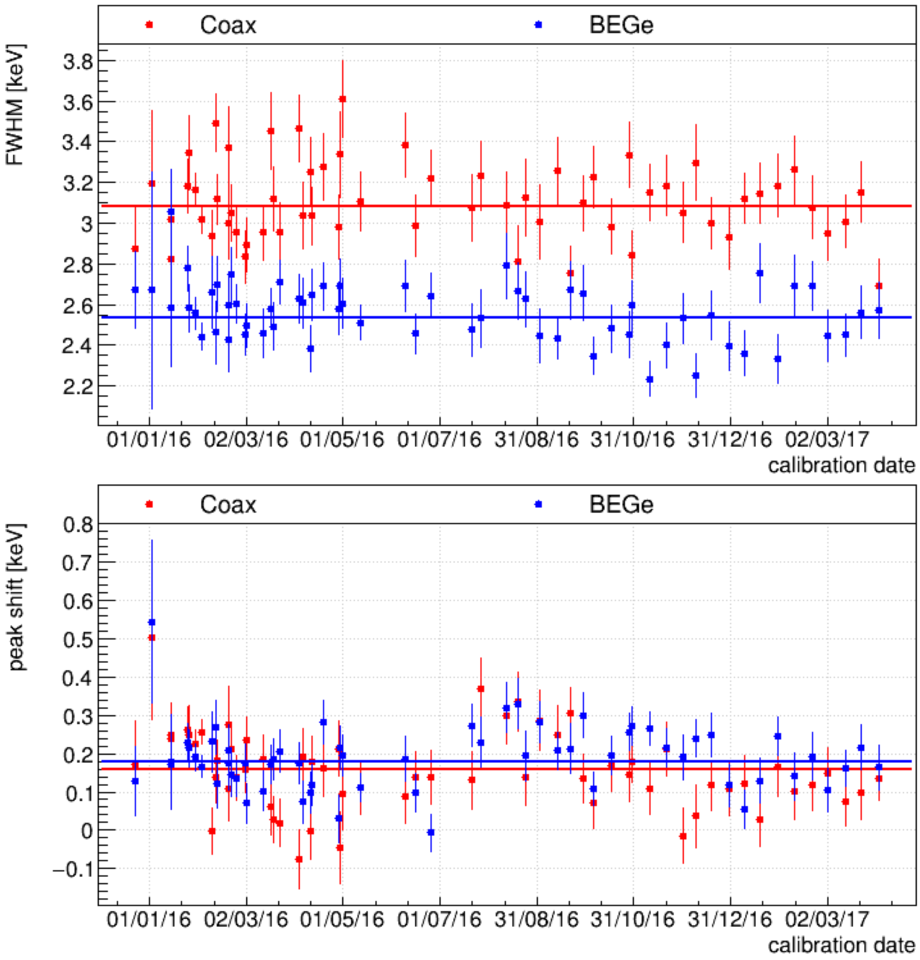

Figure D.13.: FWHM (*top*) and peak shift (*bottom*) of the 860 keV γ-line of ^{208}Tl extracted from the PII calibration runs for the Coax and BEGe data.

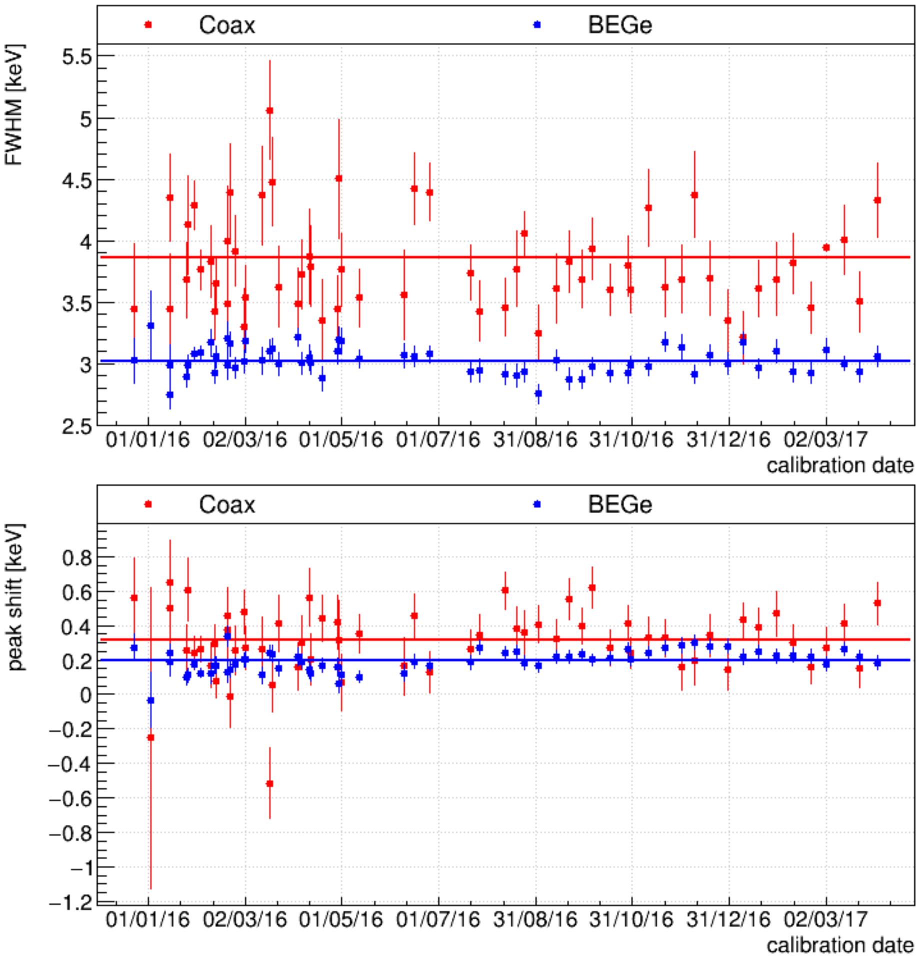

Figure D.14.: FWHM (*top*) and peak shift (*bottom*) of the 1593 keV γ-line of ^{208}Tl extracted from the PII calibration runs for the Coax and BEGe data.

Appendix E

Coincidence data set background analysis

E.1 Phase I background model

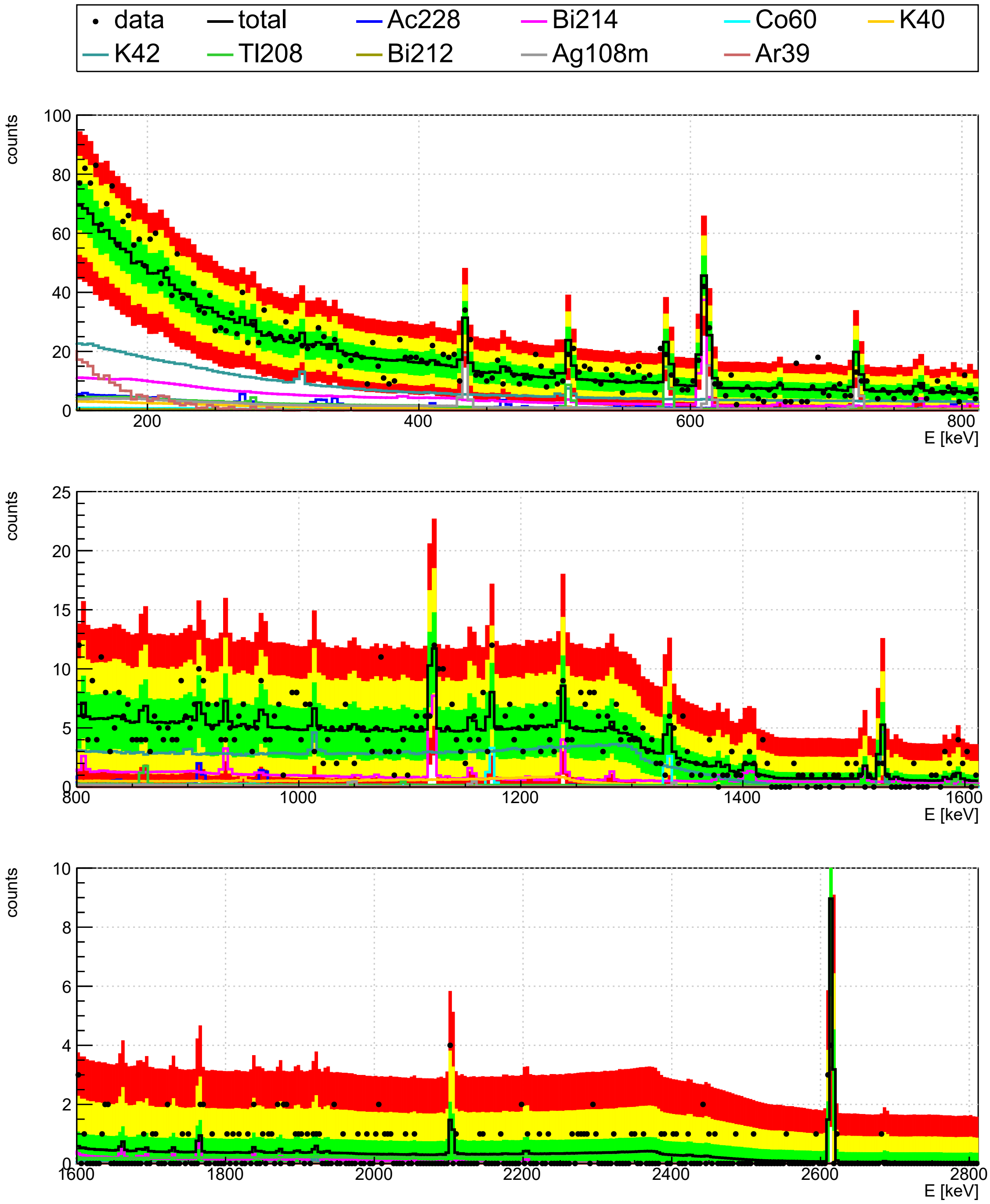

Figure E.1.: The M2 data of PI in form of the single energy spectrum in comparison to the final background model. The green, yellow and red band indicate for each bin the 68%, 95% and 99.7% smallest probability intervals of the Poisson distribution, with the expectation value given by the background model expectation. Additionally shown are the expected spectra of the individual background isotopes. A 4 keV binning is used for the spectra.

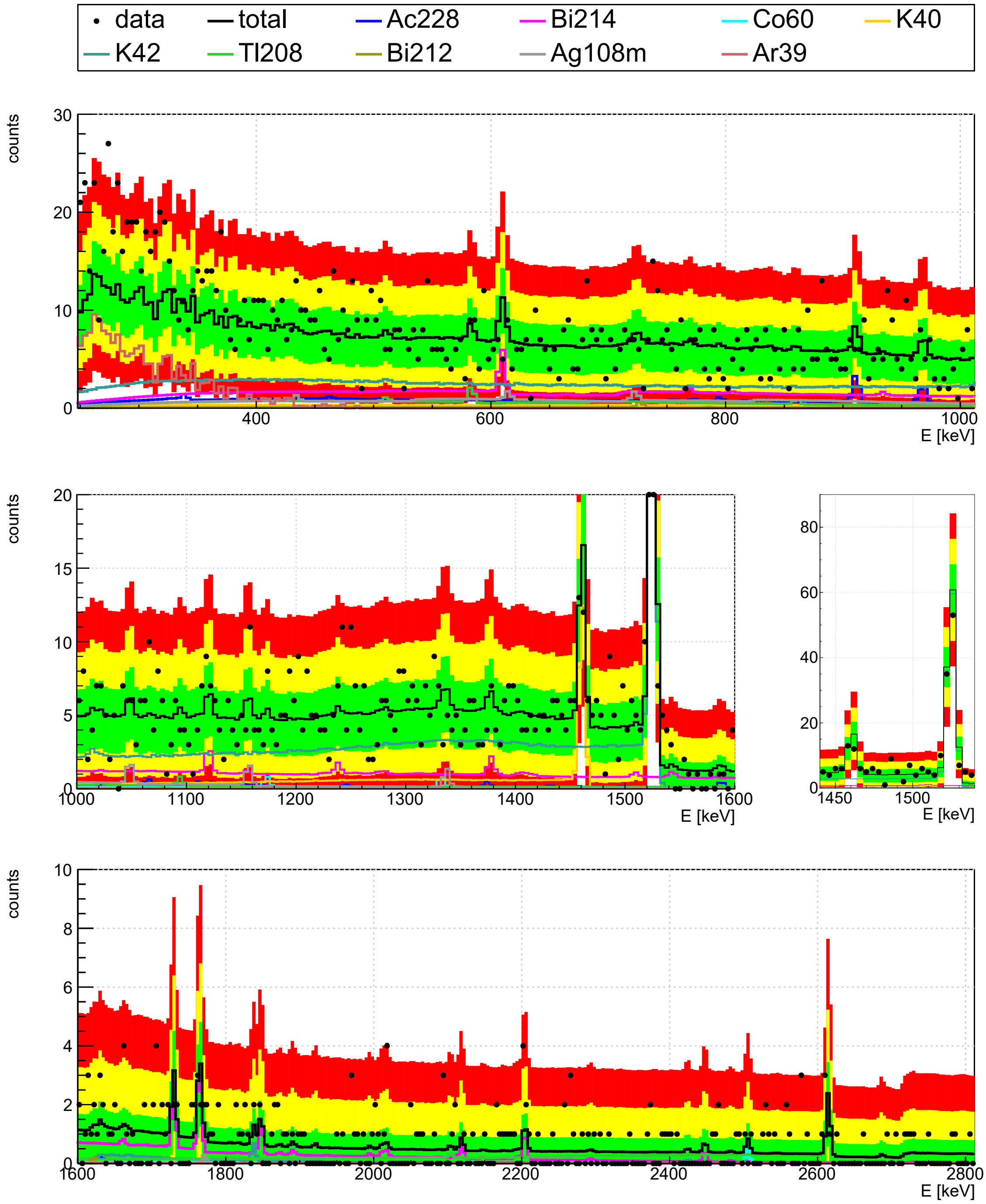

Figure E.2.: The M2 data of PI in form of the single energy spectrum in comparison to the final background model. The green, yellow and red band indicate for each bin the 68%, 95% and 99.7% smallest probability intervals of the Poisson distribution, with the expectation value given by the background model expectation. Additionally shown are the expected spectra of the individual background isotopes. A 4 keV binning is used for the spectra.

E.2 Phase II background model

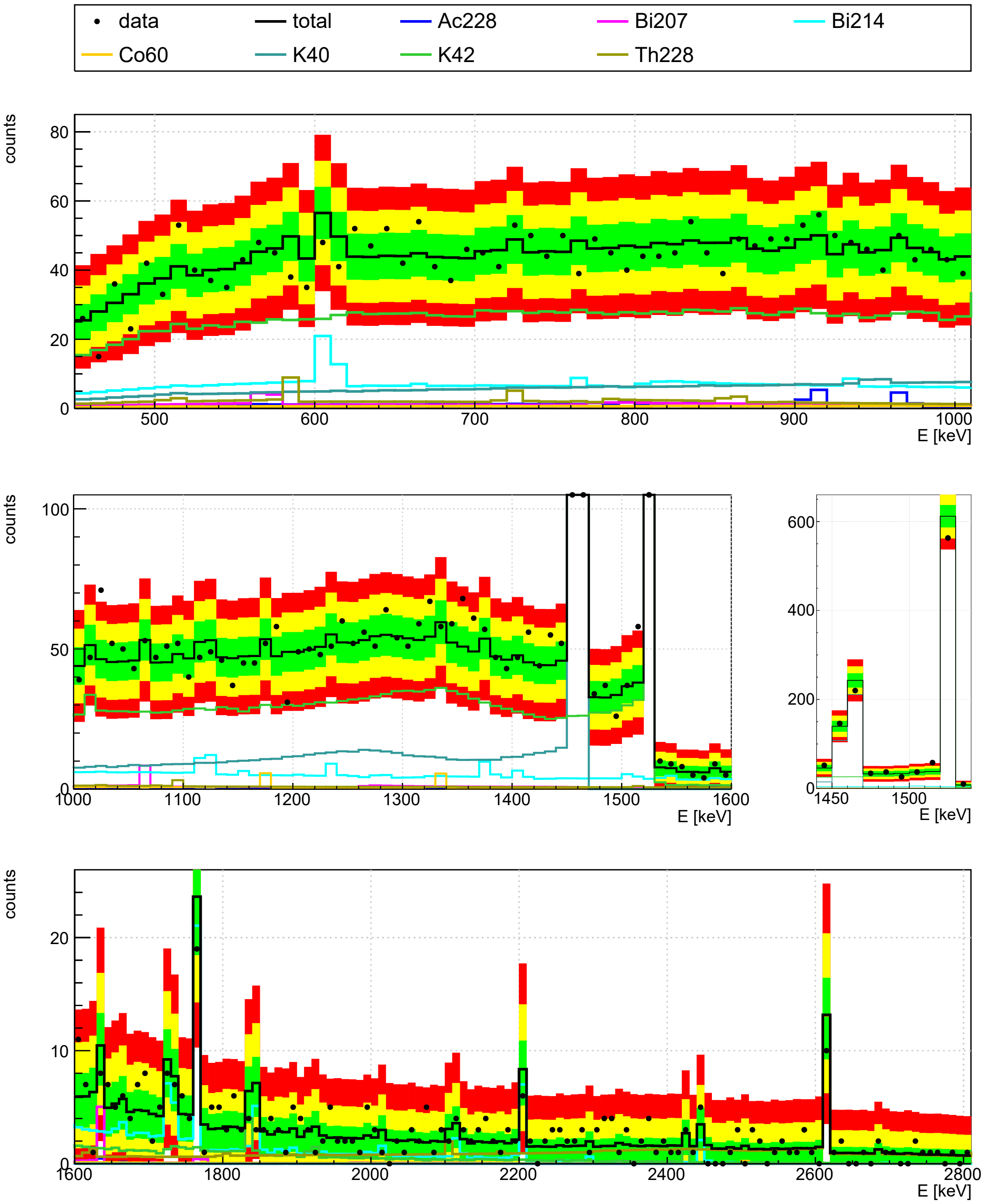

Figure E.3.: Best fit of the sum energy spectrum of the PII M2 data with a 10 keV binning. Also shown are the expected contribution by each background isotop. The green, yellow and red band indicate for each bin the 68%, 95% and 99.7% smallest probability intervals of the Poisson distribution, with the expectation value given by the best fit.

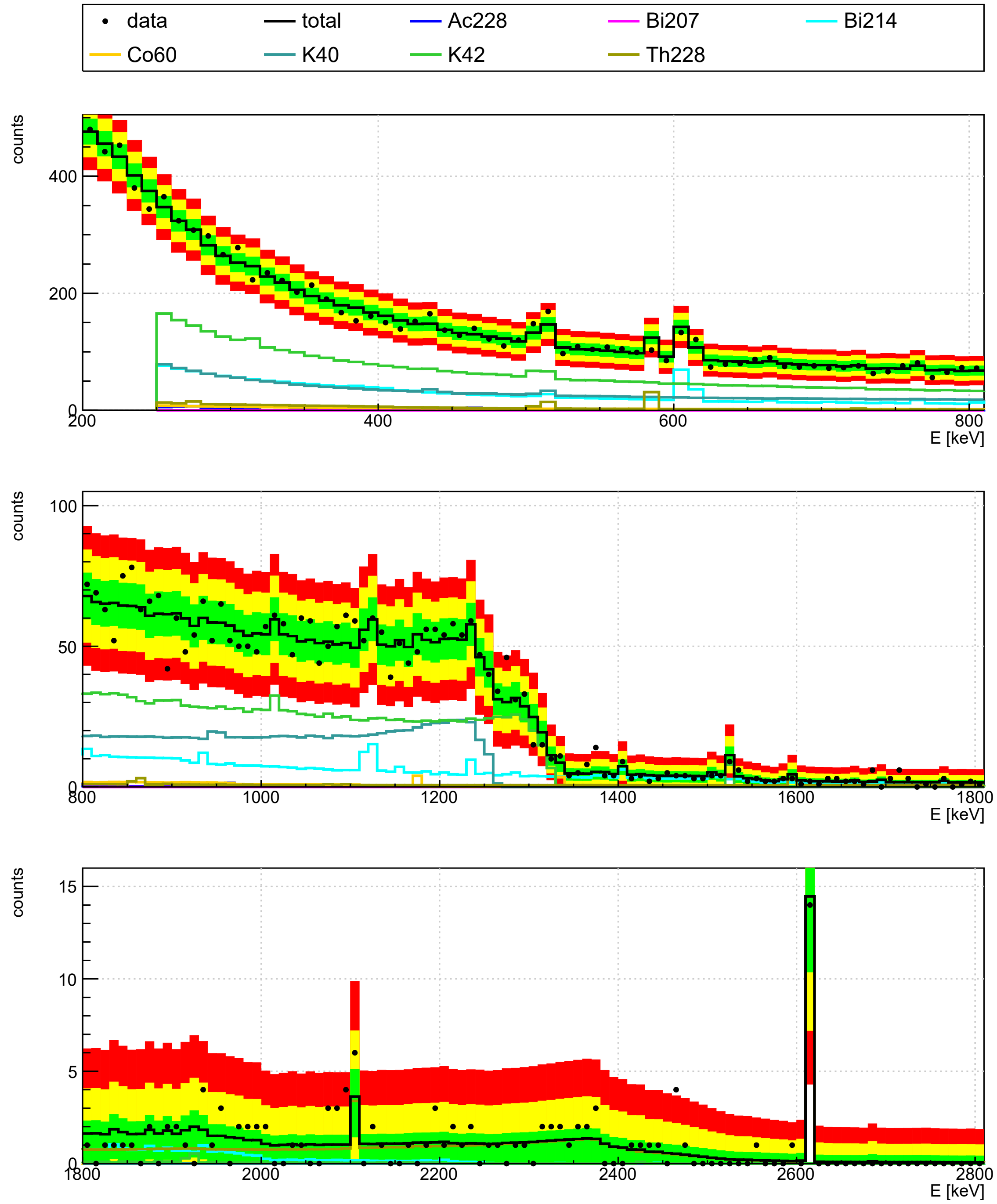

Figure E.4.: Best fit of the single energy spectrum of the PII M2 data with a 10 keV binning. Also shown are the expected contribution by each background isotop. The green, yellow and red band indicate for each bin the 68%, 95% and 99.7% smallest probability intervals of the Poisson distribution, with the expectation value given by the best fit.

		sum fit			single fit		
component		global	marg.	68%/90%	global	marg.	68%/90%
Ac228Cables	[μBq]	315	133	<425	90	19	<500
Ac228Coppershroud	[mBq]	8.1	6.3	<139	141	46	<255
Bi207Minishroud	[μBq]	51	48	(15,84)	7	8	<38
Bi214Cables	[μBq]	518	461	(236,630)	607	559	(450,660)
Bi214Fibers	[mBq]	0	0	<2.3	0	0	<5.4
Bi214Coppershroud	[mBq]	80	36	<141	173	34	<139
Co60Cables	[μBq]	121	51	(9,94)	27	15	<46
Co60Fibers	[mBq]	0	0.1	<0.9	0.2	0	<1.1
K40Holder	[mBq]	9.4	1.7	<7.7	5.0	7.3	<13.5
K40HVCables	[mBq]	5.1	4.7	(1.9,6.9)	5.5	5.0	(2.3,7.6)
K40Minishroud	[mBq]	0	0.5	<10.3	13.7	5.2	<18.6
K40Fibers	[mBq]	0	0.5	<65.0	0	0.6	<46.1
K42LAr	[μBq/kg]	80	65	(32,98)	91	46	(15,72)
K42LArRing80	[mBq/kg]	3.3	1.5	<4.4	0.0	0.1	<2.5
K42LArAbove	[mBq/kg]	1.9	1.9	(1.7,2.1)	1.9	1.9	(1.7,2.1)
K42NplusBEGe	[mBq]	1.0	1.6	(0.7,2.3)	0.3	1.0	(0.4,1.7)
K42NplusCoax	[mBq]	1.1	1.7	(0.9,2.5)	0.4	1.1	(0.5,1.7)
Th228Cables	[μBq]	422	361	(318,430)	335	306	(249,369)
Th228Fibers	[mBq]	0	0.4	<1.0	0.9	0.1	<1.8
Th228Coppershroud	[mBq]	4.4	0.2	<23.8	0.0	0.3	<30.9
p-value:		data points in interval:			data points in interval:		
0.83 (sum)		(out of	68.0%:	453 (72%)	(out of	68.0%:	528 (77%)
0.51 (single)		632)	95.0%:	609 (96%)	685)	95.0%:	660 (96%)
			99.7%:	632 (100%)		99.7%:	681 (99.4%)

Table E.1.: Results from the first preliminary fit of the sum and single energy spectrum. Given are the global mode, the marginalized mode and the 68% smallest interval. If this interval is compatible with 0, the 90% upper limit is given instead as obtained from the 90% quantile of the marginalized posteriors. Additionally given at the bottom are the p-value of the fit and the number of data points (bins) within the 68%, 95% and 99.7% probability bands given the global mode as expectation value.

E.3 MC spectra

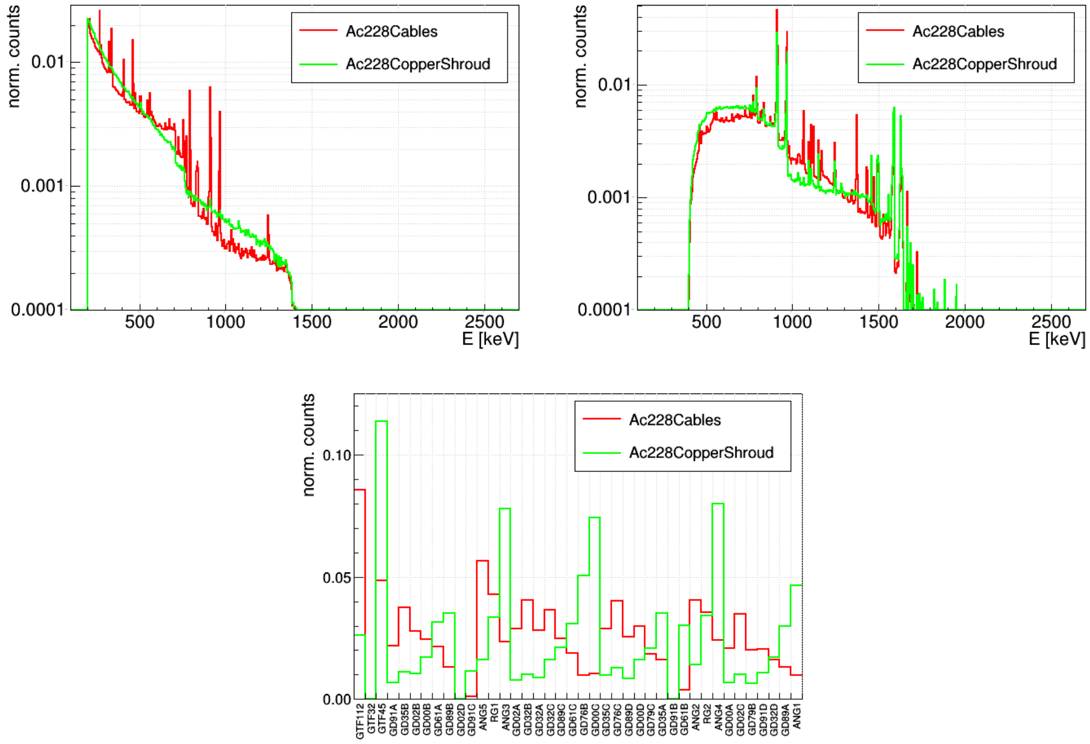

Figure E.5.: The single energy (*left*), sum energy (*right*) spectra and the distribution of total counts per detector (*bottom*) expected from MC simulations of the given components of ^{228}Ac. The spectra are normalized to an integral of 1.

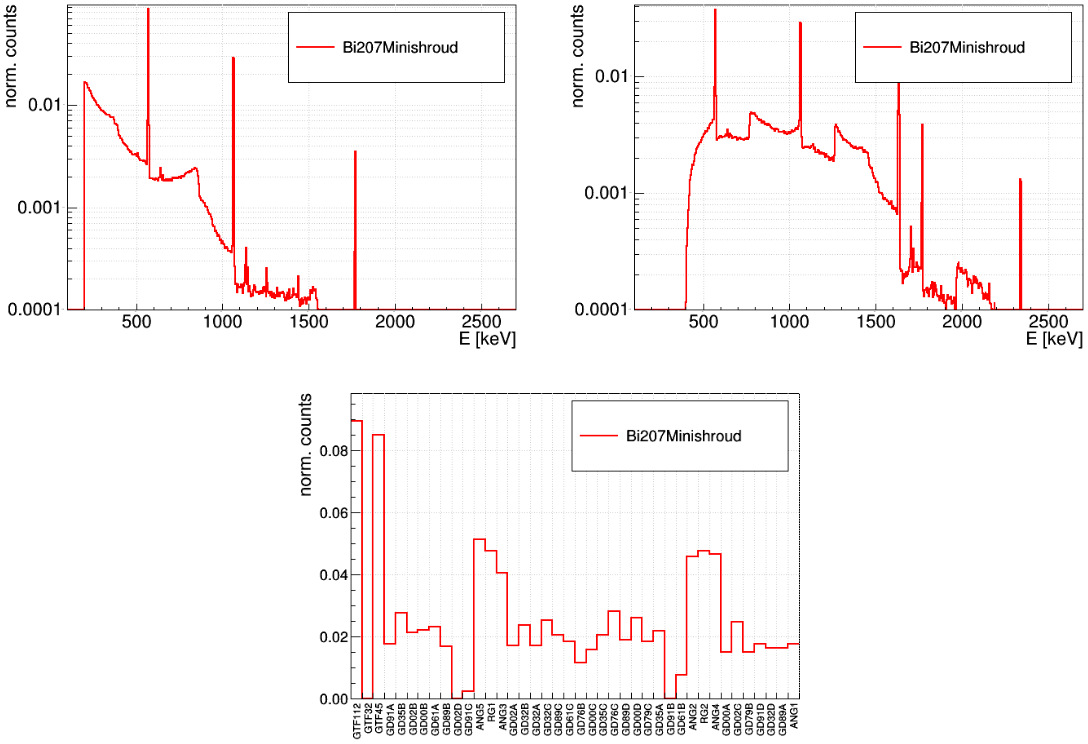

Figure E.6.: The single energy (*left*), sum energy (*right*) spectra and the distribution of total counts per detector (*bottom*) expected from MC simulations of the given component of ^{207}Bi. The spectra are normalized to an integral of 1.

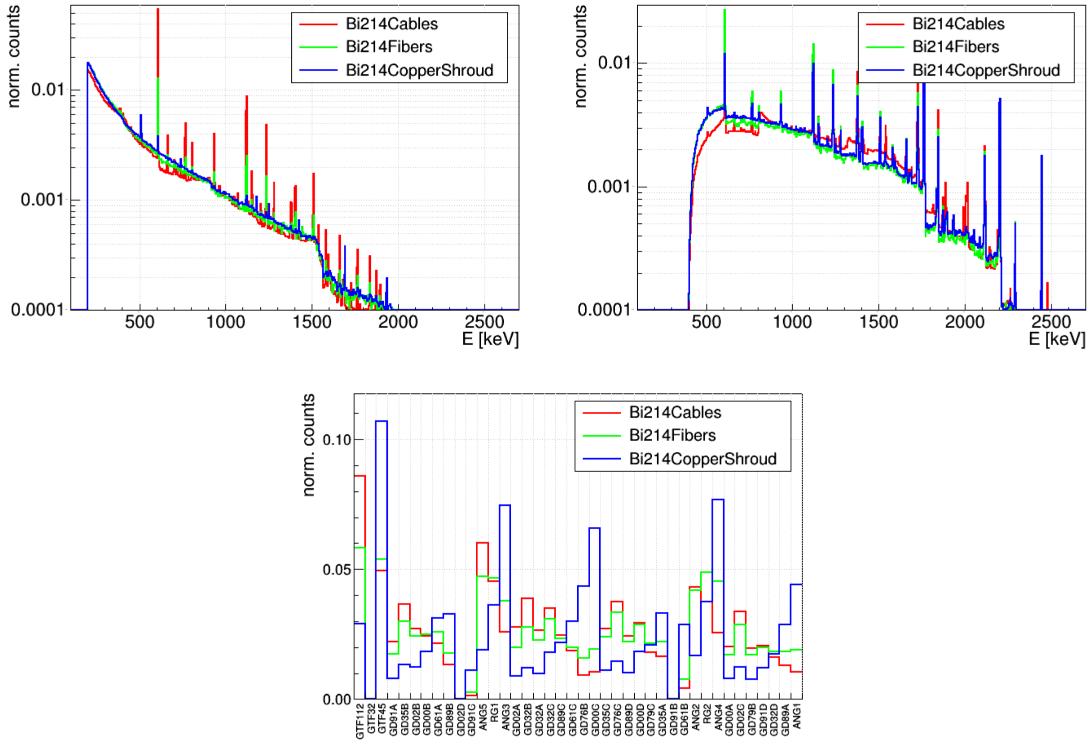

Figure E.7.: The single energy (*left*), sum energy (*right*) spectra and the distribution of total counts per detector (*bottom*) expected from MC simulations of the given component of ^{214}Bi. The spectra are normalized to an integral of 1.

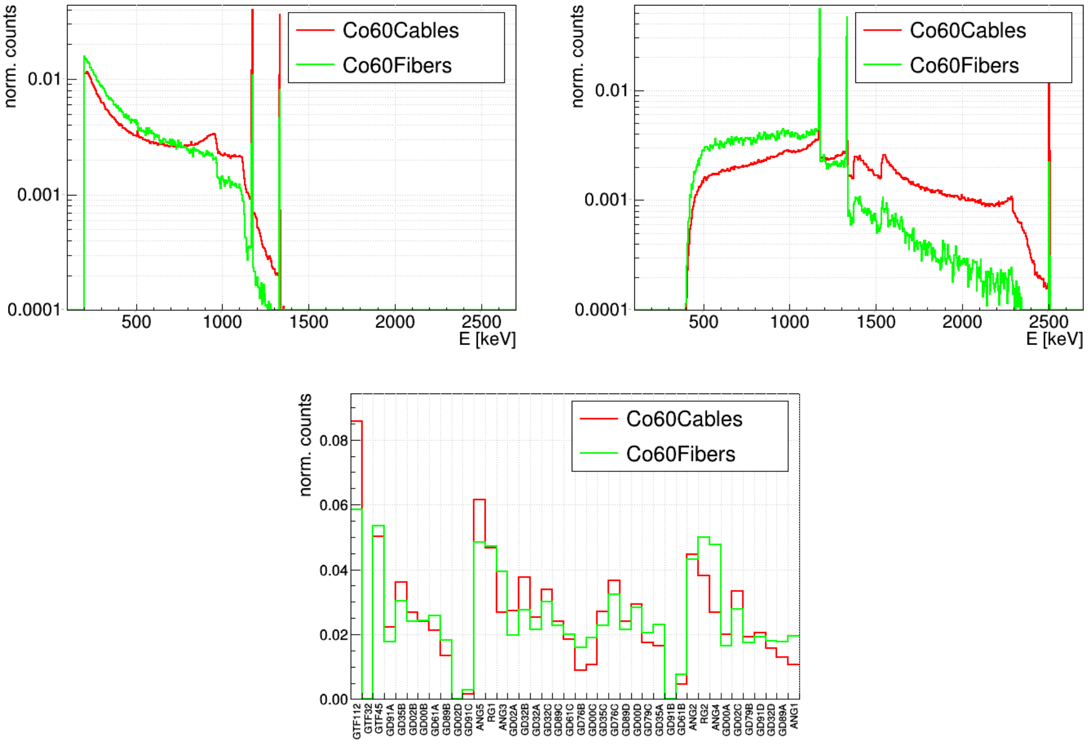

Figure E.8.: The single energy (*left*), sum energy (*right*) spectra and the distribution of total counts per detector (*bottom*) expected from MC simulations of the given component of ^{60}Co. The spectra are normalized to an integral of 1.

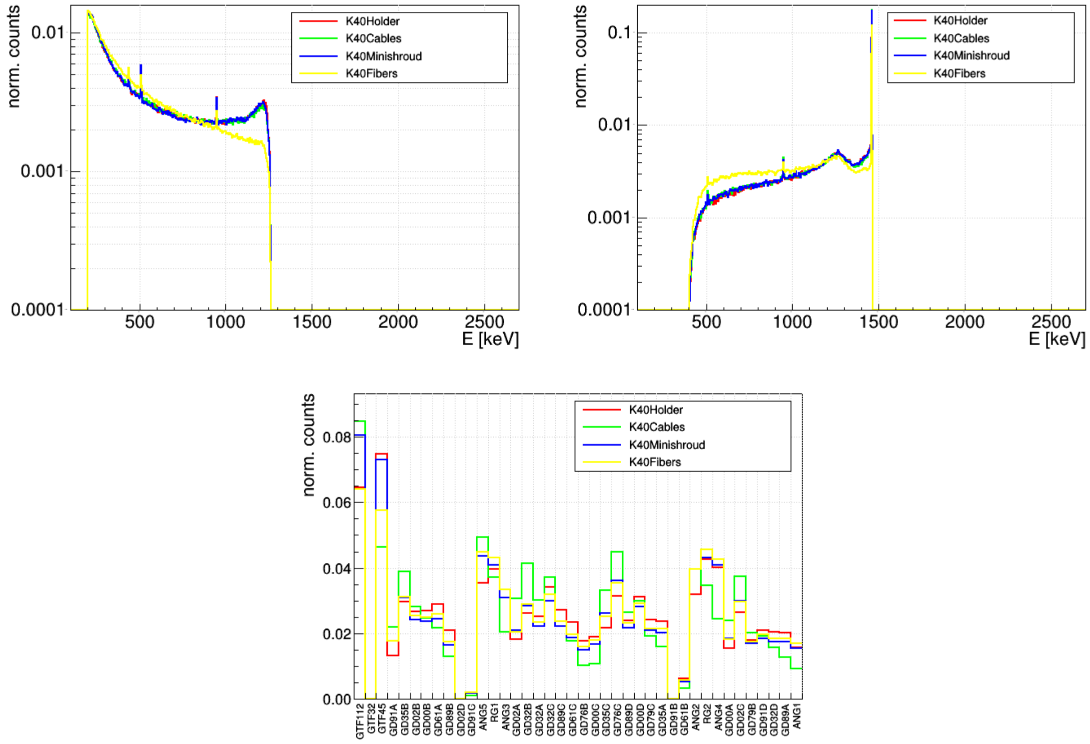

Figure E.9.: The single energy (*left*), sum energy (*right*) spectra and the distribution of total counts per detector (*bottom*) expected from MC simulations of the given components of ^{40}K. The spectra are normalized to an integral of 1.

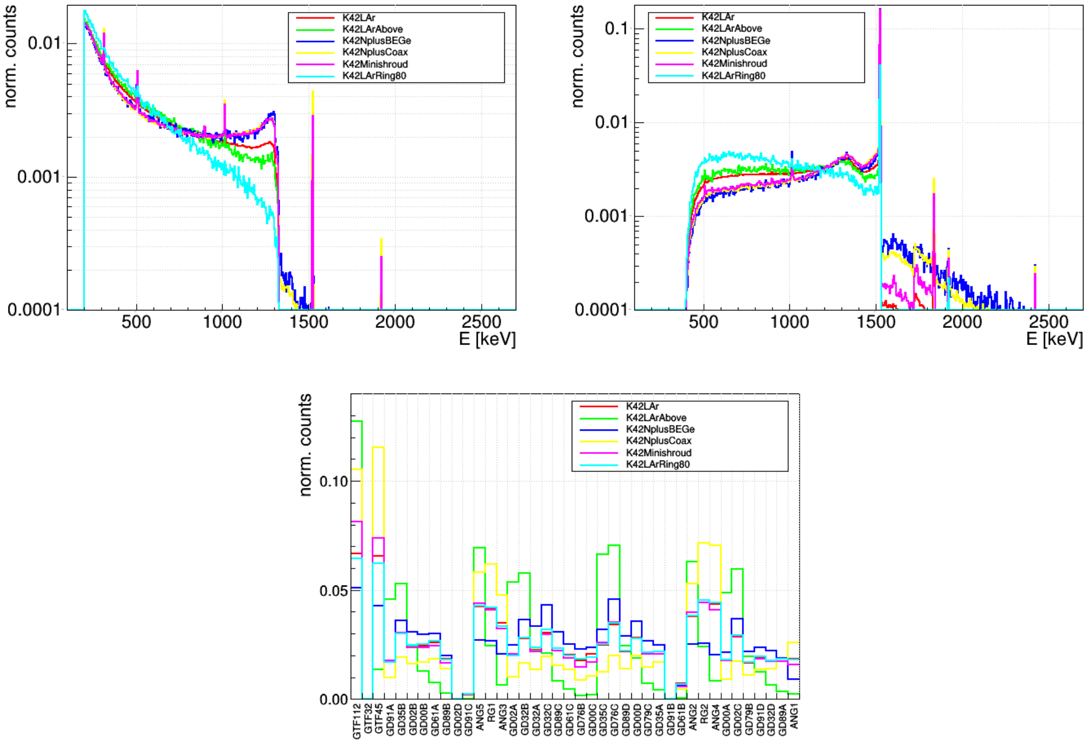

Figure E.10.: The single energy (*left*), sum energy (*right*) spectra and the distribution of total counts per detector (*bottom*) expected from MC simulations of the given components of ^{42}K. The spectra are normalized to an integral of 1.

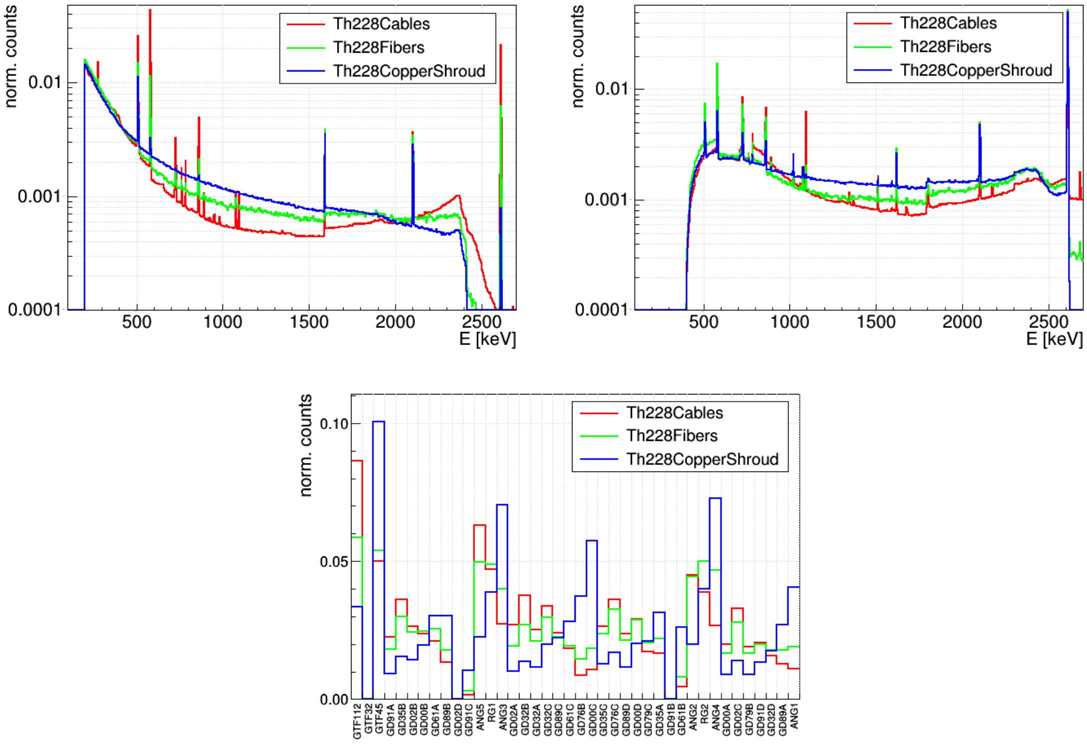

Figure E.11.: The single energy (*left*), sum energy (*right*) spectra and the distribution of total counts per detector (*bottom*) expected from MC simulations of the given components of ^{228}Th, being represented by ^{208}Tl and ^{212}Bi. The spectra are normalized to an integral of 1.

E.4 ^{42}K and ^{40}K priors

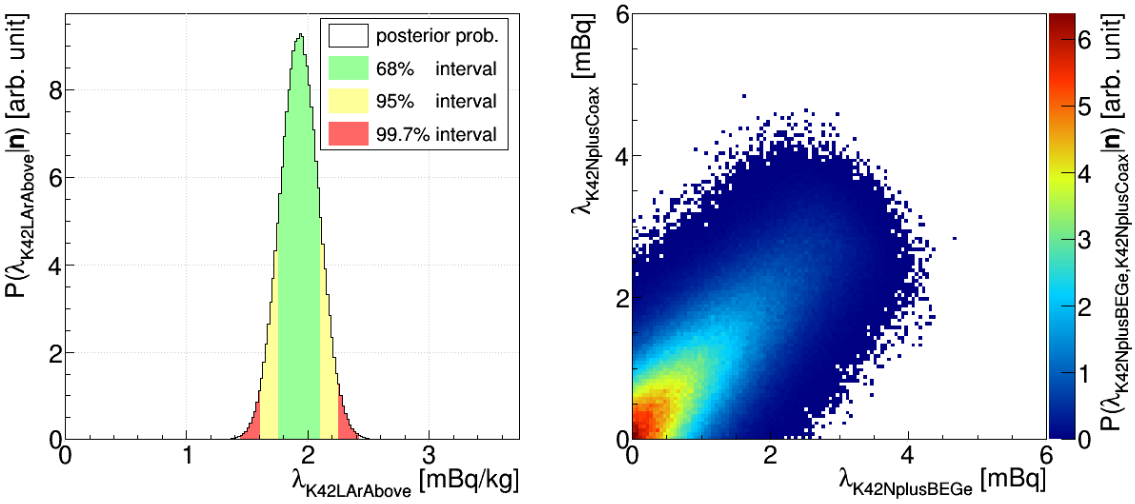

Figure E.12.: Marginalized posterior probability density distributions for the K42LArAbove (*left*) and the K42NplusCoax and K42NplusBEGe (*right*) components, obtained from the detector distribution fit of the events with a sum energy of (1524.6±7.5) keV as discussed in Ch. 6.6.2.

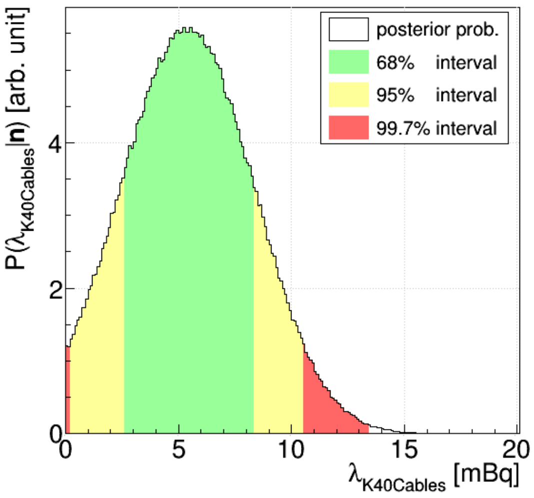

Figure E.13.: Marginalized posterior probability density distributions for the K40Cables component, obtained from the detector distribution fit of the events with a sum energy of (1460.8±7.5) keV as discussed in Ch. 6.6.3.

Appendix F

$2\nu\beta\beta$-decay to excited states

F.1 Update of events in cut regions of Phase I

In the following, the number and timestamps of events are listed, that are either removed from or added to the new cut selection due to the analysis changes to the PI data set descibed in Ch. 7.5.6, with respect to the previous analysis presented in [4, 127]:

- $0^+_{g.s.} \rightarrow 2^+_1$: One event (timestamp: 1356810423) was shifted by about 1 keV into the signal cut region. Another event (timestamp: 1346955931) got removed from SB0, due to it being classified as M3 event with the fixed energy threshold of 100 keV.
- $0^+_{g.s.} \rightarrow 0^+_1$: Two events (timestamps: 1350872647, 1350952126) are removed from SB1 and SB3 due to classification as M3 events.
- $0^+_{g.s.} \rightarrow 2^+_2$ B1: Two events (timestamps: 1345032530, 1356810423) are added to the signal cut region due to a shift of the reconstructed energy value. Three events (timestamps: 1355269850, 1351549326, 1368927784) are added to SB0, SB2 and SB3 respectively for the same reason. On the other hand, 7 events (timestamps: 1364475771, 1327316696, 1337052296, 1330396078, 1355259920, 1328820266, 1350872647) are removed from the combined sidebands, for multiplicity reasons.
- $0^+_{g.s.} \rightarrow 2^+_2$ B2: No changes in the number of counts observed.

F.2 Pair optimization plots

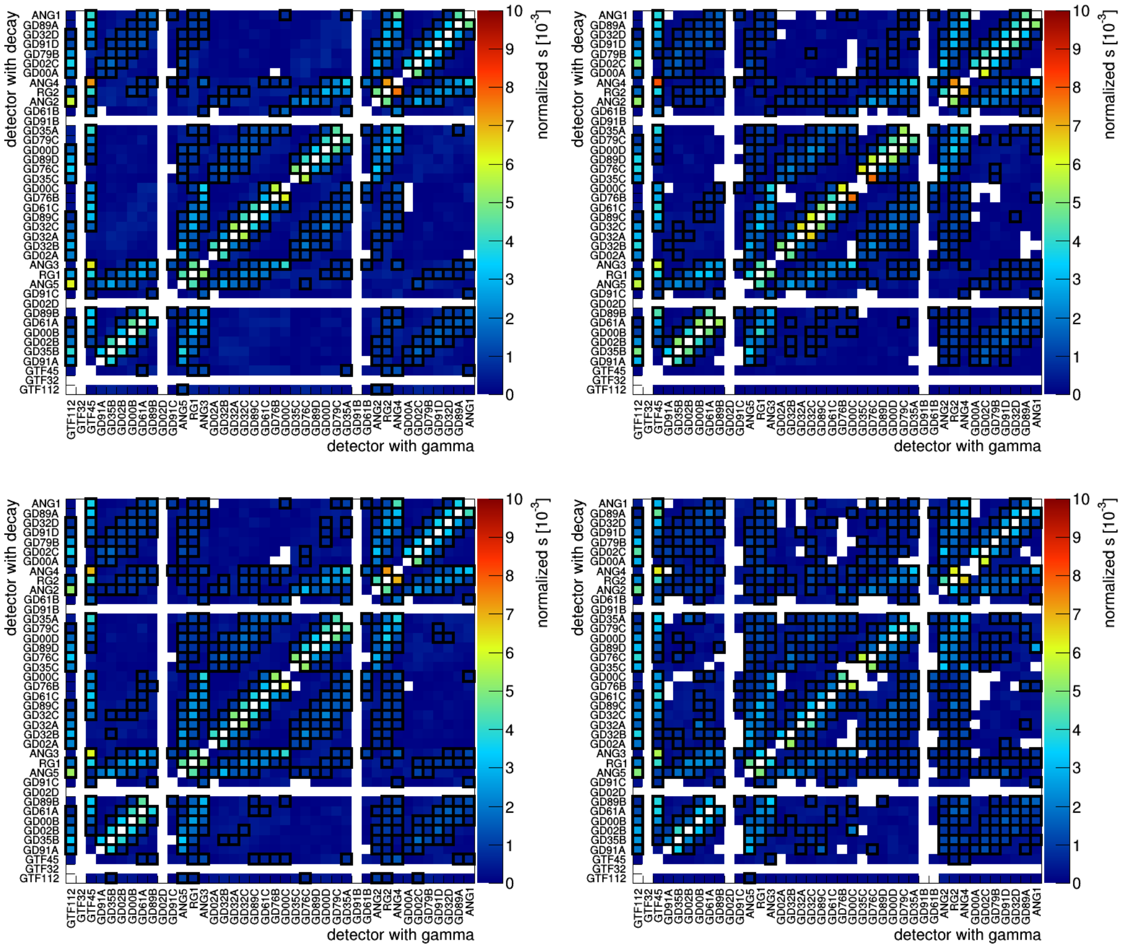

Figure F.1.: A map of detector pairs in PII, with the detector with the γ-ray energy deposition on the x-axis and the two electron energy deposition (signal decay) on the y-axis. The color code indicates the contribution of each pair to the total sensitivity to the $0^+_{g.s.} \rightarrow 0^+_1$ decay mode, as determined by the ratio between signal efficiency contribution and background contribution. Pairs with a high individual contribution are accepted for the analysis and are framed in black. A discusson of the different regions of accepted pairs can be found in Ch. 7.5.4.

F.3 Toy MC limit distributions

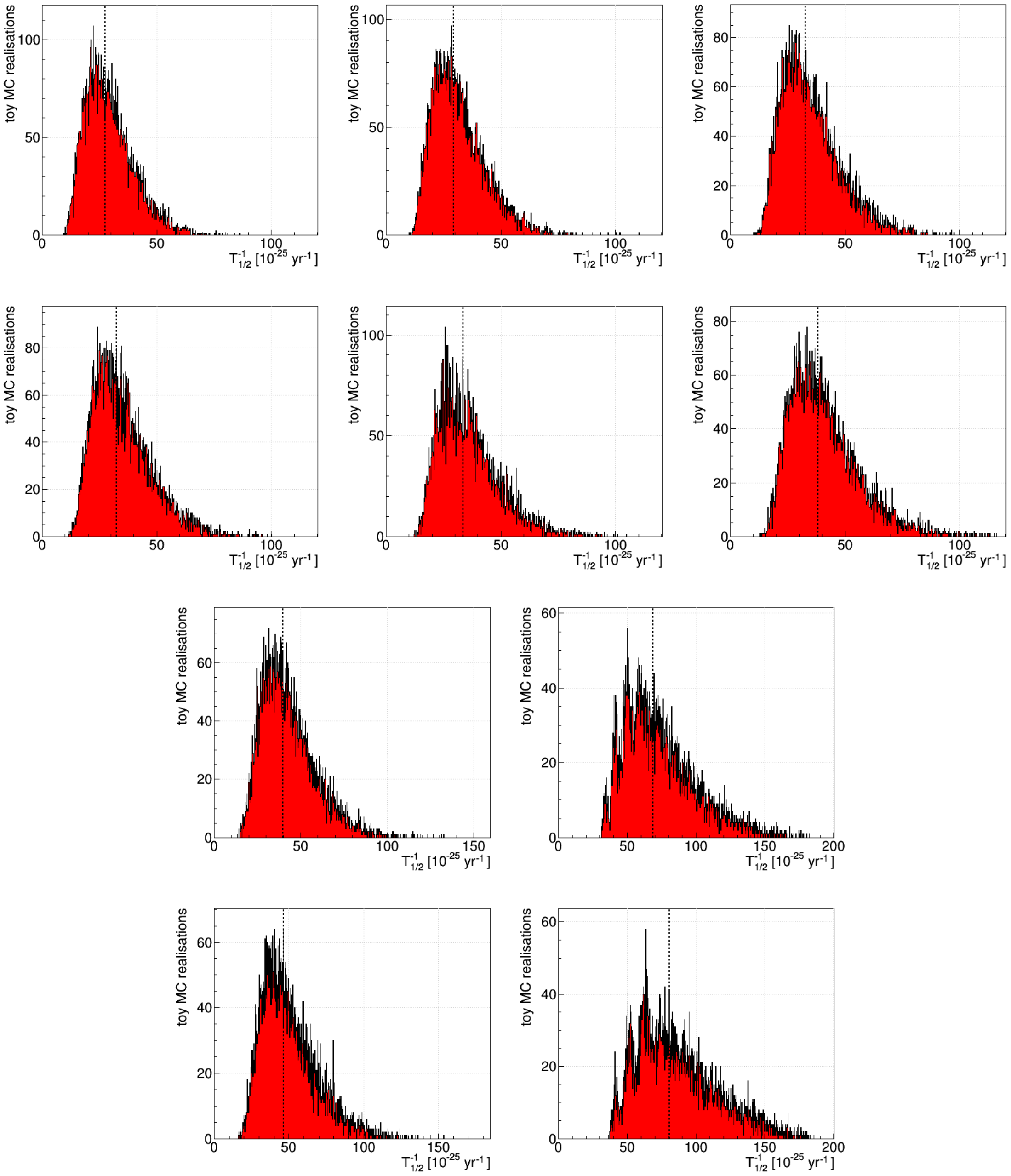

Figure F.2.: Distributions of 90% credibility upper limits on the inverse half-life of the $2\nu\beta\beta$ -decay, obtained from fits of 10,000 toy MC experiments of M2 data, generated for the background only case using the predicted counts in the signal regions given by the background model. The upper row shows the distributions for the modes $0^+_{g.s.} \rightarrow 0^+_1$ (*left*), $0^+_{g.s.} \rightarrow 2^+_1$ (*middle*) and $0^+_{g.s.} \rightarrow 2^+_2$ (*right*). The second row, shows the corresponding distributions, using the PII data only. In the third and fourth row, the distributions are given for the cases where only the first (*left*) or the second (*right*) branch of the $0^+_{g.s.} \rightarrow 2^+_2$ decay mode are taken into account for the combined PI and PII data and the PII data only, respectively. The dashed line indicates the median of each distribution. The sensitivity to set a 90% lower limit on the half-life is defined as the inverse of this median.

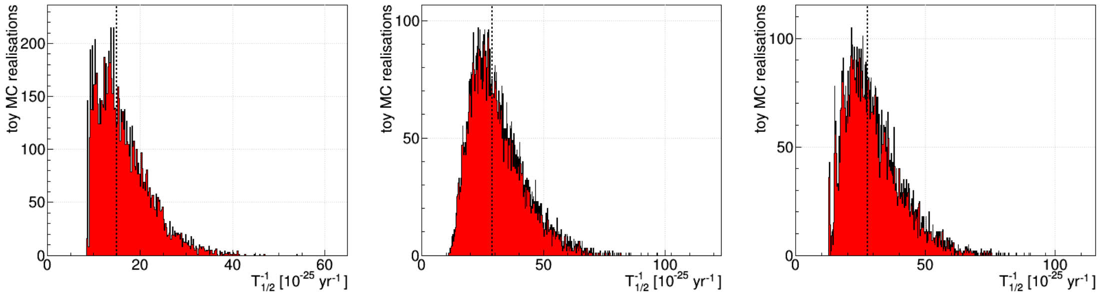

Figure F.3.: Distributions of 90% credibility upper limits on the inverse half-life obtained from fits of 10,000 toy MC experiments of M2 data with applied LAr veto of the $2\nu\beta\beta$ -decay modes $0^+_{g.s.} \rightarrow 2^+_1$ (*left*), $0^+_{g.s.} \rightarrow 2^+_2$ with both branches (*middle*) and $0^+_{g.s.} \rightarrow 2^+_2$ second branch only (*right*), generated for the background only case using the predicted counts in the signal regions given by the average of the sideband counts. The dashed line indicates the median of each distribution. The sensitivity to set a 90% lower limit on the half-life is defined as the inverse of this median.

F.4 List of events in the cut regions

Run	timestamp	E_1 [keV]	ID_1	E_2 [keV]	ID_2	E_{sum} [keV]	Cut	LAr
Run36	1345032530	561.0	ANG3	563.5	RG1	1124.5	0	0
Run36	1346336163	559.4	ANG2	322.2	ANG5	881.5	0	0
Run37	1347127032	563.0	ANG3	373.1	ANG5	936.2	0	0
Run38	1348944227	769.0	ANG5	557.4	RG1	1326.4	0	0
Run41	1356810423	801.4	ANG2	561.5	ANG4	1362.9	0	0

Table F.1.: List of events in the ROI of the $0^+_{g.s.} \to 0^+_1$ decay mode in PI, giving their timestamp, both energies and detector names, the sum energy and the LAr veto flag.

Run	timestamp	E_1 [keV]	ID_1	E_2 [keV]	ID_2	E_{sum} [keV]	Cut	LAr
Run36	1345032530	561.0	ANG3	563.5	RG1	1124.5	0	0
Run38	1348944227	769.0	ANG5	557.4	RG1	1326.4	0	0
Run41	1356810423	801.4	ANG2	561.5	ANG4	1362.9	0	0

Table F.2.: List of events in the ROI of the $0^+_{g.s.} \to 2^+_1$ decay mode in PI, giving their timestamp, both energies and detector names, the sum energy and the LAr veto flag.

Run	timestamp	E_1 [keV]	ID_1	E_2 [keV]	ID_2	E_{sum} [keV]	Cut	LAr
Run25	1322045910	295.2	ANG3	658.1	GTF112	953.3	0	0
Run31	1334314022	658.6	ANG4	431.9	RG2	1090.4	0	0
Run36	1345032530	561.0	ANG3	563.5	RG1	1124.5	0	0
Run36	1345624897	658.6	GD32B	298.5	GD32C	957.1	0	0
Run36	1345713741	299.0	ANG2	656.8	ANG5	955.8	0	0
Run36	1346336163	559.4	ANG2	322.2	ANG5	881.5	0	0
Run38	1348944227	769.0	ANG5	557.4	RG1	1326.4	0	0
Run41	1356810423	801.4	ANG2	561.5	ANG4	1362.9	0	0

Table F.3.: List of events in the ROI of the first branch of the $0^+_{g.s.} \to 2^+_2$ decay mode in PI, giving their timestamp, both energies and detector names, the sum energy and the LAr veto flag.

Run	timestamp	E_1 [keV]	ID_1	E_2 [keV]	ID_2	E_{sum} [keV]	Cut	LAr
no events survived the cut								

Table F.4.: List of events in the ROI of the second branch of the $0^+_{g.s.} \to 2^+_2$ decay mode in PI, giving their timestamp, both energies and detector names, the sum energy and the LAr veto flag.

Run	timestamp	E_1 [keV]	ID_1	E_2 [keV]	ID_2	E_{sum} [keV]	Cut	LAr
Run0054	1453820902	561.3	ANG4	652.6	GD89A	1213.9	1	1
Run0055	1454162376	559.8	GD76B	618.5	GD00C	1178.3	1	1
Run0055	1454432558	565.1	ANG2	497.3	GTF112	1062.4	1	1
Run0056	1455066967	677.8	GD35C	562.0	GD76C	1239.8	1	1
Run0056	1455723604	559.3	ANG2	253.4	GD79B	812.7	1	1
Run0056	1455779333	702.0	GD79B	564.4	GTF112	1266.3	1	1
Run0058	1457214111	562.1	GD35B	285.7	GD02C	847.8	1	1
Run0060	1458564607	557.9	ANG5	580.3	GD02A	1138.2	1	1
Run0060	1459188901	559.4	ANG2	269.5	RG2	828.8	1	1
Run0060	1459273501	344.7	ANG5	562.9	RG1	907.6	1	1
Run0060	1459731407	690.8	GD00C	564.6	GTF45	1255.4	1	0
Run0060	1459915378	510.4	GD32B	563.5	GD00D	1073.9	1	1
Run0061	1460412357	559.3	GD00A	610.6	GD02C	1170.0	1	1
Run0062	1460549741	723.3	GD76C	564.5	ANG2	1287.8	1	1
Run0062	1461665088	465.8	GD02A	558.3	GTF112	1024.1	1	1
Run0063	1462404678	564.5	RG2	867.8	ANG4	1432.3	1	1
Run0063	1462810379	562.3	GD02A	702.5	GD32B	1264.9	1	1
Run0063	1463331421	559.7	GD61A	765.0	RG1	1324.6	1	1
Run0063	1463640152	412.8	GD89A	557.5	GTF45	970.4	1	1
Run0063	1463667868	480.2	GD79C	561.2	RG2	1041.5	1	1
Run0065	1465097655	609.1	GD32C	560.7	GD89C	1169.8	1	1
Run0065	1465613823	284.1	GD02C	564.4	GTF112	848.4	1	1
Run0069	1469299852	669.1	GD76B	558.7	GD00C	1227.9	1	1
Run0070	1470194479	505.4	GD32D	561.1	ANG1	1066.5	1	1
Run0070	1470817685	558.9	GD35B	844.1	ANG5	1402.9	1	1
Run0070	1471523312	936.8	ANG5	559.0	RG1	1495.7	1	0
Run0071	1472795508	564.8	GD32D	267.0	GD89A	831.8	1	1
Run0071	1474070129	359.3	GD91A	564.7	GD35B	923.9	1	1
Run0072	1474745573	320.0	GD76C	561.7	GD89D	881.7	1	1
Run0073	1475310606	559.2	GD61A	480.6	GD32D	1039.8	1	1
Run0073	1476406041	511.4	GD35B	561.2	GD00B	1072.7	1	0
Run0073	1476804729	558.6	GD35B	354.6	GD00A	913.2	1	1
Run0073	1476983241	558.7	ANG5	311.5	GD32C	870.2	1	1
Run0073	1477077416	561.5	GD35B	266.2	ANG5	827.7	1	0
Run0073	1477777592	564.8	ANG5	295.8	GD02A	860.6	1	0
Run0074	1478665381	559.3	ANG2	1019.9	GTF112	1579.2	1	1
Run0074	1479930011	564.4	GD35C	936.8	GD76C	1501.1	1	0
Run0074	1480247332	563.8	GD35B	267.7	GD02B	831.5	1	0
Run0075	1480688657	1035.1	ANG1	559.2	GTF45	1594.3	1	1
Run0075	1481341171	897.2	ANG5	557.8	RG1	1455.0	1	0
Run0075	1481655499	596.3	GD61A	563.5	GD89B	1159.9	1	1
Run0075	1483475924	300.5	ANG5	563.1	GD32C	863.6	1	1
Run0077	1487042219	782.8	GD89D	562.1	GTF112	1344.9	1	0
Run0077	1487325253	736.6	GD02C	563.6	GTF112	1300.2	1	1
Run0077	1488485407	563.8	ANG2	496.9	GD91D	1060.7	1	1
Run0078	1491067607	288.7	GD91A	561.6	GD35B	850.3	1	1
Run0079	1492027416	561.2	ANG2	261.1	RG2	822.3	1	1
Run0079	1492182476	559.4	GD00B	690.4	ANG3	1249.8	1	0
Run0079	1492213134	559.3	GD02A	648.6	GD32B	1207.9	1	1
Run0079	1492225007	561.4	RG1	263.2	GD89C	824.6	1	1

Table F.5.: List of events in the ROI of the $0^+_{g.s.} \rightarrow 0^+_1$ decay mode in PII, giving their timestamp, both energies and detector names, the sum energy and the LAr veto flag.

Run	timestamp	E_1 [keV]	ID_1	E_2 [keV]	ID_2	E_{sum} [keV]	Cut	LAr
Run0055	1454162376	559.8	GD76B	618.5	GD00C	1178.3	1	1
Run0060	1458564607	557.9	ANG5	580.3	GD02A	1138.2	1	1
Run0061	1460412357	559.3	GD00A	610.6	GD02C	1170.0	1	1
Run0062	1461665088	465.8	GD02A	558.3	GTF112	1024.1	1	1
Run0063	1463331421	559.7	GD61A	765.0	RG1	1324.6	1	1
Run0063	1463640152	412.8	GD89A	557.5	GTF45	970.4	1	1
Run0065	1465097655	609.1	GD32C	560.7	GD89C	1169.8	1	1
Run0065	1465677253	559.8	GD02A	446.0	GD89D	1005.8	1	1
Run0069	1469299852	669.1	GD76B	558.7	GD00C	1227.9	1	1
Run0070	1470817685	558.9	GD35B	844.1	ANG5	1402.9	1	1
Run0070	1471523312	936.8	ANG5	559.0	RG1	1495.7	1	0
Run0073	1475310606	559.2	GD61A	480.6	GD32D	1039.8	1	1
Run0073	1475626060	518.3	GD35B	559.3	GD02B	1077.5	1	0
Run0075	1480688657	1035.1	ANG1	559.2	GTF45	1594.3	1	1
Run0075	1481341171	897.2	ANG5	557.8	RG1	1455.0	1	0
Run0079	1492182476	559.4	GD00B	690.4	ANG3	1249.8	1	0
Run0079	1492213134	559.3	GD02A	648.6	GD32B	1207.9	1	1

Table F.6.: List of events in the ROI of the $0^+_{g.s.} \rightarrow 2^+_1$ decay mode in PII, giving their timestamp, both energies and detector names, the sum energy and the LAr veto flag.

Run	timestamp	E_1 [keV]	ID_1	E_2 [keV]	ID_2	$\mathrm{E}_{\mathrm{sum}}$ [keV]	Cut	LAr
Run0053	1451850166	289.3	GD35A	655.5	GTF45	944.8	1	0
Run0054	1453877532	655.9	GD00C	579.8	GTF45	1235.7	1	1
Run0055	1454162376	559.8	GD76B	618.5	GD00C	1178.3	1	1
Run0056	1454902424	558.3	GD89C	336.0	GTF45	894.2	1	1
Run0056	1455723604	559.3	ANG2	253.4	GD79B	812.7	1	1
Run0058	1457012878	657.1	GD91D	475.5	GD32D	1132.6	1	1
Run0058	1457262662	342.3	ANG5	657.3	GD32C	999.6	1	1
Run0060	1458564607	557.9	ANG5	580.3	GD02A	1138.2	1	1
Run0060	1458694122	342.6	GD02B	657.3	GTF112	999.9	1	1
Run0060	1459188901	559.4	ANG2	269.5	RG2	828.8	1	1
Run0061	1460412357	559.3	GD00A	610.6	GD02C	1170.0	1	1
Run0062	1461665088	465.8	GD02A	558.3	GTF112	1024.1	1	1
Run0063	1463331421	559.7	GD61A	765.0	RG1	1324.6	1	1
Run0063	1463640152	412.8	GD89A	557.5	GTF45	970.4	1	1
Run0065	1465097655	609.1	GD32C	560.7	GD89C	1169.8	1	1
Run0065	1465170488	658.3	GD00A	516.5	GD02C	1174.9	1	1
Run0065	1465677253	559.8	GD02A	446.0	GD89D	1005.8	1	1
Run0067	1467018089	699.8	GD89D	658.4	GD00D	1358.2	1	0
Run0067	1467110000	275.7	GD02A	557.7	GD32A	833.4	1	0
Run0069	1469299852	669.1	GD76B	558.7	GD00C	1227.9	1	1
Run0069	1469540827	253.3	GD32A	657.3	GD32C	910.5	1	0
Run0070	1469876040	657.2	GD89B	312.9	ANG3	970.1	1	1
Run0070	1470817685	558.9	GD35B	844.1	ANG5	1402.9	1	1
Run0070	1471523312	936.8	ANG5	559.0	RG1	1495.7	1	0
Run0071	1474430952	657.2	ANG5	395.9	GTF112	1053.0	1	1
Run0073	1475310606	559.2	GD61A	480.6	GD32D	1039.8	1	1
Run0073	1475626060	518.3	GD35B	559.3	GD02B	1077.5	1	0
Run0073	1476804729	558.6	GD35B	354.6	GD00A	913.2	1	1
Run0073	1476983241	558.7	ANG5	311.5	GD32C	870.2	1	1
Run0074	1478665381	559.3	ANG2	1019.9	GTF112	1579.2	1	1
Run0075	1480688657	1035.1	ANG1	559.2	GTF45	1594.3	1	1
Run0075	1481341171	897.2	ANG5	557.8	RG1	1455.0	1	0
Run0075	1481765376	657.1	GD61C	375.7	GTF45	1032.8	1	1
Run0076	1485568483	657.3	GD00A	319.7	GD02C	977.0	1	1
Run0077	1487009572	658.3	ANG3	264.3	GD00C	922.6	1	1
Run0078	1490367414	609.1	ANG5	657.2	GD32B	1266.3	1	1
Run0079	1492182476	559.4	GD00B	690.4	ANG3	1249.8	1	0
Run0079	1492213134	559.3	GD02A	648.6	GD32B	1207.9	1	1

Table F.7.: List of events in the ROI of the first branch of the $0^+_{g.s.} \rightarrow 2^+_2$ decay mode in PII, giving their timestamp, both energies and detector names, the sum energy and the LAr veto flag.

Run	timestamp	E_1 [keV]	ID_1	E_2 [keV]	ID_2	$\mathrm{E}_{\mathrm{sum}}$ [keV]	Cut	LAr
Run0056	1454819620	1214.8	ANG5	300.0	RG1	1514.8	1	1
Run0065	1465482655	1217.8	ANG3	267.7	GD61C	1485.5	1	1
Run0074	1477840989	313.1	GD00A	1216.8	GTF112	1529.9	1	0
Run0075	1480959366	1215.3	GD35B	320.6	GD02B	1535.9	1	1

Table F.8.: List of events in the ROI of the second branch of the $0^+_{g.s.} \rightarrow 2^+_2$ decay mode in PII, giving their timestamp, both energies and detector names, the sum energy and the LAr veto flag.

F.5 Timestamp distributions of events in the cut regions

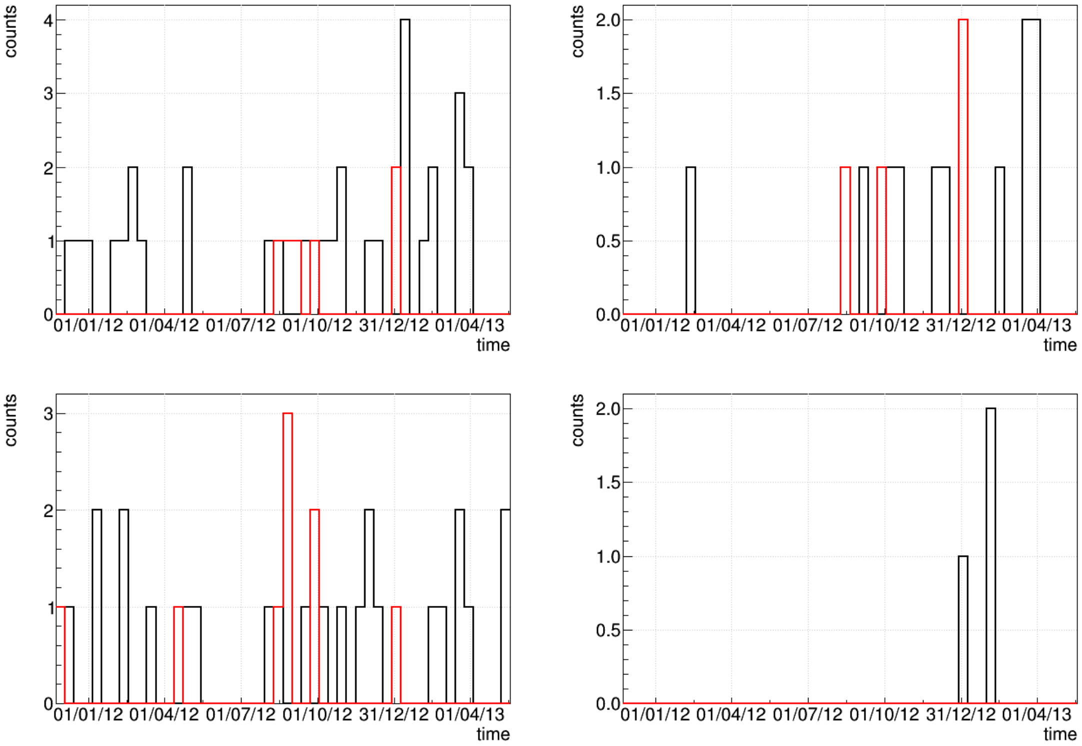

Figure F.4.: Timestamp distribution of PI events in the signal cut regions (red) and summed side-band regions (black) of the search for the $0^+_{g.s.} \to 0^+_1$ (*top left*), $0^+_{g.s.} \to 2^+_1$ (*top right*) and the first (*bottom left*) and second (*bottom right*) branch of the $0^+_{g.s.} \to 2^+_2$ $2\nu\beta\beta$-decay mode (from top to bottom.

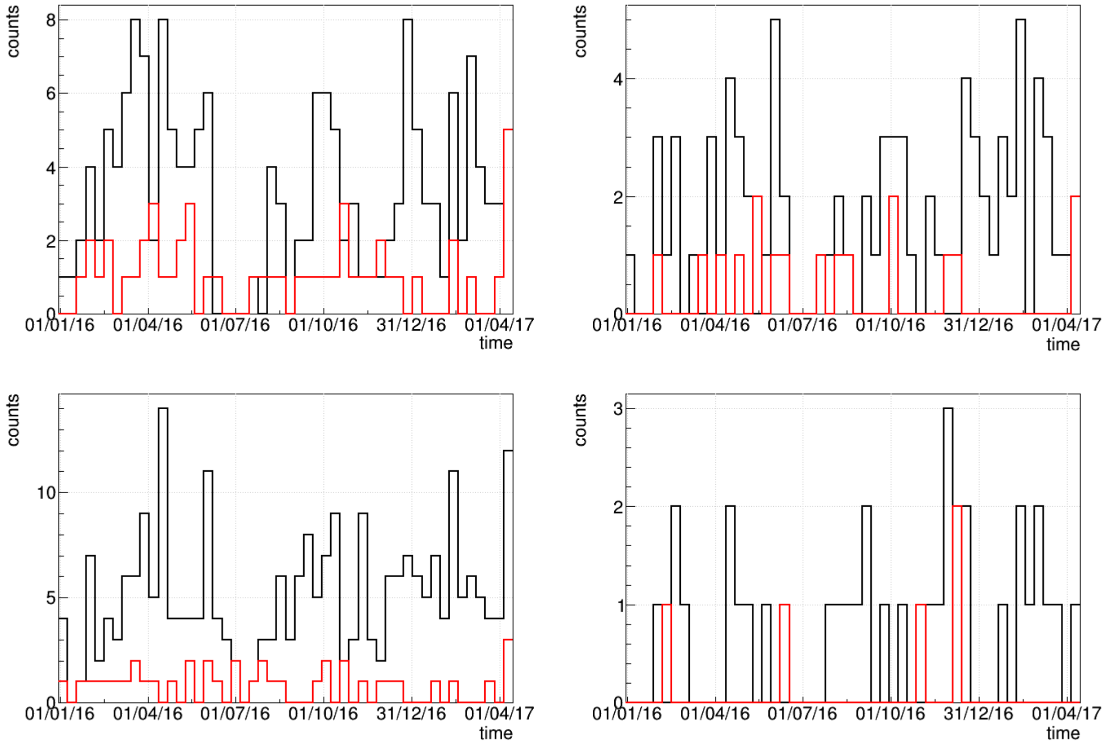

Figure F.5.: Timestamp distribution of PII events in the signal cut regions (red) and summed sideband regions (black) of the search for the $0^+_{g.s.} \to 0^+_1$ (*top left*), $0^+_{g.s.} \to 2^+_1$ (*top right*) and the first (*bottom left*) and second (*bottom right*) branch of the $0^+_{g.s.} \to 2^+_2$ $2\nu\beta\beta$-decay mode (from top to bottom.

F.6 Detector distributions of events in the cut regions

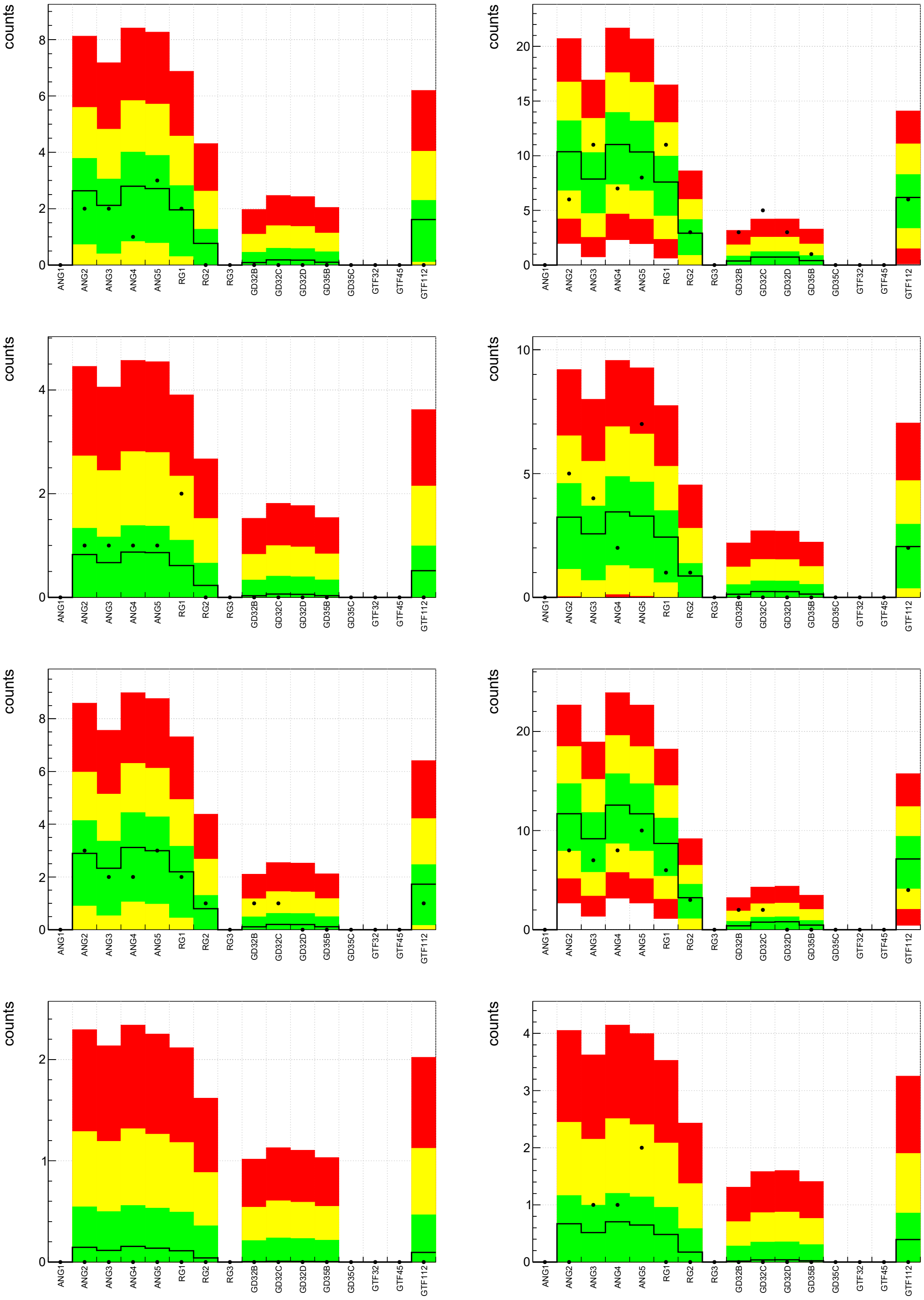

Figure F.6.: Distribution among the detectors of PI events in the signal cut regions (*left*) and summed sideband regions (*right*) of the search for the $0^+_{g.s.} \rightarrow 0^+_1$, $0^+_{g.s.} \rightarrow 2^+_1$ and the first and second branch of the $0^+_{g.s.} \rightarrow 2^+_2$ $2\nu\beta\beta$-decay mode (from *top* to *bottom*). The data is shown as black dots, the expectation from the background model is drawn as black line, in addition to the corresponding 68% (green), 95% (yellow) and 99.7% (red) smallest Poisson intervals.

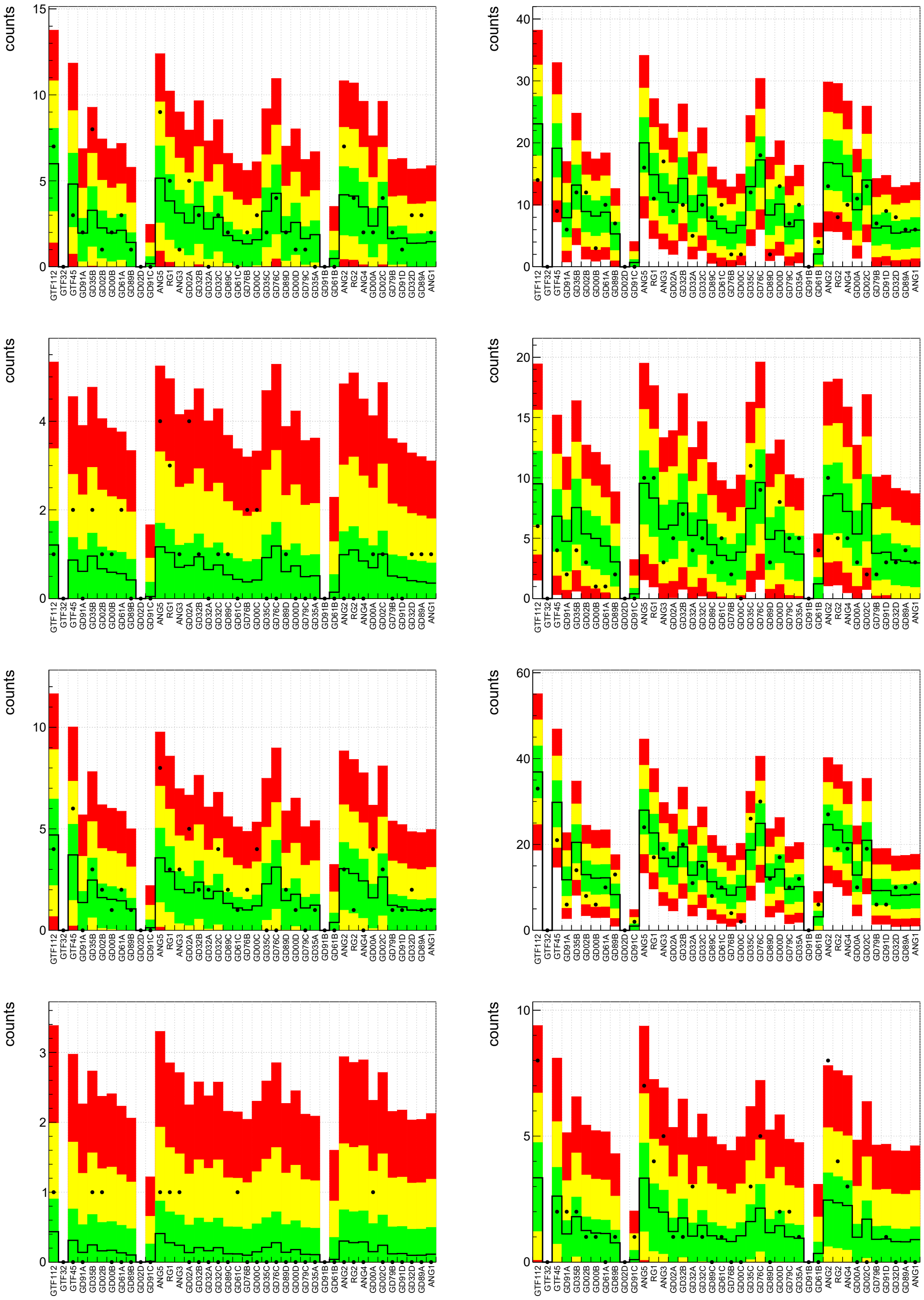

Figure F.7.: Distribution among the detectors of PII events in the signal cut regions (*left*) and summed sideband regions (*right*) of the search for the $0^+_{g.s.} \rightarrow 0^+_1$, $0^+_{g.s.} \rightarrow 2^+_1$ and the first and second branch of the $0^+_{g.s.} \rightarrow 2^+_2$ $2\nu\beta\beta$-decay mode (from *top* to *bottom*). The data is shown as black dots, the expectation from the background model is drawn as black line, in addition to the corresponding 68% (green), 95% (yellow) and 99.7% (red) smallest Poisson intervals.

Appendix G

$0\nu\beta\beta$-decay to excited states

G.1 M1 fit plots of separate data sets

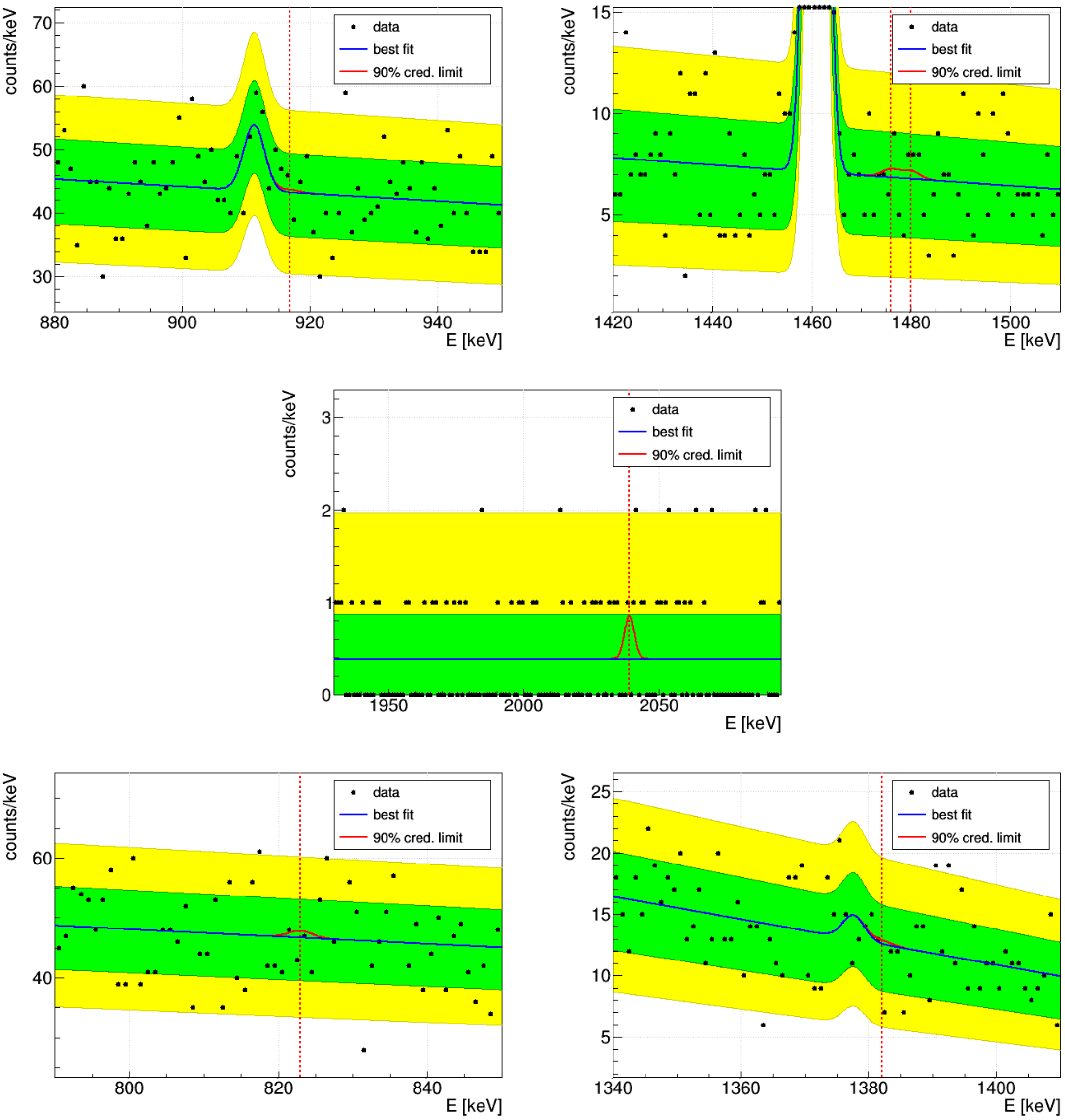

Figure G.1.: Combined unbinned spectral fit of the M1 PI-$^{\text{enr}}$Coax data set in the ROIs of the $0\nu\beta\beta$-decay analysis. A binning of 1 keV has been chosen for visualisation. The red dashed line shows the signal position. The limit is scaled to the limit obtained for the $0^+_{g.s.} \to 0^+_1$ decay in the top three plots and to the limit obtained for the $0^+_{g.s.} \to 2^+_2$ decay mode in the bottom plots. The green and yellow band represent the 68% and 95% probability band, obtained from a Poisson distribution with an expectation equal to the best fit value.

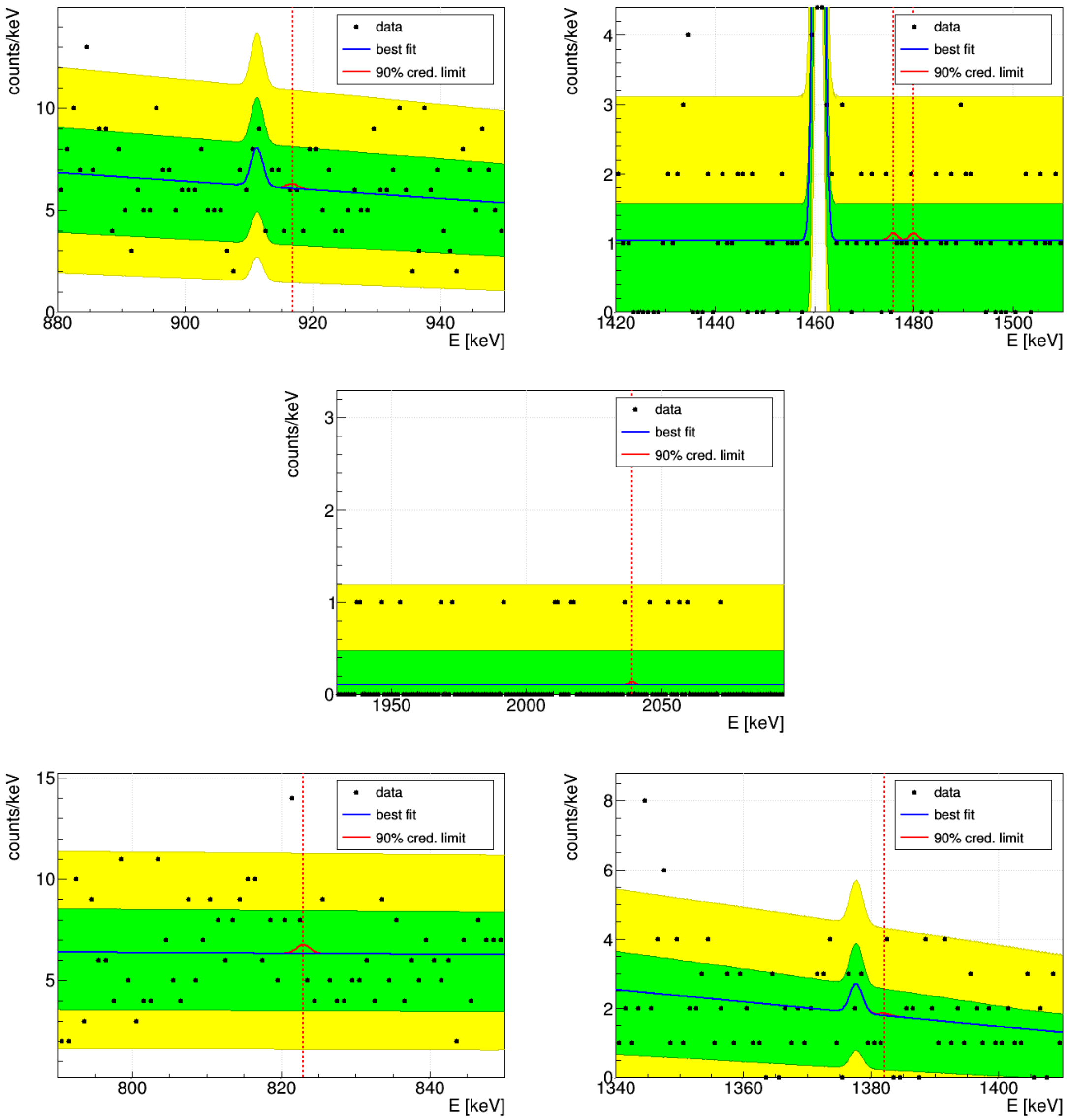

Figure G.2.: Combined unbinned spectral fit of the M1 PI-$^{\mathrm{enr}}$BEGe data set in the ROIs of the $0\nu\beta\beta$-decay analysis. A binning of 1 keV has been chosen for visualisation. The red dashed line shows the signal position. The limit is scaled to the limit obtained for the $0^+_{g.s.} \rightarrow 0^+_1$ decay in the top three plots and to the limit obtained for the $0^+_{g.s.} \rightarrow 2^+_2$ decay mode in the bottom plots. The green and yellow band represent the 68% and 95% probabililty band, obtained from a Poisson distribution with an expectation equal to the best fit value.

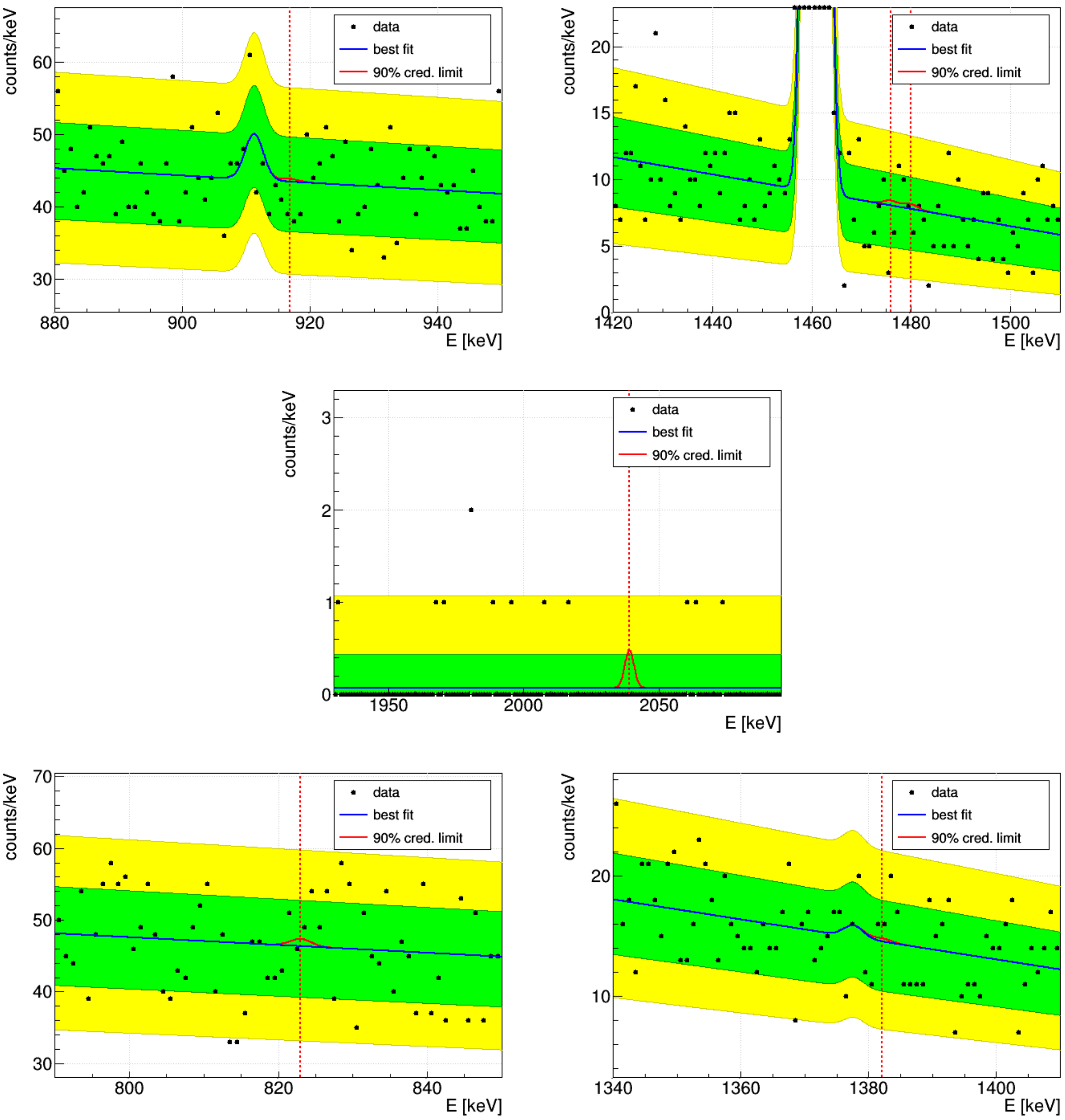

Figure G.3.: Combined unbinned spectral fit of the M1 PII-$^{\mathrm{enr}}$Coax data set in the ROIs of the $0\nu\beta\beta$-decay analysis. A binning of 1 keV has been chosen for visualisation. The red dashed line shows the signal position. The limit is scaled to the limit obtained for the $0^+_{g.s.} \rightarrow 0^+_1$ decay in the top three plots and to the limit obtained for the $0^+_{g.s.} \rightarrow 2^+_2$ decay mode in the bottom plots. The green and yellow band represent the 68% and 95% probabililty band, obtained from a Poisson distribution with an expectation equal to the best fit value.

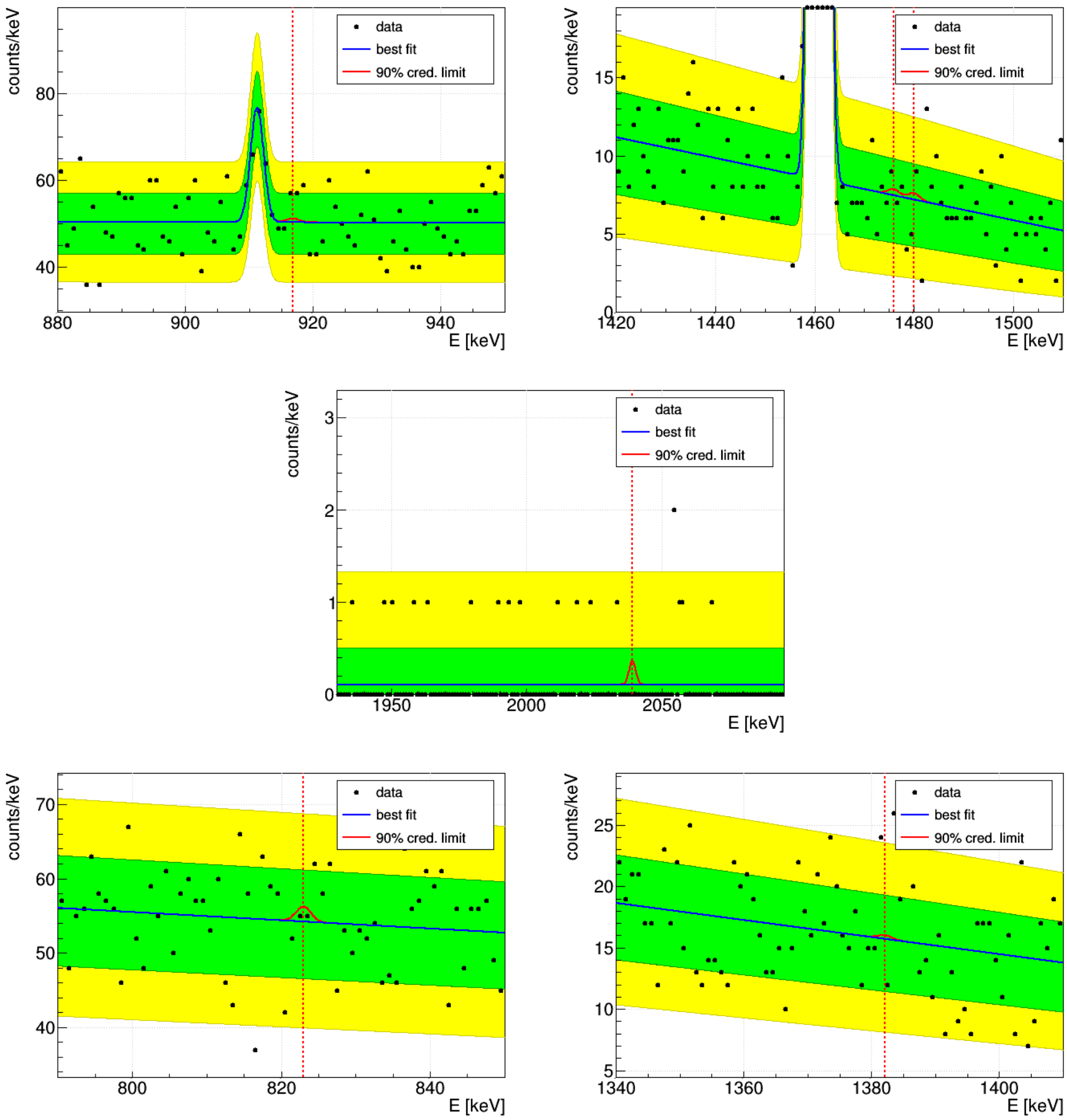

Figure G.4.: Combined unbinned spectral fit of the M1 PII-$^{\mathrm{enr}}$BEGe data set in the ROIs of the $0\nu\beta\beta$-decay analysis. A binning of 1 keV has been chosen for visualisation. The red dashed line shows the signal position. The limit is scaled to the limit obtained for the $0^+_{g.s.} \rightarrow 0^+_1$ decay in the top three plots and to the limit obtained for the $0^+_{g.s.} \rightarrow 2^+_2$ decay mode in the bottom plots. The green and yellow band represent the 68% and 95% probabililty band, obtained from a Poisson distribution with an expectation equal to the best fit value.

G.2 Toy MC limit distributions

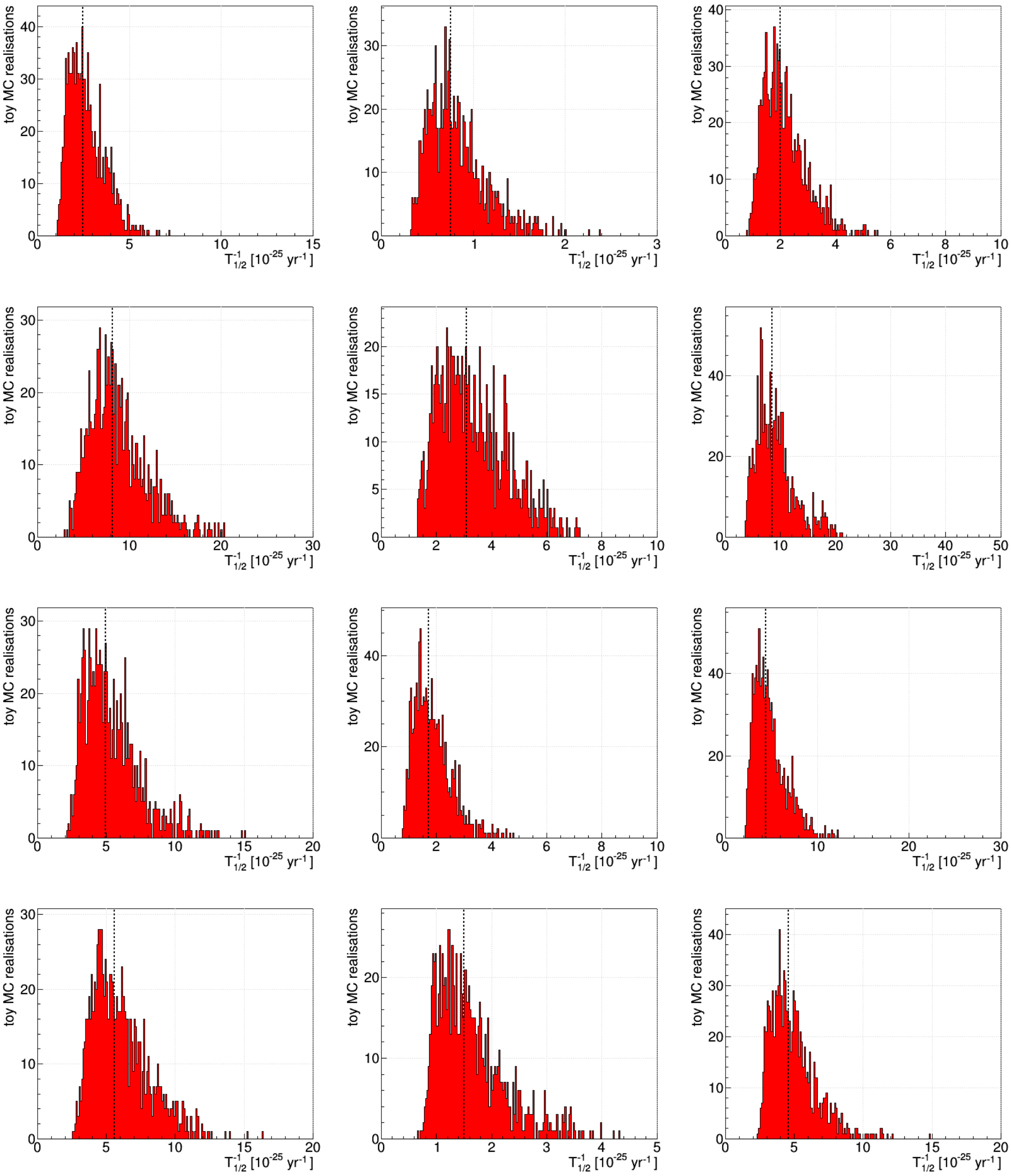

Figure G.5.: Distributions of 90% credibility upper limits on the inverse half-life obtained from fits of 1,000 toy MC experiments, generated for the background only case of M1 data for the ROIs of the $0\nu\beta\beta$ -decay modes $0^+_{g.s.} \to 0^+_1$ (*left*), $0^+_{g.s.} \to 2^+_1$ (*middle*) and $0^+_{g.s.} \to 2^+_2$ (*right*). The first row includes all data sets and ROIs. The second row excludes the ROI around the Q-value. The third and fourth row are only based on PI and PII expectations, respectively. The dashed line indicates the median of each distribution. The sensitivity to set a 90% lower limit on the half-life is defined as the inverse of this median.

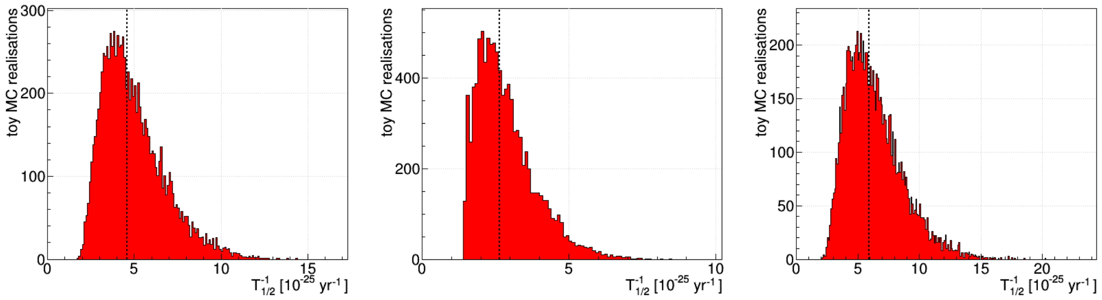

Figure G.6.: Distributions of 90% credibility upper limits on the inverse half-life obtained from fits of 10,000 toy MC experiments of M2 data of the $0\nu\beta\beta$ -decay modes $0^+_{g.s.} \rightarrow 0^+_1$ (*left*), $0^+_{g.s.} \rightarrow 2^+_1$ (*middle*) and $0^+_{g.s.} \rightarrow 2^+_2$ (*right*), generated for the background only case using the predicted counts in the signal regions given by the background model. The dashed line indicates the median of each distribution. The sensitivity to set a 90% lower limit on the half-life is defined as the inverse of this median.

G.3 Pair optimization plots

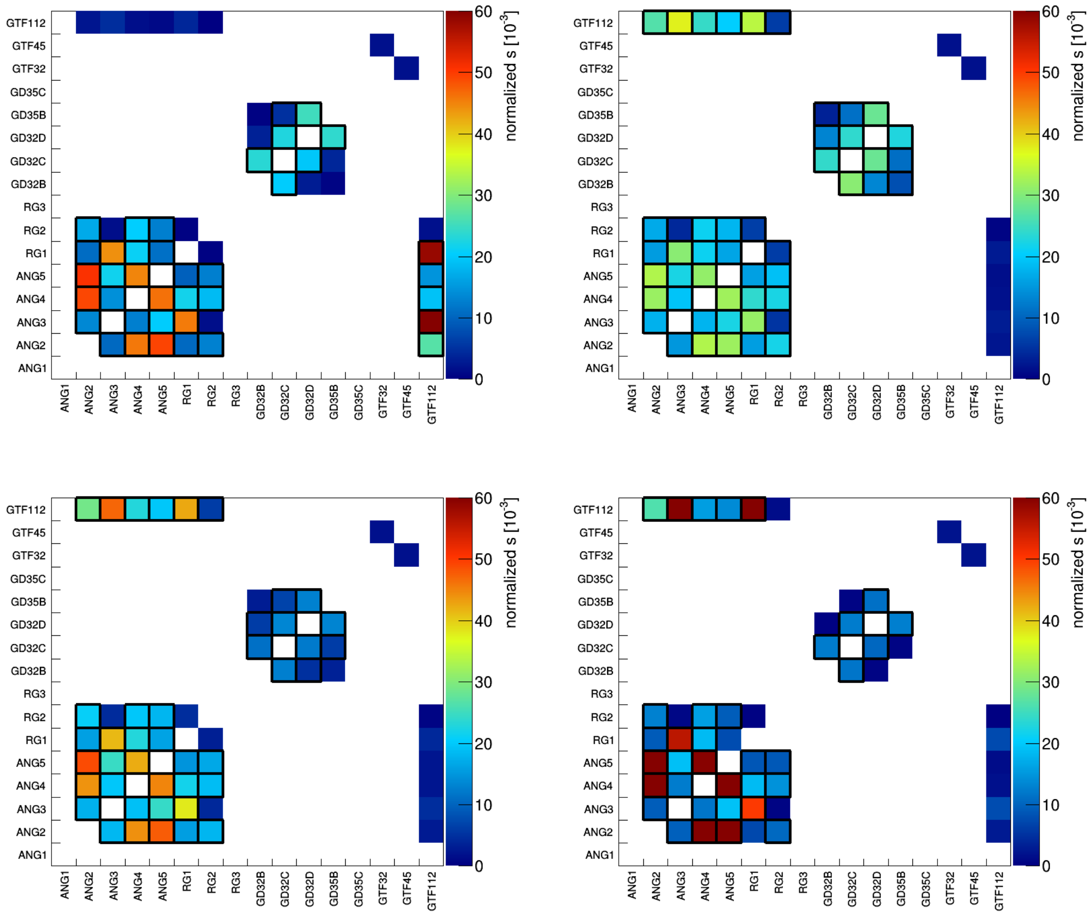

Figure G.7.: A map of detector pairs in PI, with the detector with the discrete energy deposition on the x-axis (the lower energy deposition in case of *bottom right*) and the second detector on the y-axis. The color code indicates the contribution of each pair to the total sensitivity of the cut region 1 (*top left*), 2 (*top right*), 3 (*bottom left*) and 5 (*bottom right*) of the $0^+_{g.s.} \to 0^+_1$ decay mode, as determined by the ratio between signal efficiency contribution and background contribution. Pairs with a high individual contribution are accepted for the analysis and are framed in black.

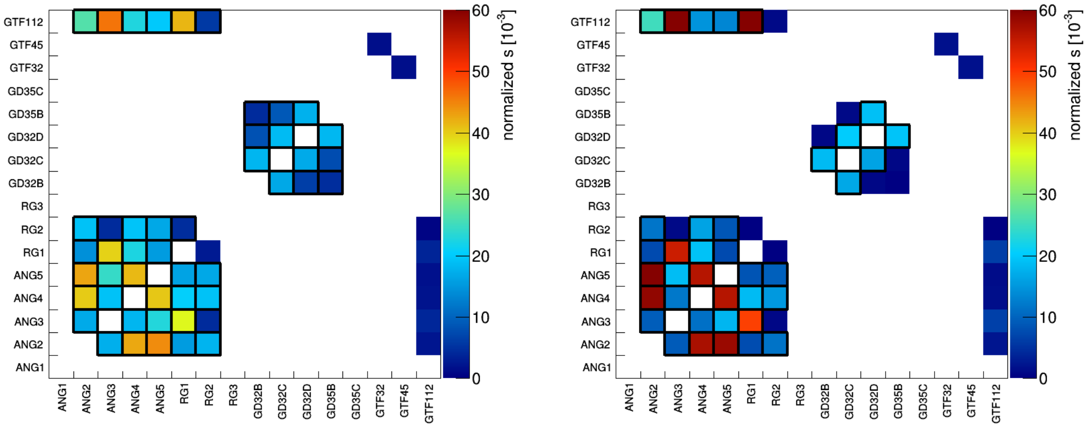

Figure G.8.: A map of detector pairs in PI, with the detector with the discrete (*left*) or lower (*right*) energy deposition on the x-axis and the second detector on the y-axis. The color code indicates the contribution of each pair to the total sensitivity of the cut region 0 (*left*) and 1 (*right*) of the $0^+_{g.s.} \rightarrow 2^+_1$ decay mode, as determined by the ratio between signal efficiency contribution and background contribution. Pairs with a high individual contribution are accepted for the analysis and are framed in black.

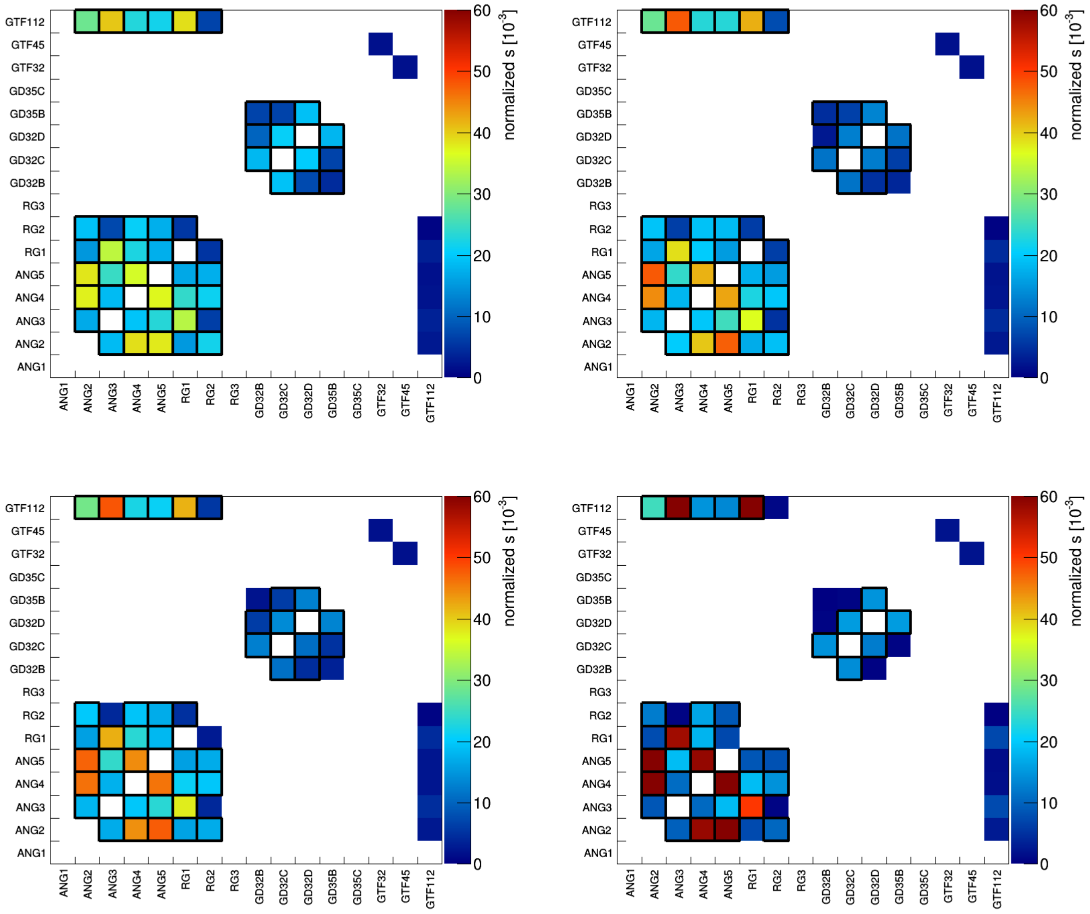

Figure G.9.: A map of detector pairs in PI, with the detector with the discrete energy deposition on the x-axis (lower energy deposition in case of *bottom right*) and the second detector on the y-axis. The color code indicates the contribution of each pair to the total sensitivity of the cut region 0 (*top left*), 1 (*top right*), 2 (*middle left*) and 5 (*bottom right*) of the $0^+_{g.s.} \rightarrow 2^+_2$ decay mode, as determined by the ratio between signal efficiency contribution and background contribution. Pairs with a high individual contribution are accepted for the analysis and are framed in black.

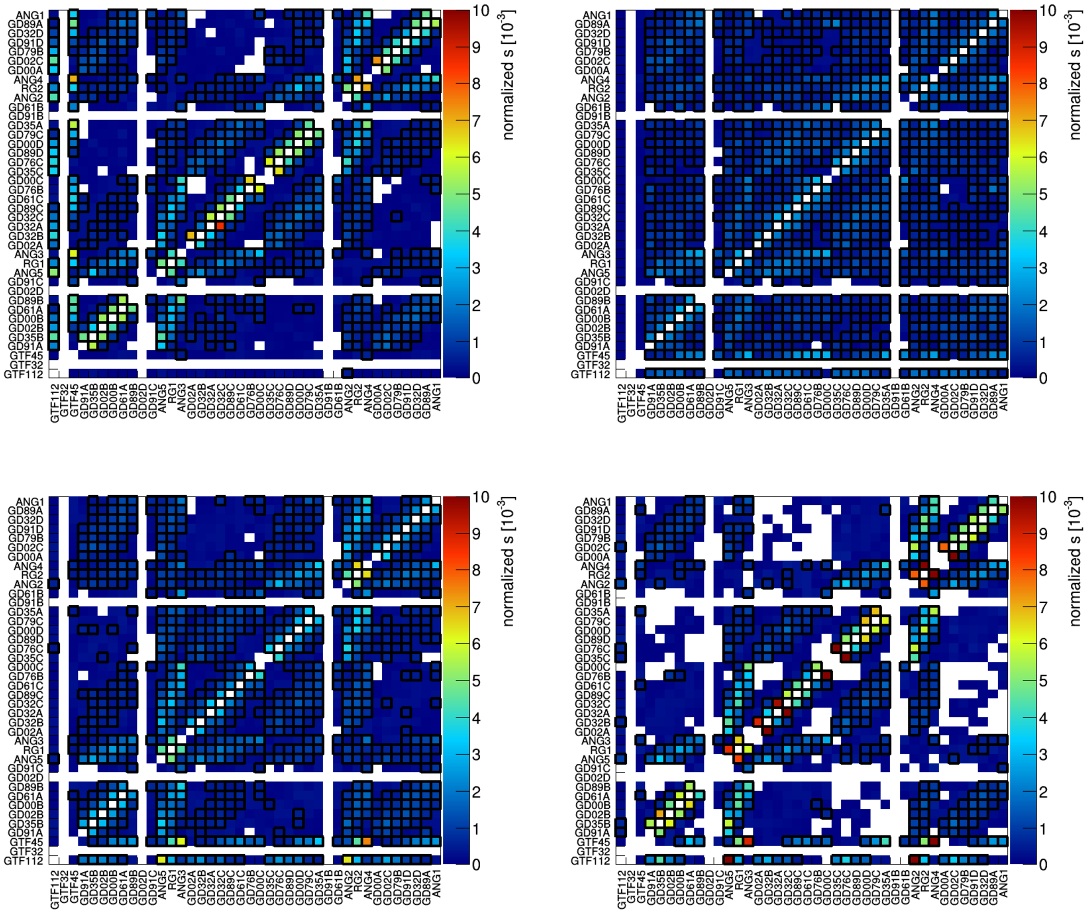

Figure G.10.: A map of detector pairs in PII, with the detector with the discrete energy deposition on the x-axis (the lower energy deposition in case of *bottom right*) and the second detector on the y-axis. The color code indicates the contribution of each pair to the total sensitivity of the cut region 1 (*top left*), 2 (*top right*), 3 (*bottom left*) and 5 (*bottom right*) of the $0^+_{g.s.} \rightarrow 0^+_1$ decay mode, as determined by the ratio between signal efficiency contribution and background contribution. Pairs with a high individual contribution are accepted for the analysis and are framed in black.

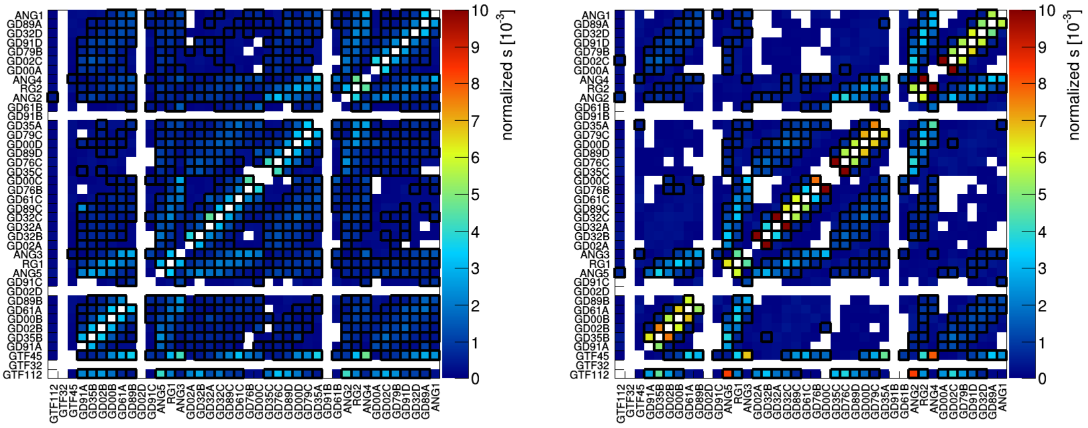

Figure G.11.: A map of detector pairs in PII, with the detector with the discrete (*left*) or lower (*right*) energy deposition on the x-axis and the second detector on the y-axis. The color code indicates the contribution of each pair to the total sensitivity of the cut region 0 (*left*) and 1 (*right*) of the $0^+_{g.s.} \rightarrow 2^+_1$ decay mode, as determined by the ratio between signal efficiency contribution and background contribution. Pairs with a high individual contribution are accepted for the analysis and are framed in black.

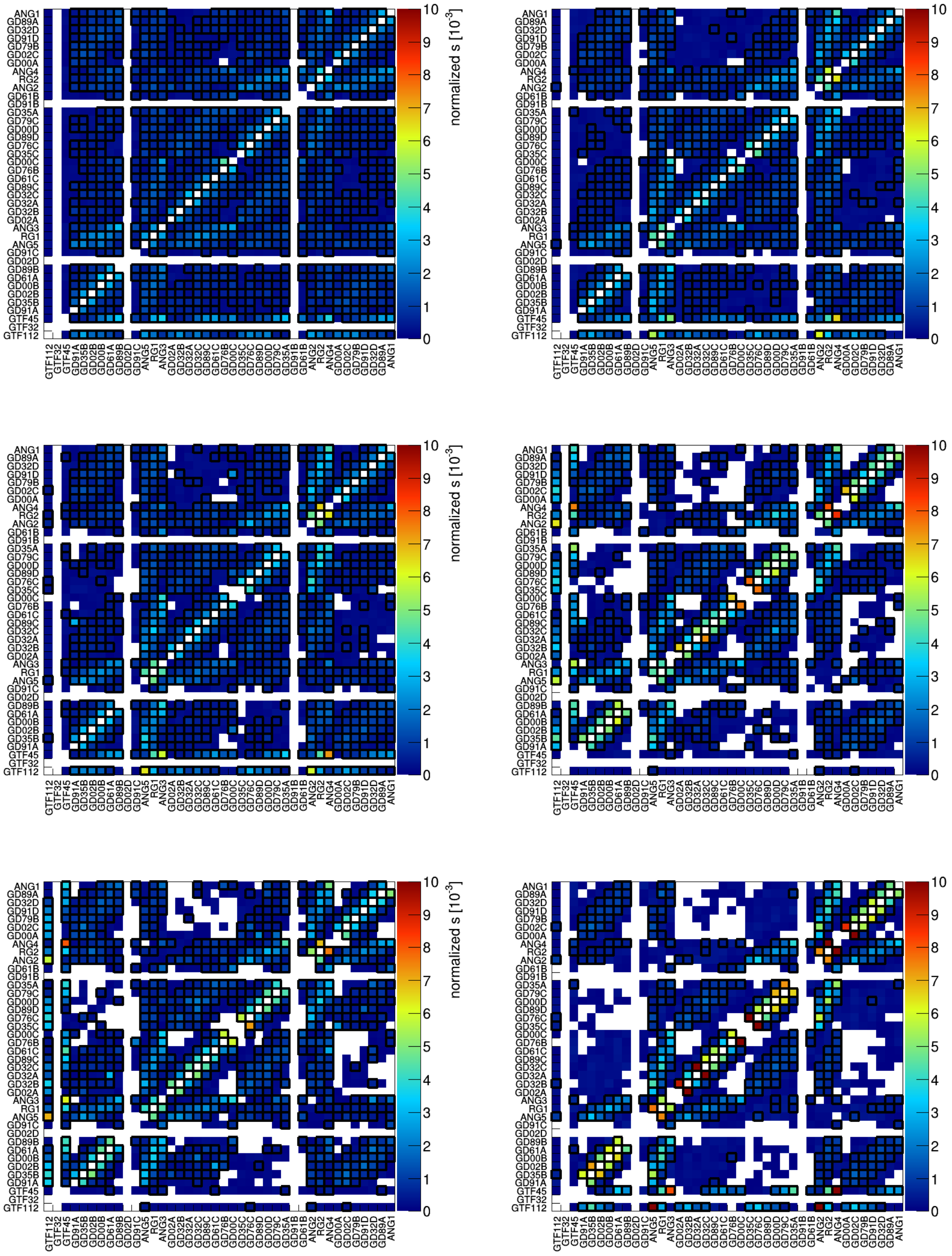

Figure G.12.: A map of detector pairs in PII, with the detector with the discrete energy deposition on the x-axis (lower energy deposition in case of *bottom right*) and the second detector on the y-axis. The color code indicates the contribution of each pair to the total sensitivity of the cut region 0 (*top left*), 1 (*top right*), 2 (*middle left*), 3 (*middle right*), 4 (*bottom left*) and 5 (*bottom right*) of the $0^+_{g.s.} \rightarrow 2^+_2$ decay mode, as determined by the ratio between signal efficiency contribution and background contribution. Pairs with a high individual contribution are accepted for the analysis and are framed in black.

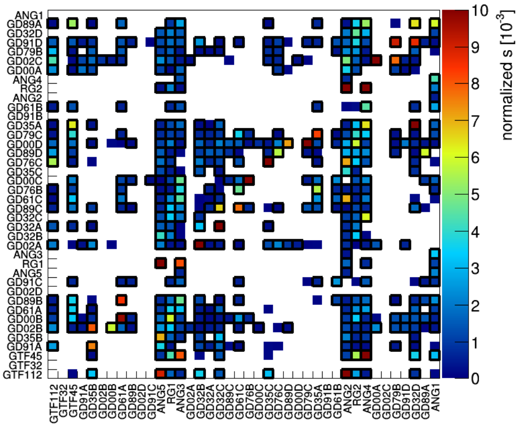

Figure G.13.: A map of detector pairs in PII, with the detector with the lower ID on the x-axis and the second detector on the y-axis. The color code indicates the contribution of each pair to the total sensitivity of the cut region 6 of the $0^+_{g.s.} \rightarrow 2^+_2$ decay mode, as determined by the ratio between signal efficiency contribution and background contribution. Pairs with a high individual contribution are accepted for the analysis and are framed in black.

G.4 Optimized signal cut regions

		Phase I							Phase II						
Region	E_{center}	w	E_{low}	E_{high}	N_p	ε [%]	b	$1-\frac{F_{\text{opt}}}{F_{\text{def}}}$	w	E_{low}	E_{high}	N_p	ε [%]	b	$1-\frac{F_{\text{opt}}}{F_{\text{def}}}$
$0^+_{g.s.} \to 0^+_1$															
Cut1	559.1	±3.2	912.5	1431.5	38	0.71	0.95	3.2	±2.2	913.1	1439.1	623	1.87	2.44	5.5
	$\vee$ 563.2														
Cut2	916.8	$^{+2.8}_{-1.8}$	100	523.8	48	1.13	3.61	17.0	±1.8	200	526.8	1061	2.25	12.9	1.8
Cut3	1475.9	±3.0	100	568.4	42	1.49	1.20	3.3	±2.2	200	567.1	775	2.03	1.82	1.1
	$\vee$ 1480.0														
Cut5	2039.1	±5.4	140	1504.2	35	0.32	0.57	10.8	±3.6	200	1499.8	424	0.52	0.81	4.4
$0^+_{g.s.} \to 2^+_1$															
Cut0	1480.0	±3.8	100	564.2	47	2.67	0.90	3.9	±2.4	200	563.0	896	4.78	0.99	7.2
Cut1	2039.1	±5.4	140	1505.2	37	0.49	0.59	4.6	±3.6	200	1504.2	444	1.13	0.79	2.2
$0^+_{g.s.} \to 2^+_2$															
Cut0	823.0	±2.8	100	1221.6	48	2.29	5.31	10.0	±1.8	200	1220.4	1019	4.62	16.1	16.7
Cut1	1382.1	±3.4	100	662.2	46	0.49	1.51	5.7	±2.4	200	661.0	836	0.71	1.60	7.3
Cut2	1480.0	±3.8	100	564.2	43	0.43	0.90	4.6	±2.6	200	563.0	850	0.57	1.14	7.1
Cut3	559.1								±2.2	834.7	1343.6	649	0.25	2.41	4.5
Cut4	657.0								±2.4	834.7	1343.6	752	0.26	0.97	4.0
Cut5	2039.1	±5.4	140	1502.2	35	0.28	0.58	14.6	±3.6	200	1505.8	443	0.50	0.81	3.2
Cut6	2039.1								±4.8	847	-	452*	0.11	0.19	1.9

Table G.1.: The optimized signal cut regions of the three decay modes of the $0\nu\beta\beta$ decay to excited states, given with their width w and the two energies that limit the region (E_{low}, E_{high}), as well as the number of accepted detector pairs N_p. Furthermore, given are the signal cut efficiency ε, background expectation b as obtained from the background model and improvement of the sensitivity achieved by the optimization, evaluated with the figure of merit F.

*) For Cut6 of the $0^+_{g.s.} \to 2^+_2$ decay mode, the energy depositions in both detectors is interchangeable. Thus the order of detectors in a pair is disregarded, which halves the number of total pairs.

G.5 Sidebands

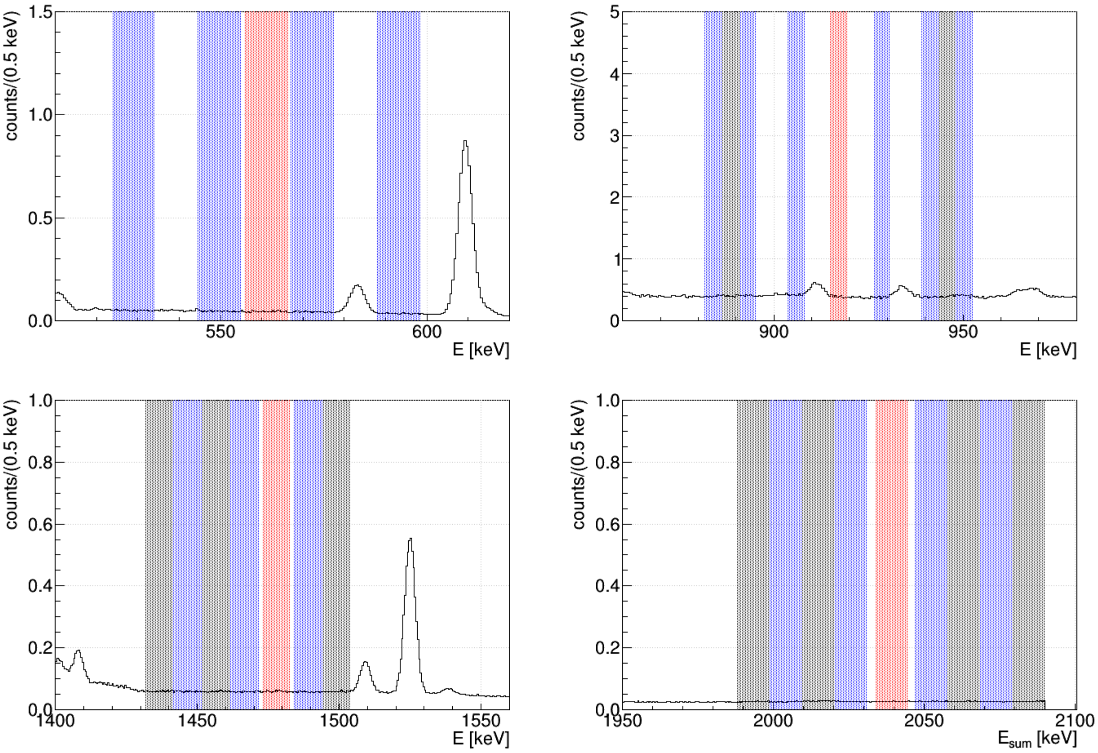

Figure G.14.: Sideband illustrations for the $0\nu\beta\beta$ $0^+_{g.s.} \to 0^+_1$ decay mode for the PI data set, Cut1 to Cut3 and Cut5.

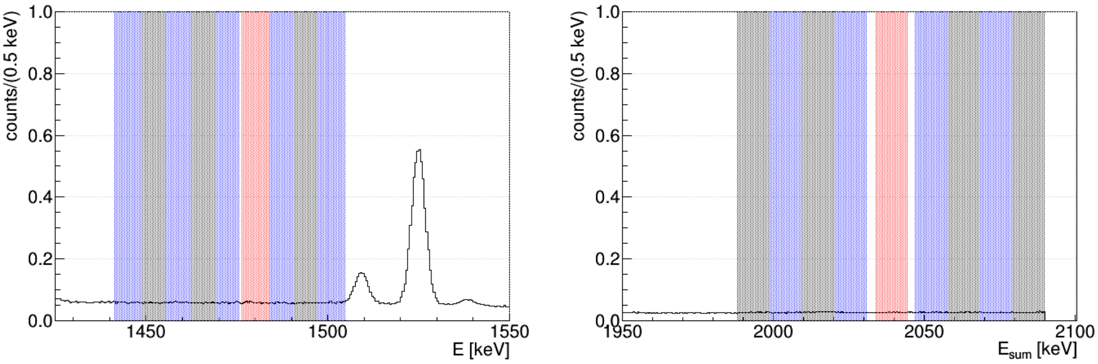

Figure G.15.: Sideband illustrations for the $0\nu\beta\beta$ $0^+_{g.s.} \to 2^+_1$ decay mode for the PI data set, Cut0 and Cut1.

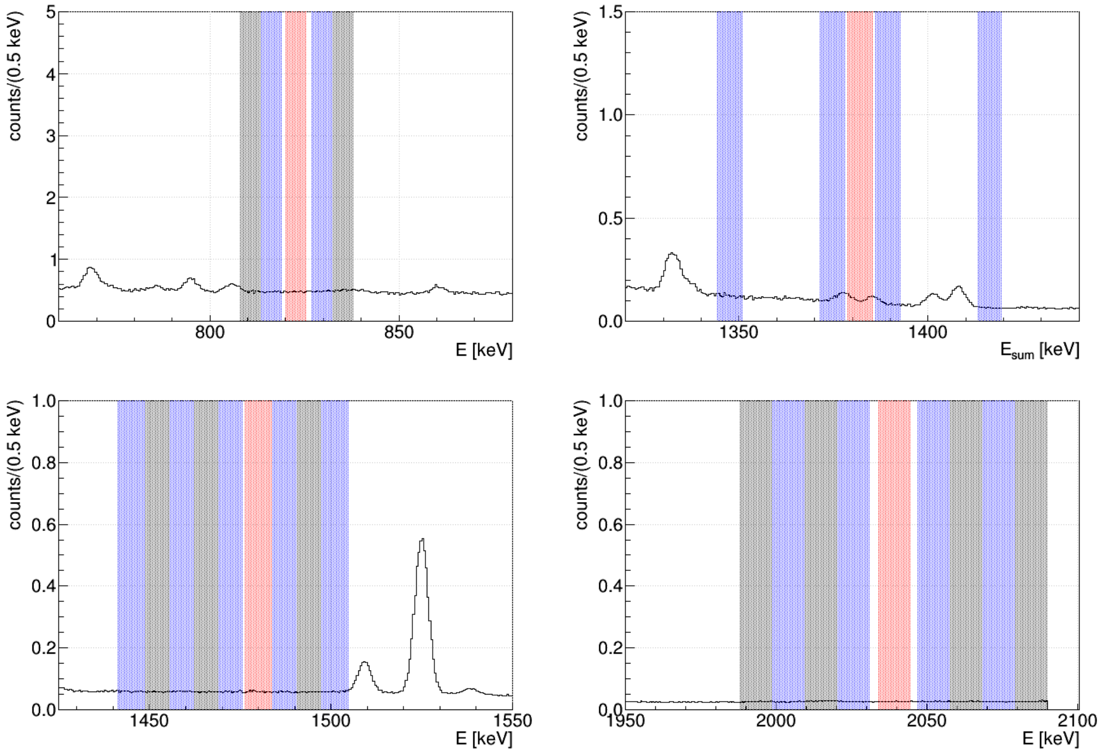

Figure G.16.: Sideband illustrations for the $0\nu\beta\beta$ $0^+_{g.s.} \rightarrow 2^+_2$ decay mode for the PI data set, Cut0-2 and Cut5.

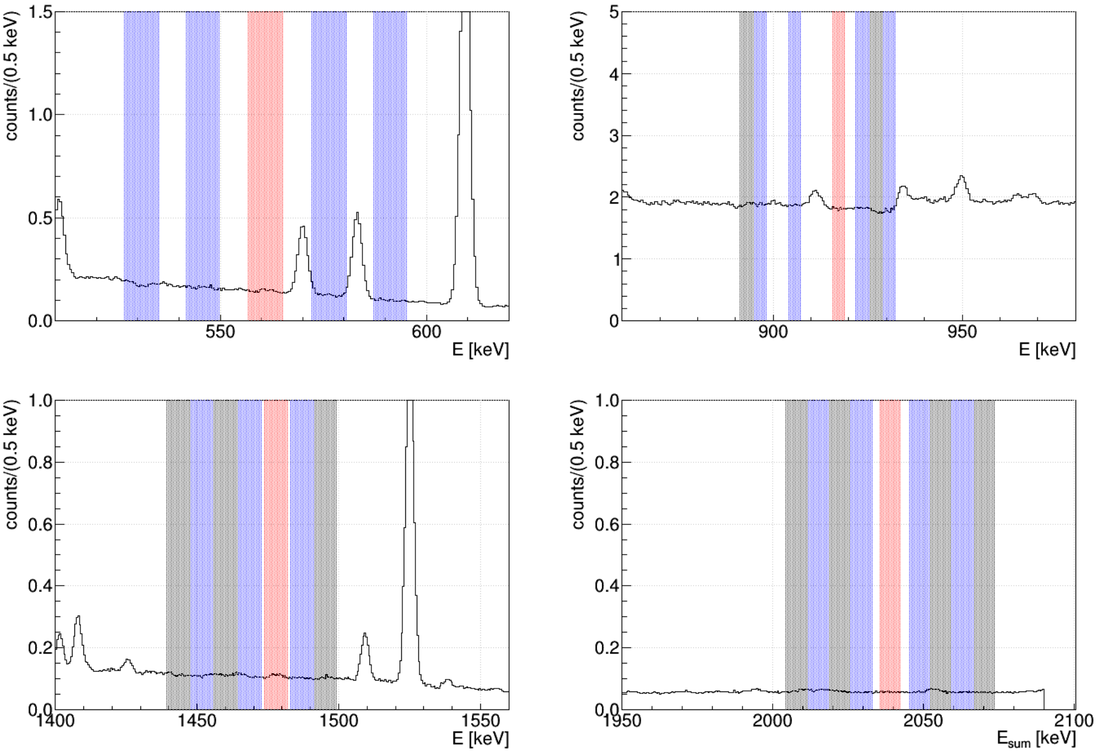

Figure G.17.: Sideband illustrations for the $0\nu\beta\beta$ $0^+_{g.s.} \rightarrow 0^+_1$ decay mode for the PII data set, Cut1 to Cut3 and Cut5.

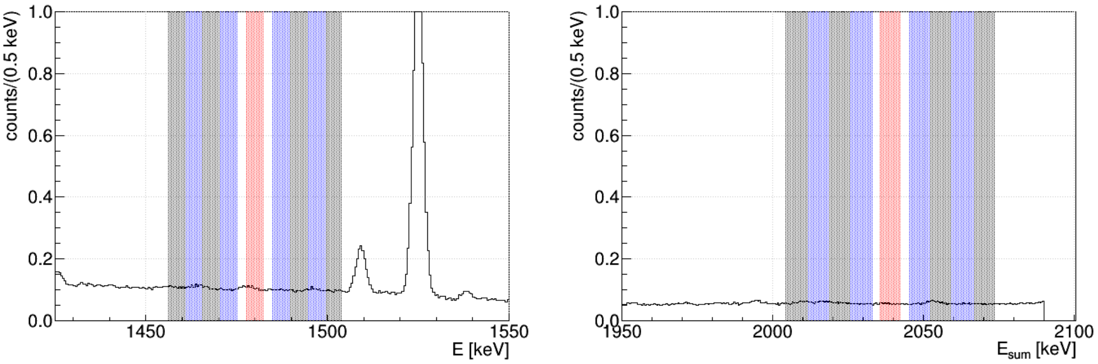

Figure G.18.: Sideband illustrations for the $0\nu\beta\beta$ $0^+_{g.s.} \rightarrow 2^+_1$ decay mode for the PII data set, Cut0 and Cut1.

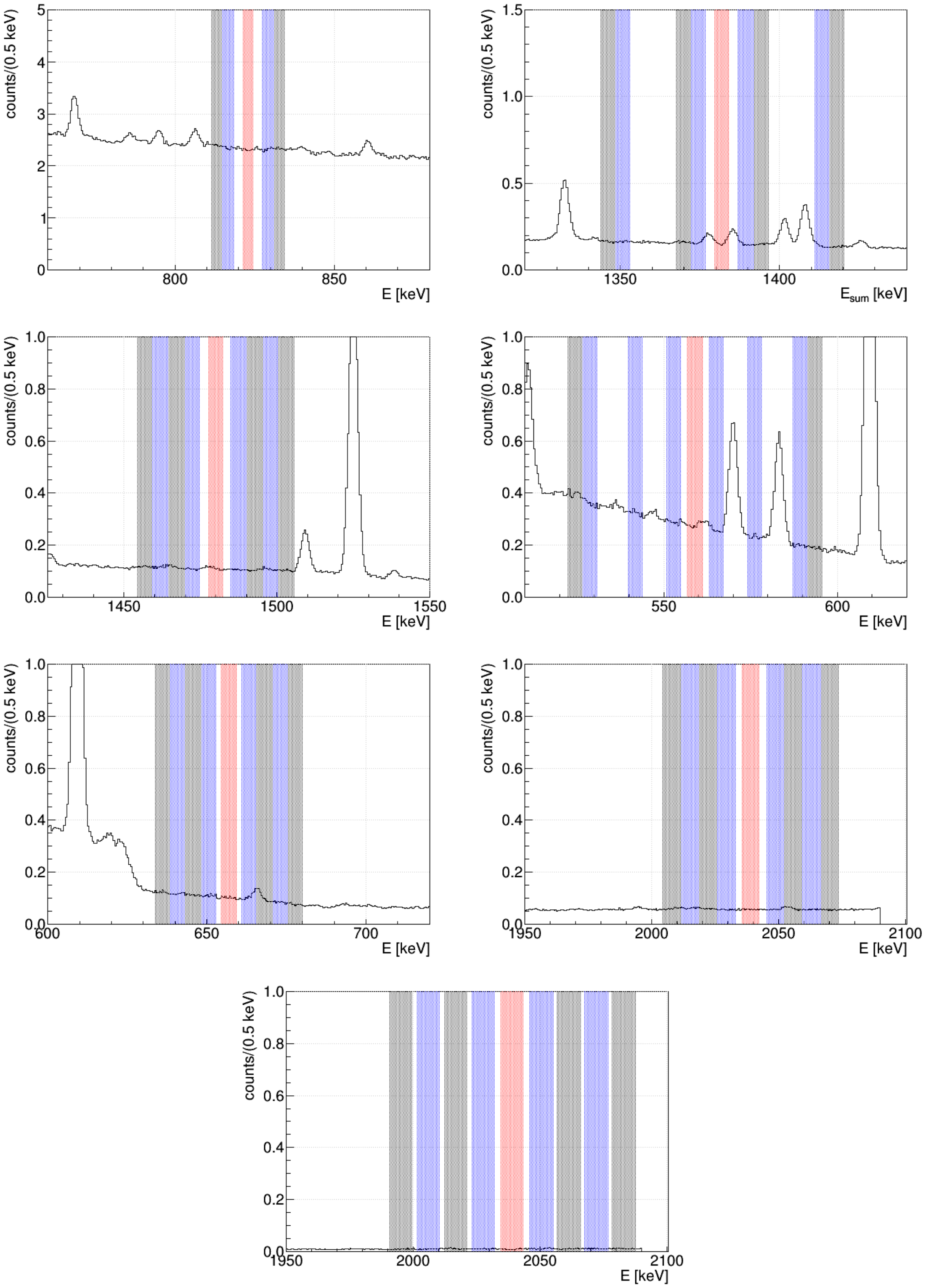

Figure G.19.: Sideband illustrations for the $0\nu\beta\beta$ $0^+_{g.s.} \rightarrow 2^+_2$ decay mode for the PII data set, Cut0 to Cut6.

PI $0^+_{g.s.} \to 0^+_1$					
Cut1			Cut2		
SB	E_{center} [keV]	$N^{\text{SB}}_{\text{MC}}$	SB	E_{center} [keV]	$N^{\text{SB}}_{\text{MC}}$
0	527.00 ∨ 531.10	1.06	0	884.1	3.66
1	547.85 ∨ 551.95	0.97	1	888.7	3.71
2	570.35 ∨ 574.45	0.90	2	893.3	3.74
3	591.20 ∨ 595.30	0.75	3	906.0	3.90
			4	928.6	3.53
			5	941.3	3.56
			6	945.9	3.66
			7	950.5	3.75
window: ±3.20 (eff. width: 5.25x2)			window: ±2.30 (eff. width: 4.60)		
$\bar{N}^{\text{SB}}_{\text{MC}}$:		0.92	$\bar{N}^{\text{SB}}_{\text{MC}}$:		3.69
$N^{\text{ROI}}_{\text{MC}}$:		0.95	$N^{\text{ROI}}_{\text{MC}}$:		3.62
Cut3			Cut5		
SB	E_{center} [keV]	$N^{\text{SB}}_{\text{MC}}$	SB	E_{center} [keV]	$N^{\text{SB}}_{\text{MC}}$
0	1434.5 ∨ 1438.6	1.21	0	1993.3	0.57
1	1444.6 ∨ 1448.7	1.20	1	2004.1	0.57
2	1454.7 ∨ 1458.8	1.19	2	2014.9	0.60
3	1464.8 ∨ 1468.9	1.17	3	2025.7	0.56
4	1487.0 ∨ 1491.1	1.17	4	2052.5	0.59
5	1497.1 ∨ 1501.2	1.19	5	2063.3	0.58
			6	2074.1	0.57
			7	2084.9	0.58
window: ±3.00 (eff. width: 5.05x2)			window: ±5.40 (eff. width: 10.80)		
$\bar{N}^{\text{SB}}_{\text{MC}}$:		1.19	$\bar{N}^{\text{SB}}_{\text{MC}}$:		0.58
$N^{\text{ROI}}_{\text{MC}}$:		1.20	$N^{\text{ROI}}_{\text{MC}}$:		0.57

Table G.2.: The positions of the sidebands (SBs) for all decay modes by their center energy and the window width. Also given is the expected background $N^{\text{SB}}_{\text{MC}}$ in each SB estimated from the background model, the average of those background expectations $\bar{N}^{\text{SB}}_{\text{MC}}$ and for comparison the background expectation in the ROI $N^{\text{ROI}}_{\text{MC}}$.

PI $0^+_{g.s.} \rightarrow 2^+_1$					
Cut0			Cut1		
SB	E_{center} [keV]	$N^{\text{SB}}_{\text{MC}}$	SB	E_{center} [keV]	$N^{\text{SB}}_{\text{MC}}$
0	1445.0	0.81	0	1993.3	0.59
1	1451.8	0.70	1	2004.1	0.59
2	1458.6	0.71	2	2014.9	0.62
3	1465.4	0.70	3	2025.7	0.58
4	1472.2	0.80	4	2052.5	0.60
5	1487.8	0.79	5	2063.3	0.60
6	1494.6	0.70	6	2074.1	0.58
7	1501.4	0.81	7	2084.9	0.59
window: ±3.80 (eff. width: 7.60)			window: ±5.40 (eff. width: 10.80)		
$\bar{N}^{\text{SB}}_{\text{MC}}$:		0.75	$\bar{N}^{\text{SB}}_{\text{MC}}$:		0.59
$N^{\text{ROI}}_{\text{MC}}$:		0.90	$N^{\text{ROI}}_{\text{MC}}$:		0.59

Table G.3.: The positions of the sidebands (SBs) for all decay modes by their center energy and the window width. Also given is the expected background $N^{\text{SB}}_{\text{MC}}$ in each SB estimated from the background model, the average of those background expectations $\bar{N}^{\text{SB}}_{\text{MC}}$ and for comparison the background expectation in the ROI $N^{\text{ROI}}_{\text{MC}}$.

PI $0^+_{g.s.} \to 2^+_2$

Cut0			Cut1		
SB	E_{center} [keV]	$N^{\text{SB}}_{\text{MC}}$	SB	E_{center} [keV]	$N^{\text{SB}}_{\text{MC}}$
0	810.6	5.49	0	1347.8	1.68
1	816.2	5.28	1	1374.7	1.57
2	829.8	5.40	2	1389.5	1.21
3	835.4	5.58	3	1416.4	0.89
window: ±2.80 (eff. width: 5.6)			window: ±3.40 (eff. width: 6.80)		
$\bar{N}^{\text{SB}}_{\text{MC}}$:		5.43	$\bar{N}^{\text{SB}}_{\text{MC}}$:		1.34
$N^{\text{ROI}}_{\text{MC}}$:		5.31	$N^{\text{ROI}}_{\text{MC}}$:		1.51

Cut2			Cut5		
SB	E_{center} [keV]	$N^{\text{SB}}_{\text{MC}}$	SB	E_{center} [keV]	$N^{\text{SB}}_{\text{MC}}$
0	1445.0	0.81	0	1993.3	0.57
1	1451.8	0.70	1	2004.1	0.57
2	1458.6	0.71	2	2014.9	0.61
3	1465.4	0.70	3	2025.7	0.56
4	1472.2	0.80	4	2052.5	0.59
5	1487.8	0.79	5	2063.3	0.58
6	1494.6	0.70	6	2074.1	0.57
7	1501.4	0.81	7	2084.9	0.59
window: ±3.80 (eff. width: 7.60)			window: ±5.40 (eff. width: 10.80)		
$\bar{N}^{\text{SB}}_{\text{MC}}$:		0.75	$\bar{N}^{\text{SB}}_{\text{MC}}$:		0.58
$N^{\text{ROI}}_{\text{MC}}$:		0.90	$N^{\text{ROI}}_{\text{MC}}$:		0.58

Table G.4.: The positions of the sidebands (SBs) for all decay modes by their center energy and the window width. Also given is the expected background $N^{\text{SB}}_{\text{MC}}$ in each SB estimated from the background model, the average of those background expectations $\bar{N}^{\text{SB}}_{\text{MC}}$ and for comparison the background expectation in the ROI $N^{\text{ROI}}_{\text{MC}}$.

PII $0^+_{g.s.} \to 0^+_1$					
Cut1			Cut2		
SB	E_{center} [keV]	$N^{\text{SB}}_{\text{MC}}$	SB	E_{center} [keV]	$N^{\text{SB}}_{\text{MC}}$
0	529.0 ∨ 533.1	3.06	0	893.0	13.6
1	543.7 ∨ 547.8	2.77	1	896.6	13.5
2	574.5 ∨ 578.6	2.20	2	905.8	13.4
3	589.2 ∨ 593.3	1.70	3	923.6	13.2
			4	927.2	12.8
			5	930.8	12.9
window: ±2.20 (eff. width: 4.25x2)			window: ±1.80 (eff. width: 3.60)		
$\bar{N}^{\text{SB}}_{\text{MC}}$:		2.43	$\bar{N}^{\text{SB}}_{\text{MC}}$:		13.2
$N^{\text{ROI}}_{\text{MC}}$:		2.47	$N^{\text{ROI}}_{\text{MC}}$:		13.1
Cut3			Cut5		
SB	E_{center} [keV]	$N^{\text{SB}}_{\text{MC}}$	SB	E_{center} [keV]	$N^{\text{SB}}_{\text{MC}}$
0	1441.3 ∨ 1445.4	1.94	0	2007.9	0.88
1	1449.8 ∨ 1453.9	1.88	1	2015.1	0.92
2	1458.3 ∨ 1462.4	1.94	2	2022.3	0.87
3	1466.8 ∨ 1470.9	1.86	3	2029.5	0.81
4	1485.0 ∨ 1489.1	1.76	4	2048.7	0.84
5	1493.5 ∨ 1497.6	1.75	5	2055.9	0.89
			6	2063.1	0.82
			7	2070.3	0.81
window: ±2.20 (eff. width: 4.25x2)			window: ±3.60 (eff. width: 7.20)		
$\bar{N}^{\text{SB}}_{\text{MC}}$:		1.86	$\bar{N}^{\text{SB}}_{\text{MC}}$:		0.86
$N^{\text{ROI}}_{\text{MC}}$:		1.86	$N^{\text{ROI}}_{\text{MC}}$:		0.82

Table G.5.: The positions of the sidebands (SBs) for all decay modes by their center energy and the window width. Also given is the expected background $N^{\text{SB}}_{\text{MC}}$ in each SB estimated from the background model, the average of those background expectations $\bar{N}^{\text{SB}}_{\text{MC}}$ and for comparison the background expectation in the ROI $N^{\text{ROI}}_{\text{MC}}$.

PII $0^+_{g.s.} \to 2^+_1$					
Cut0			Cut1		
SB	E_{center} [keV]	$N^{\mathrm{SB}}_{\mathrm{MC}}$	SB	E_{center} [keV]	$N^{\mathrm{SB}}_{\mathrm{MC}}$
0	1458.6	1.00	0	2007.9	0.86
1	1463.2	1.04	1	2015.1	0.89
2	1468.0	1.01	2	2022.3	0.85
3	1472.8	0.97	3	2029.5	0.79
4	1487.4	0.96	4	2048.7	0.81
5	1492.2	0.94	5	2055.9	0.86
6	1497.0	0.98	6	2063.1	0.80
7	1501.8	0.94	7	2070.3	0.79
window: ±2.40 (eff. width: 4.80)			window: ±3.60 (eff. width: 7.20)		
$\bar{N}^{\mathrm{SB}}_{\mathrm{MC}}$:		0.98	$\bar{N}^{\mathrm{SB}}_{\mathrm{MC}}$:		0.83
$N^{\mathrm{ROI}}_{\mathrm{MC}}$:		1.01	$N^{\mathrm{ROI}}_{\mathrm{MC}}$:		0.80

Table G.6.: The positions of the sidebands (SBs) for all decay modes by their center energy and the window width. Also given is the expected background $N^{\mathrm{SB}}_{\mathrm{MC}}$ in each SB estimated from the background model, the average of those background expectations $\bar{N}^{\mathrm{SB}}_{\mathrm{MC}}$ and for comparison the background expectation in the ROI $N^{\mathrm{ROI}}_{\mathrm{MC}}$.

PII $0^+_{g.s.} \to 2^+_2$					
Cut0			Cut1		
SB	E_{center} [keV]	$N^{\mathrm{SB}}_{\mathrm{MC}}$	SB	E_{center} [keV]	$N^{\mathrm{SB}}_{\mathrm{MC}}$
0	813.1	17.2	0	1346.0	1.58
1	816.7	16.9	1	1350.8	1.58
2	829.3	16.6	2	1369.9	1.55
3	832.9	16.7	3	1374.7	1.60
			4	1389.5	1.44
			5	1394.3	1.45
			6	1413.4	1.35
			7	1418.2	1.30
window: ±1.80 (eff. width: 3.60)			window: ±2.40 (eff. width: 4.80)		
$\bar{N}^{\mathrm{SB}}_{\mathrm{MC}}$:		16.9	$\bar{N}^{\mathrm{SB}}_{\mathrm{MC}}$:		1.48
$N^{\mathrm{ROI}}_{\mathrm{MC}}$:		16.6	$N^{\mathrm{ROI}}_{\mathrm{MC}}$:		1.58
Cut2			Cut3		
SB	E_{center} [keV]	$N^{\mathrm{SB}}_{\mathrm{MC}}$	SB	E_{center} [keV]	$N^{\mathrm{SB}}_{\mathrm{MC}}$
0	1456.8	1.23	0	524.6	3.47
1	1462.0	1.22	1	529.0	3.18
2	1467.2	1.20	2	542.0	2.85
3	1472.4	1.14	3	552.9	2.56
4	1487.6	1.11	4	565.3	2.30
5	1492.8	1.08	5	576.2	2.04
6	1498.0	1.13	6	589.2	1.76
7	1503.2	1.06	7	593.6	1.67
window: ±2.60 (eff. width: 5.20)			window: ±2.20 (eff. width: 4.40)		
$\bar{N}^{\mathrm{SB}}_{\mathrm{MC}}$:		1.16	$\bar{N}^{\mathrm{SB}}_{\mathrm{MC}}$:		2.48
$N^{\mathrm{ROI}}_{\mathrm{MC}}$:		1.15	$N^{\mathrm{ROI}}_{\mathrm{MC}}$:		2.45

Table G.7.: The positions of the sidebands (SBs) for all decay modes by their center energy and the window width. Also given is the expected background $N^{\mathrm{SB}}_{\mathrm{MC}}$ in each SB estimated from the background model, the average of those background expectations $\bar{N}^{\mathrm{SB}}_{\mathrm{MC}}$ and for comparison the background expectation in the ROI $N^{\mathrm{ROI}}_{\mathrm{MC}}$.

PII $0^+_{g.s.} \to 2^+_2$ *continued*					
Cut4			Cut5		
SB	E_{center} [keV]	$N^{\text{SB}}_{\text{MC}}$	SB	E_{center} [keV]	$N^{\text{SB}}_{\text{MC}}$
0	636.2	1.18	0	2007.9	0.87
1	641.0	1.12	1	2015.1	0.90
2	645.8	1.08	2	2022.3	0.87
3	650.6	1.07	3	2029.5	0.81
4	663.4	1.07	4	2048.7	0.84
5	668.2	1.00	5	2055.9	0.89
6	673.0	0.82	6	2063.1	0.82
7	677.8	0.74	7	2070.3	0.81
window: ±2.40 (eff. width: 4.80)			window: ±3.60 (eff. width: 7.20)		
$\bar{N}^{\text{SB}}_{\text{MC}}$:		1.01	$\bar{N}^{\text{SB}}_{\text{MC}}$:		0.85
$N^{\text{ROI}}_{\text{MC}}$:		0.99	$N^{\text{ROI}}_{\text{MC}}$:		0.82
Cut6					
SB	E_{center} [keV]	$N^{\text{SB}}_{\text{MC}}$			
0	2007.9	0.19			
1	2015.1	0.19			
2	2022.3	0.21			
3	2029.5	0.21			
4	2048.7	0.24			
5	2055.9	0.21			
6	2063.1	0.22			
7	2070.3	0.22			
window: ±4.80 (eff. width: 9.60)					
$\bar{N}^{\text{SB}}_{\text{MC}}$:		0.21			
$N^{\text{ROI}}_{\text{MC}}$:		0.19			

Table G.8.: The positions of the sidebands (SBs) for all decay modes by their center energy and the window width. Also given is the expected background $N^{\text{SB}}_{\text{MC}}$ in each SB estimated from the background model, the average of those background expectations $\bar{N}^{\text{SB}}_{\text{MC}}$ and for comparison the background expectation in the ROI $N^{\text{ROI}}_{\text{MC}}$.

G.6 List of events in the cut regions

Run	timestamp	E_1 [keV]	ID_1	E_2 [keV]	ID_2	E_{sum} [keV]	Cut	LAr
Run26	1323636860	823.6	ANG3	706.2	GTF112	1529.8	1	0
Run26	1324340992	821.1	ANG4	220.5	ANG5	1041.6	1	0
Run26	1324406684	821.2	RG1	510.7	GTF112	1331.9	1	0
Run26	1325580113	171.5	ANG3	823.9	RG1	995.4	1	0
Run37	1346918744	824.4	ANG2	777.7	RG1	1602.1	1	0
Run38	1349218103	823.7	ANG3	264.6	GTF112	1088.3	1	0
Run39a	1349981647	822.6	ANG3	385.3	ANG5	1207.9	1	0
Run39a	1350159417	821.3	RG1	146.2	GTF112	967.6	1	0
Run39a	1351108046	206.1	GD32D	821.2	GD35B	1027.3	1	0
Run42	1359717453	824.8	RG1	366.4	GTF112	1191.2	1	0
Run43	1362061647	824.8	RG1	515.8	GTF112	1340.6	1	0

Table G.9.: List of events in the ROI of Cut0 of the $0^+_{g.s.} \rightarrow 2^+_2$ decay mode in PI, giving their timestamp, both energies and detector names, the sum energy and the LAr veto flag.

Run	timestamp	E_1 [keV]	ID_1	E_2 [keV]	ID_2	E_{sum} [keV]	Cut	LAr
Run0063	1463972027	1289.0	GD91A	561.1	ANG5	1850.1	1	0
Run0070	1470817685	558.9	GD35B	844.1	ANG5	1402.9	1	1
Run0070	1471523312	936.8	ANG5	559.0	RG1	1495.7	1	0
Run0074	1478665381	559.3	ANG2	1019.9	GTF112	1579.2	1	1
Run0075	1480688657	1035.1	ANG1	559.2	GTF45	1594.3	1	1
Run0075	1481341171	897.2	ANG5	557.8	RG1	1455.0	1	0

Table G.10.: List of events in the ROI of Cut3 of the $0^+_{g.s.} \rightarrow 2^+_2$ decay mode in PII, giving their timestamp, both energies and detector names, the sum energy and the LAr veto flag.

Run	timestamp	SB	E_1 [keV]	ID_1	E_2 [keV]	ID_2	E_{sum} [keV]	Cut	LAr
Run0071	1473364772	3	923.3	GD00D	236.8	RG2	1160.1	1	1
Run0071	1473409012	3	922.2	ANG3	421.7	ANG4	1343.9	1	1
Run0072	1474759959	3	416.5	GD00B	922.0	GD91D	1338.6	1	1
Run0073	1476859330	3	922.4	GD02C	340.5	GTF112	1262.8	1	1
Run0074	1478907426	3	922.3	ANG2	247.2	RG2	1169.5	1	1
Run0075	1482218922	3	241.0	GD02A	923.6	GD32B	1164.5	1	1
Run0075	1483300373	3	924.9	GD00B	229.3	GD91D	1154.2	1	1
Run0078	1490323229	3	923.7	RG2	313.9	ANG4	1237.6	1	1
Run0056	1455087074	4	927.4	GD89C	357.5	GD00C	1284.9	1	1
Run0057	1455911292	4	927.0	GD02B	433.4	GD00B	1360.4	1	1
Run0058	1457153986	4	298.4	RG2	928.6	GD91D	1226.9	1	1
Run0060	1459656396	4	927.5	GD35A	257.4	GTF45	1184.9	1	1
Run0063	1462145939	4	318.8	GD61A	925.8	GD89B	1244.6	1	1
Run0063	1462186687	4	927.7	GD35B	274.9	GD32B	1202.6	1	1
Run0064	1464415499	4	201.2	ANG5	928.0	RG1	1129.2	1	1
Run0071	1473461816	4	928.8	GD02C	308.4	GD79B	1237.2	1	1
Run0071	1473589429	4	927.6	GD02B	318.1	GD02C	1245.7	1	1
Run0071	1474002261	4	422.7	RG2	927.7	GD02C	1350.4	1	1
Run0073	1475397784	4	333.2	GD00B	925.5	GD61A	1258.7	1	1
Run0074	1479414250	4	287.5	GD32B	925.7	GD35C	1213.2	1	1
Run0074	1479783520	4	926.3	GD32A	249.5	GD32C	1175.7	1	1
Run0076	1484895291	4	235.7	RG2	925.6	ANG4	1161.2	1	1
Run0076	1485220768	4	363.6	ANG5	928.5	GD02A	1292.1	1	0
Run0079	1491759436	4	927.8	ANG5	380.8	GD76C	1308.7	1	1
Run0054	1453820922	5	253.7	GD89C	932.5	GD61C	1186.1	1	1
Run0055	1454280955	5	237.8	ANG2	929.3	GD00A	1167.1	1	1
Run0056	1455411487	5	478.3	GD32B	929.8	ANG2	1408.1	1	0
Run0056	1455658082	5	931.8	GD35C	312.2	GD76C	1244.1	1	1
Run0063	1463650780	5	930.1	GD91A	259.0	GD02B	1189.0	1	1
Run0064	1464192335	5	213.3	GD91A	929.1	RG1	1142.4	1	1
Run0065	1465398902	5	930.5	GD02A	213.8	GD32C	1144.2	1	1
Run0067	1467108433	5	931.6	ANG4	506.8	GD91D	1438.5	1	0
Run0069	1469577119	5	502.9	GD00B	932.1	GD00A	1435.0	1	1
Run0070	1471151344	5	929.2	GD32D	226.7	GTF45	1155.8	1	0
Run0073	1477529067	5	931.0	GD00B	243.5	RG1	1174.5	1	1
Run0074	1478293932	5	932.3	GD02A	238.2	GTF112	1170.5	1	1
Run0074	1479751887	5	929.3	GD00B	276.8	GD61A	1206.1	1	1
Run0077	1488304150	5	321.9	GD00A	931.5	GD02C	1253.4	1	1
Run0078	1489582472	5	204.9	ANG5	932.3	RG1	1137.2	1	1

Table G.11.: List of events in the sidebands of Cut2 of the $0^+_{g.s.} \to 0^+_1$ decay mode in PII, giving their timestamp, the sideband ID, both energies and detector names, the sum energy and the LAr veto flag. Continued in Tab. G.12

Run	timestamp	SB	E_1 [keV]	ID_1	E_2 [keV]	ID_2	E_{sum} [keV]	Cut	LAr
Run0056	1454670669	2	907.5	GD32B	270.4	GTF112	1178.0	1	1
Run0056	1454893447	2	282.6	GD35C	906.8	GD76C	1189.5	1	1
Run0058	1456751461	2	905.4	GD00B	486.4	GD32D	1391.8	1	1
Run0060	1459712685	2	905.0	GD35A	369.5	ANG4	1274.5	1	1
Run0063	1462861676	2	401.3	GD02A	907.0	GD32B	1308.3	1	1
Run0065	1465407939	2	905.7	GD35C	280.2	GTF112	1185.8	1	0
Run0070	1470210209	2	906.0	RG2	452.5	ANG4	1358.5	1	1
Run0070	1470453408	2	282.1	GD89B	907.0	ANG3	1189.0	1	1
Run0073	1477529980	2	904.1	GD35B	454.4	GD02B	1358.6	1	1
Run0074	1478425954	2	906.6	ANG2	228.4	GD91D	1135.0	1	1
Run0074	1480498408	2	904.8	GD35B	506.8	GD02B	1411.5	1	1
Run0077	1487116970	2	904.8	ANG4	237.8	GTF45	1142.5	1	1
Run0078	1489674749	2	905.5	GD02B	497.4	ANG5	1402.9	1	1
Run0054	1453993012	1	897.5	GD32A	297.9	GD32C	1195.4	1	1
Run0060	1458559028	1	226.2	ANG3	898.0	GD00C	1124.2	1	1
Run0062	1461581396	1	253.2	GD61A	896.8	GD89B	1150.1	1	0
Run0063	1462219337	1	897.3	GD91A	288.6	ANG2	1185.9	1	1
Run0070	1469777412	1	896.0	GD89D	393.7	GD00D	1289.7	1	0
Run0070	1471357435	1	240.0	GD00D	894.8	RG2	1134.9	1	1
Run0070	1471793926	1	894.9	ANG5	494.2	RG1	1389.1	1	1
Run0071	1473588876	1	896.0	GD91A	484.7	ANG5	1380.6	1	1
Run0071	1474124518	1	896.6	ANG3	278.3	GTF112	1174.9	1	1
Run0071	1474380165	1	895.9	RG1	523.0	ANG3	1418.9	1	1
Run0073	1475210493	1	315.9	GD61A	895.5	GD89B	1211.3	1	1
Run0074	1480525990	1	898.3	GD91A	303.8	GD35B	1202.2	1	0
Run0075	1481454604	1	897.7	ANG2	203.9	GD00A	1101.6	1	1
Run0075	1481859295	1	896.8	RG1	230.0	GD32C	1126.8	1	0
Run0075	1482600755	1	206.0	GD89B	895.1	ANG3	1101.1	1	1
Run0076	1485586400	1	219.2	GD00B	897.7	GD89A	1116.9	1	1
Run0077	1488004364	1	451.7	GD00A	895.1	GD02C	1346.8	1	0
Run0078	1490142630	1	896.4	GD35B	418.0	ANG2	1314.4	1	1
Run0056	1455177824	0	894.7	ANG5	499.8	GD02A	1394.5	1	1
Run0062	1461808338	0	242.2	GD00B	893.3	GD32A	1135.5	1	1
Run0071	1473197051	0	892.5	GD89B	316.7	GTF45	1209.2	1	1
Run0073	1476355534	0	894.7	GD91A	281.0	ANG5	1175.7	1	1
Run0077	1488675764	0	893.2	GD32C	262.1	GD89D	1155.3	1	1
Run0079	1492023704	0	386.2	GD35C	893.6	RG2	1279.8	1	1

Table G.12.: Continuation of Tab. G.11.

G.7 Detector distributions of events in the cut regions

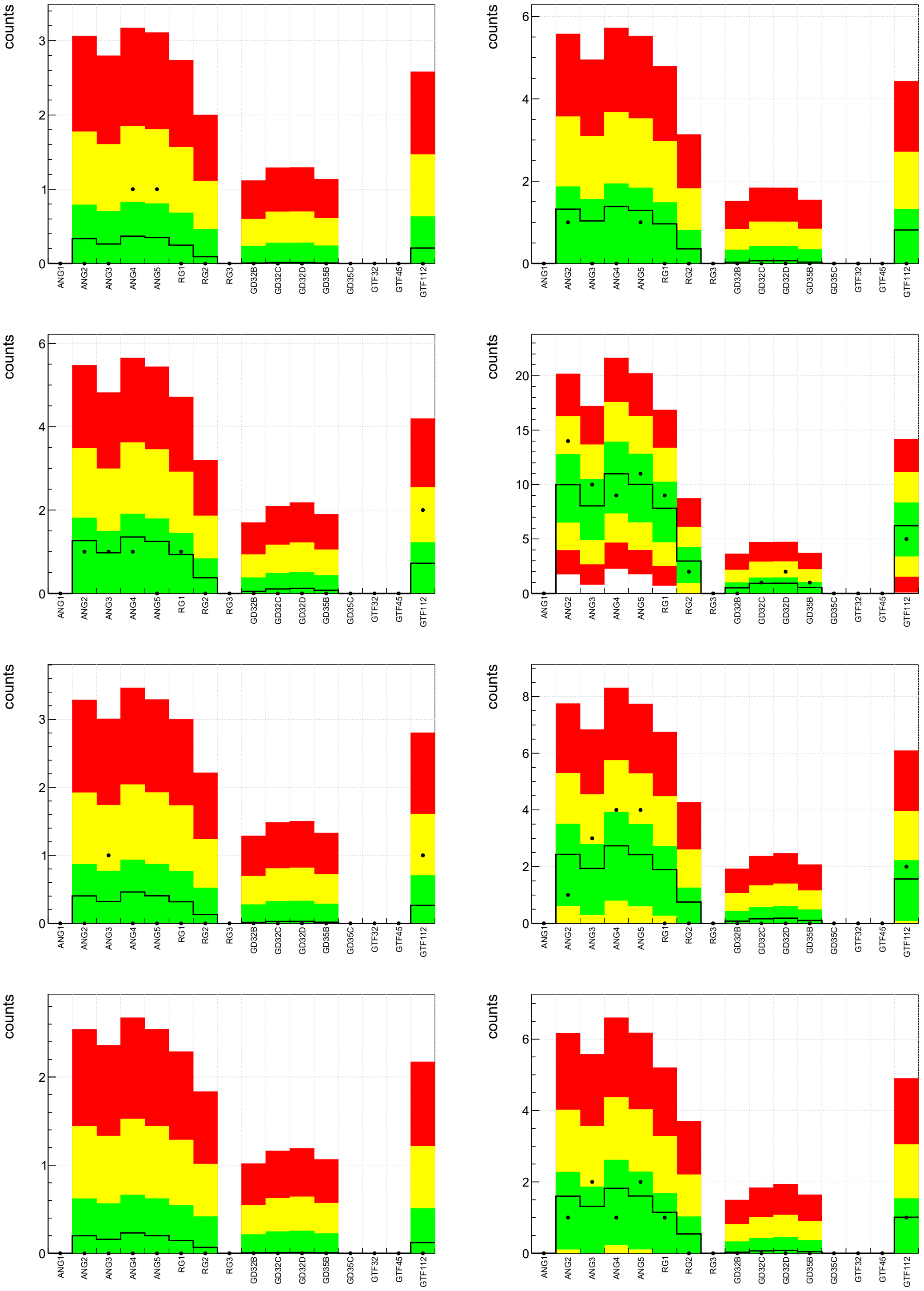

Figure G.20.: Distribution among the detectors of PI events in the signal cut regions (*left*) and summed sideband regions (*right*) of the search for the $0^+_{g.s.} \rightarrow 0^+_1$ $0\nu\beta\beta$-decay mode. From top to bottom, the plots belong to Cut1-3 and Cut5. The data is shown as black dots, the expectation from the background model is drawn as black line, in addition to the corresponding 68% (green), 95% (yellow) and 99.7% (red) smallest Poisson intervals.

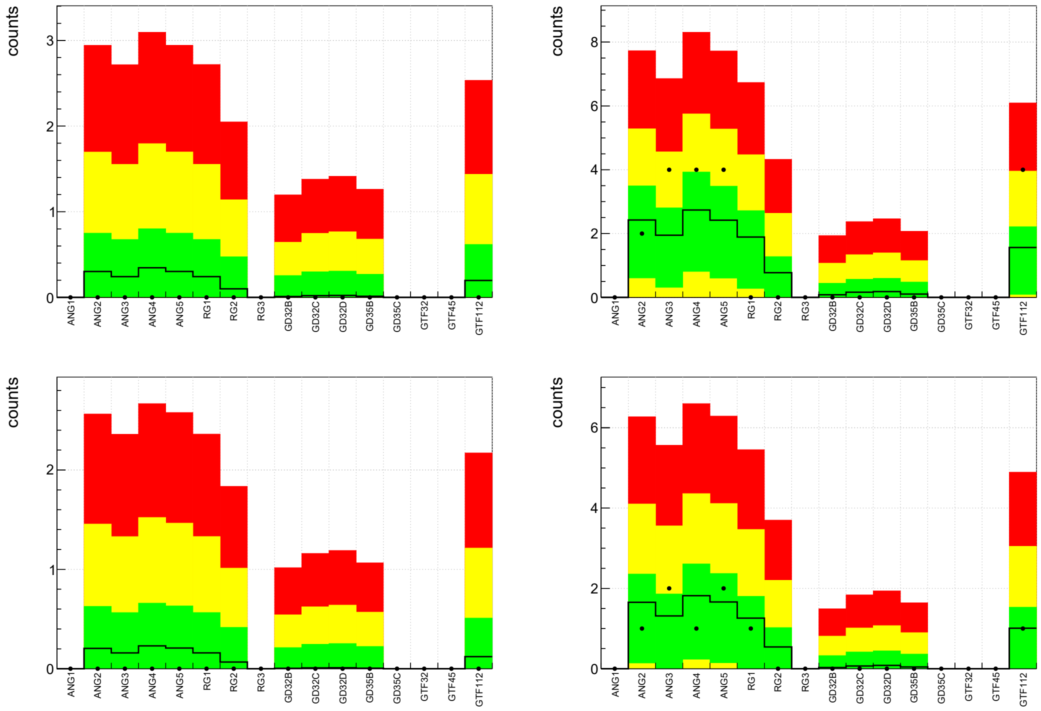

Figure G.21.: Distribution among the detectors of PI events in the signal cut regions (*left*) and summed sideband regions (*right*) of the search for the $0^+_{g.s.} \rightarrow 2^+_1$ $0\nu\beta\beta$-decay mode. From top to bottom, the plots belong to Cut0-1. The data is shown as black dots, the expectation from the background model is drawn as black line, in addition to the corresponding 68% (green), 95% (yellow) and 99.7% (red) smallest Poisson intervals.

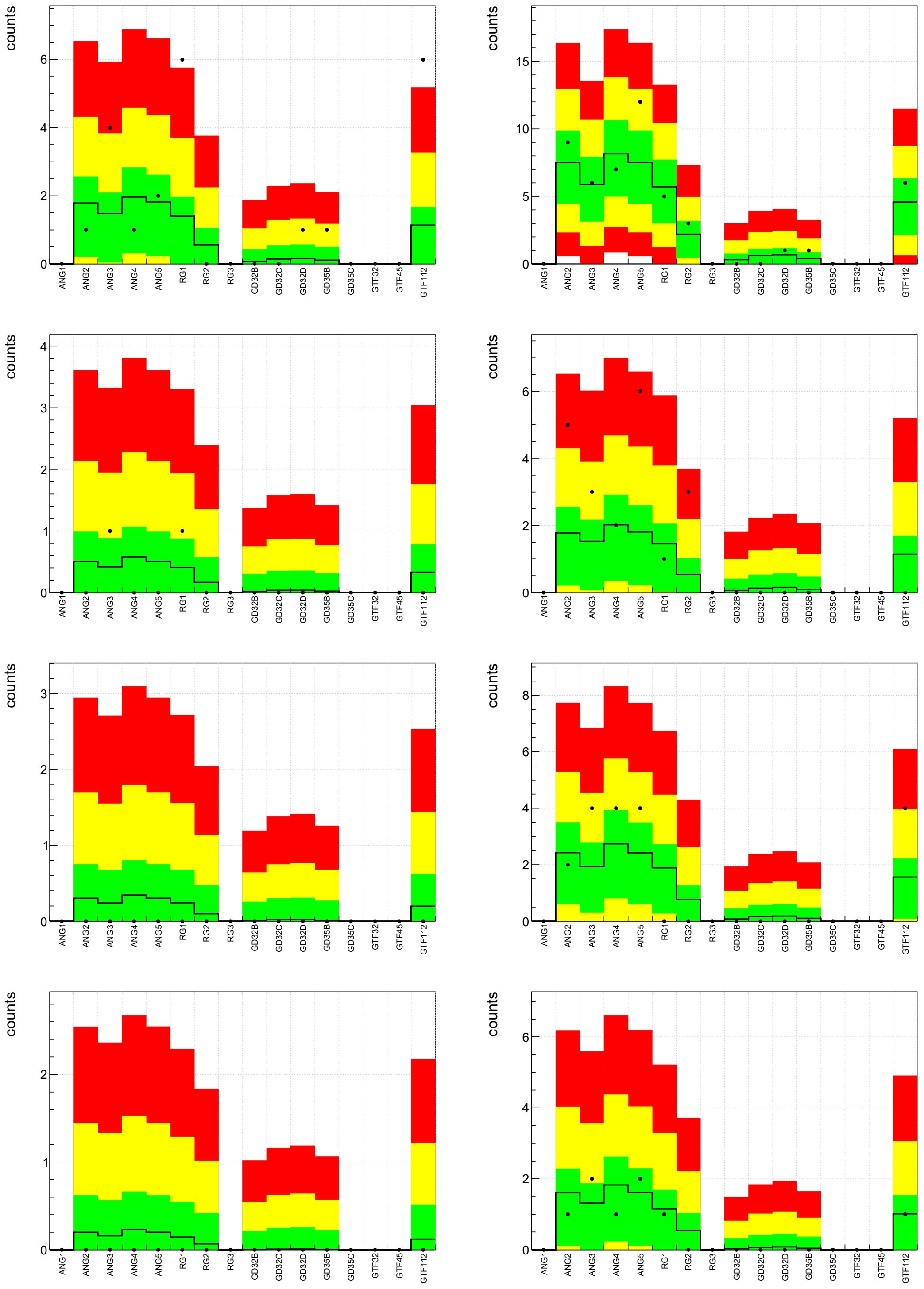

Figure G.22.: Distribution among the detectors of PI events in the signal cut regions (*left*) and summed sideband regions (*right*) of the search for the $0^+_{g.s.} \rightarrow 2^+_2$ $0\nu\beta\beta$-decay mode. From top to bottom, the plots belong to Cut0-2 and Cut5. The data is shown as black dots, the expectation from the background model is drawn as black line, in addition to the corresponding 68% (green), 95% (yellow) and 99.7% (red) smallest Poisson intervals.

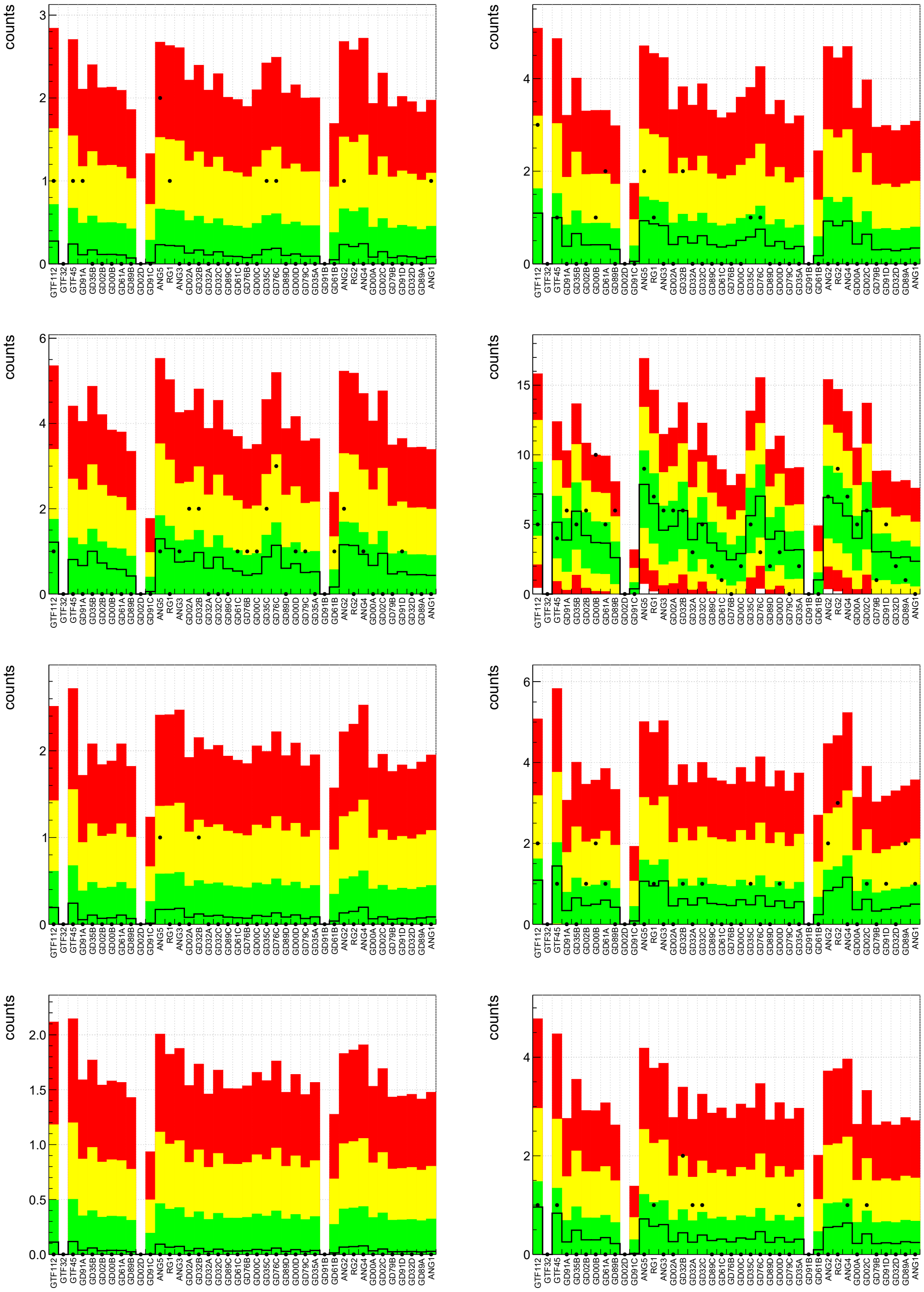

Figure G.23.: Distribution among the detectors of PII events in the signal cut regions (*left*) and summed sideband regions (*right*) of the search for the $0^+_{g.s.} \rightarrow 0^+_1$ $0\nu\beta\beta$-decay mode. From top to bottom, the plots belong to Cut1-3 and Cut5. The data is shown as black dots, the expectation from the background model is drawn as black line, in addition to the corresponding 68% (green), 95% (yellow) and 99.7% (red) smallest Poisson intervals.

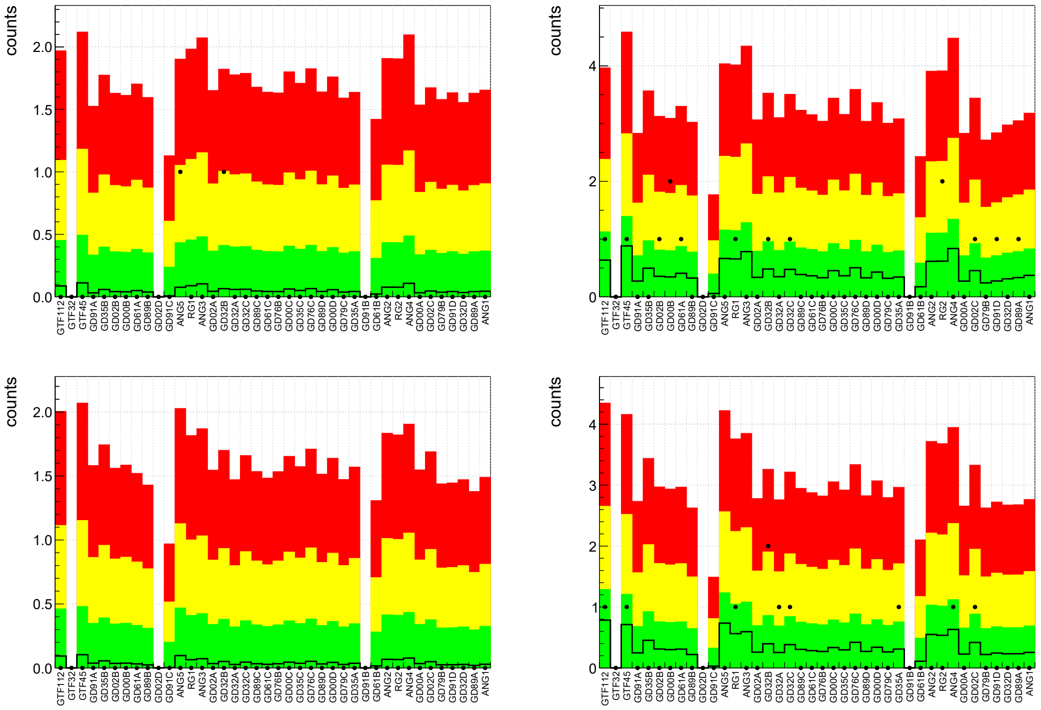

Figure G.24.: Distribution among the detectors of PII events in the signal cut regions (*left*) and summed sideband regions (*right*) of the search for the $0^+_{g.s.} \rightarrow 2^+_1$ $0\nu\beta\beta$-decay mode. From top to bottom, the plots belong to Cut0-1. The data is shown as black dots, the expectation from the background model is drawn as black line, in addition to the corresponding 68% (green), 95% (yellow) and 99.7% (red) smallest Poisson intervals.

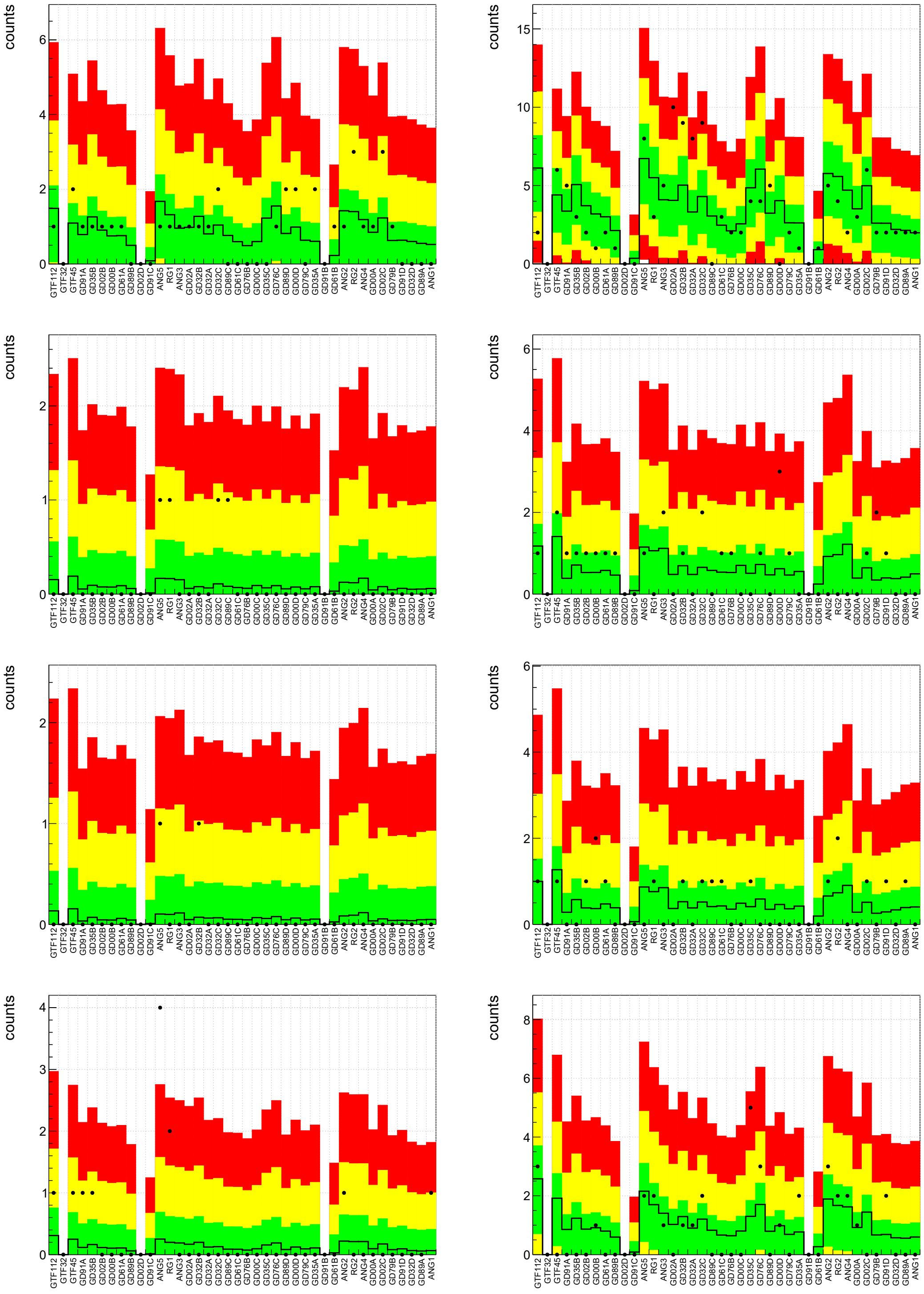

Figure G.25.: Distribution among the detectors of PII events in the signal cut regions (*left*) and summed sideband regions (*right*) of the search for the $0^+_{g.s.} \rightarrow 2^+_2$ $0\nu\beta\beta$-decay mode. From top to bottom, the plots belong to Cut0-3. The data is shown as black dots, the expectation from the background model is drawn as black line, in addition to the corresponding 68% (green), 95% (yellow) and 99.7% (red) smallest Poisson intervals.

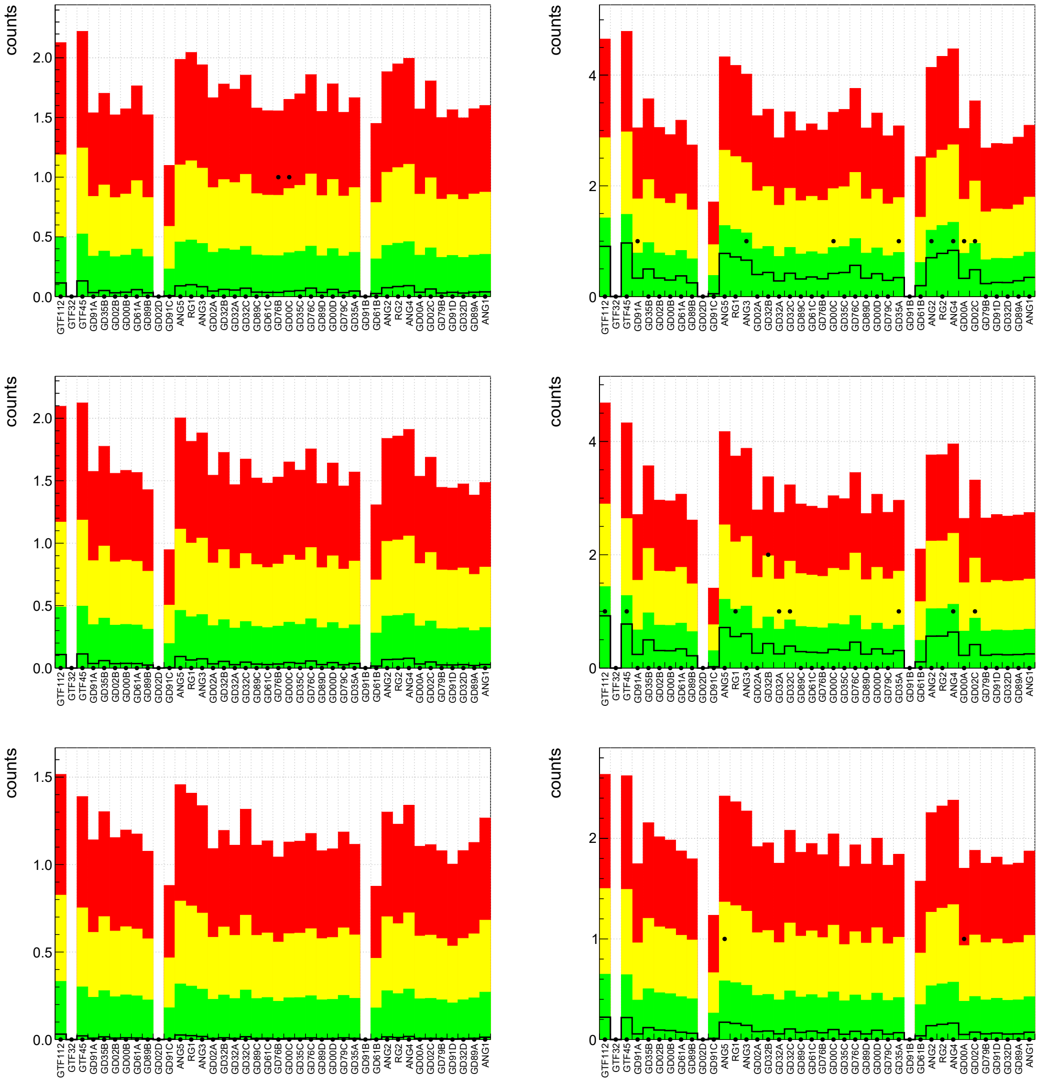

Figure G.26.: Distribution among the detectors of PII events in the signal cut regions (*left*) and summed sideband regions (*right*) of the search for the $0^+_{g.s.} \rightarrow 2^+_2$ $0\nu\beta\beta$-decay mode. From top to bottom, the plots belong to Cut4-6. The data is shown as black dots, the expectation from the background model is drawn as black line, in addition to the corresponding 68% (green), 95% (yellow) and 99.7% (red) smallest Poisson intervals.

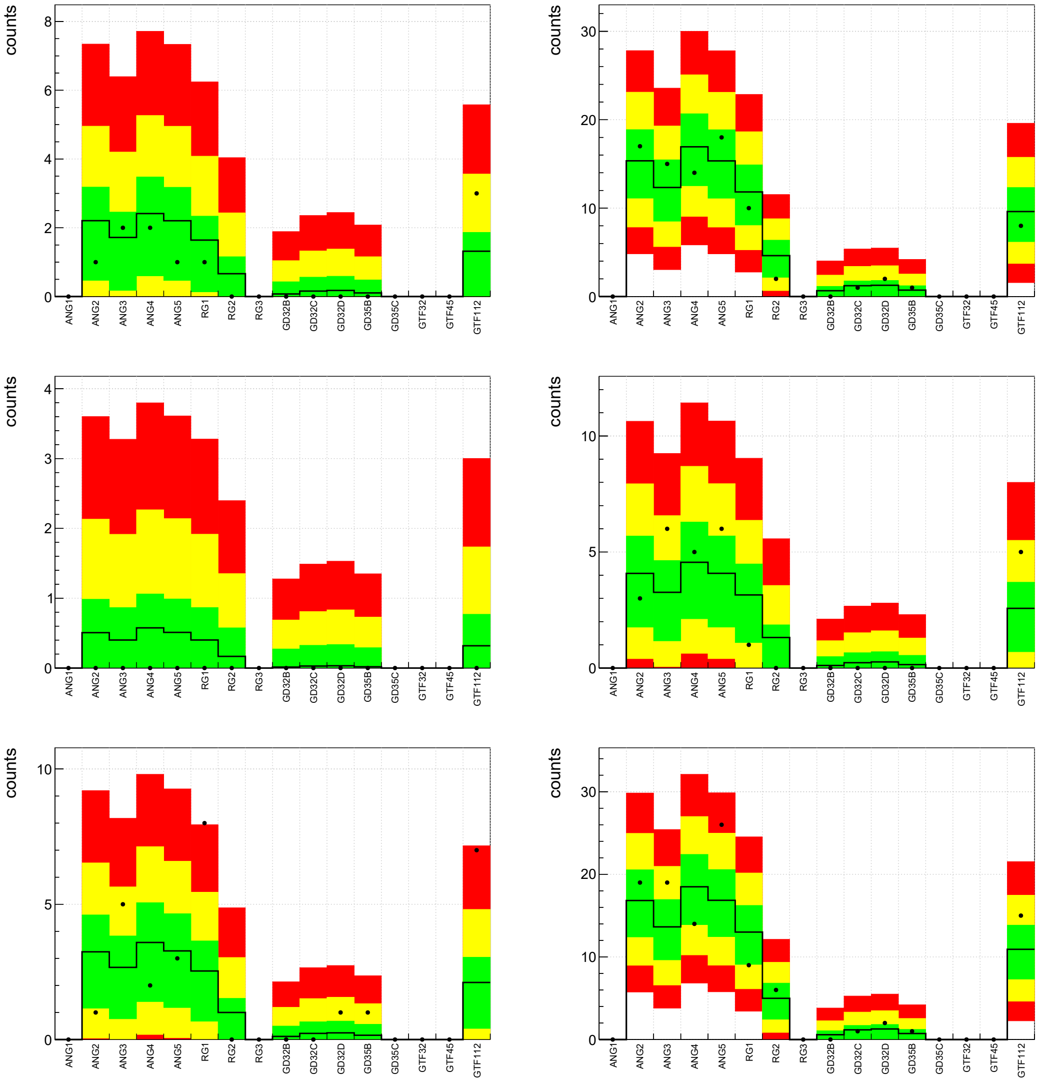

Figure G.27.: Distribution among the detectors of PI events combining all signal cut regions (*left*) and all sideband regions (*right*) of the search for the $0\nu\beta\beta$-decay, $0^+_{g.s.} \rightarrow 0^+_1$ (*top*), $0^+_{g.s.} \rightarrow 2^+_1$ (*middle*) and $0^+_{g.s.} \rightarrow 2^+_2$ (*bottom*). The data is shown as black dots, the expectation from the background model is drawn as black line, in addition to the corresponding 68% (green), 95% (yellow) and 99.7% (red) smallest Poisson intervals.

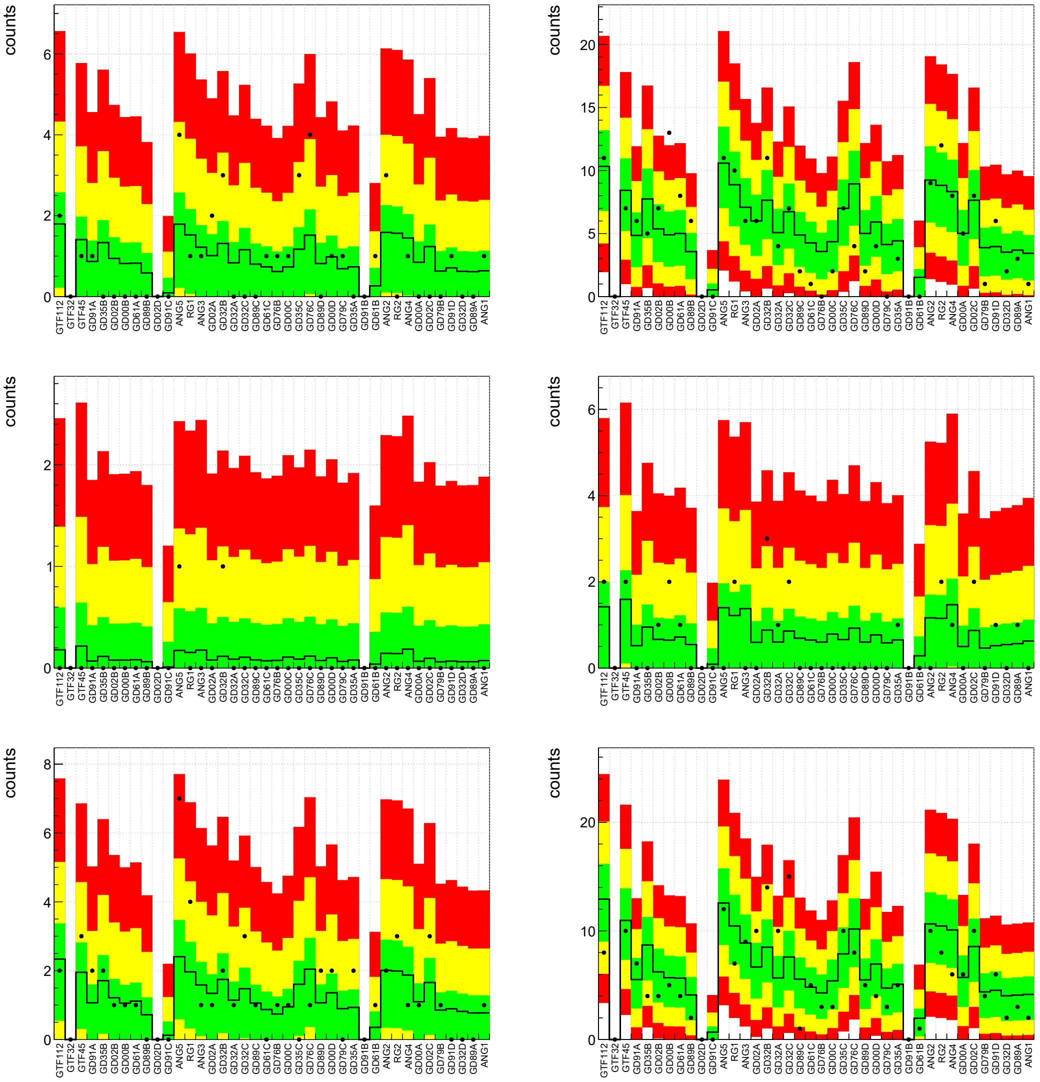

Figure G.28.: Distribution among the detectors of PII events combining all signal cut regions (*left*) and all sideband regions (*right*) of the search for the $0\nu\beta\beta$-decay, $0^+_{g.s.} \rightarrow 0^+_1$ (*top*), $0^+_{g.s.} \rightarrow 2^+_1$ (*middle*) and $0^+_{g.s.} \rightarrow 2^+_2$ (*bottom*). The data is shown as black dots, the expectation from the background model is drawn as black line, in addition to the corresponding 68% (green), 95% (yellow) and 99.7% (red) smallest Poisson intervals.

G.8 Systematic uncertainties (M2)

Uncertainty [%]	$0^+_{g.s.} \to 0^+_1$				$0^+_{g.s.} \to 2^+_1$		$0^+_{g.s.} \to 2^+_2$						
	1	2	3	5	0	1	0	1	2	3	4	5	6
Phase I													
FWHM	1.8	5.0	2.0	2.2	2.5	2.1	4.3	3.5	2.5	-	-	2.2	-
Shift	0.5	2.2	0.1	0.5	0.4	0.5	0.5	0.6	0.4	-	-	0.4	-
Combined Energy	1.8	5.5	2.0	2.2	2.5	2.2	4.3	3.5	2.6	-	-	2.2	-
DLCoax	12.1	7.1	12.1	20.5	10.1	18.4	8.3	12.2	12.3	-	-	20.1	-
DLBEGe	-	-	-	-	-	-	-	-	-	-	-	-	-
MC processes	4	4	4	4	4	4	4	4	4	-	-	4	-
Exposure	1.4	1.4	1.4	1.4	1.4	1.4	1.4	1.4	1.4	-	-	1.4	-
Phase II													
FWHM	1.0	3.3	1.4	1.7	2.2	1.6	3.2	2.2	1.9	2.0	1.7	1.7	1.5
Shift	0.9	0.6	0.2	0.7	0.7	0.6	1.3	1.2	0.5	1.5	0.8	0.7	0.5
Combined Energy	1.3	3.3	1.4	1.8	2.3	1.7	3.5	2.5	2.0	2.5	1.9	1.8	1.6
DLCoax	3.4	1.9	4.6	7.9	3.2	4.9	2.5	5.0	5.1	3.7	4.5	6.1	5.9
DLBEGe	2.5	1.4	0.9	5.5	1.7	2.3	0.8	3.5	1.5	1.1	1.6	1.4	1.4
MC processes	4	4	4	4	4	4	4	4	4	4	4	4	4
Exposure	1.1	1.1	1.1	1.1	1.1	1.1	1.1	1.1	1.1	1.1	1.1	1.1	1.1

Table G.13.: Summary of the systematical uncertainties of the expected signal counts of the search for the $0\nu\beta\beta$-decay to excited states. Shown are the uncertainties derived from the energy resolution (FWHM), the energy scale shift (Shift), the dead layer/active volume uncertainties (DLCoax, DLBEGe), the MC physics processes and the exposure for the 4 ($0^+_{g.s.} \to 0^+_1$), 2 ($0^+_{g.s.} \to 2^+_1$) and 7 ($0^+_{g.s.} \to 2^+_2$) signal cut regions of the three decay modes in PI and PII data sets.

G.9 Inverse half-life posteriors obtained with M1 and M2 data sets

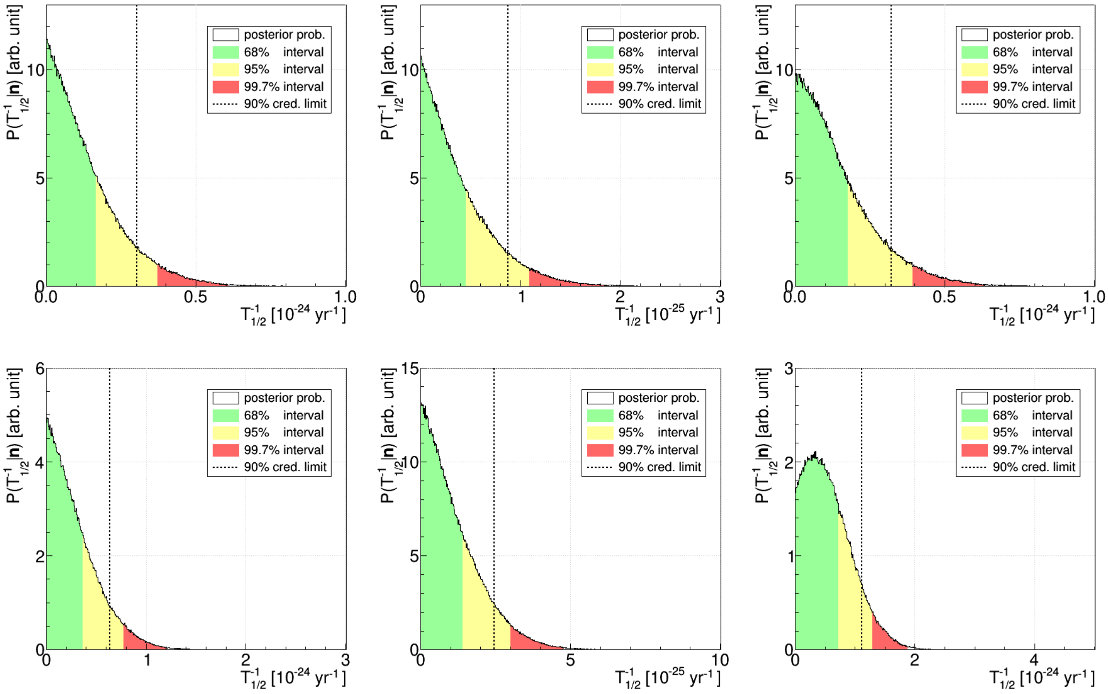

Figure G.29.: Shown is the marginalized posterior probability density distribution for $T_{1/2}^{-1}$ obtained for the $0^+_{g.s.} \rightarrow 0^+_1$ (*left*), $0^+_{g.s.} \rightarrow 2^+_1$ (*middle*) and $0^+_{g.s.} \rightarrow 2^+_2$ (*right*) decay modes using the M1 data. The smallest 68%, 95% and 99.7% intervals are filled in color. Additionally, the 90% credibility upper limit is shown as dashed line. The bottom row shows the posteriors obtained while excluding the ROI around the Q-value of the decay.

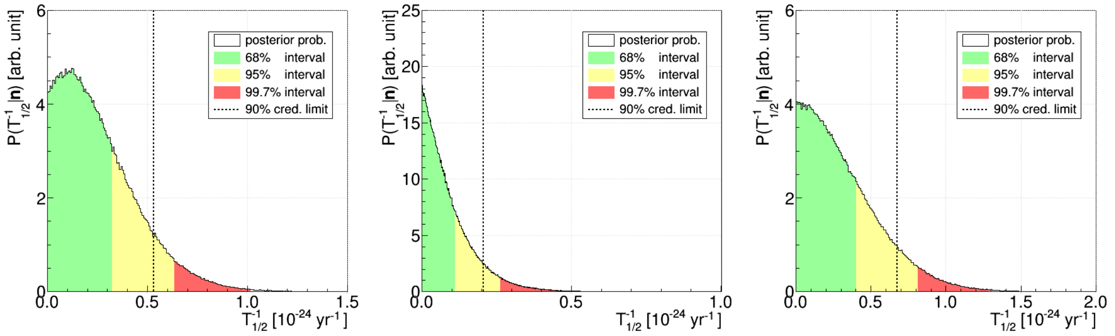

Figure G.30.: Shown is the marginalized posterior probability density distribution for $T^{-1}_{1/2}$ obtained for the $0^+_{g.s.} \rightarrow 0^+_1$ (*left*), $0^+_{g.s.} \rightarrow 2^+_1$ (*middle*) and $0^+_{g.s.} \rightarrow 2^+_2$ (*right*) decay modes using the M2 data. The smallest 68%, 95% and 99.7% intervals are filled in color. Additionally, the 90% credibility upper limit is shown as dashed line.

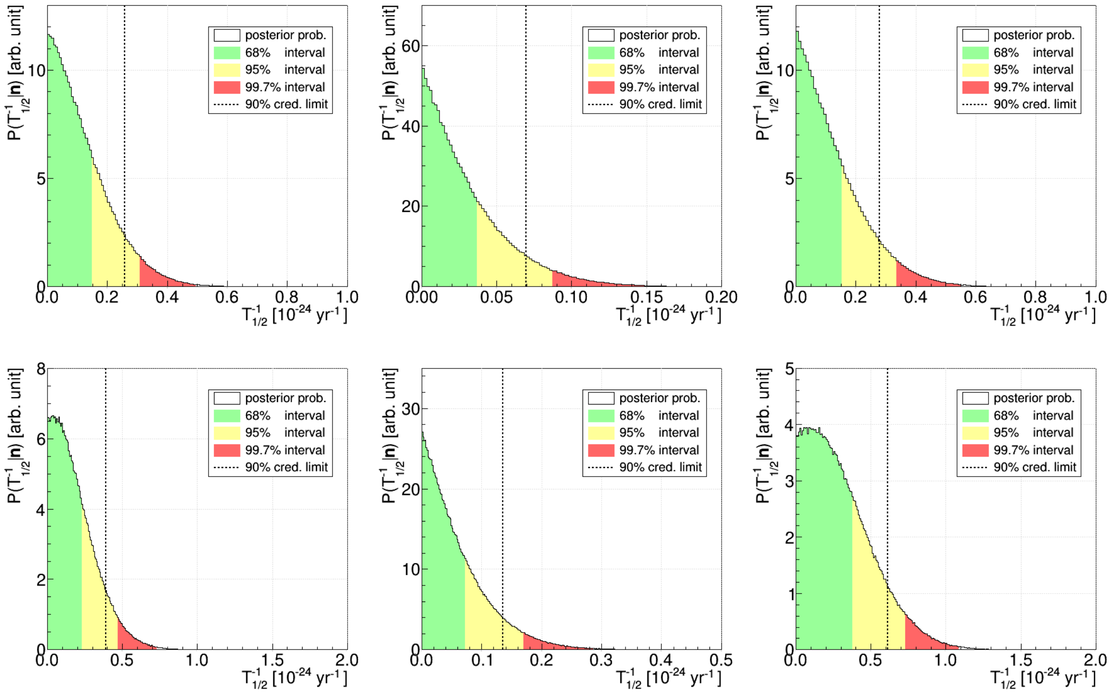

Figure G.31.: Shown is the marginalized posterior probability density distribution for $T^{-1}_{1/2}$ obtained for the $0^+_{g.s.} \rightarrow 0^+_1$ (*left*), $0^+_{g.s.} \rightarrow 2^+_1$ (*middle*) and $0^+_{g.s.} \rightarrow 2^+_2$ (*right*) decay modes by combining the M1 and M2 data. The smallest 68%, 95% and 99.7% intervals are filled in color. Additionally, the 90% credibility upper limit is shown as dashed line. The bottom row shows the posteriors obtained while excluding the ROI around the Q-value of the decay in the M1 data.

Appendix H

List of acronyms

$\beta\beta$-decay - double beta decay
$\beta^-\beta^-$-decay - double beta minus decay
$\beta^+\beta^+$-decay - double beta plus decay
$0\nu\beta\beta$-decay - neutrinoless double beta decay
$2\nu\beta\beta$-decay - two-neutrino double beta decay
ANG - ANGereichert (enriched detectors from the HdM experiment)
B1/2 - first/second de-excitation branch of $0^+_{g.s.} \rightarrow 2^+_2$ decay mode
BAT - Bayesian Analysis Toolkit
BEGe - Broad Energy Germanium
BI - Background Index
Ch. - Chapter
C.L. - Confidence Level
cts - counts
DEP - Double Escape Peak
DL - Dead Layer
EC - Electron Capture
FADC - Fast/Flash Analog to Digital Converter
FCCD - Full Charge Collection Depth
Fig. - Figure
FWHM - Full Width at Half Maximum
GD - Gerda Detector (enriched detectors produced for the Gerda experiment)
Gerda - GERmanium Detector Array
GTF - Genius Test Facility
HdM - Heidelberg-Moscow
HV - High Voltage
IGEX - International Germanium EXperiment
IH - Inverted neutrino mass Hierarchy
JFET - Junction Field Effect Transistor
LMA - Large Mixing Angle
M2 - data with energy depositions in two detectors (Multiplicity=2)
MaGe - Majorana Gerda (MC simulation framework)
MC - Monte Carlo
MCMC - Markov Chain Monte Carlo
NH - Normal neutrino mass Hierarchy
PI/PII - Phase I/II of the Gerda experiment
PMT - PhotoMultiplier Tube
PSD - Pulse Shape Discrimination
RG - Ricco Grande (enriched detectors of the IGEX experiment)
ROI - Region Of Interest
SB - SideBand
Sec. - Section
SEP - Single Escape Peak
SM - Standard Model
TPC - Time Projection Chamber
ZAC - Zero Area Cusp

Appendix I

Gerda Phase II data disclaimer

Disclaimer

At the time of writing, Phase II of GERDA is still running. This work is based only on a subset of the final Phase II data, taken from December 2015 to April 2017.
Because the characterisation of the M2 data and improvements of data quality is still in process, the data selection and processing parameters are subject to change for the final PII data set. This includes:

- A larger exposure (∼100 kg·yr) with the end of Phase II.
- Adjusting the correction of crosstalk on a run by run basis (either exclude runs with larger deviations or use matrices determined on base of physics data for selected runs).
- A correction of the energy shifts also observed in the M1 data, which may be related to the calibration process.
- The data quality and selection for natural detectors is currently under revision.

As the analyses in chapters 5 to 8 are performed in parallel to this process, analysis parameters and results are expected to change. This work presents **preliminary** Phase II results. However, analysis strategies and procedures are documented and will be applied to the final data set when available.

Bibliography

[1] M. Agostini, M. Allardt, E. Andreotti et al. *Results on Neutrinoless Double-β Decay of ^{76}Ge from Phase I of the GERDA Experiment*. Physical Review Letters **111** (12), 122503 (sep 2013). 1307.4720, URL https://link.aps.org/doi/10.1103/PhysRevLett.111.122503.

[2] M. Agostini, A. M. Bakalyarov, M. Balata et al. *Upgrade for Phase II of the Gerda experiment*. The European Physical Journal C **78** (5), 388 (may 2018). URL http://link.springer.com/10.1140/epjc/s10052-018-5812-2.

[3] M. Agostini, M. Allardt, A. M. Bakalyarov et al. *Results on $\beta\beta$ decay with emission of two neutrinos or Majorons in ^{76}Ge from GERDA Phase I: GERDA Collaboration*. European Physical Journal C **75** (9), 416 (sep 2015). 1501.02345, URL http://link.springer.com/10.1140/epjc/s10052-015-3627-y.

[4] M. Agostini, M. Allardt, A. M. Bakalyarov et al. *2$\nu\beta\beta$ decay of ^{76}Ge into excited states with GERDA phase I*. Journal of Physics G: Nuclear and Particle Physics **42** (11), 044001 (sep 2015). URL http://iopscience.iop.org/article/10.1088/0954-3899/42/11/115201/meta.

[5] W. Pauli. *Fünf Arbeiten zum Ausschliessungsprinzip und zum Neutrino. Texte zur Forschung* (Darmstadt : Wissenschaftliche Buchgesellschaft, 1977).

[6] C. L. Cowan, F. Reines, F. B. Harrison et al. *Detection of the free neutrino: A confirmation*. Science **124** (3212), 103–104 (jul 1956). URL http://www.sciencemag.org/cgi/doi/10.1126/science.124.3212.103.

[7] C. S. Wu, E. Ambler, R. W. Hayward et al. *Experimental test of parity conservation in beta decay*. Physical Review **105** (4), 1413–1415 (feb 1957). URL https://link.aps.org/doi/10.1103/PhysRev.105.1413.

[8] R. Davis Jr. and D. S. Harmer. *Attempt to observe the $Cl^{37}(\bar{\nu}e^{-})Ar^{37}$ reaction induced by reactor antineutrinos*. Bull. Am. Phys. Soc. **4**, 217 (1959).

[9] B. T. Cleveland, T. Daily, R. Davis Jr. et al. *Update on the measurement of the solar neutrino flux with the Homestake chlorine detector*. Nuclear Physics B (Proceedings Supplements) **38** (1-3), 47–53 (mar 1995). URL http://stacks.iop.org/0004-637X/496/i=1/a=505.

[10] M. Dine and A. Kusenko. *Origin of the matter-antimatter asymmetry*. Reviews of Modern Physics **76** (1), 1–30 (dec 2004). 0303065, URL https://link.aps.org/doi/10.1103/RevModPhys.76.1.

[11] J. Hosaka, K. Ishihara, J. Kameda et al. *Three flavor neutrino oscillation analysis of atmospheric neutrinos in Super-Kamiokande*. Physical Review D - Particles, Fields, Gravitation and Cosmology **74** (3), 032002 (aug 2006). 0604011, URL https://link.aps.org/doi/10.1103/PhysRevD.74.032002.

[12] Q. R. Ahmad, R. C. Allen, T. C. Andersen et al. *Measurement of the Rate of $\nu_e + d \rightarrow p + p + e$âĹŠ Interactions Produced by ^{8}B Solar Neutrinos at the Sudbury Neutrino Observatory*. Physical Review Letters **87** (7), 071301 (jul 2001). URL https://link.aps.org/doi/10.1103/PhysRevLett.87.071301.

[13] Z. Maki, M. Nakagawa and S. Sakata. *Remarks on the Unified Model of Elementary Particles*. Progress of Theoretical Physics **28** (5), 870–880 (nov 1962). URL https://academic.oup.com/ptp/article-lookup/doi/10.1143/PTP.28.870.

[14] V. Gribov and B. Pontecorvo. *Neutrino astronomy and lepton charge*. Physics Letters B **28** (7), 493–496 (jan 1969). URL http://linkinghub.elsevier.com/retrieve/pii/0370269369905255.

[15] G. Bellini, L. Ludhova, G. Ranucci et al. *Neutrino oscillations*. Advances in High Energy Physics **2014**, 1–28 (2014). URL http://www.hindawi.com/journals/ahep/2014/191960/.

[16] J. N. Bahcall, A. M. Serenelli and S. Basu. *New solar opacities, abundances, helioseismology, and neutrino fluxes*. The Astrophysical Journal **621** (1), L85–L88 (mar 2004). 0412440, URL http://dx.doi.org/10.1086/428929.

[17] B. Aharmim, S. N. Ahmed, A. E. Anthony et al. *Low-energy-threshold analysis of the Phase I and Phase II data sets of the Sudbury Neutrino Observatory*. Physical Review C **81** (5), 055504 (may 2010). 0910.2984, URL https://link.aps.org/doi/10.1103/PhysRevC.81.055504.

[18] P. Mosteiro, G. Bellini, J. Benziger et al. *Low-energy (anti)neutrino physics with Borexino: Neutrinos from the primary proton-proton fusion process in the Sun*. Nuclear and Particle Physics Proceedings **265-266**, 87–92 (aug 2015). 1508.05379, URL http://linkinghub.elsevier.com/retrieve/pii/S240560141500365X.

[19] L. Wolfenstein. *Neutrino oscillations in matter*. Physical Review D **17** (9), 2369–2374 (may 1978). arXiv:1011.1669v3, URL https://link.aps.org/doi/10.1103/PhysRevD.17.2369.

[20] S. P. Mikheev and A. b. Y. Smirnov. *Resonance Amplification of Oscillations in Matter and Spectroscopy of Solar Neutrinos*. Sov. J. Nucl. Phys. **42** (6), 913–917 (1985).

[21] W. Hampel, J. Handt, G. Heusser et al. *GALLEX solar neutrino observations: Results for GALLEX IV*. Physics Letters, Section B: Nuclear, Elementary Particle and High-Energy Physics **447** (1-2), 127–133 (feb 1999). URL http://linkinghub.elsevier.com/retrieve/pii/S0370269398015792.

[22] S. Abe, T. Ebihara, S. Enomoto et al. *Precision measurement of neutrino oscillation parameters with KamLAND*. Physical Review Letters **100** (22), 221803 (jun 2008). 0801.4589, URL https://link.aps.org/doi/10.1103/PhysRevLett.100.221803.

[23] F. P. An, J. Z. Bai, A. B. Balantekin et al. *Observation of electron-antineutrino disappearance at Daya Bay*. Physical Review Letters **108** (17), 171803 (apr 2012). 1203.1669, URL https://link.aps.org/doi/10.1103/PhysRevLett.108.171803.

[24] J. K. Ahn, S. Chebotaryov, J. H. Choi et al. *Observation of reactor electron antineutrinos disappearance in the RENO experiment*. Physical Review Letters **108** (19), 191802 (may 2012). 1204.0626, URL https://link.aps.org/doi/10.1103/PhysRevLett.108.191802.

[25] Y. Abe, C. Aberle, J. C. dos Anjos et al. *First measurement of θ_{13} from delayed neutron capture on hydrogen in the Double Chooz experiment*. Physics Letters, Section B: Nuclear, Elementary Particle and High-Energy Physics **723** (1-3), 66–70 (jun 2013). `1301.2948`, URL `http://linkinghub.elsevier.com/retrieve/pii/S0370269313003390`.

[26] K. Abe, N. Abgrall, Y. Ajima et al. *Indication of electron neutrino appearance from an accelerator-produced off-axis muon neutrino beam*. Physical Review Letters **107** (4), 041801 (jul 2011). `1106.2822`, URL `https://link.aps.org/doi/10.1103/PhysRevLett.107.041801`.

[27] A. Aguilar, L. B. Auerbach, R. L. Burman et al. *Evidence for Neutrino Oscillations from the Observation of Electron Anti-neutrinos in a Muon Anti-Neutrino Beam*. Physical Review D **64** (11), 112007 (nov 2001). `0104049`, URL `http://arxiv.org/abs/hep-ex/0104049{%}0Ahttp://dx.doi.org/10.1103/PhysRevD.64.112007`.

[28] A. A. Aguilar-Arevalo, B. C. Brown, L. Bugel et al. *Improved Search for $\bar{\nu}_\mu \rightarrow \bar{\nu}_e$ Oscillations in the MiniBooNE Experiment*. Physical Review Letters **110** (16), 161801 (apr 2013). `1303.2588`, URL `http://arxiv.org/abs/1303.2588`.

[29] Y. Fukuda, T. Hayakawa, E. Ichihara et al. *Evidence for oscillation of atmospheric neutrinos*. Physical Review Letters **81** (8), 1562–1567 (aug 1998). `9807003`, URL `https://link.aps.org/doi/10.1103/PhysRevLett.81.1562`.

[30] *NuFIT 3.2* (2018). URL `http://www.nu-fit.org`.

[31] R. B. Patterson. *Prospects for Measurement of the Neutrino Mass Hierarchy*. Annual Review of Nuclear and Particle Science **65** (1), 177–192 (oct 2015). `1506.07917`, URL `http://dx.doi.org/10.1146/annurev-nucl-102014-021916`.

[32] S. Marcocci, S. Dell'Oro, M. Viel et al. *The contribution of light Majorana neutrinos to neutrinoless double beta decay and cosmology*. Journal of Physics: Conference Series **888** (1), 023–023 (dec 2017). `1505.02722`, URL `http://stacks.iop.org/1475-7516/2015/i=12/a=023?key=crossref.b4099927366dbd853bc118234d342049`.

[33] P. Adamson, C. Ader, M. Andrews et al. *First measurement of electron neutrino appearance in NOvA*. Physical Review Letters **116** (15), 151806 (apr 2016). `1601.05022`, URL `https://link.aps.org/doi/10.1103/PhysRevLett.116.151806`.

[34] K. Abe, J. Adam, H. Aihara et al. *Measurements of neutrino oscillation in appearance and disappearance channels by the T2K experiment with 6.6$\times$10^{20} protons on target*. Physical Review D - Particles, Fields, Gravitation and Cosmology **91** (7), 072010 (apr 2015). `1502.01550`, URL `https://link.aps.org/doi/10.1103/PhysRevD.91.072010`.

[35] M. Goeppert-Mayer. *Double beta-disintegration*. Physical Review **48** (6), 512–516 (sep 1935). URL `https://link.aps.org/doi/10.1103/PhysRev.48.512`.

[36] S. R. Elliott, A. A. Hahn and M. K. Moe. *Direct evidence for two-neutrino double-beta decay in* ^{82}*Se*. Physical Review Letters **59** (18), 2020–2023 (nov 1987). URL https://link.aps.org/doi/10.1103/PhysRevLett.59.2020.

[37] W. C. Haxton and G. J. Stephenson. *Double beta decay*. Progress in Particle and Nuclear Physics **12** (C), 409–479 (1984). URL http://linkinghub.elsevier.com/retrieve/pii/0146641084900061.

[38] W. H. Furry. *On transition probabilities in double beta-disintegration*. Physical Review **56** (12), 1184–1193 (dec 1939). URL https://link.aps.org/doi/10.1103/PhysRev.56.1184.

[39] F. F. Deppisch, M. Hirsch and H. Päs. *Neutrinoless double-beta decay and physics beyond the standard model*. Journal of Physics G: Nuclear and Particle Physics **39** (12), 124007 (dec 2012). URL http://stacks.iop.org/0954-3899/39/i=12/a=124007?key=crossref.4bb9228536ff6a9ba9b494588cd82f0d.

[40] J. Engel and J. Menéndez. *Status and future of nuclear matrix elements for neutrinoless double-beta decay: A review*. Reports on Progress in Physics **80** (4), 046301 (apr 2017). 1610.06548, URL http://stacks.iop.org/0034-4885/80/i=4/a=046301?key=crossref.b5ee23ef91fa30a1f8d2ff41a378cf3f.

[41] T. Tomoda. *0+ → 2+* $0\nu\beta\beta$ *decay triggered directly by the Majorana neutrino mass*. Physics Letters, Section B: Nuclear, Elementary Particle and High-Energy Physics **474** (3-4), 245–250 (feb 2000). 9909330, URL http://linkinghub.elsevier.com/retrieve/pii/S0370269300000253.

[42] A. Gando, Y. Gando, H. Hanakago et al. *Limits on Majoron-emitting double-*β *decays of* ^{136}*Xe in the KamLAND-Zen experiment*. Physical Review C - Nuclear Physics **86** (2), 021601 (aug 2012). arXiv:1307.2929, URL https://link.aps.org/doi/10.1103/PhysRevC.86.021601.

[43] J. B. Albert, D. J. Auty, P. S. Barbeau et al. *Search for Majoron-emitting modes of double-beta decay of* ^{136}*Xe with EXO-200*. Physical Review D - Particles, Fields, Gravitation and Cosmology **90** (9), 092004 (nov 2014). 1409.6829, URL https://link.aps.org/doi/10.1103/PhysRevD.90.092004.

[44] R. N. Mohapatra. *New contributions to neutrinoless double-beta decay in supersymmetric theories*. Physical Review D **34** (11), 3457–3461 (dec 1986). URL https://link.aps.org/doi/10.1103/PhysRevD.34.3457.

[45] J. D. Vergados. *Neutrinoless double* β*-decay without Majorana neutrinos in supersymmetric theories*. Physics Letters B **184** (1), 55–62 (jan 1987). URL http://linkinghub.elsevier.com/retrieve/pii/0370269387904874.

[46] J. Schechter and J. W. Valle. *Neutrinoless double-*β *decay in* $SU(2)\times U(1)$ *theories*. Physical Review D **25** (11), 2951–2954 (jun 1982). URL https://link.aps.org/doi/10.1103/PhysRevD.25.2951.

[47] S. F. Ge, M. Lindner and S. Patra. *New physics effects on neutrinoless double beta decay from right-handed current*. Journal of High Energy Physics **2015** (10) (aug 2015). 1508.07286, URL http://arxiv.org/abs/1508.07286.

[48] J. Kotila and F. Iachello. *Phase-space factors for double-β decay*. Physical Review C - Nuclear Physics **85** (3), 034316 (mar 2012). arXiv:1209.5722v1, URL https://link.aps.org/doi/10.1103/PhysRevC.85.034316.

[49] J. Menéndez, A. Poves, E. Caurier et al. *Disassembling the nuclear matrix elements of the neutrinoless $\beta\beta$ decay*. Nuclear Physics A **818** (3-4), 139–151 (mar 2009). 0801.3760, URL http://linkinghub.elsevier.com/retrieve/pii/S0375947408008233.

[50] Y. Iwata, N. Shimizu, T. Otsuka et al. *Large-Scale Shell-Model Analysis of the Neutrinoless $\beta\beta$ Decay of ^{48}Ca*. Physical Review Letters **116** (11), 112502 (mar 2016). 1602.07822, URL https://link.aps.org/doi/10.1103/PhysRevLett.116.112502.

[51] M. Horoi and A. Neacsu. *Shell model predictions for ^{124}Sn double-β decay*. Physical Review C **93** (2), 024308 (feb 2016). URL https://link.aps.org/doi/10.1103/PhysRevC.93.024308.

[52] J. Barea, J. Kotila and F. Iachello. *$0\nu\beta\beta$ and $2\nu\beta\beta$ Nuclear Matrix Elements in the Interacting Boson Model With Isospin Restoration*. Physical Review C **91** (3), 034304 (mar 2015). 1506.08530, URL http://arxiv.org/abs/1506.08530.

[53] F. Šimkovic, V. Rodin, A. Faessler et al. *$0\nu\beta\beta$ and $2\nu\beta\beta$ Nuclear Matrix Elements, Quasiparticle Random-Phase Approximation, and Isospin Symmetry Restoration*. Physical Review C - Nuclear Physics **87** (4), 045501 (apr 2013). 1302.1509, URL https://link.aps.org/doi/10.1103/PhysRevC.87.045501.

[54] D. L. Fang, A. Faessler and F. Simkovic. *Partial restoration of isospin symmetry for neutrinoless double β decay in the deformed nuclear system of ^{150}Nd*. Physical Review C - Nuclear Physics **92** (4), 044301 (oct 2015). URL https://link.aps.org/doi/10.1103/PhysRevC.92.044301.

[55] M. T. Mustonen and J. Engel. *Large-scale calculations of the double-β decay of ^{76}Ge, ^{130}Te, ^{136}Xe, and ^{150}Nd in the deformed self-consistent Skyrme quasiparticle random-phase approximation*. Physical Review C - Nuclear Physics **87** (6), 064302 (jun 2013). 1301.6997, URL https://link.aps.org/doi/10.1103/PhysRevC.87.064302.

[56] J. M. Yao, L. S. Song, K. Hagino et al. *Systematic study of nuclear matrix elements in neutrinoless double-β decay with a beyond-mean-field covariant density functional theory*. Physical Review C **91** (2), 024316 (feb 2015). 1410.6326, URL https://link.aps.org/doi/10.1103/PhysRevC.91.024316.

[57] J. M. Yao and J. Engel. *Octupole correlations in low-lying states of ^{150}Nd and ^{150}Sm and their impact on neutrinoless double- β decay*. Physical Review C **94** (1), 014306 (jul 2016). URL https://link.aps.org/doi/10.1103/PhysRevC.94.014306.

[58] N. L. Vaquero, T. R. Rodríguez and J. L. Egido. *Shape and pairing fluctuation effects on neutrinoless double beta decay nuclear matrix elements*. Physical Review Letters **111** (14), 142501 (sep 2013). URL https://link.aps.org/doi/10.1103/PhysRevLett.111.142501.

[59] P. Puppe, A. Lennarz, T. Adachi et al. *High resolution (3He,t) experiment on the double-β decaying nuclei ^{128}Te and ^{130}Te*. Physical Review C - Nuclear Physics **86** (4), 044603 (oct 2012). URL https://link.aps.org/doi/10.1103/PhysRevC.86.044603.

[60] F. Boehm and P. Vogel. *Physics of Massive Neutrinos* (Cambridge University Bridge, 1992).

[61] R. Arnold, C. Augier, A. M. Bakalyarov et al. *Measurement of the double-beta decay half-life and search for the neutrinoless double-beta decay of ^{48}Ca with the NEMO-3 detector*. Physical Review D **93** (11), 112008 (jun 2016). 1604.01710, URL https://link.aps.org/doi/10.1103/PhysRevD.93.112008.

[62] H. V. Klapdor-Kleingrothaus, A. Dietz, L. Baudis et al. *Latest results from the HEIDELBERG-MOSCOW double beta decay experiment*. European Physical Journal A **12** (2), 147–154 (oct 2001). 0103062, URL http://link.springer.com/10.1007/s100500170022.

[63] C. E. Aalseth, F. T. Avignone, R. L. Brodzinski et al. *IGEX neutrinoless double-beta decay experiment: Prospects for next generation experiments*. Physical Review D - Particles, Fields, Gravitation and Cosmology **65** (9), 6 (may 2002). 0202026, URL https://link.aps.org/doi/10.1103/PhysRevD.65.092007.

[64] H. V. Klapdor-Kleingrothaus, I. V. Krivosheina, A. Dietz et al. *Search for neutrinoless double beta decay with enriched ^{76}Ge in Gran Sasso 1990-2003*. Physics Letters, Section B: Nuclear, Elementary Particle and High-Energy Physics **586** (3-4), 198–212 (apr 2004). URL http://linkinghub.elsevier.com/retrieve/pii/S0370269304003235.

[65] H. V. Klapdor-Kleingrothaus and I. V. Krivosheina. *The Evidence for the Observation of $0\nu\beta\beta$ Decay: the Identification of $0\nu\beta\beta$ Events From the Full Spectra*. Modern Physics Letters A **21** (20), 1547–1566 (jun 2006). URL http://www.worldscientific.com/doi/abs/10.1142/S0217732306020937.

[66] B. Schwingenheuer. *Status and prospects of searches for neutrinoless double beta decay*. Annalen der Physik **525** (4), 269–280 (apr 2013). arXiv:1210.7432v1, URL http://doi.wiley.com/10.1002/andp.201200222.

[67] M. Agostini, A. M. Bakalyarov, M. Balata et al. *Improved Limit on Neutrinoless Double-β Decay of ^{76}Ge from GERDA Phase II*. Physical Review Letters **120** (13), 132503 (mar 2018). 1803.11100, URL https://link.aps.org/doi/10.1103/PhysRevLett.120.132503.

[68] N. Abgrall, A. Abramov, N. Abrosimov et al. *The large enriched germanium experiment for neutrinoless double beta decay (LEGEND)*. In: *AIP Conference Proceedings*, Volume 1894, 020027 (2017). 1709.01980, URL http://aip.scitation.org/doi/abs/10.1063/1.5007652.

[69] J. Albert, G. Anton, I. Arnquist et al. *Sensitivity and discovery potential of the proposed nEXO experiment to neutrinoless double-β decay*. Physical Review C **97** (6), 065503 (jun 2018). URL https://link.aps.org/doi/10.1103/PhysRevC.97.065503.

[70] A. Giuliani. *The Mid and Long Term Future of Neutrinoless Double Beta Decay*. In: *XXVIII International Conference on Neutrino Physics and Astrophysics (Neutrino 2018)* (Heidelberg, Germany, 2018).

[71] P. A. R. Ade, N. Aghanim, C. Armitage-Caplan et al. *Planck 2013 results. XVI. Cosmological parameters*. Astronomy & Astrophysics **571**, A16 (nov 2013). 1303.5076, URL http://dx.doi.org/10.1051/0004-6361/201321591.

[72] C. Weinheimer. *KATRIN, a next generation tritium β decay experiment in search for the absolute neutrino mass scale*. Progress in Particle and Nuclear Physics **48** (1), 141–150 (jan 2002). URL http://linkinghub.elsevier.com/retrieve/pii/S0146641002001205.

[73] C. Kraus, B. Bornschein, L. Bornschein et al. *Final results from phase II of the Mainz neutrino mass searchin tritium β decay*. European Physical Journal C **40** (4), 447–468 (apr 2005). URL http://www.springerlink.com/index/10.1140/epjc/s2005-02139-7.

[74] V. N. Aseev, A. I. Belesev, A. I. Berlev et al. *Upper limit on the electron antineutrino mass from the Troitsk experiment*. Physical Review D - Particles, Fields, Gravitation and Cosmology **84** (11), 112003 (dec 2011). 1108.5034, URL https://link.aps.org/doi/10.1103/PhysRevD.84.112003.

[75] G. Heusser. *Low-Radioactivity Background Techniques*. Annual Review of Nuclear and Particle Science **45** (1), 543–590 (dec 1995). URL http://www.annualreviews.org/doi/10.1146/annurev.ns.45.120195.002551.

[76] National Council on Radiation Protection and Measurement. *Report No.94, Exposure of the population in the United States and Canada from natural background radiation*. Technischer Bericht, Bethesda, MD (1987).

[77] M. Ivanovich and R. S. Harmon. *Uranium-series disequilibrium: Applications to earth, marine, and environmental sciences* (Clarendon Press, Oxford (United Kingdom), 1992), 2nd Edition.

[78] E. Hoppe, A. Seifert, C. Aalseth et al. *Cleaning and passivation of copper surfaces to remove surface radioactivity and prevent oxide formation*. Nuclear Instruments and Methods in Physics Research Section A: Accelerators, Spectrometers, Detectors and Associated Equipment **579** (1), 486–489 (aug 2007). URL http://linkinghub.elsevier.com/retrieve/pii/S0168900207006882.

[79] M. Agostini, M. Allardt, A. M. Bakalyarov et al. *Limits on uranium and thorium bulk content in GERDA Phase I detectors*. Astroparticle Physics **91**, 15–21 (may 2017). 1611.06884, URL http://linkinghub.elsevier.com/retrieve/pii/S0927650516301670.

[80] G. V. Gorshkov et al. *Natural Neutron Background of the Atmosphere and the Earth Crust (in Russian)*. Moscow: AtÂŋomizdat (1966).

[81] H. Krieger. *Strahlungsphysik* (Teubner Verlag, 2004).

[82] G. F. Knoll. *Radiation Detection and Measurement, Third Edition* (John Wiley & Sons, Inc., 2000).

[83] M. Berger, J. Hubbell, S. Seltzer et al. *XCOM: Photon Cross Section Database (version 1.5)* (2010). URL `http://physics.nist.gov/xcom`.

[84] O. Klein and Y. Nishina. *Über die Streuung von Strahlung durch freie Elektronen nach der neuen relativistischen Quantendynamik von Dirac*. Zeitschrift für Physik **52** (11-12), 853–868 (nov 1929). URL `http://link.springer.com/10.1007/BF01366453`.

[85] W. Stolz. *Radioaktivität* (Teubner Verlag, 2005).

[86] M. Berger, J. Coursey, M. Zucker et al. *ESTAR, PSTAR, and ASTAR: Computer Programs for Calculating Stopping-Power and Range Tables for Electrons, Protons, and Helium Ions (version 1.2.3)* (2005). URL `http://physics.nist.gov/Star`.

[87] W. Shockley. *Currents to conductors induced by a moving point charge*. Journal of Applied Physics **9** (10), 635–636 (oct 1938). URL `http://aip.scitation.org/doi/10.1063/1.1710367`.

[88] S. Ramo. *Currents Induced by Electron Motion*. Proceedings of the IRE **27** (9), 584–585 (sep 1939). URL `http://ieeexplore.ieee.org/document/1686997/`.

[89] W. G. Pfann. *Zone melting* (John Wiley & Sons, 1958).

[90] *Canberra* (2018). URL `http://www.canberra.com/products/detectors/germanium-detectors.asp`.

[91] S. Andringa, E. Arushanova, S. Asahi et al. *Current Status and Future Prospects of the SNO+ Experiment*. Advances in High Energy Physics **2016**, 1–21 (2016). URL `http://www.hindawi.com/journals/ahep/2016/6194250/`.

[92] E. Morikawa, R. Reininger, P. Gürtler et al. *Argon, krypton, and xenon excimer luminescence: From the dilute gas to the condensed phase*. The Journal of Chemical Physics **91** (3), 1469–1477 (aug 1989). URL `http://aip.scitation.org/doi/10.1063/1.457108`.

[93] T. Doke, A. Hitachi, J. Kikuchi et al. *Absolute scintillation yields in liquid argon and xenon for various particles*. Japanese Journal of Applied Physics, Part 1: Regular Papers and Short Notes and Review Papers **41** (3 A), 1538–1545 (2002). URL `http://stacks.iop.org/1347-4065/41/i=3R/a=1538`.

[94] T. Oikari, H. Kojola, J. Nurmi et al. *Simultaneous counting of low alpha- and beta-particle activities with liquid-scintillation spectrometry and pulse-shape analysis*. International Journal of Radiation Applications and Instrumentation. Part **38** (10), 875–878 (jan 1987). URL `http://linkinghub.elsevier.com/retrieve/pii/0883288987901870`.

[95] R. Acciarri, M. Antonello, B. Baibussinov et al. *Oxygen contamination in liquid Argon: Combined effects on ionization electron charge and scintillation light*. Journal of Instrumentation **5** (5), P05003–P05003 (may 2010). `0804.1222`, URL `http://stacks.iop.org/1748-0221/5/i=05/a=P05003?key=crossref.d56a5eb1a4f52dafaf457d1a28fd1c95`.

[96] Wikipedia (2018). User: Qwerty123uiop, URL https://en.wikipedia.org/wiki/Photomultiplier#/media/File:PhotoMultiplierTubeAndScintillator.svg.

[97] R. J. Barlow. *Statistics: A Guide to the Use of Statistical Methods in the Physical Sciences* (John Wiley & Sons, 2008). URL https://books.google.com/books?id=Mv5uk3xDSo8C{&}pgis=1.

[98] R. Hoekstra, R. D. Morey, J. N. Rouder et al. *Robust misinterpretation of confidence intervals*. Psychonomic Bulletin & Review **21** (5), 1157–1164 (oct 2014). URL http://link.springer.com/10.3758/s13423-013-0572-3.

[99] A. P. Dempster. *A Selection of Early Statistical Papers of J. Neyman. University of California Press, Berkeley, 1967. x + 429 pp., illus. $14.75*. Science **160** (3828), 661–663 (may 1968). URL http://www.sciencemag.org/cgi/doi/10.1126/science.160.3828.661-b.

[100] G. J. Feldman and R. D. Cousins. *A Unified Approach to the Classical Statistical Analysis of Small Signals*. Physical Review D **57** (7), 3873–3889 (apr 1997). 9711021, URL http://dx.doi.org/10.1103/PhysRevD.57.3873.

[101] R. E. Kass and A. E. Raftery. *Bayes Factors*. Journal of the American Statistical Association **90** (430), 773 (jun 1995). URL https://www.jstor.org/stable/2291091?origin=crossref.

[102] F. Beaujean and A. Caldwell. *A test statistic for weighted runs*. Journal of Statistical Planning and Inference **141** (11), 3437–3446 (nov 2011). URL http://linkinghub.elsevier.com/retrieve/pii/S0378375811001935.

[103] F. Beaujean, A. Caldwell, D. Kollár et al. *P-values for model evaluation*. Physical Review D - Particles, Fields, Gravitation and Cosmology **83** (1), 012004 (jan 2011). 1011.1674, URL https://link.aps.org/doi/10.1103/PhysRevD.83.012004.

[104] A. Caldwell, D. Kollár and K. Kröninger. *BAT - The Bayesian analysis toolkit*. Computer Physics Communications **180** (11), 2197–2209 (nov 2009). 0808.2552, URL http://linkinghub.elsevier.com/retrieve/pii/S0010465509002045.

[105] N. Abgrall, E. Aguayo, F. T. Avignone et al. *The MAJORANA DEMONSTRATOR Neutrinoless Double-Beta Decay Experiment*. Advances in High Energy Physics **2014**, 1–18 (2014). URL http://www.hindawi.com/journals/ahep/2014/365432/.

[106] A. Gando, Y. Gando, T. Hachiya et al. *Search for Majorana Neutrinos Near the Inverted Mass Hierarchy Region with KamLAND-Zen*. Physical Review Letters **117** (8), 082503 (aug 2016). URL https://link.aps.org/doi/10.1103/PhysRevLett.117.082503.

[107] J. Shirai. *Results and future plans for the KamLAND-Zen experiment*. Journal of Physics: Conference Series **888**, 012031 (sep 2017). URL http://stacks.iop.org/1742-6596/888/i=1/a=012031?key=crossref.26f6bb15f405a225c0e9cafe102e96eb.

[108] K. Kamdin. *Understanding the SNO+ Detector*. Physics Procedia **61**, 719–723 (2015). URL http://linkinghub.elsevier.com/retrieve/pii/S1875389214007007.

[109] M. Auger, D. J. Auty, P. S. Barbeau et al. *The EXO-200 detector, part I: detector design and construction*. Journal of Instrumentation **7** (05), P05010–P05010 (may 2012). URL http://stacks.iop.org/1748-0221/7/i=05/a=P05010?key=crossref.f4eed52005c567472c6d77dde9945af9.

[110] M. Auger, D. J. Auty, P. S. Barbeau et al. *Search for neutrinoless double-beta decay in ^{136}Xe with EXO-200*. Physical Review Letters **109** (3), 032505 (jul 2012). 1205.5608, URL https://link.aps.org/doi/10.1103/PhysRevLett.109.032505.

[111] J. B. Albert, D. J. Auty, P. S. Barbeau et al. *Search for Majorana neutrinos with the first two years of EXO-200 data*. Nature **510** (7504), 229–234 (jun 2014). arXiv:1402.6956v1, URL http://www.nature.com/articles/nature13432.

[112] I. Abt et al. *GERDA - The GERmanium Detector Array for the search of neutrinoless $\beta\beta$ decays of ^{76}Ge at LNGS* (2004). URL http://www.mpi-hd.mpg.de/ge76/proposal.pdf.

[113] *Laboratori Nazionali del Gran Sasso* (2018). URL https://www.lngs.infn.it/en.

[114] K.-H. Ackermann, M. Agostini, M. Allardt et al. *The Gerda experiment for the search of $0\nu\beta\beta$ decay in ^{76}Ge*. The European Physical Journal C **73** (3), 2330 (mar 2013). URL http://link.springer.com/10.1140/epjc/s10052-013-2330-0.

[115] *GERDA homepage* (2018). URL https://www.mpi-hd.mpg.de/gerda/.

[116] K. Freund, R. Falkenstein, P. Grabmayr et al. *The performance of the Muon Veto of the Gerda experiment*. The European Physical Journal C **76** (5), 298 (may 2016). URL http://link.springer.com/10.1140/epjc/s10052-016-4140-7.

[117] M. Agostini, M. Allardt, E. Andreotti et al. *Production, characterization and operation of ^{76}Ge enriched BEGe detectors in GERDA*. European Physical Journal C **75** (2), 39 (feb 2015). 1410.0853, URL http://link.springer.com/10.1140/epjc/s10052-014-3253-0.

[118] M. Agostini, M. Allardt, E. Andreotti et al. *Pulse shape discrimination for Gerda Phase I data*. The European Physical Journal C **73** (10), 2583 (oct 2013). URL http://link.springer.com/10.1140/epjc/s10052-013-2583-7.

[119] M. Agostini, M. Allardt, E. Andreotti et al. *The background in the $0\nu\beta\beta$ experiment Gerda*. European Physical Journal C **74** (4), 2764 (apr 2014). 1306.5084, URL http://link.springer.com/10.1140/epjc/s10052-014-2764-z.

[120] N. B. Schmidt. *Neutrinoless Double Beta Decay Search in GERDA: Background Modeling and Limit Setting*. Dissertation, Technische Universität München (2014).

[121] S. Hemmer. *Study of Lepton Number Conserving and Non-Conserving Processes Using GERDA Phase I Data*. Disseration, Università degli Studi di Padova (2014).

[122] G. Zuzel and H. Simgen. *High sensitivity radon emanation measurements*. Applied Radiation and Isotopes **67** (5), 889–893 (may 2009). URL http://linkinghub.elsevier.com/retrieve/pii/S0969804309000608.

[123] G. Meierhofer, P. Grabmayr, L. Canella et al. *Prompt γ rays in ^{77}Ge and ^{75}Ge after thermal neutron capture*. The European Physical Journal A **48** (2), 20 (feb 2012). URL http://link.springer.com/10.1140/epja/i2012-12020-y.

[124] M. Agostini, D. Budjas, L. Pandola et al. *GERDA off-line analysis of HPGe detector signals* (2011). Internal document.

[125] M. Agostini, A. Lazzaro and L. Pandola. *Performance of the quality cuts in GERDA Phase I* (2013). Internal document.

[126] G. Benato. *Data Reconstruction and Analysis for the GERDA Experiment*. Dissertation, Universität Zürich (2015).

[127] B. Lehnert. *Search for $2\nu\beta\beta$ Excited State Transitions and HPGe Characterization for Surface Events in GERDA Phase I*. Dissertation, Technische Universität Dresden (2016).

[128] T. R. Rodríguez and G. Martínez-Pinedo. *Energy Density Functional Study of Nuclear Matrix Elements for Neutrinoless $\beta\beta$ Decay*. Physical Review Letters **105** (25), 252503 (dec 2010). URL https://link.aps.org/doi/10.1103/PhysRevLett.105.252503.

[129] J. Barea, J. Kotila and F. Iachello. *Nuclear matrix elements for double-β decay*. Physical Review C **87** (1), 014315 (jan 2013). URL https://link.aps.org/doi/10.1103/PhysRevC.87.014315.

[130] J. Suhonen and O. Civitarese. *Effects of orbital occupancies and spinâĂŞorbit partners on $0\nu\beta\beta$-decay rates*. Nuclear Physics A **847** (3-4), 207–232 (dec 2010). URL http://linkinghub.elsevier.com/retrieve/pii/S0375947410006305.

[131] A. Meroni, S. T. Petcov and F. Šimkovic. *Multiple CP non-conserving mechanisms of $(\beta\beta)0\nu$ -decay and nuclei with largely different nuclear matrix elements*. Journal of High Energy Physics **2013** (2), 25 (feb 2013). URL http://link.springer.com/10.1007/JHEP02(2013)025.

[132] M. Agostini, M. Allardt, A. M. Bakalyarov et al. *Background-free search for neutrinoless double-β decay of ^{76}Ge with GERDA*. Nature **544** (7648), 47–52 (apr 2017). URL http://www.nature.com/doifinder/10.1038/nature21717.

[133] M. Bauer, S. Belogurov, Y. Chan et al. *MaGe: a Monte Carlo framework for the Gerda and Majorana double beta decay experiments*. Journal of Physics: Conference Series **39**, 362–362 (may 2006). URL http://stacks.iop.org/1742-6596/39/i=1/a=097?key=crossref.bc659214a8e8c89aa9b830a88e0369e0.

[134] M. Agostini, M. Barnabé-Heider, D. Budjáš et al. *LArGe: active background suppression using argon scintillation for the Gerda $0\nu\beta\beta$-experiment*. European Physical Journal C **75** (10), 506 (oct 2015). arXiv:1501.05762v1, URL http://link.springer.com/10.1140/epjc/s10052-015-3681-5.

[135] L. Pertoldi, A.-K. Schuetz, K. von Sturm et al. *Background Budget for GERDA Phase II* (2018). Internal document.

[136] A.-K. Schütz. *To be published*. Dissertation, Eberhard Karls Universität Tübingen (2018).

[137] M. Agostini, A. M. Bakalyarov, M. Balata et al. *Background of the GERDA Experiment in Phase II*. To be published (2019).

[138] V. D'Andrea. *Improvement of Performances and Background Studies in GERDA Phase II*. Dissertation, Gran Sasso Science Institute (2017).

[139] L. Pandola. *Parameters and facts for the analysis dataset of the $0\nu\beta\beta$ decay of GERDA Phase IIb (after partial unblinding in Cracow)* (2017). Internal document.

[140] A. Kirsch. *Search for the neutrinoless double-decay in Gerda Phase I using a Pulse Shape Discrimination technique*. Dissertation, Ruperto-Carola University of Heidelberg (2014).

[141] R. Brun and F. Rademakers. *ROOT - An object oriented data analysis framework*. Nuclear Instruments and Methods in Physics Research, Section A: Accelerators, Spectrometers, Detectors and Associated Equipment **389** (1-2), 81–86 (apr 1997). URL http://linkinghub.elsevier.com/retrieve/pii/S016890029700048X.

[142] M. Agostini, L. Pandola, P. Zavarise et al. *GELATIO: a general framework for modular digital analysis of high-purity Ge detector signals*. Journal of Instrumentation **6** (08), P08013–P08013 (aug 2011). URL http://stacks.iop.org/1748-0221/6/i=08/a=P08013?key=crossref.d8a1346f280a7e98c6878e4cd7e0ed32.

[143] M. O. Deighton. *Minimum-Noise Filters with Good Low-Frequency Rejection*. IEEE Transactions on Nuclear Science **16** (5), 68–75 (1969). URL http://ieeexplore.ieee.org/document/4325476/.

[144] M. Agostini, M. Allardt, A. M. Bakalyarov et al. *Improvement of the energy resolution via an optimized digital signal processing in GERDA Phase I*. The European Physical Journal C **75** (6), 255 (jun 2015). URL http://link.springer.com/10.1140/epjc/s10052-015-3409-6.

[145] S. Agostinelli, J. Allison, K. Amako et al. *GEANT4 - A simulation toolkit*. Nuclear Instruments and Methods in Physics Research, Section A: Accelerators, Spectrometers, Detectors and Associated Equipment **506** (3), 250–303 (jul 2003). 1005.0727v1, URL http://linkinghub.elsevier.com/retrieve/pii/S0168900203013688.

[146] P. Grabmayr, R. Falkenstein, S. Hemmer et al. *Re-evaluation of enrichment fractions f_{Ge} and active volume fractions f_{av}* (2013). Internal document.

[147] H. Klapdor-Kleingrothaus, A. Dietz, I. Krivosheina et al. *Data acquisition and analysis of the double beta experiment in Gran Sasso 1990-2003*. Nuclear

Instruments and Methods in Physics Research Section A: Accelerators, Spectrometers, Detectors and Associated Equipment **522** (3), 371–406 (apr 2004). URL http://linkinghub.elsevier.com/retrieve/pii/S0168900203033515.

[148] P. Vermaercke, M. Hult, L. Verheyen et al. *Measurement of the isotopic composition of germanium by k0-INAA and INAA*. Nuclear Instruments and Methods in Physics Research Section A: Accelerators, Spectrometers, Detectors and Associated Equipment **622** (2), 433–437 (oct 2010). URL http://linkinghub.elsevier.com/retrieve/pii/S0168900209024036.

[149] S. Nisi and A. di Vacri. *Ge isotopic ratio determination in two GeO_2 samples with ICPMS* (2006). Internal document.

[150] N. S. Koshylakov, M. M. Smirnov and E. B. Gliner. *Differential Equations of Mathematical Physics* (New York: Interscience, 1964).

[151] D. A. Weston. *Electromagnetic Compatibility : Methods, Analysis, Circuits, and Measurement* (CRC Press, 2016), 3rd Edition.

[152] G. W. Phillips and K. W. Marlow. *Automatic analysis of gamma-ray spectra from germanium detectors*. Nuclear Instruments and Methods **137** (3), 525–536 (sep 1976). URL http://linkinghub.elsevier.com/retrieve/pii/0029554X76904729.

[153] G. Gilmore. *Practical Gamma-ray Spectrometry* (John Wiley & Sons, 2008).

[154] A. Sonzogni. *NuDat 2.7* (2018). URL https://www.nndc.bnl.gov/nudat2/.

[155] O. A. Ponkratenko, V. I. Tretyak and Y. G. Zdesenko. *Event generator DECAY4 for simulating double-beta processes and decays of radioactive nuclei*. Physics of Atomic Nuclei **63** (7), 1282–1287 (jul 2000). URL http://link.springer.com/10.1134/1.855784.

[156] P. Benetti, F. Calaprice, E. Calligarich et al. *Measurement of the specific activity of ^{39}Ar in natural argon*. Nuclear Instruments and Methods in Physics Research Section A: Accelerators, Spectrometers, Detectors and Associated Equipment **574** (1), 83–88 (apr 2007). URL http://linkinghub.elsevier.com/retrieve/pii/S0168900207001672.

[157] J. Kostensalo, J. Suhonen and K. Zuber. *Spectral shapes of forbidden argon β decays as background component for rare-event searches*. Journal of Physics G: Nuclear and Particle Physics **45** (2), 025202 (feb 2018). URL http://stacks.iop.org/0954-3899/45/i=2/a=025202?key=crossref.46a162a9da8ee360a00db507709e9a2e.

[158] P. M. Endt. *Supplement to Energy Levels of $A = 21 - 44$ Nuclei (VII)*. Nuclear Physics A **633** (1), 1–220 (apr 1998). URL http://linkinghub.elsevier.com/retrieve/pii/S0375947497006131.

[159] M. Laubenstein. *Personal communication* (2013).

[160] R. Arnold, C. Augier, J. Baker et al. *Measurement of double beta decay of ^{100}Mo to excited states in the NEMO-3 experiment*. Nuclear Physics A **781** (1-2), 209–226 (jan 2007). URL `http://linkinghub.elsevier.com/retrieve/pii/S0375947406006567`.

[161] A. S. Barabash, P. Hubert, A. Nachab et al. *Investigation of $\beta\beta$ decay in ^{150}Nd and ^{148}Nd to the excited states of daughter nuclei*. Physical Review C - Nuclear Physics **79** (4), 045501 (apr 2009). URL `https://link.aps.org/doi/10.1103/PhysRevC.79.045501`.

[162] M. F. Kidd, J. H. Esterline, S. W. Finch et al. *Two-neutrino double-β decay of ^{150}Nd to excited final states in ^{150}Sm*. Physical Review C - Nuclear Physics **90** (5), 055501 (nov 2014). URL `https://link.aps.org/doi/10.1103/PhysRevC.90.055501`.

[163] S. I. Vasil, A. A. Klimenko, S. B. Osetrov et al. *New Bound to the Probability of ^{76}Ge $\beta\beta$ Decay to the 0_1^+ ^{76}Se Level*. JETP Letters **72** (6), 279–281 (sep 2000). URL `http://link.springer.com/10.1134/1.1328436`.

[164] J. Suhonen. *Personal communication in [127]* (2014).

[165] F. Iachello. *Personal communication in [127]* (2014).

[166] J. Menendéz. *Personal communication in [127]* (2015).

[167] S. K. Dhiman and P. K. Raina. *Two-neutrino double-beta decay matrix elements for ground and excited states of ^{76}Ge*. Physical Review C **50** (6), R2660–R2663 (dec 1994). URL `https://link.aps.org/doi/10.1103/PhysRevC.50.R2660`.

[168] O. Civitarese and J. Suhonen. *Two-neutrino double-beta decay to excited one- and two-phonon states*. Nuclear Physics A **575** (2), 251–268 (aug 1994). URL `http://linkinghub.elsevier.com/retrieve/pii/0375947494901880`.

[169] S. Stoica and I. Mihut. *Nuclear structure calculations of two-neutrino double-beta decay transitions to excited final states*. Nuclear Physics A **602** (2), 197–210 (may 1996). URL `http://linkinghub.elsevier.com/retrieve/pii/0375947496001224`.

[170] M. Aunola and J. Suhonen. *Systematic study of beta and double beta decay to excited final states*. Nuclear Physics A **602** (2), 133–166 (may 1996). URL `http://linkinghub.elsevier.com/retrieve/pii/0375947496000875`.

[171] J. Toivanen and J. Suhonen. *Study of several double-beta-decaying nuclei using the renormalized proton-neutron quasiparticle random-phase approximation*. Physical Review C **55** (5), 2314–2323 (may 1997). URL `https://link.aps.org/doi/10.1103/PhysRevC.55.2314`.

[172] A. A. Raduta, F. Simkovic and A. Faessler. *Renormalized boson expansion for the $2\nu\beta\beta$ decay*. Journal of Physics G: Nuclear and Particle Physics **26** (6), 793–810 (jun 2000). URL `http://stacks.iop.org/0954-3899/26/i=6/a=304?key=crossref.2c9f5a2d7e4ef7262a94da1f181f63ec`.

[173] S. Unlu. *Quasi Random Phase Approximation Predictions on Two-Neutrino Double Beta Decay Half-Lives to the First 2^+ State*. Chinese Physics Letters **31** (4), 42101 (2014). URL http://stacks.iop.org/0256-307X/31/i=4/a=042101.

[174] B. J. Mount, M. Redshaw and E. G. Myers. *Double-β-decay Q values of ^{74}Se and ^{76}Ge*. Physical Review C - Nuclear Physics **81** (3), 032501 (mar 2010). URL https://link.aps.org/doi/10.1103/PhysRevC.81.032501.

[175] R. B. Firestone. *Table of Isotopes* (John Wiley & Sons, 1996), 8th Edition.

[176] G. Schatz and A. Weidinger. *Nukleare Festkörperphysik* (Teubner Verlag, 2012).

[177] L. Pandola. *Personal communication* (2013).

[178] B. Schneider. *Development of a setup for an in-situ measurement of the light attenuation of liquid argon for the GERDA experiment*. Diploma thesis, Technische Universität Dresden (2014).

[179] T. Tomoda. $0^+ \to 2^+$ *neutrinoless $\beta\beta$ decay of ^{76}Ge*. Nuclear Physics, Section A **484** (3-4), 635–646 (jul 1988). URL http://linkinghub.elsevier.com/retrieve/pii/0375947488903132.

[180] B. Maier. *Status of the Heidelberg-Moscow $\beta\beta$ experiment with ^{76}Ge*. In: *Nuclear Physics B (Proceedings Supplements)*, Volume 35, 358–362 (1994). URL http://linkinghub.elsevier.com/retrieve/pii/0920563294902763.

[181] F. Šimkovic, M. Nowak, W. A. Kamiński et al. *Neutrinoless double beta decay of ^{76}Ge, ^{82}Se, ^{100}Mo, and ^{136}Xe to excited 0^+ states*. Physical Review C - Nuclear Physics **64** (3), 355011–3550112 (aug 2001). 0107016, URL https://link.aps.org/doi/10.1103/PhysRevC.64.035501.

[182] S. Umehara, T. Kishimoto, I. Ogawa et al. *Neutrino-less double-β decay of ^{48}Ca studied by CaF_2(Eu) scintillators*. Physical Review C - Nuclear Physics **78** (5), 058501 (nov 2008). URL https://link.aps.org/doi/10.1103/PhysRevC.78.058501.

[183] C. E. Aalseth, N. Abgrall, E. Aguayo et al. *Search for Neutrinoless Double-β Decay in ^{76}Ge with the Majorana Demonstrator*. Physical Review Letters **120** (13), 132502 (mar 2018). 1710.11608, URL https://link.aps.org/doi/10.1103/PhysRevLett.120.132502.

[184] R. Arnold, C. Augier, J. Baker et al. *First results of the search for neutrinoless double-beta decay with the NEMO-3 detector*. Physical Review Letters **95** (18), 182302 (oct 2005). 0507083, URL https://link.aps.org/doi/10.1103/PhysRevLett.95.182302.

[185] A. S. Barabash and V. B. Brudanin. *Investigation of double-beta decay with the NEMO-3 detector*. Physics of Atomic Nuclei **74** (2), 312–317 (feb 2011). 1002.2862, URL http://link.springer.com/10.1134/S1063778811020062.

[186] Y. M. Gavrilyuk, A. M. Gangapshev, V. V. Kazalov et al. *Indications of $2\nu 2K$ capture in ^{78}Kr*. Physical Review C - Nuclear Physics **87** (3), 035501 (mar 2013). URL https://link.aps.org/doi/10.1103/PhysRevC.87.035501.

[187] J. Argyriades, R. Arnold, C. Augier et al. *Measurement of the two neutrino double beta decay half-life of ^{96}Zr with the NEMO-3 detector*. Nuclear Physics A **847** (3-4), 168–179 (dec 2010). 0906.2694, URL http://linkinghub.elsevier.com/retrieve/pii/S0375947410006238.

[188] E. Armengaud, C. Augier, A. S. Barabash et al. *Development of ^{100}Mo -containing scintillating bolometers for a high-sensitivity neutrinoless double-beta decay search*. European Physical Journal C **77** (11), 785 (nov 2017). 1704.01758, URL http://link.springer.com/10.1140/epjc/s10052-017-5343-2.

[189] R. Arnold, C. Augier, J. D. Baker et al. *Results of the search for neutrinoless double-β decay in ^{100}Mo with the NEMO-3 experiment*. Physical Review D - Particles, Fields, Gravitation and Cosmology **92** (7), 072011 (oct 2015). 1506.05825, URL https://link.aps.org/doi/10.1103/PhysRevD.92.072011.

[190] R. Arnold, C. Augier, J. D. Baker et al. *Measurement of the $2\nu\beta\beta$ decay half-life and search for the $0\nu\beta\beta$ decay of ^{116}Cd with the NEMO-3 detector*. Physical Review D **95** (1), 012007 (jan 2017). 1606.08494, URL https://link.aps.org/doi/10.1103/PhysRevD.95.012007.

[191] F. A. Danevich, A. S. Georgadze, V. V. Kobychev et al. *Search for 2β decay of cadmium and tungsten isotopes: Final results of the Solotvina experiment*. Physical Review C - Nuclear Physics **68** (3), 12 (sep 2003). URL https://link.aps.org/doi/10.1103/PhysRevC.68.035501.

[192] T. Bernatowicz, J. Brannon, R. Brazzle et al. *Precise determination of relative and absolute $\beta\beta$-decay rates of ^{128}Te*. Physical Review C **47** (2), 806–825 (feb 1993). URL https://link.aps.org/doi/10.1103/PhysRevC.47.806.

[193] C. Arnaboldi, C. Brofferio, C. Bucci et al. *A calorimetric search on double beta decay of ^{130}Te*. Physics Letters B **557** (3-4), 167–175 (apr 2003). URL http://linkinghub.elsevier.com/retrieve/pii/S0370269303002120.

[194] W. J. Lin, O. K. Manuel, S. Muangnoicharoen et al. *Double beta-decay of tellurium-128 and tellurium-130*. Nuclear Physics, Section A **481** (3), 484–493 (may 1988). URL http://linkinghub.elsevier.com/retrieve/pii/0375947488903417.

[195] C. Alduino, F. Alessandria, K. Alfonso et al. *First Results from CUORE: A Search for Lepton Number Violation via $0\nu\beta\beta$ Decay of ^{130}Te*. Physical Review Letters **120** (13), 132501 (mar 2018). URL https://link.aps.org/doi/10.1103/PhysRevLett.120.132501.

[196] A. P. Meshik, C. M. Hohenberg, O. V. Pravdivtseva et al. *Weak decay of ^{130}Ba and ^{132}Ba: Geochemical measurements*. Physical Review C - Nuclear Physics **64** (3), 352051–352056 (aug 2001). URL https://link.aps.org/doi/10.1103/PhysRevC.64.035205.

[197] M. Pujol, B. Marty, P. Burnard et al. *Xenon in Archean barite: Weak decay of ^{130}Ba, mass-dependent isotopic fractionation and implication for barite formation*. Geochimica et Cosmochimica Acta **73** (22), 6834–6846 (nov 2009). URL http://linkinghub.elsevier.com/retrieve/pii/S0016703709005055.

[198] J. B. Albert, G. Anton, I. Badhrees et al. *Searches for double beta decay of ^{134}Xe with EXO-200*. Physical Review D **96** (9), 092001 (nov 2017). URL https://link.aps.org/doi/10.1103/PhysRevD.96.092001.

[199] J. B. Albert, M. Auger, D. J. Auty et al. *Improved measurement of the $2\nu\beta\beta$ half-life of ^{136}Xe with the EXO-200 detector*. Physical Review C - Nuclear Physics **89** (1), 015502 (jan 2014). 1306.6106, URL https://link.aps.org/doi/10.1103/PhysRevC.89.015502.

[200] J. B. Albert, G. Anton, I. Badhrees et al. *Search for Neutrinoless Double-Beta Decay with the Upgraded EXO-200 Detector*. Physical Review Letters **120** (7), 072701 (feb 2018). 1707.08707, URL https://link.aps.org/doi/10.1103/PhysRevLett.120.072701.

[201] A. Gando, Y. Gando, H. Hanakago et al. *Measurement of the double-β decay half-life of ^{136}Xe with the KamLAND-Zen experiment*. Physical Review C - Nuclear Physics **85** (4), 045504 (apr 2012). 1201.4664, URL https://link.aps.org/doi/10.1103/PhysRevC.85.045504.

[202] R. Arnold, C. Augier, J. D. Baker et al. *Measurement of the $2\nu\beta\beta$ decay half-life of ^{150}Nd and a search for $0\nu\beta\beta$ decay processes with the full exposure from the NEMO-3 detector*. Physical Review D **94** (7), 072003 (oct 2016). 1606.08494, URL https://link.aps.org/doi/10.1103/PhysRevD.94.072003.

[203] A. L. Turkevich, T. E. Economou and G. A. Cowan. *Double-beta decay of ^{238}U*. Physical Review Letters **67** (23), 3211–3214 (dec 1991). URL https://link.aps.org/doi/10.1103/PhysRevLett.67.3211.

[204] Wikipedia (2018). User: BatesIsBack, URL https://en.wikipedia.org/wiki/Decay_chain.

[205] M. Agostini, A. M. Bakalyarov, E. Andreotti et al. *Characterization of 30 ^{76}Ge enriched Broad Energy Ge detectors for GERDA Phase II* (jan 2019). 1901.06590, URL http://arxiv.org/abs/1901.06590.

Eidesstattliche Erklärung

Hiermit versichere ich, dass ich die vorliegende Arbeit ohne unzulässige Hilfe Dritter und ohne Benutzung anderer als der angegebenen Hilfsmittel angefertigt habe. Die aus fremden Quellen direkt oder indirekt übernommenen Gedanken sind als solche kenntlich gemacht. Die Arbeit wurde bisher weder im Inland noch im Ausland in gleicher oder ähnlicher Form einer anderen Prüfungsbehörde vorgelegt.

Die Promotion wurde and der Technischen Universität Dresden, am Institut für Kern- und Teilchenphysik unter der wissenschaftlichen Betreuung von Prof. Dr. Kai Zuber durchgeführt.

Ich erkenne die Promotionsordnung der Fakultät Mathematik und Naturwissenschaften vom 23.02.2011 an.

Dresden, 18. September 2018

Thomas Wester